Yuichi Setsuhara · Toshio Kamiya ·
Shin-ichi Yamaura *Editors*

Novel Structured Metallic and Inorganic Materials

Springer

Novel Structured Metallic and Inorganic Materials

Yuichi Setsuhara · Toshio Kamiya ·
Shin-ichi Yamaura
Editors

Novel Structured Metallic and Inorganic Materials

Springer

Editors
Yuichi Setsuhara
Osaka University
Osaka, Japan

Toshio Kamiya
Tokyo Institute of Technology
Yokohama, Japan

Shin-ichi Yamaura
Tohoku University
Sendai, Japan

Present Address:
The Polytechnic University of Japan
Tokyo, Japan

ISBN 978-981-13-7610-8 ISBN 978-981-13-7611-5 (eBook)
https://doi.org/10.1007/978-981-13-7611-5

This Springer imprint is published by the registered company Springer Nature Singapore Pte Ltd.
The registered company address is: 152 Beach Road, #21-01/04 Gateway East, Singapore 189721, Singapore

Preface

This book *Novel Structured Metallic and Inorganic Materials* is based on achievements in the joint research project "Advanced Materials Development and Integration of Novel Structured Metallic and Inorganic Materials", which was carried out for 6 years (FY 2010–2015) through the cooperation of research groups in the following six institutes in Japan; the Institute for Materials Research, Tohoku University; the Materials and Structures Laboratory, Tokyo Institute of Technology; the Joining and Welding Research Institute, Osaka University; the EcoTopia Science Institute, Nagoya University; the Institute of Biomaterials and Bioengineering, Tokyo Medical and Dental University; and the Institute for Nanoscience and Nanotechnology, Waseda University.

Major objectives of the six-institute joint research project included creation of advanced metallic and inorganic materials with the novel structure, as well as development of the materials-joining technologies for development of the cutting-edge applications as environmental and energy materials, biomedical materials, and electronic materials for contributing to the creation of a safe and secure society.

In this book which consists of six parts, many scientific and technological results are organized so as to provide basics of novel structured materials in Part I and II, integration and processing of the materials in Part III, applications of the novel structured materials for environmental protection and energy in Part IV, biomedical applications in Part V, and applications for electronic devices in Part VI. Every chapter is aimed at understanding most advanced researches, by describing details from its fundamentals as much as possible. Since both fundamentals and cutting-edge topics are given in this book, it provides lots of useful information for ordinary readers as well as materials scientists and engineers who wish to consider future prospects and innovations based on *Novel Structured Metallic and Inorganic Materials*, of which contents are very unique as textbook in materials science and technology.

Furthermore, the achievements in the abovementioned joint research project have been extended further to the joint research and educational project "Creation of Life Innovation Materials for Interdisciplinary and International Researcher

Development", which has been carried out since FY 2016 via cooperation of research groups in the following six institutes in Japan; the Institute of Materials and Systems for Sustainability (former EcoTopia Science Institute), Nagoya University; the Institute for Materials Research, Tohoku University; the Laboratory for Materials and Structures (former Materials and Structures Laboratory), Tokyo Institute of Technology; the Joining and Welding Research Institute, Osaka University; the Institute of Biomaterials and Bioengineering, Tokyo Medical and Dental University; and the Research Organization for Nano and Life Innovation (former Institute for Nanoscience and Nanotechnology), Waseda University. Here, it is gratefully acknowledged that both of the projects have been financially supported by the Ministry of Education, Culture, Sports, Science and Technology (MEXT) of Japan.

Yuichi Setsuhara
Osaka University
Osaka, Japan

Toshio Kamiya
Tokyo Institute of Technology
Yokohama, Japan

Shin-ichi Yamaura
The Polytechnic University of Japan
Tokyo, Japan

Contents

Part I
Novel Structured Metallic Materials

Chapter 1
Introduction to Amorphous Alloys and Metallic Glasses

Shin-ichi Yamaura, Wei Zhang and Akihisa Inoue

Abstract The development of amorphous alloys and metallic glasses is briefly overviewed, and their structure, glass-forming ability (GFA), and physical, chemical, mechanical and magnetic properties are introduced. In particular, the history of the development of amorphous alloys and metallic glasses and the difference between amorphous alloys and metallic glasses are summarized in this chapter.

Keywords Metallic glass · Amorphous alloy · Glass transition · Rapid quench

1.1 History of the Development of Noncrystalline Alloys—From Amorphous Alloys to Metallic Glasses

Metallic materials are fundamental elements essential for our society and the importance of such metallic materials must remain constant from the past to the future. All the basic metallic materials that have been in use since ancient times are crystalline alloys in an equilibrium state with a regular atomic arrangement of the crystal lattices. This is because metallic atoms can easily move in the molten

S. Yamaura (✉) · W. Zhang · A. Inoue
Institute for Materials Research, Tohoku University, 2-1-1 Katahira Aoba, Sendai, Miyagi 980-8577, Japan
e-mail: s-yamaura@uitec.ac.jp

Present Address:
S. Yamaura
The Polytechnic University of Japan, 2-32-2 Ogawanishi-machi, Kodaira, Tokyo 187-0035, Japan

Present Address:
S. Yamaura · W. Zhang
Dalian University of Technology, No. 2 Linggong Road Ganjingzi, Dalian 116024, Liaoning, People's Republic of China

Present Address:
A. Inoue
Josai International University, 1 Gumyo, Togane, Chiba 283-8555, Japan

Y. Setsuhara et al. (eds.), *Novel Structured Metallic and Inorganic Materials*, https://doi.org/10.1007/978-981-13-7611-5_1

alloy, leading to easy phase transformation from liquid to solid phase with rearrangement of atoms just below the melting temperature.

It was already known in the 1950s that alloy thin films produced by electrodeposition or vapor deposition on a substrate which was cooled by liquid helium could possess a noncrystalline phase which is called "amorphous" phase [1]. It was subsequently reported by Duwez et al. for the first time in 1960 that the Au–Si amorphous alloy having no crystalline phase in the nonequilibrium state could be produced by using the gun method, which is an early-stage rapid solidification technique from a liquid state with a cooling rate of higher than 10^6 K/s [2]. After this discovery, many researchers became interested in the formation of amorphous alloys in a nonequilibrium state and conducted basic studies of its physical properties in the 1960s [3–5]. As an outstanding result obtained in the 1960s, it was found that the Au–Ge–Si ternary alloys showed a glass transition (to a supercooled liquid state), indicating the existence of a glassy phase like oxide glass even in metallic amorphous materials [3]. Also, the noble metal-based glassy alloys with a distinct glass transition such as the Pd–Ni–P alloy [4] and Fe-based ferromagnetic amorphous alloys such as Fe–P–C [5] alloys were found in the decade.

In the 1970s, studies on amorphous alloys were significantly proceeded. At that time, the Pd–Si amorphous alloy in ribbon shape was produced by using the centrifugal rapid quenching method. Previously, the gun method and the piston–anvil method had been used to produce amorphous alloy specimens of small pieces with many pores. So, those homogeneous amorphous alloy specimens in ribbon shape with a width of about 1 mm and a thickness of about 20 μm produced by the centrifugal rapid quenching method were suitable to study their physical properties such as mechanical strength and electrical resistivity. After that, single roller melt spinning was developed and became one of the most popular methods for producing ribbon-shaped amorphous alloy samples. In that decade, high mechanical strength of the Pd–Si [6] amorphous alloy, excellent soft magnetism of the Fe–P–B [7], Fe–P–C [8], and Fe–Si–B [9] amorphous alloys, high corrosion resistance of the Fe–Cr–Mo–P–C amorphous alloys [10], and superconductivity of the La–Au amorphous alloys [11] were reported. Furthermore, the planar melt-spinning method was developed to produce long, wide amorphous alloy ribbons and has been applied to produce soft-magnetic Fe–Si–B amorphous alloy wide ribbons for commercial distribution transformers [12].

Furthermore, amorphous alloy wires of about 100 μm in diameter were produced by using the in-rotating-water spinning method around 1980. Also, amorphous alloy powders of about 15–30 μm in diameter were produced by using high-pressure gas atomizing method [13] in this period. However, all these methods were based on rapid quenching at a cooling rate of 10^6 K/s, so the products were limited to small, thin samples.

In 1988–1990, Mg–Ln–(Cu) [14], Ln–Al–(Co, Ni, Cu) [15] (Ln: rare-earth elements), and Zr–Al–(Ni, Cu) [16] amorphous alloys having a distinct glass transition and subsequent large supercooled liquid region for 50–130 K just below the crystallization temperature were developed. The constituent atoms can readily move in this supercooled liquid, leading to the inertial relaxation. However,

crystallization is suppressed even in this relaxed state because of the stabilization of the supercooled liquid due to close packing of the constituent atoms, preventing long-range diffusion and rearrangement of atoms. This means that such high stability of the supercooled liquid against crystallization can result in an existence of amorphous phase even at a slow cooling rate, with the result that bulky amorphous alloy samples can be obtained.

Since the development of this series of bulk amorphous alloys, amorphous alloys having a distinct glass transition and subsequent large supercooled liquid region have been called "metallic glasses", "glassy alloys", or "bulk amorphous alloys", distinguishing them from conventional amorphous alloys. Metallic glasses have attracted increased interest around the world in the field of materials science and engineering. After 1993, a large number of the Zr-based, Al-based, Ti-based, Hf-based, Fe-based, Pd-based, Cu-based, Ni-based, and Co-based glassy alloys were developed [17, 18] and it was found that these glassy alloys showed a large supercooled liquid region of more than 50 K and that it was possible to produce bulk glassy alloy samples with a diameter of a few to 80 mm by using conventional rapid quenching methods such as water quenching and copper mold casting.

In 1994, three empirical rules for stabilization of the supercooled phase and synthesis of a bulky sample of glassy alloy were derived from the experimental data obtained before 1994 [17]. The rules proposed by one of the authors (A.I.) are stated as follows: (1) The alloy should contain at least three components. (2) The atomic size differences among the main constituent elements should be more than 12%. (3) The heat of mixing among the main constituent elements should be a negative large value. Based on these empirical rules, quite a large number of bulk glassy alloys were developed in the two decades after 1994.

1.2 Amorphous Alloys and Metallic Glasses

Amorphous alloys and metallic glasses can be produced by rapid quenching from a molten liquid and they possess a liquid-like random atomic arrangement. Therefore, they show quite different characteristics from crystalline alloys. In a sense, the atomic arrangement of the material must control its properties. Figure 1.1 shows schematics describing the atomic arrangement of crystalline alloy and amorphous alloy/metallic glass. As seen in the figure, an ordinary crystalline alloy has a crystal lattice such as an fcc/bcc structure and is polycrystalline with a huge number of grains and defects such as grain boundaries, segregation, voids, and dislocations. From these crystal lattice structures and microstructures, crystalline alloys show high electro-conductivity, high thermal conductivity, and large plastic deformation. On the other hand, amorphous alloys possess a liquid-like random atomic arrangement without crystal lattice and grains. The electro-conductivity of amorphous alloys is one order lower than that of crystalline alloys because of their random atomic arrangement, preventing smooth electron movement. Moreover, amorphous alloys show higher mechanical strength and lower ductility with much

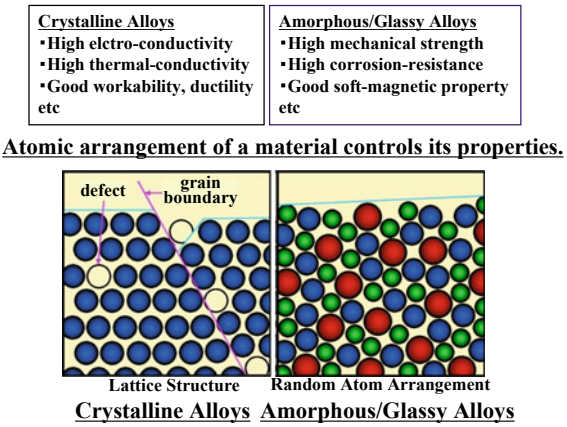

Fig. 1.1 Schematic illustrations of atomic arrangement of a nominal crystalline alloy and an amorphous/glassy alloy with their characteristic features

smaller plastic deformation than those of crystalline alloys because they have no dislocation which would play an important role for plastic deformation and also because they have no slip planes nor slip direction. It is also known that amorphous alloys show high corrosion resistance and good soft magnetism.

Figure 1.2 shows a schematic of melt-spinning equipment and an outer view of a melt-spun alloy. Melt spinning is one of the major synthesizing processes to obtain amorphous alloys. A crushed alloy ingot is put into a nozzle and then the nozzle is set inside a high-frequency induction coil. The alloy ingot is heated by the coil in a dilute Ar atmosphere or, in the case of a certain iron-based alloy, in air. After that, the molten alloy is injected onto the surface of a rotating wheel. The figure also shows an example of a melt-spun amorphous alloy. The width of the produced amorphous alloy ribbon is dependent on the width of the slit size of the nozzle and the width of the Cu wheel. The thickness of the ribbon sample is dependent on the surface speed and slit gap of the Cu wheel and the injection pressure. Extremely rapid quenching (at around 10^6 K/s) is essential to produce amorphous alloys. As well as the melt spinning is shown in Fig. 1.2, and there are also a variety of

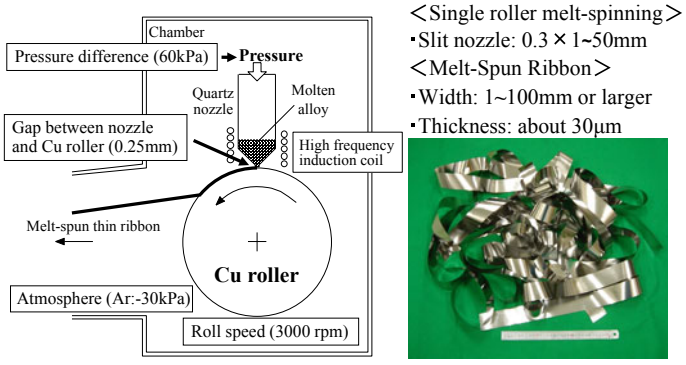

Fig. 1.2 Schematic of melt-spinning equipment and outer view of melt-spun alloy in ribbon shape

rapid quenching methods such as in-rotating-water spinning and gas atomizing to produce melt-spun amorphous alloys in thin ribbon, wire, and powder shapes. The sample size was small, so their applications were strictly limited to small ones because they need extremely rapid quenching as mentioned above. It is known that the most successful application of amorphous alloys is a low core-loss distribution transformer using the melt-spun Fe–Si–B amorphous alloy ribbons and a high-sensitive magnetic sensor using Fe–Si–B amorphous alloy fine wires produced by the in-rotating-water melt spinning.

In the late 1980s to the early 1990s, a series of compositions of amorphous alloys which showed a distinct glass transition and wide supercooled liquid region just below the crystallization temperature was developed. This type of amorphous alloys having a distinct glass transition and wide supercooled liquid region has been called "metallic glass". Metallic glass does not require an extremely high cooling rate, so it is possible to synthesize considerably larger samples than conventional amorphous alloys. Furthermore, metallic glass can show large plastic deformation in a supercooled liquid state in which the viscosity drastically decreases while conventional amorphous alloys do not show any plastic deformation. So, metallic glasses can be deformed like a Newtonian fluid in a supercooled liquid state, resulting in superplasticity with elongations up to a few tens of thousands percent. They can be potentially used for various applications for which amorphous alloys cannot be adopted due to their critical size limit and poor workability.

Figure 1.3 shows a schematic diagram of continuous cooling transformation indicating the critical cooling rate necessary to form a crystalline alloy, an amorphous alloy, and a metallic glass. As clearly seen in the figure, it is impossible to synthesize an amorphous phase with ordinary crystalline alloy compositions no

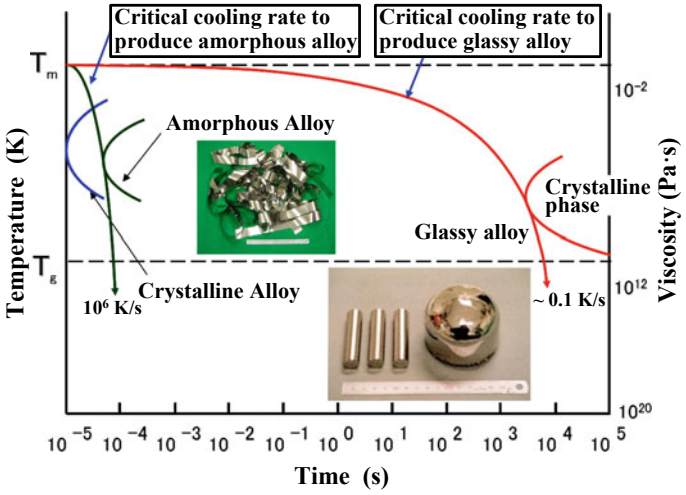

Fig. 1.3 Diagrams of continuous cooling transformation (CCT) of a conventional crystalline alloy, an amorphous alloy, and a metallic glass. T_m: Melting temperature, T_g: Glass transition temperature

matter how high the cooling rate is. In the case of amorphous alloy compositions, the C-nose region in which crystalline phase is formed shifts slightly to the longer time side, with the result that an amorphous phase can be formed at a cooling rate of order 10^6 K/s, avoiding crossing the cooling line with the C-nose region. According to a large number of previous reports, compositions of amorphous alloys are empirically obtained at around a eutectic point in a phase diagram. In the case of metallic glasses, the C-nose region shifts to the significantly longer time side, which enables the production of bulky amorphous alloys, even at a cooling rate much slower than the critical cooling rate for amorphous alloy formation. For example, the critical cooling rate for the formation of the Pd–Cu–Ni–P glassy alloy was experimentally obtained and reported to be about 0.067 K/s. It is possible to synthesize bulky ingots of this alloy up to about 80 mm in diameter, as shown in the figure. Its critical cooling rate, which is significantly lower than that of amorphous alloys, is attributed to the stabilization of the supercooled liquid phase in a glassy alloy satisfying the abovementioned empirical rules. By satisfying those empirical rules, a dense randomly packed structure in which atomic diffusion and rearrangement for crystallization are restrained geometrically during the cooling process is formed, leading to the synthesis of a bulky glass ingot having high stability of supercooled liquid.

Since the extremely high cooling rate at which amorphous alloys can be formed is not necessary to form glassy alloys, various processes to produce bulky glassy alloys, such as water quenching, injection molding, suction casting, squeeze casting, one-directional flow melting solidification, pour casting, tilt casting and cap casting, etc. have been developed and the principles of some casting methods are shown in Fig. 1.4. Among these casting methods, the most popular and widely used

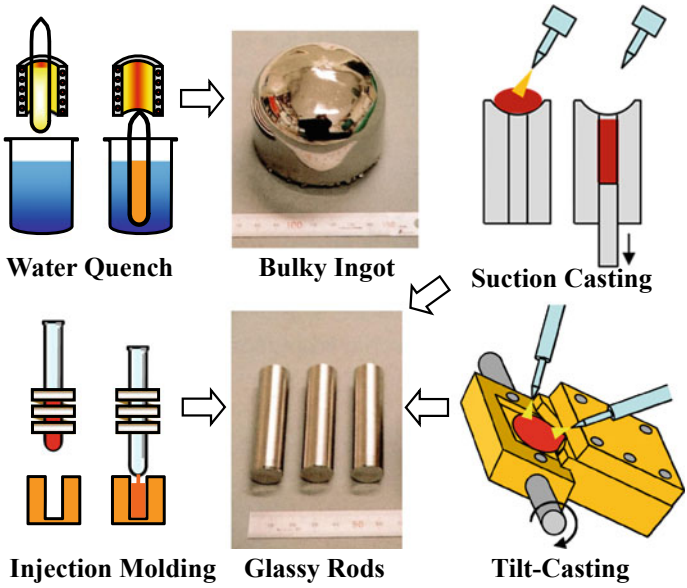

Fig. 1.4 Examples of production methods of metallic glass

method is suction casting and it has been applied to the production of bulk glassy alloys mainly up to about 5 mm. Tilt casting and cap casting invented by Yokoyama and Inoue are thought to be a better casting method than conventional Cu-mold injection casting for suppression of nucleation of casting defects because the surface area of the molten alloy does not change rapidly during casting and has been mainly applied to larger size samples with diameters above 5 mm. Furthermore, suction casting was also applied to produce glassy alloy pipes (hollow tubes). Needless to say, all the processes to produce amorphous alloys, such as melt spinning, gas atomization, vapor deposition, and so on, can also be applied to synthesize glassy alloys [19, 20].

Figure 1.5 shows examples of glassy alloy products [21–23], that is, a water-quenched ingot (upper left), tilt-cast rods (upper right), and suction-cast pipes (lower). As you see clearly in the figure, glassy alloy products can be obtained in much larger size compared with those of conventional amorphous alloys.

Figure 1.6 shows the thermal behaviors of three types of material, that is, metallic glass, amorphous alloy, and crystalline alloy, when heating at room temperature. Thermal parameters T_g, T_x, and T_m correspond to glass transition, crystallization, and melting temperatures, respectively. There is a large difference in the transformation behavior among an ordinary crystalline alloy, an amorphous alloy, and a glassy alloy. A crystalline alloy simply melts at the melting point, T_m, when heating from room temperature. An amorphous alloy transforms into a crystalline state at the crystallization temperature, T_x, and then into a molten state at $T_{m.}$. On the other hand, a metallic glass first transforms into a supercooled liquid state at the glass transition temperature, T_g, and then into a crystallization state at T_x when heating at room temperature. The viscosity steeply decreases in the supercooled liquid region ($\Delta T_x = T_g - T_x$) when heating a glassy alloy at room

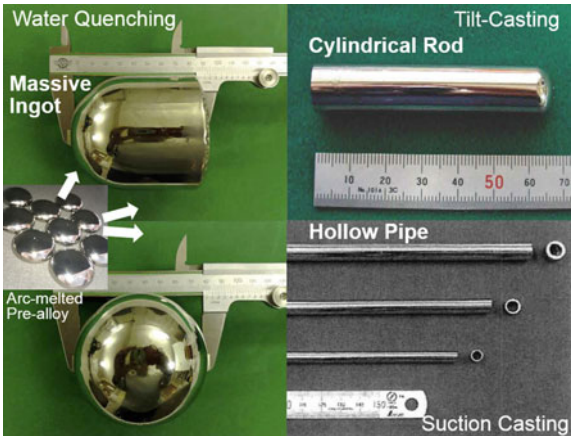

Fig. 1.5 Photographs of bulky metallic glass ingot and rods [21–23]. Massive Ingot: Reprinted from Ref. [21], Copyright 2012, with permission from Elsevier

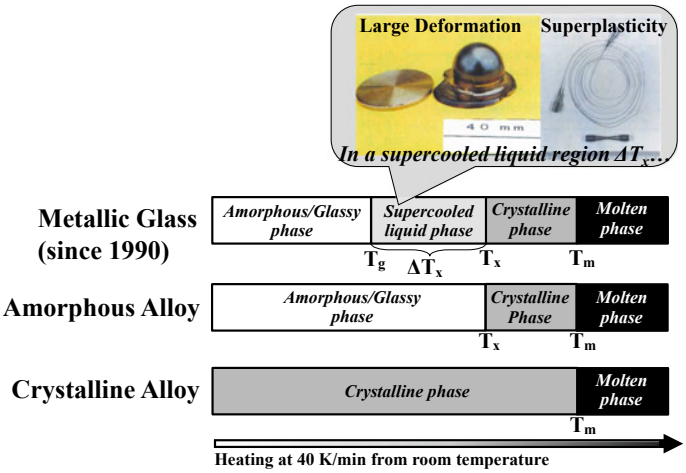

Fig. 1.6 Three different thermal behaviors of metallic glass, amorphous alloy, and crystalline alloy. T_g: Glass transition temperature, T_x: Crystallization temperature, T_m: Melting point, ΔT_x (= $T_x - T_g$): Supercooled liquid region

temperature. Such a low viscosity in the supercooled liquid region enables large plastic deformation of a glassy alloy. Amorphous alloys also have high mechanical strength but plastic deformation is difficult because of the absence of a supercooled liquid region.

Figure 1.7 shows an example of (a) an XRD pattern and (b) a DSC curve obtained from a typical glassy alloy. XRD and DSC stand for X-ray diffraction and differential scanning calorimetry, respectively. When the alloy is characterized by XRD analysis, the presence of a broad, diffuse peak is often taken to be evidence of the formation of an amorphous/glassy phase. Moreover, the thermal properties such as T_g, T_x, and ΔT_x of the amorphous/glassy alloy can be measured by obtaining the DSC curve. It is essential to obtain the XRD pattern and the DSC curve to check whether those nonequilibrium alloys are well prepared and possess a single amorphous/glassy phase or not. In Fig. 1.7a, a broad, diffuse peak called

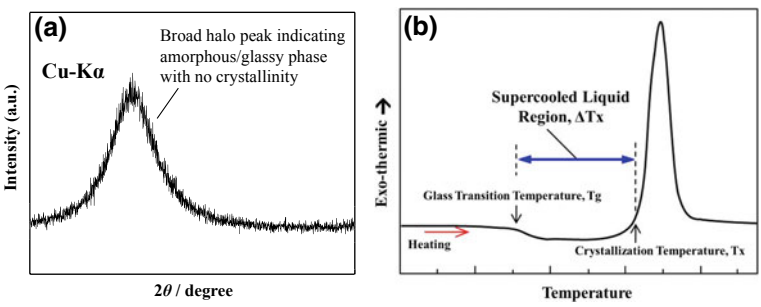

Fig. 1.7 Examples of **a** XRD pattern and **b** DSC curve of an ordinary metallic glass

"halo peak" without any sharp peaks can be seen, indicating that this alloy possesses only a single amorphous/glassy phase. The position of the halo peak shifts to a lower angle side or higher angle side depending on the averaged first neighbor atomic distance in the random atomic arrangement. In the DSC curve of a typical glassy alloy shown in Fig. 1.7b, the supercooled liquid region with endothermic reaction first appears when heating from the room temperature. The onset temperature of that endothermic reaction corresponds to the glass transition temperature, T_g. Then, crystallization occurs with a large exothermic peak when further heating, the onset temperature of the exothermic peak corresponds to the crystallization temperature, T_x. It should be noted that conventional amorphous alloys do not show distinct glass transition in the DSC curve because of the lack of stability of amorphous structure.

1.3 Characteristics of Amorphous Alloys and Metallic Glasses

Amorphous alloys and metallic glasses possess distinct characteristics, which are significantly different from those of traditional crystalline alloys, because of their random atomic arrangement. It is said that the three major properties of amorphous alloys and metallic glasses are (1) high mechanical strength, (2) high corrosion resistance, and (3) excellent soft magnetism. Moreover, metallic glass possesses (4) extremely large viscous deformability and imprintability in a supercooled liquid state, and (5) precise net castability, different from conventional amorphous alloy. Each property will be summarized briefly as follows.

1.3.1 High Mechanical Strength

Figure 1.8 shows a schematic illustration of stress–strain curves of metallic glass and steel [24]. As shown in the figure, metallic glass shows a larger strain in an elastic manner until it fractures and does not show yielding behavior that a crystalline alloy such as steel generally shows. Furthermore, metallic glass hardly shows plastic deformation at room temperature. This is because metallic glass contains no dislocations and no sliding planes that play an important role in plastic deformation of crystalline alloys. Therefore, metallic glasses inherently possess very high mechanical strength.

Figure 1.9 shows the relations between Young's modulus, E, and fracture strength, σ_f, of various crystalline alloys and metallic glasses [25]. The fracture strength σ_f of metallic glass is proportional to its Young's modulus E and is about three times larger than that of a crystalline alloy having the same Young's modulus value. On the contrary, the Young's modulus of metallic glass is about one-third that of a crystalline alloy having almost the same strength.

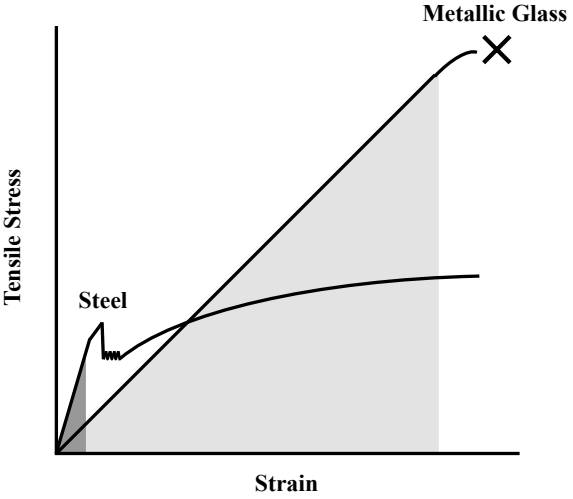

Fig. 1.8 Schematic illustration of stress–strain curves of metallic glass and steel. Reprinted from Ref. [24], Copyright 2005, with permission from AGNE Gijutsu Center

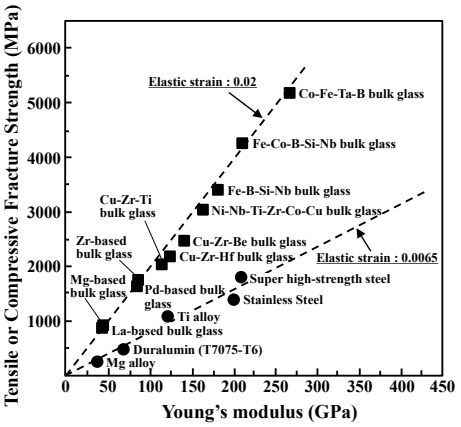

Fig. 1.9 Relations between Young's modulus and fracture strength of various crystalline alloys and metallic glasses. Reprinted from Ref. [25], Copyright 2004, with permission from Elsevier

As explained here, metallic glass possesses higher mechanical strength, a higher elastic limit, and a lower Young's modulus than conventional crystalline alloys. In Fig. 1.8, the hatched area under the stress–strain curve corresponding to an elasticity region of the metallic glass is much larger than that of the steel. This means that metallic glass can accumulate higher elastic strain energy than a crystalline alloy. For example, the elastic strain energy accumulated in the Zr-based glassy alloy having $\sigma_f = 1.7$ GPa was estimated to be five times higher than that in a typical crystalline Ti-based alloy. These characteristic features (high strength and low elastic modulus) of metallic glass are suitable for application to the face plate of a golf club head, resulting in a drastic improvement of a driving distance. Those golf clubs became commercially available in the late 1990s (see Fig. 1.10 [26]).

Fig. 1.10 Outer view of the golf clubs with face plates made of Zr-based metallic glass. Reprinted from Ref. [26], Copyright 2001, with permission from the Japan Institute of Metals and Materials

1.3.2 High Corrosion Resistance

Since amorphous alloys and metallic glasses have a random atomic arrangement, they are unstable (nonequilibrium) with higher internal energy than crystalline alloys. Actually, amorphous alloys and metallic glasses themselves easily dissolve or corrode in an aggressive environment. But soon after the surface layer of those alloys dissolves, a new passive surface film mainly consisting of corrosion-resistant elements such as Cr, Nb, and Mo can be formed. Amorphous alloys and metallic glasses do not contain any defects such as grain boundaries, dislocations, and second-phase precipitates, and such a new passive surface film becomes very homogeneous and protective. This is the reason why amorphous alloys and glassy alloys possess good corrosion resistance (see Fig. 1.11).

Figure 1.12 indicates the corrosion rates of SUS304 stainless steel, pure Cr metal, and $Fe_{42}Cr_{16}Mo_{16}C_{18}P_8$ metallic glass tested in 6 N HCl solution at 298 K after [27]. It is clearly shown that the corrosion rate of the metallic glass is significantly less than those of the stainless steel and pure Cr, successfully proving excellent corrosion resistance of the metallic glass.

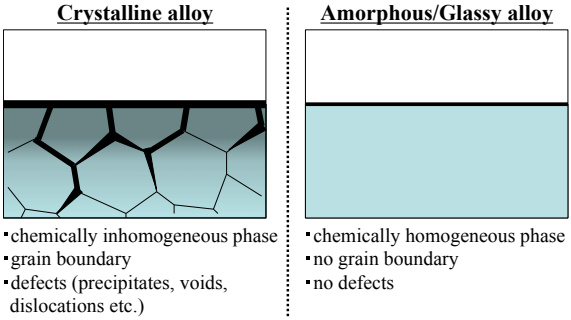

Fig. 1.11 Comparison of corrosion resistivity of crystalline alloy and metallic glass

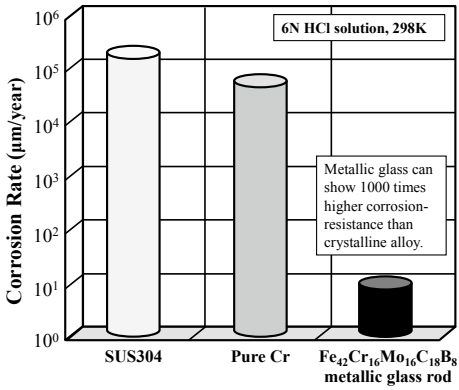

Fig. 1.12 Corrosion rates of SUS304 stainless steel, pure Cr metal, and $Fe_{42}Cr_{16}Mo_{16}C_{18}B_8$ metallic glass tested in 6N HCl solution at 298 K after [27]

1.3.3 Excellent Soft Magnetism

Amorphous alloys and metallic glasses have no magnetic anisotropy because they are three-dimensionally isotropic without crystal orientation. Furthermore, they have a homogeneous microstructure without any defects such as grain boundaries, voids, and precipitates which may cause a pinning effect of magnetic domain wall movement. Consequently, amorphous alloys and metallic glasses are intrinsically expected to possess excellent soft magnetism with high permeability [25]. Soft-magnetic materials always possess high permeability and low coercivity. As can be seen in Fig. 1.13, several amorphous alloys and metallic glasses show relatively high permeability, high saturation magnetic flux density, and also low coercivity because of their liquid-like homogeneous microstructure. In addition, the magnetic softness of bulk glass-type Fe-based alloys is better than that for ordinary

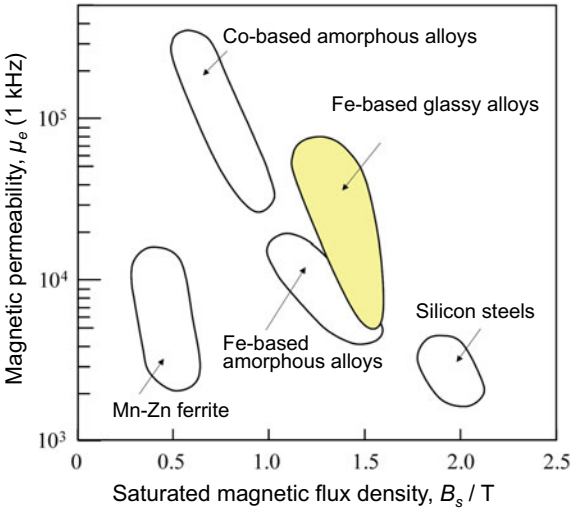

Fig. 1.13 Excellent soft-magnetic property of amorphous/glassy alloys

Fe-based amorphous alloys because of the formation of a more homogeneous medium-range ordered atomic arrangement which is the feature of bulk metallic glasses.

1.3.4 Viscous Flow Formability in the Supercooled Liquid State

Metallic glasses exhibit Newtonian viscosity in the supercooled liquid region by a nearly constant viscosity in a wide strain rate range [28]. The metallic glasses with the Newtonian flow property show good linear relation between the true stress (σ) and true strain rate ($\dot{\varepsilon}$), and the relation can be expressed as $\dot{\varepsilon}$, where k is a constant. Figure 1.14 shows a relationship between the σ and $\dot{\varepsilon}$ for La-, Zr-, Pd-, and Pt-based bulk metallic glasses [29]. The slope (m value) of the linear relation corresponds to the strain-rate sensitivity exponent and can be evaluated as 1.0, indicating the achievement of an ideal superplasticity while the conventional Al–78Zn superplastic alloy shows m = 0.5. Figure 1.15 shows a large tensile elongation of about 20,000% which has been obtained for the La–Al–Ni-based metallic glass rod subjected to pulling treatment in the supercooled liquid region. Recently, the superplastic processing has been developed for making the micro- and nanodevices on the metallic glasses by virtue of the viscous flow formability. Figure 1.16 shows a scanning electron microscopy image of the glassy streak patterns with the dimensions of 300 nm, periodic intervals of 150 nm, and a height of about 100 nm fabricated by isothermal processing of an $Fe_{55}Ni_{15}Mo_5P_{10}C_{10}B_5$ metallic glass on silicon mold in the supercooled liquid region for 120 s under an applied pressure of 100 MPa [30]. In addition, the long-scale and/or large-scale bulk metallic glass can

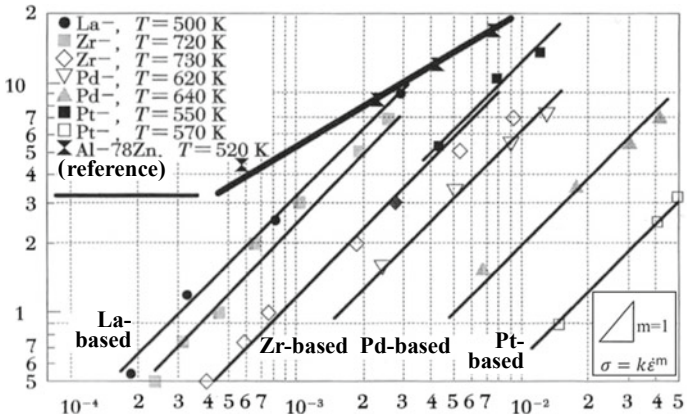

Fig. 1.14 Relationship between the true stress (σ) and true strain rate ($\dot{\varepsilon}$) for a La-, Zr-, Pd-, and Pt-based metallic glasses [29]

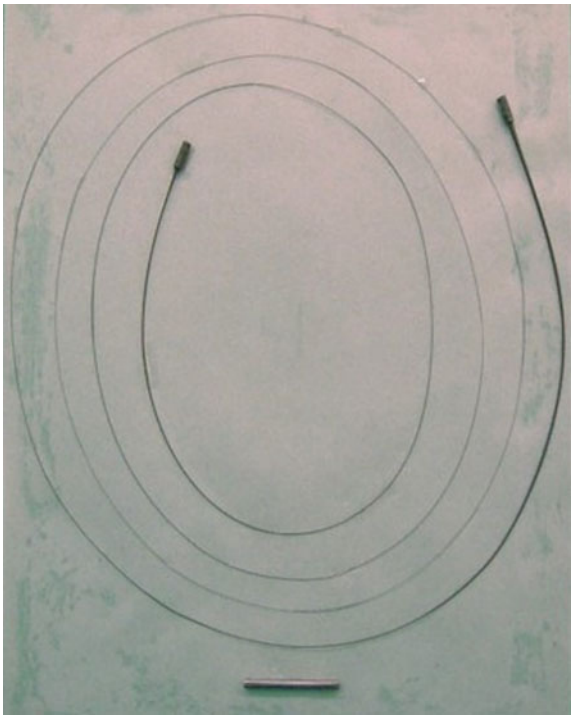

Fig. 1.15 Extended elongation in a La–Al–Ni-based BMG rod superplastically deformed up to about 20,000% in the supercooled liquid region

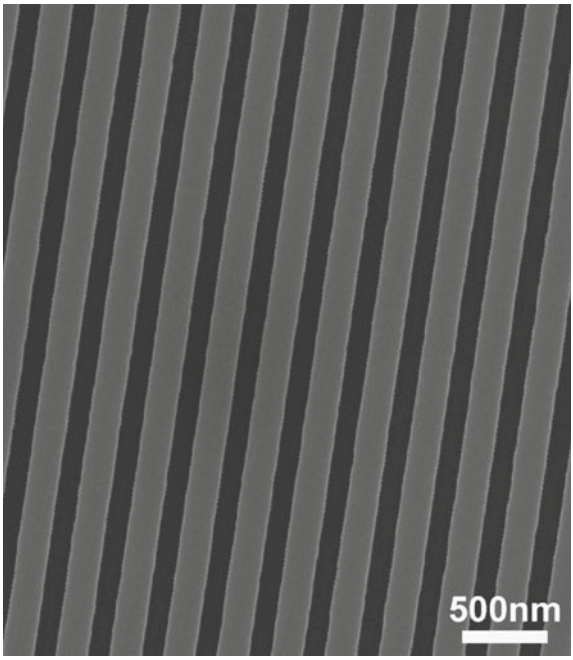

Fig. 1.16 SEM image of the $Fe_{55}Ni_{15}Mo_5P_{10}C_{10}B_5$ glassy streak pattern formed by imprinting on a silicon mold. Reprinted from Ref. [30], Copyright 2013, with permission from Elsevier

be fabricated by ejected alloy liquid joining process [31] as well as by thermoplastic consolidation of glassy powders through hot working and shape forming techniques [32, 33].

1.3.5 Precise Net Castability

Figure 1.17 shows the volume change of a metallic glass and a crystalline alloy during the cooling from the melt to the solid. As you can see in the figure, crystalline alloy reduces significantly its volume at the melting point because of phase transformation from the liquid phase with random atomic arrangement to the solid phase with regular atomic arrangement. On the contrary, metallic glass does not show a significant solidification shrinkage not like shown in crystalline alloy. This is because metallic glass solid maintains the liquid-like random atomic arrangement even at much lower temperature than the melting point. Therefore, the size and shape of the cast parts produced by casting are very close to those of the mold, and this precise net castability of metallic glass can lead to production of glassy alloy micro-parts by injection mold casting. Figure 1.18 shows excellent precise net castability and imprintability with examples of micro-gear of glassy alloy produced by near net shape casting and of mirror-like images of mold surface and cast sample surface. Figure 1.18a indicates the precisely injection mold cast Ni-based glassy

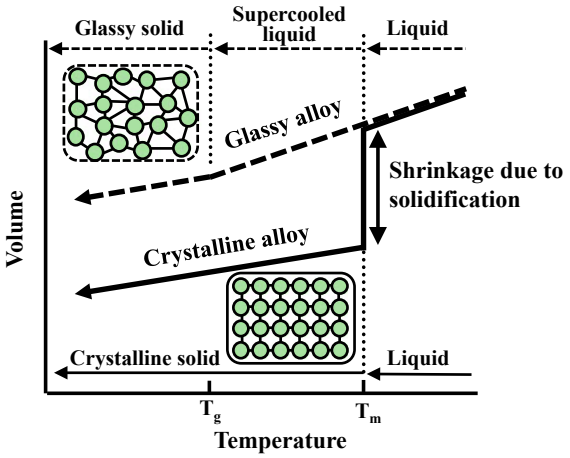

Fig. 1.17 Schematics of the volume change during cooling from the melt to the solid of a glassy alloy and a crystalline alloy

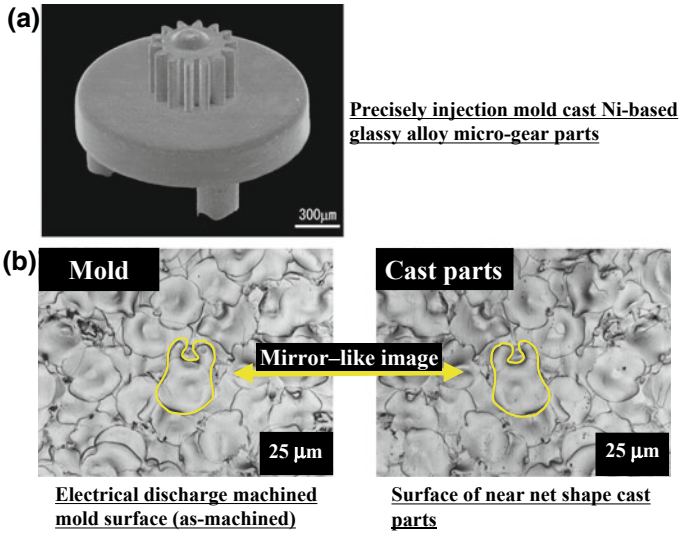

Fig. 1.18 An example showing the precise net castability and imprintability of metallic glass

alloy micro-gear. You can see that it was successfully produced without volume contraction by using a mold. Furthermore, Fig. 1.18b shows magnified images of the mold surface prepared by electrical discharge machining and the surface of the cast sample of around a same area with the mold surface. As clearly seen in the figure, the surface roughness of the mold is precisely transferred to the surface

of the glassy alloy sample. Metallic glass shows much smaller volume contraction during solidification than conventional crystalline alloy and is three-dimensionally isotropic with liquid-like random atomic arrangement, leading to the capability of precise net casting.

1.4 Standardization of Metallic Glasses

If there are casting defects in glassy specimens, those defects can easily lead to crack initiation, resulting in severe degradation of mechanical strength. Moreover, if some precipitates are formed in the glassy phase, those precipitates may prevent the formation of a protective passive surface film, resulting in degradation of corrosion resistance. So, it is significantly important to avoid casting defects during the production of metallic glasses from the viewpoint of quality and reliability particularly in mass production for engineering use. However, metallic glass is a nonequilibrium solid. It may be difficult to avoid formation of micro-defects which are nucleated by accident in the glassy phase during quenching. So, it is also difficult to produce a large quantity of glassy alloy rods and plates whose quality and reliability are guaranteed at the mass-production level. The mass-production methods of glassy alloy ingots such as rods and thick plates are not established yet while only the melt spinning for amorphous alloy thin ribbons and gas atomizing for amorphous alloy powders have been established at present. Therefore, it is very important to standardize the basic properties and the production methods of several metallic glasses selected to meet the engineering demands. The IMR research group has proposed the standardization of several metallic glasses for industrial use as listed in Table 1.1 [22]. In the table, the chemical compositions of several typical metallic glasses and their basic properties such as thermal parameters (T_g and T_x) and mechanical strength (ε_y and σ_y) can be seen. Thus, development of instrumentation techniques such as temperature control of molten alloys, control of injection pressure, and an optimized automatic casting operation is essential to stabilize and guarantee the quality and reliability of the metallic glasses by suppressing the nucleation of casting defects. Automated tilt casting is thought to be a potentially better production method of bulky metallic glasses at present. It is finally important to point out that the most important factor for mass production application is to develop a new bulk glassy alloy with much higher glass-forming ability as well as without expensive elements.

Table 1.1 Standard metallic glasses suggested by IMR research group and their basic properties [22]

	Alloy compositions		d_c (mm)	d_s (mm)	T_g (K)	T_x (K)	T_l (K)	E (GPa)	ε_y (%)	σ_y (MPa)
Z-alloy	Z1	$Zr_{50}Cu_{40}Al_{10}$ (ternary eutectic alloy)	14	10	706	792	1092	88*	2.1*	1860*
	Z2	$Zr_{55}Cu_{30}Ni_5Al_{10}$ (high glass formability)	30	10	683	767	1163	90*	2.0*	1830*
	Z3	$Zr_{60}Cu_{20}Ni_{10}Al_{10}$ (high resistance against embrittlement)	20	10	662	754	1164	80*	2.2*	1750*
	Z4	$Zr_{65}Cu_{17.5}Ni_{10}Al_{7.5}$ (high stability of supercooled liquid)	16	10	625	750	1164	82	1.9	1528
C-alloy	C1	$Cu_{36}Zr_{48}Al_8Ag_8$ (high glass formability)	25	10	683	792	1142	102	1.8	1850
	C2	$Cu_{42}Zr_{42}Al_8Ag_8$ (high mechanical strength)	15	10	705	780	1213	108	1.8	1986
T-alloy	TN	$Ti_{50}Cu_{25}Ni_{15}Zr_5Sn_5$ (high corrosion resistance)	5	3	706	765	1245	105	1.9	2070
	TP	Ti–Cu–Zr–Sn–Pd (for biomedical use)	10	5	689	739	1126	118	1.7	2000

d_c: Critical diameter of glass formation; d_s: Standard diameter; T_g: Glass transition temperature; T_x: Crystallization temperature; T_l: Melting point; E: Young's modulus; ε_y: Yield strain; σ_y: Yield stress obtained by compression test. *: Obtained by tensile test

1.5 Summary

In this chapter, development of amorphous alloys and metallic glasses was briefly overviewed. The characteristic features of amorphous alloys and metallic glasses are summarized below:

(1) Amorphous alloys and metallic glasses can be produced by rapid quenching from a molten liquid and possess liquid-like random atomic arrangement without crystallinity. Therefore, they show quite different characteristics which are different from those of crystalline alloys.
(2) The three major properties of amorphous alloys and metallic glasses are (1) high mechanical strength, (2) high corrosion resistance, and (3) excellent soft magnetism. Amorphous alloys and metallic glasses possess many other functional properties different from crystalline alloys such as high affinity to micromachining, high activity as a catalyst, and so on. These outstanding characteristics of amorphous alloys and metallic glasses originate from their random atomic arrangement.
(3) Metallic glasses possess a distinct glass transition and subsequent large supercooled liquid region just below the crystallization temperature while conventional amorphous alloys do not show a glass transition. In the supercooled liquid region, unlike amorphous alloys, metallic glass can show superplastic deformation. Moreover, metallic glass does not require an extremely high cooling rate for its formation, and can be produced in bulk as well as in precise net shape. These factors are expected to enable the use of metallic glass for a variety of applications in the future.

Metallic glasses have been developed since 1990 and basic studies of these glasses have been conducted for more than two decades. Thus, their application for engineering purposes in practice is overdue. The authors hope readers will become interested in these nonequilibrium materials called amorphous alloys and metallic glasses by reading this short article.

References

1. A. Brenner, D.E. Couch, E.K. Williams, Plating **37**, 36 (1950)
2. W. Klement, R.H. Willens, P. Duwez, Nature **187**, 869 (1960)
3. H.S. Chen, D. Turnbull, J. Appl. Phys. **38**, 3646 (1967)
4. P.L. Maitrepierre, J. Appl. Phys. **40**, 4826 (1969)
5. S.C.H. Lin, P. Duwez, Phys. Stat. Sol. **34**, 469 (1969)
6. T. Masumoto, R. Maddin, Acta Metall. **19**, 725 (1971)
7. T. Egami, P.J. Flanders, C.D. Graham Jr., Appl. Phys. Lett. **26**, 128 (1975)
8. H. Fujimori, T. Masumoto, Y. Obi, M. Kikuchi, Jpn. J. Appl. Phys. **13**, 1889 (1974)
9. M. Kikuchi, H. Fujimori, Y. Obi, T. Masumoto, Jpn. J. Appl. Phys. **14**, 1077 (1975)
10. M. Naka, K. Hashimoto, T. Masumoto, J. Jpn. Inst. Matals **38**, 835 (1974)
11. M.M. Collver, R.H. Hammond, Phys. Rev. Lett. **30**, 92 (1973)

12. E.E. Luborsky, Ferromagnetic materials, in *Handbook on the Properties of Magnetically Ordered Structures*, ed. by E.P. Wohefarth (North-Holland Publishing Company 2, 1980, Chapter 6)
13. S.A. Miller, R.J. Murphy, Scripta Metall. **25**, 673 (1979)
14. A. Inoue, M. Kohinata, A.P. Tsai, T. Masumoto, Mater. Trans. JIM **30**, 378 (1989)
15. A. Inoue, T. Zhang, T. Masumoto, Mater. Trans. JIM **30**, 965 (1989)
16. A. Inoue, T. Zhang, T. Masumoto, Mater. Trans., JIM **31**, 177 (1990)
17. C. Suryanarayana, A. Inoue, *Bulk Metallic Glasses* (CRC Press, New York, 2011, Chapter 3)
18. M. Miller, P. Liaw (ed.), *Bulk Metallic Glasses* (Springer, New York, 2010, An Overview)
19. C. Suryanarayana, A. Inoue, *Bulk Metallic Glasses* (CRC Press, New York, 2011, Chapter 10)
20. A. Inoue, Kinzoku. Mater. Sci. Technol. **75(**9) (2005) (in Japanese)
21. N. Nishiyama, K. Takenaka, H. Miura, N. Saidoh, Y. Zeng, A. Inoue, Intermetallics **30**, 19 (2012)
22. IMR News KINKEN **56**)(6) (2008) (in Japanese)
23. E. Makabe, New functional materials, fundamentals of metallic glasses and their applications to industry, in *Metallic Glass pipe* (Technosystem, Tokyo, 2009) (in Japanese)
24. K. Fujita, Kinzoku. Mater. Sci. Technol. **75**(34) (2005) (in Japanese)
25. A. Inoue, B. Shen, C.T. Chang, Acta Mater. **52**, 4093 (2004)
26. H. Kakiuchi, A. Inoue, M. Onuki, Y. Takano, T. Yamaguchi, Mater. Trans. **42**, 678 (2001)
27. S.J. Pang, T. Zhang, K. Asami, A. Inoue, Corros. Sci. **44**, 1847 (2002)
28. A. Inoue, Y. Saotome, Metals **3**, 51 (1993)
29. Y. Saotome, Sokeizai **42**, 1 (2001). (in Japanese)
30. W. Zhang, C.F. Fang, Y.H. Li, Scripta Mater. **69**, 77 (2013)
31. X.M. Wang, K. Son, A. Inoue, Mater. Trans. **49**, 1419 (2008)
32. Y. Kawamura, H. Kato, A. Inoue, Int. J. Powder Metall. **33**, 50 (1997)
33. G.Q. Xie, W. Zhang, D.V. Louzguine-Luzgin, H. Kimura, A. Inoue, Scripta Mater. **57**, 35 (2006)

Chapter 2
Applications of Amorphous Alloy/ Metallic Glass for Environmental and Energy Engineering, Electronics Engineering, and Biomedical Engineering Fields

Shin-ichi Yamaura, Wei Zhang, Rie Y. Umetsu, Guoqiang Xie and Ichiro Seki

Abstract In this chapter, metallic glasses and amorphous alloys especially developed for environmental and energy engineering, electronic engineering, and biomedical engineering by the authors' research group are overviewed. As for the achievements related to the environmental and energy engineering field, the development of the following four types of materials are presented: (1) Ni–Cr–P–B glassy alloys for bipolar plates of PEM fuel cell, (2) Au–Cu–Si–Ag glassy alloy

Present Address:
S. Yamaura (✉)
The Polytechnic University of Japan, 2-32-1 Ogawanishi-machi, Kodaira, Tokyo 187-0035, Japan
e-mail: s-yamaura@uitec.ac.jp

S. Yamaura · W. Zhang · R. Y. Umetsu · G. Xie · I. Seki
Institute for Materials Research, Tohoku University, 2-1-1 Katahira, Aoba, Sendai, Miyagi 980-8577, Japan
e-mail: wzhang@dlut.edu.cn

R. Y. Umetsu
e-mail: rieume@imr.tohoku.ac.jp

G. Xie
e-mail: xieguoqiang@hit.edu.cn

I. Seki
National Institute of Technology, Tsuyama College, 624-1, Numa, Tsuyama, Okayama 708-8509, Japan
e-mail: seki@tsuyama-ct.ac.jp

S. Yamaura · W. Zhang
Dalian University of Technology, No. 2 Linggong Road, Ganjingzi, Dalian 116024, Liaoning, People's Republic of China

G. Xie
Harbin Institute of Technology, Shenzhen 518055, People's Republic of China

Y. Setsuhara et al. (eds.), *Novel Structured Metallic and Inorganic Materials*, https://doi.org/10.1007/978-981-13-7611-5_2

with an extremely low glass transition temperature T_g for nanoimprinting in an energy- and cost-efficient manner, (3) Ni–Nb–Zr amorphous alloys for hydrogen separation, and (4) porous metals prepared by dealloying glassy/amorphous alloys for environmental catalysts. Furthermore, bonding and joining methods for metallic glasses are also evaluated and summarized. Electronic transport properties of Ni–Nb–Zr amorphous alloys are shown. Besides, effects of hydrogen absorption on the electrical resistivity and their possibilities to the applications are discussed in the viewpoint of the electronic engineering. As for the biomedical engineering field, recent progress in the developments of these biomedical BMGs, which include bioinert materials such as Ti-based BMGs, Zr-based BMGs, Fe-based BMGs and biodegradable materials such as Mg-based BMGs, Ca-based BMGs, Zn-based BMGs, and Sr-based BMGs, is described. Moreover, several metallic glasses with low magnetic susceptibility, which are promised materials for development of high-performance MRI, are described in detail.

Keywords Metallic glass · Glassy alloy · Amorphous alloy · Fuel cell · Bipolar plate · Hydrogen permeable membrane · Catalyst · Porous metal · Bonding · Joining · Nanoimprint · Temperature coefficient of resistivity · Biomedical applications · Bioinert materials · Biodegradable materials · Mechanical properties · Corrosion resistance

2.1 Development of Metallic Glasses for Environmental and Energy Engineering

Shin-ichi Yamaura and Wei Zhang

2.1.1 Introduction

Amorphous alloys and metallic glasses (glassy alloys) possess distinct characteristics different from those of conventional crystalline alloys. It is said that the three major properties of amorphous alloys and metallic glasses are (1) high mechanical strength, (2) high resistance to corrosion, and (3) excellent soft magnetism. When applied in the environment and energy engineering field, their functional properties such as soft magnetism, corrosion resistance, and micromachining capability rather than mechanical strength can be focused on. Some applications of metallic glasses in the field of environmental and energy engineering studied in the MEXT program will be overviewed in this section, in particular, glassy alloy bipolar plates for proton exchange membrane fuel cells (high corrosion resistance), amorphous alloy membranes for hydrogen separation (high hydrogen diffusivity and high hydrogen absorption), porous catalysts (characteristic microstructure), low T_g metallic glass

for design material (characteristic thermal stability), and metallic glass bonding as a peripheral technology for practical applications of metallic glass.

2.1.2 Metallic Glass for Bipolar Plates of a Proton Exchange Membrane Fuel Cell

Nowadays, fuel cells are attracting increasing interest as promising power generation systems from the viewpoint of solving energy and environmental problems. Since fuel cells can convert chemical energy of fuels directly to electricity, the efficiency of generating electricity by fuel cells is relatively higher than that by conventional thermal power generation. Theoretically, fuel cells do not emit carbon dioxide (CO_2), nitrogen oxide (NO_x) nor sulfur oxide (SO_x) gases, so their usage can contribute to the suppression of global warming. Fuel cells are considered to be the most suitable power generator in the twenty-first century [1]. The present author has attempted to develop a glassy alloy bipolar plate for the past decade. Recent research will be shown in this subsection.

The proton exchange membrane (PEM) fuel cell has been receiving considerable attention as a clean energy source that may be used in the near future, for example, for electric vehicles, home appliances, and so on because of its advantageous characteristics such as high power density and capability of low-temperature operation. The PEM fuel cell is based on the reverse reaction of water electrolysis. Theoretically, the generated voltage is 1.23 V at standard reference conditions and 1.17 V during operation at 353 K.

Figure 2.1 shows the main components of a single PEM fuel cell [2]. A single fuel cell is comprised of a proton exchange membrane, electrodes (catalyst layer + porous support), and bipolar plates. Bipolar plates are also called "separators" or "interconnectors" depending on the functions being focused on. Generally, a fuel cell stack in which single cells are connected in series is constructed because the voltage of a single cell is only about 1 V. Bipolar plates are one of the most critical components of PEM fuel cells, accounting for more than 70% of their weight and more than 40% of their cost [3]. Bipolar plates are multifunctional: They collect and conduct electricity from cell to cell, they mechanically support the stacks, they separate the fuel gas from the oxidant gas, and their flow field supplies gases to the electrodes. Bipolar plates are conventionally made from carbon graphite and from metallic materials such as stainless steel and clad material. Although carbon graphite is very stable in the corrosive environment in fuel cells, it is difficult to produce thin bipolar plates because of its brittleness. Thinner bipolar plates will lead to lighter and more compact fuel cell stacks, reducing costs and space. Many research groups have thus attempted to develop metallic materials for bipolar plates. However, the corrosive environment inside a fuel cell is detrimental to metallic materials, and dissolved metal ions damage the proton exchange membrane, resulting in a severe decrease in fuel cell performance.

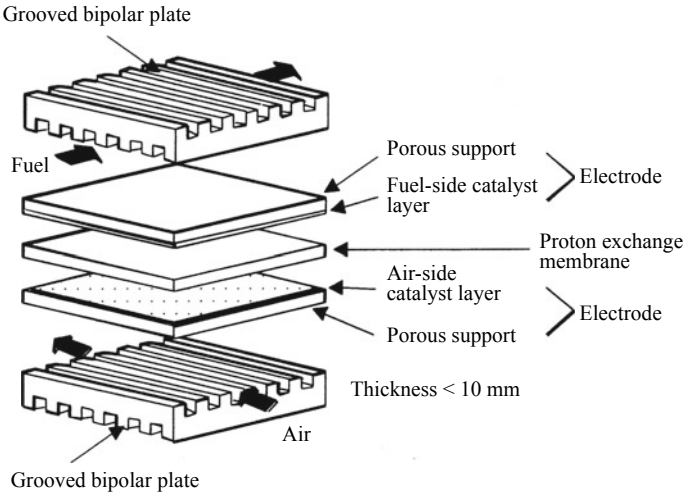

Fig. 2.1 Components of proton exchange membrane fuel cell. Reprinted from Ref. [2], Copyright 2005, with permission from the Chemical Society of Japan

Metallic glass is also a potential material for fuel cells because of its unique properties in contrast to those of crystalline alloys. The advantages of applying metallic glass for bipolar plates are as follows: (1) metallic glass deforms relatively easily under a supercooled liquid state, resulting in the capability of readily producing grooved bipolar plates, (2) metallic glass possesses extremely high corrosion resistance, suppressing an increase in contact resistance and a dissolution of metal ions which cause degradation of fuel cell performance, and (3) metallic glass possesses high mechanical strength, making it possible to produce relatively thinner bipolar plates leading to more compact fuel cells.

Experimental results for the development of glassy alloy bipolar plates are shown below.

Figure 2.2 shows some prototypes of glassy alloy bipolar plates, directly produced from glassy alloy sheets by hot pressing under a supercooled liquid state [4]. In this case, melt-spun $Ni_{60}Nb_{15}Ti_{15}Zr_{10}$ glassy alloy sheets were hot pressed by using grooved dies. In the early stage of the series of our work, melt-spun glassy sheets were used to produce bipolar plates, the alloy sheets being heated up to a temperature between the glass transition temperature T_g and the crystallization temperature T_x. As it was necessary to prepare larger melt-spun sheets than the bipolar plates themselves, it was difficult to put them into practical use. Then, the present authors group conceived the idea of glassy alloy-coated bipolar plates.

Originally, Naka et al. [5] and Yoshioka et al. [6] reported that Ni–Cr–P–B quaternary amorphous/glassy alloys showed good corrosion resistance. Subsequently, we found that those alloys can be produced by melt spinning in air showing a wide supercooled liquid region ΔT_x and no difference of thermal properties between the alloys produced in air and those in an Ar atmosphere. Besides, the T_g and T_x

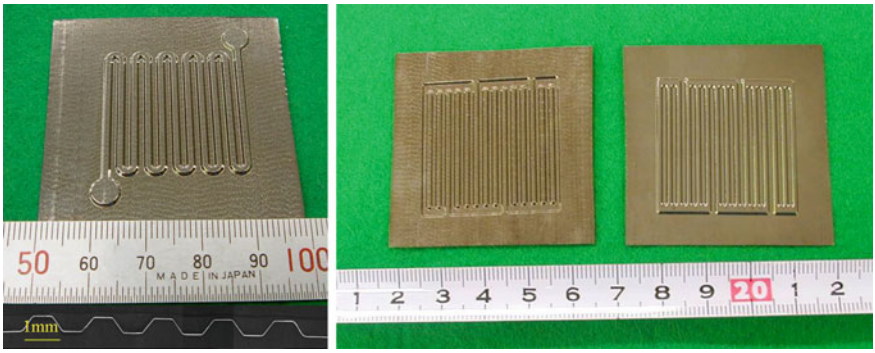

Fig. 2.2 Examples of hot-pressed $Ni_{60}Nb_{15}Ti_{15}Zr_{10}$ glassy alloy bipolar plates. Reprinted from Ref. [4], Copyright 2005, with permission from the Japan Institute of Metals and Materials

temperatures are much lower than those of the Ni–Nb–Ti–Zr glassy alloys, so the Ni–Cr–P–B quaternary alloys were adopted to produce glassy alloy-coated bipolar plates as a next step.

Figure 2.3 shows several XRD patterns obtained from the melt-spun $Ni_{80-x}Cr_xP_{16}B_4$ (x = 3–30 at.%) alloys prepared in this study [7]. No sharp distinct peaks but rather a broad halo peak is observed in the range of 25–100°. This indicates that all the alloys possess a single amorphous/glassy phase.

Thermal parameters, T_g, T_x, and ΔT_x of those alloys were then investigated and were summarized in Fig. 2.4 [7]. The alloys with Cr content of 3 and 6 at.% did not show a glass transition in the DSC measurements, so they were recognized as amorphous alloys rather than metallic glasses and were not included in Fig. 2.4. As

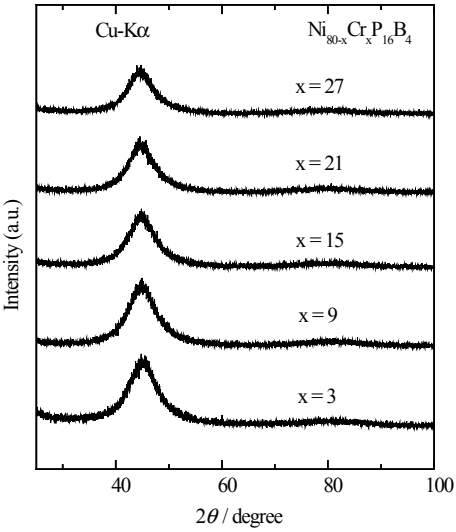

Fig. 2.3 XRD patterns of $Ni_{80-x}Cr_xP_{16}B_4$ (x = 3–27 at.%) alloys. Reprinted from Ref. [7], Copyright 2007, with permission from the Japan Institute of Metals and Materials

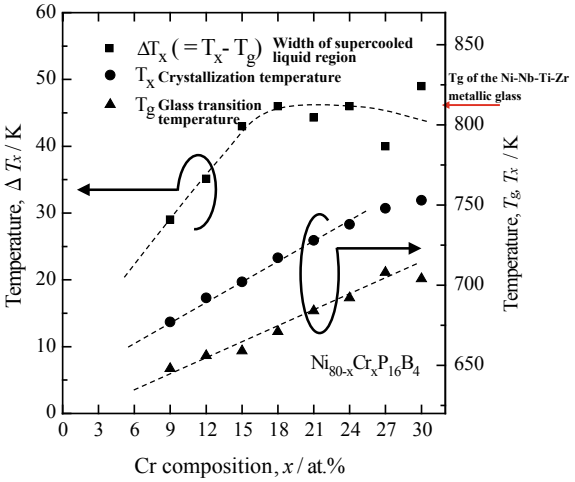

Fig. 2.4 Summarized plot of the Tg, Tx, and ΔTx of the melt-spun alloy samples as a function of Cr content. The direction of the arrows indicates the vertical axis that the curve should be referred to. Reprinted from Ref. [7], Copyright 2007, with permission from the Japan Institute of Metals and Materials

clearly seen in this figure, ΔT_x increases with increasing Cr content and finally shows a saturation at above 15 at.%Cr. In this case, it is preferable to obtain an alloy with wider ΔT_x, and also with lower T_g and T_x. Therefore, we selected the $Ni_{65}Cr_{15}P_{16}B_4$ alloy as the optimum alloy composition. The T_g, T_x, and ΔT_x values of the $Ni_{65}Cr_{15}P_{16}B_4$ glassy alloy are 659 K, 702 K, and 43 K, respectively.

Table 2.1 summarizes the results of corrosion tests conducted by immersing the alloy samples in 1 mass% sulfuric acid solution [7]. It was found that the corrosion rate of the $Ni_{65}Cr_{15}P_{16}B_4$ glassy alloy was much lower than that of the corrosion-resistant stainless steel SUS316L, clarifying that this glassy alloy showed excellent corrosion resistance.

The high-velocity oxy-fuel (HVOF) spray coating method was employed to produce a newly designed bipolar plate with glassy alloy surface film [8, 9]. Figure 2.5 shows a schematic of the HVOF spray coating method: (a) feedstock powder of the glassy alloy prepared by gas atomizing, (b) overview, and (c) cross-sectional view of the $Ni_{65}Cr_{15}P_{16}B_4$ glassy alloy-coated bipolar plate. It is very important that glassy feedstock power be prepared. In this work, the aluminum bipolar plates were prepared beforehand and then the glassy alloy was deposited on

Table 2.1 Corrosion rates of the $Ni_{65}Cr_{15}P_{16}B_4$ glassy alloys and the stainless steel SUS316L. Reprinted from Ref. [7], Copyright 2007, with permission from the Japan Institute of Metals and Materials.

Alloy composition (at.%)	Corrosion rate (mm/year)
$Ni_{65}Cr_{15}P_{16}B_4$	6.94×10^{-3}
$Ni_{56}Cr_{24}P_{16}B_4$	9.52×10^{-4}
SUS316L	1.48×10^{-2}

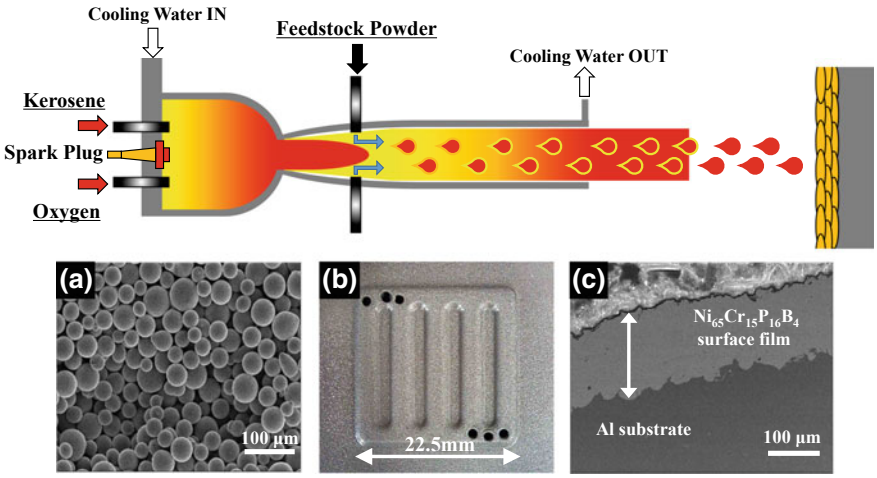

Fig. 2.5 A schematic illustration of the high-velocity oxy-fuel (HVOF) spray coating system. **a** Feedstock powder of $Ni_{65}Cr_{15}P_{16}B_4$ glassy alloy prepared by gas atomizing, **b** overview and **c** cross-sectional view of the $Ni_{65}Cr_{15}P_{16}B_4$ glassy alloy-coated bipolar plate

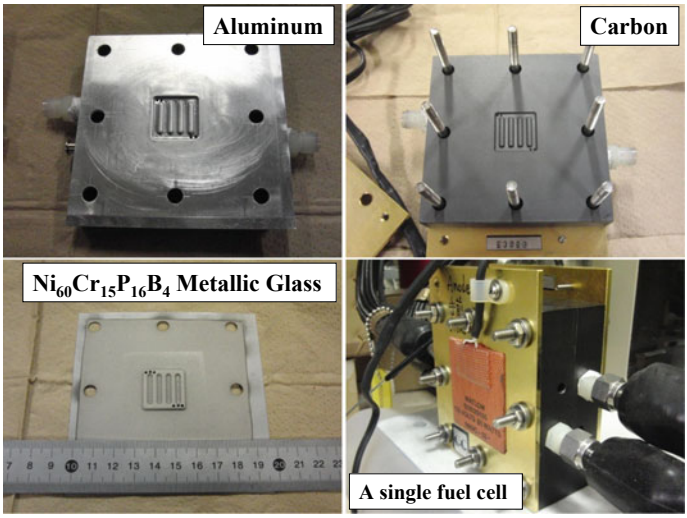

Fig. 2.6 Overviews of three different bipolar plates prepared with the same gas flow grooves prepared in this study and a single fuel cell with those plates

the surface of the aluminum bipolar plates by using HVOF spray coating. The thickness of the glassy surface film was about 200 μm as seen in Fig. 2.5c.

Figure 2.6 shows outer views of three different bipolar plates with the same groove design prepared in this work. A pair of bipolar plates of each material was prepared and used for assembling a single fuel cell.

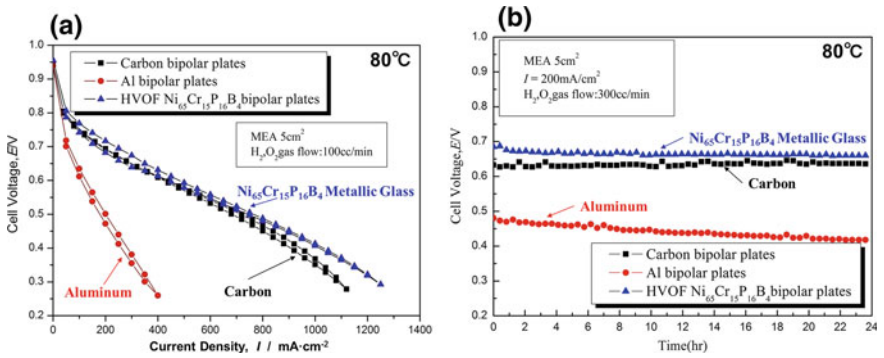

Fig. 2.7 Power generation tests of a single fuel cell with three different bipolar plates. **a** I–V measurements and **b** long time power generation tests for about 24 h. Reprinted from Ref. [8], Copyright 2010, with permission from the Japan Institute of Metals and Materials

Figure 2.7 shows the results of power generation tests conducted with a single fuel cell with different bipolar plates [8]. Figure 2.7a indicates the I–V behaviors of each single cell. The fuel cell with aluminum bipolar plates showed the greatest decrease in voltage with increasing current density among those three different bipolar plates. This may be because the aluminum bipolar plates show poorer corrosion resistance than others. The fuel cells with glassy alloy-coated bipolar plates and with graphite bipolar plates showed a current density greater than 1000 mA/cm^2 at 0.3 V. It was found that the single cell with the glassy alloy-coated bipolar plates showed very high I–V performance as well as the cell with the graphite bipolar plates. Figure 2.7b shows the results of 24-h power generation tests conducted for the fuel cells with three different bipolar plate materials. The current density was 200 mA/cm^2. The cell voltage of the fuel cell with the aluminum bipolar plates is lower than those with other bipolar plates and gradually decreased with time. On the contrary, the single cell with the glassy alloy-coated bipolar plates showed no voltage drop during the test for 24 h as was the case with graphite bipolar plates. So, the $Ni_{65}Cr_{15}P_{16}B_4$ glassy alloy-coated bipolar plate produced by the HVOF spray coating was found to have a potential for practical use for fuel cells. It was successfully demonstrated in this work that glassy alloys having inherently high corrosion resistance can be applied for bipolar plate material. The effect of hydrophilic surface treatment of the glassy alloy-coated bipolar plates on power generation performance was also studied [10] and a new proton exchange membrane which can be substituted for the Nafion film was also studied in our research program [11].

Table 2.2 Thermal parameters (T_g, T_x, ΔT_x, T_l), critical diameters (d_c), and mechanical properties (Hv, σ_{cf}, E) of newly developed Au-based BGAs (after [12])

Composition (at.%)	T_g (K)	T_x (K)	ΔT_x (K)	T_l (K)	d_c (mm)	Hv	σ_{cf} (MPa)	E (GPa)
$Au_{50}Cu_{33}Si_{17}$	383	405	22	679	1<	361	–	–
$Au_{50}Cu_{25.5}Ag_{7.5}Si_{17}$	377	419	42	652	5	353	935	65.4
$Au_{60}Cu_{15.5}Ag_{7.5}Si_{17}$	359	403	44	670	5	316	832	55.1
$Au_{65}Cu_{10.5}Ag_{7.5}Si_{17}$	342	392	50	678	4	294	726	48.4
$Au_{70}Cu_{5.5}Ag_{7.5}Si_{17}$	339	375	36	680	3	264	643	46.6

2.1.3 Au–Cu–Ag–Si Metallic Glass for Micro-/Nanodevices

Nanoimprinting is receiving a lot of attention as a mass-production method for micro-/nanodevices. Metallic glasses are suitable for making micro- and nanodevices because they are homogeneous on the nanometer scale without any defects such as grain boundaries, voids, and precipitates. For applying glassy alloys for nanoimprinting, there are strong demands for glassy alloys characterized by low glass transition temperature T_g, wide supercooled liquid region ΔT_x, high oxidation resistance, good mechanical properties, and high corrosion resistance. Zhang et al. in our group has reported that the $Au_{60}Cu_{15.5}Ag_{7.5}Si_{17}$ quaternary glassy alloys possessed an ultralow T_g of 359 K, a wide ΔT_x of 44 K and a relatively large critical

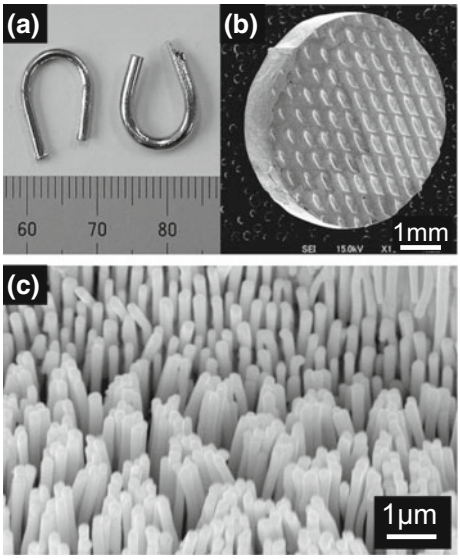

Fig. 2.8 **a** $Au_{60}Cu_{15.5}Si_{17}Ag_{7.5}$ glassy rods formed into a U shape by using two pairs of tweezers in near-boiling water (97 °C). **b** Pattern shaped by a pair of pliers on the surface of a glassy plate ($\varphi 5 \times 1.5$ mm^2) in near-boiling water. **c** SEM image of $Au_{60}Cu_{15.5}Si_{17}Ag_{7.5}$ glassy pillars formed by embossing on porous alumina. Glassy pillars with diameters of about 200 nm are formed when the alloy is heated through its supercooled liquid region (92 °C) for 180 s under an applied pressure of 100 MPa. Reprinted from Ref. [12], Copyright 2009, with permission from Elsevier

diameter of 5 mm, showing a good superplastic formability at a low temperature below 373 K [12–14].

Table 2.2 lists the thermal parameters (T_g, T_x, ΔT_x, and melting point, T_l), critical diameter (d_c), and mechanical properties (Vickers hardness, H_v, compressive fracture strength, σ_{cf} and Young's modulus, E) of the Au-based glassy alloys (after [12]). The glass transition temperatures of these alloys are about 340–380 K. Moreover, those alloys contain Au of more than 50 at.%, so their corrosion resistance is found to be better than that of stainless steel SUS316L.

Figure 2.8a shows $Au_{60}Cu_{15.5}Ag_{7.5}Si_{17}$ glassy rods formed into U shapes by two pairs of tweezers in near-boiling water (370 K) [12]. Figure 2.8b shows a small disk pressed from a glassy plate using a pair of pliers. The pattern on the surface is created by the teeth of the pliers. Figure 2.8c shows glassy nanopillars with diameters of about 200 nm fabricated by isothermal processing on porous alumina at 365 K for 180 s under an applied pressure of 100 MPa. The results shown in Fig. 2.8 indicate that the shaping, imprinting, embossing, and other fabrication processes can be conveniently applied to glassy alloys. This type of glassy alloys with ultralow T_g are good candidate materials for scientific and various other applications, including micro-/nanomachinery with energy-saving processing, high-density data recording media, and design material for jewelry and ornamentation.

2.1.4 *Amorphous Alloys for Hydrogen Permeable Membrane*

Amorphous alloys and glassy alloys having inherently lower density than the crystalline counterparts have received much attention as material for hydrogen permeable membrane because they possess a greater amount of free interior volume, leading to higher hydrogen diffusivity. In our work, hydrogen permeability of Ni–Nb–Zr amorphous alloys was studied and Pd-coated Ni–Nb–Zr amorphous alloys were found to show excellent hydrogen permeability as high as the conventional Pd–Ag alloy [15, 16]. Furthermore, pure hydrogen was successfully extracted from the reformed gas of methanol steam by using an amorphous alloy membrane [17]. Recently, improvement of thermal stability and suppression of hydrogen embrittlement of amorphous alloys have been major challenges to overcome in this research field. The details will be discussed in Chap. 20.

2.1.5 *Porous Metal Catalysts Produced from Amorphous Alloys and Metallic Glasses*

One of the potential applications of amorphous alloys and glassy alloys is thought to be their use as catalysts. Studies on catalytic properties of amorphous alloys have been conducted for decades from the early stage of amorphous alloy research. For example, Komiyama et al. reported that an amorphous alloy could improve the

activity of hydrogenation of CO [18]. In particular, Zr-, Ni-, and Pt-based amorphous alloys are good candidates for use as high-performance catalyst material.

So far, we have produced nanoporous metals by a dealloying method in which a certain element is selectively dissolved from amorphous alloys or crystalline solids. Nanoporous Pd- and Cu-based alloys have been prepared and their catalytic properties have been studied [19–21]. Furthermore, the catalytic activity of nanoparticles prepared from glassy/amorphous alloys has also been studied and reported [22–24]. The details will be discussed in Chaps. 5 and 19.

2.1.6 *Bonding and Joining of Metallic Glasses*

Metallic glasses have unlimited potential as functional materials, but in most cases only small pieces a few centimeters in diameter or in length can be produced because of the necessity of rapid quenching for producing metallic glasses. Therefore, it is important to develop bonding and joining techniques of metallic glasses to enable us to produce their larger applications in bulk. The bonding and joining of metallic glasses studied in our group (in the MEXT program) will thus be included in this article.

Generally speaking, welding of metallic glasses requires careful optimization of welding conditions, needless to say, the cooling rate after welding/remelting should be higher than the critical cooling rate to produce an amorphous phase. Nowadays, it is not difficult to obtain a high cooling rate of several hundred K/s by using modern heat sources for welding. There are three zones in a specimen subjected to

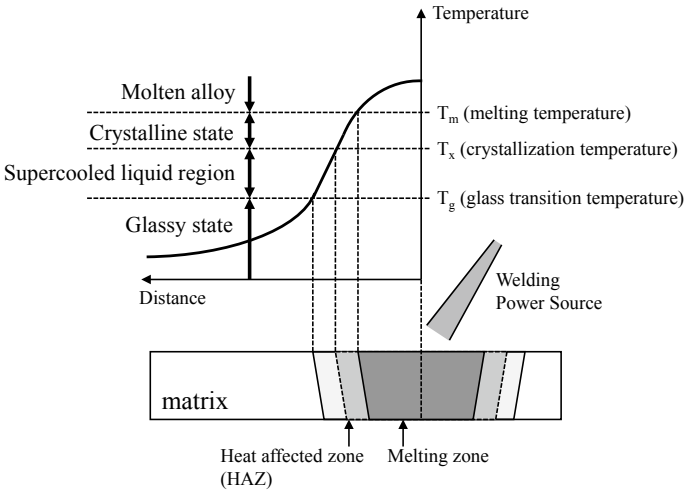

Fig. 2.9 Cross-sectional view of the glassy alloy, showing the temperature gradient from the melting zone heated by welding power source

welding: a melting zone, a heat-affected zone, and an unaffected zone, as shown in Fig. 2.9. The boundary between the melting zone and the heat-affected zone (HAZ) is the melting point, T_m, from which the maximum temperature decreases continuously to room temperature. In general, recrystallization and grain growth are observed macroscopically and the dissolution or growth of precipitates and atomic segregation are observed microscopically in conventional crystalline metals. In most cases of crystalline metals, the region heated higher than the recrystallization temperature (and below the melting point at the same time) always corresponds to the HAZ. In the case of glassy alloys, formation of the HAZ is related to the melting temperature T_m, the crystallization temperature T_x, and the glass transition temperature T_g.

In glassy alloys, the HAZ easily crystallizes after welding because of the slow cooling rate. Therefore, the cooling rate around the melting zone and the HAZ should be higher than the critical cooling rate of glassy alloys to maintain an amorphous state. Moreover, it is necessary to consider the degradation of mechanical properties of a glassy alloy in the HAZ caused not only by crystallization but also by structural relaxation even in the amorphous state. Therefore, it is necessary to reduce the thermal damage to a glassy alloy (in particular to HAZ) by decreasing the input thermal energy in the rapid heating process and by increasing the cooling rate in the subsequent rapid cooling process when welding glassy alloys.

So far, welding methods characterized by relatively low thermal energy input, such as electron beam welding, laser welding, spot welding, and solid bonding such as friction stir welding have been experimentally applied to glassy alloys. In the last part of this article, several studies on the welding process of glassy alloys are reviewed.

Glassy alloys can be easily changed from an amorphous state to a crystalline state. So, it is necessary to use a high-power heat source with narrow spot diameter and ultrahigh welding speed in order to join glassy alloys with each other [25–28]. Figure 2.10 shows the result of butt welding of $Zr_{55}Al_{10}Ni_5Cu_{30}$ glassy alloy sheets by using a 130 μm-focused fiber laser at an ultrahigh welding speed of 72 m/min

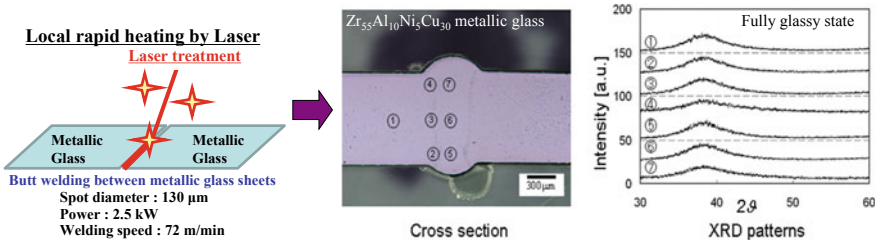

Fig. 2.10 Fiber-laser butt welding of $Zr_{55}Al_{10}Ni_5Cu_{30}$ glassy alloy. Cross section and XRD results of weld bead produced at a welding speed of 72 m/min. Reprinted from Ref. [25], Copyright 2008, with permission from Elsevier

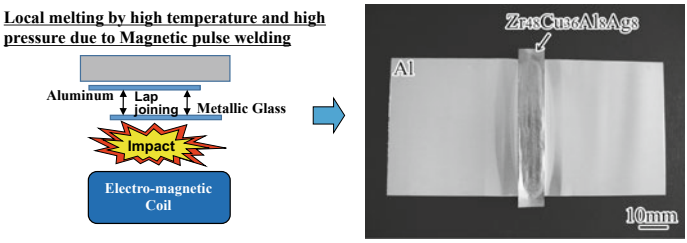

Fig. 2.11 Aluminum/glassy alloy lap joints fabricated by magnetic pulse welding. Reprinted from Ref. [27], Copyright 2009, with permission from the Japan Institute of Metals and Materials

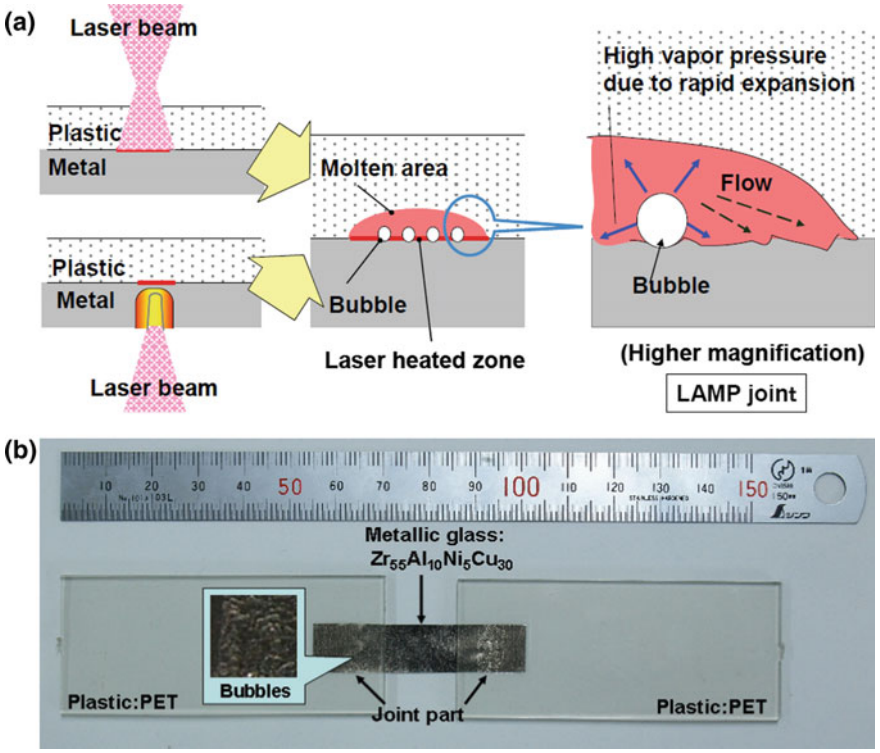

Fig. 2.12 A schematic illustration of direct joining process of $Zr_{55}Al_{10}Ni_5Cu_{30}$ glassy alloy and engineering plastic PET with a diode laser beam of linear mode, showing that small bubbles are generated which induce high pressure, resulting in the flow of melted plastic along the alloy-plastic boundary (**a**) and laser direct joint between $Zr_{55}Al_{10}Ni_5Cu_{30}$ glassy alloy and engineering plastic PET before the tensile shear test (**b**). Reprinted from Ref. [28], Copyright 2010, with permission from the Japan Institute of Metals and Materials

and a laser power of 2.5 kW [25]. The thickness of the glassy alloy sheets is 1 mm. It was found that there were no crystalline peaks in the XRD pattern obtained from each cross-sectional area shown in the figure. High-power fiber laser welding at ultrahigh welding speed was found to be applicable to glassy alloys in order to maintain the amorphous state and to avoid crystallization after welding.

Figure 2.11 shows the result of aluminum/glassy alloy lap joints successfully fabricated by magnetic pulse welding [27]. Figure 2.12 shows the result of a laser direct joint between glassy alloy and engineering plastic PET [28]. Recently, various welding and joining techniques can be applied to glassy alloys under appropriate conditions.

2.1.7 *Summary of the Studies for Environmental and Energy Engineering*

In this section, metallic glasses and amorphous alloys especially developed for the environmental and energy applications by the author's research group were overviewed. In particular, the development of four types of materials, namely, (1) Ni–Cr–P–B glassy alloys for bipolar plates of PEM fuel cell, (2) Au–Cu–Si–Ag glassy alloys with an extremely low glass transition temperature T_g for nanoimprinting in an energy- and cost-efficient manner, (3) Ni–Nb–Zr amorphous alloys for hydrogen separation, and (4) porous metals prepared by dealloying the glassy/amorphous alloys for environmental catalysts was discussed and other current achievements were shown. Furthermore, bonding and joining methods for metallic glasses were also presented and summarized here.

(1) We succeeded in showing excellent power generation performance of a single cell with $Ni_{65}Cr_{15}P_{16}B_4$ glassy alloy-coated bipolar plates as well as that with carbon graphite bipolar plates. A single cell with glass-coated bipolar plates showed no voltage drop during a long power generation test for 24 h as was also the case with carbon graphite bipolar plates. It was thus found in this work that a $Ni_{65}Cr_{15}P_{16}B_4$ glassy alloy-coated bipolar plate produced by the HVOF spray coating has a potential for practical use for the fuel cells in the future.

(2) $Au_{60}Cu_{15.5}Si_{17}Ag_{7.5}$ glassy alloy with an extremely low glass transition temperature T_g was developed for nanoimprinting, micro-/nanodevices and design material for ornaments and jewelry. Glassy alloy nanopillars were successfully produced by embossing on porous alumina in a supercooled liquid state, showing their potential as a nanoimprint material. The T_g value of $Au_{60}Cu_{15.5}Si_{17}Ag_{7.5}$ glassy alloy is 359 K, so it can be easily deformed in boiling water, leading to a decrease in manufacturing cost and energy use.

(3) Ni–Nb–Zr amorphous alloy and its derivative alloys were developed for hydrogen separation. The hydrogen permeability coefficients of those

amorphous alloys were as high as those of conventional Pd metal and Pd–Ag alloys.

(4) Several porous metals have been produced by dealloying Au-based, Pd-based, and Cu-based glassy alloys in this decade. They are to be used as environment catalysts.

Furthermore, bonding and joining methods of glassy alloy were herein reviewed. Glassy alloys were successfully bonded to each other or to other materials such as engineering plastics under optimum conditions of fiber laser welding, magnetic pulse welding, laser-assisted metal and plastic joining, and so on.

2.2 Development of Metallic Glasses for Electronic Engineering

Rie Y. Umetsu

Electron transport properties of metallic glasses are described in this section. Here, no strict distinction is made between metallic glasses and amorphous alloys from the standpoint that both are nonperiodic systems. In addition, materials mentioned here are restricted to paramagnetic or diamagnetic ones. In materials with strong or weak ferromagnetism, the electron transport properties are governed by well-localized *d*-electrons around the Fermi energy. Therefore, theoretical treatments should differ from those of nonmagnetic systems. Even in *nonmagnetic* systems, theory is strictly different depending on the kinds of the main carrier at the Fermi energy, such as *d*-electrons or *s*- and *p*-electrons. Behavior of the electrical resistivity of metallic glasses and/or amorphous alloys is often discussed in comparison with that of crystalline alloys. There are three characteristic features of the electrical resistivity of amorphous alloys as follows [29]:

1. The residual resistivity of amorphous alloys is 5–100 times higher than that of the crystalline phase.
2. The change of resistivity with temperature is very small, only a few percentage points in the temperature range below room temperature.
3. The sign of the temperature coefficient of resistivity (TCR) in amorphous alloys is positive or negative and the value is sometimes very close to zero.

Concerning the above features, there is a well-known empirical rule proposed by Mooij although it does not apply to only amorphous alloys [30]. He found a relationship between residual resistivity, ρ_0, and TCR, that is, alloys with a high value of residual resistivity ($\rho_0 > 150$ μΩ cm) tend to exhibit a negative TCR, whereas those with a low value ($\rho_0 < 150$ μΩ cm) show a positive TCR [30]. Mizutani classified five kinds of behaviors of temperature dependences of the electrical resistivity for various alloy systems [31, 32]. He also mentioned that the sign of TCR changes from positive to negative with increasing value of electrical

resistivity in the temperature range of 2–300 K and that the change of resistivity is accompanied by shortening of the mean free path down to an average atomic distance. The gradual change of the TCR can be explained by the Baym–Meisel–Cote theory based on the Boltzmann transport equation [33–35].

Historically, electron transport properties of liquid metals were discussed by Mott and Jones in their book in 1936 [36]. Next, in 1961, Ziman successfully explained the behavior of the electrical resistivity of pure liquid metals, such as Zn and Na [37]. The Ziman formula is constructed on the basis of three assumptions: (1) The electron transport properties can be described in terms of the Boltzmann transport equations. (2) Each ion acts upon the conduction electrons through a localized pseudopotential. (3) The conduction electrons are nearly free and elastic scattering is assumed. Faber and Ziman extended the Ziman formula for binary alloy systems [38], and Evans et al. replaced the pseudopotential in the Ziman formula by the muffin-tin potential so as to enable treatment of liquid transition metals having strong hybridization with the *d*-electrons [39]. In order to discuss the electrical resistivity in a temperature range well below the Debye temperature, an inelastic electron–phonon interaction was introduced by Baym to treat the thermal vibrations of ions [33]. Furthermore, temperature dependence of the dynamic structural factor in the Baym resistivity formula was considered by Meisel and Cote [34, 35].

In the model, temperature dependence of the electrical resistivity of amorphous alloys with weak paramagnetism or diamagnetism is denoted as follows [33–35]:

$$\rho = \rho_0 \exp[-2W(T)] + \rho_{\mathrm{ip}}\left(1 - \frac{2\pi}{\Lambda q_{\mathrm{D}}}\right), \tag{2.2.1}$$

where ρ_0 is the residual resistivity, $\exp[-2W(T)]$ is the Debye–Waller factor and their product is the elastic component. The second term in Eq. (2.2.1) arises from the inelastic electron–phonon interaction, and ρ_{ip} is ideal one-phonon resistivity when $\Lambda \to \infty$. Λ is the mean free path and q_{D} is the Debye wave vector. For amorphous alloys with a nonperiodic structure, Λ is small, and consequently the second term becomes negligible. Therefore, the electrical resistivity is governed by the temperature dependence of the Debye–Waller factor, not by electron–phonon scattering. If $\Lambda = 2\pi/q_{\mathrm{D}}$, electron–phonon scattering is completely absent and the resistivity in such case is approximately 200 μΩ cm for monovalent free-electron metals [35]. The characteristic features of the electron transport properties of amorphous alloys, such as the comparatively high electrical resistivity and the negative behavior of TCR are explained by the model. In the Debye–Waller factor, W is indicated as follows in the Debye approximation [40]:

$$W = \frac{3\hbar^2 k^2 T^2}{2Mk_B\Theta^3} \int_0^{\Theta/T} \left(\frac{1}{e^Z - 1} + \frac{1}{2}\right) z dz \tag{2.2.2}$$

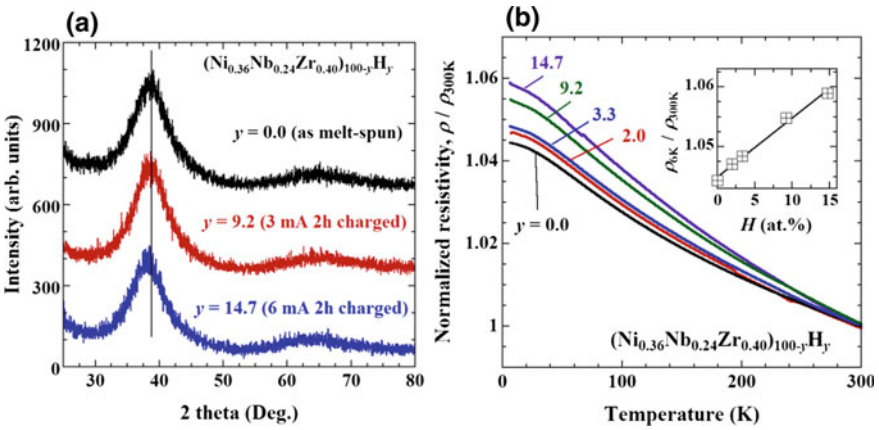

Fig. 2.13 **a** X-ray diffraction patterns of $Ni_{36}Nb_{24}Zr_{40}$ melt-spun amorphous ribbon and hydrogen-absorbed specimens [42]. **b** Temperature dependence of the normalized electrical resistivity, $\rho/\rho_{300\ K}$, for $Ni_{36}Nb_{24}Zr_{40}$ melt-spun amorphous ribbon and hydrogen-absorbed specimens for y = 0.0, 2.0, 3.3, 9.2, and 14.7 for $(Ni_{0.36}Nb_{0.24}Zr_{0.40})_{100-y}H_y$. The inset is the ratio of the resistivity, $\rho_{6\ K}/\rho_{300\ K}$, as a function of the concentration of the absorbed hydrogen. Reprinted from Ref. [42], Copyright 2013, with permission from the Japan Institute of Metals and Materials

where $\hbar$, k_B, M, and Θ are the Plank's constant, the Boltzmann constant, electron mass, and the Debye temperature, respectively. As a result, the electrical resistivity shows T^2-dependence in a low temperature range and T-linear dependence in the temperature range above the Debye temperature.

As an example, we introduce the temperature dependence of the electrical resistivity of Ni–Nb–Zr amorphous alloy ribbons and its absorbed hydrogen. It has been known that the Ni–Nb–Zr ternary alloy forms a metallic glass or amorphous phase in a wide concentration range [41]. Figure 2.13a indicates X-ray diffraction patterns of $Ni_{36}Nb_{24}Zr_{40}$ melt-spun amorphous ribbon and hydrogen-absorbed specimens [42]. The specimens were fabricated by the conventional melt-spinning technique using a single roller. The hydrogen was absorbed by electrochemical charging [42, 43]. The amount of absorbed hydrogen can be controlled by the current density during electrochemical charging and it was confirmed by the inert gas carrier melting-thermal conductivity method. In Fig. 2.13a, typical halo-patterns are observed, indicating evidence of the amorphous state. The main peaks observed around 40° slightly shift to a lower degree with increasing hydrogen absorption. This behavior indicates the occurrence of volume expansion by interstitially absorbed hydrogen.

Figure 2.13b shows the temperature dependence of the normalized electrical resistivity, $\rho/\rho_{300\ K}$, for y = 0, 2.0, 3.3, 9.2, and 14.7 for $(Ni_{0.36}Nb_{0.24}Zr_{0.40})_{100-y}H_y$ amorphous alloy ribbons. All of the resistivity exhibits negative temperature dependence as discussed above. The inset shows the ratio of the resistivity change, $\rho_{6\ K}/\rho_{300\ K}$, as a function of the concentration of the absorbed hydrogen [42]. As shown in the figure, TCR increases negatively with increasing absorbed hydrogen,

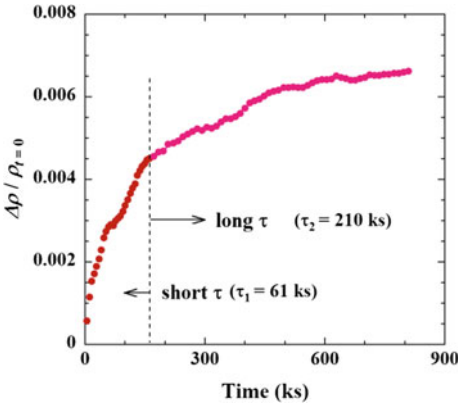

Fig. 2.14 Time dependence of the ratio of the electrical resistivity change, $\Delta\rho/\rho_{t=0}$, at room temperature just after electrochemical charging. Reprinted from Ref. [42], Copyright 2013, with permission from the Japan Institute of Metals and Materials

y. The straight line is a guide for the eyes. Although it is seen that there is a linear relationship between $\rho_{6\ K}/\rho_{300\ K}$ and the amount of absorbed hydrogen, it is somewhat difficult to clarify the origin. With regards to the origins, there are several possibilities, e.g., the change of the mean free path associated with the volume expansion, change of the Debye temperature and electronic state. In addition, impurity scattering related to the absorbed hydrogen would also have an effect. In the case of the present Ni–Nb–Zr alloy system, the electronic state would have a character due to the *d*-electrons because the alloy is constructed by the transition metal elements. However, the magnetic properties are seen not to be governed by the localized *d*-electrons. Magnetic susceptibility is in the order of 10^{-4}–10^{-5} emu/mol, and magnetization shows a negligible temperature dependence. It may be said that the main carrier at the Fermi energy is (*sp* + *d*)-electrons and the alloy system is rather close to a group of weak paramagnetism [29].

Figure 2.14 shows time dependence of the ratio of the electrical resistivity change of $Ni_{36}Nb_{24}Zr_4$ amorphous alloy ribbon just after electrochemical charging [42]. Kawashima et al. pointed out that the absorbed hydrogen in Ni–Nb–Zr amorphous alloy ribbons was distributed in the specimen with time as indicated by the fact that the morphology of the specimen gradually changed [44]. As shown in the figure, two stages of the increase of electrical resistivity are observed. Similar increasing behavior is observed in single crystalline Nb, which also absorbs hydrogen by the same method [45]. From systematic investigations, Koike et al. have suggested that the absorbed hydrogen in the Nb exhibits two stages of diffusion caused by different mechanisms. They expressed the increase of the electrical resistivity with time as follows [45, 46]:

$$\Delta\rho(t) = \Delta\rho_1(t) + \Delta\rho_2(t) + \Delta\rho_{OX}(t), \tag{2.2.3}$$

where

$$\begin{aligned}\Delta\rho_1(t) &\approx \Delta\rho_1(1-\exp(-t/\tau_1))\\ \Delta\rho_2(t) &\approx \Delta\rho_2[1-0.811(\exp(-t/\tau_2)+\frac{1}{9}\exp(-9t/\tau_2))],\\ \Delta\rho_{OX}(t) &= At\end{aligned} \tag{2.2.4}$$

Here, $\Delta\rho_1$ is the first stage change, which is due to the formation of some internal sources such as dislocations, and $\Delta\rho_2$ is the second stage, which is due to the vacancy migration from the surface [45, 47]. The third term in Eq. (2.2.3) is explained to be the correct one expressed as a linear increase with the time in the reference. Because the change of the resistivity seems to be almost saturated over 800 ks, the present experimental data were fitted by the sum of only the first and second terms. From the fitting, relaxation time τ_1 and τ_2 were obtained to be about 61 ks and 210 ks, respectively. Since the curvature of the present data is similar to that of Nb–H, it is suggested that the absorbed hydrogen and vacancy result in an increase of electrical resistivity of the Ni–Nb–Zr amorphous ribbon, which would be mainly due to the increase of the residual resistivity accompanying by impurity scattering.

As shown in the above examples, temperature dependence of the electrical resistivity can be explained by the extended Ziman formula based on the Boltzmann transport equation. The effects of the absorbed hydrogen on the electron transport properties are systematic and a unique behavior of resistivity change with the time is also observed. Furthermore, very interesting properties, such as ballistic conductivity, superconductivity, and the Coulomb-blockade oscillations have been reported in the series of Ni–Nb–Zr amorphous alloy ribbons with absorbed hydrogen [48, 49]. There is a possibility that these properties could prove to be useful for applications, such as in sensors, electrical devices, and new technology.

2.3 Development of Metallic Glasses for Applications as Biomaterials and Biomedical Materials

Guoqiang Xie

2.3.1 Introduction

With a continuously increasing aging society and the improvement of quality of life (QOL), large demands of the biological and biomedical materials are expected for a long time. The development of novel biomaterials, that are much safer and much higher quality, in terms of both biomedical and mechanical properties are of great interest for both the research scientists and clinical surgeons.

Metallic materials show a great potential for application as biological and biomedical materials, and are superior in many aspects to alternative biomaterials

such as ceramics and polymers. Pure Ti and Ti alloys, pure Zr and Zr alloys, stainless steel, and cobalt chromium alloys are widely used as artificial hip joints, artificial knee joints, bone plates, dental implants, cardiovascular stents, etc. [50–52]. Besides, pure Mg and Mg alloys, pure Zn and Zn alloys have been studied and developed as biodegradable materials aiming to be useful in the clinical cases that need temporary supporting or fixation (such as plates and screws for bone fracture fixation, stents for cardiovascular repair), without second operation to be removed after finishing their functions [53]. However, these conventional crystalline metals and alloys have disadvantages such as low strength, high Young's modulus (which can cause stress shielding), low wear resistance, prone to crevice corrosion, pitting corrosion as well as stress corrosion cracking (SCC) and high cycle fatigue failure, and incompatibility with X-ray or magnetic resonance imaging (MRI), which cause various problems in clinical application [52].

Bulk metallic glasses (BMGs) owing to their high corrosion resistance, excellent mechanical properties, and good biocompatibility [54–56] exhibit promising potential to be applied as biomaterials and biomedical materials. This potential has caused an increasing interest in studying and developing the biomedical BMGs.

In the design and development of biomedical BMGs, main chemical compositions of the conventional crystalline biomedical alloys, i.e., Ti alloys, Zr alloys, stainless steels, Mg alloys, and Zn alloys were taken as references. Based on this consideration, there are the corresponding BMGs with the same main chemical compositions explored as potential biomaterials. These BMGs can be divided into two categories, namely, bioinert group and biodegradable group. The bioinert BMG group includes Ti-based BMGs, Zr-based BMGs, Fe-based BMGs (which are also known as amorphous stainless steels), and so on. The biodegradable BMG group includes Mg-based BMGs, Ca-based BMGs, Zn-based BMGs, Sr-based BMGs, and so on. In this section, recent progress in the developments of these BMGs as novel biomedical materials will be summarized.

2.3.2 Bioinert Metallic Glasses

The original requirement of first-generation "biocompatible" materials was bioinertness [57]. BMG alloys, which have potential for use as nonabsorbable medical devices, are usually based on Ti, Zr, and Fe. Toxic or potentially harmful elements such as Be and Ni are generally to be avoided, if possible. As summarized in Table 2.3, the bioinert BMG group includes members such as Ti-based BMGs, Zr-based BMGs, and Fe-based BMGs. Their alloy compositions, fabrication methods, and mechanical properties are also summarized in Table 2.3.

Ti-based BMGs are promising materials for applications to biomedical fields due to their high corrosion resistance, excellent mechanical properties, and good biocompatibility. Many Ti-based BMGs have been developed in the framework of the Ti–Ni–Cu and Ti–Zr–Cu–Ni alloy systems [92]. However, these Ti-based BMGs contain Ni and/or Be, etc., which are not suitable to be in contact with human body

Table 2.3 Summary of bioinert BMG alloy systems and their mechanical properties

BMG system	Alloys composition	Preparation method	Critical diameter (mm)	Compressive fracture strength (σ_f) (MPa)	Young's modulus (E) (GPa)	Vickers hardness (Hv) (kg mm^{-2})	Reference
Ti-based	Ti–Zr–Cu–Pd	Arc melting/Cu mold casting	7	1950	82	–	[58, 59]
	Ti–Zr–Cu–Pd–Sn	Arc melting/Cu mold casting	4–12	1970–2150	95	650	[60–62]
		Spark plasma sintering (SPS)	over 15	2060	94–103	–	[63]
	Ti–Zr–Cu–Pd–M (M: Nb, Ta, Ag, Au, Pt, Si, Fe, Cr)	Arc melting/Cu mold casting	2–5	1670–2150	80–119	–	[64–68]
	Ti–Cu–Hf–Si	Arc melting/Cu mold casting	3	1685	95	–	[69]
	Ti–Cu–Zr–Fe–Sn–Si–Ag	Arc melting/Cu mold casting	7	2080	100.4 ± 0.1	588 ± 6	[70]
Zr-based	Zr–Cu–Fe–Al	Arc melting/Cu mold casting	13	1498-1690 (yield strength)	–	434–563	[71, 72]
	Zr–Cu–Fe–Al–Ag	Arc melting/Cu mold casting	3–10	1640–1720	68–82	–	[73, 74]
	Zr–Cu–Fe–Al–Ag–Ti	Arc melting/Cu mold casting	–	1450–1580	70–78	443–460	[75]
	Zr–Cu–Fe–Al–Nb Zr–Cu–Fe–Al–Ti	Arc melting/Cu mold casting	–	1795	72	–	[76]
	Zr–Cu–Al–Ag	Arc melting/Cu mold casting	25	1790–1953 (yield strength)	–	–	[77, 78]
	Zr–Co–Al Zr–Co–Al–Ag Zr–Co–Al–Nb	Arc melting/tilt casting	18	1830 (tensile strength); 2070	83	–	[79–82]
	Zr–Cu–Pd–Al–Nb	Arc melting/Cu mold casting	18–20	1700–2150	82	–	[83, 84]

(continued)

Table 2.3 (continued)

BMG system	Alloys composition	Preparation method	Critical diameter (mm)	Compressive fracture strength (σ_f) (MPa)	Young's modulus (E) (GPa)	Vickers hardness (Hv) (kg mm^{-2})	Reference
	Zr–Cu–Al–Ti	Arc melting/Cu mold casting	6	–	83	–	[85]
	Zr–Pd–Fe–Al	Arc melting/Cu mold casting	6	1500	–	411–422	[86]
Fe-based	Fe–Co–Cr–Mo–C–B–Y	Arc melting/Cu mold casting	16	3500	–	1253	[87]
	Fe–Co–Cr–Mo–C–B–Er	Arc melting/Cu mold casting	2–4	4070–4100	200	–	[88]
	Fe–Cr–Mo–C–B–Er	Arc melting/Cu mold casting	3–12	4040–4200	209–220	1122	[88, 89]
	Fe–Cr–Mo–P–C–B	Arc melting/Cu mold casting	2.5–3	3150–3550	176–183	845–974	[90]
	Fe–Cr–Mo–Mn–C–B–Y	Arc melting/Cu mold casting	2–5	–	–	–	[91]
	Fe–Mo–C–B–Er	Arc melting/Cu mold casting	3	4000	204	1122	[89]

because of the cellar toxicity, limiting the application of Ti-based BMGs in biomedical fields. Recently, Ni- and Be-free Ti–Zr–Cu–Pd BMGs with high strength and good corrosion resistance make it possible to create novel Ti-based BMG implants [59]. However, relative low glass-forming ability (GFA) (with critical diameter of 7 mm) restricted the biomedical applications. Large critical diameter and excellent mechanical properties of BMGs are the fundamental requirement for applications. The influence of small amounts of additional elements on the formation and properties of Ti–Zr–Cu–Pd bulk glassy alloys was studied. Minor Sn addition improved the glass-forming ability (with a critical diameter of 12 mm), thermal stability, and plasticity of the Ti–Zr–Cu–Pd alloy system [62]. High strength and distinct plastic strain were observed in the stress–strain curves for Nb-, Ta-, and noble elements (such as Au and Pt)-added Ti–Zr–Cu–Pd alloys. Especially, yield strength exceeding 2050 MPa, low Young's modulus of about 80 GPa and distinct plastic strain of 8.5% and 10% corresponding to serrated flow sections were obtained in the 3 at.% Nb-, and 1 at.% Pt-added alloys, respectively [64, 66, 67]. Using the gas-atomized Ti-based (Ti–Zr–Cu–Pd–Sn) glassy alloy powders, the Ti-based BMGs with a diameter over 15 mm exhibited high density, high strength, as well as good corrosion resistance can be produced by a spark plasma sintering (SPS) process [63]. Studies of corrosion behavior of the Ti-based BMGs in different kinds of simulated body fluids have shown that the Ti-based BMGs exhibited passive behavior at the open-circuit potential with a low corrosion rate; a susceptibility to localized corrosion in the form of pitting corrosion; the localized corrosion resistance was statistically equivalent to, or better than, the conventional crystalline biomedical alloys, including pure Ti and Ti-based biomedical alloys (such as Ti–6Al–4V) [60, 65], 316L stainless steel [93]. The additions of the minor Nb or Ta also exhibited higher corrosion resistance [67]. The Ti-based BMGs exhibited low SCC susceptibility in simulated body fluid. A bioactive calcium phosphate compound layer was obtained after two-step treatment on the Ti-based BMGs [94].

Because Zr with Ti has similar chemical characters, Zr-based BMGs are also suggested to use as biomaterials. The biomedical Zr-based BMGs have been featured with a high hardness that is about twice to three times of that for conventional crystalline biomedical 316L SS, Ti alloys and Zr alloys, and high yield strength that is considerably higher than that of those abovementioned conventional crystalline metallic biomaterials. The elastic strains around 2% with low modulus of 68–83 GPa were obtained. The modulus was lower than that of 316 L stainless steel (about 200 GPa) and Ti–6Al–4V alloy (110–125 GPa). In addition, the Zr-based BMGs also exhibited a considerably large plastic strain. For example, the plastic deformation of Zr–Cu–Pd–Al–Nb BMGs exceeded 20% [84]. In comparison with conventional crystalline Zr and Zr-based alloys, Ti and Ti-based alloys, and 316L stainless steel, the Zr-based BMGs showed evidently a lower passive current density, much higher pitting potential, suggesting that the passive films formed on the Zr-based BMGs are more protective than on the abovementioned control groups, indicating their enhanced corrosion resistance behavior [83]. The high corrosion resistance of the biomedical Zr-based BMGs can be attributed to the formation of the passive films, mainly composed of ZrO_2, on the surface of the

alloy. Adding Nb [95] and Ag [96] are beneficial for the corrosion resistance, especially enhanced the corrosion resistance against pitting corrosion.

Compared to Ti-based or Zr-based BMGs, Fe-based BMGs have very low costs, making them quite attractive for any large-scale biomedical applications. Moreover, they also have reasonably good glass-forming ability (GFA) and can be easily prepared by traditional Cu mold casting/cooling methods. However, up to date, most of developed Fe-based BMGs are soft magnetic materials as functional and structural materials, for example, power inductor and soft magnetic cores and not suitable for biomedical applications considering their magnetic properties. In clinical, magnetic resonance imaging (MRI) diagnosis is inhibited with the presence of magnetic implants in body because they become magnetized in the intense magnetic field of the MRI instrument, which may produce image artifacts and therefore prevent exact diagnosis. To decrease the artifacts, medical devices with low magnetic susceptibility are required. Nonmagnetic Fe-based BMGs were first developed by Ponnambalam et al. in 2003 and are called as "amorphous steel" [97] because their composition is similar to that of stainless steel, i.e., both of the stainless steel and amorphous steel contain Fe, C, Cr, and Mo elements. The amorphous steels have glass-forming ability high enough to form single-phase glassy rods with diameters reaching 16 mm [87]. The tensile fracture strengths of at least 3000 MPa, and high plastic strains up to 3.6% were obtained. The ductility of the Fe-based BMGs can be significantly enhanced by properly tuning the alloy compositions [90]. It is well known that conventional biomedical stainless steels (3l6L SS and 304 SS) are usually prone to localized attack and Ni ion release in long-term applications due to their poor corrosion resistance because of the aggressive biological effects [98]. The developed Fe-based BMGs have higher pitting potential values and lower corrosion current density values both in Hank's solution and in artificial saliva solution and have quite lower ion releasing than that of 316L SS [99].

2.3.3 Biodegradable Metallic Glasses

Besides the joint replacements that need permanent prosthesis implantation in the human body, there are many other clinical cases, such as bone fracture, cardiovascular diseases, in which the temporary implant materials are needed. The fixation or mechanical support are temporarily needed during the healing process of the injured or pathological tissue, and after that, the implants accomplish their mission and will no longer function in human body. In this case, biodegradable materials are the optimal choice as these materials do their job while healing and new tissue forming occur and degrade in the human body thereafter. As summarized in Table 2.4, the biodegradable BMG group includes members such as Mg-based BMGs, Ca-based BMGs, Zn-based BMGs, and Sr-based BMGs. Their alloy compositions, fabrication methods, and mechanical properties are summarized in Table 2.4 as well.

Table 2.4 Summary of biodegradable BMG alloy systems and their mechanical properties

BMG system	Alloys composition	Preparation method	Critical diameter (mm)	Compressive fracture strength (σ_f) (MPa)	Young's modulus (E) (GPa)	Vickers hardness (Hv) (kg mm^{-2})	Reference
Mg-based	Mg–Zn–Ca	Induction melting/Cu mold casting	1–5	700–930	47.6–48.2	220	[100–102]
		Spark plasma sintering (SPS)	over 15	–	–	–	[103]
	Mg–Zn–Ca–Ag	Induction melting/Cu mold casting	2	722–759	49–63	–	[104]
	Mg–Zn–Ca–Sr	Induction melting/Cu mold casting	4–6	787–848	48.5–49.4	250–256	[105]
	Mg–Cu–Gd	Spark plasma sintering (SPS)	over 15	–	–	73	[106]
	Mg–Cu–Y	Spark plasma sintering (SPS)	over 15	–	–	91	[106]
	Mg–Cu–Y–Si	Induction melting/Cu mold casting	2.6	–	~66	~408	[107]
Ca-based	Ca–Mg–Zn	Induction melting/Cu mold casting	0.9–6	~364	20–46	71–145	[108, 109]
	Ca–Mg–Zn–Sr–Yb	Induction melting/Cu mold casting	4	370	19.4	–	[110]
	Ca–Zn–Mg–Yb	Induction melting/Cu mold casting	2	600	31.9	–	[111]
	Ca–Zn–Mg–Li	Induction melting/Cu mold casting	5	530	23.4	138	[112]

(continued)

Table 2.4 (continued)

BMG system	Alloys composition	Preparation method	Critical diameter (mm)	Compressive fracture strength (σ_f) (MPa)	Young's modulus (E) (GPa)	Vickers hardness (Hv) (kg mm^{-2})	Reference
Zn-based	Zn–Ca–Mg–Yb	Induction melting/Cu mold casting	2	640–663	36.6	–	[111, 113]
Sr-based	Sr–Mg–Zn	Induction melting/Cu mold casting	3	–	19.7	–	[114]
	Sr–Mg–Zn–Li	Induction melting/Cu mold casting	3	–	18.4	–	[114]
	Sr–Mg–Zn–Yb–Cu	Induction melting/Cu mold casting	3	408	20.6	–	[115]

2.3.4 Porous Bulk Metallic Glasses

Developments of the large size and high strength BMGs without toxic and allergic elements make it possible to create BMG implants. However, one of the major problems concerning metallic implants in the orthopedic industry, especially with hip replacement implants, is the large mismatch (about an order of magnitude) between the Young's modulus of the metallic implant and that of cortical bone. The much higher stiffness of the metal carries a majority of any applied stresses, creating a stress shielding effect for the more compliant bone and leaving it effectively unstressed. Cortical bone, when left unstressed, resorbs into the body in a process termed as disuse atrophy. This resorption weakens the implant/cortical bone interface and can lead to implant loosening and the eventual need for a painful revision surgery. One way to overcome the problem is to reduce Young's modulus of metallic implants by introducing pores.

Oh et al. [116] reported that the porous Ti having Young's modulus comparable to the human bone was fabricated by hot-pressing method, while the strength was lower than that of bone. By spark plasma sintered the mixture of the gas-atomized Ti-based glassy alloy powders and solid salt (NaCl) powders, followed by leaching treatment into water to eliminate the salt phase, high strength, and large size (the diameter exceeding 15 mm) porous Ti-based BMGs with low Young's modulus, which is comparable to that of bone, were produced [117]. The pores are homogeneously distributed in the whole sintered samples. The porosity can be controlled by controlling the volume fraction of the adding salt phase. Corrosion behavior of the produced porous Ti-based BMG samples with various porosities was investigated by polarization process in Hanks' solution. The porous Ti-based BMGs with various porosities exhibited a similar polarization process. The potentiodynamic polarization curves showed that the anodic current density in the porous Ti-based BMGs slowly increased during anodic polarization, suggesting the crevice corrosion mechanism.

2.3.5 Summary of the Studies for Biomedical Engineering

In this section, recent progress in the developments of bulk metallic glasses (BMGs) for applications as biomaterials and biomedical materials was described and summarized. These biomedical BMGs were divided into two categories, namely, bioinert group and biodegradable group. The bioinert BMG group included Ti-based BMGs, Zr-based BMGs, and Fe-based BMGs. The biodegradable BMG group included Mg-based BMGs, Ca-based BMGs, Zn-based BMGs, and Sr-based BMGs. These BMGs did not contain toxic or non-biocompatible elements (e.g., Ni or Be), and exhibited high strength, high elastic strain limit, low Young's modulus, excellent corrosion resistance, and good biocompatibility. Using a spark plasma sintering (SPS) process, large-sized BMGs and porous BMGs having approximate Young's

modulus with that of bone were developed. These excellent properties make the BMGs become competent candidates for application to biomedical fields.

2.4 Low Magnetic Susceptibility Metallic Glasses for Magnetic Resonance Imaging

Ichiro Seki

2.4.1 Introduction

Implant materials are requiring high reliability mechanically for human actions. Because metallic materials have high mechanical strength and high corrosion resistance commonly, they are selected as the implant materials. In the human bodies, the implanted materials have to endure against corrosion caused by an ionic solution like biological fluid. Therefore, stainless steels, Co-Cr-based alloys, and Ti-based alloys, which are typically high corrosion resistance materials, are selected. On the other hand, in recent medical examinations, magnetic resonance imaging (MRI) technique is treated for high-quality diagnosis and early detection of serious diseases. At the medical examinations using magnetic resonance imaging (MRI) technique, the implanted materials cause fake images calling as artifacts [118, 119], and are often causing degradation of the quality of the medical examinations by the artifacts. The artifacts are caused strongly depending on magnitude of magnetization of the metallic materials, and are observableness for the stainless steels. The magnitude of magnetization is systematically compared by magnetic susceptibility for typical nonferrous metal without ferromagnetic materials. The magnetic susceptibilities of typical implant materials such as Co–Cr–Mo and Ti–6Al–4V alloys are known as $7.5 \times 10^{-6}\,\mathrm{cm^3\,g^{-1}}$ and $3.0 \times 10^{-6}\,\mathrm{cm^3\,g^{-1}}$, respectively [120]. In viewpoint of only low magnetic susceptibility, although the magnetic susceptibilities of ceramics such as Alfa-alumina whose magnetic susceptibility is $-0.363 \times 10^{-6}\,\mathrm{cm^3\,g^{-1}}$ [121] are suitable, ceramics have problem for reliability of mechanical strength. Particularly, ceramics is typically embrittlement and is weak for impact stress. In following sentences, from viewpoint of the metallic materials having low magnetic susceptibility, two kinds of metallic glasses, which are based on Zr and Mg, are briefly introduced.

2.4.2 Magnetic Susceptibility of Zr-Based Metallic Glass Alloys

Zirconium having high corrosion resistance and mechanical strength are suitable for the biomaterial material use. Moreover, the magnetic susceptibility of zirconium is lower than the recent titanium-based biomaterials and is quite low than the common

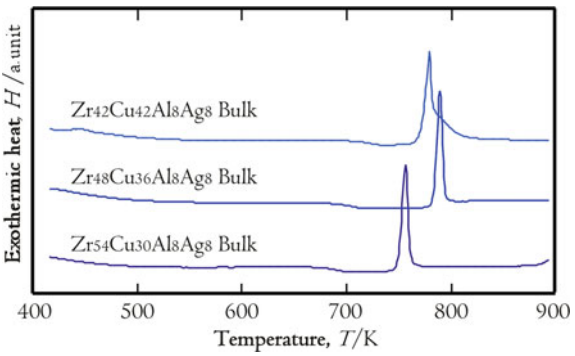

Fig. 2.15 Thermal properties of the $Zr_{54-X}Cu_{30+X}Al_8Ag_8$ metallic glasses at heating

metallic materials based on transition metals. Therefore, zirconium is one of desirable materials for MRI, because a problem of the artifacts caused by metallic materials becomes small. For the zirconium-based alloys of biomaterial material use, recently, Suyalatu et al. have reported Zr-based 3 at.%Mo containing alloy, whose magnetic susceptibility is 1.03×10^{-6} cm^3 g^{-1} [120]. Nomura et al. have also reported $Zr_{48}Cu_{36}Al_8Ag_8$ metallic glass alloy, whose magnetic susceptibility is 0.8×10^{-6} cm^3 g^{-1} [122]. The magnetic susceptibility of the Zr–Cu-based metallic glass alloys having typical high glass-forming ability [77] is also systematically reported as dependence of the alloy composition [123]. In this section, a relationship of the magnetic susceptibility and the alloy composition of metallic glass alloys are mentioned.

Figure 2.15 shows thermal properties of the $Zr_{54-X}Cu_{30+X}Al_8Ag_8$ metallic glass alloys at heating by constant heating ratio. A glass-forming ability of the metallic glasses is conveniently evaluated by magnitude of regions of ΔT, which is differential of a glass transition temperature (T_g) showed by a little endothermic behavior before crystallizations and crystallization temperature (T_c) showed by large exothermic behavior. Thus, the glass-forming ability of $Zr_{48}Cu_{36}Al_8Ag_8$ metallic glass alloy is highest in this series alloys, and is interpreted. On the other hand, the magnetic susceptibility is experimentally determined from a magnetization depending on magnitude of a magnetic field, and is listed in Table 2.5 for the $Zr_{54-X}Cu_{30+X}Al_8Ag_8$ metallic glass alloys. The magnitude of magnetic susceptibility of the alloys is slightly effected by shaping of the samples such as ribbon and bulk, but is mainly effected by the zirconium content of the alloys actually, i.e., the magnetic susceptibility of the alloys is linearly changed depending on the alloy composition rather than the magnitude of glass-forming ability of the metallic glass alloy.

The magnetic susceptibility of metallic martials of Pauli-type paramagnets is also conveniently expressed by simply sum of two contributions of the conduction electrons, χ_{free}, and ion in closed shell, χ_{ion}, as follows [124, 125]:

$$\chi_{est} = \chi_{free} + \chi_{ion}$$

$$\chi_{free} = 2/3 \cdot \mu_B^2 \cdot N(E_F)$$

Table 2.5 Magnetic susceptibilities of the $Zr_{54-X}Cu_{30+X}Al_8Ag_8$ metallic glass alloys

Alloy composition	Measured values		Estimated magnetic susceptibility $10^{-5} \times cm^3/mol$			Glass transition or crystallization temperature, T/K		
	χmeas $10^{-5} \times cm^3/mol$	γ mJ/molK^2	χ_{free}	χ_{ion}	χ_{est}	T_g	T_{x1}	ΔT_x
$Zr_{54}Cu_{30}Al_8Ag_8$ Bulk	9.256	2.377	13.654	−1.732	11.922	676.86	749.88	73.02
$Zr_{48}Cu_{36}Al_8Ag_8$ Bulk	8.288	2.052	11.786	−1.758	10.027	684.35	783.74	99.39
$Zr_{42}Cu_{42}Al_8Ag_8$ Bulk	6.897	1.651	9.485	−1.785	7.700	705.11	773.58	68.47
$Zr_{54}Cu_{30}Al_8Ag_8$ Ribbon	6.171	2.377	13.654	−1.732	11.922	–	–	–
$Zr_{48}Cu_{36}Al_8Ag_8$ Ribbon	4.957	2.052	11.786	−1.758	10.027	–	–	–
$Zr_{42}Cu_{42}Al_8Ag_8$ Ribbon	4.548	1.651	9.485	−1.785	7.700	–	–	–
$Zr_{36}Cu_{48}Al_8Ag_8$ Ribbon	3.558	1.212	6.962	−1.812	5.150	–	–	–
$Zr_{30}Cu_{54}Al_8Ag_8$ Ribbon	3.044	0.770	4.424	−1.839	2.585	–	–	–

$$N(E_F) = 3\gamma/2\pi^2 k_B^2$$

$$\chi_{ion} = -N_0 \cdot Z_e \cdot \mu_0 \cdot e^2 \cdot \left(r^2\right)/6m_0$$

Here, χ_{free} is expressed by μ_B and $N(E_F)$, which are Bohr magnetron and number of the electrons at the Fermi energy, respectively. Moreover, $N(E_F)$ can be expressed by γ and k_B, which are electronic specific heat coefficient and Boltzmann constant, respectively. From γ for the Zr–Cu binary amorphous alloys given by Garoche and Bigot [126], γ for the $Zr_{54-X}Cu_{30+X}Al_8Ag_8$ metallic glass alloys can be roughly expected. On the other hand, χ_{ion} is theoretically expressed by N_0, Z_e, μ_0, e, r, and m_0, which are Avogadro number, number of electrons in closed shell, permeability in vacuum, electric charge of an electron, radius of an electron orbit, and mass of electrons, respectively. The values of the χ_{ion} for general ion species have been systematically and theoretically determined by Angus et al. [127], and are listed in Table 2.5. The measured and estimated magnetic susceptibilities for the alloys are showing similar behavior depending on alloy composition, and are showing within same order. Consequently, the magnetic susceptibility of the alloy is only depending on the alloy composition except for alloy structure such as glassy structure, and it can be simply estimated theoretically.

2.4.3 Mg-Based Metallic Glasses for MRI

Desirable materials for MRI are requiring lower magnetic susceptibility explained in the previous part for Zr-based metallic glass alloys. The magnetic susceptibility of metallic glasses is basically depending on the alloy composition. Therefore, from the magnetic susceptibility of magnesium reported as 6.3×10^{-6} cm^3 mol^{-1} [121], it can be simply expected that the magnetic susceptibility of Mg-based metallic glasses is also low. On the other hand, because a corrosion resistance of the magnesium is quite low in a quasi-biometric solutions, i.e., an absorption rate of magnesium into a human body is quite fast, it is ordinary considered that a treatment of the magnesium is difficult for a bone replacement material. However, the faster absorption rate of magnesium is also focused for the bone replacement material of a self-extinction type. The bone replacement material is usually substituted for a broken bone in human body by a medical treatment, and the material will become unnecessarily depending on the healing of the affected part. If conventional implant materials are used inside a human body to repair bone-fractures, they should be removed by a second surgery after completion of osteosynthesis. But it is so painful for the patients to undergo a surgery again. Herein, in the case of treating of the self-extinction materials made by the magnesium-based material, the medical treatment to remove the substitution becomes unnecessary, i.e., from a point of view of a regenerative medicine, resolvability materials such kinds of magnesium-based materials become suitable with controlling of corrosion

Table 2.6 Magnetic susceptibility of the Mg–Zn metallic glasses

Alloy composition	Density 10^3 kg/m^3	Measured values χmeas $10^{-5} \times$ cm^3/mol	Atomic weight g/mol	e/a	Estimated magnetic susceptibility $10^{-5} \times$ cm^3/mol		
					χ_{free}	χ_{ion}	χ_{est}
$Mg_{75}Zn_{25}$	2.685	1.629	34.58	4.50	1.127	−0.603	0.524
(2nd)		0.888	35.40	4.70			
$Mg_{73}Zn_{27}$	2.773		35.40	4.70	1.137	−0.62812	0.509
Mg70Zn30	2.979	0.749	36.63	5.00	1.132	−0.6658	0.467
(2nd)		0.416					
$Mg_{67}Zn_{33}$	3.149	0.294	37.87	5.30	1.137	−0.70348	0.434
(2nd)		0.599					
(3rd)		0.852					
(4th)		0.605					
$Mg_{64}Zn_{36}$	3.173	0.642	39.10	5.60	1.178	−0.74116	0.436
$Mg_{61}Zn_{39}$	–	0.631	40.33	5.90		−0.77884	–
$Mg_{66}Zn_{29}Ag_5$	3.370	0.396	42.68	5.37	1.183	−0.85223	0.330
$Mg_{65}Zn_{30}Ca_5$	2.906	0.538	37.42	5.00	1.168	−0.70345	0.464
$Mg_{65}Zn_{30}Ca_4Ag_1$	3.081	0.416	38.10	5.09	1.143	−0.73514	0.408
$Mg_{63}Zn_{30}Ca_4Ag_3$	3.148	0.393	39.77	5.27	1.173	−0.81358	0.360

resistance in human body. In this section, the magnetic susceptibility of the magnesium-based alloys is mentioned.

Table 2.6 lists magnetic susceptibilities of measured and expected values of Mg–Zn metallic glass alloys. The measured values are determined by superconducting quantum interference device (SQUID) magnetometer at 300 K up to 2 T (20 kOe). The estimated values are determined by the relation "$\chi_{est} = \chi_{free} + {}_{ion}$" similar with the relation mentioned for the Zr-based metallic glass alloys. Here, χ_{free} is estimated from the previous relation, and is also estimated from the following equation [124]:

$$\chi_{free} = 2/3 \cdot \mu_B^2 \cdot N(E_F) \approx 1.243 \times 10^{-6}(A/\rho)^{2/3}(e/a)^{1/3}$$

Here, A, ρ, and e/a are atomic weight, density, and a number of the electrons per atom. The χ_{ion} can be determined by the manner of Angus et al. [127]. For the composition dependence of the estimated magnetic susceptibility of the alloys, because the magnetic susceptibility of zinc is -9.15×10^{-6} cm^3 mol^{-1} [121], the magnetic susceptibility of that becomes small slightly depending on increasing of zinc content. Moreover, the estimated magnetic susceptibilities of the alloys are also corresponding to the measured values within same order. However, because the magnetic susceptibility of Mg-based metallic glasses is small enough, the difference of that seems to be hiding in error ranges of the measured magnetic susceptibilities of the alloy in this case.

For an application of the magnesium and magnesium-based alloys as the bone replacement material, the corrosion resistance of magnesium and magnesium alloys is quite small, and the magnesium in human body is reacted with a water expressed by the following reaction [128]:

$$Mg + 2H_2O = Mg(OH)_2 + H_2$$

Here, although the magnesium is known as harmlessness and one of essential elements for the human body, and is effective for bone metabolism, a dissolution rate of a substitution materials made of the pure magnesium into human body is commonly 3 or 4 times faster than a bone replacement rate [129]. Moreover, because much hydrogen gas is generated in human body faster than an absorption rate into the human body, an air bubble is formed, and it is desirable to avoid the phenomena. Therefore, when the magnesium alloy as the bone replacement material is treating, increasing the corrosion resistance to decrease the dissolution rate in the human body is necessary. The corrosion resistance of magnesium-based metallic glass alloys has been investigated by Qin et al. [104], and is reported to be delayed by a doped calcium and silver. The magnetic susceptibility for the calcium and silver-doped Mg-based metallic glasses is also investigated and is listed in Table 2.6. From the comparison, because the effect of the doped calcium and silver for the magnetic susceptibility is not significant, the manner of calcium and silver dope for the Mg-based metallic glasses is effective for increasing of corrosion resistance with saving of the magnetic property influencing for MRI.

References

1. J. Larminie, A. Dicks, *Fuel Cell Systems Explained*, 2nd edn. (Wiley, UK, 2003)
2. The Chemical Society of Japan (ed.), *Fuel Cell* (Maruzen, Tokyo, 2005)
3. H. Tsuchiya, O. Kobayashi, Int. J. Hydrog. Energy **29**, 985 (2004)
4. A. Inoue, T. Shimizu, S. Yamaura, Y. Fujita, S. Takagi, H.M. Kimura, Mater. Trans. **46**, 1706 (2005)
5. M. Naka, K. Hashimoto, T. Masumoto, J. Non-Cryst. Solids **34**, 257 (1979)
6. H. Yoshioka, K. Asami, A. Kawashima, K. Hashimoto, Corros. Sci. **27**, 981 (1987)
7. M. Yokoyama, S. Yamaura, H.M. Kimura, A. Inoue, Mater. Trans. **48**, 3176 (2007)
8. S.C. Kim, S. Yamaura, Y. Shimizu, K. Nakashima, T. Igarashi, A. Makino, A. Inoue, Mater. Trans. **51**, 1609 (2010)
9. S.C. Kim, S. Yamaura, T. Igarashi, Y. Shimizu, K. Nakashima, A. Makino, A. Inoue, J Japan Inst Meals **75**, 122 (2011). (in Japanese)
10. S. Yamaura, K. Katsumata, M. Hattori, T. Yogo, Mater. Trans. **54**, 1324 (2013)
11. M. Hattori, S. Yamaura, W. Zhang, W. Sakamoto, T. Yogo, J. Membr. Sci. **488**, 166 (2015)
12. W. Zhang, H. Guo, M.W. Chen, Y. Saotome, C.L. Qin, A. Inoue, Scripta Mater. **61**, 744 (2009)
13. H. Guo, W. Zhang, C.L. Qin, J.B. Qiang, M.W. Chen, A. Inoue, Mater. Trans. **50**, 1290 (2009)
14. E. Guo, W. Zhang, M.W. Chen, Y. Saotome, M. Fukuhara, A. Inoue, Metall. Mater. Trans. **A42**, 1486 (2011)
15. S. Yamaura, Y. Shimpo, H. Okouchi, M. Nishida, O. Kajita, H.M. Kimura, A. Inoue, Mater. Trans. **44**, 1885 (2003)
16. S. Yamaura, M. Sakurai, M. Hasegawa, K. Wakoh, Y. Shimpo, M. Nishida, H.M. Kimura, E. Matsubara, A. Inoue, Acta Mater. **53**, 3703 (2005)
17. S. Yamaura, S. Uemiya, H.M. Kimura, A. Inoue, Mater. Sci. For. **561–565**, 1319 (2007)
18. A. Yokoyama, H. Komiyama, H. Inoue, T. Masumoto, H.M. Kimura, J. Catalysis. **68**, 355 (1981)
19. Z.H. Dan, F.X. Qin, T. Wada, S. Yamaura, G.Q. Xie, Y. Sugawara, I. Muto, A. Makino, N. Hara, Electrochim. Acta **108**, 512 (2013)
20. Z.H. Dan, F.X. Qin, S. Yamaura, Y. Sugawara, I. Muto, N. Hara, J. Alloy. Compd. **581**, 567 (2013)
21. Z.H. Dan, F.X. Qin, S. Yamaura, G.Q. Xie, A. Makino, N. Hara, J. Electrochem. Soc. **161**, C120 (2014)
22. M. Zhao, K. Abe, S. Yamaura, Y. Yamamoto, N. Asao, Chem. Mater. **26**, 1056 (2014)
23. M. Ozawa, S. Kato, K. Kobayashi, T. Yogo, S. Yamaura, Jpn. J. Appl. Phys. **55**, 01AG05 (2016)
24. M. Ozawa, T. Yogo, S. Yamaura, J. Jpn. Soc. Powder Metallurgy. **63**, 29 (2016)
25. Y. Kawahito, T. Terajima, H. Kimura, T. Kuroda, K. Nakata, S. Katayama, A. Inoue, Mater. Sci. Eng., B **148**, 105 (2008)
26. T. Tsumura, S. Hamada, H.M. Kimura, A. Inoue, K. Nakata, Trans. JWRI **40**, 45 (2011)
27. M. Watanabe, S. Kumai, Hagimoto, G.Q. Zhang, K. Nakayama, Mater. Trans. **50**, 1279 (2009)
28. Y. Kawahito, Y. Niwa, T. Terajima, S. Katayama, Mater. Trans. **51**, 1433 (2010)
29. U. Mizutani, *Introduction to the Electron Theory of Metals*. Cambridge University Press (2001)
30. J.H. Mooij, Phys. Status Solidi A **17**, 521–530 (1973)
31. U. Mizutani, Prog. Mater Sci. **28**, 97–228 (1983)
32. U. Mizutani, Phys Stat Solidi (b) **176**, 9–30 (1993)
33. G. Baym, Phys. Rev. **135A**, 1691–1692 (1964)
34. L.V. Meisel, P.J. Cote, Phys. Rev. B **16**, 2978–2980 (1977)
35. L.V. Meisel, P.J. Cote, Phys. Rev. B **17**, 4652–4659 (1978)

36. N.F. Mott, H. Jones, *The Theory of the Properties of Metals and Alloys* (Clarendon Press, Oxford, 1936)
37. J.M. Ziman, Phil. Mag. **6**, 1013–1034 (1965)
38. T.E. Faber, J.M. Ziman, Phil. Mag. **11**, 153–173 (1965)
39. R. Evans, D.A. Greenwood, P. Lloyd, Phys. Lett. **35A**, 57–58 (1971)
40. S.R. Nagel, J. Vassiliou, P.M. Horn, B.C. Giessen, Phys. Rev. B **17**, 462–467 (1978)
41. H. Kimura, A. Inoue, S. Yamaura, K. Sasamori, M. Nishida, Y. Shinpo, H. Okouchi **44**, 1167–1171 (2003)
42. R.Y. Umetsu, H. Yoshida, M. Fukuhara, S. Yamaura, M. Matsuura, T. Sasaki, T. Sekiguchi, M. Saito, J. Mizuno, H. Kawarada, Mater. Trans. **54**, 1339–1342 (2013)
43. R.Y. Umetsu, H. Yoshida, M. Fukuhara, S. Yamaura, T. Sasaki, T. Sekiguchi, M. Saito, J. Mizuno, H. Kawarada, Open J. Metal. **3**, 45–49 (2013)
44. A. Kawahima, S. Yamaura, N. Ohtsu, H. Kimura, A. Inoue, Mater. Trans. **47**, 1523–1526 (2006)
45. H. Koike, Y. Shizuku, A. Yazaki, Y. Fukai, J. Phys.: Condens. Matter **16**, 1335–1349 (2004)
46. J. Crank, *The Mathematics of Diffusion* (Clarendon Press, Oxford, 1975)
47. T. Iida, Y. Yamazaki, T. Kobayashi, Y. Iijima, Y. Fukai, Acta Mater. **53**, 3083–3089 (2005)
48. M. Fukuhara, A. Kawashima, S. Yamaura, A. Inoue, Appl. Phys. Lett. **90**, 203111 (2007)
49. M. Fukuhara, H. Yoshida, K. Koyama, A. Inoue, Y. Miura, J. Appl. Phys. **107**, 033703 (2010)
50. M. Long, H.J. Rack, Biomater. **19**, 1621 (1998)
51. M. Niinomi, Metall. Mater. Trans. A **33**, 477 (2002)
52. M. Geetha, A.K. Singh, R. Asokamani, A.K. Gogia, Prog. Mater. Sci. **54**, 397 (2009)
53. Y.F. Zheng, X.N. Gu, F. Witte, Mater. Sci. Eng., R **77**, 1 (2014)
54. A. Inoue, A. Takeuchi, Acta Mater. **59**, 2243 (2011)
55. A. Inoue, Acta Mater. **48**, 279 (2000)
56. W.L. Johnson, MRS Bull. **24**, 42 (1999)
57. L.L. Hench, Sci. **208**(4446), 826 (1980)
58. S.L. Zhu, X.M. Wang, F.X. Qin, A. Inoue, Mater. Sci. Eng., A **459**, 233 (2007)
59. S.L. Zhu, X.M. Wang, F.X. Qin, M. Yoshimura, A. Inoue, Mater. Trans. **48**, 2445 (2007)
60. J.J. Oak, D.V. Louzguine-Luzgin, A. Inoue, J. Mater. Res. **22**, 1346 (2007)
61. S.L. Zhu, X.M. Wang, A. Inoue, Intermet. **16**, 1031 (2008)
62. S.L. Zhu, G.Q. Xie, F.X. Qin, X.M. Wang, A. Inoue, Mater. Trans. **53**, 500 (2012)
63. G.Q. Xie, F.X. Qin, S.L. Zhu, A. Inoue, Intermet. **29**, 99 (2012)
64. F.X. Qin, X.M. Wang, G.Q. Xie, A. Inoue, Intermet. **16**, 1026 (2008)
65. J.J. Oak, D.V. Louzguine-Luzgin, A. Inoue, Mater. Sci. Eng., C **29**, 322 (2009)
66. F.X. Qin, G.Q. Xie, Z.H. Dan, A. Inoue, Appl. Mech. Mater. **148–149**, 241 (2012)
67. F.X. Qin, G.Q. Xie, S.L. Zhu, Z.H. Dan, Mater. Sci. Forum **750**, 23 (2013)
68. S.L. Zhu, G.Q. Xie, A. Inoue, Z.D. Cui, X.J. Yang, W. Zhang, Mater. Sci. Forum **833**, 79 (2015)
69. G. Wang, H.B. Fan, Y.J. Huang, J. Shen, Z.H. Chen, Mater. Des. **54**, 251 (2014)
70. S.J. Pang, Y. Liu, H.F. Li, L.L. Sun, Y. Li, T. Zhang, J. Alloys Compd. **625**, 323 (2015)
71. K. Jin, J.F. Löffler, Appl. Phys. Lett. **86**, 241909 (2005)
72. Q.S. Zhang, W. Zhang, G.Q. Xie, D.V. Louzguine-Luzgin, A. Inoue, Acta Mater. **58**, 904 (2010)
73. Z. Liu, K.C. Chan, L. Liu, J. Alloys. Compd. **487**, 152 (2009)
74. Y. Liu, Y.M. Wang, H.F. Pang, Q. Zhao, L. Liu, Acta Biomater. **9**, 7043 (2013)
75. N.B. Hua, L. Huang, W.Z. Chen, W. He, T. Zhang, Mater. Sci. Eng., C **44**, 400 (2014)
76. L. Liu, C.L. Qiu, C.Y. Huang, Y. Yu, H. Huang, S.M. Zhang, Intermet. **17**, 235 (2009)
77. Q.S. Zhang, W. Zhang, A. Inoue, Mater. Trans. **48**, 629 (2007)
78. Q.S. Zhang, W. Zhang, A. Inoue, Mater. Trans. **48**, 1272 (2007)
79. T. Wada, F.X. Qin, X.M. Wang, M. Yoshimura, A. Inoue, N. Sugiyama, R. Ito, N. Matsushita, J. Mater. Res. **24**, 2941 (2009)

80. A. Kawashima, T. Wada, K. Ohmura, G.Q. Xie, A. Inoue, Mater. Sci. Eng., A **542**, 140 (2012)
81. S.L. Zhu, G.Q. Xie, H. Wang, F.X. Qin, AIP Conf. Proc. **1518**, 668 (2013)
82. B.R. Guan, X.T. Shi, Z.H. Dan, G.Q. Xie, M. Niinomi, F.X. Qin, Intermet. **72**, 69 (2016)
83. C.L. Qiu, Q. Chen, L. Liu, K.C. Chan, J.X. Zhou, P.P. Chen, S.M. Zhang, Scr. Mater. **55**, 605 (2006)
84. S.L. Zhu, G.Q. Xie, F.X. Qin, X.M. Wang, A. Inoue, J. Mech. Behav. Biomed. Mater. **13**, 166 (2012)
85. L. Li, L.L. Shi, Z.D. Zhu, Q. He, H.J. Ai, J. Xu, Mater. Sci. Eng., C **33**, 2113 (2013)
86. Z. Liu, K.C. Chan, L. Liu, Mater. Trans. **52**, 61 (2011)
87. J. Shen, Q.J. Chen, J.F. Sun, H.B. Fan, G. Wang, Appl. Phys. Lett. **86**, 151907 (2005)
88. X.J. Gu, S.J. Poon, G.J. Shiflet, Scr. Mater. **57**, 289 (2007)
89. X.J. Gu, S.J. Poon, G.J. Shiflet, J. Mater. Res. **22**, 344 (2007)
90. X.J. Gu, S.J. Poon, G.J. Shiflet, M. Widom, Acta Mater. **56**, 88 (2007)
91. H. Fang, X. Hui, G. Chen, J. Alloys Compd. **464**, 292 (2008)
92. G.Q. Xie, F.X. Qin, S.L. Zhu, Mater. Trans. **54**, 1314 (2013)
93. M.L. Morrison, R.A. Buchanan, A. Peker, P.K. Liaw, J.A. Horton, J. Non-Cryst. Solids **353**, 2115 (2007)
94. F.X. Qin, S.L. Zhu, Z.H. Dan, A. Kawashima, G.Q. Xie, J. Alloys Compd. **615**, S123 (2014)
95. L. Liu, C.L. Qiu, Q. Chen, S.M. Zhang, J. Alloys Compd. **425**, 268 (2006)
96. N. Hua, L. Huang, J. Wang, Y. Cao, W. He, S. Pang et al., J. Non-Cryst. Solids **358**, 1599 (2012)
97. V. Ponnambalam, S.J. Poon, G.J. Shiflet, V.M. Keppens, R. Taylor, G. Petculescu, Appl. Phys. Lett. **83**, 1131 (2003)
98. M.H. Fathi, M. Salehi, A. Saatchi, V. Mortazavi, S.B. Moosavi, Dent. Mater. **19**, 188 (2003)
99. Y.B. Wang, H.F. Li, Y. Cheng, S.C. Wei, Y.F. Zheng, Electrochem. Commun. **11**, 2187 (2009)
100. X.J. Gu, G.J. Shiflet, F.Q. Guo, S.J. Poon, J. Mater. Res. **20**, 1935 (2005)
101. Y.Y. Zhao, E. Ma, J. Xu, Scr. Mater. **58**, 496 (2008)
102. B. Zberg, P.J. Uggowitzer, J.F. Löffler, Nat. Mater. **8**, 887 (2009)
103. F.X. Qin, Z.H. Dan, G.Q. Xie, Mater. Sci. Forum **783–786**, 1931 (2014)
104. F.X. Qin, G.Q. Xie, Z.H. Dan, S.L. Zhu, I. Seki, Intermet. **42**, 9 (2013)
105. H.F. Li, S.J. Pang, Y. Liu, L.L. Sun, P.K. Liaw, T. Zhang, Mater. Des. **67**, 9 (2015)
106. F.O. Méar, G.Q. Xie, D.V. Louzguine-Luzgin, A. Inoue, Mater. Trans. **50**, 588 (2009)
107. K.M. Liu, H.T. Zhou, B. Yang, D.P. Lu, A. Atrens, Mater. Sci. Eng., A **527**, 7475 (2010)
108. G. Wang, P.K. Liaw, O.N. Senkov, D.B. Miracle, M.L. Morrison, Adv. Eng. Mater. **11**, 27 (2009)
109. J.D. Cao, N.T. Kirkland, K.J. Laws, N. Birbilis, M. Ferry, Acta Biomater. **8**, 2375 (2012)
110. H.F. Li, X.H. Xie, K. Zhao, Y.B. Wang, Y.F. Zheng, W.H. Wang et al., Acta Biomater. **9**, 8561 (2013)
111. W. Jiao, H.F. Li, K. Zhao, H.Y. Bai, Y.B. Wang, Y.F. Zheng et al., J. Non-Cryst. Solids **357**, 3830 (2011)
112. J.F. Li, D.Q. Zhao, M.L. Zhang, W.H. Wang, Appl. Phys. Lett. **93**, 171907 (2008)
113. W. Jiao, K. Zhao, X.K. Xi, D.Q. Zhao, M.X. Pan, W.H. Wang, J. Non-Cryst. Solids **356**, 1867 (2010)
114. K. Zhao, J.F. Li, D.Q. Zhao, M.X. Pan, W.H. Wang, Scr. Mater. **61**, 1091 (2009)
115. H.F. Li, K. Zhao, Y.B. Wang, Y.F. Zheng, W.H. Wang, J. Biomed. Mater. Res. B **100**, 368 (2012)
116. I.H. Oh, N. Nomura, N. Masahashi, S. Hanada, Scr. Mater. **49**, 1197 (2003)
117. G.Q. Xie, F.X. Qin, S.L. Zhu, D.V. Louzguine-Luzgin, Intermet. **44**, 55 (2014)
118. J. Olsrud, J. Latt, S. Brockstedt, B. Romner, I.M. Bjorkman-Burtscher, J Magn. Reson. Imaging **22**, 433 (2005)
119. F. Shafiei, E. Honda, H. Takahashi, T. Sasaki, J. Dent. Res. **82**, 602 (2003)

120. Suyalatu, R. Kondo, Y. Tsutsumi, H. Doi, N. Nomura, T. Hanawa, Acta Biomater. **7**, 4259 (2011)
121. The Chemical Society of Japan, *Handbook of Chemistry Basic Crochet II* (Maruzen Co., 2004), p. 633 (in Japanese)
122. N. Nomura, G.Q. Xie, K. Son, Y. Tsutsumi, H. Doi, A. Inoue, T. Hanawa, *Proceedings of the Visual-JW2010* (2010), p. 326
123. I. Seki, R.Y. Umetsu, G.Q. Xie, N. Nomura, X.M. Wang, T. Hanawa, Mater. Trans. **54**, 1356 (2013)
124. U. Mizutani, *Introduction to the Electron Theory of Metals* (Cambridge University Press, 2001), p. 44
125. K. Oki, T. Eguchi, *Fundamental of Electron Theory of Metals* (Uchidaroukakuho, 2003), p. 69 (in Japanese)
126. P. Garoche, J. Bigot, Phys. Rev. B **28**, 6886 (1983)
127. W.R. Angus, Proc. R. Soc. Lond. **A136**, 569 (1932)
128. M.P. Staiger, A.M. Pietak, J. Huadmai, G. Dias, J. Biomater. **27**, 1728 (2006)
129. The Japan Institute of Metals, *Metals for Medicine* (The Japan Institute of Metals, 2010), p. 137 (in Japanese)

Chapter 3
Ti-Based Biomedical Alloys

Mitsuo Niinomi and Masaaki Nakai

Abstract Titanium (Ti) and its alloys are currently getting much attention for structural biomaterials, because they are much advantageous as compared with other metallic biomaterials such as biomedical stainless steels and Co-based alloys, and their practical uses in implant devices are widely spreading. In this paper, types of Ti alloys for biomedical applications are first described. Pure Ti, (α + β)-type, and β-type Ti alloys for biomedical applications including general β-type Ti alloys, superelastic and shape-memory β-type Ti alloys, Young's modulus self-adjustable β-type Ti alloys, and β-type Ti alloys for reconstructive implants are then described.

Keywords Titanium alloy · Superelasticity · Shape-memory effect · Young's modulus self-adjustability · Reconstructive implants

3.1 Introduction

Titanium (Ti) and its alloys are attracting a lot of attention for biomedical applications such as implants for failed bone replacement, which are shown in Fig. 3.1 [1], because they exhibit excellent specific strength and corrosion resistance, no allergic problems, and the best biocompatibility among the metallic biomaterials. Pure Ti and Ti-6Al-4V ELI are still the most widely used for biomedical applications among the Ti alloys, and they occupy most of the market of Ti-based

M. Niinomi (✉)
Institute for Materials Reserach, Tohoku University, Sendai, Japan
e-mail: niinomi@imr.tohoku.ac.jp

Graduate School of Science and Technology, Meijo University, Nagoya, Japan

Graduate School of Engineering, Osaka University, Osaka, Japan

Institute of Materials and Systems for Sustainability, Nagoya University, Nagoya, Japan

M. Nakai
Faculty of Science and Technology, Kindai University, Osaka, Japan

Y. Setsuhara et al. (eds.), *Novel Structured Metallic and Inorganic Materials*, https://doi.org/10.1007/978-981-13-7611-5_3

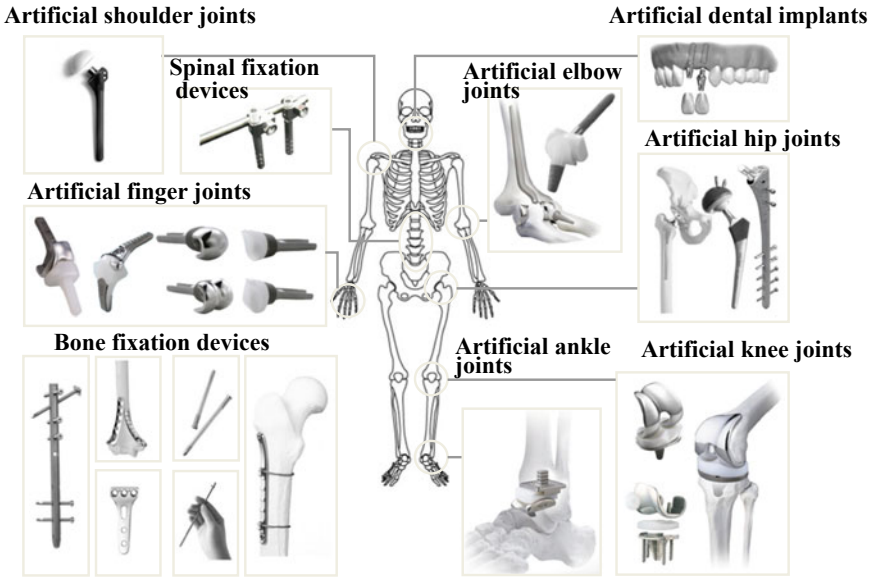

Fig. 3.1 Schematic drawings of various implants for replacing failed hard tissue. Reprinted from Ref. [1], Copyright 2010, with permission from The Japan Institute of Metals and Materials

biomaterials. However, these alloys were basically optimized to be structural materials for aerospace applications. Therefore, Ti alloys for biomedical applications are required, and hence, research on Ti alloys composed of nontoxic and allergy-free elements is being pursued and was started [2–4]. Ti alloys containing nontoxic and allergy-free elements developed in the early stages are mainly ($\alpha + \beta$)-type. Afterward, the mechanical biocompatibility of the biomaterials was considered as an important factor and, therefore, research of β-type Ti alloys, which are advantageous from that point of view began and is still increasing [1, 5, 6].

Among all the studies addressing this topic, the developments of materials for biomedical applications such as the developments of new Ti alloys exhibiting superelasticity and shape-memory Ti alloys composed of nontoxic elements are attracting a lot of attentions [7–12]. These superelastic or shape-memory characteristics are expected to result in new applications of these metallic materials other than the medical field.

Focusing on the spinal devices, in order to satisfy the demands of both surgeons, demanding materials with a high Young's modulus, and patients, who need materials with a low Young's modulus, Young's modulus-adjustable β-type Ti alloys are being developed.

Furthermore, the direct or indirect evaluation of biocompatibility using animals [13] or cells [14, 15], and the measurement of the mechanical performance [16–18] using indicators such as fatigue, fretting fatigue, and fracture toughness are also intensely studied.

Three groups of Ti and its alloys (commercially pure Ti (CP-Ti), (α + β)-type Ti alloys, and β-type Ti alloys) for biomedical applications are discussed in this section. Biomedical instruments made of Ti and its alloys are introduced.

3.2 Types of Ti Alloys for Biomedical Applications

Titanium alloys are generally classified into α-type, (α + β)-type, and β-type according to their primary constitutional phases. The α-type Ti alloys are composed of single-phase α-microstructures, while the β-type Ti alloys are composed of single-phase β-microstructures. The (α + β)-type Ti alloys are composed of two-phase (α + β)-microstructures. The α- and β-phases have hexagonal close-packed (hcp) and body-centered cubic (bcc) structures, respectively: the latter possessing a lower atomic density than the former. These characteristics are depicted in Fig. 3.2 [19]. The three phases appear according to the stability of the Ti phase, which changes with the β-stabilizing elements, as shown in Fig. 3.3. Between the stable α- and β-phases, the metastable α′ martensite with an hcp structure, the α″ martensite with an orthorhombic structure, and the ω-phase with a hexagonal or trigonal structure can be formed.

Therefore, the Young's modulus, which is a very important property from the viewpoint of mechanical biocompatibility with the bone, is typically smaller in β-type Ti alloys than in α- or (α + β)-type Ti alloys.

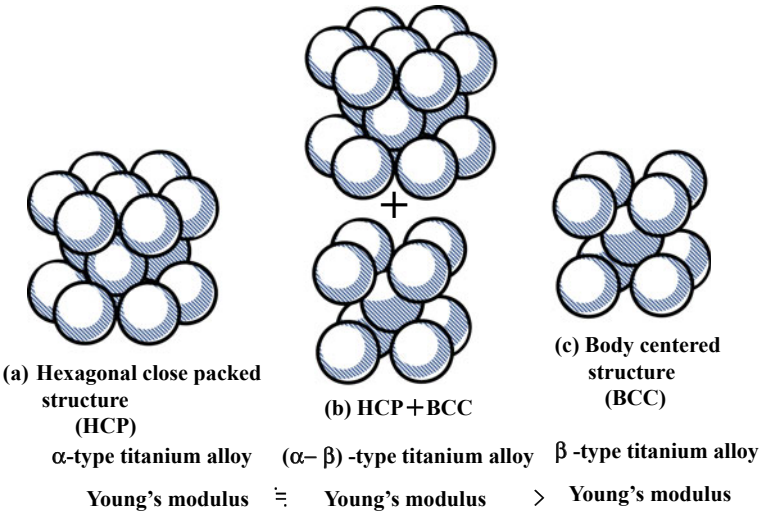

Fig. 3.2 Schematic explanation of α-, (α + β)-, and β-type titanium alloys based on crystal structure, and order of largeness of Young's modulus [19]

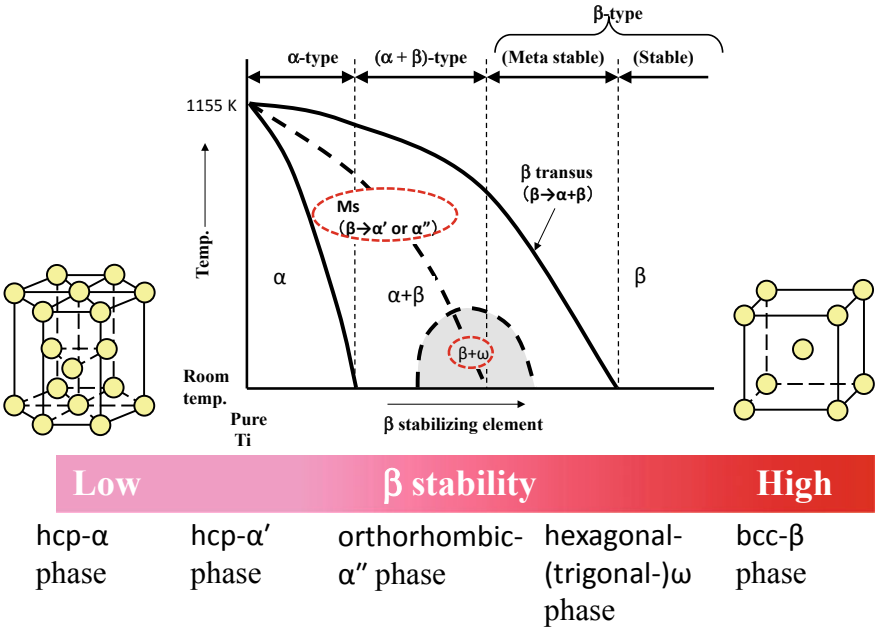

Fig. 3.3 Relationship between schematic phase diagram of titanium alloys and β stability

3.3 Pure Ti

Four grades Ti for implant devices are ASTM standardized, which is the standard specification for unalloyed Ti for surgical implant applications (UNS R50250, UNS R50400, UNS R50550, UNS R50700) designated as ASTM F67 [20]. They are also standardized as per ISO and JIS designated as ISO 5832-2 [21] and JIS T 7401-1 [22], respectively. The chemical compositions of these four-grade pure Ti materials are listed in Table 3.1 [20]. The content of impurities, such as nitrogen (N), iron (Fe), and oxygen (O) increase by increasing the number of the grade. For pure Ti, the increase in the content of impurities leads to a rise in the strength and to a decrease in the elongation (ductility). Therefore, the strength increases as ductility decreases when the number of the grade in pure Ti is increased.

3.4 (α + β)-Type Ti Alloys

Pure Ti and its alloys such as Ti-6Al-4V extra low interstitial (ELI) are widely used for biomedical applications. Ti-6Al-4V ELI is a (α + β)-type Ti alloy. Ordinary Ti-6Al-4V, which is a common purity alloy, is also used for biomedical

Table 3.1 Chemical requirements for four-grade pure titanium

Element	Composition, mass%			
	Grade 1 (UNS R50250)	Grade 2 (UNS R50400)	Grade 3 (UNS R50550)	Grade 4 (UNS R50700)
Nitrogen, max	0.03	0.03	0.05	0.05
Carbon, max	0.08	0.08	0.08	0.08
Hydrogen, max	0.015	0.015	0.015	0.015
Iron, max	0.20	0.30	0.30	0.50
Oxygen, max	0.18	0.25	0.35	0.40
Titanium	Balance	Balance	Balance	Balance

Reprinted from Ref. [20], with permission from ASTM

applications. These two alloys are standardized as per ASTM F136 (UNS R56401), [23] and F1472 (UNS R56400) [24], respectively. Ti-6Al-4V ELI is also standardized in ISO designated as per ISO 5832-3 [25], while Ti-6Al-4V is standardized as per in JIS, designated as JIS T 7401-2 [26]. Ti-3Al-2.5V is standardized for biomedical applications as per ASTM designated as ASTM F-2146 (UNS R56320) [27]. Pure Ti and α + β type Ti alloys, including Ti-6Al-4V ELI, Ti-6Al-4V, and Ti-3Al-2.5V were originally designed to be used as in the general structural materials in particular for aerospace structures and only later they were adopted for biomedical applications.

The toxicity of the β stabilizing element of V was later realized [28, 29]. Therefore, V in the Ti-6Al-4V was replaced by another β stabilizing element such as Fe or Nb, which are considered to be safer for the body as compared to V. Ti-5Al-2.5Fe and Ti-6Al-7Nb, which are also (α + β)-type Ti alloys, have been introduced [30]. Ti-5Al-2.5Fe has been registered in the ISO standardization only (ISO 5832) [31], while Ti-6Al-7Nb has been registered in ASTM (ASTM F 1295 (UNS R56700), ISO (ISO 5832-11), and JIS (JIS T7401-5) standardizations [32–34]. Therefore, it can be said that the development of Ti alloys optimized for implantation in living bodies began with the introduction of these alloys. Based on the same concept, other (α + β)-type biomedical Ti alloys like Ti-6Al-6Nb-1Ta and Ti-6Al-2Nb-1Ta have been proposed [35, 36]. The latter was originally produced to be structural Ti alloy for military use, and then has been registered in JIS standardization (JIS T7401-3) [37]. Subsequently, (α + β)-type Ti alloys that do not contain V or Al, namely Ti-15Zr-based and Ti-15Sn-based alloys were developed such as Ti-15Sn-4Nb-2Ta-0.2Pd and Ti-15Zr-4Nb-2Ta-0.2Pd [38]. Ti-15Zr-based alloy has been registered in JIS standardization (JIS T7401-4) [39].

3.5 β-Type Ti Alloys

3.5.1 General β-Type Ti Alloys

Stress shielding is an inhomogeneous stress transfer between the implant and the bone. The stress transfers predominantly through the implant because the modulus (Young's modulus) of the metal implant is generally much higher than that of bone. This effect leads to bone absorption, which causes the loosening of the implant or refracture of the bone after the implant removal. Therefore, a metallic biomaterial with a similar modulus to that of the bone (i.e., a low-modulus metallic biomaterial) was required. The moduli of the Ti alloys are the lowest among the main metallic biomaterials [30]. The elastic modulus of the (α + β)-type Ti-6Al-4V (around 110 GPa) is much lower than those of stainless steel and Co-based alloys (around 180 and 210 GPa, respectively) [40]. As mentioned above, Ti alloys are classified into α-type, (α + β)-type, and β-type alloys. The moduli of the β-type titanium alloys is lower than those of the α-type and (α + β)-type alloys because the crystal structure of the α phase (main component phase of the α-type Ti alloys) is hexagonal close-packed (hcp), while that of the β phase (main component phase of the β-type titanium alloys) is body-centered cubic (bcc). Thus, low-modulus β-type Ti alloys for biomedical applications are being developed.

The low-modulus Ti alloys developed for biomedical applications are all β-types containing nontoxic and allergy-free elements. The first low-modulus β-type Ti alloy developed for biomedical applications was Ti-13Nb-13Zr [41], which is registered in the ASTM standard designated as ASTM F1713 [42]. Other similar alloys were then developed, such as Ti-12Mo-6Zr-2Fe (TMZF) [43] registered in ASTM standard (ASTM F1813 (UNS R58120)) [44], Ti-15Mo [45] registered in ASTM (ASTM F2066) (UNS R58150) [46], Ti-16Nb-10Hf (Tiadyne 1610) [47], Ti-15Mo-5Zr-3Al [48] standardized as per ISO and JIS designated as ISO 5832-14 [49] and JIS T 7401-6 [50], Ti-35.3Nb-5.1Ta-7.1Zr (TNZT: TiOsteum) [51] (ASTM Task Force F-04.12.23) [52], and Ti-29Nb-13Ta-4.6Zr (TNTZ) [53]. Later, Ti-11.5Mo-6Zr-4.5Sn was also registered in ASTM (ASTM F 1713(UNS R58130)) [54]. Since then, many low-modulus β-type Ti alloys have been developed or are under study. Recently, low-modulus β-type Ti alloys composed of low-cost elements such as Fe, Cr, Mn, Sn, and Al have been proposed, owing to consumption of resources of high-cost elements such as the rare metals Nb, Ta, Mo, and Zr. Examples of these alloys include Ti-10Cr-Al [55], Ti-Mn [56], Ti-Mn-Fe [57], Ti-Mn-Mo [58], Ti-Mn-Al [59], Ti-Cr-Al [60], Ti-Sn-Cr [61], Ti-Cr-Sn-Zr [62], Ti-(Cr, Mn)-Sn [63], and Ti-12Cr [64].

The selected low-modulus β-type Ti alloys for biomedical applications are listed in Table 3.2 [40]. The Young's moduli of the representative β-type Ti alloys are shown in Fig. 3.4 [65] together with those of the representative α- and (α + β)-type Ti alloys. These data were obtained under solution-treated conditions. Many of the β-type Ti alloys for biomedical applications show Young's moduli of around 80 GPa under the solution-treated conditions.

Table 3.2 β-type titanium alloys with low Young's modulus developed up to date

β-type titanium alloy	ASTM standard	ISO standard	JIS standard
Ti-13Nb-13Zr	ASTMF F1713	–	–
Ti-12Mo-6Zr-2Fe (TMZF)	ASTM F1813	–	–
Ti-12Mo-5Zr-5Sn	–	–	–
Ti-15Mo	ASTM F2066	–	–
Ti-16Nb-10Hf (Tiadyne 1610)	–	–	–
Ti-15Mo-2.8Nb-0.2Si	–	–	–
Ti-15Mo-5Zr-3Al	–	ISO 5832-14	JIS T 7401-6
Ti-30Ta	–	–	–
Ti-45Nb	–	–	–
Ti-35Zr-10Nb	–	–	–
Ti-35Nb-7Zr-5Ta (TNZT: TiOsteum)	ASTM Task Force 4.12.23	–	–
Ti-29Nb-13Ta-4.6Zr (TNTZ)	–	–	–
Ti-35Nb-4Sn	–	–	–
Ti-11.5Mo-6Zr-4.5Sn	ASTM F 1713	–	–
Ti-50Ta	–	–	–
Ti-8Fe-8Ta	–	–	–
Ti-8Fe-8Ta-4Zr	–	–	–
Ti-35Nb-2Ta-3Zr	–	–	–
Ti-22.5Nb-0.7Zr-2Ta	–	–	–
Ti-23Nb-0.7Ta-2.0Zr-1.2O (Gum Metal)	–	–	–
Ti-28Nb-13Zr-0.5Fe (TNZF)	–	–	–
Ti-24Nb-4Zr-7.9Sn (Ti2448)	–	–	–
Ti-7.5Mo	–	–	–
Ti-12Mo-3Nb	–	–	–
Ti-12Mo-5Ta	–	–	–
Ti-12Cr	–	–	–
Ti-30Zr-7Mo	–	–	–
Ti-30Zr-3Mo-3Cr	–	–	–
Ti-5Fe-3Nb-3Zr	–	–	–

Reprinted from Ref. [40], Copyright 2012, with permission from Elsevier

3.5.2 Superelastic and Shape-Memory β-Type Ti Alloys

A shape-memory TiNi alloy is still expected to be used for biomedical applications, particularly, for stents and guide wires of catheters. However, Ni is a high-risk element concerning allergic problems, although protection methods can be used to prevent the dissolution of Ni ions in the human body. Therefore, a Ni-free shape-memory alloy was developed for biomedical applications, and to date, many Ni-free β-type Ti alloys have been tested.

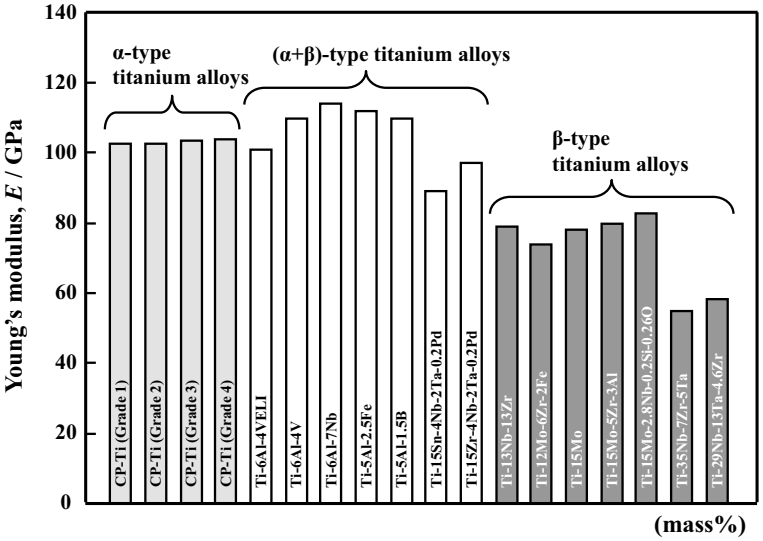

Fig. 3.4 Young's moduli of representative α-type, (α + β)-type, and β-type titanium alloys [65]

The selected Ni-free shape-memory alloys, which generally also exhibit superelasticity, are listed in Table 3.3 [66] and can be roughly divided in four groups: (i) Ti-Nb systems alloys [67–80], (ii) Ti-Mo system alloys [81–85], (iii) Ti-Ta system alloys [86], and (iv) Ti-Cr system alloys [87].

The addition of a small amount of oxygen (O) or nitrogen (N) enhances the superelastic performance of Ni-free Ti-based alloys, because they decrease the starting temperature of the martensite transformation. In general, the total elastic recovery strain is around 3% for Ni-free shape-memory Ti alloys. Microstructural control (i.e., the texture formation caused by a thermomechanical treatment) is also important to enhance the superelastic performance. For example, around 6% total

Table 3.3 Representative Ni-free shape-memory and superelastic alloys

Alloy system	Superelastic and shape-memory alloy
Ti-Nb system	Ti-Nb, Ti-Nb-O, Ti-Nb-Sn, Ti-Nb-Al, Ti-22Nb-(0.5-2.0)O (at.%), Ti-Nb-Zr, Ti-24Nb-2Zr (at.%), Ti-Nb-Zr-Ta, Ti-Nb-Zr-Ta-O, Ti-Nb-Mo, Ti-Nb-Ta-Zr-N, Ti-22Nb-6Ta (at.%), Ti-Nb-Au, Ti-Nb-Pt, Ti-Nb-Ta, Ti-Nb-Pd, Ti-29Nb-13Ta-4.6Zr (TNTZ), Ti-24Nb-4Zr-8Sn (mass%)
Ti-Mo system	Ti-Mo-Ga, Ti-Mo-Ge, Ti-Mo-Sn, Ti-Mo-Ag, Ti-5Mo-(2-5)Ag (mol%), Ti-5Mo-(1-3)Sn (mol%), Ti-Sc-Mo
Ti-Ta system	Ti-50Ta (mass%), Ti-50Ta-4Sn (mass%), Ti-50Ta-10Zr (mass%)
Ti-Cr system	Ti-7Cr-(1.5, 3.0, 4.5)Al (mass%)

Reprinted from Ref. [66], Copyright 2012, with permission from Woodhead Publishing

elastic recovery strain can be obtained for Ti-Nb-Al system alloys because of their texture [88]. It has been reported that around 6% of total elastic recovery strain is obtained in Ti-Nb-Zr, Ti-Nb-Zr-Ta, Ti-Nb-Zr-Ta-O, and Ti-Nb-Zr-Ta-N system alloys [74].

3.5.3 *Young's Modulus Self-adjustable β-Type Ti Alloys*

Spinal fixation devices are generally composed of rods, plugs, and screws, as shown in Fig. 3.5(b) [89]. The rods, in particular, bend when manually handled by surgeons within the small space inside the patients' bodies for in situ spine contouring [64]. The bent shape should be maintained and therefore, the bend back of the bent rod, called as springback, should be prevented. The amount of springback in implant rods should be small so that the implant offers better handling ability during operations. The amount of springback is considered to depend on both the strength and Young's modulus of the implant rod. If two implant rods having the same strength but different Young's moduli are used, the one with the lower modulus will show a greater spring back, as shown in Fig. 3.6 [89]. Patients require low Young's modulus for stress shielding inhibition, whereas surgeons require a high Young's modulus in order to prevent springback. To satisfy these conflicting demands at the same time, it should be possible to change Young's modulus to a higher value only at the bent sections of the rod at room temperature deformation, allowing Young's modulus of the rest of the rod to have a lower value [64]. Among the nonequilibrium phases such as the α′ martensite-, α″ martensite-, and ω-phases, the ω-phase has a higher Young's modulus than the β-phase, as already shown in Fig. 3.3.

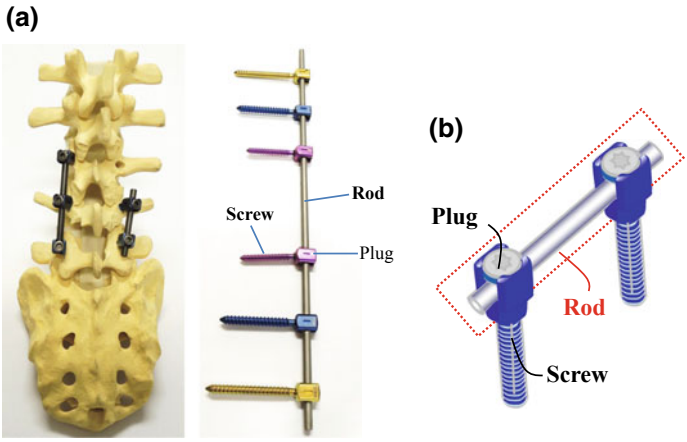

Fig. 3.5 **a** Images and **b** schematic drawing of spinal fixation system consisting of rods, screws, and plugs. Reprinted from Ref. [89], Copyright 2013, with permission from The Japan Institute of Metals and Materials

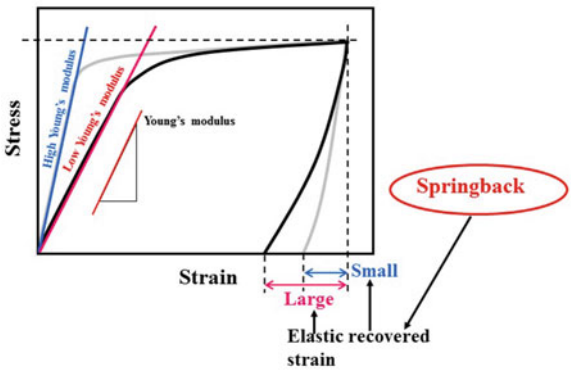

Fig. 3.6 The relationship between Young's modulus and springback. Reprinted from Ref. [89], Copyright 2013, with permission from The Japan Institute of Metals and Materials

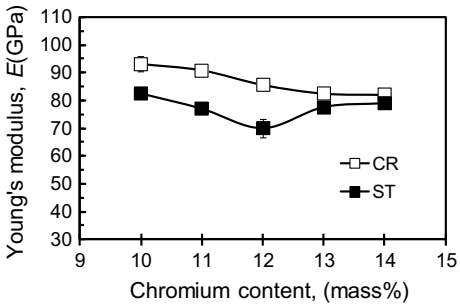

Fig. 3.7 Young's modulus of Ti-(10-14)Cr alloys subjected to solution treatment (ST) and 10% reduction cold rolling (CR) as a function of Cr (chromium) content. Reprinted from Ref. [90], Copyright 2012, with permission from Elsevier

Therefore, if the ω phase is induced by deformation (bending) on the interested part only, the conflicting demands might be satisfied. Figure 3.7 [90] shows Young's moduli of Ti-(10-14)Cr alloys subjected to solution treatment (ST) and cold rolling (CR), where cold rolling at a reduction ratio of 10% was carried out to simulate the deformation. The increase in Young's modulus is the highest at a Cr content of 12 mass%. To achieve a higher degree than that of Ti-12Cr, which has an athermal ω-phase, O is added to the alloy owing to its ability to suppress the formation of the athermal ω-phase. Finally, Ti-11Cr-0.2O, which exhibits a higher increase in the Young's modulus by CR than those of Ti-11Cr-(0.40, 0.60)O and Ti-12Cr-(0.20, 0.40, 0.60)O has been developed, as shown in Fig. 3.8 [90].

Figure 3.9 [91] shows comparison profiles of the ratio of springback per unit of load as a function of the applied strain for TNTZ, Ti-12Cr, and Ti-6Al-4V ELI (Ti64 ELI). The ratios of springback per unit of load of all the alloys show a similar trend, initially decreasing significantly and then remaining approximately stable while the applied strain increases. Among the mentioned alloys, Ti-11Cr-0.2O, which reaches a very low and stable springback value when the applied strain is greater than 2%, exhibits a minimal ratio of springback per unit stress. This value is much lower than that of TNTZ and is the closest to that of Ti64 ELI among the compared alloys.

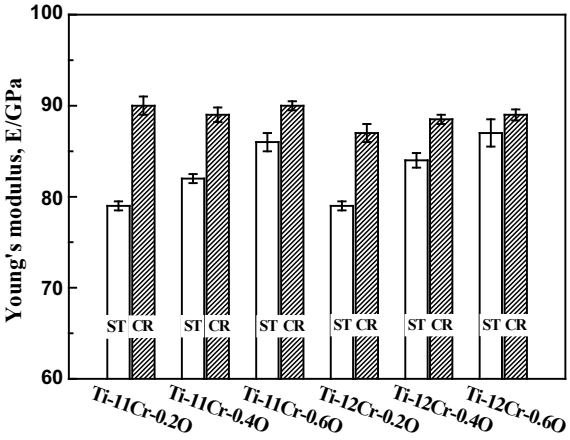

Fig. 3.8 Young's moduli of Ti-(11, 12) Cr-(0.2, 0.6) O alloys subjected to solution treatment (ST) and 10% reduction cold rolling (CR). Reprinted from Ref. [90], Copyright 2012, with permission from Elsevier

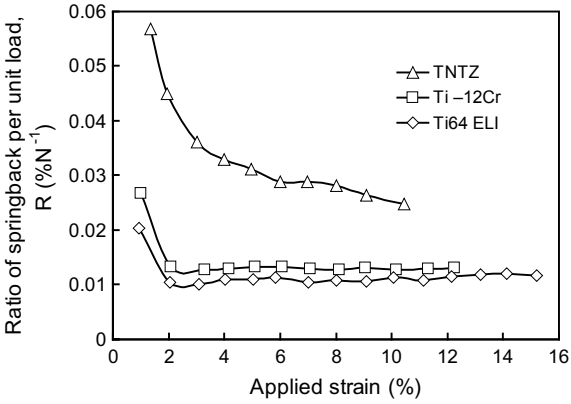

Fig. 3.9 Ratio of spring back per unit load as a function of applied strain for Ti-12Cr, Ti64 ELI, and TNTZ, and strains for calculation of the spring back ratio. Reprinted from Ref. [91], Copyright 2014, with permission from Elsevier

3.5.4 β-Type Ti Alloys for Reconstructive Implants

In particular situation, internal fixation devices are implanted into the bone marrow such as (i) the femoral, tibial, and humeral marrows, (ii) the screws used for bone plate fixation [92], and (iii) the implants used for children, which would otherwise grow into the bone. In these cases, it is essential to remove the internal fixation device after surgery in accordance with certain specific criteria including significant local symptoms, such as: (i) palpable hardware, (ii) wound dehiscence/exposure of hardware, or (iii) returning to contact sportletes [93, 94]. The assimilation of the removable internal fixation devices with the bone, owing to calcium phosphate precipitation might cause the refracture of the bone during the operation of removal. Therefore, in these circumstances, it is essential to prevent the adhesion of the alloys to the bone tissues, hence, the calcium phosphate precipitation.

Zr and Ti belong to the same group of elements in the periodic table, have the same crystal structure, and show unlimited solubility with each other [95, 96]. The toxicities of Ti and Zr are similar, and the latter expected to be an effective element for solution strengthening Zr is expected to be an effective element for solution strengthening [97, 98]. It has been reported that Zr has the ability to prevent the precipitation of calcium phosphate, which is the main component of the human bones [99], and that Ti alloys with Zr contents exceeding 25 mass% inhibit the formation of calcium phosphate [100]. Furthermore, when the Zr content exceeds 56 mass% the tensile strength remains fairly high but the elongation decreases [101]. Binary Ti-Zr alloys with high Zr contents exhibited high strength [100, 102, 103] and excellent biocompatibility [97]. On the basis of this analogy, biomedical Ti-Zr-based alloys such as Ti-Zr-Nb [104], Ti-Zr-Nb-Ta [105], and Ti-Zr-Al-V [101] alloys have been recently developed. Ti-30Zr-5Mo [106] was also developed with regard to the concept of novel Ti alloys for removable implants. Furthermore, Ti-30Zr-7Mo [106], Ti-30Zr-5Cr [107], and Ti-30Zr-3Cr-3Mo [107] showed self-tuning Young's moduli in addition to an easy removal from bones.

3.5.5 Summary

Ti and its alloys are still attracting attention for biomedical applications because their biological and mechanical biocompatibilities are generally better than those of other metallic biomaterials. Not only biological and mechanical biocompatibilities but also a behavior similar to that of living bone is required from metallic biomaterials. Ti alloys containing the metastable β-type phase can satisfy such requirements because of a deformation-induced phase. One example of this is Young's modulus self-adjustable β-type Ti alloy mentioned in this chapter. Development of such kinds of Ti alloys for biomedical applications is highly desirable in the future.

References

1. T. Nakano, Properties and evaluation methods in living body environment, in *Metals for Medicine*, ed. by T. Hanawa (Japan Institute of Metals and Materials, 2010), p. 184
2. D. Kuroda, M. Niinomi, M. Morinaga, Y. Kato, T. Yashiro, Mat. Sci. Eng. A **A243**, 244 (1998)
3. M. Niinomi, Mater. Jpn. **37**, 843 (1998)
4. Y. Okazaki, S. Rao, T. Tateishi, Y. Ito, Mat. Sci. Eng. A **A243**, 250 (1998)
5. P. Kovacs, J.A. Davidson, in *Titanium '92*, ed. by F.H. Froes, I. Caplan (TMS, 1993), p. 2705
6. T. Ahmed, M. Lomg, J. Silvestri, C. Ruiz, H.J. Rack, A new low modulus, biocompatible titanium alloy, in *Titanium '95*, ed. by P.A. Blenkinsop, W.J. Evans, H.M. Flower (The Institute of Materials, 1996), p. 1760

7. K. Nitta, S. Watanabe, N. Masahashi, H. Hosoda, S. Hanawa, Ni-free Ti-Nb-Sn shape memory alloys, in *Structural Biomaterials for the 21st Century*, ed. by M. Niinomi, T. Okabe, E.M. Taleff, D.R. Lesuer, H.F. Lippard (TMS, 2001), p. 25
8. Y. Daimatsu, A. Yamamoto, H. Hosoda, S. Miyazaki, Shape memory characteristics of Ti-Mo-Ga for biomedical applications, in *Collected Abstract Fall Meeting of JIM* (2001), p. 401
9. H. Hosoda, A. Yamamoto, S. Miyazaki, Mechanical properties of Ti-Mo-Ge shape memory alloy for biomedical applications, in *Collected Abstract Fall Meeting of JIM* (2001), p. 401
10. H. Hiromoto, F. Mizuno, T. Hanawa, C. Kuroda, H. Hosoda, K. Wakashima, S. Miyazaki, Polarization behavior of Ti-Mo-Al shape memory alloy in simulated body liquid, in *Collected Abstract Annual Meeting of JIM* (2002), p. 443
11. M. Ikeda, Y. Nakamura, N. Takahama, Effect of Zr contents on heat treatment behaviors and phase constitution of Ti-50 mass% Ta-Zr alloy, in *Collected Abstract Annual Meeting of JIM* (2003), p. 130
12. T. Maeshima, T. Eto, H. Uchiyama, K. Uchiyama, M. Nishida, Development of Ti-Sc-Mo shape memory alloy, in *Annual Meeting of JIM* (2003), p. 134
13. T. Hatori, K. Morikawa, S. Niwa, M. Niinomi, A. Suzuki, Bone tissue reaction to new β titanium low rigidity alloy: rabit study on bone healing remodeling and atrophy in intramedullary fracture fixation, in *Proceedings of International Conference on Biomechanics combined with the Annual Scientific Meeting of Taiwanese Society of Biomechanics* (2001), p. 28
14. Y. Okazaki, S. Asao, S. Rao, T. Tateishi, J. Jpn. Inst. Met. **60**, 902 (1996)
15. A. Yamamoto, T. Kobayashi, N. Maruyama, K. Nakazawa, M. Sumita, J. Jpn. Inst. Met. **59**, 463 (1995)
16. T. Akahori, M. Niinomi, K. Fukunaga, I. Inagaki, Met. Mat. Trans. A **31A**, 1949 (2000)
17. M. Niinomi, T. Akahori, K. Ishimizu, Fatigue and fretting fatigue of biomaterials, Ti-29Nb-13Ta-45.6Zr, in air and simulated body environment, in *Materials Lifetime Science and Engineering*, ed. by P.K. Liaw, R.A. Buchana, D.L. Klarstrom, R.P. Wei, D.G. Harlow (TMS, 2003), p. 223
18. K. Nakazawa, M. Sumita, N. Maruyama, J. Jpn. Inst. Met. Mater. **63**, 1600 (1999)
19. M. Niinomi, C.J. Boehlert, Titanium alloys for biomedical applications, in *Advances in Metallic Biomaterials, Tissues, Part 1: Materials and Biological Reactions*, ed by M. Niinomi, T. Narushima, M. Nakai. Springer Series in Biomaterials Science and Engineering Series, vol. 3, ed. by M. Wang (Springer, 2015), p. 179
20. ASTM F67: Standard specification for unalloyed titanium, for surgical implant applications (UNS R50250, UNS R50400, UNS R50550, UNS R50700) (ASTM International, West Conshohocken, PA, USA)
21. ISO 5832-2: Implants for surgery—metallic materials—part 2: Unalloyed titanium (ISO, Vernier, Geneva, Switzerland)
22. JIS T7401-1: Titanium materials for surgical implant applications, Part 1: unalloyed titanium (JIS, Tokyo, Japan)
23. ASTM F136: Standard specification for wrought titanium-6aluminum-4vanadium ELI (extra low interstitial) alloy for surgical implant applications (UNS R56401) (ASTM International, West Conshohocken, PA, USA)
24. ASTM F1472: Standard specification for wrought titanium-6aluminum-4vanadium alloy for surgical implant applications (UNS R56400) (ASTM International, West Conshohocken, PA, USA)
25. ISO 5832-3: Implants for surgery—metallic materials—part 3: wrought titanium 6-aluminium 4-vanadium alloy (ISO, Vernier, Geneva, Switzerland)
26. JIS T7401-2: Titanium materials for surgical implant applications part 2: wrought titanium 6-aluminium 4-vanadium alloy (JIS, Tokyo, Japan)
27. ASTM F 2146: Standard specification for wrought titanium-3aluminum-2.5vanadium alloy seamless tubing for surgical implant applications (UNS R56320) (ASTM International, West Conshohocken, PA, USA)

28. R. Zwicker, K. Buheler, R. Mueller, H. Beck, H.J. Schmid, in *Titanium '80: Science and Technology*, vol. 2, ed. by H. Kimura, O. Izumi (The Metallurgical Society of AIME, 1980), p. 505
29. M. Semlitsch, F. Staub, H. Webber, Biomed. Tech. **30**, 334 (1985)
30. M. Niinomi, Met. Mat. Trans. A **33**, 477 (2002)
31. ISO 5832: Implant for surgery—metallic materials—part 10: wrought titanium 5-aluminum 2.5-iron alloy (ISO, Vernier, Geneva, Switzerland)
32. ASTM F1295: Standard specification for wrought titanium-6aluminum-7niobium alloy for surgical implant applications (UNS R56700) (ASTM International, West Conshohocken, PA, USA)
33. ISO 5821-11: Implants for surgery—metallic materials—part 11: wrought titanium 6-aluminium 7-niobium alloy (ISO, Vernier, Geneva, Switzerland)
34. JIS T7401-5: Titanium materials for surgical implant applications part 5: wrought titanium 6-aluminium 7-niobium alloy (JIS, Tokyo, Japan)
35. Military Specification, MIL-T-9046 J, Code A-3 (1991)
36. Y. Sasaki, K. Doi, T. Matsushita, Kinzoku **66**, 812 (1996)
37. JIS T7401-3: Titanium materials for surgical implant applications part 3: wrought titanium 6-aluminium 2-niobium 1-tantalum alloy (Tokyo, Japan)
38. Y. Okazaki, Y. Ito, A. Ito, T. Tateishi, New titanium alloys to be considered for medical implants, in *Medical Applications of Titanium and Its Alloys*, ed. by S.A. Brown, J.E. Lemons. ASTM STP 1272 (ASTM, West Conshohocken, PA, USA, 1996), p. 45
39. JIS 7401-4: Titanium materials for surgical implant applications part 4: wrought titanium 15-zirconium 4-niobium 4-tantalum alloy (Tokyo, Japan)
40. M. Niinomi, M. Nakai, J. Hieda, Acta Biomater. **8**, 3888 (2012)
41. A.K. Mishra, J.A. Davidson, R.A. Poggie, P. Kovacs, T.J. Fitzgerald, Mechanical and tribological properties and biocompatibility of diffusion hardened Ti-13Nb-13Zr—A new titanium alloy for surgical implants, in *Medical Applications of Titanium And Its Alloy*, ed. by S.A. Brown, J.E. Lemons. ASTM STP 1272 (ASTM, West Conshohocken, PA, USA, 1996), p. 96
42. ASTM F1713: Standard specification for wrought titanium-13niobium-13zirconium alloy for surgical implant applications (UNS R58130) (ASTM International, West Conshohocken, PA, USA)
43. K.K. Wang, L.J. Gustavson, J.H. Dumbleton, Microstructure and properties of a new beta titanium alloy, Ti-12Mo-6Zr-2Fe, developed for surgical implants, in *Medical Applications of Titanium and Its Alloy*, ed. by S.A. Brown, J.E. Lemons. ASTM STP 1272 (ASTM, West Conshohocken, PA, USA, 1996), p. 76
44. ASTM F1813: Standard specification for wrought titanium–12 molybdenum–6 zirconium–2 iron alloy for surgical implant (UNS R58120) (ASTM International, West Conshohocken, PA, USA)
45. L.D. Zardiackas, D.W. Mitchell, J.A. Disegi, Characterization of Ti-15Mo beta titanium alloy for orthopedic implant, in *Medical Applications of Titanium and Its Alloy*, ed. by S.A. Brown, J.E. Lemons. ASTM STP 1272 (ASTM, West Conshohocken, PA, USA, 1996), p. 60
46. ASTM F2066: Standard specification for wrought titanium-15 molybdenum alloy for surgical implant applications (UNS R58150) (ASTM International, West Conshohocken, PA, USA)
47. K. Wang, Mater. Sci. A **213**, 134 (1996)
48. S.G. Steinemann, P.A. Mausli, S. Szmukler-Moncler, M. Semlitsch, H.E. Pohler Hintermann, S.M. Perren, in *Titanium '92, Science and Technology*, ed. by F.H. Froes, I. Caplan (Warrendale, PA, 1993), p. 2689
49. ISO 5832-14: Implants for surgery—metallic materials—part 14: wrought titanium 15-molybdenum 5-zirconium 3-aluminium alloy (ISO, Vernier, Geneva, Switzerland)
50. JIS T7401-6: Titanium materials for surgical implant applications part 6: wrought titanium 15-molybdenum 5-zirconium 3-aluminium alloy (JIS, Tokyo, Japan)

51. T. Ahmed, M. Long, J. Silvestri, C. Ruiz, H.J. Rack, A new low modulus, biocompatible titanium alloy, in *Titanium '95, Science and Technology*, vol. II, ed. by P.A. Blenkinsop, W. J. Evans, H.M. Flower (Institute of Metals, London, UK, 1996), p. 1760
52. ASTM designation draft #3: Standard specification for wrought taitanium-35Niobium-7zirconium-5tantalum alloy for surgical implant applications (UNS R58350) (ASTM, Philadelphia, PA, USA)
53. M. Niinomi, T. Hattori, K. Morikawa, T. Kasuga, A. Suzuki, H. Fukui, S. Niwa, Mater. Trans. **43**, 2970 (2002)
54. ASTM F1713: Standard specification for wrought titanium-13niobium-13zirconium alloy for surgical implant applications (UNS R58130) (ASTM International, West Conshohocken, PA, USA), p. 29
55. S. Hatanaka, M. Ueda, M. Ikeda, M. Niinomi, Adv. Mater. Res. **89–91**, 232 (2010)
56. M. Ikeda, M. Ueda, R. Matsunaga, M. Ogawa, M. Niinomi, Mater. Trans. **50**, 2737 (2009)
57. M. Ikeda, M. Ueda, T. Kinoshita, M. Ogawa, M. Niinomi, Mater. Sci. Forum **706–709**, 1893 (2012)
58. P.F. Santos, M. Niinomi, H. Liu, M. Nakai, K. Cho, T. Narushima, Development and performance of a Ti-based beta-type alloy for biomedical applications using Mn and Mo additions, in *Abstract of Innovative Research for Biosis-Abiosis Intelligent Interface Symposium, The 6th International Symposium for Interface Oral Health Science*, Gonryo Kaika, Sendai, Japan, 18–19 January 2016, p. 66
59. M. Ikeda, M. Ueda, R. Matsunaga, M. Niinomi, Mater. Sci. Forum **654–656**, 855 (2010)
60. M. Ikeda, D. Sugano, Mater. Sci. Eng., C **25**, 377 (2005)
61. S. Ashida, H. Kyogaku, H. Hosoda, Mater. Sci. Forum **706–709**, 1943 (2012)
62. Y. Murayama, S. Sasaki, Univ. Res. J. Niigata Inst. Tec. **14**, 1 (2009)
63. Y. Kasano, T. Inamura, H. Kanetaka, S. Miyazaki, H. Hosoda, Mater. Sci. Forum **654–656**, 2118 (2010)
64. M. Nakai, M. Niinomi, X.F. Zhao, X.L. Zhao, Mater. Lett. **65**, 688 (2011)
65. M. Nakai, M. Niinomi, K. Cho, K. Narita, Enhancing functionalities of metallic materials by controlling phase stability for use in orthopedic implants, in Interface *Oral Health Science 2014*, ed. by K. Sasaki, O. Suzuki, N. Takahashi (Springer, 2015), p. 79
66. M. Niinomi, Shape memory, super elastic and low Young's modulus alloys, in *Biomaterials for Spinal Surgery*, ed. by L. Ambrosio, E. Tanner (Woodhead Publishing Ltd, 2012), p. 462
67. H.Y. Kim, Y. Ikehara, J.I. Kim, H. Hosoda, S. Miyazaki, Acta Mater. **54**, 2419 (2006)
68. J.I. Kim, H.Y. Ki, H. Hosoda, S. Miyazaki, Mater. Trans. **46**, 852 (2005)
69. E. Takahashi, T. Sakurai, S. Watanabe, N. Masahashi, S. Hanada, Mater. Trans. **43**, 2978 (2002)
70. K. Nitta, S. Watanabe, N. Masahashi, H. Hosoda, S. Hanada, Ni-free Ti-Nb-Sn shape memory alloys, in *Structural Biomaterials for the 21st Century*, ed. by M. Niinomi, T. Okabe, E.M. Taleff, D.R. Lesuer, H.E. Lippard (TMS, Warrendale, PA, USA, 2001), p. 25
71. H. Hosoda, Y. Fukui, T. Inamura, K. Wakashima, S. Miyazaki, K. Inoue, Mater. Sci. Forum **426–432**, 3121 (2003)
72. T. Inamura, H. Hosoda, K. Wakashima, S. Miyazaki, Mater. Trans. **46**, 1597 (2005)
73. H. Kim, H.Y. Ki, T. Inamura, H. Hosoda, S. Miyazaki, Mater. Sci. Eng., A **403**, 334 (2005)
74. H.Y. Kim, H. Hosoda, S. Miyazaki, Development of super elastic Ti-Nb system alloys for biomedical applications, in *Collected abstracts of the 2007 Spring Meeting of JIM* (2007), p. 91
75. Y. Ohmatsu, J.I. Kim, H.Y. Kim, H. Hosoda, S. Miyazaki, Shape memory characteristics of Ti-Nb-Mo alloys for biomedical applications, in *Collected Abstracts of the 2003 Spring Meeting of JIM* (2003), p. 144
76. Y. Al-Zain, H.Y. Kim, H. Hosoda, T.H. Nam, S. Miyazaki, Acta Mater. **58**, 4212 (2010)
77. H.Y. Kim, T. Sasaki, K. Okutsu, J.I. Kim, T. Inamura, H. Hosoda, S. Miyazaki, Acta Mater. **54**, 423 (2006)

78. N. Oshika, S. Hashimoto, J.I. Kim, H.Y. Kim, Y. Ohmatsu, H. Hosoda, S. Miyazaki, Shape memory characteristics of Ti-Nb-Au alloys for biomedical applications, in *Collected Abstracts of the 2003 Fall Meeting of JIM* (2003), p. 149
79. D. Ping, Y. Mitarai, F. Yin, Scripta Mater. **52**, 1287 (2005)
80. M. Niinomi, Multifunctional low-rigidity β-type Ti-Nb-Ta-Zr system alloys as biomaterials, in *Interface Oral Health Science 2007*, ed. by K. Sasaki, O. Suzuki, N. Takahashi, asso ed. by M. Watanabe, O. Okuno (2007), p. 75
81. H. Hosoda, N. Hosoda, S. Miyazaki, Trans. MRS-J. **26**, 243 (2001)
82. H.Y. Kim, Y. Ohmatsu, J.I. Kim, H. Hosoda, S. Miyazaki, Mater. Trans. **45**, 1090 (2004)
83. N. Hosoda, A. Yamamoto, H. Hosoda, S. Miyazaki, Mechanical properties of Ti-Mo-Ge shape memory alloys for biomedical applications, in *Collected Abstracts of the 2001 Fall Meeting of JIM* (2001), p. 401
84. T. Maeshima, M. Nishida, Mater. Trans. **45**, 1096 (2004)
85. T. Maeshima, M. Nishida, Mater. Trans. **45**, 1101 (2004)
86. M. Ikeda, S. Komatsu, Y. Nakamura, Mater. Trans. **45**, 1106 (2004)
87. M. Ikeda, D. Sugano, S. Masuda, M. Ogawa, Mater. Trans. **46**, 1604 (2005)
88. H. Hosoda, S. Miyazaki, J. Jpn. Soc. Mech. Eng. **107**, 509 (2004)
89. M. Niinomi, Materia. Jpn. **525**, 219 (2013)
90. X.F. Zhao, M. Niinomi, M. Nakai, J. Hieda, Acta Biomater. **8**, 2392 (2012)
91. H.H. Liu, M. Niinomi, M. Nakai, J. Hieda, K. Cho, J. Mech. Behav. Biomed. **30**, 205 (2014)
92. E. Kobayashi, M. Ando, Y. Tsutsumi, H. Doi, T. Yoneyama, M. Kobayashi, T. Hanawa, Mater. Trans. **48**, 301 (2007)
93. G.K. Kambouroglou, T.S. Axelrod, A brief report. J. Hand. Surg. **23**, 737 (1998)
94. S.D. Cook, E.A. Renz, R.L. Barrack, K.A. Thomas, A.F. Harding, R.J. Haddad, M. Milicic, Clin. Orthop. Relat. Res. (236) (1985)
95. I. Thibon, D. Ansel, T. Gloriant, J. Alloy. Compd. **470**, 127 (2009)
96. T. Albrektsson, H.A. Hansson, B. Ivarsson, Biomater. **6**, 97 (1985)
97. Y. Ikarashi, K. Toyoda, E. Kobayashi, H. Doi, T. Yoneyama, H. Hamanaka, T. Tsuchiya, Mater. Trans. **46**, 2260 (2005)
98. Y. Tsutsumi, D. Nishimura, H. Doi, N. Nomura, T. Hanawa, Mater. Sci. Eng., C **29**, 1702 (2009)
99. T. Hanawa, O. Okuno, H. Hamanaka, J. Jpn. Inst. Met. **56**, 1168 (1992)
100. E. Kobayash, S. Matsumoto, H. Doi, T. Yoneyama, H. Hamanaka, J. Biomed. Mater. Res. **29**, 943 (1995)
101. E. Kobayashi, H. Doi, T. Yoneyama, H. Hamanaka, S. Matsumoto, K. Kudaka, J. J. Dent. Mater. **14**, 321 (1995)
102. W.F. Ho, W.K. Chen, S.C. Wu, H.C. Hsu, J. Mater. Sci. Mater. Med. **19**, 3179 (2008)
103. A.G. Imgram, D.N. Williams, H.R. Ogden, J. Less-Common Met. **4**, 217 (1962)
104. M. Takahashi, E. Kobayashi, H. Doi, T. Yoneyama, H. Hamanaka, J. Jpn. Inst. Met. **64**, 1120 (2000)
105. G.J. Yang, T. Zhang, J. Alloy. Compd. **392**, 291 (2005)
106. X.L. Zhao, M. Niinomi, M. Nakai, T. Ishimoto, T. Nakano, Mater. Sci. Eng., C **31**, 1436 (2011)
107. X.L. Zhao, M. Niinomi, M. Nakai, G. Miyamoto, T. Furuhara, Acta Biomater. **7**, 3230 (2011)

Chapter 4
Mn-Based Ferromagnetic Alloys

Yoshifuru Mitsui and Rie Y. Umetsu

Abstract Magnetic properties of Mn-based alloys and compounds are rich in the variety of their magnetism because the magnetic moment of Mn varies from almost zero to 5 μ_B depending on its environment and its sign of exchange interaction changes with the distance between Mn atoms. Mn-based alloys and compounds with large magnetic anisotropy are recently being focused on with regard to their applications to perpendicular magnetic films and alternate materials of permanent magnets. Although it is generally thought that magnetic anisotropy originates from large spin–orbit interaction due to heavy elements, such as Pt, Pd, and rare earth elements, some Mn-based alloys and compounds indicate comparatively large magnetic anisotropy without such heavy elements. MnAlGe pseudo-two-dimensional compound with a Cu_2Sb-type structure is thought to be a candidate for perpendicular magnetic films. Clarification of the mechanism of magnetic properties is needed to improve the characteristics desired for applications. MnBi has been considered to be an alternate material for permanent magnet; however, a problem exists in which a single phase of MnBi is difficult to obtain. Among some ingenious fabrication processes, it has been found that solid-state reaction in a magnetic field is effective to improve the reaction. The application of a magnetic field during the reaction enhances not only the fabrication of a single phase of MnBi but also the assembly of the crystal orientation.

Keywords Magnetic anisotropy · Magnetic moment · Curie temperature · Exchange interaction · In-field heat treatment

Y. Mitsui (✉)
Graduate School of Science and Engineering, Kagoshima University, 1-21-35 Korimoto, Kagoshima 890-0065, Japan
e-mail: mitsui@sci.kagoshima-u.ac.jp

R. Y. Umetsu
Institute for Materials Research, Tohoku University, 2-1-1 Katahira, Aoba-ku, Sendai 980-8577, Japan

Y. Setsuhara et al. (eds.), *Novel Structured Metallic and Inorganic Materials*, https://doi.org/10.1007/978-981-13-7611-5_4

4.1 Introduction

Mn-based alloys and compounds have various magnetic properties. Basically, pure Mn has four phases: α, β, γ, and δ. The α phase has a body-center-cubic-type unit cell containing 58 Mn atoms composing four kinds of Mn sites. Its magnetism is antiferromagnetic having a Néel temperature of 95 K [1]. Although the ground state of the β phase is enhanced Pauli paramagnetism, antiferromagnetic ordering or spin-glass-like-magnetism is induced by substitution of elements, such as Al, Co, Ru, Rh, and Os [2, 3]. The crystal structure is also cubic type with 20 Mn atoms in the unit cell and it has two kinds of inequivalent Mn sites. The γ phase is a face-centered-cubic structure and shows paramagnetism at around 1100 K. It is hard to obtain the γ phase at room temperature by quenching of pure Mn; however, stabilization is possibly by substitution of certain elements, and the obtained phase exhibits antiferromagnetism with a Néel temperature of about 480 K [4]. Because of its high stability of antiferromagnetic ordering, γ-MnIr is applied to the pinning layer in a tunnel-magnetoresistance multilayer for a magnetic head. The δ phase has a body-centered-cubic structure, and there is a theoretical report that its ground state is antiferromagnetic [5].

As mentioned above, even pure Mn has four kinds of phases. In the alloys and compounds, Mn atoms have a magnetic moment from almost zero to 5 μ_B depending on the environment [6], and it is well known that the exchange interaction between Mn atoms changes from antiferromagnetic to ferromagnetic depending on distance. When the Mn atoms are close to each other, their magnetic moments prefer antiferromagnetic coupling, whereas when they are far from each other, ferromagnetic coupling is preferred. Ni_2MnAl Heusler alloy is unique because the magnetic property is significantly sensitive to the degree of order. That is, $L2_1$-type ordering indicates ferromagnetic ordering, whereas $B2$-type disorder exhibits antiferromagnetic ordering [7]. This behavior is explained by the fact that the disorder introduces a close Mn–Mn bond distance with antiferromagnetic coupling. Among ferromagnetic Mn-based alloys and compounds, MnAl, MnZn, MnBi, MnGa, MnGe, MnAlGe, MnZnSb, are known to have a large magnetic anisotropy. These materials have a uniaxial magnetic crystalline anisotropy constant on the order of $\sim 10^6$ J/m^3, which is comparable to that of a rare-earth-based permanent magnet and $L1_0$-type FePt, CoPt, and FePd. Because the magnetization of Mn-based ferromagnetic materials is not so high, their characteristic as permanent magnets is inferior to that of rare-earth-based permanent magnets. However, the recent trend of the element strategy encourages investigation of these materials [8]. Especially, in the field of spintronics, ferromagnetic materials with large magnetic anisotropy but comparatively low magnetization are highly desired [9, 10].

In the present chapter, the focus is on two kinds of Mn-based ferromagnets. One is MnAlGe pseudo-two-dimensional compounds with a Cu_2Sb-type structure. Not only the magnetic anisotropy and magnetization, but also the degree of the Curie temperature, T_C, is very important for applications. The relationship between T_C

and the distance between Mn layers will be discussed. The other is MnBi compound with a NiAs-type structure. Although the compound has been considered to have high potential as an alternative permanent magnet, it is very difficult to obtain a single phase because of the segregation during peritectic reactions. Applying magnetic fields during the solid-state reaction improves the fabrication of MnBi as well as the crystal orientation.

4.2 Magnetic Properties of Mn-Based Layered Compounds MnAlGe and MnGaGe

In this section, magnetic properties of a MnAlGe pseudo-two-dimensional compound and its related material of MnGaGe are introduced. They have a tetragonal Cu_2Sb-type structure, and Mn atoms are aligned two dimensionally in the *c*-plane. There are two layers, one composed only of Mn atoms and the other composed of nonmagnetic elements of Al(Ga)/Ge stacked in the *c*-axis direction (Fig. 4.1). Lattice parameters *a* and *c* are reported to be 0.3913 nm and 0.5933 nm for MnAlGe [11], and 0.3966 nm and 0.5885 nm for MnGaGe [12], respectively. Magnetic moment and magnetic structure for MnAlGe have been shown by neutron diffraction to have magnetic moments of Mn with 1.70 μ_B at 4.2 K [13]. The

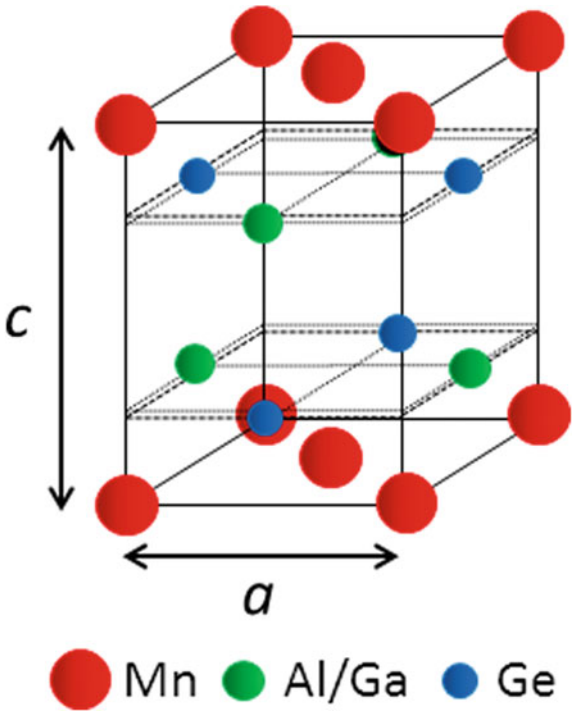

Fig. 4.1 Crystal structure of MnAlGe and MnGaGe compounds with a Cu_2Sb type. Layers composed of only Mn atoms or of nonmagnetic elements stacked in the *c*-axis direction. The Al/Ga and Ge layers slightly shift

Table 4.1 Lattice parameters a and c, magnetic moment of Mn at 4.2 K m_{Mn}, uniaxial magnetic anisotropy constant K_u, the Curie temperature T_C for MnAlGe and MnGaGe compounds after [11–13]

	a, c (nm)	m_{Mn} (μ_B)	K_u ($\times 10^6$ J/m^3)	T_C (K)	References
MnAlGe	0.3913, 0.5933	1.70	0.97	519	[11, 13]
MnGaGe	0.3966, 0.5885	1.66		458	[12]

uniaxial magnetic anisotropy constant and T_C obtained by magnetic measurements are listed in Table 4.1. Investigations of MnAlGe film were made in the 1970s and 80s by some groups [14–17]. It has been reported that crystalized islands of MnAlGe are distributed in nonmagnetic amorphous state by annealing up to a certain temperature [17]. Recently, Mizukami et al. succeeded in fabricating epitaxy film on a MgO substrate and showed perpendicular magnetic anisotropy [10]. They also reported a Gilbert damping constant of $\sim$0.05, whereas the theoretical value is much smaller than the experimental one.

As well as magnetic anisotropy, T_C is also very important for the applications. Substitution effects on T_C for MnAlGe have been investigated and unique results indicating that only Cr substitution for Mn enhances T_C have been reported [18, 19]. In order to investigate the effects of substitution on T_C for the MnGaGe series, some experiments were performed [20]. Three kinds of specimens of $(Mn_{0.8}Cr_{0.2})GaGe$, MnGaGe, and $(Mn_{0.8}Fe_{0.2})GaGe$ were fabricated by induction melting, and obtained ingots were annealed at 773 K. Figure 4.2 shows powder X-ray diffraction patterns for $(Mn_{0.8}Cr_{0.2})GaGe$, MnGaGe, and $(Mn_{0.8}Fe_{0.2})GaGe$ compounds at room temperature, together with the calculated pattern for MnGaGe, reported lattice parameters being used here [11]. Intensities of most of the observed peaks coincide with the simulated patterns except for two peaks indexed as 101 and 301 reflections as indicated by arrows in the figure. The powdered specimens may

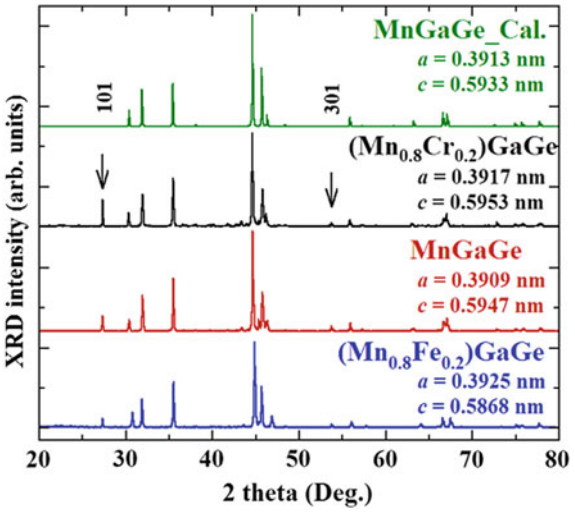

Fig. 4.2 Powder X-ray diffraction patterns for $(Mn_{0.8}Cr_{0.2})GaGe$, MnGaGe, and $(Mn_{0.8}Fe_{0.2})GaGe$ compounds, together with calculated pattern as MnGaGe using lattice parameters from the literature [11]. Reprint from Ref. [20], Copyright 2014, with permission from IEEE

be somewhat oriented. Lattice parameter a is not sensitive to the substitution, whereas c is slightly expanded by Cr substitution and shrunk by Fe. Using these specimens, magnetization curves were measured at 4.2 K. The saturation magnetizations of $(Mn_{0.8}Cr_{0.2})GaGe$ and MnGaGe were almost the same, or slightly increased by Cr substitution. On the other hand, magnetization was decreased by Fe substitution.

Figure 4.3 indicates thermomagnetization curves measured under a magnetic field of 1 T for the three specimens. T_C is defined at the minimum point in the temperature derivative of the thermomagnetization curves and indicated by arrows in the figure. Similar behavior of the substitution effects on T_C is observed in the MnGaGe series. Even the enhancement of magnetization is slight, T_C being enhanced by about 40 K for replacement of 20% Mn by Cr. To focus on the relationship between T_C and lattice parameters, that is, distance between Mn atoms or Mn layers, the data are summarized in Fig. 4.4 [20]. The figure indicates lattice parameters a and c as functions of T_C for the MnAlGe and MnGaGe series. Although lattice parameter a is almost constant, it seems that T_C increases with an increase of lattice parameter c. This would mean that the exchange interaction is governed by the distance between Mn layers. Another effective way to investigate the relationship between T_C and the atomic distance is to confirm T_C under pressure. The effect of pressure on T_C has been reported by Kanomata et al., although the results are opposite to the presented ones [21]. They measured T_C as a function of pressure and obtained the value of the pressure coefficient of T_C: dT_C/dP = 3.2 K/GPa. This means that T_C increases with applied pressure. During the experiments, however, the pressure was applied hydrostatically, and thus not only the c-axis but

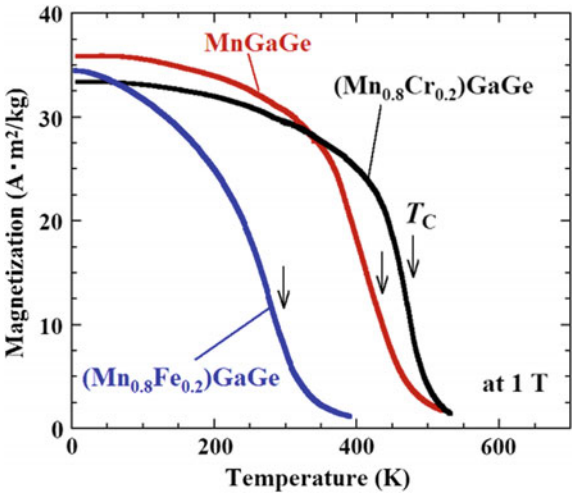

Fig. 4.3 Thermomagnetization curves measured under a magnetic field of 1 T for $(Mn_{0.8}Cr_{0.2})GaGe$, MnGaGe, and $(Mn_{0.8}Fe_{0.2})GaGe$ compounds. The Curie temperature T_C is indicated by arrows. Reprint from Ref. [20], Copyright 2014, with permission from IEEE

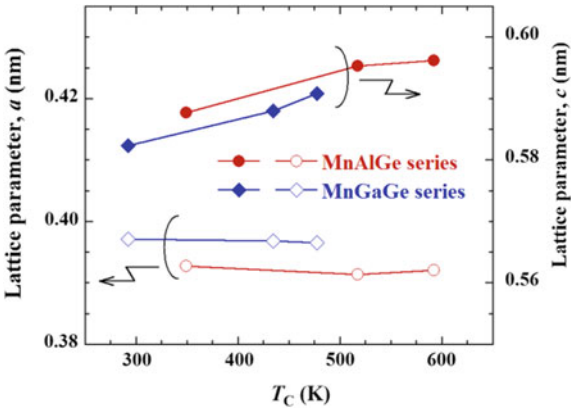

Fig. 4.4 Lattice parameters a and c as functions of the Curie temperature, T_C for MnAlGe and MnGaGe series. Reprint from Ref. [20], Copyright 2014, with permission from IEEE

also the a-axis shrunk. Kanomata et al. also investigated pressure effects on the lattice parameters and obtained linear compressibility of 2.3 and 2.9 $\times$ 10^{-3}/GPa for the a-axis and the c-axis, respectively [22]. This result indicates that the compressibility of the two axes is of the same order. A change of the lattice parameter a, that is, the Mn–Mn atomic distance should be taken into consideration when discussing magnetic properties.

At the end of the present chapter, we have added some comments on the magnetic anisotropy in MnAlGe. Magnetic anisotropy of magnetic materials generally originates from two contributions, that is, magnetic dipole–dipole interaction and single ion spin energy in the crystalline field. These interaction energies have been roughly estimated by magnetic measurements of a MnAlGe single crystal [13]. The dipole–dipole interaction energy has been considered to have a negative value from ground state up to T_C and it is one order smaller than the uniaxial magnetic anisotropy constant. Therefore, it is considered that the main part of the magnetic anisotropy energy would be due to single ion spin energy. Recently, magnetocrystalline anisotropy has been theoretically calculated in MnAl and MnGa with an $L1_0$-type structure [23]. Although their crystal structures are different from MnAlGe with the Cu_2Sb type, they are similar to the concept of Mn-based layered compounds. Theoretical studies have reported that the magnetic anisotropy energy would originate from the favorable electronic structure of MnAl and MnGa. That is, the hybridization through spin–orbit interaction between the occupied and unoccupied 3d states located near the Fermi energy dominates the magnetic anisotropy energy [23]. The density of states for MnAlGe and MnGaGe has been reported by Motizuki et al., who pointed out that the hybridizations between Mn-3d and Al-3p or Ge-4p states are not so strong and that a large spin splitting occurs only for the Mn-3d bands [24]. In order to enhance the magnetic anisotropy energy in Mn-layered compounds, Mn-3d states may need some itinerant character. However, in such case, the magnetic moment of Mn becomes smaller than that expected from a localized Mn atom. In this situation, materials with a large magnetic anisotropy energy and a small magnetic moment are preferable in the field of spintronics but

not suitable as alternative materials for permanent magnets. A singular situation may be necessary to provide both large magnetic anisotropy and high magnetization in Mn-based layered compounds.

4.3 In-Magnetic-Field Annealing of MnBi

Ferromagnetic compound MnBi with a hexagonal NiAs-type structure also has a large magnetic moment and a high Curie temperature. The magnetic moment has been reported to be 3.9 μ_B/Mn at 0 K [25]. The Curie temperature was 628 K due to the first-order magnetic phase transition from ferromagnetic MnBi to paramagnetic phase. The high-temperature phase with paramagnetism has been reported to have a distorted Ni_2In structure [26]. The composition of the high-temperature phase was $Mn_{1.08}Bi$, slightly different from the low-temperature MnBi phase [27]. The extrapolated Curie temperature of the MnBi phase has been reported to be 720 K [28, 29]. It should be noted that MnBi has a positive thermal coefficient of magnetic crystalline anisotropy K_u, which has a peak of $\sim$2.3 MJ/m^3 over 500 K [30, 31]. First-principle calculation for MnBi was performed, resulting in improvement of K_u by substitution of Sn [32]. As MnBi has a high K_u above room temperature, MnBi/NdFeB and MnBi/SmFeN hybrid magnets have so far been evaluated [33–35]. It is reported that the substitution of MnBi for NdFeB partially recovered the decrease of coercivity above room temperature [33].

It is difficult to obtain a single MnBi phase due to the segregation of Mn. Unreacted Mn and Bi critically decrease the magnetization of Mn–Bi. For synthesizing a high fraction of the MnBi phase, various preparation methods have been performed. For example, Yoshida et al. synthesized MnBi by arc melting in He gas [36]. In other studies, amorphous Mn–Bi was prepared by rapid solidification [37–39]. The fraction of crystallized MnBi phase from an amorphous Mn–Bi was over 95 wt.% [37]. The obtained grain size of crystallized MnBi was 20–30 nm, resulting in a high coercivity of 25 kOe at 540 K [38]. Yang et al. performed magnetic separation of ferromagnetic MnBi, diamagnetic Bi, and paramagnetic Mn [40]. Recently, a MnBi phase prepared by hot compaction, and high coercivity of $H_c >$ 30 kOe above 450 K was obtained [41]. On the other hand, processing in a magnetic field influences the functions of the materials. Magnetic field processing has realized three-dimensional orientation of materials [42, 43], growth of larger single crystals of silicon, and so on.

In the case of ferromagnetic materials, the ferromagnetic phases with large magnetization stabilize under a magnetic field by the gain of Zeeman energy, examples being change of phase equilibrium of the Fe–C system [44–46] and the Bi–Mn system [47, 48]. In addition, the diffusion coefficient and the morphology, such as crystal orientation, the grain alignment, grain size, and so on, were controlled by annealing under a magnetic field. For example, the suppression of the diffusion coefficient of carbon in iron has been reported [49]. In other studies, the

in-field annealing improved the coercivity field of Nd–Fe–B permanent magnets [50] and the magnetostriction of the $TbFe_2$-based alloys [51].

In-field heat treatments for synthesizing Bi–Mn have also been performed [52–55]. The morphology of Bi–Mn alloys is also influenced by in-field annealing, resulting in uniaxial aligned and coarsened ferromagnetic MnBi grains in the Bi-rich matrix [53–55]. These magnetic field effects were explained by uniaxial crystallization of the MnBi phase and rotation of the ferromagnetic MnBi grains in a Bi-rich matrix under a magnetic field [55].

In this section, among the recent techniques for synthesizing MnBi, the in-field reactive sintering method is described for solid-state sintering (Mn solid + Bi solid → MnBi) and liquid-state sintering (Mn solid + Bi liquid → MnBi) [56–58]. These in-field syntheses were carried out at 523 K and 533 K, which were just below the eutectic point of Bi–Mn system and just above the melting point of Bismuth, respectively. For performing reactive sintering in a magnetic field, the sample was heated in an electric furnace utilized for the cryogen-free superconducting magnet. Details of the electric furnace for in-field annealing can be found in Ref. 59.

Figure 4.5 shows X-ray diffraction patterns of bulk samples sintered at 15 T for 1 day in solid- and liquid-state reactions [58]. *00l* diffraction of the MnBi phase was strongly observed for both in-field sintered samples. The obtained fraction of the MnBi phase is 82 wt.% for the solid-state reaction and 71 wt.% for the liquid-state reaction. On the other hand, the fraction of MnBi phase obtained by the solid-state reaction in a zero field was only 9 wt.%. As mentioned above, a high fraction and highly oriented MnBi phase can be obtained by in-field reactive sintering. Furthermore, in-field reactive sintering realized enhancement of the reaction [58].

Figure 4.6 shows typical magnetic properties of in-field sintered samples [58]. In both curves, anisotropic magnetic properties can be clearly observed. The easy axis is parallel to the thickness of the pellet, which is parallel to the *c*-axis of the hexagonal structure. Thus, in-field heat treatment realized anisotropic magnetic properties due to the synthesis of the uniaxial-oriented crystal.

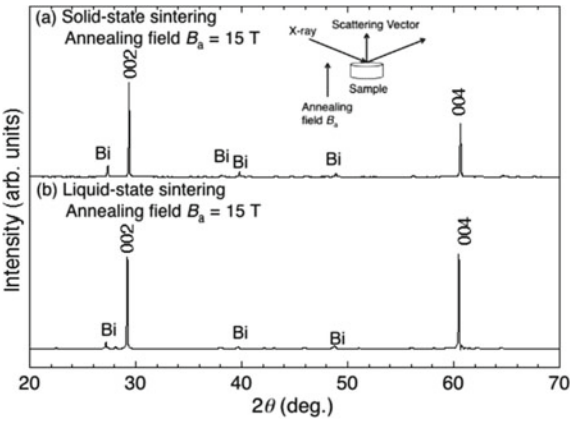

Fig. 4.5 Bulk X-ray diffraction patterns of Bi–Mn samples sintered by solid-state sintering (**a**) and liquid-state sintering (**b**). The inset figure indicates the relationship between the sample, the scattering vector of X-ray, and the direction of annealing field B_a. Reprint from Ref. [58], Copyright 2016, with permission from AIP Publishing LLC

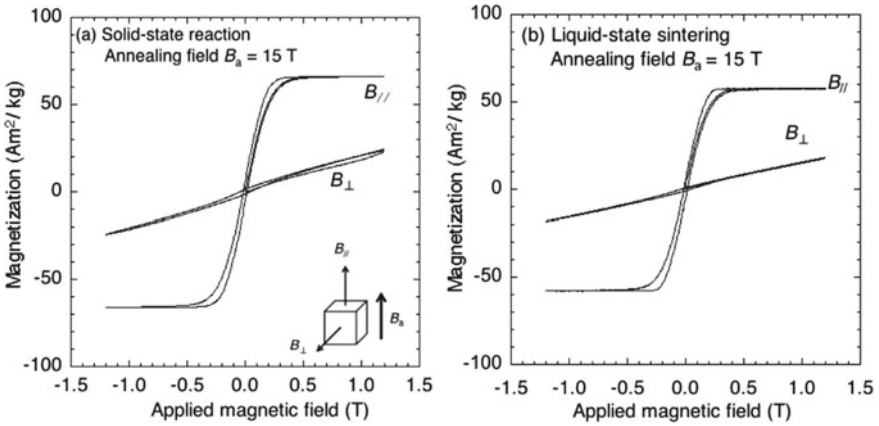

Fig. 4.6 Magnetization curves for the samples sintered by solid- (**a**) and liquid-state sintering (**b**). $B_{//}$, $B_\perp$ is the measured magnetic field direction, which is parallel and perpendicular to the thickness of the pellet. The inset in (**a**) indicates the relationship between $B_{//}$, $B_\perp$ and the annealing field directions. Reprint from Ref. [58], Copyright 2016, with permission from AIP Publishing LLC

As described above, the effects of the magnetic field on reactive sintering from Mn and Bi powder were found to be as follows:

(1) Enhancement of reactions.
(2) Synthesis of the uniaxial-oriented MnBi phase.

The origin of the magnetic field effects for the reaction in the Bi–Mn system was not investigated in detail. However, it is expected that the in-field annealing will be one of the methods for preparing the anisotropic ferromagnetic bulk materials. Although the in-field reaction realized the synthesis of the uniaxial-oriented MnBi phase, magnetic properties need to be improved. For example, as seen in Fig. 4.6, the coercivity is low. Magnetic properties heavily depend on morphology, such as grain size, crystal orientation, and so on. These morphologies depend on the size of the raw powder, annealing temperature, and annealing time. Thus, the optimization of experimental conditions is required to improve the magnetic properties of MnBi.

References

1. T. Yamada, N. Kunitomi, Y. Nakai, D.E. Cox, G. Shirane, J. Phys. Soc. Jpn. **28**, 615–627 (1970)
2. H. Nakamura, K. Yoshimoto, M. Shiga, M. Nishi, K. Kakurai, J. Phys. Condens. Matter **9**, 4701–4728 (1997)
3. M. Miyakawa, R.Y. Umetsu, M. Ohta, A. Fujita, K. Fukamichi, T. Hori, Phys. Rev. B **72**, 054420 (2005)
4. Y. Endoh, Y. Ishikawa, J. Phys. Soc. Jpn. **30**, 1614–1627 (1971)

5. J. Hafner, D. Spišák, Phys. Rev. B **72**, 144420 (2005)
6. N. Môri, T. Mitsui, J. Phys. Soc. Jpn. **25**, 82–88 (1967)
7. K.R.A. Ziebeck, P.J. Webster, J. Phys. F: Metal Phys. **5**, 1756–1766 (1975)
8. J.M.D. Coey, J. Phys. Condens. Matter **26**, 064211 (2014)
9. B. Balke, G.H. Fecher, J. Winterlik, C. Felser, Appl. Phys. Lett. **90**, 152504 (2007)
10. S. Mizukami, A. Sakuma, T. Kubota, Y. Kondo, A. Sugihara, T. Miyazaki, Appl. Phys. Lett. **103**, 142405 (2013)
11. S.N.S. Murthy, R.J. Begum, C.S. Somanathan, M.R.L.N. Murthy, J. Appl. Phys. **40**, 1870–1871 (1969)
12. G.B. Street, E. Sawatzky, K. Lee, J. Appl. Phys. **44**, 410–413 (1973)
13. K. Shibata, H. Watanabe, H. Yamauchi, T. Shinohara, J. Phys. Soc. Jpn. **35**, 448–451 (1973)
14. D.D. Bacon, E.A. Nesbitt, R.C. Sherwood, J.H. Wernick, U.S. Patent 95707 (1970)
15. R.C. Sherwood, E.A. Nesbitt, J.H. Wernick, D.D. Bacon, A.J. Kurtzig, R. Wolfe, J. Appl. Phys. **42**, 1704–1705 (1971)
16. K. Lee, E. Sawatzky, J.C. Suits, J. Appl. Phys. **44**, 1756–1758 (1973)
17. J. Strzeszewski, J. Magn. Magn. Mater **15–18**, 1103–1104 (1980)
18. H. Ido, T. Kamimura, K. Shirakawa, J. Appl. Phys. **55**, 2365–2366 (1984)
19. T. Kamimura, H. Ido, K. Shirakawa, J. Appl. Phys. **57**, 3255–3257 (1985)
20. R.Y. Umetsu, Y. Mitsui, Y. Isamu, T. Teruaki, H. Kawarada, IEEE Trans. Magn. **50**, 1001904 (2014)
21. T. Kanomata, T. Suzuki, H. Yoshida, T. Kaneko, J. Magn. Magn. Mater **104–107**, 1957–1958 (1992)
22. T. Kanomata, T. Kawashima, T. Kaneko, H. Takahashi, N. Mōri, Jpn. J. Appl. Phys. **30**, 541–544 (1991)
23. Y. Kota, A. Sakuma, J. Phys. Soc. Jpn. **83**, 034715 (2014)
24. K. Motizuki, T. Korenari, M. Shirai, J. Magn. Magn. Mater **104–107**, 1923–1924 (1992)
25. R.R. Heikes, Phys. Rev. **99**, 446–447 (1955)
26. B.W. Roberts, Phys. Rev. **104**, 607–616 (1956)
27. T. Chen, J. Appl. Phys. **45**, 2358–2360 (1974)
28. B.A. Huberman, Phys. Rev. B **12**, 2741–2746 (1975)
29. K. Koyama, T. Onogi, Y. Mitsui, Y. Nakamori, S. Orimo, K. Watanabe, Mater. Trans. **48**, 2414–2418 (2007)
30. T. Chen, W.E. Stutius, IEEE Trans. Mag. **10**, 581–586 (1974)
31. X. Guo, X. Chen, Z. Altounian, J.O. Strom-Olsen, Phys. Rev. B **46**, 14578–14582 (1992)
32. A. Sakuma, Y. Manabe, Y. Kota, J. Phys. Soc. Jpn. **82**, 073704 (2013)
33. S. Cao, M. Yue, Y.X. Yang, D.T. Zhang, W.Q. Liu, J.X. Zhang, Z.H. Guo, W. Li, J. Appl. Phys. **10**, 07A740 (2011)
34. D.T. Zhang, W.T. Geng, M. Yue, W.Q. Liu, Q.M. Lu, J.X. Zhang, Z.H. Guo, W. Li, J.A. Sundararajan, Y. Qiang, J. Appl. Phys. **115**, 17A746 (2014)
35. N.V. Rama Rao, A.M. Gabay, G.C. Hadjipanayis, IEEE Trans. Magn. **49**, 3255–3257 (2013)
36. H. Yoshida, T. Shima, T. Takahashi, H. Fujimori, Mater. Trans. JIM **40**, 455–458 (1999)
37. X. Guo, A. Zaluska, Z. Altounian, J.O. Strom-Olsen, J. Mater. Res. **5**, 2648 (1990)
38. J.B. Yang, Y.B. Yang, X.G. Chen, X.B. Ma, J.Z. Han, Y.C. Yang, S. Guo, A.R. Yan, Q.Z. Huang, M.M. Wu, D.F. Chen, Appl. Phys. Lett. **99**, 082505 (2011)
39. T. Saito, R. Nishimura, D. Nishio-Hamane, J. Magn. Magn. Mater. **349**, 9–14 (2014)
40. J.B. Yang, W.B. Yelon, W.J. James, Q. Cai, M. Kornecki, S. Roy, N. Ali, Ph l'Heritier, J. Phys. Condens. Matter **14**, 6509–6519 (2002)
41. N.V. Rama Rao, A.M. Gabey, G.C. Hadjipanayis, J. Phys. D: Appl. Phys. **46**, 062001 (2013)
42. T. Kimura, C. Chang, F. Kimura, M. Maeyama, J. Appl. Cryst. **42**, 535–537 (2009)
43. M. Yamaki, S. Horii, M. Haruta, J. Shimoyama, Jpn. J. Appl. Phys. **51**, 010107 (2012)
44. J.-K. Choi, H. Ohtsuka, Y. Xu, W.-Y. Choo, Scr. Mater. **43**, 221–226 (2000)
45. Y.D. Zhang, C.S. He, X. Zhao, Y.D. Wang, L. Zuo, C. Esling, Sol. Stat. Phenom. **105**, 187 (2005)

46. Y. Mitsui, Y. Ikehara, K. Takahashi, S. Kimura, G. Miyamoto, T. Furuhara, K. Watanabe, K. Koyama, J. Alloy. Compd. **632**, 251–255 (2015)
47. K. Koyama, Y. Mitsui, E.S. Choi, Y. Ikehara, E.C. Palm, K. Watanabe, J. Alloy. Compd. **509**, L78–L80 (2011)
48. Y. Mitsui, K. Koyama, K. Watanabe, Mater. Trans. **54**, 242–245 (2013)
49. H. Fujii, S. Tsurekawa, Phys. Rev. B **83**, 054412 (2011)
50. H. Kato, T. Miyazaki, M. Sagawa, K. Koyama, Appl. Phys. Lett. **84**, 4230–4232 (2004)
51. Q. Wang, Y. Liu, T. Liu, P. Gao, K. Wang, Appl. Phys. Lett. **101**, 132406 (2002)
52. H. Morikawa, K. Sassa, S. Asai, Mater. Trans. **39**, 814–818 (1998)
53. H. Yasuda, I. Ohnaka, Y. Yamamoto, A.S. Wismogroho, N. Takezawa, K. Kishio, Mater. Trans. **44**, 2550–2554 (2003)
54. Y. Liu, J. Zhang, S. Cao, G. Jia, X. Zhang, Z. Ren, X. Li, C. Jing, K. Deng, Solid State Commun. **138**, 104–109 (2006)
55. C. Lou, Q. Wang, T. Liu, N. Wei, C. Wang, J. He, J. Alloy Compd. **505**, 96–100 (2010)
56. Y. Mitsui, R.Y. Umetsu, K. Koyama, K. Watanabe, J. Alloy Compd. **615**, 131–134 (2014)
57. Y. Mitsui, K. Abematsu, R.Y. Umetsu, K. Takahashi, K. Koyama, J. Magn. Magn. Mater. **400**, 304–306 (2016)
58. K. Abematsu, Y. Mitsui, A. Taira, D. Miyazaki, A. Takaki, R.Y. Umetsu, K. Takahashi, K. Koyama, AIP Conf. Proc. **1763**, 020010 (2016)
59. K. Watanabe, S. Awaji, K. Kimura, Jpn. J. Appl. Phys. **36**, L673–L675 (1997)

Chapter 5
Functional Materials Developed in IMR

Fengxiang Qin, Zhenhua Dan, Wei Zhang, Soyalatu, Mitsuo Niinomi, Takeyuki Nakamoto, Takahiro Kimura and Takashi Nakajima

Abstract In this chapter, three functional materials developed in IMR are introduced. The first one is nanoporous metals produced by dealloying Ti-based amorphous alloys. Its process and surface analyses are briefly described. Moreover, Zr-based Zr–Ti gradient material as a biocompatible material is introduced and its microstructure and mechanical properties are summarized. Finally, the Fe–Co alloy thin films were prepared to apply for energy harvesters and their magnetostriction is briefly summarized.

Keywords Nanoporous material · Metallic glass · Catalyst · Biocompatible material · Gradient material · Magnetostriction

F. Qin · Z. Dan · W. Zhang (✉) · Soyalatu · M. Niinomi · T. Nakajima
Institute for Materials Research, Tohoku University, 2-1-1 Katahira, Aoba, Sendai 980-8577, Japan
e-mail: wzhang@dlut.edu.cn

F. Qin
School of Materials Science and Engineering, Nanjing University of Science and Technology, Nanjing 210094, China

Z. Dan
School of Materials Science and Engineering, Nanjing TECH University, Nanjing 210009, China

W. Zhang
Dalian University of Technology, 2 Linggong Road, Ganjingzi, Dalian 116024, Liaoning, China

T. Nakamoto
Institute of Materials and Systems for Sustainability, Nagoya University, Furo-cho, Chikusa, Nagoya 464-8603, Japan

T. Kimura
Machining & Molding Section, Technology Research Institute of Osaka Prefecture, 2-7-1 Ayumino, Izumi, Osaka 594-1157, Japan

T. Nakajima
Tokyo University of Science, 6-3-1 Niijuku, Katsushika, Tokyo 125-8585, Japan

Y. Setsuhara et al. (eds.), *Novel Structured Metallic and Inorganic Materials*, https://doi.org/10.1007/978-981-13-7611-5_5

5.1 Nanoporous Metals

Fengxiang Qin, Zhenhua Dan and Wei Zhang

Recently, the nanoporous materials have been the focus of much attention due to their potential in various applications, but especially as catalyst, sensors, and actuators [1–3]. The dealloying process, the selective dissolution of a less noble alloying element in an aqueous solution, was found to be an effective method of fabricating nanoporous metals such as copper, silver, gold, platinum, etc. [4]. The dealloying processes are impacted by many parameters, such as the alloy compositions, the solution composition and temperature, and the treatment time [4–6]. Amorphous alloys can be characterized by their disordered atomic-scale structure and an absence of the grain boundaries and weak spots typical of crystalline materials [7, 8]. Therefore, there are high expectations of amorphous alloys as metals which, due to the homogeneity in the matrix, are likely to be able to form uniform nanoporous structures more readily than crystalline alloys. The selection of an appropriate electrolyte for dealloying is of critical importance. Monolithic nanoporous copper was fabricated from crystalline Al–Cu [4], Mn–Cu [9, 10], and Al–Zn–Cu [11]. The dealloying process has not been used to fabricate a nanoporous Cu structure using the binary Ti–Cu amorphous alloy system. For reactions with Ti-based materials, fluoride ions seem effective [12] since the solubility of CuF_2 chemicals was reported as 0.075 g/100 g H_2O [13], which is much lower than that of TiF_4 or $[TiF_6]^{2-}$ species. From an electrochemical perspective, the standard electrode potentials of Ti and Cu (−1.630 V versus the standard hydrogen electrode (SHE) for Ti/Ti^{2+} and 0.342 V vs. SHE for Cu/Cu^{2+}) differ as much as 1972 mV [13], which promises to be a great driving force for dealloying Ti from binary Ti–Cu alloys. Meanwhile, the Ti–Cu melt-spun ribbons are in a chemically and physically homogeneous amorphous state. It is therefore expected that homogeneous nanoporousity can be formed without preferential dissolution, and that by dealloying amorphous binary Ti–Cu alloys in HF solutions. In this chapter, we report the fabrication of nanoporous copper (NPC) from binary Ti–Cu amorphous alloys. The starting material, amorphous binary Ti_xCu_{100-x} (x = 30, 40, 50 and 60 at.%) alloys, was immersed in an HF solution under a free corrosion condition. The concentrations of HF solution were 0.027 M (pH 3.3), 0.133 M (pH 2.9), and 0.651 M (pH 2.6), hereafter referred as Sol-1, Sol-2, and Sol-3, respectively.

5.1.1 Morphology of As-dealloyed Ti–Cu Alloys

As previous work presented, as-spun $Ti_{40}Cu_{60}$, $Ti_{50}Cu_{50}$, and $Ti_{60}Cu_{40}$ ribbons are amorphous state by the identification of XRD technique [14]. Figure 5.1 shows the nanoporous structure of as-spun $Ti_{50}Cu_{50}$ ribbons after 600 s, 1.8 ks, 3.6 ks, and 10.8 ks of immersion in Sol-1, Sol-2, and Sol-3. After 600 s of immersion, pores a

few tenths of nanometers in size were formed except where there were some crack-like voids a few hundred nanometers in length due to the selective leaching of Ti-rich elements. After 1.8 ks of immersion, a structure similar to an interpenetrated bicontinuous mode was formed. The porous structure formed in all three dimensions due to the successive dealloying in the depth directions.

After 600 s, 1.8 ks, 3.6 ks, and 10.8 ks of immersion in Sol-2 (Fig. 5.1b1–4), the length scales of the bicontinuous ligaments increased from several tenths nanometers to hundredths nanometers. The larger pores in Sol-3 than those in Sol-1 and Sol-2 can be attributed to the difference in the concentration of the HF solutions. The NPCs formed in three solutions are similar in morphology and the length scale of the

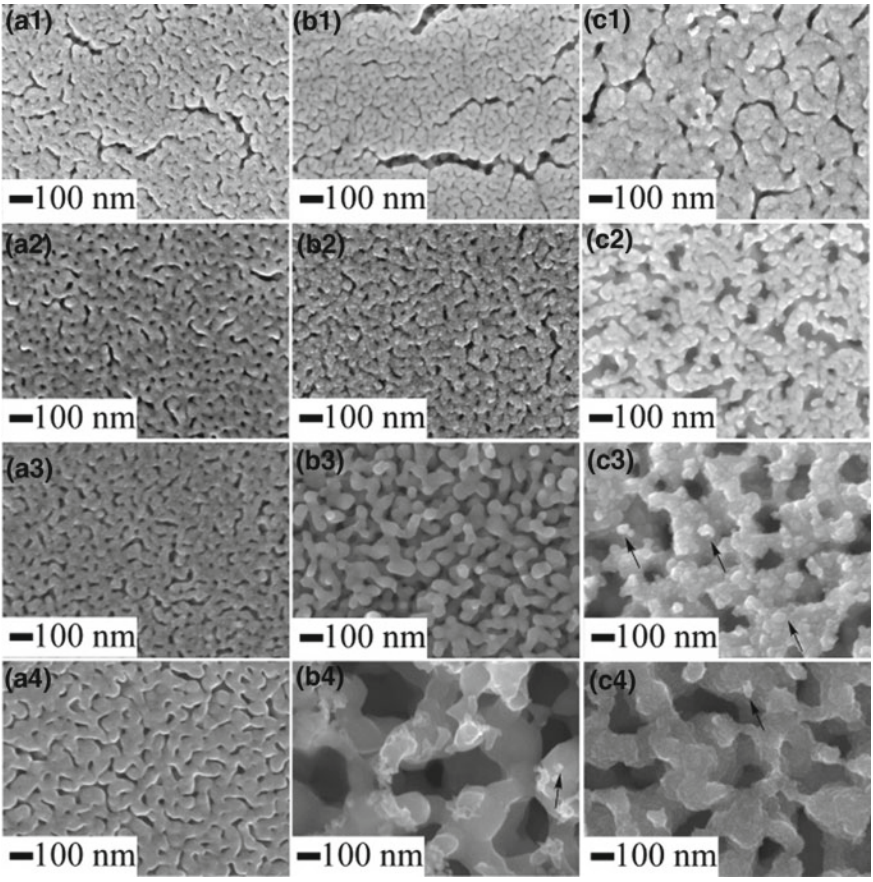

Fig. 5.1 SEM morphology of as-dealloyed Ti50Cu50 ribbon treated in Sol-1 **a** after 600 s (**a1**), 1.8 ks (**a2**), 3.6 ks (**a3**), and 10.8 ks (**a4**); in Sol-2 **b** after 600 s (**b1**), 1.8 ks (**b2**), 3.6 ks (**b3**), and 10.8 ks (**b4**); in Sol-3 **c** after 600 s (**c1**), 1.8 ks (**c2**), 3.6 ks (**c3**), and 10.8 ks (**c4**) under an open-to-air free corrosion condition at 298 K. Reprinted from Ref. [14], Copyright 2012, with permission from Elsevier

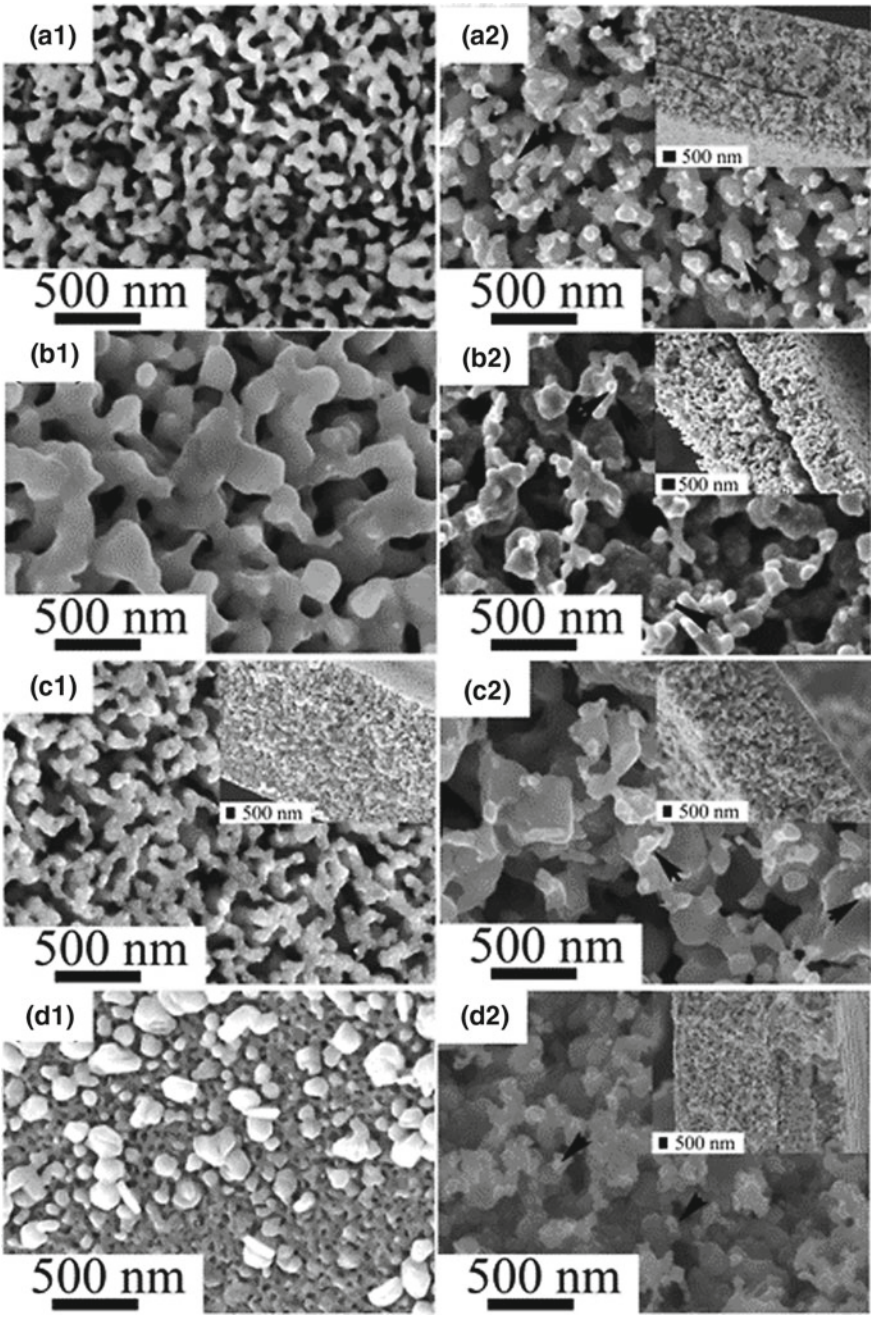

Fig. 5.2 SEM morphology of as-dealloyed $Ti_{60}Cu_{40}$ ribbons immersed in Sol-1 (**a1**) and Sol-2 (**a2**), $Ti_{50}Cu_{50}$ in Sol-1 (**b1**) and Sol-2 (**b2**), $Ti_{40}Cu_{60}$ in Sol-1 (**c1**) and Sol-2 (**c2**), and $Ti_{30}Cu_{70}$ in Sol-1 (**d1**) and Sol-2 (**d2**) for 43.2 ks at an open-to-air free corrosion condition. Reprinted from Ref. [14], Copyright 2012, with permission from Elsevier

ligament of the NPC is larger in more concentrated HF solutions. Figure 5.2 shows the morphology of as-dealloyed Ti_xCu_{100-x} (x: 30, 40, 50, and 60 at.%) ribbons after immersion in Sol-1 and Sol-2 for 43.2 ks. The as-dealloyed Ti–Cu ribbons are porous with some Cu nanoparticles at the edge of the pores with sizes ranging from several tenths of nanometers to few hundred nanometers, marked by the arrows in Figs. 5.1 and 5.2. Those Cu nanoparticles might be due to the rearrangement of the dissolved Cu atoms during the dealloyings [15]. Despite the monolithic characteristic, the NPC ribbons are brittle, and are commonly curly. The as-dealloyed ribbons exhibit an open, bicontinuous interpenetrating ligament-channel structure with length scales of one to several hundred nanometers in Sol-2. The cross-sectional views show the NPCs were three-dimensional structures, and the size of the pores of the NPCs decreased as atomic ratios of the Cu in the Ti–Cu ribbons increased. Moreover, the cross-sectional view of the pores shows an increase in size with increased concentrations of the HF solutions. In the case of the $Ti_{30}Cu_{70}$ ribbons treated in Sol-1, the NPCs were not obtained and the precipitation on the surface occurred. When the titanium atoms in the surface region were dissolved out during dealloying, the residual Cu has the smaller difference in the standard electrode potentials between the NPC and Cu electrode. The dealloying reactions hardly proceeded further to leach Ti atoms in the inner $Ti_{30}Cu_{70}$ matrix due to the deprivation of the large difference in the standard electrode potentials.

5.1.2 Characteristics of As-dealloyed Ti–Cu Alloys

Figure 5.3a, b, c shows the bright-field TEM images, selected-area diffraction patterns (SADP), and the high-resolution TEM (HR-TEM) image of as-dealloyed $Ti_{50}Cu_{50}$ ribbons immersed in Sol-2 for 43.2 ks. The three-dimensional bicontinuous porous structure is clearly visible, and the pore size varies from a few tenths of nanometers to several hundred nanometers. Meanwhile, some nanoparticles with several tenths of nanometers in size can be observed outside the nanopores. As shown in Fig. 5.3b, the diffraction rings marked at the lower part were assigned to Cu (111), (200), (220), and (311). On the other hand, those marked at the upper part were assigned to Cu_2O (110), (111), (200), (211), (220), and (311). The amount of Cu_2O species was small due to the weak intensity of the corresponding diffraction rings. Summarily, the SADP proved that the as-dealloyed ribbons are consisted of face-centered cubic (fcc) Cu and small amount of Cu_2O. The HR-TEM image shows that the NPCs have a polycrystalline structure, indicating the original Cu atoms were rearranged to form a crystalline structure as they were dealloyed [15]. In order to confirm the elements state before and after immersion in HF solutions, XPS analysis was performed. The results are shown in Fig. 5.4 and Table 5.1. The XPS spectra from the native surface of the as-spun $Ti_{50}Cu_{50}$ ribbon over a wide binding energy region exhibited peaks of carbon, oxygen, titanium, and copper. The C1s peaks were so-called contaminant carbon on the top of surface of the sample. All the oxygen came from surface oxide. The O1s spectra measured were composed of

two peaks at 529.8 and 531.2 eV, which were assigned to OM oxygen and OH oxygen, respectively. The OM oxygen denotes oxygen with a Ti–O bond. As shown in Fig. 5.4, peaks at 932.4 and 952.2 eV are observed on the Cu 2p spectrum region, without a satellite peak between the 2p3/2 and 2p1/2 peak which is the characteristics of the peak for oxidized Cu, indicating that Cu exists in metal state. The Ti 2p spectra are composed of two main peaks, which are identified as Ti 2p1/2 and Ti 2p3/2, mainly originating from TiO_2 (as shown in Fig. 5.4 and Table 5.1). After immersion in Sol-2 for 43.2 ks, in survey spectrum, no titanium peak was detected, meaning that all titanium was dealloyed completely during the process of immersion. A weak satellite peak can be observed between Cu 2p3/2 and 2p1/2 and the small amount of Cu was oxidized to be CuO. However, the amount of Cu_2O was relatively higher than CuO, but it is very limited compared to the Cu metal. As shown in Fig. 5.3, it is known that the as-dealloyed $Ti_{50}Cu_{50}$ composed of fcc Cu phase and Cu_2O. These Cu_2O and CuO are believed originating from oxidization of the outer surface due to the large surface area of nanoporous structure. In addition, no fluoride species were detected on the surface of the as-dealloyed Ti–Cu ribbons by XPS analysis, which indicates that the fluoride ions combined with Ti^{4+}, O^{2-} to form the highly soluble species.

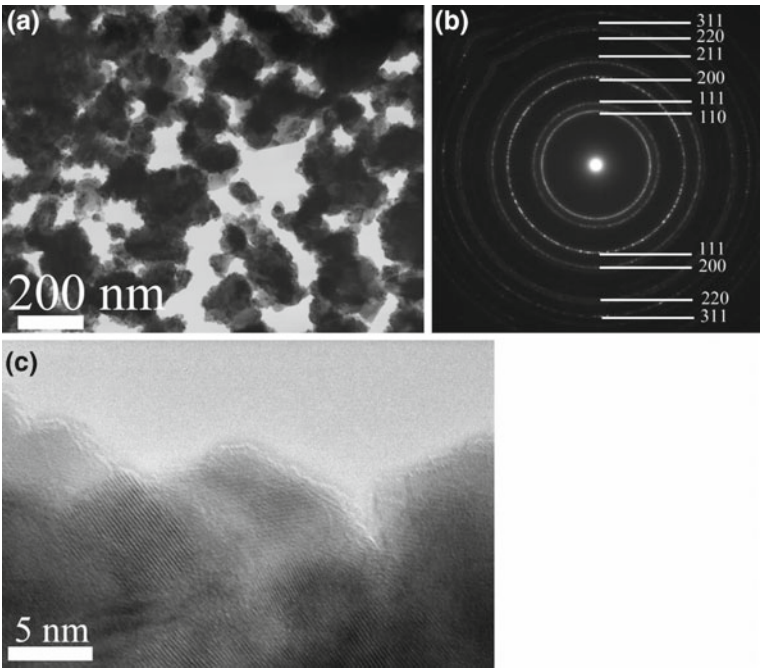

Fig. 5.3 Bright field TEM image (**a**), SADP (**b**) and high-resolution TEM images (**c**) of as-dealloyed $Ti_{50}Cu_{50}$ ribbon treated in Sol-2 for 43.2 ks at free corrosion conditions at 298 K. Reprinted from Ref. [14], Copyright 2012, with permission from Elsevier

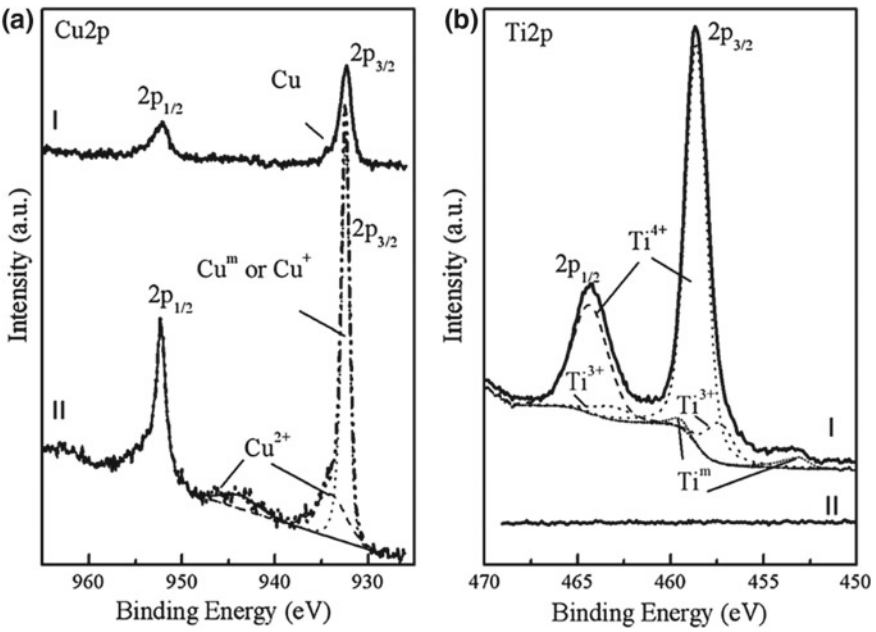

Fig. 5.4 Cu (**a**) and Ti (**b**) XPS peaks of as-spun $Ti_{50}Cu_{50}$ ribbon before (I) and after (II) dealloying in Sol-2 for 43.2 ks. Reprinted from Ref. [14], Copyright 2012, with permission from Elsevier

Table 5.1 Ratios of the corresponding Cu2p3, Ti2p, O1s, and C1s of as-spun $Ti_{50}Cu_{50}$ ribbons and as-dealloyed $Ti_{50}Cu_{50}$ ribbons treated in Sol-2 for 43.2 ks. Reprinted from Ref. [14], Copyright 2012, with permission from Elsevier

As-spun $Ti_{50}Cu_{50}$			As-dealloyed $Ti_{50}Cu_{50}$	
Name	At. Conc. %	Mass Conc. %	At. Conc. %	Mass Conc. %
Cu2p3	1.87	6.02	11.17	37.97
Ti2p	14.78	35.83	0	0
O1s	36.91	29.9	23.18	19.84
C1s	46.44	28.25	65.65	42.19

5.1.3 Discussion

The as-spun $Ti_{50}Cu_{50}$ ribbons were also immersed in 1 M HCl and 1 M HNO_3 solutions for 1296 ks under free corrosion conditions at 298 K. No porous structures were obtained, and the ribbons were locally attacked with a few micrometer-ordered pits formed. On the whole, $Ti_{50}Cu_{50}$ alloy showed high stability in HCl and HNO_3 solutions. The presence of a native TiO_2 layer, confirmed by XPS analysis, can be assumed to have protected the substrate from the corrosion

attack of Cl^- and NO_3^- ions. It can be concluded, therefore, that the hydrofluoric acid played a key role in a breakdown of the barrier of the native Ti_2O layer and further dissolution of the Ti elements existing in the binary Ti–Cu alloys. After the dissolution of the native oxide layer is completed, HF solution reacts with Ti atoms in the Ti–Cu clusters. The Ti atoms reacted with abundant HF species to form TiF_4 and hydrogen gas, and then the TiF_4 continued reacting with F^- ions to form the water-soluble $[TiF_6]^{2-}$ species [16]. As the Ti atoms gradually dissolved from the Ti–Cu clusters, the Cu atoms rearranged to form the NPCs with a nanoscaled fcc structure. Chen et al. [11] reported the fabrication of NPCs from $Cu_{30}Mn_{70}$ ribbons succeeded in HCl solutions. The different reactions occurred to Mn and Ti alloying metals resulted from the different stabilities of the binary alloys in HCl and HF solutions, which was actually determined by the nature of the native oxide layer on the initial surface. The selection of the treatment solutions should be considered from the perspectives of the dissolution of the protection layers. Nanoporous copper reduced from an amorphous Ti–Cu alloy with a high surface area has potential applications as catalysts or sensors.

In conclusion, binary amorphous Ti_xCu_{100-x} (x = 30, 40, 50, and 60 at.%) alloys were prepared by arc melting and the melt-spun method. As-spun ribbons were dealloyed in various concentrations of HF solutions for different immersion times. An interpenetrating three-dimensional bicontinuous nanoporous structure of copper was formed after dealloying. The pore size is from tenths of nanometers to hundredths of nanometers, depending on the alloy composition, HF concentration, and the treatment time. Fluoride ions played a key role in dissolving the native TiO_2 oxide layer and forming highly soluble $[TiF_6]^{2-}$ species. This method of fabricating nanoporous copper from homogeneous amorphous binary Ti–Cu alloys is considered effective for preparation of nanosized catalysts.

5.2 Zr-Based Zr–Ti Gradient Material Fabricated by Selective Laser Melting Process for Bone Plate Applications

Soyalatu, Mitsuo Niinomi, Takeyuki Nakamoto and Takahiro Kimura

5.2.1 Introduction

Ti and its alloys are candidate materials for preparing bone plates because of their good mechanical properties, outstanding corrosion resistance, and good biocompatibility, which result in tight bonding with newly formed bone [17, 18]. However, implanted bone plates must sometimes be removed after healing of the bone fracture. In such cases, the addition of a zirconium coating to Ti and Ti alloy bone plates is useful because Zr prevents tight bonding with bone [19]. Recently, additive

manufacturing (AM) has received attention as a method of fabricating coatings [20]. In the present study, fabrication of Zr-based Zr–Ti gradient material for the use in bone plates via SLM is investigated.

5.2.2 *Zr-Based Zr–Ti Gradient Material Fabricated via SLM*

In this study, Ti plates were prepared along with the Zr powder (average particle diameter of <32 μm) used to coat them. Ti/Zr composites were fabricated via SLM. The microstructures were characterized via using a scanning electron microscopy (SEM) and an electron backscatter diffraction (EBSD, Quanta 200 3D SEM-TSL) analysis. The hardness of the composites was evaluated using a nanoindentation tester. Optical microscopy (OM) and SEM micrographs of the top surface of a Ti/Zr composite fabricated via SLM are shown in Fig. 5.5. The images show fully dense, layered martensitic structures. Figure 5.6 shows SEM images and electron probe microanalyzer (EPMA) element maps of a vertical cross section of the track created by a laser beam in the top layer. The concentration of Ti and Zr vary gradually because of fusion. Laser melting affects only the top layer of Zr. This first layer also exhibits a martensitic structure, as shown in Fig. 5.5c. As shown in Fig. 5.7a, this martensitic state is also confirmed by EBSD inverse pole figure (IPF) maps of the vertical cross section of the Ti/Zr composite. This first layer is important with regard to Zr coating, as previous researchers have reported that Ti coatings on Co–Cr substrates show cracks in the interfacial region [21]. In this study, no crack is shown in the Ti/Zr composite material (Fig. 5.6a, b), because Zr forms a substitutional solid solution with Ti and the two elements have similar physical properties.

Figure 5.8 shows the Vickers hardness of the top layer of the Ti/Zr composite. This martensitic structure exhibits higher Vickers hardness than that of the matrix, and has no micro-cracks. This study examines one layer of melted Zr on Ti plate, but and the SLM technique can easily repeat deposition. It means that further several layers of pure Zr can be fabricated on Ti. The SLM method can fabricate gradient functional implant devices, and the fabricated Zr–Ti gradient material may be useful in applications that require a removable bone plate.

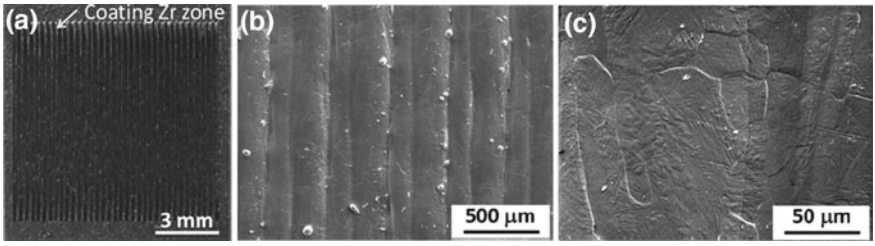

Fig. 5.5 **a** Optical microscope image of top surface of Ti/Zr composite, **b** SEM low magnified image of Zr coating layer, and **c** SEM magnified image of **b** showing its microstructure

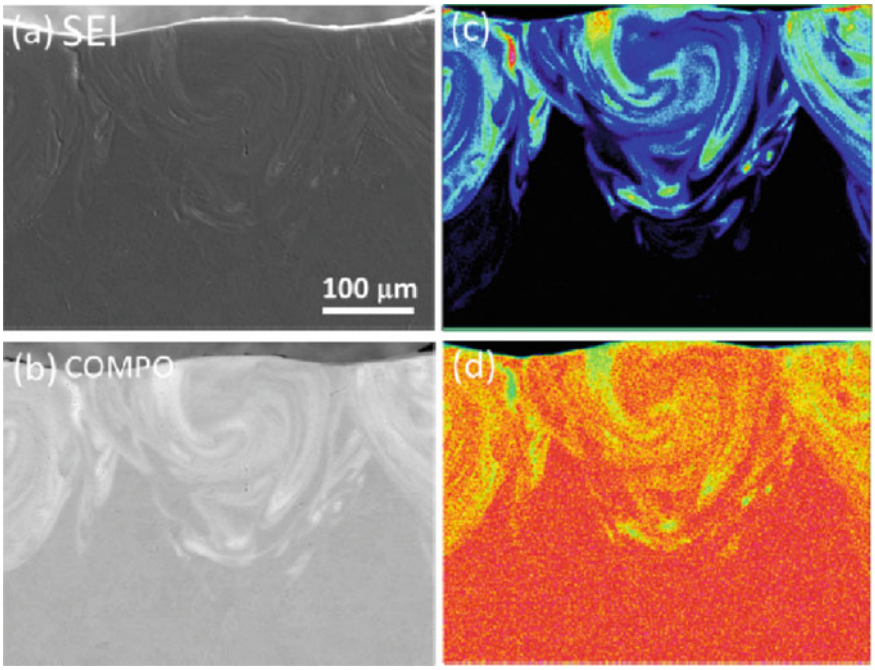

Fig. 5.6 SEM image and EPMA element maps of vertical cross section of Ti/Zr composite: **a** SEM image, **b** COMPO SEM image, **c** Zr element map, and **d** Ti element map

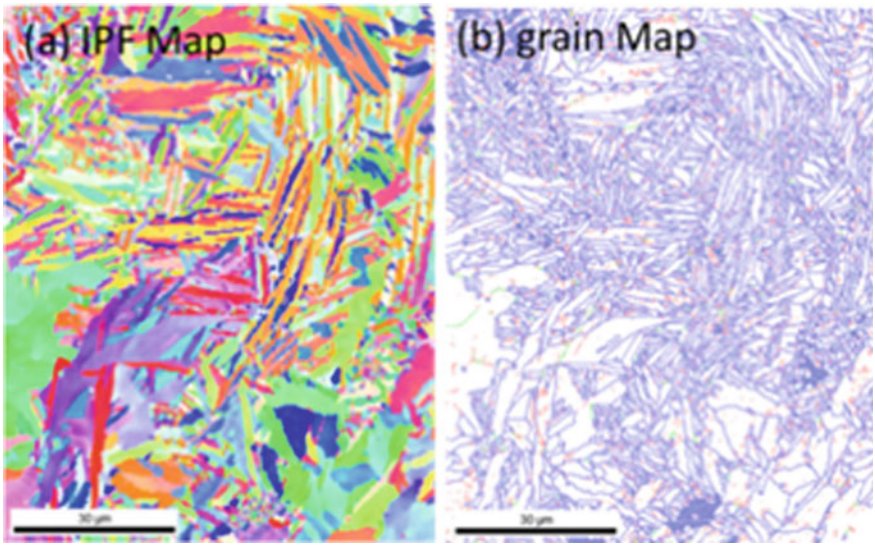

Fig. 5.7 **a** EBSD IPF maps of the vertical cross section of Ti/Zr composite and **b** grain map of the same region

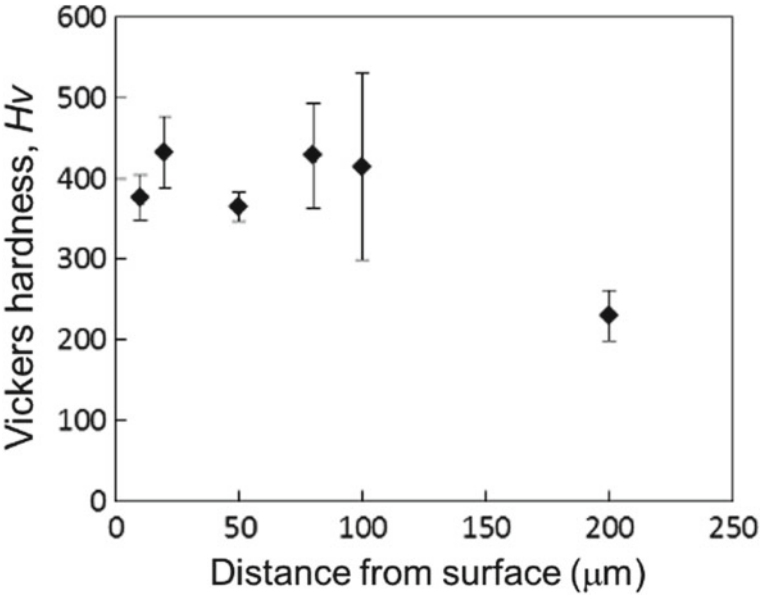

Fig. 5.8 Vickers hardnesses of Ti/Zr composite layers evaluated via nanoindentation testing

5.2.3 Summary

In this work, a Zr-based Zr–Ti gradient material was fabricated via selective laser melting (SLM). A single layer of Zr fabricated by SLM on Ti plate has been examined in this study, but the SLM technique can easily repeat deposition. It means that further several layers of pure Zr layer can be fabricated on Ti. Thus, this SLM method can be employed to fabricate gradient functional bone plates.

5.3 Magnetostrictive Fe–Co Alloy Thin Film

Takashi Nakajima

There has been strong interest in developing magnetostrictive thin films for novel sensors, actuators, and vibration energy harvesting devices [22–24]. Rare-earth-based magnetostrictive materials, represented by Terfenor-D (Tb–Dy–Fe), have played a key role for developing such applications owing to their large magnetostriction of more than 2000 ppm [25–30]. However, there has also been demand for establishing rare-earth-free magnetostrictive materials.

In recent years, the strong magnetomechanical coupling originating from the heterogeneity at the phase boundaries of Fe-based alloys has attracted great research

interest. Hunter et al. prepared compositional gradient Fe–Co alloy thin films using a combinatorial sputtering technique, and they found significant magnetostriction enhancement at the (fcc + bcc)/bcc phase boundary [31]. The effective magnetostriction was 260 ppm for an $Fe_{34}Co_{66}$ thin film quenched from 1073 K, and the intrinsic magnetostriction of the ideally oriented film was estimated to be more than 1000 ppm. Yamaura et al. reported the effect of the forging and cold rolling for the bulk Fe–Co alloy [32]. The as-forged Fe–Co with the Co content of 75 at.% alloy reached the largest magnetostriction of 108 ppm, and subsequent cold-rolling treatment further increased the magnetostriction up to 140 ppm. The enhancement of the magnetostriction was also interpreted by the interfacial effect at the (fcc + bcc)/bcc phase boundary and crystal orientation. In this section, we report on the annealing temperature dependence of the magnetostriction of Fe–Co alloy thin films to focus on the interfacial effect on magnetostriction [33].

Fe–Co alloy thin films were sputter deposited on quartz glass substrates. The substrates were 20 mm long, 5 mm wide, and approximately 60–70 μm thick for inducing the appropriate strain. The films were fabricated at a substrate temperature of 623 K under an Ar pressure of 1.0 Pa and a sputtering power of 100 W. The composition of the films was chosen to be $Fe_{32}Co_{68}$ in order to obtain an fcc and/or bcc phase by annealing between 673 and 1173 K [34]. The samples were annealed at various temperatures for 60 min in an evacuated glass tube and quenched by immersing the tube in ice water.

Figure 5.9 shows the phase diagram [34] and XRD patterns of the Fe–Co alloy thin films quenched from various temperatures. The crystalline phase of the Fe–Co alloy thin films was examined by XRD patterns as shown in Fig. 5.9b. A bcc single phase was observed when the annealing temperature was less than 1093 K. As the temperature increased, the crystal structure exhibited a coexisting phase of bcc and fcc between 1113 and 1143 K and fcc single phase above 1153 K. Thus, the crystal structures that are consistent with the conventional phase diagram shown in Fig. 5.9a are successfully obtained.

The evaluation of the magnetostriction was performed using the cantilever deflection technique, which allows the magnetostriction λ to be determined from the field-induced bending of the cantilevered sample as shown in Fig. 5.10a [35]. The displacement of the cantilever was induced by an alternating magnetic field parallel ($H_{\parallel}$) and perpendicular ($H_{\perp}$) to the in-plane direction of the substrate. The saturation magnetostriction λ_s was calculated using the following expression:

$$\lambda_s = \frac{(\Delta s_{\parallel} - \Delta s_{\perp}) E_s t_s^2 (1 + v_f)}{18 E_f t_f L l (1 - v_s)} \tag{1}$$

where $H_{\parallel}$ and $\Delta s_{\perp}$ are the maximum position change of the laser spot on the position sensitive detector (PSD) induced by $H_{\parallel}$ and $H_{\perp}$, respectively. E is the Young's modulus, v the Poisson's ratio, t the thickness, l the distance between the clamping edge to the laser spot on the sample, and L the optical travel distance from the incident point at the sample. The subscripts "s" and "f" denote "substrate", and

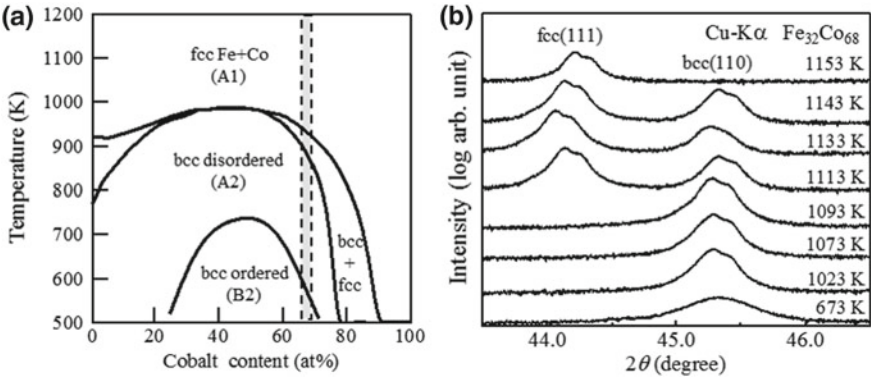

Fig. 5.9 **a** Phase diagram of the Fe–Co alloy and **b** annealing temperature dependence of XRD patterns Fe–Co alloy thin films. Reprinted from Ref. [33], Copyright 2014, with permission from the Japan Institute of Metals and Materials

"film," respectively. The magnetostriction for each sample was calculated from the field-induced butterfly loops as a result of magnetostrictive behavior, as shown in Fig. 5.10b. Figure 5.10c shows the annealing temperature dependence of λ_s for the Fe–Co alloy thin films. As the annealing temperature increased, λ_s gradually increased, reaching a maximum of 159 ppm at 1073 K and then it drastically decreased. The λ_s of the sample annealed at 1073 K is almost three times larger than that of the sample annealed at 673 K. As shown in the phase diagram and

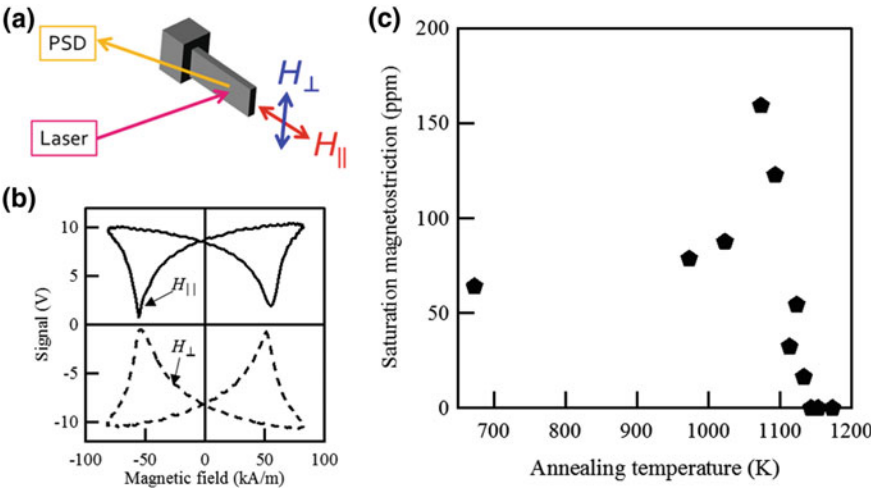

Fig. 5.10 **a** Schematic image of the magnetostiction measurement. **b** Magnetostrictive behavior as detected by cantilever deflection method. **c** Annealing temperature dependence of magnetostriction of Fe–Co alloy thin films. Reprinted from Ref. [33], Copyright 2014, with permission from the Japan Institute of Metals and Materials

XRD results, it is clear that λ_s is greatly enhanced near the bcc/fcc coexisting phase. The λ_s decreased with increasing the fcc phase, and the tendency is consistent with the results of bulk samples [32]. It is reported that the λ_s of Fe–Co alloy with single fcc phase exhibited negative magnetostriction. Therefore, the excessive fcc phase should cancel the net magnetostriction.

The origin of the magnetostriction enhancement in Fe–Co alloy is considered to result from the reorientation of the tetragonal precipitates at the (fcc + bcc)/bcc phase boundary [31]. If it is true, we can see the inhomogeneous magnetic microstructure at the phase boundary. Then, we conducted magnetic force microscopy (MFM) measurements to investigate the magnetic microstructure. Figure 5.11a is the superposed image of the AFM and MFM images of the sample annealed at 1093 K. The AFM image was obtained by tapping mode for the first scan and the MFM image was obtained for the second scan by monitoring the phase shift in the resonant cantilever oscillation, keeping the cantilever height constant above the sample surface configuration. As shown in Fig. 5.11a, the image exhibits an inhomogeneous contrast near the grain boundaries. As seen in the line profile of the height and the phase shift shown in Fig. 5.11b, the height and phase shift were not identical. The degree of the phase shift provides information on the magnetic field gradient between the cantilevered tip and the Fe–Co surface. Therefore, these results suggest that the local magnetization is enhanced around the grain interfaces of the Fe–Co alloy thin film. The magnetization increase at the grain boundaries serves as strong evidence for the presence of inhomogeneous crystal structure including the tetragonal precipitates, which supports the magnetic domain rotation model as the mechanism for the magnetostriction enhancement of the Fe–Co alloy system.

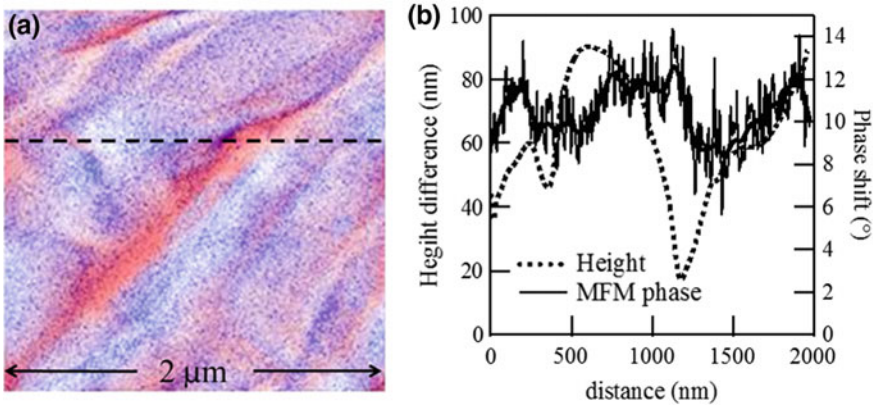

Fig. 5.11 **a** Superposed image of AFM and MFM images of Fe–Co alloy thin film annealed at 1093 K. **b** Profiles of height and phase shift upon dashed lines in **a**. Reprinted from Ref. [33], Copyright 2014, with permission from the Japan Institute of Metals and Materials

Acknowledgements This work was supported in part by the Global COE program "Materials Integration International Centre for Education and Research, Tohoku University" MEXT, Japan. Thanks are also extended to Mr. K. Kobayashi for his help in the TEM observation (FX.Q, Z.D., and W.Z.).

References

1. Y. Ding, M.W. Chen, J. Erlebacher, J. Am. Chem. Soc. **126**, 6876 (2004)
2. K. Bonroy, J.M. Friedt, F. Frederix, W. Laureyn, S. Langerock, A. Campitelli, M. Sara, G. Borghs, B. Goddeeris, P. Declerck, Anal. Chem. **76**, 4299 (2004)
3. D. Kramer, R.N. Viswanath, J. Weissmüller, Nano Lett. **4**, 793 (2004)
4. Z.H. Zhang, Y. Wang, Z. Qi, W.H. Zhang, J.Y. Qin, J. Frenzel, J. Phys. Chem. C **113**, 12629 (2009)
5. J.C. Thorp, K. Sieradzki, L. Tang, P.A. Crozier, A. Misra, M. Nastasi, D. Mitlin, S.T. Picraux, Appl. Phys. Lett. **88**, 033110 (2006)
6. X.G. Wang, Z. Qi, C.C. Zhao, W.M. Wang, Z.H. Zhang, J. Phys. Chem. C **113**, 13139 (2009)
7. W.K. Jun, R.H. Willens, P. Duwez, Nat. **187**, 869 (1960)
8. A. Inoue, Acta Mater. **48**, 279 (2000)
9. A.J. Smith, D.L. Trimm, Annu. Rew. Mater. Res. **35**, 127 (2005)
10. J.R. Hayes, A.M. Hodge, J. Biener, A.V. Hamza, J. Mater. Res. **21**, 2611 (2006)
11. L.Y. Chen, T. Fujita, Y. Ding, M.W. Chen, Adv. Funct. Mater. **20**, 2279 (2010)
12. Y.A. Buslaev, V.A. Bochkareva, N.S. Nikolaev, Russ. Chem. Bull. **11**, 361 (1962)
13. D.R. Lide, CRC handbook of chemistry and physics, 84th edn. (CRC Press, LLC, Boca Raton, London, New York, Washington, DC, 2003–2004)
14. Z.H. Dan, F.X. Qin, Y. Sugawara, I. Muto, N. Hara, Intermet. **29**, 14 (2012)
15. J. Erlebacher, J. Electrochem. Soc. **151**, C614 (2004)
16. P. Roy, S. Berger, P. Schmuki, Angew. Chem. Int. Ed. **50**, 2904 (2011)
17. M. Niinomi, Metall. Mater. Trans. **A33**, 477 (2002)
18. M. Niinomi, J. Mech. Behav. Biomed. Mater. **1**, 30 (2008)
19. Y. Tsutsumi, D. Nishimura, H. Doi, N. Nomura, T. Hanawa, Mater. Sci. Eng., C **C29**, 1702 (2009)
20. M. Das, K. Bhattacharya, S.A. Dittrick, C. Mandal, V.K. Balla, T.S. Sampath Kumar, A. Bandyopadhyay, I. Manna, J. Mech. Behav. Biomed. Mater. **29**, 259 (2014)
21. P. Fox, S. Pogson, C.J. Sutcliffe, E. Jones, Sur. Coat. Tech. **202**, 5001 (2008)
22. D.J. Bell, T.J. Lu, N.A. Fleck, S.M. Spearing, J. Micromech. Microeng. **15**, S153 (2005)
23. A. Ludwig, E. Quandt, J. Appl. Phys. **87**, 4691 (2000)
24. M.R.J. Gibbs, E.W. Hill, P.J. Wright, J. Phys. D: Appl. Phys. **37**, R237 (2004)
25. A.E. Clark, *Ferromagnetic Materials* (North-Holland, Amsterdam, 1980)
26. N.C. Koon, C.M. Williams, B.N. Das, J. Magn. Magn. Mater. **100**, 173 (1991)
27. H. Szymczak, J. Magn. Magn. Mater. **200**, 425 (1999)
28. H. Uchida, U.H. Matsumura, H. Kaneko, J. Magn. Magn. Mater. **239**, 540 (2002)
29. A.G. Olabi, A. Grunwald, Mater. Des. **29**, 469 (2008)
30. V.H. Babu, G. Markandeyulu, A. Subrahmanyam, Appl. Phys. Lett. **90**, 252513 (2007)
31. D. Hunter, W. Osborn, K. Wang, N. Kazantseva, J. Hattrick-Simpers, R. Suchoski, R. Takahashi, M.L. Young, A. Mehta, L.A. Bendersky, S.E. Lofland, M. Wuttig, I. Takeuchi, Nat. Commun. **2**, 518 (2011)
32. S. Yamaura, T. Nakajima, T. Satoh, T. Ebata, Y. Furuya, Mat. Sci. Eng. B **193**, 121 (2015)
33. T. Nakajima, T. Takeuchi, I. Yuito, K. Kato, M. Saito, K. Abe, T. Sasaki, T. Sekiguchi, S. Yamaura, Mater. Trans. **55**, 556 (2014)
34. I. Ohnuma, H. Enoki, O. Ikeda, R. Kainuma, H. Ohtani, B. Sundman, K. Ishida, Acta Mater. **50**, 379 (2002)
35. A.C. Tam, H. Schroeder, IEEE Trans. Magn. **25**, 2629 (1989)

Part II
Novel Structured Inorganic Materials

Chapter 6
Exotic Crystal Structures and Electronic Structures in Novel Structured Inorganic Materials

Toshio Kamiya, Hidenori Hiramatsu, Keisuke Ide, Takayoshi Katase and Hideo Hosono

Abstract Ionic materials like oxides have a variety of crystal/atomic structures owing to the coexistence of long-range Coulomb interaction and short-range covalent bonds, which often produce natural nanostructures embedded in their crystal structures. Such structures and materials can be sources of unusual electronic structures and nonconventional materials properties and functions. This chapter reviews such exotic crystal structures in relation to their electronic structures and properties. It will be discussed for what applications such oxides can have advantages over the conventional functional materials such as Si.

Keywords Ionic crystal · Natural nanostructure · Ionic bonds · Covalent bonds · Low dimensional electronic structures

6.1 Introduction

Oxide functional materials are now employed in many commercially available products. For example, transparent conductive oxides (TCOs) such as ITO (In_2O_3:Sn), GZO (ZnO:Ga), and FTO (SnO_2:F) are used as transparent electrodes in thin film solar cells, touch panels, and flat-panel displays (FPDs). Piezoelectric oxides are used in nanometer-controllig actuators as in atomic force microscopes, and gyro sensors and accelerometer sensors in smart phones, ferroelectric oxides are used as ferroelectric random access memory in Sony's FeliCa cards, electrochromic oxides are used in a part of anti-dazzle car mirrors, and high-K dielectrics are used in Si ULSI circuits and chip capacitors. Among them, the most successful one is amorphous oxide semiconductor (AOS) [1–3] thin-film transistors (TFTs) now employed in many flat-panel displays ranging from very high-resolution liquid crystal displays to large size (up to 88 in. diagonal prototype as of 2018) organic light-emitting diode (OLED) TVs. Considering

T. Kamiya (✉) · H. Hiramatsu · K. Ide · T. Katase · H. Hosono
Tokyo Institute of Technology, Tokyo, Japan
e-mail: kamiya.t.aa@m.titech.ac.jp

Y. Setsuhara et al. (eds.), *Novel Structured Metallic and Inorganic Materials*, https://doi.org/10.1007/978-981-13-7611-5_6

semiconductor materials, ionic oxide semiconductors have unique properties largely different from conventional covalent semiconductors such as Si and GaAs.

Here, we like to discuss why the oxide semiconductors can make such better devices for some purposes than the conventional semiconductor devices. On the other hand, we should also consider the fact that it would be very difficult to find such advantages if the targets of the oxide devices are the same as those of the conventional semiconductors, because their electronic structures are largely different, and the ultimate carrier mobility would be smaller for the ionic oxides than for the conventional semiconductors due to the stronger carrier scattering originating from polar phonons and also due to the lower symmetry, and more complex structures. That means, we must reconsider the possibility of functional oxide materials and find suitable applications according to the electronic structures and properties inherent to oxides.

The most important features of oxides are associated with a variety of crystal structures and constituent elements. This wide variety provides many chemical, optical, electronic, and magnetic functions, which would be favorable for developing multi-/coupled functional materials and devices. In addition, some oxides have peculiar nanostructures embedded in crystal structures (e.g., see Fig. 6.1). These are distinguishing features from conventional semiconductors because Si, GaAs, GaN, etc. have almost the same crystal structures (remind that zinc blend and wurtzite-type structures are derivatives of the diamond structure). Although the present device technology fabricates quantum wells using time and money

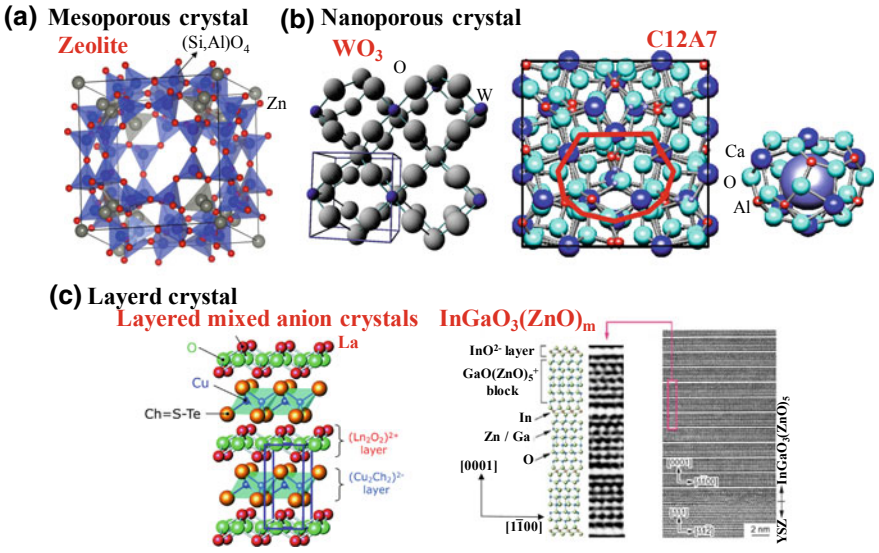

Fig. 6.1 Natural nanostructures in oxide crystals. **a** Mesoporous crystals, **b** nanoporous crystals, and **c** layered crystals. The right figure in "C12A7" shows a cage structure extracted from the shadowed area in the left figure. Free oxide ion in the cage is illustrated as a large sphere in the right figure but neglected in the left figure for simplicity

consuming artificial superlattice processes, such oxides have natural "quantum well/dot structures" as seen in Fig. 6.1 and might provide natural systems for the mesoscopic electronic applications. We also like to note that another important advantage is related to the strong ionicity of oxides. That is, oxides can have large electron mobility even in amorphous structures due partly to the strong iconicity, and also have lower density defects than in covalent amorphous semiconductors such as a-Si, which will be discussed later on.

6.2 Electronic Structure of Oxides

6.2.1 Formation of Band Gap

The electronic structures of oxides are largely different from those of covalent semiconductors. For example for Si, conduction band minimum (CBM) and valence band maximum (VBM) are made of antibonding (sp^3 σ*) and bonding states (sp^3 σ) of Si sp^3 hybridized orbitals, respectively, and its bandgap is formed of the energy splitting of the σ* − σ levels (Fig. 6.2a). In contrast, as oxides have strong ionicity, CBM and VBM are usually formed of different ionic species, respectively. The most important factor to understand electronic structures in ionic crystals is Madelung potential. When metal atoms and oxygen atoms come close, charge transfer occurs due to large differences in electron affinities and ionization potentials, which ionizes these atoms (Fig. 6.2b). The ions form negative electrostatic potential at the cationic sites and positive potential at the anionic sites (this is the Madelung potential), which consequently stabilizes the charged ion states in the crystal structure (Fig. 6.2c). Therefore, CBMs are made mainly of the unoccupied orbitals of metal cation while VBMs of fully-occupied 2p orbitals of oxygen ion in typical oxides (note that these are not the cases for transition metals, lanthanide, and actinide; their *d* and *f* orbitals may locate near VBM or in the band gap). Main group oxides have large bandgaps because the large Madelung potential increases the energy splitting between the metal unoccupied orbitals and the occupied oxygen 2p orbitals.

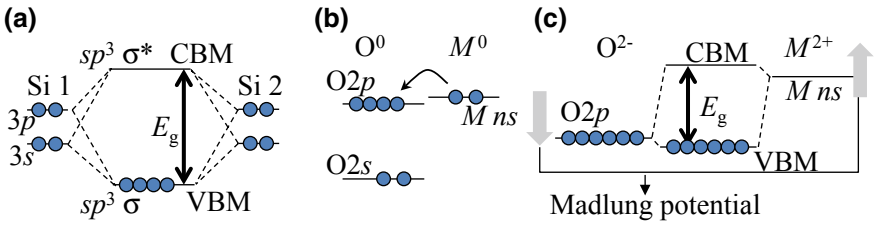

Fig. 6.2 Formation of the energy gap in **a** covalent semiconductor (e.g., Si), and **b**, **c** ionic semiconductors ($M^{2+}O^{2-}$). **b** Energy levels of neutral atoms in a vacuum. **c** The atoms are ionized in a crystal structure and form large Madelung potential and large bandgap

For transparent conducting oxides (TCOs) such as In_2O_3, ZnO, and SnO_2, CBMs are made mainly of *s* orbitals with a large principle quantum number *n* (e.g., $n = 5$ for Sn and In). These *s* orbitals have large spatial size and forms large hybridization even with second neighbor metal cations, which reduces the electron effective mass and thus contributes to large mobilities such as >200 $cm^2/(Vs)$ in undoped single crystal TCOs. Such oxides can be a good electrical conductor as long as high-density carrier doping is possible.

6.2.2 *Electron Transport and Defect Levels in n-Type AOSs*

The above electronic structure explains the peculiar properties of AOSs. Usually, amorphous semiconductors exhibit much-deteriorated carrier transport properties than associated crystalline materials as known in hydrogenated amorphous silicon (a-Si:H) and chalcogenides. This is because the chemical bonds in the covalent semiconductors are made of sp^3 or *p*-type orbitals with strong spatial directivity. Therefore, the strained chemical bonds form rather deep and high-density localized states (known as Anderson localization) below CBM and above VBM, causing carrier trapping (compare the real space images of Fig. 6.3a, b). In contrast, as CBMs of oxides are in general made of spherical extended *s* orbitals of metal ions, and their overlaps with neighboring metal *s* orbitals are not altered largely by disordered local structures. Electronic levels of CBM are, therefore, insensitive to local strained bonds, and electron transport is not affected significantly (Fig. 6.3c, d) [2, 4, 5].

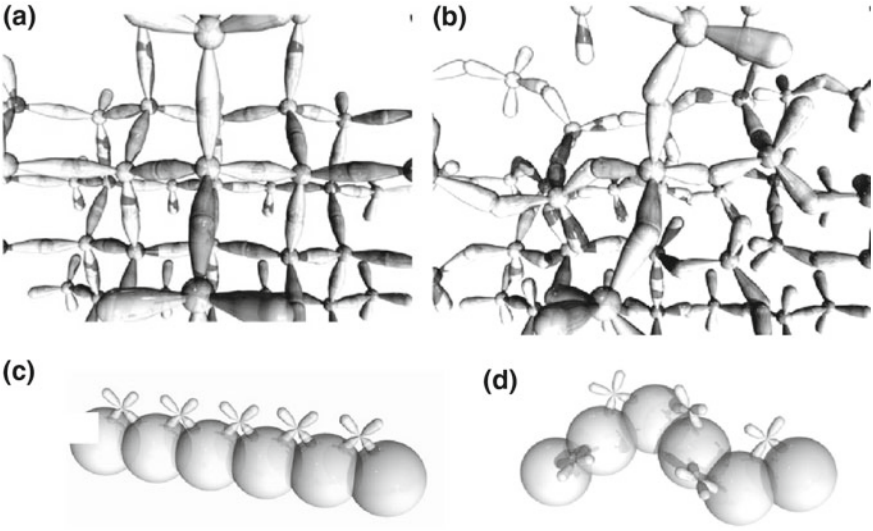

Fig. 6.3 Illustrative images of carrier transport paths in **a** crystalline Si, **b** amorphous Si, **c** crystalline oxide semiconductor, and **d** AOS

This chemical bonding view is confirmed by first-principles pseudo-band structure calculations [6].

Such a view of the electronic structures can also explain the different behaviors in defects. In covalent semiconductors, a dangling bond forms a nonbonding state and thus a singly occupied defect level is formed near the middle of the band gap (compare Fig. 6.4a, b). Such defect level can work both as electron trap and hole trap and is very serious for electronic devices both for n-type and p-type ones; therefore, these defects must be reduced, e.g., to $<10^{16}$ cm^{-3} for a-Si:H solar cells and TFTs by hydrogen termination (hydrogen passivation). For oxides (Fig. 6.4c, d), an oxygen vacancy (V_O) would form a metal cation nonbonding state but it would be located in the conduction band. Such in-band defect level does not affect most of the semiconductor devices because the Fermi level in those devices are varied within the band gap. Recent first-principles calculation and experimental data suggests that V_O in some oxide semiconductors such as ZnO and AOSs form deep electron traps because the V_O has rather large free space and forms a quantum dot-like electronic level in V_O, which trap the electrons released by the formation of the oxygen deficiency [7–10] (such deep electron traps are observed in AOSs by hard X-ray photoemission spectroscopy [11]). Even in such case, the deep fully occupied electron trap does not deteriorate the operation characteristics of n-type devices, and this is actually the case for AOS TFTs [2, 11].

The above explanations are confirmed by the following facts on AOSs. We have reported that AOSs in Cd–Ge–O and In–Ga–Zn–O systems (a-IGZO) exhibit large electron Hall mobilities [4, 5]. Figure 6.5a shows electron transport properties of a-IGZO with the nominal chemical composition of $InGaO_3(ZnO)_1$ in comparison with single crystalline $InGaO_3(ZnO)_1$ (sc-IGZO) [14, 15, 12, 13]. Hall mobility increases with increasing the carrier concentration, and Hall mobilities greater than 10 $cm^2(Vs)^{-1}$ are obtained when carrier concentration exceeds $\sim 10^{18}$ cm^{-3}. Carrier

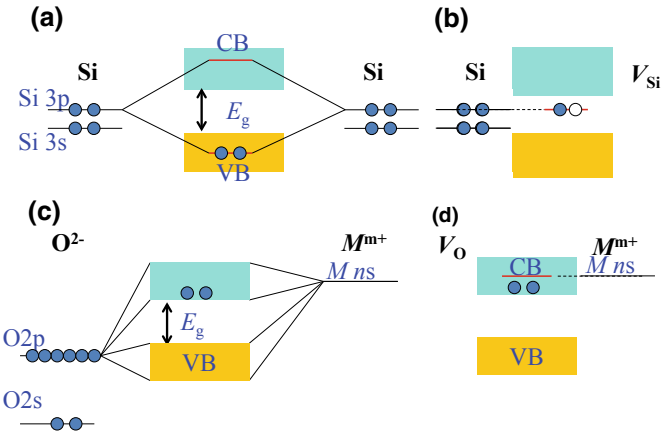

Fig. 6.4 Schematic energy diagrams of **a**, **b** covalent semiconductors and **c**, **d** oxide semiconductors. **a**, **c** Ideal crystals with no defect, **b** with Si vacancy (V_{Si}), and with O vacancy (V_O)

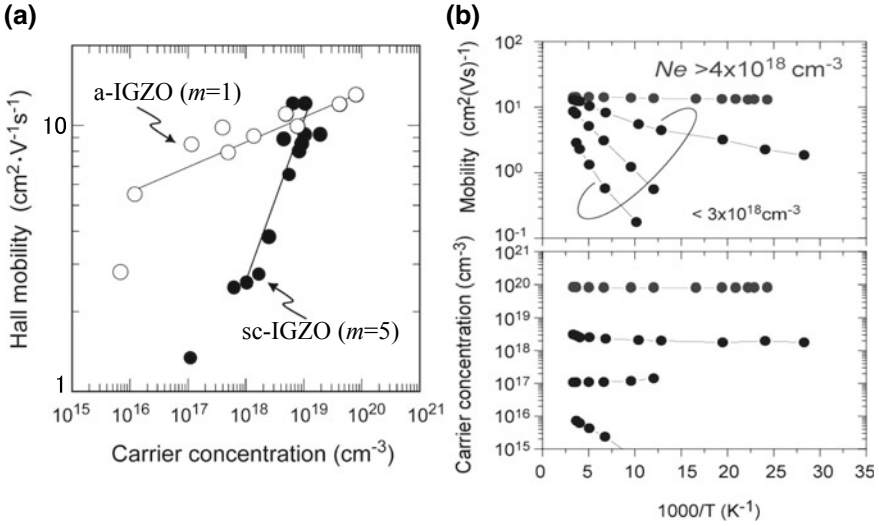

Fig. 6.5 **a** Relationship between Hall mobility and electron concentration measured at room temperature for sc-IGZO and a-IGZO films. **b** Temperature dependence of electron mobility and concentration for a-IGZO films with varied electron concentrations

transport is controlled by thermal activation at low carrier concentrations, while degenerate conduction is attained when the carrier concentration exceeds a threshold value $N_{th} = 4 \times 10^{18}$ cm^{-3} (Fig. 6.5b). Similar behavior is observed in sc-IGZO. Note that these behaviors are different from conventional crystalline semiconductors such as Si because carrier mobility usually decreases with increasing carrier concentration due to ionized impurity scattering in highly doped materials. We found that this peculiar behavior is explained by percolation conduction associated with the carrier transport potential barriers in the conduction band formed by the disordered structures in sc-IGZO and a-IGZO [16]. Note that sc-IGZO has structural randomness embedded in its crystal structure as Zn and Ga share the same crystallographic sites, which causes the amorphous-like carrier transport behaviors.

6.3 Materials Design for Wide Band Gap p-Type Semiconductors

6.3.1 Guiding Principles for p-Type Transparent Oxide Semiconductors

In contrast to n-type oxide semiconductors, it is much difficult to attain good p-type conduction in oxides because hole transport paths in typical oxides are made mainly of O 2*p* orbitals (Figs. 6.2c and 6.6a) but they are rather localized. Therefore, hole

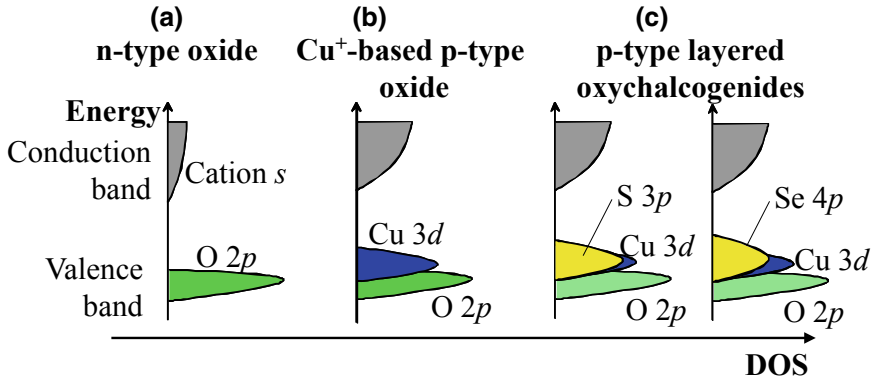

Fig. 6.6 Simplified electronic structures in oxide semiconductors. **a** Typical n-type oxide. CBM is composed mainly of metal *s* orbitals and VBM of O 2*p* orbitals. **b** Cu^+-based *p*-type oxides. VBM is made of hybridized orbitals of Cu 3*d* and O 2*p*, which raises the energy level of VBM and forms more conductive hole transport paths. **c** Oxychalcogenides. Hybridization of VBM is enhanced by the intervention of chalcogen *p* orbitals. The energy level of VBM is raised and the hole effective mass is reduced as the atomic number of the chalcogenide ion is increased

effective masses are rather large, and VBM levels are deep. The former results in small hole mobilities and the latter causes difficulty in hole doping. These are the reason why only n-type oxides were known for TCOs before 1997.

A way to attain p-type conduction is to increase the dispersion of VBM and also raise the VBM, which would be achieved by (i) decreasing the nearest neighboring oxygen–oxygen distance, (ii) using hybridization of metal orbitals whose energy levels are close to those of O 2*p* (Fig. 6.6b), or (iii) employing more extended orbitals for anions (Fig. 6.6c). We adopted the approach (ii) and selected Cu^+-based oxides because the energy levels of Cu 3*d* are close to those of O 2*p* levels. In addition, the closed shell configuration of Cu^+ $3d^{10}$ was expected not to give optical absorption due to *d*–*d* or O 2*p*–Cu 3*d* transitions, and therefore the Cu^+-based oxides meet the requirements of TOS (transparency for visible light). Following this guiding principle, Profs. Kawazoe and Hosono group found a delafossite-type crystal, $CuAlO_2$, as the first p-type TOS in 1997 [17], followed by the findings of a series of p-type TOSs, $CuGaO_2$ [18], and $SrCu_2O_2$ [19].

6.3.2 *Better P-Type Transparent Oxide Semiconductors: Layered Oxychalcogenides*

However, the hole mobilities and concentrations of the Cu^+-based TOSs are far from satisfactory. Thus, we then extended the guiding principle to the approach (iii). We employed chalcogenides to form VBM largely hybridized with Cu^+ $3d^{10}$ orbitals. To satisfy the condition to maintain large bandgaps, we chose layered

oxychalcogenides, *Ln*CuO*Ch* (*Ln* = lanthanide, *Ch* = chalcogen) [20]. It is composed of alternate stacking of $(Ln_2O_2)^{2+}$ and $(Cu_2Ch_2)^{2-}$ layers along the [001] direction (Fig. 6.1c). This layered structure would be a key for the wide bandgap. Simple chalcogenides, Cu_2S and Cu_2Se, have rather small bandgaps of ~1.2–1.4 eV [17, 18], but, e.g., LaCuOS has a much larger bandgap of ~3.2 eV. As the bandgaps of *Ln*CuO*Ch* are mainly determined by the Cu*Ch* layers (discussed later), this difference in the bandgaps is attributed to the layered structure, where the low dimensional chemical bonding networks suppress band dispersions (see Ref. [19] for a similar crystal $La_2CdO_2Se_2$).

As we expected, *Ln*CuO*Ch* exhibits good p-type conduction. Mobility becomes larger with an increase in the Se content in $LaCuO(S_{1-x}Se_x)$. Since Se 4*p* orbitals have larger spatial spread than that of S 3*p* orbitals, hybridization with Cu 3*d* becomes larger and thereby hole mobility increases as the Se content increases (Fig. 6.7a, b). The largest hole mobility ~8 $cm^2(Vs)^{-1}$, which is comparable to that of p-type GaN:Mg, was obtained in LaCuOSe [20]. Degenerate p-type conduction with a moderately large hole mobility of ~4 $cm^2(Vs)^{-1}$ was attained in Mg-doped LaCuOSe. In addition, it was found that excitons were stable even at room temperature and sharp excitonic photoluminescence (PL) was observed (Fig. 6.7c) [21].

6.3.3 *Two-Dimensional Electronic Structure in LaCuO*Ch

LaCuOSe has a distinct difference from GaN:Mg. Mg-doping to LaCuOSe increased the hole concentration up to 2×10^{20} cm^{-3} and carrier transport changed to degenerate conduction [22]. We like to note that degenerate p-type conduction has not been attained in any transparent semiconductors even including GaN:Mg. In addition, unlike conventional semiconductors, the moderately large hole mobility (~4 $cm^2(Vs)^{-1}$) and intense PL are maintained even in the heavily doped

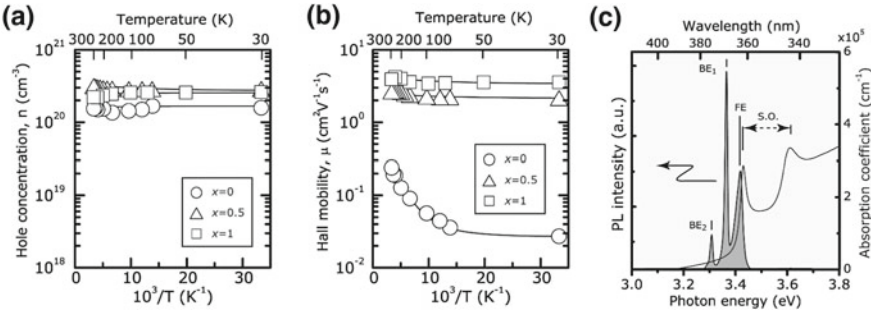

Fig. 6.7 Opto-electronic properties of $LaCuO(S_{1-x}Se_x)$. Temperature dependences of **a** hole concentration and **b** hole mobility of Mg-doped $LaCuO(S_{1-x}Se_x)$. **c** Optical absorption and photoluminescence spectra measured at 10 K for undoped LaCuOSe

LaCuOSe:Mg, although high-density carriers, in general, reduce carrier mobility and exciton lifetime.

Optical absorption spectra measured at 10 K (Fig. 6.7c) showed a stepwise structure with sharp peaks just on the edges of the steps [23]. Such stepwise structure is similar to those observed in semiconductor artificial superlattices and would reflect the two-dimensional density of states of LaCuOSe. *Ab initio* electronic structure calculations explain well these unusual properties. The band structure is highly anisotropic and hole effective mass is smaller in the Γ-X direction than in the Γ-Z direction (Fig. 6.8a) [24], which implies the electronic structure is highly two-dimensional. Projected density of states (PDOS) showed that the VBM is mainly composed of hybridized orbitals of Cu 3*d* and Se *p* orbitals and the CBM of Cu 4*s*. Thus, the bandgap is formed almost solely of the CuSe layer. In contrast, the LaO layer has a larger energy gap than the CuSe layer has (Fig. 6.8b). This characteristic structure explains the moderately large hole mobility and intense PL in the heavily doped LaCuOSe:Mg. In LaCuOSe:Mg, Mg ions are thought doped in the LnO layer. Holes are generated from acceptor levels made from the Mg dopants, which are then transferred to the CuSe layer because it forms hole transport paths as seen in the high hole density region illusrated by the white area in Fig. 6.8c. This electronic structure spatially separates the conducting holes from the ionized acceptors (Mg^{2+}). As a consequence, carrier scattering is effectively suppressed. That is, a modulation doping structure is naturally formed in the layered oxychalcogenides. The large exciton binding energy (∼50 meV) [21] is also associated with the hole confinement effect in the two-dimensional CuSe layers.

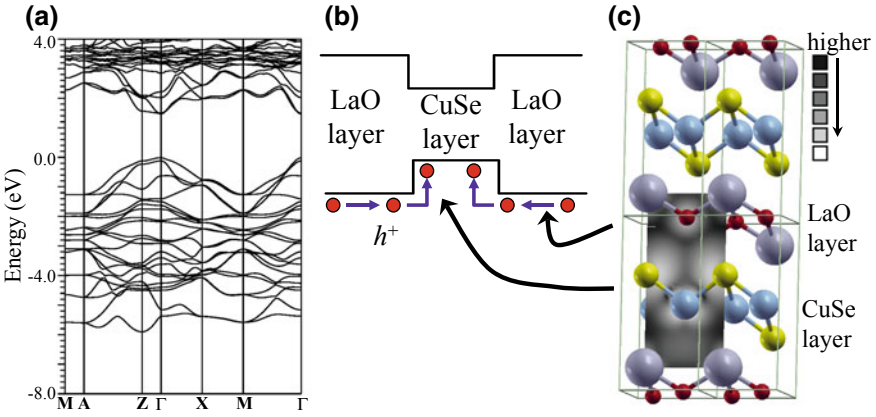

Fig. 6.8 Two-dimensional electronic structure in LnCuOSe. **a** Band structure of LaCuOSe, **b** schematic illustration of the electronic structure near the bandgap, and **c** hole density map

6.4 Doping

6.4.1 Empirical Doping Limit Rule

To make wide bandgap electronic functional materials, carrier doping is important. However, it is also known that wider band gap materials are more difficult to dope carriers. More exactly, wide bandgap materials can dope either only to n-type or p-type. This would be explained in the band alignment diagram (Fig. 6.9), where the CBM and VBM levels measured from the vacuum level (E_V) are aligned. It tells that electron doping is easy if the CBM is deeper than 3.8 eV from E_V, while hole doping is easy if the VBM is shallower than 5.7 eV from E_V [25]. This doping limit suggests the maximum band gap for bipolar semiconductors would be limited to ~2.0 eV.

6.4.2 Break the Empirical Doping Limit by Natural Nanostructure

To overcome the empirical rule, new ideas would be required. An example is the nanoporous crystal, $12CaO{\cdot}7Al_2O_3$ (C12A7), shown in Fig. 6.1b. Its cubic unit cell has a lattice parameter of 1.199 nm and consists of 12 cages (~0.4 nm in inner diameter, the right figure of "C12A7" in Fig. 6.1b). As the cage framework is

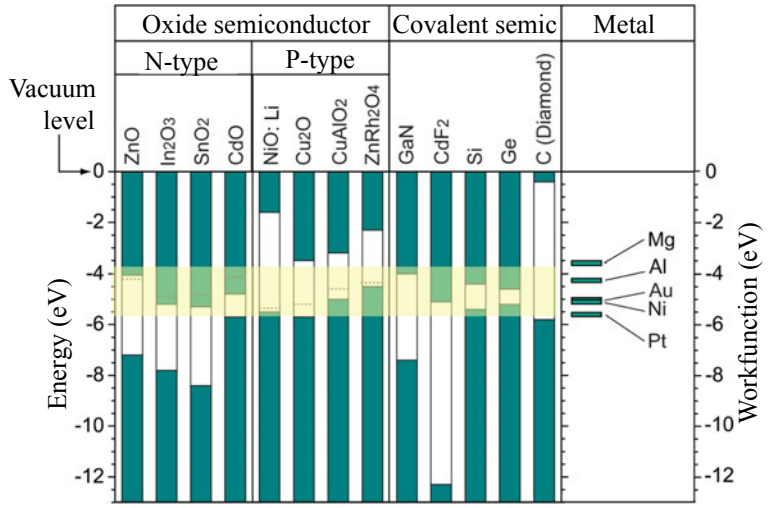

Fig. 6.9 Band alignment of representative semiconductors to explain empirical doping rule. The energy is measured from the vacuum level. For comparison, work functions of metals are shown on the right

charged positively (the averaged formal charge is +1/3*e* per cage), 2 cages out of the 12 cages clathrate an O^{2-} ion each (free oxide ions). This exotic structure has led to the appearance of many new functions by replacing the free oxide ions with other active anions. Abundant O^- ions, which are known as the "strongest oxidant," are formed at $\sim 2 \times 10^{20}$ cm^{-3} if C12A7 is annealed in dry oxygen gas at 600–800 °C [26]. Substitution of the free oxide ions with hydrogen creates high-density H^- ions in the cages (C12A7:H^-). C12A7:H^- is an electrical insulator like stoichiometric C12A7 and C12A7:O^-, while it exhibits persistent electronic conduction (Fig. 6.10a, see "C12A7:H^- + UV-irradiated")) and coloration after irradiated with UV light (Fig. 6.10b). The conductivity increases to >0.3 Scm^{-1} (Fig. 6.9a) and new optical absorption bands appear at the same time at $\sim$0.4 and 2.8 eV [27]. It is recovered to the insulating and colorless transparent state by heating at $\sim$350 °C. Further, it is possible to replace all the free oxygen ions with electrons (C12A7:e^-), which forms a new inorganic electride [28] ("electride" is a crystalline salt in which stoichiometric amounts of electrons are served as anions [29, 30]). C12A7:e^- exhibits electronic conduction with conductivities greater than 100 Scm^{-1} without UV irradiation (Fig. 6.10a, b).

These functions originate from the exotic active anions in the cages of C12A7. It was found that unusually shallow Madelung potential in the cages stabilizes these exotic anionic states (see Refs. [31, 32], and Fig. 6.11). Carrier transport mechanism in C12A7:e^- was discussed using *ab initio* embedded cluster calculations and a polaron conduction mechanism was proposed [33, 34].

The band structure of C12A7:e^- calculated by density functional theory (Fig. 6.12a) shows that the Fermi level (E_F) is located at 1–2 eV below the edge of the fundamental bandgap of the cage framework [35]. The density map of the encaged electrons (Fig. 6.12b) shows that the electrons are loosely confined in the cages. Such electronic structure lets us expect that C12A7:e^- might have a small work function and exhibit good electron emission properties. Indeed efficient electron emission was observed even at room temperature. Field emission-type

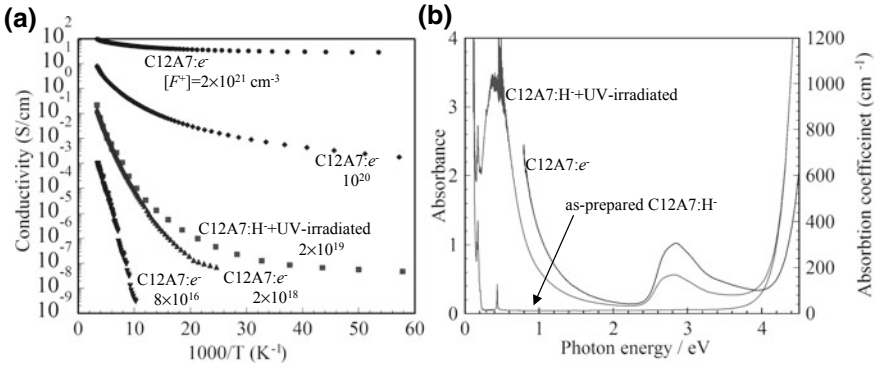

Fig. 6.10 Electron conducting C12A7. **a** Temperature dependences of conductivity, and **b** UV light-induced coloration in C12A7:H^-

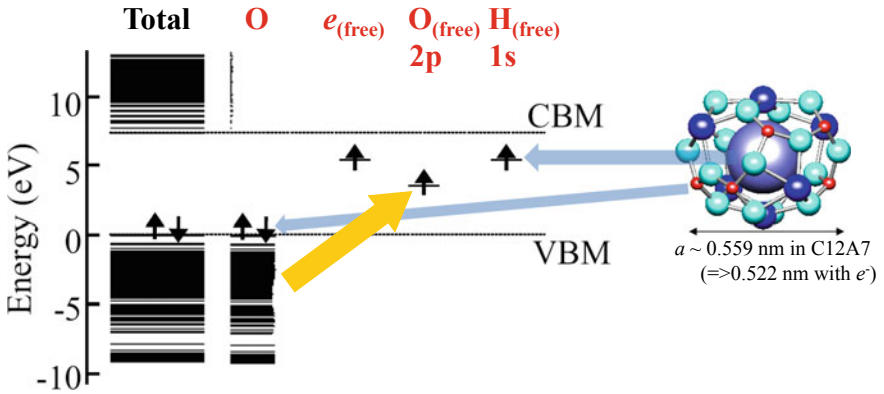

Fig. 6.11 Effect of Madelung potential on the charge states of atoms encaged in C12A7

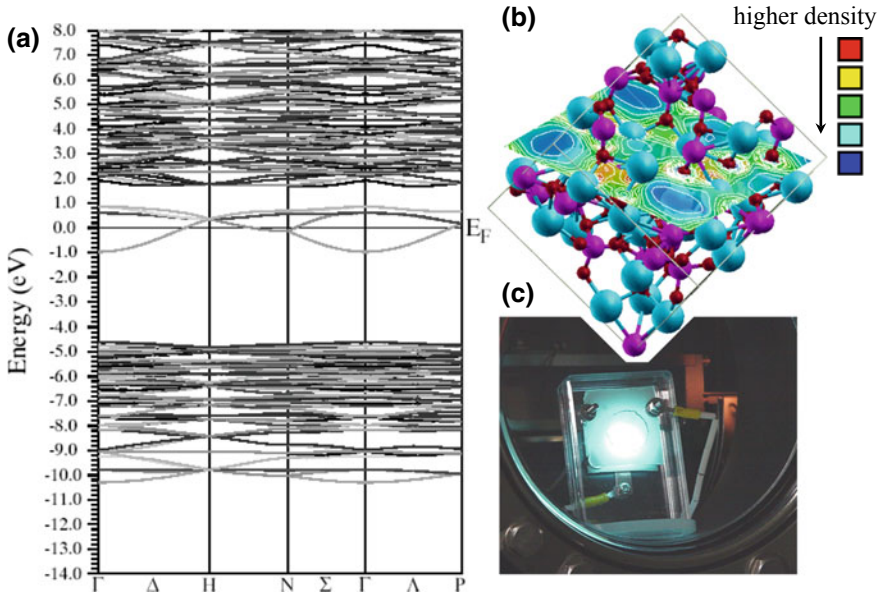

Fig. 6.12 Electronic structure of C12A7:e^-. **a** Band structure using the symmetric rigid crystal structure model. The bands around E_F are those of the electrons in the cages. CBM is located ~2 eV above E_F. **b** Density map of the encaged electrons superimposed on the crystal structure of C12A7:e^-. Blue region shows higher electron density areas. **c** Operation of field emission display device using C12A7:e^- as electron emitter. ZnO:Zn was used for phosphor

light-emitting devices displayed bright light emission clearly visible in typical ambient light (Fig. 6.12c) [35]. The work function was estimated from the electron emission characteristics provided very small values of ~0.6 eV. In contrast,

ultraviolet photoelectron spectroscopy gave a larger work function value of ~3.7 eV [36].

On the other hand, it is difficult to use the crystalline C12A7:e^- for practical applications such as displays because its fabrication requires very high temperatures >1000 °C, which is incompatible with the process temperature of FPDs (usually ≤350 °C). For FPD applications, amorphous C12A7:e^- is developed, and applied to OLED [37]. Crystalline C12A7:e^- now finds new applications such as ammonia synthesis catalysts as the forms of, e.g., Ru-loaded C12A7:e^- [38].

References

1. K. Nomura, H. Ohta, A. Takagi, T. Kamiya, M. Hirano, H. Hosono, Nat. (Lond.) **432**, 488–492 (2004)
2. T. Kamiya, K. Nomura, H. Hosono, Sci. Technol. Adv. Mater. **11**, 044305-1–23 (2010)
3. T. Kamiya, H. Hosono, *Handbook of Visual Display Technology* (2016), pp. 1111–1144
4. H. Hosono, N. Kikuchi, N. Ueda, H. Kawazoe, J. Non-Cryst. Sol. **198–200**, 165–169 (1996)
5. S. Narushima, M. Orita, M. Hirano, H. Hosono, Phys. Rev. B **66**, 035203-1–8 (2002)
6. T. Kamiya, K. Nomura, M. Hirano, H. Hosono, Phys. Stat. Solidi. (C) **5**, 3098–3100 (2008)
7. A.F. Kohan, G. Ceder, D. Morgan, C.G. Van de Walle, Phys. Rev. B **61**, 15019 (2000)
8. F. Oba, S.R. Nishitani, S. Isotani, H. Adachi, I. Tanaka, J. Appl. Phys. **90**, 824 (2001)
9. A. Janotti, C.G. Van de Walle, Phys. Rev. B **76**, 165202 (2007)
10. T. Kamiya, K. Nomura, H. Hosono, Phys. Stat. Solidi. A **207**, 1698–1703 (2010)
11. K. Nomura, T. Kamiya, H. Yanagi, E. Ikenaga, K. Yang, K. Kobayashi, M. Hirano, H. Hosono, Appl. Phys. Lett. **92**, 202117-1–3 (2008)
12. M. Orita, H. Ohta, M. Hirano, S. Narushima, H. Hosono, Phil. Mag. B **81**, 501–515 (2001)
13. H. Hosono, N. Kikuchi, N. Ueda, H. Kawazoe, K. Shimidzu, Appl. Phys. Lett. **67**, 2663–2665 (1995)
14. K. Nomura, H. Ohta, K. Ueda, T. Kamiya, M. Hirano, H. Hosono, Appl. Phys. Lett. **85**, 1993–1995 (2004)
15. A. Takagi, K. Nomura, H. Ohta, H. Yanagi, T. Kamiya, M. Hirano, H. Hosono, Thin Sol. Films **486**, 38–41 (2005)
16. T. Kamiya, K. Nomura, H. Hosono, Appl. Phys. Lett. **96**, 122103-1–3 (2010)
17. H. Kawazoe, M. Yasukawa, H. Hyodo, M. Kurita, H. Yanagi, H. Hosono, Nat. **389**, 939–942 (1997)
18. K. Ueda, T. Hase, H. Yanagi, H. Kawazoe, H. Hosono, H. Ohta, M. Orita, M. Hirano, J. Appl. Phys. **89**, 1790–1793 (2001)
19. A. Kudo, H. Yanagi, H. Hosono, H. Kawazoe, Appl. Phys. Lett. **73**, 220–222 (1998)
20. K. Ueda, S. Inoue, S. Hirose, H. Kawazoe, H. Hosono, Appl. Phys. Lett. **77**, 2701–2703 (2000)
21. H. Hiramatsu, K. Ueda, K. Takafuji, H. Ohta, M. Hirano, T. Kamiya, H. Hosono, J. Appl. Phys. **94**, 5805–5808 (2003)
22. H. Hiramatsu, K. Ueda, H. Ohta, M. Hirano, T. Kamiya, H. Hosono, Appl. Phys. Lett. **82**, 1048–1050 (2003)
23. K. Ueda, H. Hiramatsu, H. Ohta, M. Hirano, T. Kamiya, H. Hosono, Phys. Rev. B **69**, 155305-1–4 (2004)
24. S. Inoue, K. Ueda, H. Hosono, Phys. Rev. B **64**, 245211-1–5 (2001)
25. H. Hosono, Jpn. J. Appl. Phys. **52,** 090001-1–13 (2013)
26. K. Hayashi, M. Hirano, S. Matsuishi, H. Hosono, J. Am. Chem. Soc. **124**, 738–739 (2002)
27. K. Hayashi, S. Matsuishi, T. Kamiya, M. Hirano, H. Hosono, Nat. **419**, 462–465 (2002)

28. S. Matsuishi, Y. Toda, M. Miyakawa, K. Hayashi, T. Kamiya, M. Hirano, I. Tanaka, H. Hosono, Sci. **301**, 626–629 (2003)
29. J.L. Dye, Sci. **247**, 663–668 (1990)
30. J.L. Dye, Sci. **301**, 607–608 (2003)
31. T. Kamiya, H. Ohta, H. Hiramatsu, K. Hayashi, K. Nomura, S. Matsuishi, K. Ueda, M. Hirano, H. Hosono, Microelectr. Eng. **73–74**, 620–626 (2004)
32. T. Kamiya, H. Hosono, Jpn. J. Appl. Phys. **44**, 774–782 (2005)
33. P.V. Sushko, A.L. Shluger, K. Hayashi, M. Hirano, H. Hosono, Phys. Rev. Lett. **91**, 126401-1–4 (2003)
34. P.V. Sushko, A.L. Shluger, K. Hayashi, M. Hirano, H. Hosono, Thin Sol. Films **445**, 161 (2003)
35. Y. Toda, S. Matsuishi, K. Hayashi, K. Ueda, T. Kamiya, M. Hirano, H. Hosono, Adv. Mater. **16**, 685–689 (2004)
36. Y. Toda, H. Yanagi, E. Ikenaga, J.J. Kim, M. Kobata, S. Ueda, T. Kamiya, M. Hirano, K. Kobayashi, H. Hosono, Adv. Mater. **19**, 3564–3569 (2007)
37. H. Hosono, J. Kim, Y. Toda, T. Kamiya, S. Watanabe, Proc. Natl. Acad. Sci. U.S.A. **114**, 233–238 (2017)
38. M. Kitano, Y. Inoue, Y. Yamazaki, F. Hayashi, S. Kanbara, S. Matsuishi, T. Yokoyama, S.-W. Kim, M. Hara, H. Hosono, Nat. Chem. **4**, 934–940 (2012)

Chapter 7
Interface-Related Magnetic Phenomena in Novel Heterostructures

Tomoyasu Taniyama

Abstract Magnetic properties of materials relevant to the interface or surface provide a promising artificial material basis for the strategic design of spintronic devices. Giant magnetoresistance (GMR), spin accumulation, and spin transfer torque (STT), etc. are typical examples of such interface-related magnetic phenomena. Recent enormous and rapid growth of technology also allows to control magnetization orientation, magnetic phases, and spin polarization by manipulating the interface with an electric field without using either a magnetic field or an electric current. This leads to a drastic reduction in the power consumption. A full understanding of the interface-related magnetic phenomena is thus of crucial importance for the development of a major new direction of less energy dissipative spintronics. In this chapter, selected topics of interface-related magnetic phenomena and the fundamental physics underlying are described, placing a special emphasis on electric-field-induced strain transfer effect on the magnetic properties in multiferroic heterostructures.

Keywords Interface-related magnetic phenomena · Spintronic devices · Electric-field-induced strain transfer · Multiferroic heterostructures

7.1 Introduction

Magnetism is one of the most exciting collective phenomena in condensed matter, attracting a steadily increasing number of researchers from both fundamental and application perspectives. This chapter starts with a brief description of the fundamentals of magnetism [1]. The principal mechanism of magnetism or various magnetic orderings, e.g., ferromagnetism, antiferromagnetism, helimagnetism, spin glass, etc. lies in the exchange interaction between the magnetic moments or spin angular momentums of constituent atoms in a material. Since the exchange

T. Taniyama (✉)
Department of Physics, Nagoya University, Furo-cho, Chikusa-ku, Nagoya 464-8602, Japan
e-mail: taniyama.tomo@nagoya-u.jp

Y. Setsuhara et al. (eds.), *Novel Structured Metallic and Inorganic Materials*, https://doi.org/10.1007/978-981-13-7611-5_7

interaction Hamiltonian H_{ex} is given by the sum of the scalar product of the neighboring spins (Eq. (7.1)), the exchange interaction determines the relative orientation of the magnetic moments so as to minimize the total exchange energy.

$$H_{ex} = -2 \sum_{<i,j>} J_{ij} \boldsymbol{S}_i \cdot \boldsymbol{S}_j \tag{7.1}$$

where J_{ij} is the exchange constant and $\boldsymbol{S}_{i(j)}$ is the spin angular momentum of an atom labeled by the position $i(j)$. The exchange interaction is also a direct and straightforward consequence of the combination of the Pauli exclusive principles and the Coulomb interaction between electrons, clearly indicating that the geometrical arrangement of the surrounding atomic spins in a material strongly influences the magnetism. It is therefore intuitively understood that magnetic properties are extremely sensitive to the atomic arrangement at the interface, and hence distinct magnetic properties would appear.

There are three magnetic properties that are crucial from the application perspective, that is, (1) whether the material is ferromagnetic (FM) or not, (2) which direction the magnetic moments orient preferentially, and (3) how conduction electrons with either spin-up or spin-down transport in magnetic materials. Because almost magnetic applications so far utilize FM materials, stable ferromagnetism is obviously the first necessary prerequisite. The issue (2) is associated particularly with magnetic information technology or spintronics, where binary information is stored in magnetic elements by switching the orientation of the magnetic moments. The issue (3) is also related to spintronic applications such as GMR or tunnel magnetoresistance (TMR) in FM/nonmagnetic (NM)/FM trilayered structures and the high and low resistance states that depend on the relative orientation of magnetization of the two FM layers read the binary information in magnetic media. In this article, my focus is particularly on the issues (2) and (3) in multiferroic heterostructures since the issue (1) is related to more intrinsic properties of a material rather than interface properties. However, it is worth noting that FM ordering has been demonstrated to occur exclusively at the surface of 4*d* metals such as Pd and Rh even if 4*d* metals are paramagnetic in bulk, although it is beyond the scope of this chapter [1–3].

7.2 Interface-Related Magnetic Anisotropy

7.2.1 Magnetoelastic Anisotropy

As briefly described in the previous section, controlling the magnetization orientation of an FM material is one of the most important issues for developing novel magnetic information or spintronic devices. Generally, the magnetization orientation can be obtained by minimizing the total magnetic free energy F composed of magnetocrystalline anisotropy energy, magnetostatic (shape-induced) energy, interface

anisotropy energy, and magnetoelastic energy [4, 5]. In the Cartesian reference frame (x_1, x_2, x_3), the total energy is given by Eq. (7.2) as a function of the direction cosines m_i (i = 1, 2, 3) of the unit vector $\boldsymbol{m} = \boldsymbol{M}/M_S$, where $\boldsymbol{M}$ and M_S are the magnetization vector and the saturation magnetization of the FM layer, respectively.

$$\begin{aligned} F = {} & K_1\left(m_1^2m_2^2 + m_2^2m_3^2 + m_3^2m_1^2\right) + K_2m_1^2m_2^2m_3^2 \\ & + \frac{1}{2}\mu_0 M_S^2\left(N_1m_1^2 + N_2m_2^2 + N_3m_3^2\right) + \frac{K_S}{t}m_3^2 \\ & + \left(\frac{B_1^2}{2c_{11}} - \frac{B_2^2}{2c_{44}}\right)\left(m_1^2 + m_2^2\right)m_3^2 + B_1\left(u_1m_1^2 + u_2m_2^2\right) \\ & + B_2u_6m_1m_2 - B_1\left[\frac{B_1}{6c_{11}} + \frac{c_{12}}{c_{11}}\left(u_1 + u_2\right)\right]m_3^2 \end{aligned} \tag{7.2}$$

where K_1 and K_2 are the magnetocrystalline anisotropy constants of fourth and sixth order at constant strains u, t is the FM layer thickness, K_s is the parameter that characterizes the sum of the specific interface energies, N_i are the diagonal components of the tensor of demagnetizing factors, B_1 and B_2 are the magnetoelastic coefficients, and c_{11}, c_{12}, and c_{44} are the elastic stiffnesses at fixed $\boldsymbol{M}$. If we assume a magnetic thin film on a substrate, the crystal symmetry is obviously broken at the film/substrate interface, clearly giving rise to the interface anisotropy that is first predicted by Néel (fourth term in Eq. (7.2)) [6]. In addition to the contribution arising from the symmetry breaking at the interface, a misfit strain locally generated close to the interface also causes the interface anisotropy. If the misfit strain is transferred throughout the film, it can be considered as a part of the magnetoelastic anisotropy terms in Eq. (7.2) (sixth, seventh, and eighth terms).

Figure 7.1a schematically illustrates the interface misfit strain-induced magnetic anisotropy in the Fe/multi-domain ferroelectric (FE) $BaTiO_3$(001) (BTO(001)) heterostructure, where magnetoelastic anisotropy becomes visible [7–9]. Since BTO possesses the tetragonal crystal structure with lattice parameters of a = 3.992 Å and c = 4.036 Å at room temperature, two different domains appear at the interface, i.e., a-domains with the rectangular-shaped lattice and c-domains with the square-shaped one as illustrated in Fig. 7.1b. When an Fe film is grown epitaxially on the surface of the BTO(001) with the in-plane lattice orientation $[110]_{Fe}//[100]_{BTO}$, a misfit strain is transferred from BTO to Fe, thereby the magnetoelastic anisotropy shows up, according to Eq. (7.2). Figure 7.1c shows the polar plot of the remanent magnetization normalized by the saturation magnetization, representing the in-plane magnetoelastic anisotropy [7]. As seen in Fig. 7.1c, the in-plane symmetry of the remanent magnetization of Fe on an a-domain of BTO is of twofold, while that on a c-domain is of fourfold. The different magnetic anisotropy on the two domains is obviously a result of the sixth and seventh terms of Eq. (7.2).

Another example of the magnetoelastic anisotropy can be seen in Cu/Ni multilayers on GaAs(100) [10]. Since the lattice parameters of Cu and Ni bulk are 3.615 Å and 3.524 Å, respectively, the lattice misfit between them results in a perpendicular magnetic anisotropy (PMA) associated with the Néel type interface anisotropy and

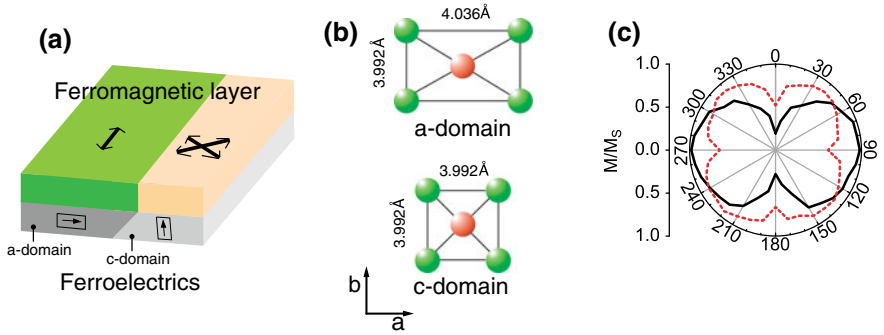

Fig. 7.1 **a** Schematic illustration of a ferromagnetic/ferroelectric multiferroic heterostructure. Magnetoelastically induced magnetic anisotropy is depicted as arrows. **b** Lattice structure of *a*-domain and *c*-domain of BTO. **c** Normalized remanent magnetization of an Fe layer on an *a*-domain (black solid curve) and a *c*-domain (red dotted curve) of BTO. Reprinted with permission from [8] Copyright 2012 American Institute of Physics; https://doi.org/10.1063/1.4773482

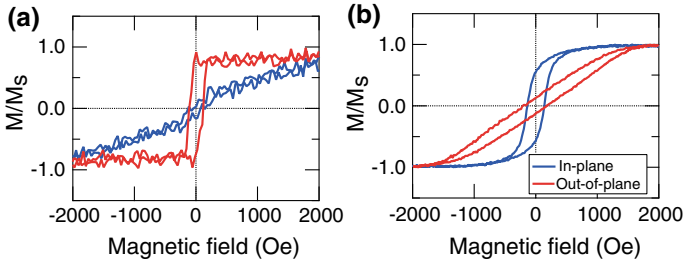

Fig. 7.2 Normalized magnetization curves of **a** $[Cu(9\ nm)/Ni(2\ nm)]_5$ and **b** $[Cu(9\ nm)/Ni(9\ nm)]_5$ multilayers for both in-plane and out-of-plane magnetic fields. The $[Cu(9\ nm)/Ni(2\ nm)]_5$ multilayer shows perpendicular magnetic anisotropy due to tensile misfit strain in the Ni layers. Reprinted with permission from [10] Copyright 2014 American Institute of Physics; https://doi.org/10.1063/1.4862969

bulk magnetoelastic anisotropy. Figure 7.2a, b shows the magnetization curves of a $[Cu(9\ nm)/Ni(2\ nm)]_5$ multilayer and a $[Cu(9\ nm)/Ni(9\ nm)]_5$ multilayer. When the Ni layer is thin enough, the interface-related magnetic anisotropy is greater than the in-plane magnetostatic anisotropy, leading to a PMA as seen in Fig. 7.2a. In a thicker Ni layer, on the other hand, the magnetostatic anisotropy dominates the magnetization orientation, forcing the magnetization to lie in the plane as shown in Fig. 7.2b.

7.2.2 *Unidirectional Anisotropy Due to Exchange Bias Effect*

Interface exchange coupling between an FM layer and an uncompensated antiferromagnetic (AFM) layer also induces a different kind of anisotropy [11]. When the

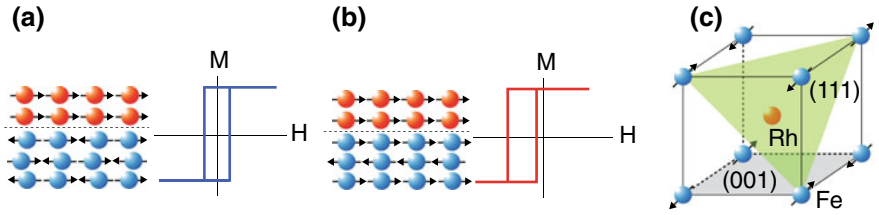

Fig. 7.3 **a** Schematic illustrations of an FM/compensated AFM interface and a hysteresis curve with no exchange bias. **b** an FM/uncompensated AFM interface and a hysteresis curve with exchange bias. **c** Magnetic structure of AFM FeRh with the compensated AFM (001) planes and uncompensated FM (111) planes. Reprinted with permission from [12] Copyright 2014 American Institute of Physics; https://doi.org/10.1063/1.4900619

spin alignment of the AFM layer is compensated at the interface as depicted in Fig. 7.3a, the averaged exchange coupling energy vanishes, giving rise to no additional magnetic anisotropy. However, if the AFM layer has the layer-by-layer alternate AFM arrangement of ferromagnetically aligned monolayers as shown in Fig. 7.3b, then the exchange coupling at the interface generates an exchange-biased magnetic field in the FM layer and a shift in the macroscopic magnetization versus magnetic field curve occurs, accordingly. This is termed exchange bias effect typically observed in FM/AFM bilayer systems such as Fe/FeRh as shown in Fig. 7.3c [12]. In a more quantitative manner, Meiklejohn and Bean proposed a model of exchange bias, in which the exchange bias field H_{EB} is expressed using the interface energy difference $\Delta\sigma$ between the opposite orientations of the FM layer in an FM/AFM bilayer.

$$H_{EB} = \frac{\Delta\sigma}{2M_{FM}t_{FM}} \tag{7.3}$$

where M_{FM} is the magnetization of the FM layer and t_{FM} is the thickness of the FM layer. In this model, $H_{EB} = 0$ for the compensated interface, while the uncompensated interface leads to a nonvanishing $H_{EB} = J_{ex}/\mathrm{M_{FM}t_{FM}a^2}$, where J_{ex} is the exchange coupling constant and a is the lattice parameter.

7.3 Electric Field Effect on Magnetic Properties

7.3.1 Electric Field Control of Magnetic Domain Walls

In general, an FM material is composed of magnetic domains separated by thin magnetic domain walls, in which the magnetic moments rotate from the direction in a magnetic domain to that in the neighboring magnetic domain. Recently, manipulation of magnetic domain walls has attracted great interest for its potential applications in newly developed spintronic memory devices. A racetrack memory is

a typical example, where binary information stored in magnetic domains can be read by controlling the position of magnetic domain walls in an FM wire via STT or spin–orbit torque [13]. In order to drive the magnetic domain walls, however, inevitable energy dissipation occurs due to Joule heating by flowing an electric current through the FM wire. Hence, another less energy dissipative technology to drive magnetic domain walls is now an essential prerequisite.

One of the approaches to controlling magnetic domain walls is to use the magnetoelastic coupling effect at the interface of FM/FE heterostructures [14, 15]. As described in Sect. 7.2.1, a misfit strain at the interface leads to an additional magnetic anisotropy due to the magnetoelastic energy. If the FE layer consists of two FE domains with different crystalline symmetries, the interface misfit strain should divide the FM layer into two FM domains separated by the FM domain wall that is pinned at the FE domain boundary. This indicates that the FM domain wall can be manipulated by moving the FE domain boundary by an electric field since the FM domain wall is pinned at the FE domain boundary while moving. Figure 7.4 depicts the schematic illustration of an Fe/BTO heterostructure, where the Fe layer has two different FM domains separated by the FM domain wall pinned at the FE *a*-*c* domain boundary. When an electric field is applied to the BTO across the layer plane, the *c*-domain starts growing by the sideway movement of the FE domain boundary, driving the FM domain wall simultaneously. Figure 7.5 demonstrates the reversible electric-field-driven motion of the FM domain wall of an Fe layer. While a positive electric field moves the FM domain wall upward, a negative electric field moves it downward. The reversible motion of the FM domain wall can be achieved by driving the FE *a*-*c* domain boundary without using electric currents, allowing to develop FM domain-wall-related spintronic devices that can be operated at very low energy consumption.

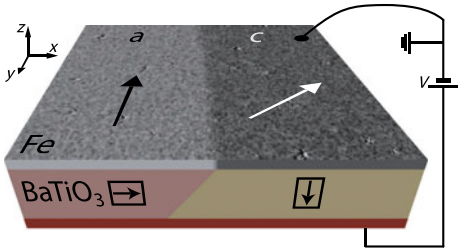

Fig. 7.4 Schematic illustration and Kerr microscopy image of the Fe/$BaTiO_3$ heterostructure with ferroelectric *a*- and *c*-domains. Arrows indicate the direction of ferroelectric polarization in the $BaTiO_3$ substrate and the direction of magnetization in the Fe film in zero magnetic field. Electric fields are applied across the $BaTiO_3$ substrate. Reprinted with permission from [14] Copyright 2015 American Physical Society; https://doi.org/10.1103/physrevx.5.011010

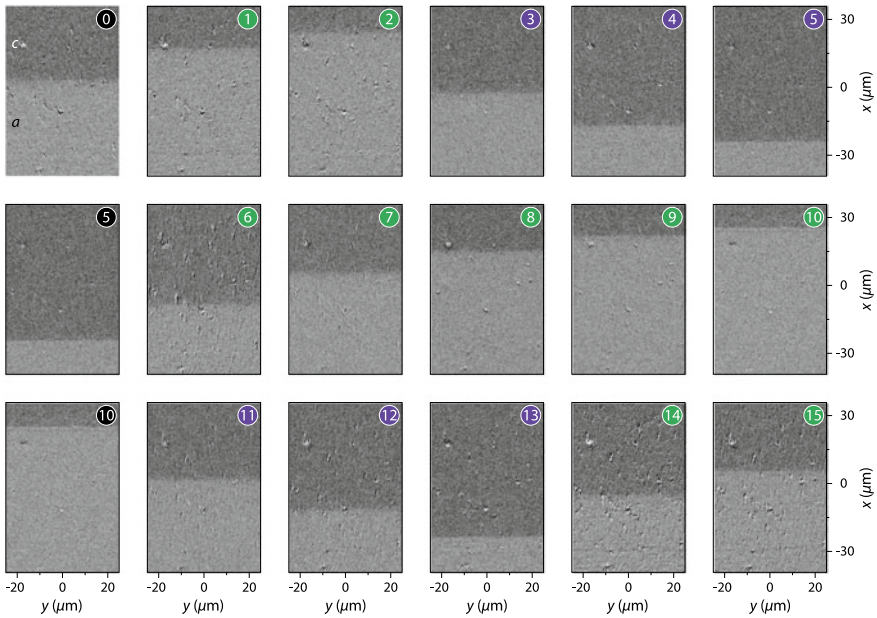

Fig. 7.5 Kerr-microscopy images illustrating the motion of a magnetic domain wall in an Fe film during the application of positive (green circles) and negative (violet circles) voltage pulses across the $BaTiO_3$ substrate. Black circles indicate that no voltage pulse is applied between two consecutive images. The electric field is 2 kV/cm. Reprinted with permission from [14] Copyright 2015 American Physical Society; https://doi.org/10.1103/physrevx.5.011010

7.3.2 *Electric Field Control of Perpendicular Magnetization*

As discussed in Sect. 7.2.1, a misfit strain at the interface gives rise to a PMA in Cu/Ni multilayers, associated with the magnetoelastic energy. Since the PMA of the Ni layers originates from the lattice expansion of Ni at the Cu/Ni interfaces, relaxation of the lattice expansion or artificial compression of the lattice could switch the magnetization orientation from out-of-plane to in-plane. An FM/FE heterostructure is again a suitable material basis to induce the switching of the magnetization between out-of-plane and in-plane. Similar to the electric-field-driven domain wall motion shown in the previous section, the application of an electric field induces *a*-*c* domain transformation of BTO in a Cu/Ni multilayer/BTO heterostructure, thereby the lattice expansion at the Cu/Ni interfaces is relaxed due to compressive strain transfer from BTO to the multilayer [16]. The additional compressive strain weakens the PMA and in-plane magnetization orientation is favored due to the magnetostatic energy arising from the thin film geometry. With this approach, Fig. 7.6 demonstrates electric-field-induced magnetization switching from out-of-plane to in-plane in a Cu/Ni multilayer/BTO heterostructure. While the out-of-plane magnetization curve (magneto-optical Kerr

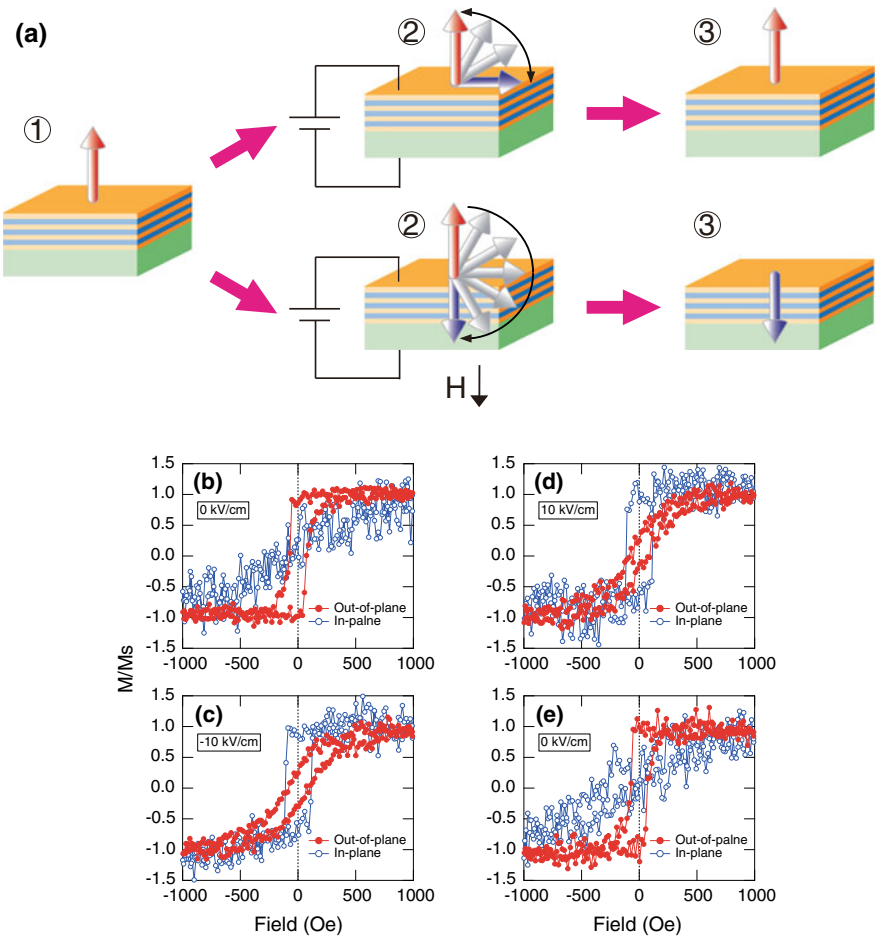

Fig. 7.6 **a** Schematic illustration of perpendicular magnetization switching by an electric field. (**b**–**e**) Normalized out-of-plane and in-plane magnetic hysteresis curves of a Cu/Ni multilayer recorded while sequentially applying an electric field of **b** E = 0 kV/cm, **c** E = 10 kV/cm, **d** E = −10 kV/cm and **e** E = 0 k/Vcm across $BaTiO_3$. Reprinted with permission from [16]. Copyright 2015 Nature Publishing Group; https://doi.org/10.1038/am.2015.72

hysteresis curve) is open and square-shaped before applying an electric field, the hysteresis curve becomes slanted with an electric field, clearly indicating that the magnetization switching occurs due to interface strain transfer. Once the electric field is removed, the PMA is recovered due to the relaxation of the FE domain structure from *c*-domains to *a*-domains.

It is obvious that 180° magnetization reversal by an electric field is also of vital importance for high-density magnetic memory and recording applications. In Cu/Ni multilayer/BTO heterostructures, even 180° magnetization reversal can be achieved if a small magnetic field that breaks the symmetry of out-of-plane magnetic

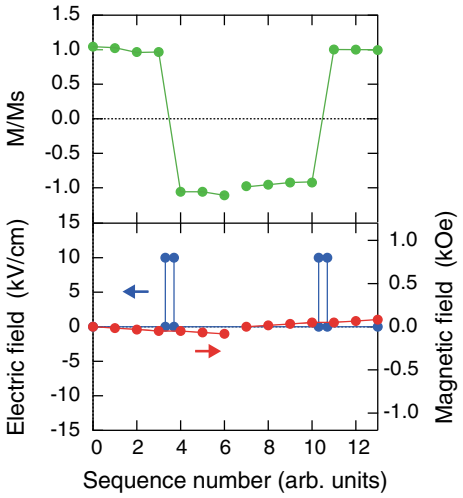

Fig. 7.7 Experimental demonstration of 180° magnetization reversal with an electric field of 10 kV/cm and a magnetic field of ±50 Oe. Reprinted with permission from [16]. Copyright 2015 Nature Publishing Group; https://doi.org/10.1038/am.2015.72

anisotropy is applied in addition to an electric field. Figure 7.6a depicts the schematic illustration of the 180° magnetization reversal processes. When an electric field is applied across the BTO layer, *a-c* FE domain transformation causes the magnetization to reorient from out-of-plane to in-plane. If a small magnetic field is added downward under the electric field, the magnetization direction is slightly tilted out-of-plane downward and the 180° magnetization reversal toward the other magnetic easy direction is achieved when the electric field is switched off. This magnetization reversal can be demonstrated by magneto-optical Kerr measurements as shown in Fig. 7.7.

7.4 Electric Field Control of Magnetic Phases

Besides electric field control of the magnetization direction in magnetic heterostructures as demonstrated in Sects. 7.3.1 and 7.3.2, magnetic phases such as ferromagnetic, antiferromagnetic phases, etc. are also found to be controllable by an electric field, relying on the magnetoelastic effect at the interface. One of the examples can be seen in B2-ordered FeRh/BTO heterostructures [17]. FeRh is a well-known material that exhibits intriguing magnetic properties, e.g., the AFM-FM phase transition at around 380 K upon heating [18, 19], where the AFM-FM phase transition has its origin in the subtle balance between the AFM interactions and the FM interactions via conduction electron spins. Recent work has demonstrated that the AFM-FM phase transition can be controlled by injecting spin-polarized electrons in FeRh wires via STT, spin accumulation [20, 21], and Joule heating [22, 23]. Another aspect of this magnetic phase transition is associated with strong spin–lattice coupling, which causes a lattice expansion of 0.3% at the AFM-FM phase transition [24]. The strong spin–lattice coupling intuitively reminds us that

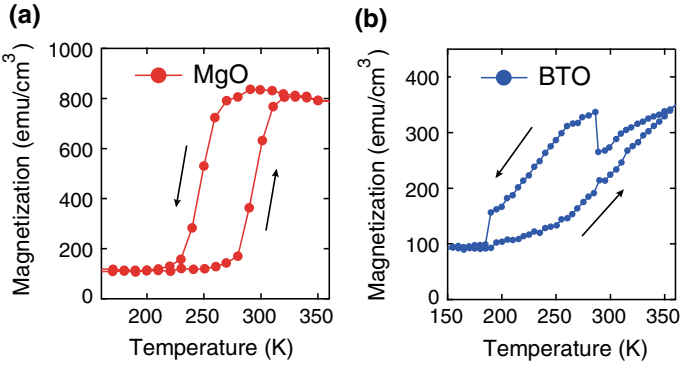

Fig. 7.8 Temperature dependence of magnetization of **a** Ga-FeRh/MgO and **b** Ga-FeRh/BTO measured in a magnetic field of 500 Oe applied in-plane along [110] of Ga-FeRh. Reprinted with permission from [25]. Copyright 2014 American Institute of Physics; https://doi.org/10.1063/1.4861455

the magnetic phases of FeRh can be tuned by inducing lattice strain artificially. In order to investigate the strain effect on the magnetic phase of FeRh, FeRh/BTO heterostructures have been used since the lattice constants and the crystal symmetry of BTO suddenly change at the successive structural phase transitions of BTO [4, 25], thereby large strain is transferred from BTO to FeRh across the interface. Figure 7.8 shows the temperature dependence of magnetization of a Ga-doped FeRh/BTO heterostructure, where sudden jumps of the magnetization are clearly seen at the tetragonal (T) to orthorhombic (O) and the O to rhombohedral (R) phase transitions [26]. The jump in the magnetization at the T-O phase transition arises from the switching of the magnetization orientation due to the magnetoelastic coupling at the interface, while that at the O-R phase transition originates from strain-induced FM-AFM phase transition: a large areal compressive strain of 0.75% occurs at the O-R transition.

Since BTO undergoes *a-c* FE domain transformation in an electric field as described before (Fig. 7.9a), the electric-field-induced domain transformation and the resultant strain transfer enable us to control the magnetic phases of FeRh. Figure 7.9b shows a representative result of the electric-field-induced variation of the magnetic coercivity of an FeRh thin film/BTO heterostructure. When an electric field is applied across the BTO, *a-c* FE domain transformation occurs and the lattice compression at the interface leads to the instability of the FM phase. Consequently, the AFM phase becomes more stable. The instability of the FM phase thus results in the reduction in the magnetic coercivity. These results clearly demonstrate that the magnetic phase of FeRh can be manipulated by a pure electric field.

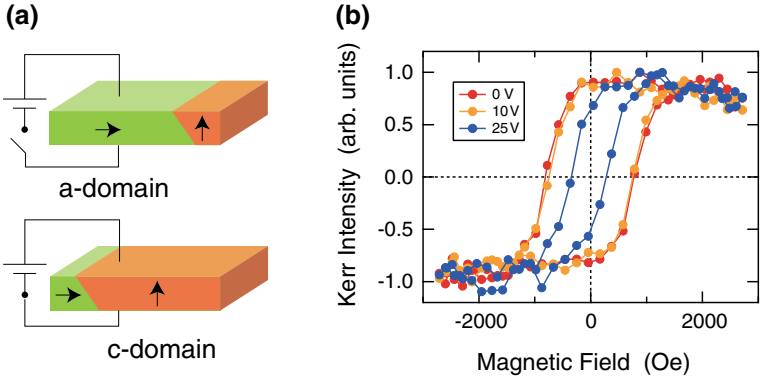

Fig. 7.9 **a** Schematic illustration of electric-field-induced FE *a-c* domain transformation. **b** Electric-field-induced variation of the magnetic coercivity of an FeRh/BTO heterostructure

7.5 Electric Field Control of Spin Polarization

The spin polarization P of electrons in an FM material is another critical parameter since it principally determines the magnetoresistance of GMR and tunnel magnetoresistance (TMR) devices. The spin polarization is generally related to the spin-dependent electronic structure through the following definition:

$$P = \frac{D_{\uparrow}(\varepsilon_F) - D_{\downarrow}(\varepsilon_F)}{D_{\uparrow}(\varepsilon_F) + D_{\downarrow}(\varepsilon_F)} \tag{7.4}$$

where $D_{\uparrow(\downarrow)}(\varepsilon_F)$ is the spin-up (down) density of states at the Fermi energy ε_F. If the spin polarization could be manipulated artificially, this leads to a vastly expanded range of design possibilities of spintronic devices. In order to manipulate the spin polarization, one of the promising approaches is to modulate the lattice of an FM material via interface strain. Because the spin-dependent electronic structure, in turn, the spin polarization is very sensitive to the lattice variation, strain transfer across the interface of the heterostructure gives rise to a significant change in the spin polarization. This means that, provided that strain transfer is generated in FM/FE heterostructures by applying an electric field due to inverse piezoelectric and piezoelastic effects, the spin polarization of the FM layer can be controlled electrically [27, 28]. Figure 7.10 demonstrates a marked change in the magnetoresistance measured with and without a lateral electric field of 66 kV/cm for a Co/Cu/Fe GMR wire/BTO heterostructure. Electric field dependence of the change in the magnetoresistance, which is termed electro-magnetoresistance (EMR), is presented in Fig. 7.10d. The results clearly show that the application of an electric field transverse to the wire axis yields an enhancement in the magnetoresistance. As discussed above, the magnetoresistance is a direct function of the spin polarization

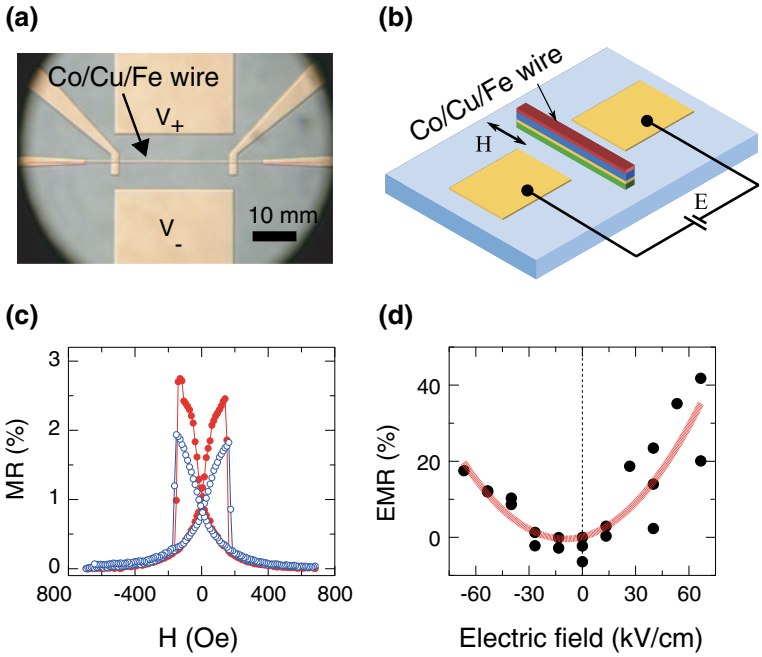

Fig. 7.10 **a** Photograph and **b** schematic illustration of a Co (30 nm)/Cu (5 nm)/Fe (12 nm) GMR wire/BTO heterostructure. **c** Magnetoresistance curves measured with and without a lateral transverse electric field of 66 kV/cm in the R phase of BTO. **d** Electro-magnetoresistance versus electric field in the R phase of BTO. Reprinted with permission from [26] Copyright 2015 American Institute of Physics; https://doi.org/10.1063/1.4929339

of the FM layers involved in the heterostructure, indicating that the spin polarization, in particular, of the Fe layer in contact with BTO is manipulated by an electric field.

7.6 Summary and Outlook

I have reviewed interface-related effects on the magnetic properties, particularly focusing on the electric-field-induced strain transfer effect in FM/FE multiferroic heterostructures toward less energy dissipative magnetization controlling technology in spintronic devices. Electric field control of magnetic domain walls, perpendicular magnetization, magnetic phases, and spin polarization has been demonstrated via strain transfer across the interface. Since the heterostructures focused in this chapter consist of ferroelectrics, there are some obstacles to be overcome for practical use in spintronic devices. One of the obstacles is the polarization fatigue that is related with the intrinsic properties of ferroelectrics. Polarization fatigue causes a serious failure of device operation due to the redox

reaction at the interface arising from the motion of oxygen ions and vacancies. However, it is worth noting that the use of perovskite-type oxides such as $SrBi_2Ta_2O_9$ could circumvent this difficulty as demonstrated in recent work [29]. Retention failure, where a built-in potential destabilizes the FE polarization states, is another critical issue to be carefully considered [30]. For practical device fabrication, integration with Si technology is also another challenging issue. Recent reports have succeeded in the growth of $SrTiO_3$ films on Si without interfacial chemical reaction, which is an encouraging progress for exploiting multiferroic heterostructures compatible with Si technology [31]. Although these issues we face are rather challenging, artificial control of the interfaces in multiferroic heterostructures and the electric field effect are now on the horizon. The author thus envisages that further investigation of interface-related magnetic phenomena and its artificial control both offer a very promising venue for the development of novel spintronic and magnetic devices.

References

1. T. Tsurumi, H. Hirayama, M. Vacha, T. Taniyama, *Nanoscale Physics for Materials Science* (Tayler & Francis, New York, 2009), p. 207
2. T. Shinohara, T. Sato, T. Taniyama, Phys. Rev. Lett. **91**, 197201 (2003)
3. T. Taniyama, E. Ohta, T. Sato, Europhys. Lett. **38**, 195 (1997)
4. T. Taniyama, J. Phys.: Cond. Matter **27**, 50400 (2015)
5. N.A. Pertsev, Phys. Rev. B **78**, 212102 (2008)
6. L. Néel, J. Phys. Radium **15**, 225 (1954)
7. Y. Shirahata, T. Nozaki, G. Venkataiah, H. Taniguchi, M. Itoh, T. Taniyama, Appl. Phys. Lett. **99**, 022501 (2011)
8. T.H.E. Lahtinen, Y. Shirahata, L. Yao, K.J.A. Franke, G. Venkataiah, T. Taniyama, S. van Dijken, Appl. Phys. Lett. **101**, 262404 (2012)
9. G. Venkataiah, E. Wada, H. Taniguchi, M. Itoh, T. Taniyama, J. Appl. Phys. **113**, 17C701 (2013)
10. Y. Shirahata, E. Wada, M. Itoh, T. Taniyama, Appl. Phys. Lett. **104**, 032404 (2014)
11. W.H. Meiklejohn, C.P. Bean, Phys. Rev. **105**, 904 (1957)
12. I. Suzuki, Y. Hamasaki, M. Itoh, T. Taniyama, Appl. Phys. Lett. **105**, 172401 (2014)
13. S. Parkin, S.-H. Yang, Nat. Nanotechnol. **10**, 195 (2015)
14. K.J.A. Franke, B.V. de Wiele, Y. Shirahata, S.J. Hämäläinen, T. Taniyama, S. van Dijken, Phys. Rev. X **5**, 0110101 (2015)
15. G. Venkataiah, Y. Shirahata, M. Itoh, T. Taniyama, Appl. Phys. Lett. **99**, 102506 (2011)
16. Y. Shirahata, R. Shiina, D.L. Gonzalez, K.J.A. Franke, E. Wada, M. Itoh, N.A. Pertsev, S. van Dijken, T. Taniyama, NPG Asia Mater. **7**, e198 (2015)
17. R.O. Cherifi, V. Ivanovskaya, L.C. Phillips, A. Zobelli, I.C. Infante, E. Jacquet, V. Garcia, S. Fusil, P.R. Briddon, N. Guiblin, A. Mougin, A.A. Ünal, F. Kronast, S. Valencia, B. Dkhil, A. Barthélémy, M. Bibes, Nat. Mater. **13**, 345 (2014)
18. M. Fallot, Ann. de Phys. **10**, 291 (1938)
19. J.S. Kouvel, C.C. Hartelius, J. Appl. Phys. **33**, 1343 (1962)
20. I. Suzuki, T. Naito, M. Itoh, T. Taniyama, Appl. Phys. Lett. **107**, 082408 (2015)
21. T. Naito, I. Suzuki, M. Itoh, T. Taniyama, J. Appl. Phys. **109**, 07C911 (2011)
22. T. Moriyama, N. Matsuzaki, K.-J. Kim, I. Suzuki, T. Taniyama, T. Ono, Appl. Phys. Lett. **107**, 122403 (2015)

23. N. Matsuzaki, T. Moriyama, M. Nagata, K.J. Kim, I. Suzuki, T. Taniyama, T. Ono, Jpn. J. Appl. Phys. **54**, 073002 (2015)
24. L. Zsoldos, Phys. Status Solidi B **20**, K25 (1967)
25. G. Venkataiah, Y. Shirahata, I. Suzuki, M. Itoh, T. Taniyama, J. Appl. Phys. **111**, 033921 (2012)
26. I. Suzuki, M. Itoh, T. Taniyama, Appl. Phys. Lett. **104**, 022401 (2014)
27. S. Savitha Pillai, H. Kojima, M. Itoh, T. Taniyama, Appl. Phys. Lett. **107**, 072903 (2015)
28. H. Kojima, T. Naito, H. Muraoka, E. Wada, I. Suzuki, Y. Shirahata, M. Itoh, T. Taniyama, J. Appl. Phys. **113**, 17C713 (2013)
29. C.A. de Araujo, J.D. Cuchiaro, L.D. McMillan, M.C. Scott, J.F. Scott, Nature **374**, 627 (1995)
30. M. Dawbar, K.M. Rabe, J.F. Scott, Rev. Mod. Phys. **77**, 1083 (2005)
31. M.P. Warusawithana, C. Cen, C.R. Sleasman, J.C. Woicik, Y. Li, L.F. Kourkoutis, J.A. Klug, H. Li, P. Ryan, L.-P. Wang, M. Bedzyk, D.A. Muller, L.-Q. Chen, J. Levy, D.G. Schlom, Science **324**, 367 (2009)

Chapter 8
Microstructure Design for Oxide/ Non-oxide Ceramics for Structural Applications

Fumihiro Wakai

Abstract Mechanical properties of ceramics, such as hardness, strength, and fracture toughness depend not only on electronic/crystal structures but also on their microstructures. The processing–property–microstructure relations and the principles of microstructural design will be critically reviewed in this section. The mechanical reliability of brittle ceramics is improved by decreasing the flaw size during the sintering process. The continuum theory of sintering is useful to find a way to suppress defects formation. The improvement of toughness is an alternative way to improve reliability. A novel nano/microstructure design was proposed to develop the strong and tough nanocrystalline ceramics recently.

Keywords Sintering · Densification · Sintering stress · Fracture toughness · Toughening mechanism

8.1 Ceramics for Structural Applications

8.1.1 Engineering Ceramics

Based on excellent mechanical properties, engineering ceramics are used for structural applications in the field of technology such as energy and environmental technology, transportation and production technology, as well as biological and medical technology. Ceramics are inorganic, nonmetallic materials such as oxides, nitrides, carbides, borides, and their composites. Examples of engineering ceramics are listed below:

Oxides: SiO_2, Al_2O_3, ZrO_2, Mullite ($3Al_2O_3{\cdot}2SiO_2$)
Nitrides: AlN, BN, TiN, Si_3N_4, SiAlONs (solid solution of Si_3N_4 and Al_2O_3)
Carbides: B_4C, SiC, TiC.

F. Wakai (✉)
Laboratory for Materials and Structures, Institute of Innovative Research, Tokyo Institute of Technology, Tokyo, Japan
e-mail: wakai.f.aa@m.titech.ac.jp

Y. Setsuhara et al. (eds.), *Novel Structured Metallic and Inorganic Materials*, https://doi.org/10.1007/978-981-13-7611-5_8

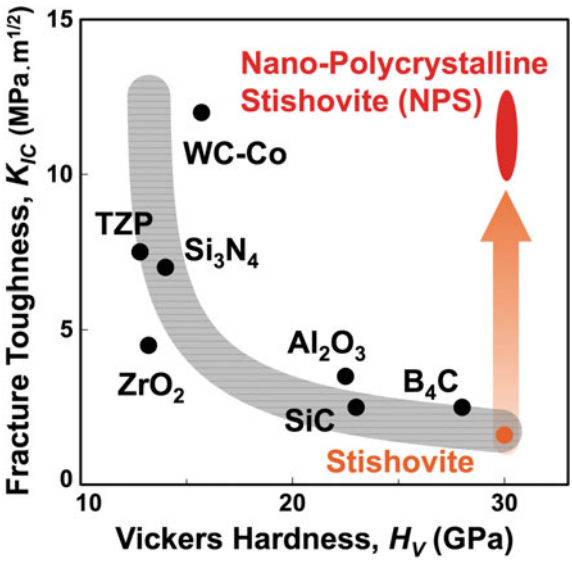

Fig. 8.1 Relation between hardness and fracture toughness

Excellent hardness, wear resistance, and thermomechanical properties of non-oxides arise from the covalent nature of atomic bonding. Moreover, some oxides such as alumina (Al_2O_3) and stishovite (a high-pressure phase of SiO_2) exhibit high hardness. Hard ceramics are used as cutting tools, forming dies, refractory non-oxides for steel industry, and casting tools. However, these hard ceramics show no ductility, so that catastrophic brittle fracture occurs unpredictably without any plastic deformation. The enhancement of reliability and damage tolerance are critical issues for the development of high-performance ceramics in order to extend their range of applications for mechanical engineering. The attainment of both hardness and toughness (damage tolerance) is a vital requirement for engineering ceramics. But, usually, these properties are mutually exclusive as shown in Fig. 8.1. High-toughness ceramics with high strength and wear resistance are targets of materials development for the future.

8.1.2 Microstructure–Property–Processing Relations

While intrinsic properties of a single crystal such as elastic constants and hardness are controlled by the constituent of atomic elements, crystal structures, the nature of atomic bonding, electric structures, and point defects, characteristic properties of polycrystalline materials are affected by their microstructures, e.g., grain size, grain shape, size distribution, pore volume, pore distribution, phase distribution, and alignment of these factors or texture. These microstructures are controlled by processing, so that the microstructure design through processing is the key for improving mechanical properties.

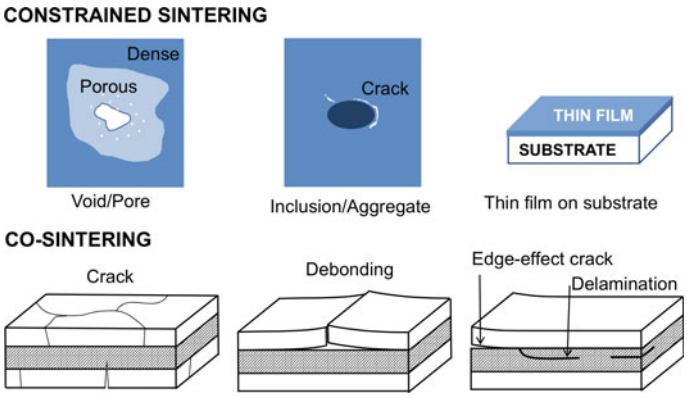

Fig. 8.2 Generation of defects during the sintering process

For example, fracture strength, σ_f of brittle material is determined by the Griffith criterion as

$$\sigma_f = YK_c/\sqrt{a} \tag{8.1}$$

where K_c is the fracture toughness, a is the flaw size, and Y is a geometry parameter. The mechanical failure of ceramics occurs unpredictably from defects/flaws that are introduced during processing, either surface finishing or sintering. Typical preexistent defects include large voids, cracks around inclusions/aggregates, which are formed by internal stresses generated during sintering [5]. One approach for achieving materials having high reliability is to decrease the flaw size by improving processing of the ceramic material since such voids and cracks are generated during the sintering process (Fig. 8.2). The continuum mechanics of sintering is an important theory to understand the stress distribution which arises in the processing due to nonuniform shrinkage rate, thereby, predicting how defects are evolved during sintering. In Sect. 8.2, the mechanics of sintering is described in order to predict the development of defects. An alternative approach to improve the reliability is to make materials with high fracture toughness strong, tough, and damage-tolerant ceramics requires nano/microstructure design to utilize toughening mechanisms at different scales. An approach for making toughened novel-structured ceramics is described in Sect. 8.3.

8.2 Sintering Process of Ceramics

8.2.1 Continuum Mechanics of Sintering in Macroscopic Scale

Sintering [11] is a thermal process that transforms powder compacts into complex-shaped components. Dimensional control of components is fundamental

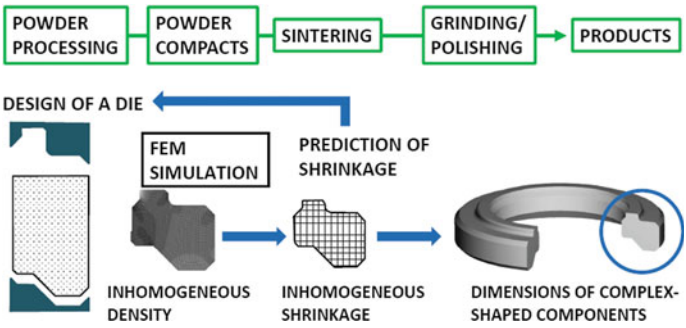

Fig. 8.3 Powder processing and sintering for making ceramic components

to meet the required tolerance specifications. Figure 8.3 shows the powder processing and sintering for making components schematically [12]. Heterogeneous density distribution in powder compacts may lead to inhomogeneous shrinkage in sintering. The continuum theory of sintering is of considerable help in predicting the dimension and shape of products or in designing industrial processes using computer simulation by finite element method (FEM). The sintering is a densification process, where the volume of a powder compact decreases with time. In the macroscopic description of deformation, the strain rate $\dot{E}_{ij}$ is a linear response to applied stress, either hydrostatic Σ_m or deviatoric Σ'_{ij}, and a thermodynamic driving force, i.e., the sintering stress Σ^s

$$\dot{E}_{ij} = \frac{\Sigma'_{ij}}{2G} + \delta_{ij}\frac{\Sigma_m - \Sigma^s}{3K} \tag{1}$$

where G and K are the shear viscosity and the bulk viscosity, respectively [2, 20, 21].

The continuum model is useful in analyzing the effect of applied stress in stress-assisted sintering such as hot pressing, spark plasma sintering, and hot isostatic pressing. It is also useful to predict the internal stresses, which are generated from the difference in shrinkage rate in constrained sintering [8]. The sintering stress is the thermodynamic driving force for shrinkage, but it may induce tensile stress that hinders shrinkage, enlarges void space, or makes cracks, when shrinkage is constrained by inhomogeneous packing density or aggregates/inclusions (Fig. 8.2). For example, in the sintering of thin film on a substrate, tensile stress is generated inside the film. This stress is proportional to the free sintering strain rate, which is caused by the sintering stress. The sintering stress, the driving force for shrinkage, generates internal stress in the film, which suppress shrinkage in constrained sintering. Such internal stresses induce cracks, debonding, or delamination in co-sintering of low temperature co-fired ceramics (LTCC) and solid oxide fuel cell (SOFC) [4].

8.2.2 Micro–Meso–Macro Relationship for Sintering Mechanics

Processing exerts essential influence on structural reliability through relations among the powder processing, the distribution of packing density, the defect formation, and the microstructure of the material [13]. If we know the origin of the sintering force and how to control it, we will be able to predict the defect development and the reliability of material. The macroscopic sintering stress is a physical quantity, which can be measured by sinter forging experimentally [9]. Microscopically the sintering stress is determined, in principle, from the knowledge of microstructures (Fig. 8.4). The concept of sintering stress was originally defined for equilibrium states, where the mechanical stress just balances the internal surface tension forces so that the porous materials does not shrink. It has been determined rigorously for periodically arranged particles in equilibrium, either isotropic [29] or anisotropic [28]. Actually, sintering is a nonequilibrium process, where gradients in the curvature lead to surface diffusion that changes the particle shape at elevated temperatures. Numerical simulation revealed that sintering force is the driving force for shrinkage and neck growth in sintering of two particles for coupled grain boundary diffusion and surface diffusion [25] and viscous sintering [27]. The analysis of sintering force is a basis for bridging the microscopic and the macroscopic models because the sintering stress arises from sintering forces acting among a huge number of particles. The theoretical modeling can help interpret experimental results particularly in complex sintering problems like sinter forging and constrained sintering [24].

8.2.3 Observation of Microstructure Evolution During Sintering

Advances in X-ray microtomography allow the observation of complex pore structures in three dimensions. It reveals real microstructural evolution during

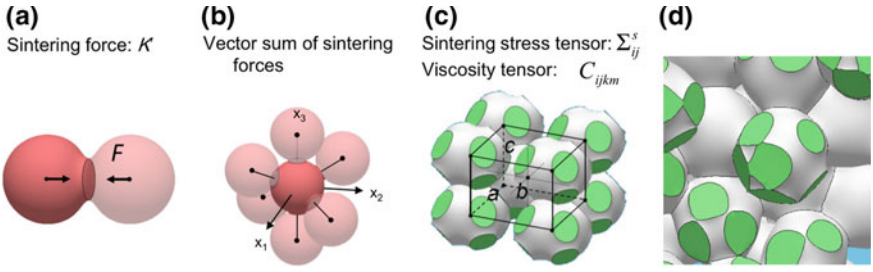

Fig. 8.4 Micromechanics in sintering. **a** Interaction between two particles, **b** multi-particles interaction, **c** periodic equilibrium structure, **d** random nonequilibrium structure

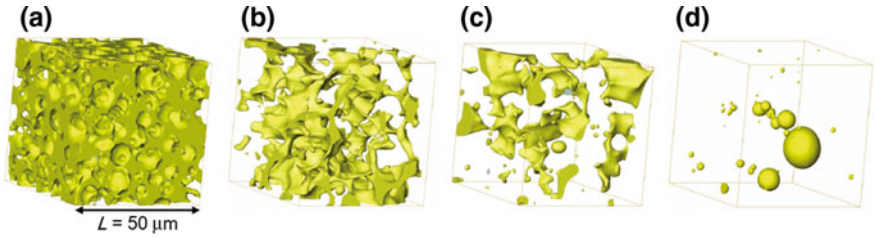

Fig. 8.5 Evolution of pore space in sintering: **a** stage 1 (relative density ρ = 63.5%), **b** stage 2 (87.8%), **c** stage 3 (94.1%), **d** stage 4 (98.4%). Reprinted from [26], Copyright 2014, with permission from Elsevier

sintering and provides an opportunity to analyze the local particle arrangements and nonuniformity at the particle scale [3]. Consider, for example, the pore space evolution in viscous sintering of spherical glass particles as shown in Fig. 8.5 [26]. In the initial stage (Fig. 8.5a), the pore structure is a continuous network with numerous circular holes resulting from contacts between particles. As holes expand with the neck growth, pore channels are pinched off, breaking the continuous network into fragments: closed pores are formed one by one in the intermediate stage (Fig. 8.5b, c). Complicated shaped pores become spherical in the final stage of sintering (Fig. 8.5d).

The macroscopic shrinkage in sintering is a result of the microstructural evolution that is driven by capillarity. The shape and form of pore structures, either open or closed, generate the sintering stress, which in turn is a driving force for shrinkage. The microstructural evolution in viscous sintering of glass is simply described by the fluid mechanics. In this case, the sintering stress in nonequilibrium porous structure is expressed by surface energy tensor, which is defined only by pore geometry [23]. The initial particle packing is slightly anisotropic usually due to tape casting. The sintering stress tensor was analyzed for X-ray computed microtomography data on the constrained sintering of glass films, which were cast on rigid substrates [3]. The average sintering stress in the thickness direction was the largest. The anisotropy in the sintering stress between the thickness direction and in-plane direction was observed. The anisotropy decreased with the microstructural evolution, and then, disappeared at the final stage [26]. The analysis of sintering stress tensor provides a novel method to investigate anisotropy and heterogeneities, which are introduced during powder processing.

8.3 Microstructure Design for Tough and Strong Ceramics

8.3.1 Toughening Mechanisms

The fracture resistance of ceramic materials is increased with crack extension by toughening mechanisms [6, 14] such as crack bridging [1], microcracking, or phase

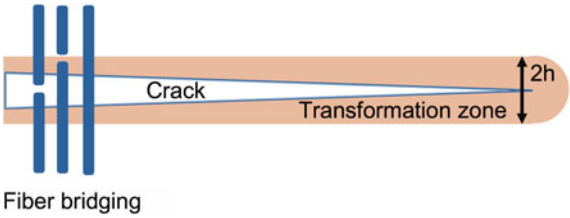

Fig. 8.6 Schematic diagram for toughening mechanisms by crack bridging and phase transformation

transformation [7, 16] as shown in Fig. 8.6. The crack bridging toughening contributes to enhanced fracture toughness of fiber-reinforced composites, silicon nitride with elongated matrix grains [22]. The enhanced fracture toughness of zirconia-based ceramics is derived from stress-induced tetragonal to monoclinic phase transformation [10]. Materials with rising resistance-curve (R-curve) lead to an increase in the strength compared to a material with the same intrinsic toughness and a flat R-curve [15]. The R-curves can be measured by using specimens with macrocracks (mm size) or with microcracks ($\sim$100 μm size). R-curves depend on specimen geometry, and they are not materials constants [17]. But, the early part of the R-curve, which is relatively insensitive to specimen geometry, provides the information on factors related to microscopic toughening mechanisms. The evaluation of R-curves with crack extension less than 10 μm is critical for the design of ceramic microstructures with both high strength and high toughness because the allowable flaw size is small in ceramics. The toughening mechanisms so far known are effective in microscale, then, they require the crack extension of more than a few micrometers to increase the fracture resistance.

8.3.2 A Novel Structured Nanocrystalline Ceramics

Stishovite is a high-pressure phase of silicon dioxide (SiO_2) stable at pressures above 9 GPa, and metastable at ambient conditions. While low-pressure phases, e.g., quartz and coesite, consist of networks of corner-sharing SiO_4 tetrahedra, stishovite possesses the rutile structure and is described as chains of edge-sharing SiO_6 octahedra. Stishovite is 60% more compact than quartz and has the highest hardness (33 GPa) of any stable/metastable oxide under ambient temperatures. Only diamond and cubic boron nitride are industrially used materials that are harder than stishovite. Hard materials with the limited ability of plastic deformation tend to be brittle, then, the fracture toughness of a single crystal is 1.6 MPa $m^{1/2}$. Recently, it is found that nanocrystalline stishovite with the average grain size of 127 nm had a fracture toughness of 13 MPa $m^{1/2}$ [18]. The fracture surface showed a unique characteristic "worm-like texture" as shown in Fig. 8.7. This discovery shows that the nanocrystalline stishovite attains both excellent hardness and toughness, which are vital requirements for structural materials.

Transformation of metastable stishovite with sixfold coordination to the stable phase with fourfold coordination often occurs through the intermediate amorphous

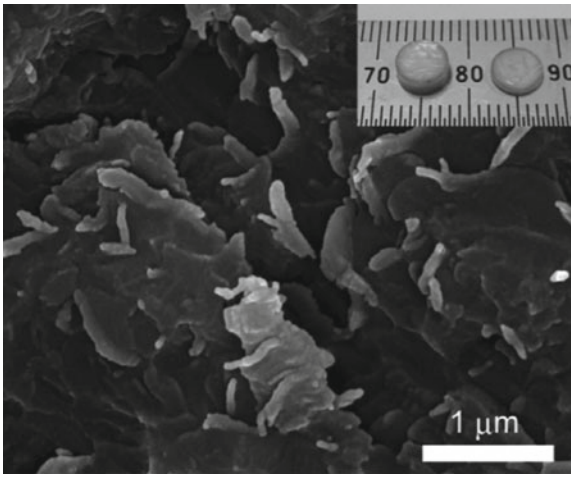

Fig. 8.7 Fracture surface of nanocrystalline stishovite. Reprinted from [18], Copyright 2012, with permission from Elsevier

state, because the Gibbs free energy of stishovite is higher than that of amorphous SiO_2 at any temperature above 0 K at ambient pressure. The direct transition of crystal to the amorphous state, which is analogous to melting, is triggered by heating at 1 bar, or decompression at room temperature. The terms, amorphization/vitrification, and melting are used for the transition below and above the glass transition temperature. The amorphization accompanies a volume expansion up to about 100%. The amorphization is induced by fracture since the tensile stress, which is equivalent to negative pressure, can be very large at the crack tip. The formation of the amorphous phase with the thickness of a few tens of nanometers was observed on the fracture surface by X-ray absorption near edge structure (XANES) spectroscopy [19]. In analogy to the transformation toughening of zirconia where the metastable tetragonal phase transforms to stable monoclinic phase at the crack tip, the fracture-induced amorphization can be a toughening mechanism of stishovite. In order to understand why the nanometer-thick amorphous layer can increase the fracture resistance significantly, a micro-mechanical test method using micro-cantilever beam specimens was developed to determine the very early part of resistance-curve of nanocrystalline SiO_2 stishovite [30]. The crack growth resistance of stishovite increased from 4 to 8 MPa $m^{1/2}$ with crack extension about 1 mm (Fig. 8.8).

It was revealed that this novel toughening mechanism was effective even at length scale of nanometer due to narrow transformation zone width of a few tens of nanometers and large dilatational strain (from 60 to 95%) associated with the transition of crystal to an amorphous state. There exists a toughening mechanic which can operate at nanoscale. This finding will provide a motivation to search for other nanoscale toughening mechanisms in many structural materials, such as ceramics, composites, nanocrystalline materials, and also, synthetic materials with hierarchical architecture.

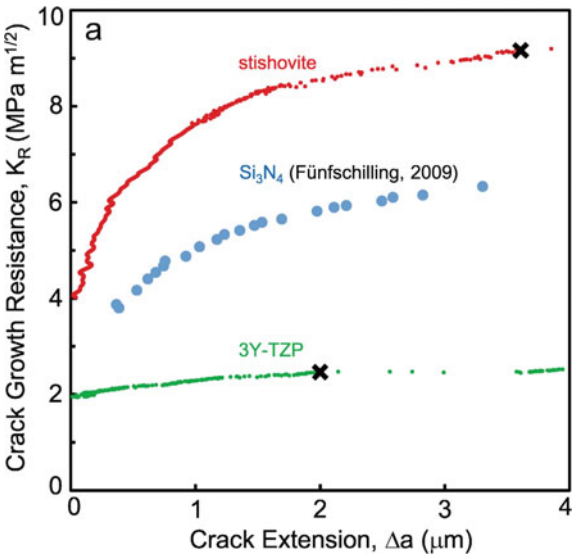

Fig. 8.8 Microscopic R-curve behavior of nanocrystalline stishovite, silicon nitride, and zirconia (Y-TZP). Reprinted from [30], Copyright 2015, with permission from Springer

References

1. P.F. Becher, Microstructural design of toughened ceramics. J. Am. Ceram. Soc. **74**, 255–269 (1991)
2. R.K. Bordia, G.W. Scherer, On constrained sintering—I. constitutive model for a sintering body. Acta Metall. Mater. **36**, 2393–2397 (1988)
3. D. Bernard, O. Guillon, N. Combaret, E. Plougonve, Acta Mater. **59**, 6228–6338 (2011)
4. P.Z. Cai, D.J. Green, G.L. Messing, Constrained densification of alumina/zirconia hybrid laminates, I: experimental observations of processing defects. J. Am. Ceram. Soc. **80**, 1929–1939 (1997)
5. A.G. Evans, Structural reliability: a processing-dependent phenomenon. J. Am. Ceram. Soc. **65**, 127–137 (1982)
6. A.G. Evans, Perspective on the development of high-toughness ceramics. J. Am. Ceram. Soc. **72**, 187–206 (1990)
7. A.G. Evans, R.M. Cannon, Toughening of brittle solids by martensitic transformation. Acta Metall. **34**, 761–800 (1986)
8. D.J. Green, O. Guillon, J. Rödel, Constrained sintering: a delicate balance of scales. J Euro Ceram Soc **28**, 1451–1466 (2008)
9. O. Guillon, J. Rödel, R.K. Bordia, Effect of green-state processing on the sintering stress and viscosity of alumina compacts. J. Am. Ceram. Soc. **90**, 1637–1640 (2007)
10. R.H.J. Hannink, P.M. Kelly, B.C. Muddle, Transformation toughening in zirconia-containing ceramics. J. Am. Ceram. Soc. **83**, 461–487 (2000)
11. S.J.L. Kang, *Sintering* (Elsevier Butterworth-Heinemann, Burlington, MA, 2005)
12. T. Kraft, H. Riedel, Numerical simulation of solid state sintering; model and application. J. Euro. Ceram. Soc. **24**, 345–361 (2004)
13. F.F. Lange, Powder processing science and technology for increased reliability. J. Am. Ceram. Soc. **72**, 3–5 (1989)
14. M.E. Launey, R.O. Ritchie, On the fracture toughness of advanced materials. Adv. Mater. **21**, 2103–2110 (2009)

15. D.B. Marshall, Strength characteristics of transformation-toughened zirconia. J. Am. Ceram. Soc. **69**, 173–180 (1986)
16. R.M. McMeeking, A.G. Evans, Mechanics of transformation-toughening in brittle materials. J. Am. Ceram. Soc. **65**, 242–246 (1986)
17. D. Munz, What can we learn from R-curve measurements? J. Am. Ceram. Soc. **90**, 1–15 (2007)
18. N. Nishiyama et al., Synthesis of nanocrystalline bulk SiO_2 stishovite with very high toughness. Scripta Mater. **67**, 955–958 (2012)
19. N. Nishiyama et al., Fracture-induced amorphization of polycrystalline SiO_2 stishovite: a potential platform for toughening in ceramics. Sci. Rep. **4**, 6558 (2014)
20. E.A. Olevsky, Theory of sintering: from discrete to continuum. Mater. Sci. Eng. R **23**, 41–100 (1998)
21. H. Riedel, H. Zipse, J. Svoboda, Equilibrium pore surfaces, sintering stresses and constitutive equations for the intermediate and late stages of sintering—II. diffusional densification and creep. Acta Metall. Mater. **42**, 445–452 (1994)
22. F.L. Riley, Silicon nitride and related materials. J. Am. Ceram. Soc. **83**, 245–265 (2000)
23. F. Wakai, Mechanics of viscous sintering on the micro- and macro-scale. Acta Mater. **61**, 239–247 (2013)
24. F. Wakai, R.K. Bordia, Microstructural evolution and anisotropic shrinkage in constrained sintering and sinter forging. J. Am. Ceram. Soc. **95**, 2389–2397 (2012)
25. F. Wakai, K. Brakke, Mechanics of sintering for coupled grain boundary and surface diffusion. Acta Mater. **59**, 5379–5387 (2011)
26. F. Wakai, O. Guillon, Evaluation of sintering stress from 3-D visualization of microstructure: case study of glass films sintered by viscous flow and imaged by X-ray microtomography. Acta Mater. **66**, 54–62 (2014)
27. F. Wakai, K. Katsura, S. Kanchika, Y. Shinoda, T. Akatsu, K. Shinagawa, Sintering force behind the viscous sintering of two particles. Acta Mater. **109**, 292–299 (2016)
28. F. Wakai, Y. Shinoda, Anisotropic sintering stress for sintering of particles arranged in orthotropic symmetry. Acta Mater. **57**, 3955–3964 (2009)
29. F. Wakai, Y. Shinoda, T. Akatsu, Methods to calculate sintering stress of porous materials in equilibrium. Acta Mater. **52**, 5621–5631 (2004)
30. K. Yoshida et al., Large increase in fracture resistance of stishovite with crack extension less than one micrometer. Sci. Rep. **5**, 10993 (2015)

Part III
Integration and Processing of Novel Structured Materials

Chapter 9
Gas Tungsten Arc Welding

Manabu Tanaka

Abstract Gas tungsten arc welding (GTAW) utilises an intense electric arc formed between a non-consumable tungsten electrode and the workpiece to generate controlled melting within the weld joint. Essentially, the arc can be used as if it was an extraordinarily hot flame. The stability of the tungsten electrode and the option to use totally inert gas mixtures if desired means that the process can be very clean and easy to implement. It is also a process with the potential to deliver relatively high-power densities to the workpiece, and so can be used on even the most refractory metals and alloys. In this chapter, principles of GTAW including energy transport, momentum transport and weld pool behaviour which are required to understand and control heat source properties of GTAW are reviewed in detail. Furthermore, future trends of applications of GTAW are also described.

Keywords Arc welding · Tungsten · Arc plasma · Heat source properties

9.1 Introduction

Gas tungsten arc welding (GTAW) first made its appearance in the USA in the late 1930s, where it was employed for welding aluminium airframes. It was an extension of the carbon arc process, with tungsten replacing the carbon electrode. The new tungsten electrode, together with an inert helium shielding gas atmosphere, reduced weld metal contamination to the extent that highly reactive metals such as aluminium and magnesium could be welded successfully. For a time, the process was known as 'heliarc' in the USA. Other countries substituted the less expensive argon for helium and referred to the process as 'argon arc'. Later, these distinctions were dropped and the process became known as tungsten inert gas (or TIG)

M. Tanaka (✉)
Joining and Welding Research Institute, Osaka University,
11-1 Mihogaoka, Ibaraki, Osaka 576-0047, Japan
e-mail: tanaka@jwri.osaka-u.ac.jp

Y. Setsuhara et al. (eds.), *Novel Structured Metallic and Inorganic Materials*, https://doi.org/10.1007/978-981-13-7611-5_9

welding. More recently, the term gas tungsten arc (GTA) has been introduced to signify that the shielding gas may not necessarily be inert.

GTAW is known for its versatility and high joint quality. It can be used with a wide variety of materials, including highly reactive or refractory metals. It may be operated manually at lower currents (e.g. 50–200 A) for single-pass joining of relatively thin sections, or multi-pass welding of thicker sections that have appropriate V- X- or similar-type edge preparations.

During the 1960s, the process was extended to much higher current range, allowing the arc forces to play a significant role in increasing weld penetration. At currents above about 250 A, the arc tends to deform the weld pool surface, with the effect increasing as the current is increased further. This mode of operation is generally automated, and in its early manifestations gave rise to terms such as high current, buried arc, and subsurface arc TIG (or GTAW). Plasma arc welding also has its origins in the GTAW process. More recent innovations have included the introduction of active fluxes (A-TIG), dual shield GTAW, guided GTAW, keyhole GTAW, and laser-GTAW hybrid processes.

Understanding of the GTAW process involves input from many disciplines. Although appearing relatively simple, application of the process involves many choices including electrode size and composition, electrode tip geometry, power supply characteristics, electrode polarity, shielding gas, welding current, and voltage settings. Each of these will be related to the type of material and its joint geometry. The complexities and the importance of the GTAW process have stimulated research which is still very active more than 60 years after its introduction.

9.2 Principles

9.2.1 Energy Transport

GTAW utilises an intense electric arc ignited between a non-consumable tungsten electrode and the workpiece to produce controlled melting within the weld joint. Essentially, the arc can be used as if it was an extraordinarily hot flame. The stability of the tungsten electrode and the option to use totally inert gas mixtures if desired means that the process can be very clean and easy to implement. It is also a process with the potential to deliver relatively high-power densities to the workpiece, and so can be used on even the most refractory metals and alloys. It can be misleading to refer to arc temperatures as a measure of melting ability, but the intent can be captured in the measure of power density. Using this one finds that GTAW processes produce power densities at the weld pool of up to 100 W/mm^2. For comparison, this is at least an order of magnitude greater than is available from an oxyacetylene flame. The power density delivered to the workpiece is important in determining the process efficiency and can be a significant constraint when using with highly conductive metals such as copper.

Under standard conditions, all shielding gases are extremely good electrical insulators because of the small degree of ionisation of the gas. The current densities typical of welding arcs (of the order of tens of amps per square millimetre) can only be achieved if a high concentration of charged particles can be generated and maintained in the conducting channel. In arcs, the necessary populations of electrons and ions are maintained by thermal ionisation and this requires temperatures of about 10 000 K and above.

The degree of ionisation of a gas can be expressed as a function of temperature by the Saha equation [1]. The resultant conductivity is then determined from consideration of the charge mobilities, as can be found in standard texts, e.g. [2] and [3]. An example of dependence of conductivity of argon on temperature is shown in Fig. 9.1 [1].

It is now known that the current density in an arc column has a limiting value under normal conditions. Once this limit is reached further increases in total current only distribute the current over larger areas of the anode, with no appreciable change in peak current density on the arc axis [4]. In the case of argon, the conductivity increases until doubly ionised argon appears at about 22 000 K. At this point, the resistance provided by the doubly charged ions outweighs the benefit of the increased number of electrons and so conductivity reaches a local maximum (see Fig. 9.1). Once this temperature has been reached in a particular region, further increases in current will tend to expand the current distribution into the adjacent, slightly low-temperature regions [5].

For a very preliminary research of the welding arc, its main section can be treated as one-dimensional, i.e. as a function of radius, r, only. Such an approach, introduced by Glickstein in 1981, began with a simple model for the positive column in which ohmic heating was balanced against radial thermal conduction:

$$\sigma E^2 = \frac{-1}{r}\frac{d}{dr}\left(rk\frac{dT}{dr}\right)dr \tag{9.1}$$

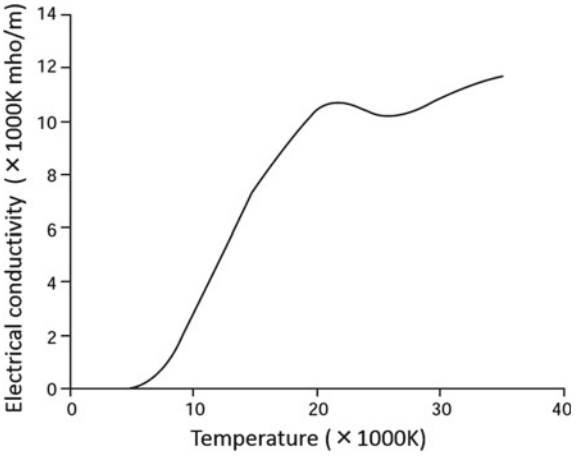

Fig. 9.1 Dependence of the electrical conductivity of argon on temperature from 3000 to 30 000 K

In the above equation, σ is the electrical conductivity, E is the electric field, r is the radius from the arc axis, k is the thermal conductivity and T is the temperature. Equation (9.1) is known as the Elenbaas–Heller equation. This equation can be corrected for additional energy losses through radiation, S(T), [1] and it is then known as the 'corrected Elenbaas–Heller', Eq. (9.2):

$$\sigma E^2 = \frac{-1}{r}\frac{d}{dr}\left(rk\frac{dT}{dr}\right)dr + S(T) \tag{9.2}$$

Since the electrical and thermal conductivities of shielding gases have complicated temperature dependencies, as shown in Fig. 9.1, these equations can only be solved numerically. Nevertheless, the view of an arc in which radial conduction and radiation balance ohmic heating is easily visualised and so is useful in developing a qualitative understanding of arc behaviour. For example, Glickstein's solutions predicted that helium arcs should be much broader than those of argon despite peak temperatures and current density distributions being similar. Consequently, helium arcs should require higher voltages than argon arcs do—as is observed—since the energy is derived from the electric field. Similarly, it can be appreciated that vapour contamination or minor additions of a gas of lower ionisation potential should significantly alter the arc configuration.

An appreciation of the welding arc with the Elenbaas–Heller equation has two fundamental limitations: there is no consideration of the regions connecting the plasma to the electrodes and the omission of convection within the arc.

The very narrow regions between the electrode surfaces and the arc proper are known as sheath regions. In these regions, the high temperatures ($\sim$10 000 K) needed for good electrical conductivity in the gas cannot be sustained due to the cooling provided by the cold electrodes (even the boiling temperature of iron is thousands of degrees below that required for argon to conduct well). Consequently, the electrical conductivity of the gas will be extremely low. Because of the high resistivity close to the electrodes the electric field of the arc will be very much stronger in these regions than elsewhere. This is equivalent to saying that the field has a nonzero divergence and according to Maxwell's equations must be associated with the presence of net electric charge:

$$\nabla \cdot E = \frac{\rho}{\varepsilon_0} \tag{9.3}$$

Or, in one dimension:

$$\rho = \varepsilon_0 \frac{dE}{dx} \tag{9.4}$$

Consequently, sheath regions will be bounded by regions of charge, one on the electrode surface and the other at the interface with the plasma. This latter constitutes a region of space charge. The corresponding voltage drops are sometimes known as 'fall' voltages (see Fig. 9.2).

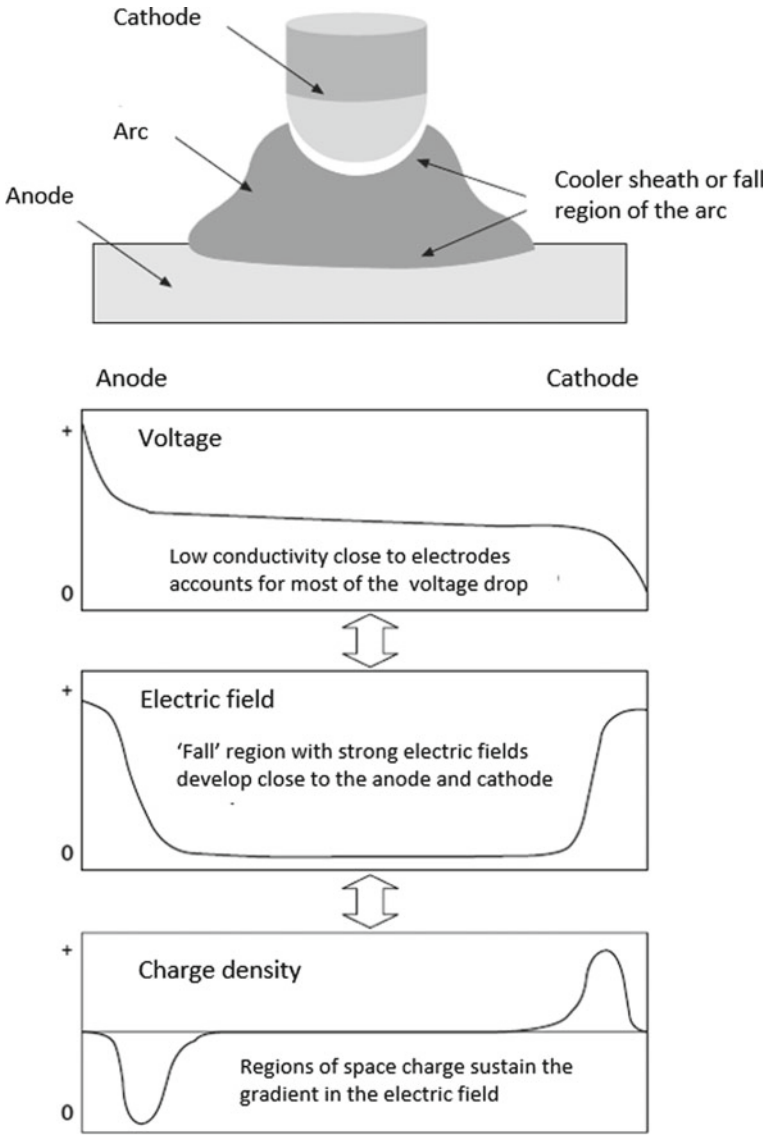

Fig. 9.2 Schematic illustrations of the variation in voltage, electric field and charge densities with position along an arc discharge

The sheath regions are extremely important to determine the particular characteristics of an arc and to establish the overall energy balance. In welding arcs, the predominant charge carriers are electrons and these must be continually replenished by being drawn out of the cathode and across the cathode sheath. Liberating electrons from a metal surface requires a considerable amount of energy—each

electron absorbing at least an amount eϕ where ϕ is the work function of the surface (typically 2–4 V). If the metal is suitably refractory (such as tungsten or hafnium), this can be provided by the high temperature of the electrode and is then known as thermionic emission. In this case, the electrons effectively evaporate from the surface. If the temperature of the electrode is not high enough, the electrons must gain their energy from the very high-strength field between the surface and the surrounding space charge. This is termed field emission. GTAW is generally operated in the thermionic emission mode. Electron emission is aided by the presence of oxides and other surface impurities.

The electrons leave the arc by crossing the anode sheath and entering the anode, which is usually the workpiece. The anode sheath is believed to be of the order of one electron mean free path in width, to be consistent with its relatively low temperature. In crossing this and entering the anode, the electron transports a considerable portion of the total energy flux. The energy contribution of each electron to the anode includes its thermal energy, the energy it absorbs from the anode fall, and its energy of condensation, eϕ. In some cases, this can amount to as much as 80% of the total energy flow into the anode. The other major source of energy transport to the anode is conduction and here the characteristics of the shielding gas become important. For example, helium is far more conductive than is argon and consequently delivers more heat—hence, the perception that it makes an arc 'hotter'. Gases such as hydrogen and nitrogen exhibit what is known as 'reactive thermal conductivity'. They dissociate at high temperatures with the absorption of significant amounts of energy, only to recombine and release this energy in the cooler regions such as the anode sheath. So these gases are also associated with 'hot' arcs. In addition to electron absorption and conduction, convection and radiation also transport energy. Convection in particular becomes very important as currents rise above 40 A or so [6] and may be the dominating transport mechanism outside the sheath regions. Convective flow is powered by Lorentz forces associated with the passage of the high welding currents and has an impact on the momentum as well as on energy transferred to the weld pool. Present numerical models of welding arcs endeavour to incorporate all these effects [6, 7] but there is still much development to be done.

9.2.2 Momentum Transport

At currents below about 200 A, the gas tungsten arc has many characteristics of an ideal flame. It can be chemically inert, it produces very high heat fluxes to the workpiece, and it appears to produce almost no disturbance to the molten metal it produces. But despite the absence of metal transfer, the arc does transport momentum and this becomes important at higher currents. The momentum transfer and several of the resultant forces on the weld pool are due to Lorentz forces generated within the arc. These forces can give rise to high-velocity plasma jets. Similar forces also occur within the pool and are one of the drivers for circulation

within it. The strength of these forces is dependent on the magnitude of the welding current ($F \propto I^2$) and its geometric distribution. The latter dependency is in turn related to variables such as electrode composition and geometry, and choice of gas shield composition. In order to model a welding arc, one might begin by considering the motion of an individual element of the plasma. Thus, each element of the arc fluid is accelerated in proportion to the net force acting on it:

$$\rho \frac{dv}{dt} = \rho\left(\frac{dv}{dt} + v \cdot \nabla v\right) = \text{net force per unit volume} \tag{9.5}$$

where ρ is the (incompressible) fluid density, v is its velocity and t is the time. The net force per unit volume in an arc will include the Lorentz term J × B, the pressure gradient—∇P, and a 'diffusion' term that accounts for viscous damping, η∇2v. The resultant equation is a modified Navier–Stokes equation for an incompressible fluid, and reads

$$\rho \frac{dv}{dt} = -\rho v \cdot \nabla v - \nabla P + J \times B + \eta \nabla^2 v \tag{9.6}$$

Solving this equation for an arc is challenging since the parameters are strongly coupled, rendering the system non-linear. In general, several different equations must be satisfied simultaneously (e.g. conservation of mass, energy, charge and momentum) and numerical methods must be used for their solution. The work of [6] provides a comprehensive treatment of this problem.

However, as is often the case, much can be learned by considering simplified approximations. One such approximation is to ignore viscosity, as done by [8]. He treated the arc as a truncated cone with the welding current, I, flowing between the two electrodes, a tungsten tip with an emission area of cross-sectional radius R_e and the weld pool surface of larger radius R_a. With the assumption that the current density is constant over any chosen radial cross section, the net force normal to the pool was found to be

$$F = \frac{\mu I^2}{8\pi}\left(1 + 2\ln\frac{R_a}{R_e}\right) \tag{9.7}$$

The ratio R_a/R_e is known as the arc expansion ratio.

Converti identified the two J × B components contributing to the net Lorentz force acting on the arc. Current flowing through an arc generates a circumferential magnetic field, $B_\theta(r)$, perpendicular to both the axial and radial vectors. Consequently, both axial and radial components of the arc current will interact with this field to give rise to forces. The axial component ($J_z \times B_\theta$) generates a compressive, or pinch force while any radial component ($J_r \times B_\theta$, due to arc expansion) results in an axially directed force. These two forces give rise to a radial pressure gradient and a fluid flow (the plasma jet), respectively. The radial pressure gradient produces a static pressure that squeezes the plasma against the terminating

electrodes. On the other hand, the fluid flow contributes to a dynamic pressure that acts only on surfaces that change the velocity of the fluid stream.

Evaluation of Eq. (9.7) indicates that the arc force increases with the square of the welding current. Furthermore, experimental observation [9] and calculations based on reasonable estimates of the arc expansion ratio [10] show that the magnitude is of the order of 3×10^{-5} I^2 grams weight. So, for example, an arc carrying 100 A would exert a relatively insignificant force of about 300 mg weight, whereas at 500 A the force would be nearer 7.5 g weight. The latter is sufficient to displace a significant volume of weld metal, molten stainless steel having a density of about 7 g/cm^3.

Evidently, the larger portion of the arc force derives from the dynamic pressure term $(\mu/4\pi) \ln (R_a/R_e)$. Consequently, changing the arc expansion ratio will alter the arc force generated at a given current. Now, in the case where the tungsten electrode is the cathode, there is good evidence that the emission current is approximately proportional to emission area. In fact, measured values for emission current densities vary slightly around about 150 A/mm^2, depending on electrode composition [11] and welding current [12]. Consequently, the arc expansion ratio can be increased by measures such as reducing the angle of the electrode taper or changing the electrode composition. Other factors, such as choice of shielding gas and electrode diameter can also alter the expansion ratio by changing the thermal balance at either electrode.

The arc pressure is a measure of the arc force per unit area at any given point over the weld pool. Generally, arc pressure is a maximum on or close to the arc axis and is often modelled as having a Gaussian distribution. Arc pressure is sensitive to changes in the distribution of the arc force and so is significantly altered by factors such as redistribution of the current and changes in gas viscosity. For example, the arc pressures in a helium arc are significantly lower than those in an argon arc at the same current because high-temperature helium is more viscous than argon and therefore distributes the arc force over a wider area.

9.2.3 Weld Pool Behaviour

To complete a model of the GTAW process, it is necessary to consider the behaviour of the liquid weld metal. The weld pool can be a very active part of the welding process, with significant energy and momentum transport taking place within it. In addition to Lorentz forces, the weld pool is subjected to variations in surface tension, buoyancy, Marangoni and 'aerodynamic' plasma drag forces. Finally, at higher currents, the pool surface can be highly distorted and this can modify current and gas flow within the arc, as well as produce another surface tension-based driver for the flow of the liquid metal (see below). In general, however, forces associated with gradients in surface tension are believed to dominate flow within the pool.

The flow resulting from gradients in surface tension is often referred to as Marangoni flow [1]. Normally, surface tension decreases with increasing temperature, so that the weld pool surface will have a higher surface tension at the edges than at the centre. As a result, the hotter weld metal at the centre is drawn across the surface to the edges, thereby establishing a circulation that transports heat directly to the edges of the pool, favouring the formation of a wide, shallow weld puddle. Under appropriate conditions, this effect can be reversed by surface-active elements such as sulphur, phosphorus and selenium. These elements lower the surface tension in the cooler regions of molten metal, but are dissipated at higher temperatures. In such circumstances, the temperature coefficient of surface tension can become positive (that is, surface tension could increase with temperature) and reverse the expected direction of flow. This circulation transports heat to the bottom of the pool rather than to the edges, to produce deep, narrow weld pools. In this way, the performance of specific welding procedures can be compromised by heat-to-heat variations in sulphur content within a given type of stainless steel, for example. Lorentz forces also promote 'centre-down' circulation within the pool (see Fig. 9.3).

When the arc current exceeds about 150 A, the weld pool surface becomes noticeably concave in response to the arc forces. The degree of metal displacement increases with increasing current and becomes an important influence on process

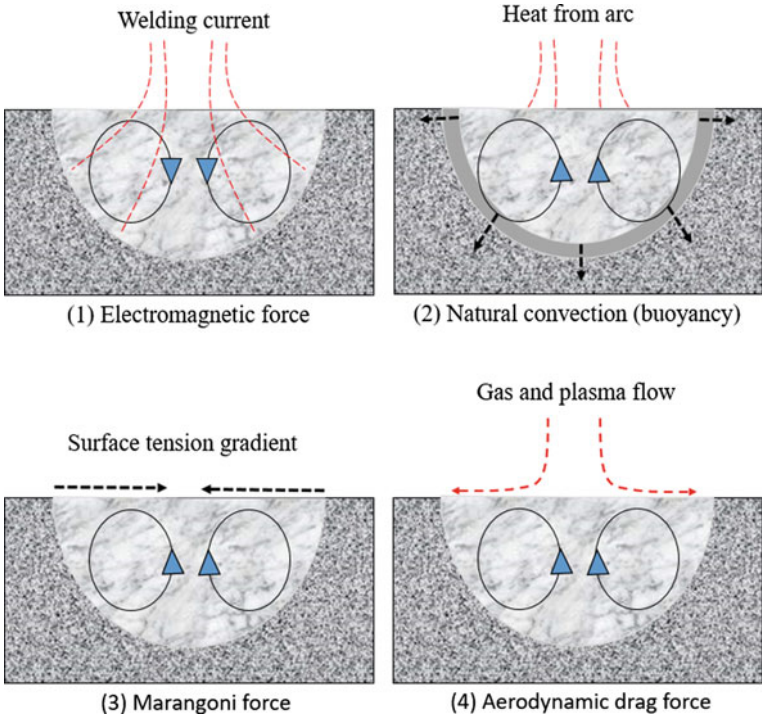

Fig. 9.3 Flow directions induced by four possible motive forces in arc welding

performance above about 250 A. The displacement of the weld pool is visible as a terminating crater if the weld is abruptly terminated. Such craters are interesting for several reasons. For example, their presence indicates that the liquid displaced by the arc forces does not simply accumulate around the edges of the pool but actually gets frozen into the weld bead. The amount of material required to fill the crater has been referred to as the 'deficit' [10]. Although the shape of the crater may differ from the depression of the pool during welding, it is evident that the deficit is conserved. Hence, measurement of the deficit, via the terminating crater, can be used to provide useful insights into the weld pool dynamics.

The use of measurements of deficit is illustrated by the data presented in Fig. 9.4. The data is from experiments involving GTA bead-on-plate welds on stainless steel using alternately argon and helium shielding gas. What is evident in each case is an abrupt and large increase in deficit over small changes in current. These changes correspond to similarly large changes in penetration (Fig. 9.5). The implication is that an inadvertent choice of welding parameters near such transition regions could result in serious weld inconsistencies.

Models that balance arc forces against the combined effects of buoyancy and surface tension [10] could explain sudden changes in deficit. Essentially, the argument is as follows. If the width of a weld pool is fixed and the arc force is gradually increased from zero, surface distortion will be resisted by buoyancy and by surface tension. These forces increase as the curvature increases, and hence deficit rises relatively slowly. However, the resistance provided by surface tension has a maximum value ($2\mu r\gamma$) that corresponds to the surface becoming vertical at some radius r. Further increase in arc force beyond this value causes proportionately much greater displacement as it is now only limited by the weaker buoyant forces.

Models that can describe weld pool surface geometry begin with the assumption of a 'free surface'. This means that the pool surface moves until the net pressure change across it is zero. Pressures arise from surface tension, buoyancy and arc pressure. Because the net pressure is zero everywhere, the surface is at a local

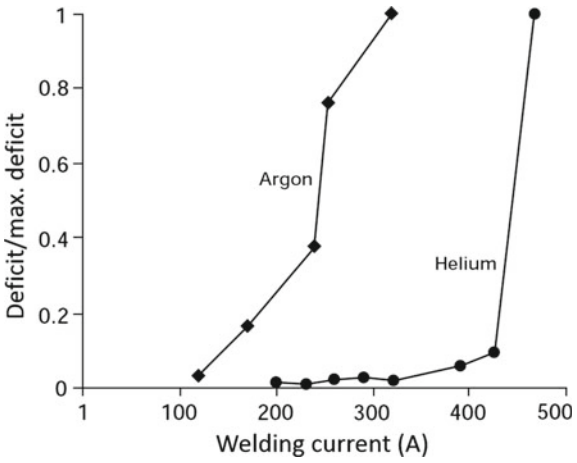

Fig. 9.4 Variation in deficit with current for melt-in mode GTAW

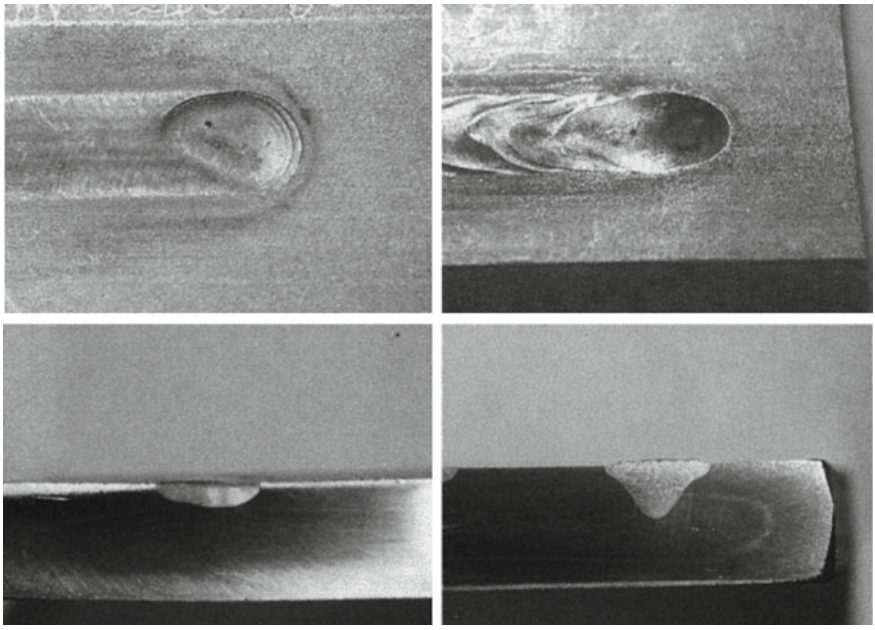

Fig. 9.5 Visual evidence of abrupt changes in deficit for bead-on-plate welds on stainless steel. Both welds were made using argon shielding and at the same welding speed and voltage. Left 240 A, right 255 A

minimum in energy. Of course the surface is attached to the parent material at the boundary of the pool. It follows that when the boundary moves as the heat source moves along the joint, the distorted surface moves with it (If it did not then its shape would change, its surface energy increase and it would experience a restoring force acting to realign it with the moved boundary). This automatically drives liquid metal from the leading to trailing edge of the pool and so is another potential driver for fluid flow within the pool.

9.3 Future Trends of Applications

There are a number of misconceptions and genuine limitations relating to GTAW and these must be addressed if the process is to retain its relevance in the future. The 'basic' GTAW process has been hampered by its low penetration and consequent poor productivity. As a production tool, it tends to be used when quality or other overriding issues demand it. It is argued that the process has much more to offer and has illustrated this with the detailed description of two of its many variants. It is suggested that this realisation that GTAW has 'more to offer' will be increasingly appreciated, particularly as fabrication operations become more

integrated and mechanised. One of the historical impediments to the seamless integration of welding into production lines has been poor joint fitup and the consequent need for a degree of adaptability that was only available with manual intervention. This impediment is rapidly being removed as component tolerances improve, welding processes become more tolerant and control systems are made more intelligent and responsive. This trend will suit the lower deposition welding processes such as GTAW and should renew the search for innovative ways of exploiting this very elegant process.

Many of the changes to GTAW over recent times have been forecast correctly to be in the area of the equipment used to implement the process [13, 14]. This area covers power sources, control systems, monitoring, viewing and data acquisition [14]. This trend is expected to continue in the future, with the increasing availability of significant computational power driving the process in the direction of greater adaptability and user-friendliness. Occupational health and safety as well as environmental issues is also becoming more important and concerns about electromagnetic radiation and its potential to interfere with computerised equipment, metal fume and overall power requirements will all lead to further changes in equipment and practices.

However, the opportunity for new variants is expected to continue and to produce some very productive processes. One example of this is the recent research into hybrid processes and particularly laser plus GTAW [15, 16]. Hybrid welding refers to a situation where two processes (in this case, laser welding and GTAW) are coupled together to act as a single point. The coupling between the laser beam and the gas tungsten arc produces a number of synergistic effects that enhance the best features of each process. For example, the laser not only provides deep penetration but also stabilises the anode spot of the arc. As one result, the gas tungsten arc then can be operated in the more efficient DCEN mode, even when welding aluminium. At the same time, the arc broadens the weld pool at the plate surface, improves the laser to material coupling and relaxes the very high joint tolerances required for laser welding. It also provides additional heat input and an improved weld profile with reduced notch angles. In one set of trials on a 2 mm aluminium 3% magnesium alloy, [15] reported an increase in welding speed from 5 m/min for the laser to 8 m/min with the hybrid process. The GTAW operated alone could only be operated in the ac mode at 2 m/min.

Another innovation, in GTAW, is the newly reported guided GTAW or GGTAW process [17]. In this variant, the main arc is established between a short, hollow tungsten electrode and the workpiece. However, a separately powered electrode positioned above the main electrode provides a lower current ‘pilot arc’. This arc is constricted in passing through the hollow main electrode. The result is two concentric arcs, the inner of which has a high energy density and is relatively stiff. The inner arc has the effect of stiffening or ‘guiding’ the main arc, hence the name of the process. This process is anticipated to have some advantages over both GTAW and plasma arc.

In summary, GTAW is a particularly elegant welding process because of its apparent simplicity and appeal to fundamental physical principles. It is also

becoming far more productive and versatile than popular images of the process suggested. The likely scenario is that this process will continue to be developed in new and imaginative ways for many years to come.

References

1. J.F. Lancaster, *The Physics of Welding*, 2nd edn. (IIW publication, Pergamon Press, Oxford and New York etc., 1986)
2. P. Lorrain, D. Corson, *Electromagnetic Fields and Waves*, 2nd edn. (W.H. Freeman and Co., San Francisco, 1970)
3. R. Papoular, *Electrical Phenomena in Gases* (Iliffe Books, London, 1965)
4. C.E. Jackson, Weld. J. **39**(4), 129s–140s (1960)
5. C.B. Shaw Jr., Weld. J. **54**(2), 33s–44s (1975)
6. P. Zhu, J.J. Lowke, R. Morrow, J. Phys. D Appl. Phys. **25**, 1221–1230 (1992)
7. J.J. Lowke, P. Kovitya, H.P. Schmidt, J. Phys. D Appl. Phys. **25**(11), 1600–1606 (1992)
8. J. Converti, Plasma jets in welding arcs, Ph.D. Thesis, Mechanical Engineering, MIT (1981)
9. A.A. Erokhin, Avtom. Svarka **7**, 21–26 (1979)
10. B.L. Jarvis, Keyhole gas tungsten arc welding: a novel process variant, Ph.D. Thesis, Mechanical Engineering, University of Wollongong (2001)
11. F. Matsuda, M. Ushio, A. Sadek, Development of GTA electrode materials, in *The 5th International Symposium of the Japanese Welding Society* (Tokyo, April 1990)
12. I. Adonyi-Bucurdiu, A study of arc force effects during submerged gas tungsten arc Welding, *PhD Dissertation* (State University, The Ohio, 1989)
13. W. Lucas, *TIG and Plasma Welding* (Woodhead Publishing Ltd, Cambridge, UK, 1990)
14. P. Muncaster, *Practical TIG (GTA) Welding* (Abington Publishing, Cambridge, UK, 1991)
15. U. Dilthey, H. Keller, Laser arc hybrid welding, in *Proceedings of 7th International Welding Symposium* (Kobe, 2001)
16. T. Ishide, S. Tsubbota, M. Watanabe, K. Ueshiro, Development of YAG laser and arc hybrid welding method. Int. Inst. Welding Document Doc No. XII-1705–02 (2002)
17. Y. Zhang, W. Lu, Y. Liu, Weld. J. **12**, 40–45 (2003)

Chapter 10
Laser Welding

Seiji Katayama

Abstract This chapter describes characteristics of laser welding, features of main lasers used for welding, factors affecting weld penetration, laser welding phenomena including behavior of laser-induced plume, keyhole behavior, and melt flows in a molten pool during laser welding. It also refers to elucidation of formation of welding defects, preventive procedures of such defects, and examples of laser joining results of dissimilar metals and metal to plastic or CFRP, monitoring and adaptive control results during welding, and industrial applications as a recent trend for laser welding.

Keywords Laser welding · CO_2 laser · YAG laser · Fiber laser · Diode laser · Fiber delivery · Welding phenomena · Welding defects · Laser-induced plume · Deep penetration · Welding conditions · Dissimilar metals joining · Monitoring · Industrial applications

10.1 Characteristics of Laser Welding

Welding is the most versatile and realistic joining method applicable to the construction of products in many industrial fields. A laser is one of the high-power-density or the high-energy-density heat sources. Therefore, "laser welding" is recognized as an advanced process to join materials with a laser beam of high power and high-energy density. The power density distribution of a laser beam and the consequent geometry of a weld bead are schematically shown in Fig. 10.1, in comparison with the profiles of arc, plasma, and electron beam. Welding with an arc is most widely used, thanks to cheap apparatuses and easy production of good joints, but the penetration of an arc weld bead is not so deep. Plasma welding can produce slightly deeper penetration than arc welding due to higher power/energy density. An electron beam can produce the deepest weld

S. Katayama (✉)
Osaka University, Suita, Japan
e-mail: katayama@jwri.osaka-u.ac.jp

Y. Setsuhara et al. (eds.), *Novel Structured Metallic and Inorganic Materials*, https://doi.org/10.1007/978-981-13-7611-5_10

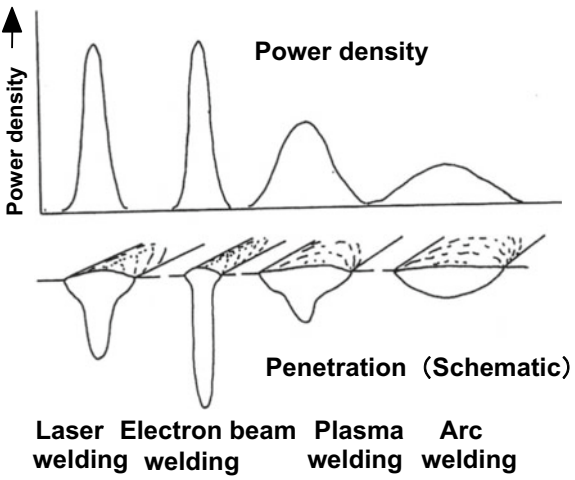

Fig. 10.1 Power densities for typical welding heat sources, and geometry of weld beads obtained at respective densities

bead, but vacuum conditions, a chamber for X-ray protection for human beings, and sometimes demagnetization for steel plates are required. On the other hand, a laser beam of high power/energy density can also produce a deep and narrow penetration weld easily in the shielding gas such as helium (He), argon (Ar), or sometimes nitrogen (N_2) under the air environment. Moreover, much deeper weld beads can be produced with a laser beam at low welding speeds even in low vacuum. The depths of laser welds are almost equal to those of electron beam welds. Among all the welding processes, laser welding can produce a variety of joints of metals or plastics ranging from very thin sheets of about 0.01 mm thickness to thick plates of about 100 mm thickness, and has gained great popularity as promising joining technology with high quality, high precision, high performance, high speed, good flexibility, and low distortion [1–4]. It can also achieve robotization, reduced manpower, full automation, and systematization in production lines. Consequently, applications of laser welding are increasing together with the development of novel laser apparatuses and joining processes. In order to properly apply pulsed or continuous wave (PW or CW, in short) lasers to welding or joining, it is important to know the specifications and capability of laser apparatuses, the factors affecting weld penetration and welding defects, and the mechanisms and behavior of welding as well as to evaluate the weldability of materials and the mechanical properties of welded joints.

10.2 Lasers for Welding

The kind and characteristics of the main lasers used for welding are summarized in Table 10.1. Typical CO_2 and Nd:YAG laser systems are schematically represented in Fig. 10.2. CO_2 lasers of 10.6 μm in wavelength are developed as high beam

Table 10.1 Kinds and characteristics of lasers for welding (April 1, 2016)

CO_2 laser (Wavelength: 10.6 μm; far-infrared ray)	
Laser media	CO_2–N_2–He mixed gas (Gas)
Average power [CW]	50 kW (Maximum)
(Normal)	1–15 kW
Merit	Easier high power (Efficiency: 10–20%)
Lamp-pumped YAG laser (Wavelength: 1.06 μm; near-infrared ray)	
Laser media	Nd^{3+}:$Y_3Al_5O_{12}$ garnet (Solid)
Average power [CW]	10 kW (Cascade-type max and fiber-coupling max)
(Normal)	50–7 kW (Efficiency: 1–4%)
Merits	Fiber delivery, and easier handling (good flexibility)
Laser diode (LD) (Wavelength: 0.8–1.0 μm; near-infrared ray)	
Laser media	InGaAsP, etc. (Solid)
Average power [CW]	8 kW (Stack type Max.), 50 kW (Fiber delivery Max.)
Merits	Compact and high efficiency (20–50%)
LD-pumped solid-state laser (Wavelength: About 1.06 μm; near-infrared ray)	
Laser media	Nd^{3+}:$Y_3Al_5O_{12}$ garnet (Solid), etc.
Average power [CW]	13.5 kW (Fiber-coupling Max.)
[PW]	6 kW (Slab type max.)
Merits	Fiber delivery, high brightness, and high efficiency (10–20%)
Disk laser (Wavelength: 1.03 μm; near-infrared ray)	
Laser media	Yb^{3+}:YAG or YVO_4 (Solid), etc.
Average power [CW]	16 kW (Cascade-type Max.)
Merits	Fiber delivery, high brightness, high efficiency (15–25%)
Fiber laser (Wavelength: 1.07 μm; near-infrared ray)	
Laser media	Yb^{3+}:SiO_2 (Solid), etc.
Average power [CW]	100 kW (Fiber-coupling Max.)
Merits	Fiber delivery, high brightness, high efficiency (20–35%)

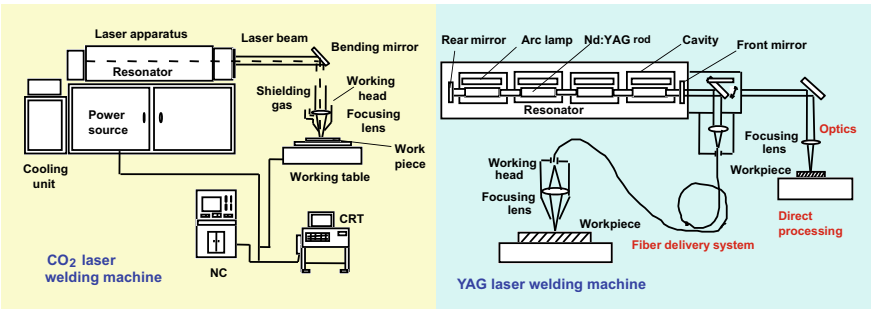

Fig. 10.2 Schematic representation of CO_2 and YAG laser welding system

quality and easy achievement of higher power, the maximum laser power reaches up to about 50, and 1–15 kW power levels have been mainly utilized in welding of steels, automotive components, airplanes, ships, etc. Inconvenient problems considered in CO_2 laser welding are as follows: (1) High-power lasers should be delivered by mirrors but not by an optical fiber, and (2) an Ar plasma, which can be easily formed in Ar shielding gas, reduces weld penetration depth especially in high-power laser welding. Therefore, there is no increase in applications of CO_2 laser to welding. Lately, CO_2 lasers are still used for cutting. In addition, CO_2 lasers of 9.6 μm in wavelength are chiefly used for drilling of resins for mobile phones, etc.

Fiber delivery, which is used in lamp- or LD-pumped Nd:YAG, diode, Yb:disk, and Yb:fiber lasers, is representative of good flexibility and desired in most industrial applications. Nd:YAG lasers of 1.06 μm in wavelength can be delivered through an optical fiber and are operated in CW or PW mode. PW lasers are used in welding of small parts such as battery cases, electric components, glass frames, etc. CW lasers of 2–7 kW power have been employed for laser welding of tailored blanks, aluminum cars, Zn-coated steel sheets, stainless steel pipes, tanks, etc. after such applications of CO_2 lasers. The lamp-pumped Nd:YAG lasers have a drawback of low electrical efficiency (the ratio of laser output to electrical input) of less than 4%.

Consequently, the development of high-power CO_2 and YAG lasers has already been stopped. Instead, laser diode (LD)-pumped solid-state (YAG) lasers have been developed up to 6 to about 10 kW. However, the development of these lasers has also been stopped due to lower electrical efficiency and lower beam quality than LD-pumped disk and fiber lasers. Recently, disk and fiber lasers are more expected in terms of high power, high efficiency, and high beam quality than lamp- or LD-pumped YAG lasers.

In the twenty-first century, thereafter, developments of lasers with high power and high beam quality have been concentrated upon diode lasers (DL or LD) themselves, and LD-pumped disk and fiber lasers. Diode lasers have high electrical efficiency of 30–60%. Direct or fiber-delivered diode lasers mounted to robots are used for welding of thin sheets of aluminum alloys, steels, stainless steels, plastics, and so on and for brazing of Zn-coated steels, etc. The drawback of diode lasers was a bad beam quality, but recently diode lasers of 2 and 4 kW in the maximum power newly developed have high beam quality equivalent to that of disk lasers.

High power, high electrical efficiency, and high beam quality are achieved by disk and fiber lasers. The disk laser and the fiber laser with the high electrical efficiency of 25–40% and the maximum power of 16 kW and 100 kW, respectively, are commercially available. Their beam qualities are extremely high as the beam parameter products (BPP) are smaller than 10 mm * mrad. Disk and fiber lasers are both utilized as heat sources for remote welding, as shown in Fig. 10.3. Remote laser welding with a robot and a scanner is the most promising joining technology of high speed and high production. Further applications of these lasers are evolved to welding for electrical components, cars, trains, bridges, pipelines, ships, airplanes, and so on.

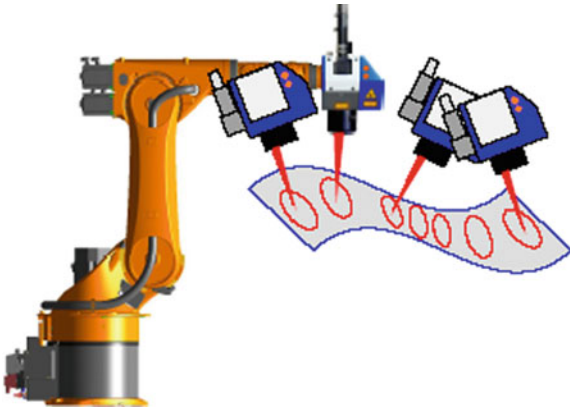

Fig. 10.3 Schematic of remote welding system using solid-state laser

10.3 Laser Welding Phenomena

Welded joints are produced in a variety of joints, as indicated in Fig. 10.4. Butt and lap joints are commonly welded with PW or CW lasers. Typical phenomena during PW and CW laser welding are schematically illustrated in Fig. 10.5. Depending upon the laser irradiation time and the power density, a spot or bead weld is formed in the morphology of a heat-conduction type or a keyhole type. When a laser beam is shot on the metallic plate, the absorption of laser energy is caused by the interaction against free electrons in the metal, the electrons transfer inside the band, and the interaction of moving electrons against metal lattice, defects, imperfection, and potential perturbation. The temperature of the plate surface rises by the transfer from laser energy to thermal energy. The laser absorption increases slightly with an

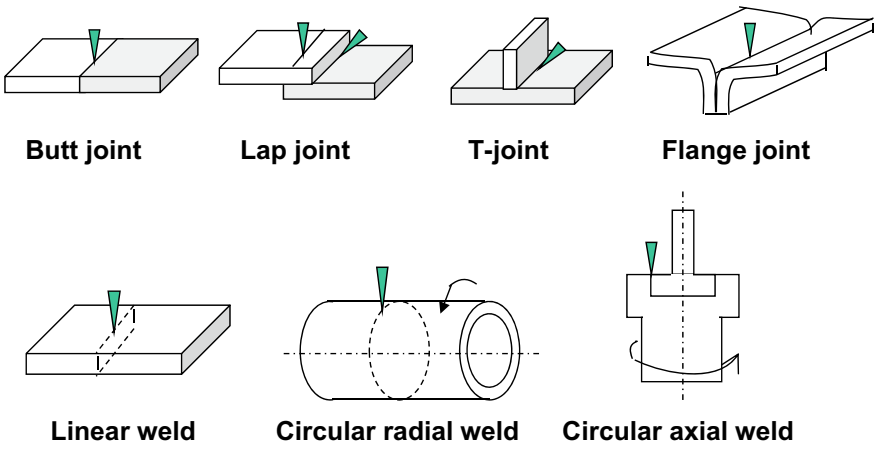

Fig. 10.4 Schematic of typical examples of laser-welded joints

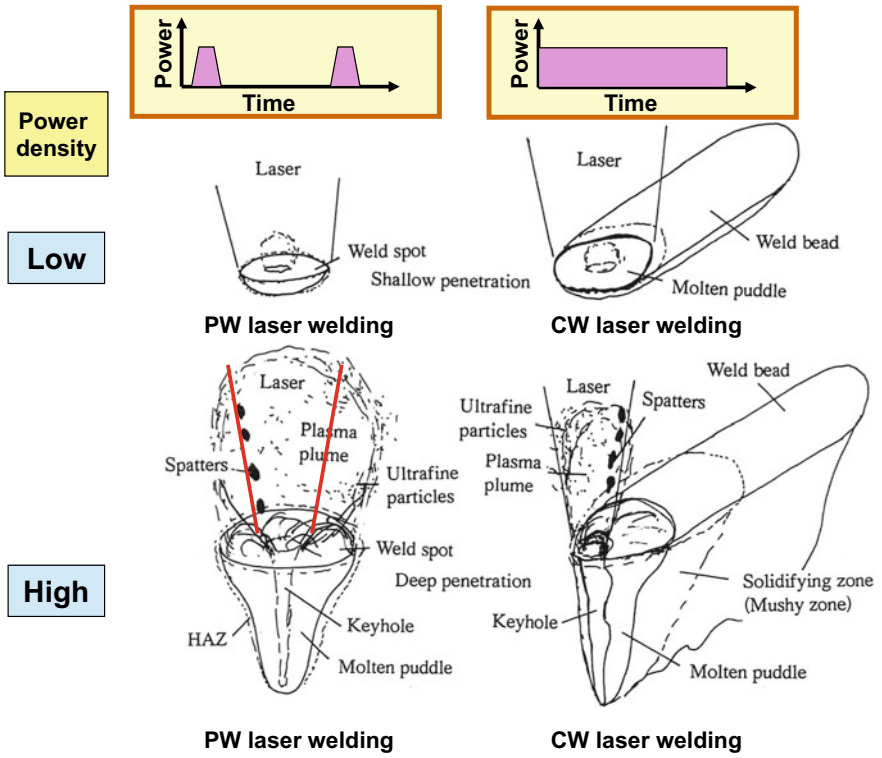

Fig. 10.5 Schematic illustration of spot and bead welding phenomena with PW and CW laser, showing heat-conduction type shallow penetration and keyhole type deep penetration depending upon laser power density

increase in the temperature in the solid and considerably above the melting temperature, and the temperature of the laser-irradiated area rises higher to the boiling temperature. A cavity or a keyhole is formed by recoil pressure due to violent evaporation. A coupling (absorption) coefficient of laser energy into the metal is schematically shown in Fig. 10.6. It increases according to the temperature and surface conditions. Since the laser absorption is extremely high in the case of a keyhole formation, a keyhole type of deep penetration welding is regarded as an efficient joining process. A bright plume of evaporated metallic atoms and vapors is ejected from laser-irradiated part, especially a keyhole. Spattering of melt droplets, caused by a strong stream of the ejected plume, sometimes occurs from the inlet of a keyhole.

The cross sections of laser weld beads in an aluminum alloy produced by CO_2 laser welding at 5 kW in the shielding gas of He, N_2, or Ar are shown in Fig. 10.7. The penetration depths at both welding speeds are shallower in the order of He, N_2, and Ar. Examples of high-speed video pictures during CO_2 laser welding under the abovementioned same conditions are shown in Fig. 10.8. Ar and N plasma are seen in the respective gases although He plasma is not observed during welding. It is

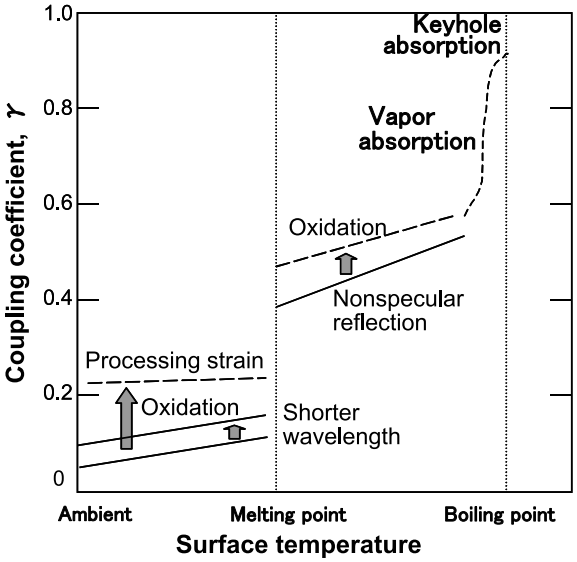

Fig. 10.6 Coupling coefficient of laser energy into metal such as steel or aluminum alloy as a function of temperature and affecting factor

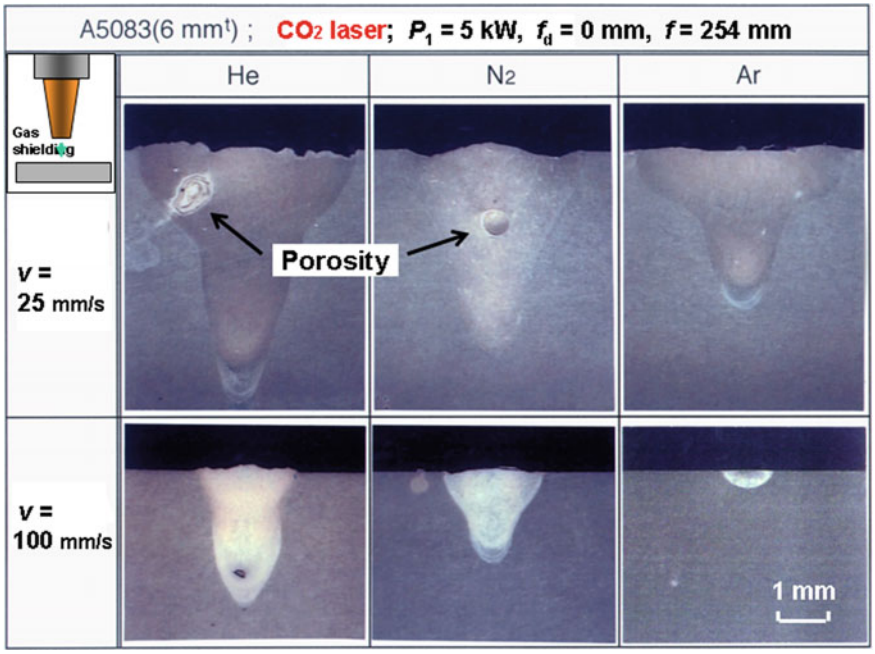

Fig. 10.7 Cross-sectional photos of CO_2 laser weld beads, made at 25 and 100 mm/s in He, N_2, and Ar coaxial shielding gas

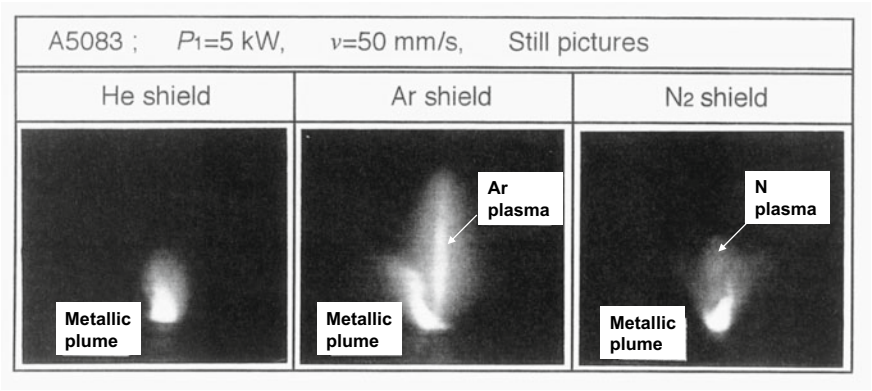

Fig. 10.8 High-speed video pictures of induced plume and gas plasma during CO_2 laser welding in He, N_2, and Ar coaxial shielding gas

well understood that the decrease in CO_2 laser weld penetration especially in Ar or N_2 gas is attributed to the stable formation tendency and size of Ar and N plasma. In welding with a high-power CO_2 laser, He ratio of more than 50% is required to produce a deep penetration weld by preventing a gas plasma.

The formation situations of a laser-induced plume and/or plasma and their effects on the weld penetration are summarized in Fig. 10.9. The formation of Ar or N plasma is easy in the case of welding with CO_2 laser of more than 5 kW power, while a laser-induced plume is only formed from a keyhole during YAG, disk, or

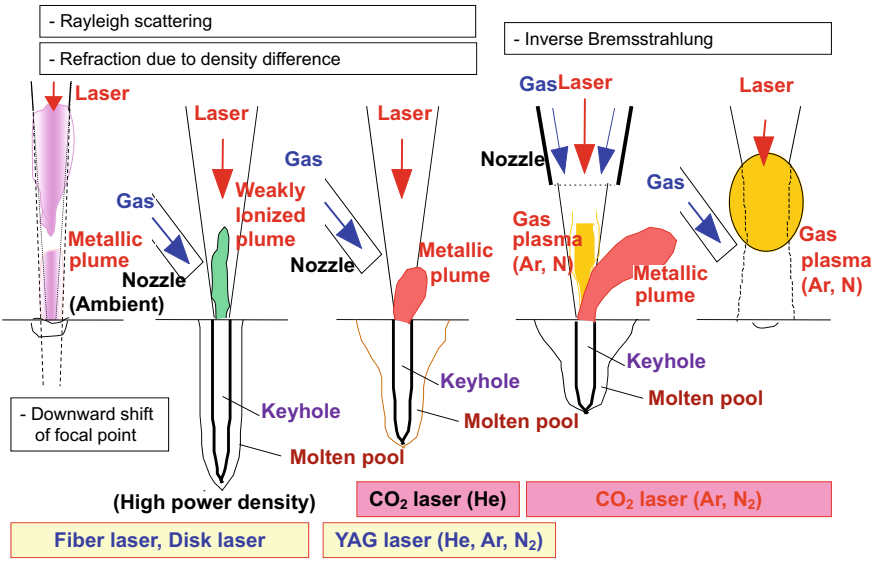

Fig. 10.9 Schematic illustration of plume and plasma formation during laser welding and their respective physical effects on weld penetration in no gas or He, N_2, and Ar shielding gas

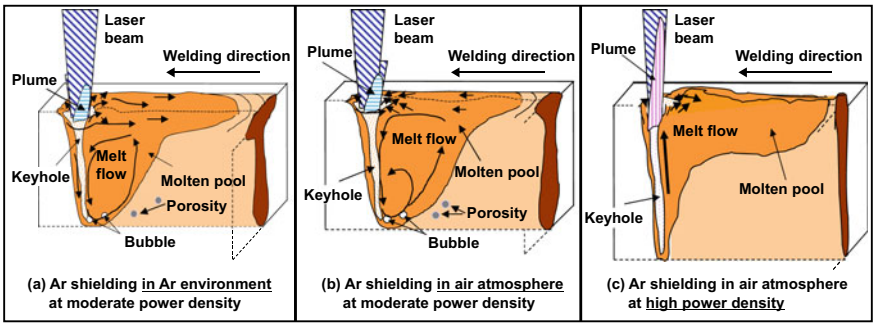

Fig. 10.10 Schematic representation of melt flows in molten pool and weld bead geometry, showing effects of **a** outer or **b** inner surface flows due to surface tension, and **c** high power density on weld penetration

fiber laser welding. The interaction between the CO_2 laser beam and the gas plasma is interpreted in terms of the absorption due to Inverse Bremsstrahlung, whose effect is about 100 times greater than that of YAG, disk, or fiber laser. The temperature of a plume during welding with the laser of about 1 μm wavelength is estimated to be about 3000–6000 K depending upon the high power density from about 1 kW/mm^2–1 MW/mm^2. In fact, such temperatures fluctuate between 3000 and 9000 K. The effects of the plume are attributed to refraction due to the difference in density between the plume and the environment as well as Rayleigh scattering due to the formation of ultrafine particles. In the case of a tall plume and the consequent wide formation range of low refraction index due to the formation of a high temperature area during remote welding, the weld penetration is drastically changed to be shallower from the keyhole type to the heat-conduction mode (at the focal point) due to the beam refraction and the downward shift of the focal point. As far as the height of the plume or low refractive index area (namely, the interaction length of the plume to a laser beam) is suppressed by a fan or a blower of shielding gas or an air, a deep penetration weld can be produced.

Melt flows in the molten pool and near the surface are interpreted by observing with X-ray transmission in-situ imaging system and high-speed video cameras. It is consequently understood that the weld penetration depth is determined chiefly by the keyhole depth, and partly by the melt downward flow around the keyhole tip and by the thermal conduction from the keyhole tip, as shown in Fig. 10.10. Melt flows of the surface in the molten pool are affected by the surface tension of the melt and the shear stream due to a plume ejected strongly from a keyhole inlet, resulting in the typical shapes of wide or narrow weld beads near the surface.

10.4 Laser Weld Penetration and Welding Defects

Small parts are made by spot welding with a pulsed laser. Deep penetration welds are easily formed with the increase in the pulse width near the focal point of a focusing lens as shown in Fig. 10.11. However, the maximum depths of sound laser spot

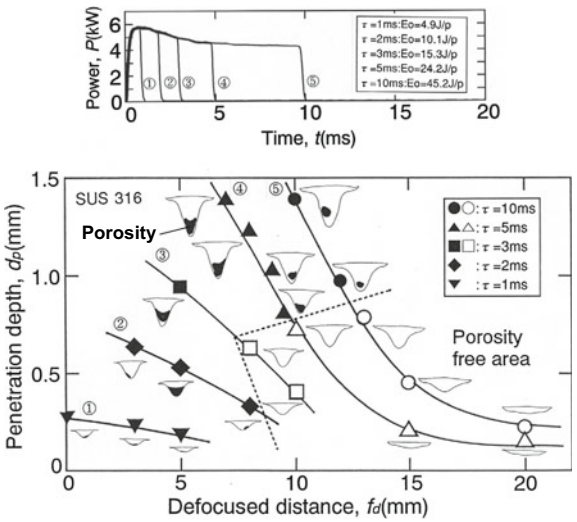

Fig. 10.11 Effects of pulse length and defocused distance on penetration depth and porosity formation in pulsed YAG laser spot welding of type 316 steel

welds should be normally less than 1.5 mm or 3 mm under controlled conditions, because porosity is easily formed especially even in the shallow weld with extremely short-time irradiation and deep welds made with a laser of rectangular pulse shape. Pulse shaping of slow rising and falling power is carried out to reduce spattering and porosity, respectively. Spot welds produced by a pulsed laser of several millisecond durations (for example, in aluminum alloys such as A5083, stainless steels such as AISI 310S, or Ni-based alloys) are very susceptible to solidification cracking because of easy formation of residual liquid along grain boundaries due to rapid solidification of cellular dendrites tips. Additional low powers for suppression of rapid solidification of dendrites tips are required to reduce such solidification cracking.

Deeply penetrated welds are effectively produced in high-power CW laser welds. The penetration depths of stainless steel welds made with fiber lasers of different beam diameters at 6 and 10 kW in Ar shielding gas are indicated in Fig. 10.12. In fiber laser welding at high power, deep penetration can be achieved even with Ar shielding gas, although the penetration is reduced due to Inverse Bremsstrahlung absorption by the formation of Ar gas plasma in the case of CO_2 laser welding with Ar shielding [3]. The penetration is shallower with the increase in the welding speed, and at high speeds, is deeper at higher power density of a smaller beam diameter. It is understood that the effect of laser power is more dominant at low speeds. The penetration is deeper at 10 kW than at 6 kW at the speed of less than 3 m/min (50 mm/s). At low welding speeds, porosity is easily formed, while no porosity is present at high welding speeds, but humping or spattering leading to underfilling occurs depending upon the smaller or wider beam diameter, respectively. Under some conditions, welding defects such as porosity, cracks, humping, underfilling, and so on are easily formed.

Based upon the X-ray transmission observation results, bubbles and porosity formation situations are shown together with keyhole behavior and melt flows in Fig. 10.13 [5]. At very slow welding speed, an unstable keyhole is easily formed and

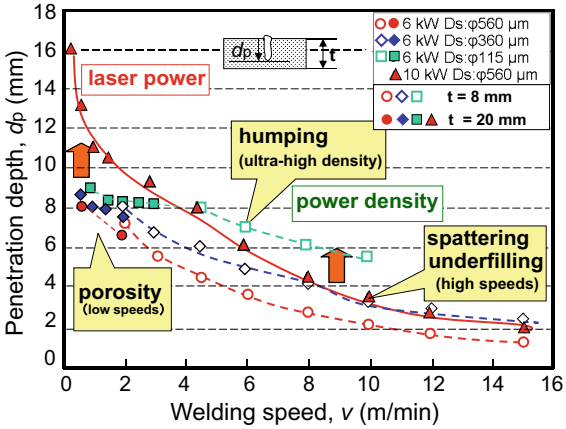

Fig. 10.12 Effect of beam diameter (power density) and welding speed on penetration depth of type 304 stainless steel weld made with 6 and 10 kW fiber laser

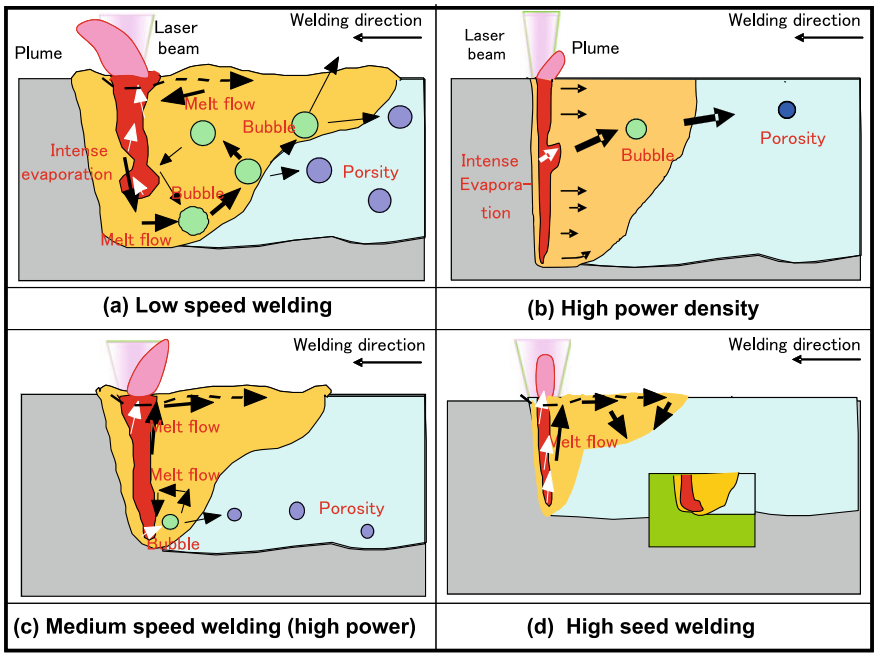

Fig. 10.13 Molten pool, keyhole behavior, and melt flows in laser welding, and effect of welding speed on porosity formation situations

leads to the formation of bubbles, since a laser beam is irradiated on the wall, which causes the melt downward flows to produce a bubble by closing the bottom keyhole. In this case, the bubbles sometimes disappear from the molten pool surface by flowing

up during welding. Porosity is more easily formed by the generation of bubbles from the tip of the keyhole at slow welding speed. Such large bubbles resulting in pores or porosity are generated from evaporation of keyhole (front) wall. Such porosity is prevented by full penetration welding. Pulse modulation is sometimes effective. In the case of high power density due to a 0.2 mm small focal beam, bubbles leading to pores or porosity are formed from the middle part of a full penetration keyhole (the location of about 5 mm below the focal point). In steels or austenitic stainless steels, porosity is absent due to the ejected plume upward at high welding speed.

According to the gas analyses of porosity, a large amount of shielding gas, a small amount of hydrogen (H), and sometimes a small amount of nitrogen (N) are detected [6]. It is generally considered that the bubbles have the same compositions as a keyhole such as a large number of evaporated vapors and a small number of the other elements composing of a shielding gas, and N (nitrogen) or O (oxygen) in air. Vapors and O make oxide films on the porosity inside surface, and the rest metallic vapors also deposit on the porosity surface as the temperature falls. Consequently, a shielding gas is mainly left inside the porosity, and H is contained because it can diffuse into the porosity during and after welding.

Porosity can be reduced or prevented by choosing proper conditions of high welding speeds, vacuum or a proper shielding gas for the metal, pulse modulation, and full penetration with a laser beam of moderate beam diameter.

The relationship between cracking susceptibility, laser welding process and the plate thickness is schematically summarized in Fig. 10.14 [7]. Cracking susceptibility is the highest in spot welding with a pulsed laser and is the lowest with CW laser welding of thin sheet (of about 1–3 mm thickness) under the proper welding conditions. However, it is noted that a rotational crack may occur when the full

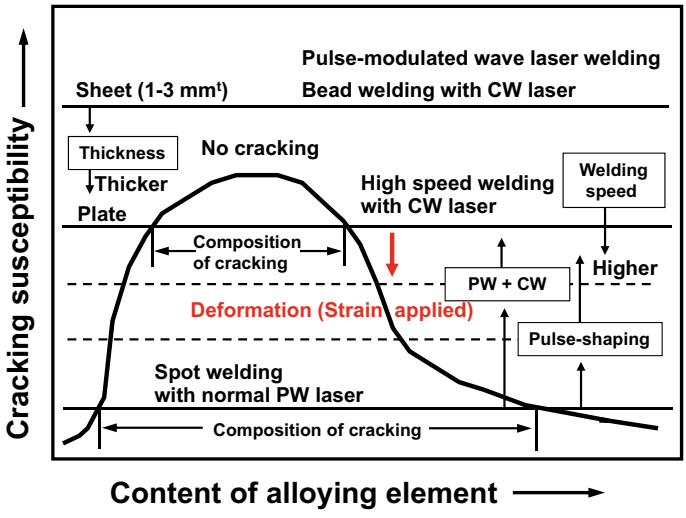

Fig. 10.14 Effects of laser welding process, welding speed, plate thickness, and alloying composition on weld cracking sensitivity of certain alloy system

penetration welding of thin sheets starts near the end. In order to reduce or prevent weld hot cracking, it is necessary to take measures from the viewpoints of both material or metallurgical and mechanical factors. In laser welding, therefore, the following measures are considered: (i) Proper selection of the base metal, its thickness and weld fusion zone geometry, (ii) proper control of molten pool compositions using a filler wire, and (iii) adoption of proper welding conditions for narrowing a mushy zone as well as suppression of rapid solidification and rapid tensile strain during solidification.

10.5 Evolution of Laser Welding

In low and high vacuum, sound extremely deep penetration welds can be produced, as shown in Fig. 10.15. The penetration depths of laser welds produced at low speeds in vacuum (under even low vacuum conditions) are comparable to those of electron beam welds [8]. Laser welding is also applicable to joining similar or dissimilar plastics, dissimilar metals such as cast irons and steels, steels and aluminum alloys, or metals and plastics [5]. It has recently been demonstrated that strong lap joints could be produced between steels and light metals such as aluminum or magnesium alloys, and in the same way between metals such as steels, stainless steels, aluminum alloys and titanium alloys, and engineering plastics such as PA (polyamide), PET (polyethylene terephthalate), and PC (polycarbonate) [9]. Figure 10.16 [10] shows appearances of the laser lap joints between Type 304 stainless steel and PET plastic sheets before and after the tensile shear test. Small

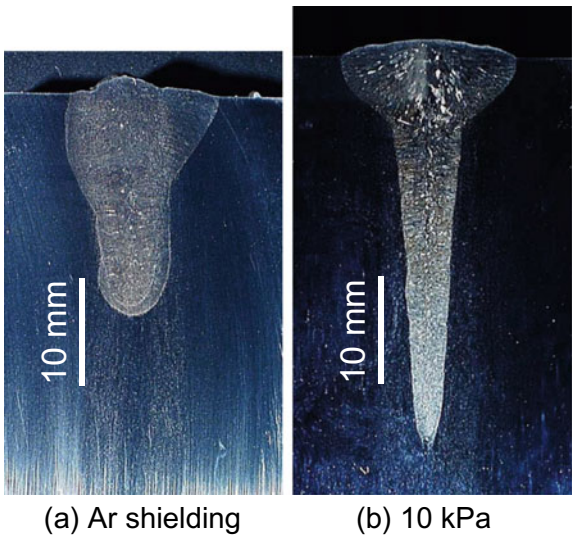

Fig. 10.15 Cross-sectional photos of laser welds in type 304 steel produced with 10 kW fiber laser at 0.3 m/min in Ar shielding gas at 1 atm (**a**) and under low vacuum of 10 kPa (**b**)

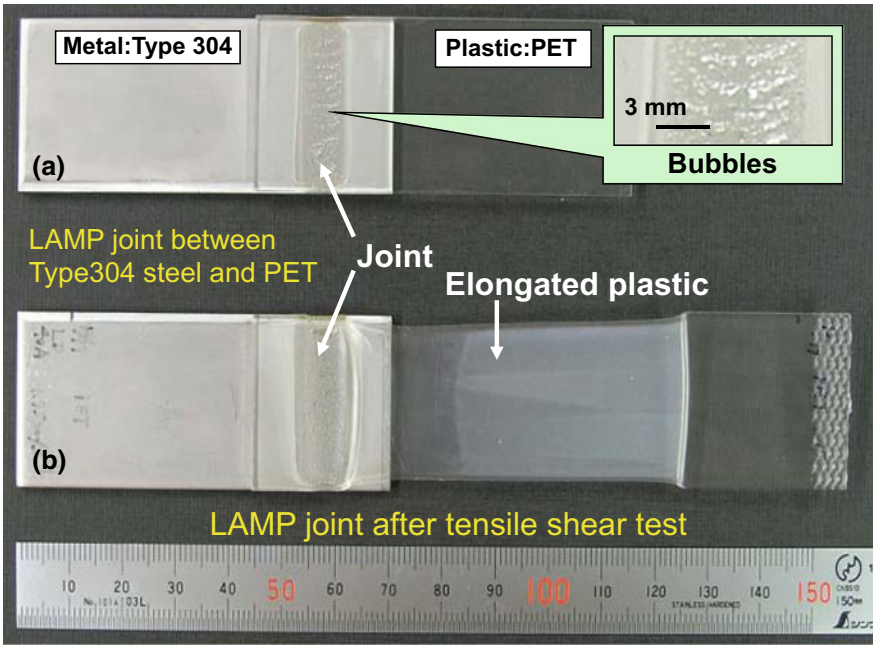

Fig. 10.16 Laser lap joints of 3-mm-thick type 304 steel plate and 2-mm-thick PET plastic sheet before and after tensile shear test, showing that bubbles are formed in melted zone in PET during joining and that elongation of PET base plastic occurs during testing

bubbles are formed in the melted plastic near the joint interface, and the elongation of the PET base plastic is demonstrated. Figure 10.17 [10] exhibits cross-sectional SEM and TEM photos near the interface of the joint at higher magnification and diffraction patterns from typical points. Cr_2O_3-type oxide film is identified, and it is observed that such oxide films always exist as an intermediate layer between plastic and metal for any combinations. SEM and TEM photos clearly exhibit that a strong joint is produced, and that laser joining is performed partly by chemical or physical bonding of melted plastic on a thin oxide film covering the base metal. These results signify a feasibility of the production of a strong joint between metal and plastic sheet. Laser direct joining mechanisms of metal and plastic lap sheets are considered as follows: Laser is shot through the transparent plastic sheet or directly on the metal plate, and then the plate is heated to melt the plastic near the joint interface. Some bubbles are generated to play a role of forcing the activated melted plastic to flow the metal surface. Tight joining of metal to plastic is performed through mechanisms of chemical, physical (Van der Waals force), and mechanical (anchor effect) bonding. Laser joining of metal plate to GFRP (glass fiber-reinforced plastics; PA matrix) or CFRP (glass fiber-reinforced plastics; PA matrix) sheet was also confirmed to be successfully performed [11].

In-process monitoring, online sensing or adaptive control system during laser welding is required to produce a sound high-quality laser weld [3, 4]. Reflection of

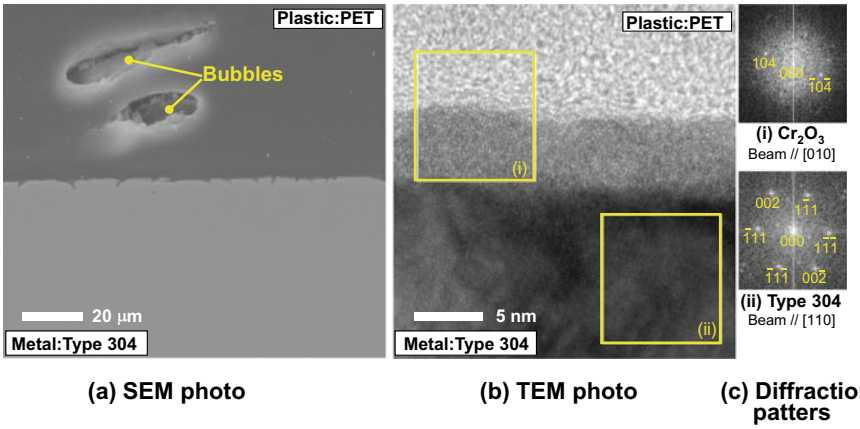

Fig. 10.17 SEM and TEM photos of cross-sectional near joint interface between type 304 steel plate and PET plastic sheet, and diffraction patterns and analyzed results of gray and dark parts, showing Cr_2O_3 oxide and type 304 steel, respectively

a laser beam and heat radiation from a laser-irradiated part and a molten pool are important candidates for monitoring signals. The later is also used for feedback or adaptive control for the production of a constant weld bead width. Direct observation of phenomena during laser welding is also important in terms of understanding of formation mechanisms of welding defects. As shown in Fig. 10.18, online sensing system on the basis of the location relationship between a keyhole and butt-joint line from observation pictures during laser welding has been developed [12]. Moreover, the special focusing optic utilizing the other laser beam in addition to the main laser for welding, which can predict the weld bead depth by monitoring the reflection light from a keyhole tip during welding, is commercially available [13]. It can also control the penetration depth at desired one under some conditions. Recently, such researches are greatly advanced and the systems are employed in practical applications.

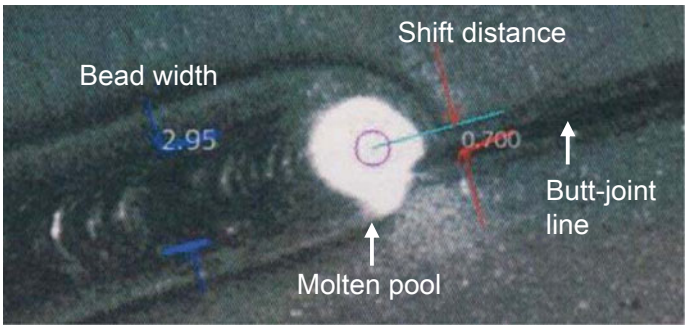

Fig. 10.18 Imaging observation photo for in-process sensing

Acknowledgements The contents in this chapter are mostly referred to those in the article "laser welding" of McGraw-Hill Encyclopedia of Science and Technology, Vol. 9 (2012), pp. 707–714, as well as "Introduction: fundamentals of laser welding" in "Handbook of laser welding technologies" of Woodhead Publishing Ltd. written by Seiji Katayama. The author would like to appreciate the permission of this article to these companies.

References

1. S. Katayama, Laser welding. Ferum (Bulletin Iron Steel Inst. Japan **17-1**, 18–29 (2012). (in Japanese)
2. S. Katayama, Laser welding of aluminum alloys. Keikinzoku (J. Japan Inst. Light Metals) **62–2**, 75–83 (2012). (in Japanese)
3. S. Katayama, New development in laser welding, in *New Developments in Advanced Welding*, ed. by N. Ahmed (Woodhead Publishing in Materials, 2005), pp. 158–197
4. S. Katayama, Understanding and improving process control in pulsed and continuous wave laser welding, in *Advances in Laser Materials Processing—Technology, Research And Applications*, ed. by J. Lawrence, J. Pou, D.K.Y. Low (Woodhead Publishing in Mechanical Engineering, 2010), pp. 181–210
5. S. Katayama, Y. Kawahito, Visualization of welding phenomena with high speed video camera and X-ray transmission real-time observation system. J. High Temp. Soc. **33–3**, 118–127 (2007). (in Japanese)
6. S. Katayama, N. Seto, J.D. Kim, A. Matsunawa, Formation mechanism and suppression procedures of porosity in high power laser welding aluminum alloys, in *Proceedings of ICALEO '98, LIA*, vol. 85, Sec. C (Orlando, 85, 1998), pp. 24–33
7. S. Katayama, Solidification phenomena of weld metals (3)—mechanism and susceptibility of solidification cracking. J. Light Metal Weld. Construct. **38–9**, 417–427 (2000). (in Japanese)
8. S. Katayama, Y. Abe, M. Mizutani, Y. Kawahito, Development of deep penetration welding technology with high brightness laser under vacuum. Phys. Proc. **12**-Part 1, 75–80 (2011)
9. S. Katayama, Laser welding of dissimilar materials. Rev. Laser Eng. **38–8**, 594–602 (2010). (in Japanese)
10. S. Katayama, Y. Kawahito, Laser direct joining of metal and plastic. Scripta Mater. **59–12**, 1247–1250 (2008)
11. S. Katayama, K.-W. Jung, Y. Kawahito, High power laser cutting of CFRP, and laser direct joining of CFRP to metal. Proc. of 29th ICALEO 2010, **103**, 333–338 (2010)
12. Private communication from Tamari Industry, Co., Ltd
13. M. Kogel-Hollacher, B. Michelt, M. Schoenleber, Inline inspection of micro and macro welds, in *Proceedings of the 83rd Laser Materials Processing Conference* (JLPS, Osaka, 2015), pp. 83–87

Chapter 11
Friction Stir Welding

Hidetoshi Fujii

Abstract Several material designs using friction stir welding (FSW) are demonstrated. The FSW is solid-state processing techniques, which can be used for many processes such as welding and surface modification. In particular, this method is very useful for the material design of transformable materials such as steel and Ti alloys. When the FSW of steel is performed below the A_1 point, the optimal microstructure consisting of very fine ferrite and globular cementite is obtained, regardless of the carbon content. When the FSW of Ti alloys is performed below the β transus, equiaxed grains of approximately 1–2 μm are obtained, and thus the mechanical properties, such as fatigue and toughness, are expected to improve.

Keywords Recrystallization · Transformation · Severe deformation · FSW · Steel

11.1 Features of the Friction Stir Welding

During friction stir welding (FSW), the materials are maintained in the solid state [1]. Accordingly, this new method has a variety of excellent advantages that have already been used for various industrial applications such as trains, ships, automobiles, and civil engineering structures for Al alloys [2–9].

In FSW, an approximate ϕ10–20 cylindrical tool rotating at a high speed is brought into contact with the materials which generates heat, as shown in Fig. 11.1a; thus, the two materials are welded using the frictional heat due to the friction and deformation of the materials [3, 4]. As shown in Fig. 11.1b, the tool consists of a large diameter part (Shoulder) and a small tip part (Probe). Only the probe is inserted into the materials, and the tool is moved along the butt interface, the materials are welded through plastic flow and recrystallization caused by the tool.

The maximum temperature is below the melting point, which indicates that the welding is performed in the solid state; accordingly, the reduction in the joint

H. Fujii (✉)
Joining and Welding Research Institute, Osaka University, Osaka 567-0047, Japan
e-mail: fujii@jwri.osaka-u.ac.jp

Y. Setsuhara et al. (eds.), *Novel Structured Metallic and Inorganic Materials*, https://doi.org/10.1007/978-981-13-7611-5_11

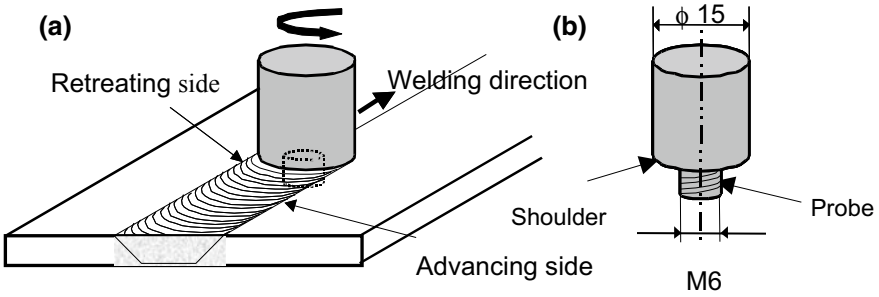

Fig. 11.1 Principles of FSW and tool shape

strength is much lower than that for conventional welding. In some cases, the joint strength is higher than the base metal. In particular, in the case of steel, the heat-affected zone (HAZ) is not generally softened, thus a 100% joint efficiency can be easily obtained [10–17], except for some special steels, such as high-strength steel [18].

Figure 11.2 shows a schematic illustration of a joint, and Fig. 11.3 shows actual microstructures of a 1080 aluminum alloy joint at a cross section [4, 19]. An equiaxial and recrystallized structure of several microns is formed at the center of the joint, and this area is called the stir zone (SZ). Outside of the stir zone, a thermomechanically affected zone (TMAZ) is formed, where elongated grains are formed due to the plastic deformation by the tool. Outside the TMAZ, a heat-affected zone (HAZ) is present, which is not affected by the plastic deformation, but affected by the heat.

The characteristics of the friction stir welding are as follows:

1. It is a solid-phase welding. Accordingly, coarsening of the crystal grains of the joint is suppressed, thus, any reduction in strength is small during the welding. Furthermore, in some cases, it is also possible to improve the strength from that of the base metal due to the refined crystal grains caused by the stirring action of the rotating tool.
2. The deformation is small, which is less than one/several numbers of that from arc welding (MIG).
3. It can be applied to the 2000 series and 7000 series Al alloys, a cast material or a composite material, which are normally difficult to weld.

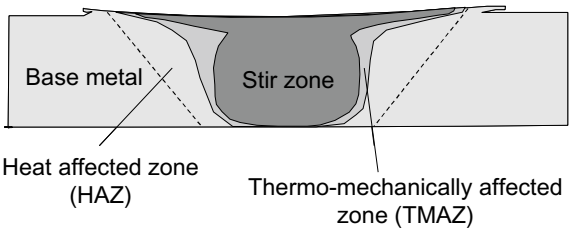

Fig. 11.2 Schematic illustration of a joint

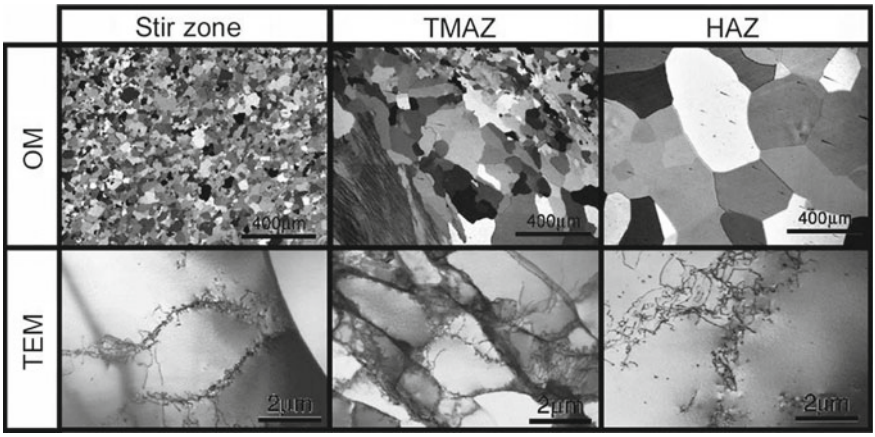

Fig. 11.3 Microstructures of a 1080 aluminum alloy joint. **a** Macrostructure, **b** optical microscope and TEM observations. Micrographs courtesy of Professor Y. S. Sato

4. It is suitable for welding dissimilar materials.
5. Pretreatment or groove processing is not required.
6. Fumes, sputtering, or ultraviolet rays are not generated during the welding.
7. Pores, cracks, and other defects are unlikely to form.
8. A shielding gas is not required in the case of welding Al alloys.
9. In principle, no filler is required.
10. There is almost no evaporation of the alloy components during the welding.
11. Professional skills are unnecessary.
12. A welding license is currently not required.
13. Steel can be welded below its A_1 temperature. In this case, no transformation occurs even for the welding of steel.

On the other hand, it has the following problems:

1. High rigidity jigs are required.
2. Since the permissible range of the gap is narrow, it is necessary to control the gap and any misalignment of the joint.
3. Complicated shapes of the members, such as filet joints, are difficult to weld.
4. A keyhole remains at the end of the welding.
5. Bonding failure called a kissing bond is likely to be produced on the back of the plate.
6. It is generally limited to low-melting-point metals.

However, these problems have been examined from various angles in the past, and some of them are currently being resolved. For more information, please refer to specialized books [4]. In particular, with respect to (6), as described in this chapter, it has become possible to weld many materials.

11.2 Tool for High-Temperature Alloys

Most practical structures welded using FSW are made of Al alloys. Thus, it is desired to establish an FSW technology for relatively high melting point materials such as steel and Ti alloys. When joining aluminum alloys, an SK or SKD tool steel, such as SKD61, is widely used. For the FSW of steels, on the other hand, high strength, toughness, wear resistance, and nonreactive properties at high temperature are required for the tool materials. In the initial study, a W alloy [10, 11] and Mo alloy [11] have been used for the tool materials, and, subsequently, ceramic materials, such as polycrystalline cubic boron nitride (PCBN) tools [20, 21] and coated Si_3N_4 [22], and tungsten carbide [13–15, 17] have been used. Recently, a high-strength and long-life Co alloy tool [23] and Ir alloy tool [24, 25] have also been developed in Japan, which have made significant progress toward commercialization. While the tungsten carbide tool is not suitable for welding over 1000 °C, it is suitable for the FSW at the low temperatures of about 650–850 °C, which enables the FSW below the A_1 point [13–15]. Thus, it is desirable to select the proper tool depending on the welding temperature and the material properties.

11.3 Friction Stir Welding of Ti Alloys—A Metal Accompanied by Transformation

A typical Ti alloy, the Ti-6Al-4V alloy, is an α + β two-phase structure alloy at room temperature, and it becomes a β single phase above the β transus of 980 °C. For such a material having a transformation, it is possible to make a new type of structure controlled by the FSW.

When performing a normal FSW, the temperature during welding exceeds the β transus, and the lamellae α-phase is formed while maintaining the crystallographic relationship during cooling. Accordingly, a microstructure consisting of the lamellar α phase that precipitated in the β phase is obtained [26, 27]. On the other hand, it has become apparent in recent years that the joint microstructure and mechanical properties can be controlled by performing the welding below the β transus, and the utility of FSW is shown [28–31]. Thus, by changing the welding conditions for Ti alloys, it is possible to obtain an arbitrary lamellar or equiaxed microstructure. Figure 11.4 indicates the maximum temperature and the cooling rate at the center on the back surface of a 2-mm-thick Ti-6Al-4V alloy plate under various welding conditions using a ϕ12 WC-based tool. The cooling rate at this time is the average value during the cooling period from the maximum temperature up to 500 °C.

The highest temperature reached under the welding conditions of 1000 rpm–400 mm/min is at 1050 °C, which exceeds the 980 °C of the β transus. Furthermore, the cooling rate is much higher than that under the other conditions, because the welding speed is greater. In general, although both the tool rotation rate

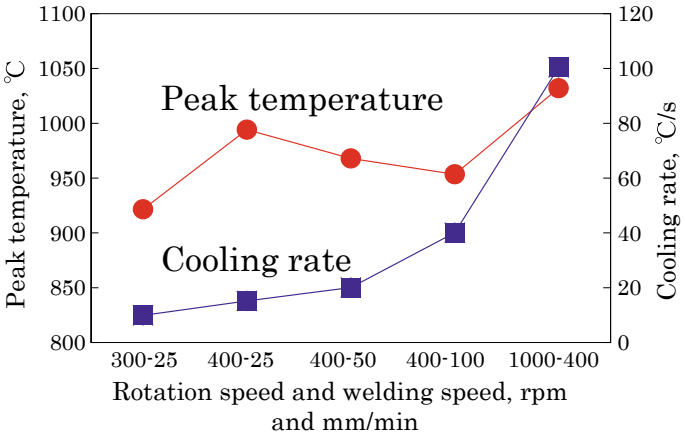

Fig. 11.4 Peak temperature and cooling rate under various welding conditions for Ti-6Al-4V alloy. Reprinted from Ref. [28], Copyright 2013, with permission from Elsevier

and welding speed can affect the maximum temperature during the welding, the rotation rate has a greater effect. On the other hand, the welding speed has a greater effect on the cooling rate during the welding.

As the welding speed increases at the same rotation rate, the maximum temperature decreases, and the cooling rate increases. In general, as the maximum temperature is higher, the prior β grain size increases, because the grain growth occurs in the β-phase temperature range. On the other hand, as the cooling rate increases, the lamellar structure becomes finer.

Under the welding conditions of 300 rpm–25 mm/min, the maximum temperature is the lowest at about 920 °C, which is considered to be clearly lower than the β transus temperature. Under this condition, very fine grains are obtained in the stir zone, but the prior β grains are not observed. This microstructure is obtained by recrystallizing both the alpha and beta grains at the same time in the α + β phase region by FSW. The size of the equiaxed grains is approximately 1–2 μm. Because the mechanical properties, such as fatigue and toughness, are expected to improve by obtaining the equiaxed microstructure, it is considered to be a more desirable microstructure.

Based on all the abovementioned results, the relationship between the maximum temperature, the cooling rate, and the microstructure can be summarized, as shown in Fig. 11.5. The equiaxed microstructure is obtained when the maximum temperature is less than the β transus during the welding. When the maximum temperature is higher than the β transus, on the other hand, a lamellar structure is obtained. In the case of the formed lamellar structure, the prior β grain size increases as the maximum temperature increases. The microstructure is fine as the temperature is reduced. On the other hand, the α lamellar structure formed in the prior β grains is refined as the cooling rate is greater.

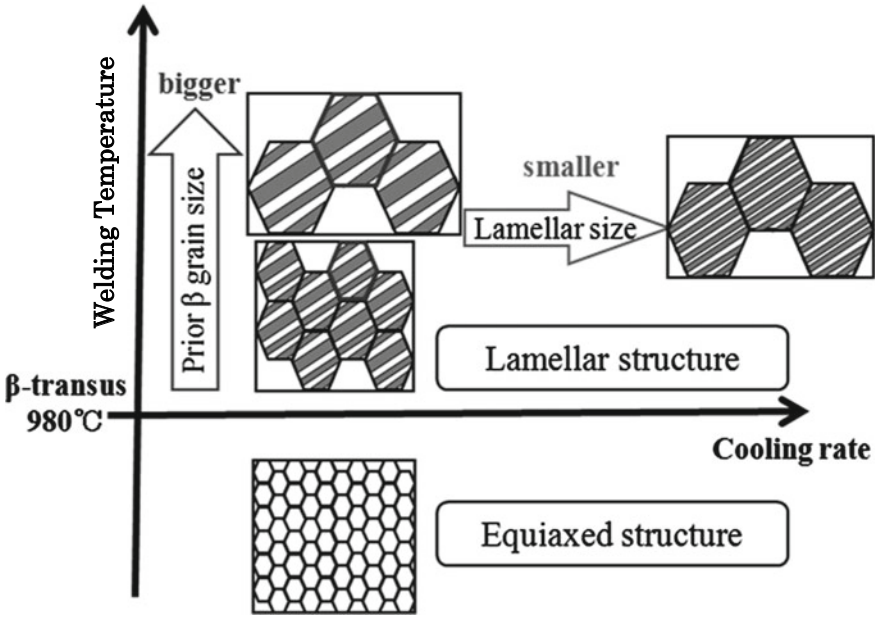

Fig. 11.5 Effects of the welding temperature and cooling rate on the microstructure in the stir zone of Ti alloys. Reprinted from Ref. [28], Copyright 2013, with permission from Elsevier

11.4 Non-transformation Friction Stir Welding of Carbon Steel

Since Thomas et al. showed the potential for the FSW of steel in 1999 [32], several papers have been published on the FSW of steel such as carbon steel, [10–17, 33, 34], pure iron, steel IF (low-carbon steel) [13, 35–37], and stainless steel [38–43]. However, unlike the FSW of aluminum alloys or austenitic stainless steels, the FSW of carbon steel is accompanied by a transformation, similar to the Ti alloys. Accordingly, by controlling the transformation during the FSW, the joint strength can be significantly changed, and various phenomena are observed [13–15, 34, 35].

Figure 11.6 [14] shows the typical microstructures of a high-carbon steel, S70C (0.70% C), which is close to the eutectoid composition. When normal fusion welding is used for such a material, the joint is very brittle and thus the welding is very difficult, because brittle martensite is formed in the entire joint. When the welding speed is decreased, the cooling rate is decreased. In this case, a pearlite-based microstructure is formed, while almost 100% martensite is formed at a typical welding speed such as 400 mm/min. Thus, the amount of martensite can be controlled by the welding conditions.

By reducing the rotational speed, on the other hand, the peak temperature can mainly be decreased. Under the 200 rpm–400 mm/min welding conditions using a

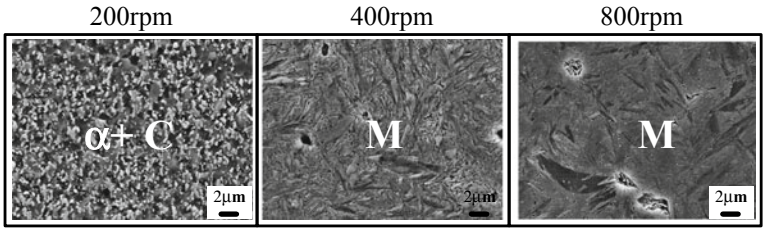

Fig. 11.6 Change in the microstructure of a high-carbon steel, S70C (0.70% C) stir zone formed below and above the A_1. M: martensite, α: ferrite, C: globular cementite. Reprinted from Ref. [14], Copyright 2007, with permission from Elsevier

WC-based tool, the peak temperature is below the A_1 point (723 °C), indicating that the welding can be performed without any transformation [14]. In this case, the resulting microstructure consists of a very refined ferrite and globular cementite, which is the ideal microstructure with both good strength and ductility. When the rotation speed is increased, the peak temperature exceeds the A_1 point, thus a very hard and brittle microstructure is formed, while at 200 rpm, the hardness is slightly increased from the base material, and the joint ensures a sufficient strength and elongation.

Because this method can be performed, regardless of the carbon content of steel, it may induce a significant change in the design and welding method of various structures in the future. By performing welding at the low temperature of about 700–900 °C, which was not possible before, a flexible strength design becomes possible in response to the user's requests. A tungsten carbide (WC) tool is very effective for this purpose.

This method can naturally be used for hypereutectoid steels. Figure 11.7 [44, 45] shows the Charpy absorbed energy of SK85 (0.85% C) joints. When the peak

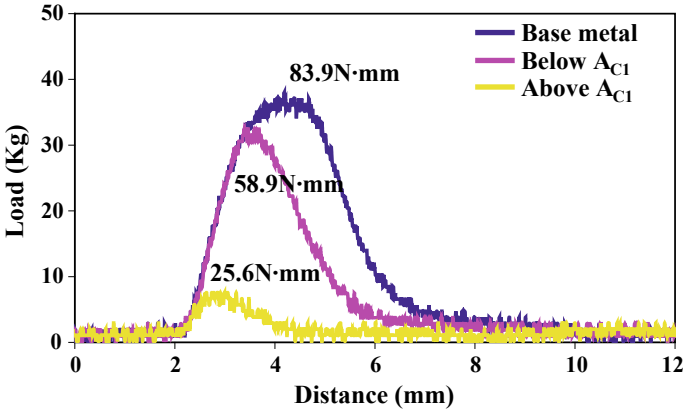

Fig. 11.7 Effect of peak temperature on Charpy absorbed energy of SK85 (0.85% C) joints. Reprinted from Ref. [45], Copyright 2010, with permission from Elsevier

temperature is below the A_1 point, the absorbed energy is increased by about three times when compared to the joint obtained above the A_1 point. The fracture surfaces are also significantly changed.

11.5 Austenite Stabilizing Method by Friction Stir Welding

Friction stir welding is a kind of large deformation process. Recently, a stabilization phenomenon of austenite was reported [46]. This phenomenon is caused by the large deformation of the austenite, when the friction stir welding is performed in the austenite temperature range. Even in the thermal cycle in which the martensite is usually formed, the martensite does not form, while the austenite remains.

Figure 11.8 shows a phase map of the weld center of a friction stir welded Cr steel with the composition of 0.1 wt% C, 8 wt% Cr, 2 wt% W, 0.2 wt% V, and 0.04 wt% Ta. The friction stir welding was carried out at a constant 100 mm/min welding speed, while changing the tool rotation rate in the range of 100–300 rpm. At 100 rpm, the welding temperature was below the point A_1 (850 °C), but it exceeded the A_1 at 300 rpm. At 200 rpm, the temperature of the upper half, which was in contact with the tool, exceeded the A_1, but the temperature of the lower half was lower than the A_1 point.

When the welding was performed at the tool rotational speed of 100 rpm, the body-centered cubic (bcc) ferrite can be obtained. When welding at 300 rpm, on the other hand, the face-centered cubic austenite is observed over the entire surface. At this time, when this alloy is simply cooled at a comparable cooling rate, a mixed structure of ferrite and martensite is obtained. Due to the high deformation during the friction stir welding, the austenite is stabilized even in a composition where the austenite is not stable, then the austenite is retained even at room temperature. As a reference, the Ms point of this steel without any deformation is 400 °C. The dislocation density in the steel increases due to the high deformation during the

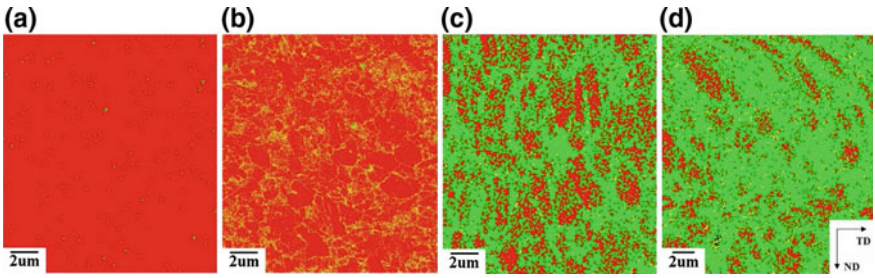

Fig. 11.8 Phase map at the weld center of a friction stir welded Cr steel. The red color indicates ferrite and the green color indicates austenite. **a** 100 rpm, **b** 200 rpm lower half, **c** 200 upper half, **d** 300 rpm. Reprinted from Ref. [46], Copyright 2014, with permission from Elsevier

friction stir welding, and thus the generation of martensite with the volume expansion is restricted [46].

Most importantly, the stabilization of austenite induces the transformation-induced plasticity (TRIP) effects [47] for the alloy compositions, in which the TRIP does not normally occur, and thus the strength and elongation of the joints exceed those of the base material. In other words, the retained austenite changes to martensite during the tensile test. Figure 11.9 shows the stress–strain curve of the joints obtained at three different rotation rates. At 100 rpm, the joint shows almost the same strength as the base material, because no transformation occurs during the welding, whereas in the case of 200 or 300 rpm, the strength and elongation of the joints significantly exceed those of the base material. The fact that a compatible strength with the base material was obtained is also revolutionary.

The above phenomenon is not only for a specific steel. The following results are obtained when performing the friction stir welding of a structural steel having the chemical compositions as shown in Table 11.1 (JIS-SCM420 Cr–Mo steel). Each transformation point can be calculated from the chemical composition of the steel as follows: the A_1 point is 740 °C, the A_3 point is 833 °C, and the Ms point is 429 °C [48]. In order to improve its hardenability, Cr, Mn, and Mo have been added to this steel, and thus the formation of ferrite and pearlite is moderately suppressed.

In the stir zone, the fcc phase, which represents the retained austenite, is observed at a few percents in the bcc base material [49]. The average area ratio of

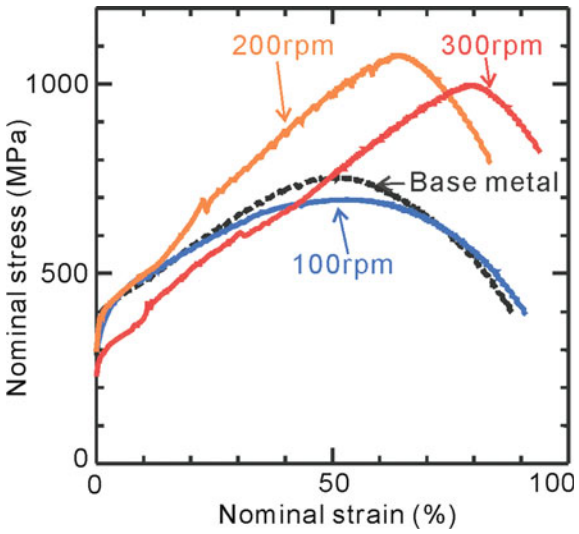

Fig. 11.9 Nominal stress–strain curves of the Cr steel joints obtained at three different rotation rates. Reprinted from Ref. [46], Copyright 2014, with permission from Elsevier

Table 11.1 Chemical compositions of SCM420 steel (mass%)

	Fe	C	Si	Mn	P	S	Cu	Cr
SCM420	Bal.	0.202	0.237	0.608	0.008	0.000	0.103	1.07

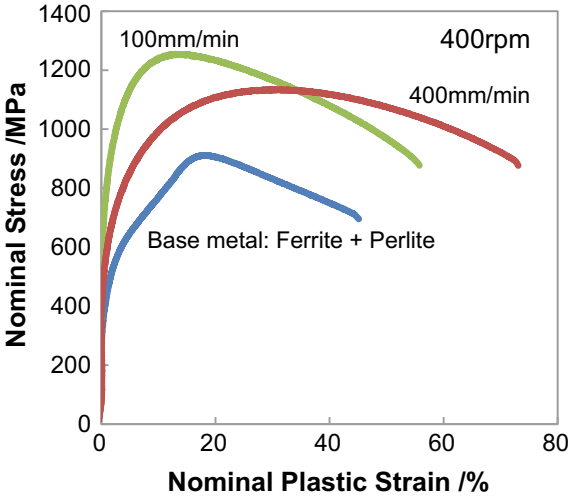

Fig. 11.10 Nominal stress–nominal strain curve of the SCM420 steel stir zones obtained at different welding speeds. Rotation rate: 400 rpm. Reprinted from Ref. [49], Copyright 2016, with permission from Elsevier

the austenite at 100 mm/min and 400 mm/min is 2.0% and 3.0%, respectively, although this was not observed in the base material. Thus, stabilization of the austenite can be achieved by the friction stir welding, which cannot be obtained by only a simple thermal cycle.

Figure 11.10 shows the nominal stress–nominal strain curve of the obtained stir zones and base metal [49]. Both joints show a higher yield strength and tensile strength than the base metal. The base material has a ferrite–pearlite structure, and the stir zone has a complex microstructure consisting of fine ferrite, martensite, and retained austenite. This difference in the microstructure has led to improvement in the strength of the stir zone. On the other hand, the elongation has been improved for both joints compared to the base metal. When comparing the two joints, the joint obtained at the welding speed of 400 mm/min has a greater elongation. This is because the quantity of the retained austenite content in the joint is high.

Figure 11.11 shows an X-ray diffraction profile measured before and after the tensile test of the friction stir welded joint at the welding speed of 400 mm/min. The peak of the austenite was not seen in the base material, but observed in the stir zone before the tensile test. After the tensile test, on the other hand, the peak of the austenite is not observed even in the stir zone. These results indicate that a martensitic transformation from the retained austenite occurred during the tensile test, suggesting that the TRIP effect causes such excellent tensile properties of the joints. A larger amount of the retained austenite at 400 mm/min causes a greater elongation.

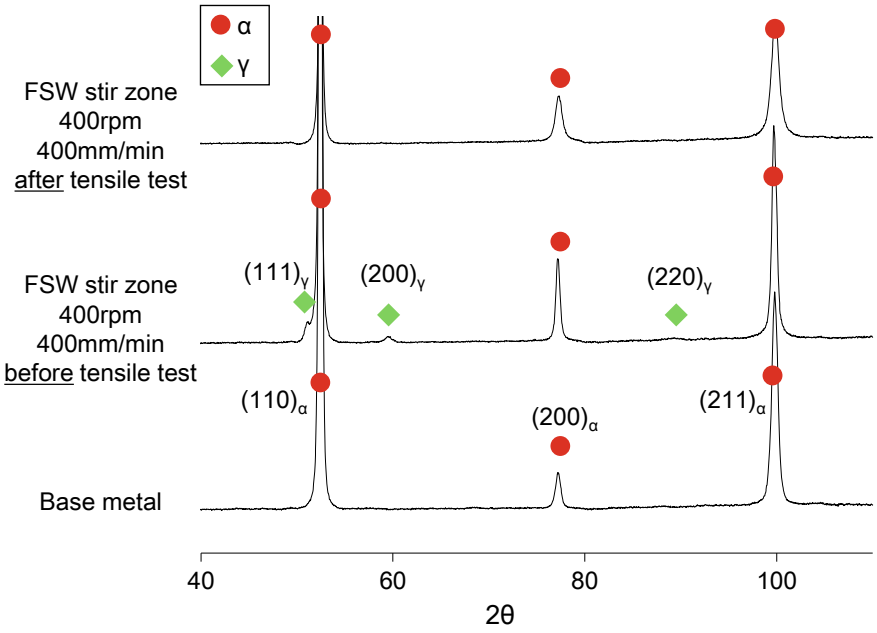

Fig. 11.11 X-ray diffraction profile measured before and after the tensile test of the friction stir welded joint at the welding speed of 400 mm/min and rotation rate of 400 rpm

11.6 Summary

Friction stir welding (FSW) was initially used only as a welding method, but some other applications, such as surface modification, have been proposed. In particular, the surface modification of steel, such as for knives, has already been commercialized, and much research is being performed on the FSW of high-temperature materials such as steel and Ti alloys. In addition, the FSW without transformation and the stabilization phenomenon of austenite are very useful for practical applications, as shown in this chapter. FSW has a variety of possibilities for material designs as well as welding. The FSW of stainless steel over 1 m/min and 8000 spots or more using one cheap tool for the spot FSW of steel seems to be linked to future technologies. Even now, new technologies have been continuously developed, and further development is also expected in the future.

References

1. W.M. Thomas, E.D. Nicholas, J.C. Needhan, M.G. Murch, P. Temple-Smith, C.J. Dawes, *International Patent Application PCT/GB92/02203 and GB Patent Application 9125978.8* (UK Patent Office, London, 6 Dec 1991)
2. R. Nandan, T. DebRoy, H.K.D.H. Bhadeshia, Prog. Mater. Sci. **53**, 980–1023 (2008)
3. R.S. Mishra, Z.Y. Ma, Mater. Sci. Eng. R **50**, 1–78 (2005)
4. *Friction Stir Welding*, ed. by Japan Welding Society, Sampo Shuppan (2006)
5. H. Okamura, K. Aota, M. Ezumi, J. Jpn. Inst. Light Met. **50**, 166–171 (2000)
6. G. Campbell, T. Stotler, Weld. J. **78**, 45–47 (1999)
7. M.R. Johnsen, Weld. J. **78**, 35–39 (1999)
8. K.E. Knipstron, B. Pekkari, Weld. J. **76**, 55–57 (1997)
9. C.J. Dawes, W.M. Thomas, Weld. J. **75**, 41–45 (1996)
10. T.J. Lienert, W.L. Stellwag, Jr., B.B. Grimmett, R.W. Warke, Weld. J., **82**, 1S–9S (2003)
11. P. Reynolds, W. Tang, M. Posada, J. DeLoach, Sci. Technol. Weld. Join. **8**, 455 (2003)
12. A. Ozekcin, H.W. Jin, J.Y. Koo, N.V. Bangaru, R. Ayer, Intern. J. Offshore Polar Eng. **14**, 284 (2004)
13. H. Fujii, L. Cui, N. Tsuji, M. Maeda, K. Nakata, K. Nogi, Mater. Sci. Eng. A **429**, 50–57 (2006)
14. L. Cui, H. Fujii, N. Tsuji, K. Nogi, Scripta Mater. **56**, 637–640 (2007)
15. L. Cui, H. Fujii, N. Tsuji, K. Nakata, K. Nogi, R. Ikeda, M. Matsushita, ISIJ Int. **47-2,** 299–306 (2007)
16. Y.S. Sato, H. Yamanoi, H. Kokawa, T. Furuhara, ISIJ Int. **48**, 71–76 (2008)
17. T. Saeid, A. Abdollah-zadeh, H. Assadi, F. Malek Ghaini, Mater. Sci. Eng. A **496**, 262–268 (2008)
18. M. Matsushita, Y. Kitani, R. Ikeda, M. Ono, H. Fujii, Y.D. Chung, Sci. Tech. Weld. Join. **16**, 181 (2011)
19. C.D. Sorensen, T.W. Nelson, S.M. Packer, in *Proceedings of 3rd International Symposium* (FSW, TWI, Kobe, Japan, 2001, CD-ROM)
20. Y.S. Sato, S.H.C. Park, H. Kokawa, Metall. Mater. Trans. **32A,** 3033 (2001)
21. M. Collier, R. Steel, T.W. Nelson, C. Sorensen, S. Packer, Mater. Sci. Forum **426**, 3011 (2003)
22. R. Ohashi, M. Fujimoto, S. Koga, R. Ikeda, M. Ono, in *Proceedings of 7th International FSW Symposium* (Awaji, Japan, 20–22 May, 2008, CD-ROM, 2-2)
23. http://www.tohoku.ac.jp/japanese/newimg/pressimg/20100326_01.pdf
24. T. Miyazawa, Y. Iwamoto, T. Maruko, H. Fujii, Sci. Tech. Weld. Join. **16,** 188–192 (2011)
25. T. Miyazawa, Y. Iwamoto, T. Maruko, H. Fujii, Sci. Tech. Weld. Join. **16,** 207–212 (2012)
26. S. Mironov, Y. Zhang, Y.S. Sato, H. Kokawa, Scripta Mater. **59**, 511–514 (2008)
27. S. Mironov, Y.S. Sato, H. Kokawa, Acta Mater. **57**, 4519–4528 (2009)
28. K. Kitamura, H. Fujii, Y. Iwata, Y.S. Sun, Y. Morisada, Mater. Design **46**, 348–354 (2013)
29. S. Yoon, R. Ueji, H. Fujii, Microstructure and texture distribution of Ti-6Al-4V alloy joints friction stir welded below β-transus temperature. J. Mater. Process. Technol. **229**, 390–397 (2016)
30. S. Yoon, R. Ueji, H. Fujii, Effect of initial microstructure on Ti-6Al-4V joint by friction stir welding. Mater. Design **88**, 1269–1276 (2015)
31. S. Yoon, R. Ueji, H. Fujii, Effect of rotation rate on microstructure and texture evolution during friction stir welding of Ti-6Al-4V plates. Mater. Charact. **106**, 352–358 (2015)
32. W.M. Thomas, P.L. Threadgill, E.D. Nicholas, Sci. Technol. Weld. Join. **4**, 365–371 (1999)
33. R. Ayer, D.P. Fairchild, S.J. Ford, N.E. Nissley, A. Ozekcin, in *Proceedings of 7th International FSW Symposium* (Awaji, Japan, 20–22 May, 2008, CD-ROM, 9B-1)
34. R. Ueji, H. Fujii, L. Cui, A. Nishioka, K. Kunishige, K. Nogi, Mater. Sci. Eng. A **423**, 324–330 (2006)

35. H. Fujii, R. Ueji, Y. Takada, H. Kitahara, N. Tsuji, K. Nakata, K. Nogi, Mater. Trans. **47**, 239–242 (2006)
36. S. Mironov, Y.S. Sato, H. Kokawa, Acta Mater. **56**, 2602–2614 (2008)
37. M. Mehranfara, K. Dehghanib, Mater. Sci. Eng. A **528**, 3404–3408 (2011)
38. T. Ishikawa, H. Fujii, K. Genchi, S. Iwaki, S. Matsuoka, K. Nogi, ISIJ Int. **49**, 897–901 (2009)
39. S.H.C. Park, Y.S. Sato, H. Kokawa, K. Okamoto, S. Hirano, M. Inagaki, Scripta Mater. **49**, 1175 (2003)
40. A.P. Reynolds, W. Tang, T. Gnaupel-Herold, H. Prask, Scripta Mater. **48**, 1289 (2003)
41. Y.S. Sato, T.W. Nelson, C.J. Sterling, Acta Mater. **53**, 637 (2005)
42. X.K. Zhu, Y.J. Chao, J. Mater. Process. Technol. **146**, 263 (2004)
43. A. Chabok, K. Dehghani, Mater. Sci. Eng. A **528**, 309–313 (2010)
44. Y.D. Chung, H. Fujii, R. Ueji, K. Nogi, Sci. Eng. Weld. Join. **14**, 233–238 (2009)
45. Y.D. Chung, H. Fujii, R. Ueji, N. Tsuji, Scripta Mater. **63**, 223–226 (2010)
46. H. Fujii, R. Ueji, Y. Morisada, H. Tanigawa, Scripta Mater. **70**, 39–42 (2014)
47. J. Angle, J. Iron Steel Inst. **177**, 165 (1954)
48. T. Araki, Steels, Maruzen (1970)
49. T. Miura, R. Ueji, H. Fujii, H. Komine, J. Yanagimoto, Mater. Design **90**, 915–921 (2016)

Chapter 12
Soldering Process

Hiroshi Nishikawa

Abstract Soldering is the major micro-joining process for assembling printed circuit boards of electronic products and is an important method of joining two metals without melting of base metals. In light of the remarkable progress in recent years in electronic products, the micro-joining process represented in soldering to incorporate devices and components into such products has become an essential technology. It can be truly said that soldering and electronics assembly technology have progressed with electronic products. In this chapter, the status of development and research of soldering and cutting edge joining process substituting for soldering are explained. In particular, in the first half, we will discuss development in Japan concerning lead-free solder, and the second half will look into research on materials with the potential to replace high-lead-containing solder for high-temperature applications.

Keywords Lead-free solder · High-temperature bonding · Nanoporous bonding (NPB)

12.1 History and Definition of Soldering

12.1.1 Sn-Pb Solder

Soldering has an extremely long history, and it has been indispensable as a process to join both similar and dissimilar metals. Lead-based solder seems to date to 3800 B.C., when it was used for artistic purposes to produce ornaments. This process has been developed through repeated trial and error over many years. In addition, understanding of the phenomena and characteristic related to soldering, such as wetting, diffusion, and dissolution, has been deepened to develop and establish this process.

H. Nishikawa (✉)
Joining and Welding Research Institute, Osaka University, Ibaraki, Japan
e-mail: nisikawa@jwri.osaka-u.ac.jp

Y. Setsuhara et al. (eds.), *Novel Structured Metallic and Inorganic Materials*, https://doi.org/10.1007/978-981-13-7611-5_12

Solder is defined in the Japanese Industrial Standards (JIS) as a "filler metal with a liquidus temperature of less than 450 °C". It is also referred to as "soft solder". A typical example of soldering is a joining for a printed circuit board (PCB) with high density in electronics products. The number of joints on one board for the products exceeds several thousand points. One major advantage of the soldering is that it can join thousands of parts collectively. Another advantage is that the soldering can be conducted under the melting point of base metals. For a long time, the most widely used solder was the Sn-Pb eutectic alloy, which has a melting point of 183 °C. To be able to form a metallic bond with Cu at such a low temperature is the key reason why the Sn-Pb eutectic solder has been used worldwide for so long. The advantages of soldering are listed below.

- Enables a simultaneous joining of multiple points.
- Enables the formation of interconnection without melting or significant damage to the base metal.
- Enables interconnection of dissimilar materials.
- Enables interconnection with superior electric and thermal properties.
- Enables hermetic sealing.
- Easily automated.

Further, the Sn-Pb eutectic solder had been the conventional filler metal for electric and electronic assembly because the eutectic temperature of the Sn-Pb alloy is not high enough to cause significant damage to the components when it is mounted on the board, and there is also limited deformation of PCBs containing resins. Furthermore, the quality of joints using the Sn-Pb eutectic solder is also high because of the good wettability to the metal surface of the board [1].

For many years, the Sn-Pb eutectic solder was commonly used as a solder material worldwide. However, in the last decade, lead-free solders become common filler materials for soldering due to the restriction of the use of certain hazardous substances (RoHS) in EU [2]. RoHS directive prohibits lead and five other materials for electrical and electronic equipment. Then, awareness of environmental harmonization and the demand to reduce environmental load, free of hazardous substances are being promoted with urgency for them. So there was a switch to lead-free solder, in which the quantity of harmful substances such as Pb was under the permissible amount, and incidentally, the maximum permissible amount of Pb allowed in lead-free solder under JIS Z 3282 is 0.10 mass% [3]. Lead-free soldering technology has matured now.

12.1.2 Lead-Free Solder

In the 1990s, research on lead-free solder had been actively conducted in university and industry, and prospective materials that could substitute for the Sn-Pb eutectic solder were investigated for issues concerning material and joint characteristics

such as (1) melting point, (2) wettability, (3) joint reliability (mechanical, electrical and chemical), (4) cost, and (5) evaluation and test methods.

Figure 12.1 shows the main binary alloys with eutectic temperature or liquidus temperature of less than 450 °C. In descending order of melting points, metals can be arranged as Au, Pb, Sn, In, Bi, and Ga, and it can be seen that Sn is the only lead-free metal with a melting temperature near that of the conventional Sn-Pb eutectic solder. Mg (200 °C), Zn (199 °C), and Cd (176 °C) are among the elements with eutectic temperatures close to the temperature of the Sn-Pb eutectic solder, but from the perspectives of wettability and environmental consciousness, none of them can be used. As a result, Sn-3.5Ag (221 °C) and Sn-0.7Cu (227 °C) have been deemed as suitable replacements for the Sn-Pb eutectic solder. However, since the melting temperatures of binary alloys are clearly higher than that of the Sn-Pb eutectic solder, most research conducted between 1995 and 2000 focused on lowering the melting point of Sn-Ag binary alloy by adding In and Bi. In addition, the effects of adding In and Bi on issues such as the melting point of the alloy, wettability, mechanical qualities, and reliability of the joints were discussed [4–7].

Table 12.1 lists some lead-free solders and lead-free solders can be classified according to the melting temperature range. They are divided into the five systems in the JIS Z 3282 and ISO 9453 (2006). There are classified into the following five systems: (1) high temperature, (2) middle high temperature, (3) middle temperature, (4) middle low temperature, and (5) low temperature, separated by the liquidus line

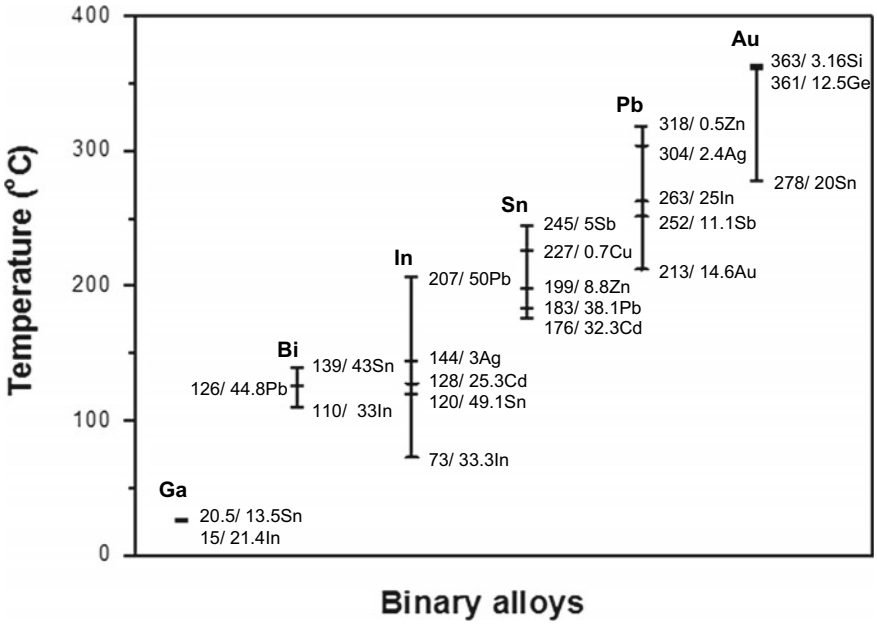

Fig. 12.1 Melting temperature of binary alloys with eutectic temperature or liquidus temperature of less than 450 °C

Table 12.1 Lead-free solder and their melting temperature range listed in standards

Solder		Composition, mass%	Solidus (°C)	Liquidus (°C)
High temperature: solidus more than 217 °C liquidi more than 225 °C	Sn-Sb	Sn-5Sb	238	241
	Sn-Cu	Sn-0.7Cu	227	228
	Sn-Cu-Ag	Sn-0.7Cu-0.3Ag	217	226
	Sn-Ag	Sn-5Ag	221	240
Mid–high temperature: solidus more than 217 °C liquidus less than 225 °C	Sn-Ag	Sn-3.5Ag	221	221
	Sn-Ag-Cu	Sn-3Ag-0.5Cu	217	219
		Sn-3.5Ag-0.7CU	217	217
		Sn-3.8Ag-0.7Cu	217	217
Mid temperature: solidus less than 217 °C and more than 150 °C liquids more than 200 °C	Sn-Ag-Bi-Cu	Sn-2.5Ag-1Bi-0.5Cu	213	218
	Sn-In-Ag-Bi	Sn-4In-3.5Ag-0.5Bi	207	212
		Sn-8In-3.5Ag-0.5Bi	196	206
Mid–low temperature: solidus more than 150 °C liquidus less than 200 °C	Sn-Zn	Sn-9Zn	198	198
	Sn-Zn-Bi	Sn-8Zn-3Bi	190	196
Low temperature: solidus less than 150 °C liquidi less than 200 °C	Sn-Bi	Sn-58Bi	139	139
	Sn-In	Sn-52In	119	119

and solidus line temperatures. The most common lead-free solders in the world are Sn-Ag-Cu system solders such as Sn-3.0mass%Ag-0.5mass%Cu solder for both flow and reflow soldering in Japan. In the United States and Europe, it is standard for solder compositions to contain large amounts of Ag and Cu such as Sn-3.8Ag-0.7Cu. The ternary eutectic temperature of the Sn-Ag-Cu system is 217 °C. Furthermore, with high Ag prices, we are beginning to consider the use of Sn-1.0Ag-0.5Cu as well as Sn-0.3Ag-0.7Cu, particularly in flow soldering in Japan.

12.2 Soldering Process

Soldering is an important process for assembling printed circuit boards of electronic products. Soldering process can be classified into three types; flow soldering, reflow soldering, and manual soldering. Flow soldering using a molten solder bath has been in wide used for many years and is suitable for through-hole mounting due to its cost advantages and high throughput for high-volume products. It mainly contains three methods: dip soldering, drag soldering, and wave soldering. Then, manual soldering is the traditional process used to join parts and component leads to lands on the board using a soldering iron and flux-cored solder wire. The correct selection of appropriate heat input and the shape of a soldering tip are important to achieve solder joints without defect.

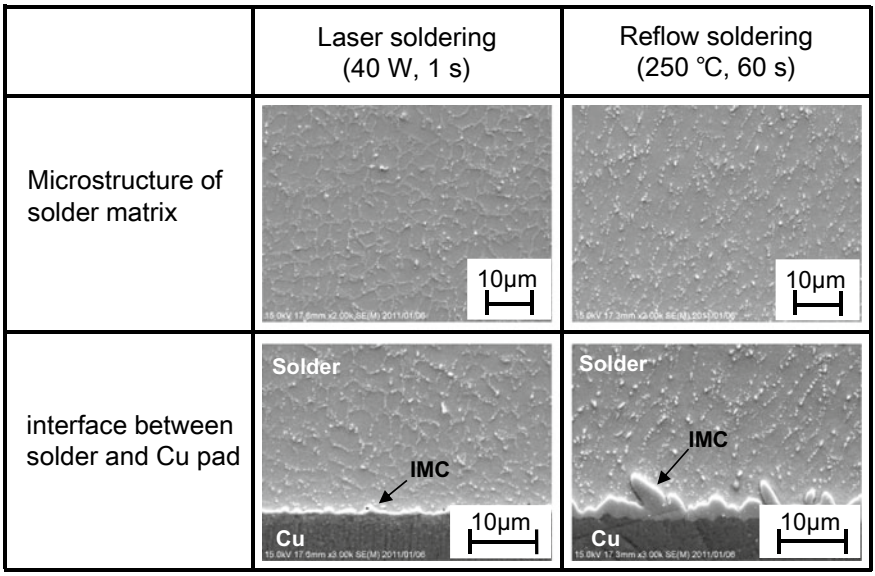

Fig. 12.2 Scanning electron microscopy (SEM) micrographs of the solder matrix and the interface between the solder and Cu pad after laser and reflow soldering

Reflow soldering is the latest major process by the industry for surface mounted components and high-density fine pitch packaging by using a solder paste. The available heating methods of reflow soldering include infrared, hot gas, convection, laser, and so on. Under reflow soldering, both heating and cooling steps are important to the solder joint quality. It is understood that the heating and cooling rate of the reflow process contributes to the final microstructure of the solder joint. For example, as shown in Fig. 12.2, the microstructure of the solder matrix for laser soldering is different from that for reflow soldering using a furnace. In laser soldering, the size of the primary β-Sn phase is smaller than that of reflow soldering. This size difference occurs because the cooling rate of laser soldering is much faster compared with that of reflow soldering. Then, as shown in Fig. 12.2, laser soldering is effective for reducing the formation of intermetallic compound layer (IMC) at the solder/Cu pad interface and ensuring the impact reliability of the joint [8]. So, to use appropriate heating method and heating conditions for reflow soldering is important to achieve solder joints without defect.

12.3 Characteristics of Lead-Free Solder

Compared to the Sn-Pb eutectic solder, the well-known characteristics of the Sn-Ag-Cu system solders are: (1) higher melting temperature ranges, (2) poor wettability on base metals, (3) hardness of mechanical property, and (4) higher

dissolution rate of solid metals. (1) and (2) are extremely basic issues, but practically, Sn-Ag-Cu system solders can be used without the issues through improvements in lead-free solder mounting technology such as a heating profile and chemical flux revision.

On the other hand, for (3), there are concerns due to stress concentration in the solder/substrate interface. Since this issue is significantly related to matters such as drop impact resistance for portable devices including cellular phones and laptops, an evaluation method for overcoming this problem is currently underway [9]. This issue also has a significant relationship with the thermal fatigue characteristics of solder, which are crucial to long-term reliability.

Concerning (4), the results of the immersion test of copper in molten solder kept at a constant temperature indicates that Cu dissolution rate is clearly higher in Sn-3.5Ag lead-free solder than in Sn-Pb eutectic solder. This high dissolution of solid metal in molten lead-free solder and higher heating temperature due to a higher melting point of the solder cause issues such as Cu line and Cu pad disappear. Cu electrode thinning, and loss in fine bonding, which decrease the reliability of the joints. Additionally, issues such as damage to stainless steel solder baths and manual soldering iron tip used in flow soldering devices are becoming pronounced. It was reported that the dissolution of iron in molten solder does occur and the dissolution rate of iron in lead-free solders is greater than that in the conventional Sn-Pb eutectic solder [10].

Although widespread use of Sn-Ag-Cu system solders as a standard composition will not lead to a major change in the basic composition, there are attempts to improve the existing characteristics by adding a minor element to overcome those shortcomings mentioned above along with other issues. The effect of minor elements such as In, Ni, and Co has been explored to improve the properties of solder and interfacial reactions [11–14]. For example, the effect of the addition of In on binary eutectic Sn-3.5Ag solder was investigated [11]. They reported that microstructure of the solder and the morphology of secondary phases in the solder matrix changed accordingly. In the case of Ni and Co, the reactions between Cu and the Sn-2.5Ag solders doped with 0.03 wt%Fe, Co, Ni were studied [12]. They reported that adding Fe, Co, or Ni produced a much thinner Cu3Sn layer at the interface in solid-state aging and thinner Cu3Sn layers might translate into better solder joint strength. Then adding Fe and Co to reduce damage to iron-based materials such as Fe plating were effective [10, 14].

By simply observing the process temperature and areas where Sn-Ag-Cu solder can be used, it can be inferred that the lead-free soldering process has matured. On the other hand, because of the diversification of electronic products and technological progress, there are certain temperature and areas where there is an unfilled demand for a switch to lead-free or where this switch is delayed. Figure 12.3 shows melting temperatures of main lead-free solders in a wide temperature range where there is a demand for harmful substance-free joint materials due to the diversification of electronic products in recent years. As shown in this figure, the focus of research and development on lead-free technology in Japan has transitioned to how to establish new interconnection technologies in low-temperature regions less than 150 °C as well as high-temperature regions more than 250 °C.

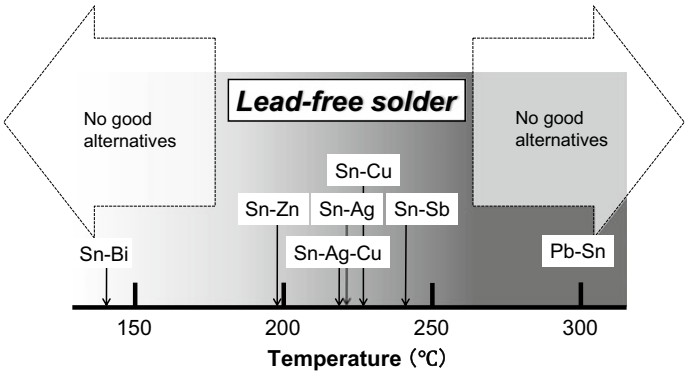

Fig. 12.3 Melting temperatures of main lead-free solders and demand for harmful substance-free joint materials

12.4 High-Temperature Bonding

The RoHS directive currently exempts the use of high-lead-containing solders for high-temperature soldering, as high-temperature soldering is a key technology for electronic component assembly and other high-temperature applications. Pb-based solders such as Pb-5Sn and Pb-10Sn have been used for the high-temperature application. However, there is no guarantee that the exemption will last. The replacement of Pb-based solder is preferable; however, no suitable alloys, and materials have been developed. A strong drive thus exists to find lead-free alternatives for high-temperature joining process. Several materials and joining processes have been proposed as alternatives to high-lead-containing solders. In the case of an alloy, Au-, Zn- and Bi-based alloys have been investigated as lead-free solder, but their widespread use is unlikely because of their inferior properties and high costs [15–21].

Then, as a new joining process, sintering process using particles have also been proposed as solder alternatives. Bonding conditions and shear strength of the joints using some kinds of particles such as Ag nanoparticles, Cu nanoparticle, and oxides are summarized in Table 12.2 [22–28]. Generally, some metals such as Ag and Cu have high electrical and thermal conductivities compared to Sn-based solders. These metals tend to have high melting temperatures. These properties make them suitable for high-temperature joining process. For instance, one candidate process that might be applicable for joining at a lower temperature is sintering. Standard sintering procedure still requires relatively high joining temperature, although the sintering temperature of the metallic particle is below its melting point. However, related to using nanoparticles, it is well known that metallic nanoparticles sinter and melt at temperatures lower than that for the bulk metal. The sintering behavior of nanoparticles is of significant interest and the sintering behavior of metallic nanoparticles has been exploited to join components to substrate.

Table 12.2 Bonding conditions and shear strength of the joints using particles in the literatures

Bonding material	Substrate	Bonding temperature (°C)	Bonding time (s)	Pressure (MPa)	Atmosphere	Shear strength (MPa)	References
Ag nanoparticle	Cu	300	300	5	Air	40	[22]
Ag nanoparticle	Ni/Ag plated Cu	250	1800	5	Air	50	[23]
Ag_2O	Ag plated Cu	300	150	2.5	Air	20	[24]
Cu + Ag nanoparticle	Cu	350	300	10	Air	50	[25]
Cu nanoparticle	Cu	300	300	5	Hydrogen	More than 30	[26]
Cu nanoparticle	Cu	400	300	15	Nitrogen + Oxygen	40	[27]
Cu_2O_2 powder	Cu	350	300	1.2	Hydrogen	20	[28]

As shown in Table 12.2, Ide et al. reported achieving Cu-to-Cu bonding using silver metallo-organic nanoparticles at 300 °C and an applied pressure of 1 or 5 MPa; shear strength of the resulting was 25–40 MPa [22]. Bonding was believed to occur because of the large surface energy contributed by the nanoscale particles. As Cu-to-Cu bonding using copper nanoparticles, Nishikawa et al. reported that the effect of joining conditions on the shear strength of Cu-to-Cu joints using copper nanoparticle paste was investigated and joints that were bonded at 400 C for 300 s under an applied pressure of 15 MPa showed high shear strength around 40 MPa [27]. However, there are some drawbacks of joining process using nanoparticle pastes, for example, it is difficult to produce suitable nanoparticle pastes for the process conditions and the residual organic materials after the joining process can induce unexpectedly large gaps and voids in the joint area [23, 29].

To address these issues, we focus on nanoporous metals that are fabricated through the dealloying method and propose that nanoporous bonding (NPB) using a nanoporous metal without the need for any solvent, organic substance or flux [30]. A feasibility study has been conducted to determine whether a nanoporous metal can be used for new joint material and the effect of bonding conditions on the shear strength of NPB was investigated. Figure 12.4a shows scanning electron microscopy (SEM) image of surface morphology of Au nanoporous sheet dealloyed by immersing the sheet into 60% nitric acid at 25 ºC for 4 h, and Fig. 12.4b shows the effect of bonding temperature on the shear strength of the Cu-to-Cu disc joints using Au nanoporous sheet with dealloying time of 4 h. The specimens were heated for 30 min with 20 MPa applied pressure under a nitrogen atmosphere. The shear strength of the disc joints increased with increasing bonding temperature. When the bonding temperature was set to 350 °C, we could achieve an average shear strength of around 25 MPa. The shear strength is higher than that of Pb-5Sn solder, which is around 20 MPa. In the case of Ag nanoporous sheet, NPB using Ag nanoporous

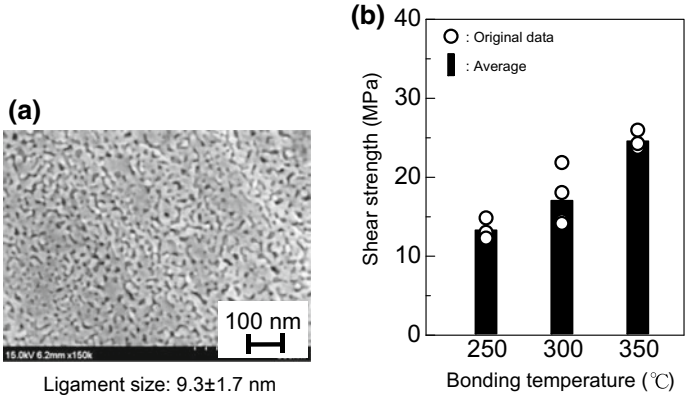

Fig. 12.4 Bonding test results using Au nanoporous sheet. **a** SEM images of surface microstructure of Au nanoporous sheet after dealloying at 25 °C for 4 h. **b** Effect of bonding temperature on the shear strength of Cu-to-Cu disc joints using Au nanoporous sheet with dealloying time of 4 h. (Bonding time: 30 min, Applied pressure: 20 MPa, Atmosphere: N_2)

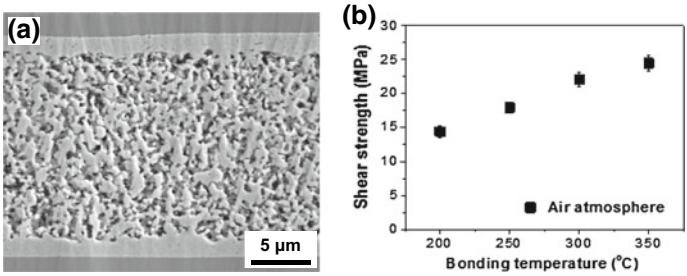

Fig. 12.5 Bonding test results using Ag nanoporous sheet. **a** SEM images of ENIG-finished Cu disc joint using Ag nanoporous sheet with dealloying time of 3 h at 75 °C. **b** Effect of bonding temperature on the shear strength of ENIG-finished Cu disc joints using Ag nanoporous sheet with. (Bonding time: 30 min, Applied pressure: 20 MPa, Atmosphere: Air)

sheet without any organic substances was also successfully demonstrated. Figure 12.5a shows SEM image of the NPB joint using ENIG(electroless Ni/immersion Au)-finished Cu discs, and Fig. 12.5b shows the effect of bonding temperature on the shear strength of the ENIG-finished Cu disc joints using Ag nanoporous sheet with dealloying time of 3 h at 75 ºC. The SEM image reveals that the Ag layer has a dense/porous sandwich structure, wherein the dense layer provides interfacial bonding between Ag and ENIG, and the dense layer exhibits good contact with the ENIG surface. Then, as shown in Fig. 12.5b, the shear strength in the air was 14.4 MPa at 200 ºC and gradually increased with increasing bonding temperature up around 25 MPa at 350 °C. The NPB joints exhibited shear strengths of more than 20 MPa above 300 °C. Consequently, NPB joints using Au nanoporous and Ag nanoporous metals can be achieved with sufficient bonding strength and this NPB is expected to be an alternative to high-Pb-containing solder. The further innovation of micro-joining processes is a key to meeting the demands for diversification of electronic products.

References

1. R.J. Klein Wassink, *Soldering in Electronics*, 2nd edn. (Electrochemical Publications Ltd., Scotland, 1989), p. 27
2. Official Journal of the European Union, Directive 2011/65/EU of the European Parliament and of the Council of 8 June 2011 on the restriction of the use of certain hazardous substances in electrical and electronic equipment (recast)
3. JIS Z 3282 Soft solders – chemical compositions and forms (2006)
4. I. Artaki, A.M. Jackson, J. Electron. Mater. **23**, 757 (1994)
5. P.T. Vianco, J.A. Rejent, J. Electron. Mater. **28**, 1127 (1999)
6. M.I. Kim, J.K. Moon, J.P. Jung, Mater. Trans. **43**, 1791 (2002)
7. K.S. Kim, T. Imanishi, K. Suganuma, M. Ueshima, R. Kato, Microelectron. Reliab. **47**, 1113 (2007)
8. H. Nishikawa, N. Iwata, J. Mater. Process. Technol. **215**, 6 (2015)

9. T. Daito, H. Nishikawa, T. Takemoto, Microelectron. Reliab. **53**, 2005 (2013)
10. T. Takemoto, T. Uetani, M. Yamazaki, Solder. Surf. Mt. Technol. **16**, 9 (2004)
11. W.K. Choi, S.W. Yoon, H.M. Lee, Mater. Trans. **42**, 783 (2001)
12. Y.W. Wang, Y.W. Lin, C.T. Tu, C.R. Kao, J. Alloys Compd. **478**, 121 (2009)
13. I.E. Anderson, J.C. Foley, B.A. Cook, J. Harringa, R.L. Terpstra, O. Unal, J. Electron. Mater. **30**, 1050 (2001)
14. H. Nishikawa, A. Komatsu, T. Takemoto, Mater. Trans. **46**, 2394 (2005)
15. V. Chidambaram, J. Hattel, J. Hald, Mater. Des. **31**, 4638 (2010)
16. Y.C. Liu, J.W.R. Teo, S.K. Tung, K.H. Lam, J. Alloys Compd. **448**, 340 (2008)
17. V. Chidambaram, J. Hald, J. Hattel, J. Alloys Compd. **490**, 170 (2010)
18. M. Rettenmayr, P. Lambracht, B. Kempf, C. Tschudin, J. Electron. Mater. **31**, 278 (2002)
19. N. Kang, H.S. Na, S.J. Kim, C.Y. Kang, J. Alloys Compd. **467**, 246 (2009)
20. T. Takahashi, S. Komatsu, H. Nishikawa, T. Takemoto, J. Electron. Mater. **39**, 1241 (2010)
21. J.M. Song, H.Y. Chuang, Z.M. Wu, J. Electron. Mater. **35**, 1041 (2006)
22. E. Ide, S. Angata, A. Hirose, K.F. Kobayashi, Acta Mater. **53**, 2385 (2005)
23. J. Yan, G. Zou, A. Wu, J. Ren, A. Hu, Y.N. Zhou, J. Electron. Mater. **41**, 1924 (2012)
24. T. Morita, Y. Yasuda, E. Ide, Y. Akada, A. Hirose, Mater. Trans. **49**, 2875 (2008)
25. Y. Morisada, T. Nagaoka, M. Fukusumi, Y. Kashiwagi, M. Yamamoto, M. Nakamoto, J. Electron. Mater. **39**, 1283 (2010)
26. T. Ishizaki, R. Watanabe, J. Mater. Chem. **22**, 25198 (2012)
27. H. Nishikawa, T. Hirano, T. Takemoto, N. Terada, Open Surf. Sci. J. **3**, 60 (2011)
28. Y. Yasuda, E. Ide, T. Morita, Open Surf. Sci. J. **3**, 123 (2011)
29. H. Yu, L. Li, Y. Zhang, Scr. Mater. **66**, 931 (2012)
30. M.S. Kim, H. Nishikawa, Scr. Mater. **92**, 43 (2014)

Chapter 13
Metallurgical Characterization of Joined Materials

Kazuhiro Ito

Abstract This chapter describes the two typical examples of joining performance of structural and functional materials from the point of view of metallurgical characterization. At first, friction stir processing (FSP) is an effective grain refinement technique. FSP was conducted in the topmost 1-mm-thick layer of the steel welds, achieving increase of its fatigue strength and toughness. The FSP provided, for example, ultrafine equiaxial ferrite grains covered with thin layer cementite in a certain condition, based on characterization using transmission electron microscope. Second, a thin Ti-based self-formed barrier (SFB) formed by annealing a Cu(Ti) alloy film deposited on dielectrics at elevated temperature is one of the solutions to achieve low resistance and high reliability of Cu interconnects in ultra-large-scale integration devices. Identification of SFB was conducted using the electron diffraction, X-ray photoelectron spectroscopy, and Rutherford backscattering spectrometry techniques. That identification indicates that SFB consists of mainly amorphous Ti oxides, and its growth is concluded to be controlled by a thermally activated process.

Keywords Friction stir processing · Welds · Fatigue strength · Cu interconnects · Diffusion barriers

13.1 Introduction

This chapter describes characterization of joined materials for clarification of fundamental mechanisms controlling the joining performance of structural and functional materials. In the author's research experiences, metallurgical solutions are presented for increasing fatigue strength/life of steel welds as an example of

K. Ito (✉)
Joining and Welding Research Institute, Osaka University, Ibaraki, Osaka, Japan
e-mail: ito@jwri.osaka-u.ac.jp

Y. Setsuhara et al. (eds.), *Novel Structured Metallic and Inorganic Materials*, https://doi.org/10.1007/978-981-13-7611-5_13

structural materials in Sect. 13.2 and for low-resistivity and high-reliability Cu interconnects in ultra-large-scale integration (ULSI) devices as an example of functional materials in the Sect. 13.3.

13.2 Microstructure-Controlled Increase of Fatigue Strength and Toughness

13.2.1 Issues to Be Addressed in Mechanical Properties of Steel Welds

Fatigue strength of steel materials ordinary increases with increasing their yield stress, but fatigue strength of their weld joints does not increase [1]. To increase fatigue strength of their weld joints, various surface treatment techniques such as ultrasonic peening [2–8], hammer peening [9–12], shot peening [13, 14], and laser peening [15] have been studied. The techniques provide compressive residual stress beneath the surface of the materials due to compressive plastic deformation at the surface. It means that the techniques make fatigue strength (the positive sign) look larger by adding compressive residual stress (the negative sign) to improve its appearance. However, it may not contribute to the improvement of their toughness.

On the other hand, friction stir processing (FSP), which is based on the principle of friction stir welding, is an effective surface microstructural modification technique to increase fatigue strength of weld joints for aluminum alloys [16, 17]. Similarly, FSP on the steel weld joints can increase its fatigue strength [18]. FSP provides grain refinement and homogenization. The following sections are presented as a practical example of microstructural modification-related increase of fatigue strength and Charpy absorbed energy in the tungsten inert gas (TIG)-welded SS400 plates.

13.2.2 Fatigue Strength Increase by FSP Microstructural Modification

The automated TIG welding was conducted on commercially available 5-mm-thick SS400 steel plates. FSP was performed on weld beads with small tungsten carbide tools containing a 12-mm-diameter shoulder and a 0.8-mm-long and 4-mm-diameter probe. FSP tools were operated in Ar atmosphere in applied stress control with counterclockwise rotation at 400 rpm and 140 mm/min (hereafter FSP (H)) and at 200 rpm and 400 mm/min (hereafter FSP(L)) in welding direction. Figure 13.1 shows surface and cross-sectional optical images of TIG-welded SS400 steel plates without FSP, with FSP(H), and with FSP(L). The weld metal was at upper part center of the plates, and the heat-affected zone (HAZ), which exhibits a

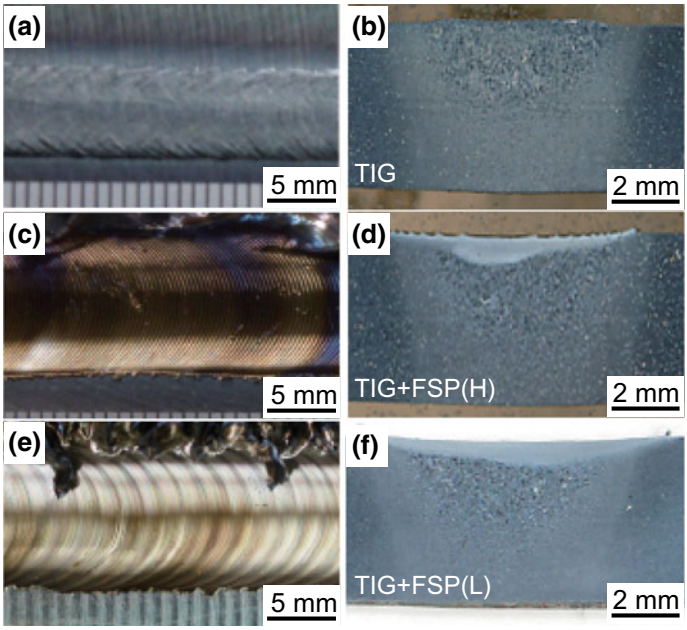

Fig. 13.1 Surface and cross-sectional optical images of TIG-welded SS400 steel plates, **a**, **b** without FSP, **c**, **d** with FSP(H), and **e**, **f** with FSP(L)

grayish-white contrast, surrounds the periphery of the weld metal (Fig. 13.1b). The FSP-modified region exhibits smooth grayish-white contrast at upper parts of the TIG welds with about 1 mm in depth from the surface, and covered TIG welds and HAZ (Fig. 13.1d, f). The heat input produced by FSP(L) was lower than that by FSP(H).

Figure 13.2 shows relationship between applied stress amplitude $((\sigma_{max} - \sigma_{min})/2)$ and number of cycles to failure in three-point bending fatigue tests for these TIG-welded specimens with and without FSP. The specimens for three-point bending fatigue tests had a size of $2.7 \times 60 \times 5$ mm^3 and were prepared perpendicular to the TIG-welded and FSP beads. The three-point bending fatigue tests were conducted at room temperature (RT) with a sinusoidal waveform at 20 Hz with a stress ratio of 0.1 (a ratio of σ_{max} to σ_{min}) and with length of the support span and radius of the punch were 25 mm and 5 mm, respectively. The number of cycles to failure of the TIG-welded specimens exhibited log-linear increase with decreasing stress amplitude (broken line). Similarly, the TIG+FSP(H) and TIG +FSP(L) specimens with FSP(H) exhibited log-linear increase of the number of cycles to failure in the stress amplitude range between 270 and 315 MPa (solid lines), and their increasing rate was higher than that of the TIG-welded specimens and that of TIG+FSP(L) (a red line) was much higher than that of TIG+FSP(H) (a blue line). The TIG+FSP(H) and TIG+FSP(L) specimens exhibited 5.6×10^5 and more than 5.0×10^6 cycles to failure at an applied stress amplitude of 270 MPa,

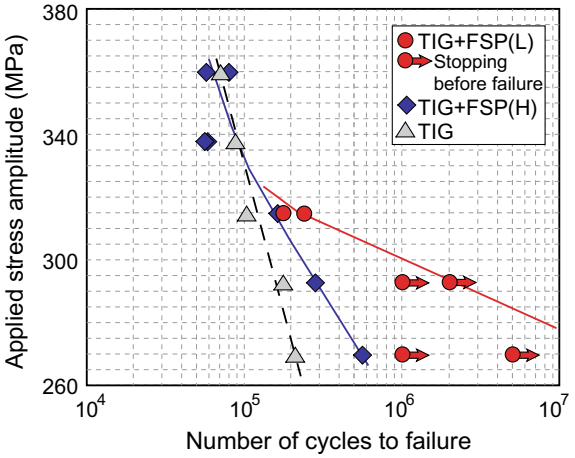

Fig. 13.2 S-N curves (stress amplitude vs. number of cycles to failure) of the TIG-welded, TIG+FSP(H), and TIG+FSP(L) specimens in three-point bending fatigue tests at RT

respectively. Those are about 170% and more than 2000% increase in comparison with the number of cycles to failure for the TIG-welded specimens. The displacements of the TIG+FSP specimens were remarkably smaller than those of the TIG-welded specimens. Similarly, the displacement of the TIG+FSP(L) specimens at σ_{max} was obviously smaller than that of TIG+FSP(H) specimens. Noted that decreasing heat input by lower rotation speed and higher traveling speed (FSP(L)) dramatically increased fatigue resistance.

Microstructures of the TIG-welded, TIG+FSP(H), and TIG+FSP(L) specimens were observed by scanning electron microscopy (SEM) equipped with an electron backscattering diffraction (EBSD) pattern detector and transmission electron microscopy (TEM). Figure 13.3 shows portions of cross-sectional SEM/EBSD images beneath the surface of TIG-welded, TIG+FSP(H), and TIG+FSP(L) specimens. FSP(H) and FSP(L) produced microstructure consisting of ultrafine equiaxial

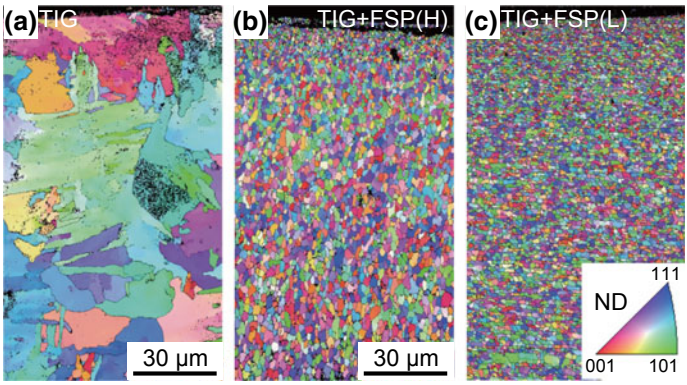

Fig. 13.3 Cross-sectional SEM-EBSD images of **a** the TIG-welded, **b** TIG+FSP(H), and **c** TIG +FSP(L) specimens

ferrite grains with average grain sizes of about 2.6 μm (Fig. 13.3b) and 1.9 μm (Fig. 13.3c), respectively. EBSD detected the crystal orientation of the grains with the designating crystal structure, and body-centered-cubic ferrite was detected in Fig. 13.3. The color indicates a grain normal direction (ND), which is parallel to crystal orientation depicted in an inset figure in Fig. 13.3c. EBSD was simultaneously characterized by rolling direction and transverse direction in addition to ND. The as-welded coarse grains were observed in the region below the FSP-modified microstructure (at any depth in the range of about 1 to 5 mm from the surface), which is similar to the SEM/EBSD image obtained beneath the surface of the TIG-welded specimens (Fig. 13.3a). In the boundary between the ultrafine grains and TIG-welded coarse grains, grains elongated and slanting downward were observed. Increasing three-point bending fatigue resistance of the TIG welds with FSP can be explained mainly by increasing stiffness of a surface portion due to microstructure consisting of ultrafine grains produced by FSP. Decreasing FSP heat input promoted further refinement of surface microstructure, leading to a significant increase in their fatigue strength/life.

Figure 13.4a shows a portion of transverse-sectional TEM bright-field image beneath the surface of the TIG+FSP(L) specimen. The bright-field image was provided using transmission electrons. The TEM bright-field image with higher magnification indicates black contrast at grain boundary of ultrafine ferrite grains (Fig. 13.4a). To identify ferrite grains and the phase at grain boundary, selected area diffraction (SAD) should be taken. The SAD image taken in the area surrounded by a red circle in Fig. 13.4a is shown in Fig. 13.4b. Many diffraction spots are observed and those are arranged regularly, and the distance from the electron beam center and the diffraction spot pattern would provide the crystal structure and plane index of a candidate phase. Figure 13.4b indicates that a single crystalline cementite is located at the grain boundary. A dark-field image taken using the diffraction spot of (210) indicated by a white circle in Fig. 13.4b is shown in

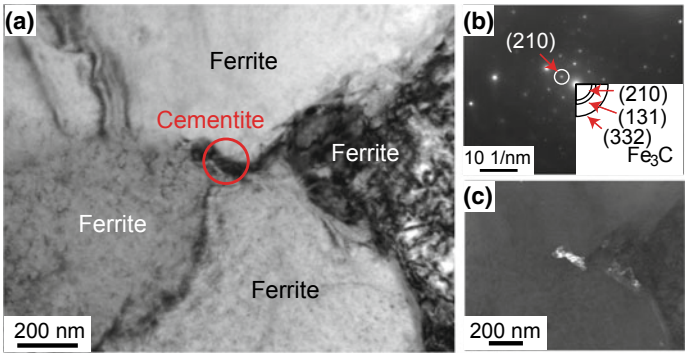

Fig. 13.4 A cross-sectional TEM bright-field image in a stir zone of FSP(L) fabricated on the TIG weld in SS400 steel plates. **b** A SAD image obtained from the ferrite-grain boundary indicated by a red circle in **a**. **c** A dark-field image taken using the diffraction spot of (210) indicated by a white circle in **b**

Fig. 13.4c. The phase originated only from the diffraction spot can be seen in the dark-field image. The layer-type grain with white contrast can be seen at the grain boundary in Fig. 13.4c. It looks a layer of cementite with thickness of several 10 nm. Based on similar TEM analysis, ferrite-grain boundaries were almost fully covered with layers of cementite. The microstructure consisting of ultrafine ferrite grains surrounded by layers of cementite increased fatigue strength. The TIG+FSP (H) specimen provided similar microstructure consisting of ultrafine ferrite grains and cementite phases at ferrite-grain boundaries. Its layer thickness became relatively thicker with increasing heat input. In addition, some of them segregated in grain boundary triple points into mass. Grain refinement as well as such the distribution of cementite contributes increasing fatigue strength of welds with FSP, and its difference in the increase between the TIG+FSP(L) and TIG+FSP(H) specimens can be explained by the difference of ferrite-grain sizes, and cementite morphology and distribution.

13.2.3 Charpy Absorbed Energy Increase by FSP Microstructural Modification

Microstructure consisting of ultrafine ferrite grains and cementite phases at ferrite-grain boundaries is not on the Fe–C binary phase diagram and related diagrams. This can be a stress-induced new microstructure supported by FSP. Noted that cementite is generally believed to be a brittle phase, and its presence at the grain boundary is expected to degrade ferrite-grain-boundary toughness. However, if cementite at ferrite-grain boundaries degraded its toughness, its fatigue strength might be degraded. But actually it did not. Thus, to clarify high toughness of the FSP-modified microstructure, the 2.5-mm-thick subsize specimens with a size of 10 $\times$ 55 $\times$ 2.5 mm^3 for Charpy impact tests were prepared. The FSP-modified microstructure was obtained in a limited area from the surfaces, and thus two sides of the TIG-welded plates were thinned to 3.5 mm in thickness. FSP was performed on each side of the plates with a small tungsten carbide tool. To make the FSP-modified regions deeper/thicker, the tool probe length was made longer (1.3 mm) than 0.8 mm for the preparation of the specimens for the three-point bending fatigue tests. The specimens were prepared perpendicular to the TIG-welded and FSP beads. The V notch with 2 mm in depth was produced in the center of the surface with a size of 55 $\times$ 2.5 mm^2 which is based on JIS Z2242. The Charpy impact tests were conducted at 196 °C and in the temperature range between –110 and 40 °C. Fracture surfaces of the TIG-welded specimens with and without FSP were observed by optical microscopy and SEM after the Charpy impact tests.

Figure 13.5 shows temperature dependence of Charpy absorbed energy of the TIG-welded, TIG+FSP(H), and TIG+FSP(L) specimens. The plotted values of Charpy absorbed energy were simply four times as much as the values obtained

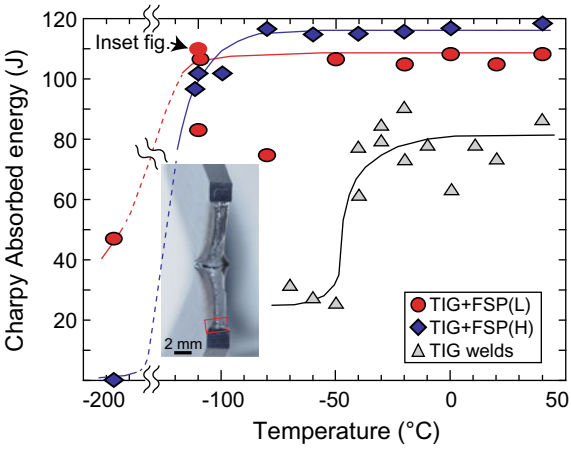

Fig. 13.5 Temperature dependence of Charpy absorbed energy of the TIG-welded, TIG+FSP(H), and TIG+FSP(L) specimens, and inset figure exhibits an optical image of the TIG+FSP (L) specimen fractured after a Charpy impact test at −110 °C as shown in a black arrow

using the 2.5-mm-thick subsize specimens. The values of the TIG+FSP(H) and TIG +FSP(L) specimens were much larger than those of the TIG-welded specimens in all the temperature ranges. The TIG+FSP(H) and TIG+FSP(L) specimens exhibited about 120 J and 110 J, respectively, in the temperature range between −110 and 40 °C, in comparison with about 80 J in the temperature range between −40 and 40 °C for the TIG-welded specimens. The value at −196 °C of the TIG+FSP(L) specimen exhibited about 50 J, while that of the TIG+FSP(H) specimen exhibited about 0 J. This indicates that a part of the FSP(L)-modified microstructure still remained ductile at −196 °C.

Figure 13.6 shows SEM images of a fracture surface of the TIG+FSP(L) and TIG+FSP(H) specimens after Charpy impact tests at −196 °C. The M-shaped fracture surface was observed at the end portion of the V notch for the TIG+FSP(L) specimen (Fig. 13.6a), and the enlarged SEM image of a red square area in Fig. 13.6a shows dimple fracture similar to the case at −110 °C. The M-shaped fracture surface is attributed to the remained TIG welds at the specimen center. This

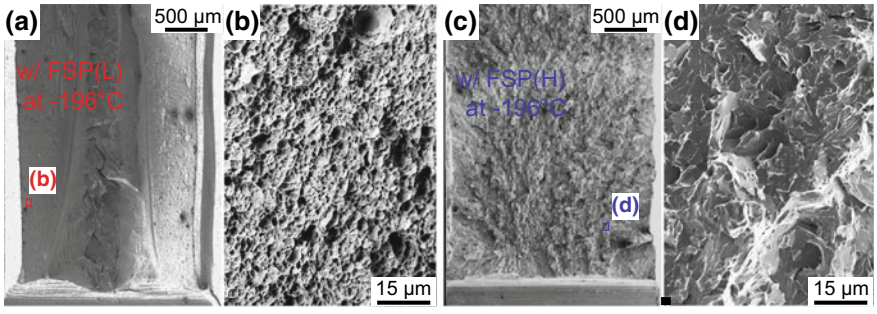

Fig. 13.6 SEM images of a fracture surface of **a**, **b** TIG+FSP(L) and **c**, **d** TIG+FSP(H) specimens after Charpy impact tests at −196 °C. **b**, **d** enlarged SEM images in areas surrounded by squares in **a** and **c**, respectively

indicates that FSP(L)-modified microstructure remains ductile at −196 °C. However, the Charpy absorbed energy at −196 °C decreased to about 50 J (Fig. 13.5), and thus brittle fracture could be partly existed in the FSP(L) modified regions. On the other hand, it is hard to see plastic deformation at the end portion of the V notch for the TIG+FSP(H) specimen, and uniform brittle fracture surface was observed (Fig. 13.6c). Enlarged SEM images of a blue square area in Fig. 13.6c show brittle fracture with river patterns, indicating that FSP(H) modified microstructure did not remain ductile at −196 °C. This is consistent with the Charpy absorbed energy of about 0 J at 196 °C (Fig. 13.5). Further grain refinement provided by FSP(L) with lower heat input than FSP(H) can decrease brittle–ductile transition temperature, although the ultrafine ferrite-grain boundaries covered with brittle cementite layers. Cementite is generally believed to be a brittle phase, but it did not degrade the Charpy absorbed energy. This suggests that FSP modification for a topmost area of the welds is useful to increase fracture toughness as well as fatigue strength of the welds, and the grain size of ultrafine grains formed by FSP plays an important role in the increment.

13.3 Cu Interconnects in ULSI Devices Using Cu(Ti) Alloy Films

Ultra-large-scale integration (ULSI) is a kind of assembly controlling the joining performance of functional materials, and its technology contributes significantly to our electronic information society. ULSI consists of transistors as the switching devices and interconnects that connect between switches. Scaling down of transistors significantly contributes to device performance. Scaling down the transistor size by, for example, one and a half, both the voltage and gate delay similarly scaling down, and the power dissipation becomes one-fourth. Then device feature size has reduced from micron-scale era into nanoscale era.

On the contrary, interconnect delay increased with decreasing gate size, although the gate delay decreased. This suggests that total device delay reaches the minimum at a critical gate size, and that further scaling down makes it increase. This leads to changing Al interconnects into Cu interconnects, since Cu has a lower electrical resistivity than Al, although Cu-interconnect metallurgy is entirely different from Al-interconnect metallurgy in the issue of ULSI technology. For example, Cu dry etching is somehow difficult, and thus a dual-damascene method is used for making Cu interconnects. First, a groove is digged via so-called trench, and then Cu film is electrochemically deposited, and finally, chemical–mechanical polishing was conducted. One of the other issues is that Cu easily diffuses into dielectrics by which Cu interconnect is surrounded. Thus, refractory metals and compounds such as Ta and TaN are deposited between Cu and dielectrics as a diffusion barrier.

Large resistance–capacitance (RC) delay has been one of the critical issues in Cu-interconnect fabrication as the device feature size has reduced to nanometer

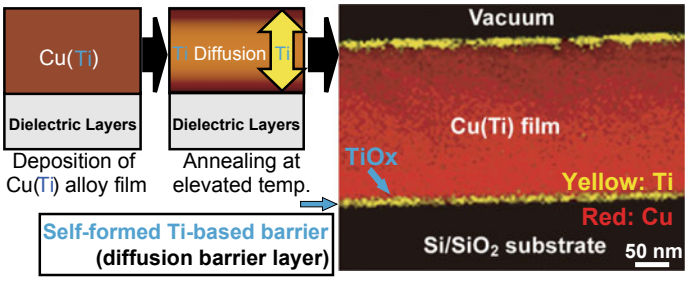

Fig. 13.7 Schematic illustrations of Ti-based self-formed barrier (SFB) synthesis using Cu(Ti) alloy films annealed at elevated temperature and its TEM/EDS mapping result [27]

scale [19]. Resistivity increase due to barrier layers is becoming significant with the reduction in line width of the Cu interconnects. Moriyama et al. [20] and Shimada et al. [21] reported that significant resistivity increase is observed when the line width decrease to smaller than 100 nm and a very thin barrier layer (<5 nm) is required for the interconnects with a line width of ~45 nm (an average grain size of 450 nm) to achieve an effective interconnect resistivity of less than 4 μΩcm. One of the various methods to reduce the volume of barrier layers in Cu interconnects [22–30] is annealing Cu alloy seeds at elevated temperatures, which is conventionally called a self-formed barrier (SFB) technique. The SFB technique is essential for reaction of solute atoms with dielectrics as shown in Fig. 13.7. The Ti atoms in the Cu(Ti) alloy seeds can react with many kinds of dielectrics such as SiO_2, SiOC, SiCO, and SiCN, resulting in the formation of SFB with different compositions [29]. In the following sections, characterization of Ti-based SFB using TEM/energy-dispersive X-ray spectroscopy (EDS), X-ray photoelectron spectroscopy (XPS), and Rutherford backscattering spectrometry (RBS), and examples applied Ti-based SFB to the Cu dual-damascene interconnect for 45-nm node of ULSI are presented.

13.3.1 Identification of Ti-Based SFB Using XPS

Figure 13.8 [28] shows cross-sectional TEM images and SAD images taken from an area marked with a broken circle in the TEM images for an annealed Cu(Ti)/SiO_2 (Fig. 13.8a) and Cu(Ti)/Low-k1 (Fig. 13.8c) samples. Thin Ti-based SFB layers are formed at the interfaces between a Cu(Ti) alloy film and dielectrics. They consisted of polycrystalline TiSi on SiO_2 (Fig. 13.8b) and TiC on Low-k1 (Fig. 13.8d). The kinds of the Ti compounds formed in the Ti-based SFB depended on the kinds of dielectrics.

Although the amorphous phases in the barrier were not directly identified by the TEM/SAD and secondary ion mass spectrometry analyses, an XPS technique with simultaneous Ar etching was employed to investigate the structure of the Ti-based

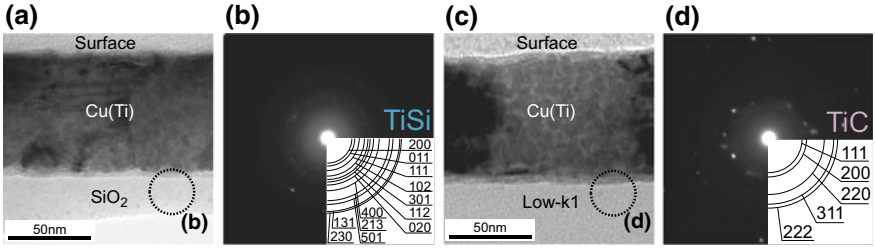

Fig. 13.8 Cross-sectional TEM images of the **a** Cu(Ti)/SiO_2 and **c** Cu(Ti)/Low-k1 after annealing at 600 °C for 2 h in Ar, respectively. **b** and **d** are SAD images taken from the areas marked with broken circles in **a** and **c** [28] (Copyright 2007 The Japan Society of Applied Physics)

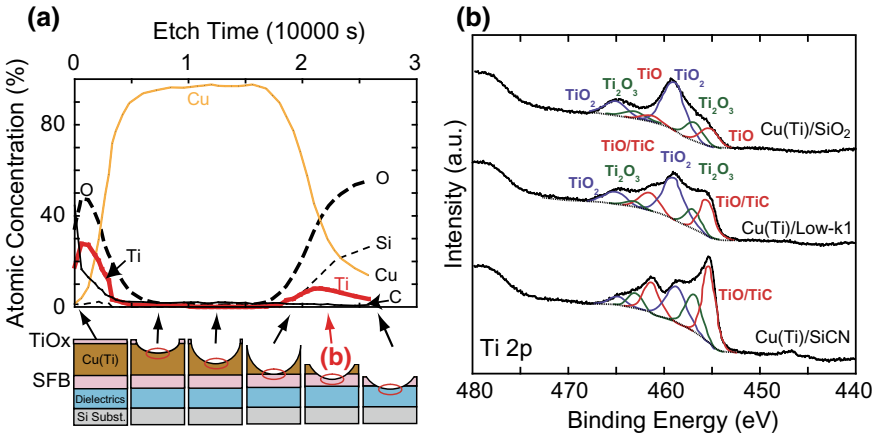

Fig. 13.9 **a** A XPS depth profile of the Cu(Ti)/SiO_2 sample after annealing in UHV at 600 °C for 2 h and **b** portions of XPS spectra around the binding energies of Ti 2p obtained from the middle of the Ti-based SFB formed in Cu(Ti)/dielectrics after annealing in UHV at 600 °C for 2 h [30] (Copyright 2011 The Japan Society of Applied Physics)

SFB and its compositions systematically with dielectrics. Figure 13.9a shows a typical example of elemental depth profiles of the Cu(Ti)/SiO_2 sample after annealing in ultrahigh vacuum (UHV) at 600 °C for 2 h obtained by XPS wide scans with simultaneous Ar etching (a schematic view of the measurements depicted below the profile) [30]. Ti segregation was observed around etch times between 18,000 and 25,000 s (at the interface), where oxygen and Si atoms were also detected. To identify composition of the Ti-based SFB, XPS narrow scans around the binding energies of Ti 2p, C 1 s, Si 2p, and N 1 s were performed. Portions of the XPS spectra around the binding energies of Ti 2p (460 eV [31, 32]) obtained from the middle of Ti-based SFB (etch time of about 21,600 s) are shown in Fig. 13.9b. They varied with dielectrics and were fitted by the sum of the XPS spectra of TiO/TiC, TiO_2, Ti_2O_3, and a background. Similarly, XPS spectra around the binding energies of C 1 s, Si 2p, and N 1 s were fitted. Based on the fitting,

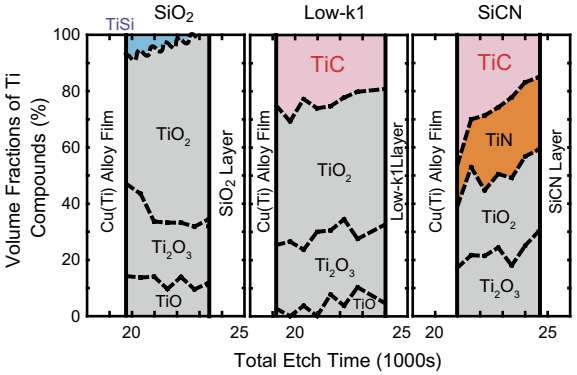

Fig. 13.10 Depth dependence of volume fractions of Ti compounds in the Ti-based SFB formed on the SiO2, low-k1, and SiCN layers after annealing in UHV at 600 °C for 2 h [30] (Copyright 2011 The Japan Society of Applied Physics)

volume fractions of TiC, TiSi, TiN, TiO_2, Ti_2O_3, and TiO phases were determined by a ratio of each peak area to sum of peak areas.

Summary of the results is shown in Fig. 13.10, which is depth dependence of composition of the Ti-based SFB in the annealed Cu(Ti)/dielectrics samples. In the Cu(Ti)/SiO_2 sample, Ti-based SFB mainly consisted of Ti oxides. The Ti oxides were in amorphous state, since crystalline Ti oxides were not detected by TEM/SAD analyses (Fig. 13.8a). A small amount of TiSi was observed in the Cu(Ti)/SiO_2, and its volume fraction increased near the interface between a Cu(Ti) alloy film and Ti-based SFB. Similarly, Ti-based SFBs in the other samples (Low-k1 and SiCN) consisted of a large amount of amorphous Ti oxides (50–75%), as shown in Fig. 13.10. The crystalline TiC was observed in the annealed Cu(Ti)/Low-k1 and Cu(Ti)/SiCN samples. TiN observed in the annealed Cu(Ti)/SiCN sample was in the amorphous state. The volume fractions of a crystalline TiC phase were estimated to be about 20%, and they have occupied a small part of the Ti-based SFB. This is in good agreement with the previous study [29]. The crystalline Ti compounds such as TiC and TiSi tended to form beneath the Cu(Ti) alloy films. Some SAD patterns obtained in Cu(Ti)/Low-k1 and Cu(Ti)/SiCN samples showed the orientation relationship between crystalline TiC and Cu grains (not shown here). This is one of the evidence that TiC formed beneath the Cu(Ti) alloy films. On the other hand, the amorphous phases such as TiO_x tended to form above the dielectric layers. Noted that a small amount of Cu was involved in the Ti-based SFB probably as Cu_2O based on XPS analysis. The set of amorphous Ti-oxide phases were believed to form continuously above the dielectric layers, and play an important role to prevent Cu diffusion into the dielectrics.

13.3.2 Ti-Based SFB Growth Characterized by RBS

The Ti-based SFB was formed by reaction between Ti atoms in Cu(Ti) alloy films and constituent elements such as O, Si, and C in dielectrics. This suggests that the growth of the Ti-based SFB depends on reaction temperature, time, and Ti

concentration in the Cu(Ti) alloy film. To characterize growth mechanism of the Ti-based SFB, its thickness was ordinarily observed by SEM and/or TEM as a function of reaction temperature and time. However, the Ti-based SFB consisted of multiple phases and preparation of many TEM samples due to nm-scale thickness of the Ti-based SFB is complicated. Thus, growth of the Ti-based SFB was characterized using RBS. Figure 13.11 shows principle of the RBS measurement and an example of refinement plots placed upon the RBS spectrum of Cu(Ti)/Low-k1 after annealing at 400 °C for 2 h [33]. The estimated molar amount of Ti atoms (n) is consistent with the molar amount of Ti atoms reacted with dielectrics, which follows the reaction formula:

$$n = Z \cdot \exp(-E/RT) \cdot t^m, \tag{13.1}$$

where Z is a pre-exponential factor and E is the activation energy for the reaction. The value of n is calculated by the following RBS theory [34]. The peak area (A) of an element in an RBS spectrum in the product of the incident beam dose (Q), the number of the element atoms in a unit of area (N), the scattering cross section of the element atom (σ), and the solid angle of the detector (Ω):

$$A = Q \cdot N \cdot \sigma \cdot \Omega. \tag{13.2}$$

The value of n was estimated by dividing N by Avogadro's number of N_A:

$$n(\mathrm{mol/m^2}) = N/N_A = A/(N_A \cdot \sigma \cdot \Omega \cdot Q). \tag{13.3}$$

The Ti peak depicted in Fig. 13.11b, for example, was fitted by a Gaussian curve and an error function, and the A value was determined from the area under the fitted curve. The values of Q, Ω, and σ of Ti atoms were 3.12×10^{13} (10 μC), 3×10^{-3} (steradian), and 6.28×10^{-29} m^2 (0.628 barn), respectively.

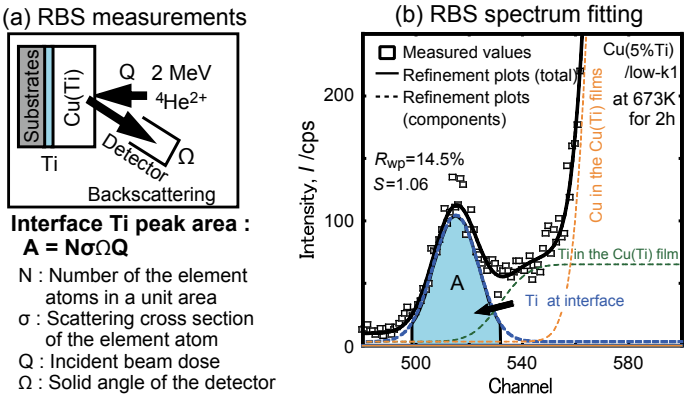

Fig. 13.11 **a** RBS measurement principle and **b** a fitting example of RBS spectrum for Cu(Ti)/Low-k1 after annealing at 400 °C for 2 h [33]

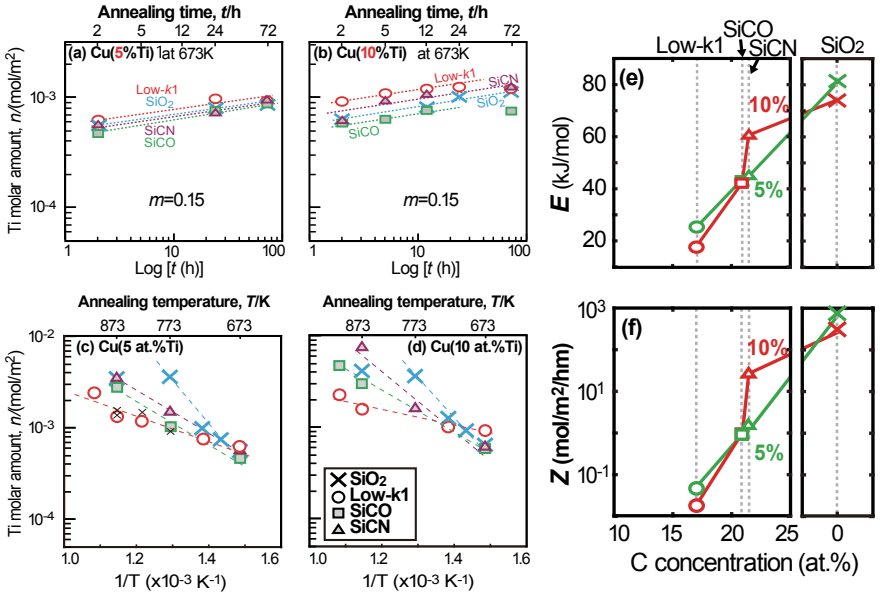

Fig. 13.12 **a**, **b** Plots of log n versus log t for Cu(Ti)/dielectrics after annealing in UHV at 400 °C and **c**, **d** Arrhenius plots of log n versus log $1/T$ for Cu(Ti)/dielectrics after annealing in UHV for 2 h. **e** Activation energies of E and **f** values of Z of the Cu(Ti)/dielectrics after annealing in UHV as a function of C concentration of the dielectrics [33]

Figure 13.12a, b shows plots of log n versus log t for Cu(Ti)/dielectrics with the initial Ti concentrations of 5 at.% and 10 at.%, respectively, after annealing in UHV at 400 °C. Those exhibit the growth behaviors of the Ti-rich SFB. The log n values were found to be proportional to the log t values in all the samples, regardless of the initial Ti concentration in the alloy films or the kinds of dielectric layers. The m values were estimated from the slopes of the log n versus log t lines. They were almost similar for all the samples regardless of the kinds of dielectric layers at each initial Ti concentration in the alloy films. The similar m values suggest that growth of the Ti-rich SFB was controlled by a similar mechanism, suggesting that growth of the Ti-rich SFB is not controlled by lattice diffusion but by grain boundary and/or interface diffusion. Arrhenius plots of log n versus $1/T$ in Cu(Ti)/dielectrics for the initial Ti concentrations of 5 at.% and 10 at.% are shown in Fig. 13.12c and d, respectively. The linear relationship suggests that the formation of the Ti-based SFB was controlled by a thermally activated process. Slopes of the log n versus $1/T$ lines at the initial Ti concentration of 5 at.% and 10 at.% were similar, corresponding to the behaviors indicated in Fig. 13.12a, b. Activation energies, E, were estimated from the slopes of the log n versus $1/T$ lines.

The E values were plotted as a function of C concentration of the dielectric layers in Fig. 13.12e. The E values at the initial Ti concentration of 5 at.%Ti and 10 at.%Ti were similar. The E values for the samples consisting of dielectric layers

containing carbon (except SiO_2) tended to decrease with decreasing C concentration (decreasing k), and those without carbon (SiO_2) were much higher than others. This indicates that the reaction of the Ti atoms in the alloy films with the low-k layers is the most easily thermally activated process. Also, composition of the dielectric layers is suggested to play an important role in the reaction of the Ti atoms with dielectric layers, and the carbon may be a key element to control the reaction. This is similar to the formation rule of Ti compounds (TiC or TiSi) in the Ti-rich interface layers. The pre-exponential factors, Z, were estimated from intercepts of the slopes in the log n versus log t lines (Fig. 13.12a, b) and log n versus $1/T$ lines (Fig. 13.12c, d). The Z values estimated from two different sets of data were the same at each initial Ti concentration and dielectric layer. The Z values of the Cu (Ti)/dielectrics after annealing in UHV were plotted as a function of C concentration of the dielectric layers, which is similar to the E behavior (Fig. 13.12f). The pre-exponential factor shows the frequency with which the Ti atoms meet elemental reactants in the dielectric layers. The frequency was low in the samples with low-k, and was high in the samples with SiO_2. In consequence, coefficients of the reaction rate ($Z \cdot \exp(-E/RT)$) were insensitive to C concentration in the dielectric layers at the initial Ti concentrations of 5 at.% and 10 at.%. These factors lead to the conclusion that growth of the Ti-based SFB is controlled by chemical reactions, represented by the Z and E values, of the Ti atoms with the dielectric layers, although there are few diffusion processes possible in all the samples since the m values suggest that it is controlled by grain boundary and/or interface diffusion. We believe the activation energy relates the chemical bonding energy in the insulator, and Z value relates the frequency that Ti atoms meet elemental reactants such as O, C, and N in the insulators.

13.4 Summary

Surface microstructural modification by FSP is effective and practical for increasing fatigue strength and Charpy absorbed energy of the TIG-welded SS400 plates. What became clear in the research activities are threefold:

1. FSP(L) and FSP(H) produced microstructure beneath the TIG-welded surface, consisting of ultrafine ferrite grains with average grain sizes of about 1.9 μm and 2.6 μm, respectively. Decreasing heat input in FSP provided further grain refinement, and the ferrite grains were surrounded with layers of cementite;
2. TIG+FSP(L) and TIG+FSP(H) specimens exhibited more than 5.0×10^6 cycles and 5.6×10^5 cycles to failure at an applied stress amplitude of 270 MPa, respectively. Those are more than 2000% and about 170% increase in comparison with the number of cycles to failure for the TIG-welded specimens;
3. Charpy absorbed energies for the TIG+FSP(L) and TIG+FSP(H) specimens exhibited about 110 J in the temperature range between −110 and 40 °C, in comparison with about 80 J in the temperature range between −40 and 40 °C

for the TIG-welded specimens. The value at −196 °C of the TIG+FSP(L) specimen exhibited about 50 J, in contrast, that of the TIG+FSP(H) specimen exhibited about 0 J.

Deposition of Cu(Ti) alloy films on dielectrics and annealing at elevated temperature provides a self-formed diffusion barrier as well as an adhesion layer at the interface between the Cu(Ti) alloy film and dielectrics, and the formation was characterized by TEM/SAD for crystalline phases, XPS for amorphous phases, and RBS for growth of the Ti-based SFB. The Ti-based SFB technique can be applied to Cu dual-damascene interconnects. What became clear in the research activities are twofold:

4. XPS analyses showed that the Ti-based SFB consisted of mainly amorphous Ti oxides. Formation of amorphous or crystalline Ti compounds such as TiC, TiN, and TiSi was dependent on the kind of dielectric. Those amounts were lower than that of amorphous Ti oxides;
5. RBS analyses showed that Ti-based SFB growth is controlled by a thermally activated process. The E and Z values decreased with decreasing C concentration in dielectrics, suggesting that the growth is controlled by chemical reactions of Ti atoms with dielectrics.

Acknowledgements This work of functional materials was supported by a Grant-in-Aid for Scientific Research from the Ministry of Education, Culture, Sports, Science and Technology (15206069 & 18360324), the Nanotechnology Program on Cu Thin Films from the New Energy and Industrial Technology Development Organization (NEDO) of Japan, Shorai Foundation for Science and Technology (Ito), and Research Fellowships of the Japan Society for the Promotion of Science for Young Scientists (Kohama). Authors would like to thank M. Murakami, The Ritsumeikan Trust for advices on the whole study, thank K. Ohmori, K. Mori, and K. Maekawa, Renesas Technology Corp., and T. Ohnishi, Kobe Steel Ltd. for Cu dual-damascene interconnects using a Cu(Ti) alloy seed, and thank S. Sonobayashi and H. Sugimura, Department of Materials Science and Engineering, Kyoto University, for XPS measurements.

References

1. K. Anami, C. Miki, Progr. Struct. Eng. Mater. **3**, 86–94 (2001)
2. S. Roy, J.W. Fisher, B.T. Yen, Int. J. Fatigue **25**, 1239–1247 (2003)
3. A. Galtier, E.S. Statnikov, Weld. World **48**, 61–66 (2004)
4. B.N. Mordyuk, G.I. Prokopenko, J. Sound Vib. **308**, 855–866 (2007)
5. W. Ting, W. Dongpo, H. Lixing, Z. Yufeng, Int. J. Fatigue **31**, 644–650 (2009)
6. D. Yin, D. Wang, H. Jing, L. Huo, Mater. Des. **31**, 3299–3307 (2010)
7. X. Zhao, D. Wang, L. Huo, Mater. Des. **32**, 88–96 (2011)
8. A. Abdullah, M. Malaki, A. Eskandari, Mater. Des. **38**, 7–18 (2012)
9. C.M. Branco, V. Infante, R. Baptista, Fatigue Fract. Eng. Mater. Struct. **27**, 785–798 (2004)
10. L. Hacini, N. Van Lê, P. Bocher, Exp. Mech. **49**, 775–783 (2009)
11. R. Simoneau, D. Thibault, J.-L. Fihey, Weld. World **53**, 124–134 (2009)
12. M. Tai, C. Miki, Weld. World **58**, 307–318 (2014)
13. W.B. Lee, G.H. Kim, K.I. Moon, Y. Lee, ISIJ Int. **49**, 1972–1974 (2009)

14. N.A.C. Lah, A. Ali, N. Ismail, L.P. Chai, A.A. Mohamed, Mater. Des. **31**, 312–324 (2010)
15. Y. Sakino, Y. Sano, R. Sumiya, Y.-C. Kim, Sci. Technol. Weld. Join. **17**, 402–407 (2012)
16. C.B. Fuller, M.W. Mahoney, Metall. Mater. Trans. A **37**, 3605–3615 (2006)
17. J. da Silva, J.M. Costa, A. Loureiro, J.M. Ferreira, Mater. Des. **51**, 315–322 (2013)
18. K. Ito, T. Okuda, R. Ueji, H. Fujii, C. Shiga, Mater. Des. **61**, 275–280 (2014)
19. M.T. Bohr, Y.A. El-Mansy, IEEE Trans. Electron. Dev. **45**, 620 (1998)
20. M. Moriyama, M. Shimada, H. Masuda, M. Murakami, Trans. Mater. Res. Soc. Jpn. **29**, 51 (2004)
21. M. Shimada, M. Moriyama, K. Ito, S. Tsukimoto, M. Murakami, J. Vac. Sci. Technol., B **24**, 190 (2006)
22. K. Namba, T. Ishigami, M. Enomoto, S. Kondo, H. Shinriki, D. Jeong, A. Shimizu, N. Saitoh, W.-M. Ki, S. Yamamoto, T. Kawasaki, T. Nakada, N. Kobayashi, in *Proceedings of AMC* (2006), pp. 269
23. H. Wojcik, M. Friedemann, F. Feustelt, M. Albert, S. Ohsiekt, J. Metzgert, J. Voss, J.W. Bartha, C. Wenze, in *Proceedings of IITC* (2007), pp.19
24. D. Jeong, H. Inoue, H. Shinriki, in *Proceedings of IITC* (2008), pp. 95
25. J. Koike, M. Wada, Appl. Phys. Lett. **87**, 041911 (2005)
26. T. Usui, K. Tsumura, H. Nasu, Y. Hayashi, G. Minamihara, H. Toyoda, S. Ito, H. Miyajima, K. Watanabe, M. Shimada, A. Kojima, Y. Uozumi, H. Shibata, in *Proceedings of IITC* (2005), pp. 188
27. S. Tsukimoto, T. Morita, M. Moriyama, K. Ito, M. Murakami, J. Electron. Mater. **34**, 592 (2005)
28. K. Ito, S. Tsukimoto, M. Murakami, Jpn. J. Appl. Phys. **46**, 1942 (2007)
29. K. Kohama, K. Ito, S. Tsukimoto, K. Mori, K. Maekawa, M. Murakami, J. Electron. Mater. **37**, 1148 (2008)
30. K. Kohama, K. Ito, Y. Sonobayashi, K. Ohmori, K. Mori, K. Maekawa, Y. Shirai, M. Murakami, Jpn. J. Appl. Phys. **50**, 04DB03 (2011)
31. A.A. Galuska, J.C. Uht, N. Marquez, J. Vac. Sci. Technol., A **6**, 110–122 (1988)
32. W. Gopel, J.A. Anderson, D. Frankel, M. Jaehnig, K. Phillips, J.A. Schafer, G. Rocker, Surf. Sci. **139**, 333–346 (1984)
33. K. Kohama, K. Ito, K. Mori, K. Maekawa, Y. Shirai, M. Murakami, J. Electron. Mater. **38**, 1913 (2008)
34. W.K. Chu, J.W. Mayer, M.A. Nicolet, *Backscattering Spectrometry* (Academic, San Diego, 1978), pp. 91–92

Chapter 14
Plasma Processes for Functionalization and Control of Materials Surface

Yuichi Setsuhara

Abstract Low-temperature and low-damage processing of materials is required for formation of advanced devices with inorganic/organic hybrid structure, including flexible electronics, photovoltaic cells, and biomaterials. For formation of high-quality organic/inorganic hybrid devices, low-temperature, and low-damage formation of high-quality inorganic functional layers (semiconductor and/or transparent conductive oxide) on organic materials is required and ultra-fine control of interface structure is significant for avoiding considerable degradation of the organic materials. In this chapter, low-temperature and low-damage processes with plasma process technology have been described on the basis of low-damage plasma production with low-inductance antenna (LIA) modules for sustaining inductively coupled radio-frequency discharges, which can provide high-density and low-damage plasmas.

Keywords Plasma process · Low-temperature and low-damage process · Inorganic/organic device · Flexible device · Inductively coupled plasma · Low-inductance antenna

14.1 Introduction

Plasma process technologies, which have been developed intensively and extensively worldwide for more than three decades since last century, have made significant progress as key manufacturing technologies for leading development of a variety of industrial applications [1] ranging from surface modification of materials [2, 3], protective coatings [4, 5] to advanced technologies including flat-panel displays (FPDs) [6], thin-film photovoltaic cells [7], biomaterials [8], and microelectronics [9, 10].

Y. Setsuhara (✉)
Joining and Welding Research Institute, Osaka University, 11-1 Mihogaoka, Ibaraki, Osaka 567-0047, Japan
e-mail: setsuhara@jwri.osaka-u.ac.jp

Y. Setsuhara et al. (eds.), *Novel Structured Metallic and Inorganic Materials*, https://doi.org/10.1007/978-981-13-7611-5_14

New challenges are still in progress to explore novel applications including nanomaterial synthesis and nano precision control of materials surface. In other words, the plasma process technologies have been developed and are developed as key technologies to explore innovations. Especially, low-damage processing of soft materials (polymers, biomaterials) [7] attract great attention for the development of next-generation devices in inorganic/organic hybrid materials, which are expected to offer a wide range of applications including flexible electronics [11] and advanced ULSIs [12]. As a means of low-temperature processes and nanostructure formation, plasma processes are considered as one of the most promising technologies.

For successful development of plasma process technologies for the formation of organic/inorganic hybrid devices, it is significant to avoid unwanted degradation of organic materials due to exposure with ions [13, 14], radicals [15], photons [16], and electrons [17] during plasma processes because the bond-dissociation energies of soft materials are comparatively lower than those of inorganic materials. Among these processes, the plasma process damage due to ion bombardment is closely related to bond-dissociation energies of the organic materials. The bond-dissociation energies are, in general, about 4 eV for the C–CH_3 bond, about 5 eV for the O–C(=O) bond, and about 8 eV for C=O bond [18]. In case of elastic collision of an Ar^+ ion with a carbon atom, it is required to lower the ion energy below $\sim$7 eV in order to avoid bond dissociation of the O–C(=O) bond assuming head-on collision of the Ar^+ ion with the carbon atom [19]. Thus, it is significant to develop plasma process technologies, which can lower ion energy impinging onto the surface during the process.

In order to meet abovementioned requirements, low-damage plasma process technologies have been developed via employing low-inductance antenna (LIA) modules [20] to sustain inductively coupled plasma (ICP), which can provide one of the solutions to realize high-density plasma production with lowered sheath edge potential and active control of power deposition profiles over large area. [19–29] Ion energy distributions measured with a mass-separated ion energy analyzer showed significantly lowered ion energy at the sheath edge as low as 5 eV [27].

In this chapter, low-damage plasma process technologies are described on the basis of plasma production with the LIA modules to sustain radio-frequency inductively coupled discharges, which can provide one of the solutions to realize high-density and low-damage plasma production and active control of power deposition profiles over a large area. Furthermore, the development of low-damage plasma process technology is required for low-temperature formation of high-quality inorganic functional layers on organic materials. As one of the applications gathering intensive attention for flexible electronics, the low-damage plasma source has been applied to low-temperature formation of a-$InGaZnO_4$ (a-IGZO) [30–33] as transparent high-mobility semiconductor material for advanced FPDs via plasma-assisted sputter deposition [34], with which a-IGZO thin-film transistor with mobility as high as 15 $cm^2\ V^{-1}\ s^{-1}$ was successfully formed from the as-deposited a-IGZO layer without post annealing.

14.2 Inductively Coupled RF Plasma for Low-Damage Process

Plasma sources widely employed for materials processing are summarized in Fig. 14.1, in which typical regions of discharge conditions are illustrated in accordance with discharge gas pressure and frequency of the power source. The plasma sources shown in Fig. 14.1 are designated in terms of the discharge regimes. With DC voltage shown in the bottom part of Fig. 14.1, a variety of plasmas can be sustained via DC magnetron, DC arc, and vacuum cathodic arc discharges. With higher frequencies, nonequilibrium plasmas (gas temperature is much less than electron temperature) can be generated at lower gas pressure regions. With increasing gas pressures, thermalization of electrons with heavy particles (gas molecules and ions) tends to elevate gas temperatures to generate the so-called thermal plasmas (gas temperature is equivalent to electron temperature), however, control of discharge generation can avoid the gas heating to generate nonequilibrium plasmas, in which gas temperature is maintained to be much less than the electron temperature, via employing special designs including electrodes to be covered with dielectric materials, selection of gas species, gas flow control, and application of pulse voltage or RF voltage rather than DC voltage. Power sources with frequencies as high as the radio frequency (RF) are widely used for sustaining RF magnetron plasma, capacitively coupled plasma (CCP), and inductively coupled plasma (ICP). The RF power sources are also used to generate thermal plasmas at higher pressure regions through inductive coupling. Microwave power sources are employed to produce electron cyclotron resonance (ECR) plasma and surface wave plasma (SWP). The microwave power sources can also be used for the production of thermal plasmas and microplasmas.

Among the variety of the plasma sources, the ICP can be generated by applying RF current at frequencies of 0.1–100 MHz to antenna conductor [1, 10]. Inductive

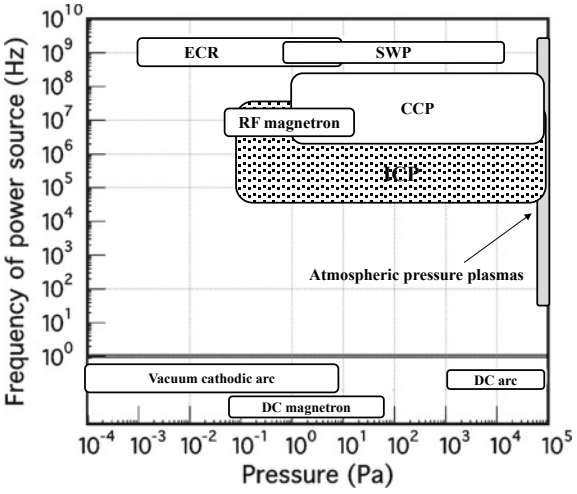

Fig. 14.1 Plasma sources widely employed for materials processing

electric field $\boldsymbol{E}_{\mathrm{ind}}$ is induced by sinusoidal temporal variation of RF magnetic field $\boldsymbol{B}_{\mathrm{rf}}$ via RF current, following the Faraday's law of induction (rot $\boldsymbol{E}_{\mathrm{ind}} = -\partial \boldsymbol{B}_{\mathrm{rf}}/\partial t$) and the inductive electric field accelerates electrons to sustain discharge. The vector differential equation implies that (a) the electric field induced by the RF antenna conductor is in parallel along the antenna conductor and (b) the strength of the induced electric field is in proportion to the amplitude of the RF current and the frequency of the RF current.

Typical plasma density (electron density or ion density) of ICP is in the range of 10^{10}–10^{12} cm^{-3}, which is one or two orders of magnitude higher than that in capacitively coupled RF plasmas (CCP), in gas pressures in the range of 10^{-1}–10^{3} Pa. In these typical discharge conditions, the electron temperature is much higher than gas temperature, and thus, the ICPs generated in low-pressure regions are in non-equilibrium state. Whereas, the ICPs sustained at higher pressures tend to be thermalized to attain thermal equilibrium with increasing pressure.

An electrical circuit representation of ICP antenna and schematic illustrations of RF voltage distribution along the antenna are shown in Fig. 14.2. When a sinusoidal RF current I_{rf} is applied to the ICP antenna with an inductance L, the RF voltage arising at the power end of the antenna V_1 is given by $V_1 = \omega L I_{\mathrm{rf}}$, where ω is an angular frequency of the RF current. Assuming that the RF current leakage to the plasma is neglected, the RF voltage may be linearly distributed along the antenna electrode as schematically illustrated in Fig. 14.2. Here, it is noted out that the RF voltage is always present at the powered end of the antenna, and thus, the electrostatic coupling of the RF voltage to the plasma is always present in the generation of ICPs.

Reduction of the electrostatic coupling of RF antenna voltages to the plasma is of great importance for ICP generation with lowered plasma potential, which is significant for low-damage high-quality processing of materials. Furthermore,

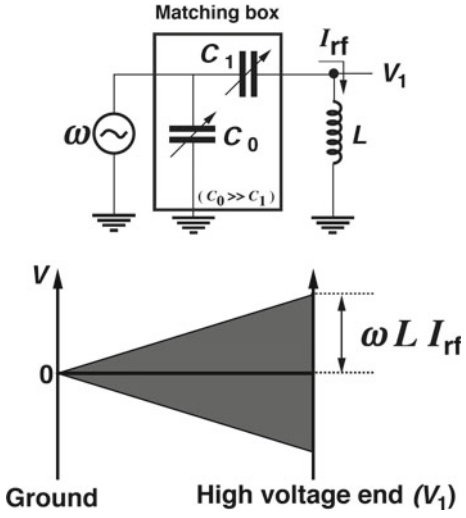

Fig. 14.2 Electrical circuit representation of ICP antenna and RF voltage distribution along the antenna

considering the plasma source designs to satisfy the requirement for enlargement of plasma sources toward a meter scale, increase of an antenna inductance, and hence increase of an RF voltage amplitude arising at the antenna terminals cannot be avoided with increasing source size, when the source employs a large loop-shaped antenna.

Feasibility of high-density plasma production with suppressed electrostatic coupling by lowering the RF voltage of the internal antenna has been demonstrated via (a) the employment of antenna configurations with lowered antenna inductance, which is roughly proportional to the square of turn numbers and the area size of the loop, (b) lowering of the RF voltage amplitude by the antenna termination with a blocking capacitor, and (c) dielectric isolation of the antenna conductor from plasma [20]. As a novel technology to achieve low-voltage operation of ICPs suitable for producing large area source with low-damage process capability, an internal antenna configuration with multiple "low-inductance antenna (LIA) module", as schematically shown in Fig. 14.3, was proposed [20]. The ICP production using the LIA modules exhibited stable production of plasmas at RF input powers of 3 kW to attain densities approaching as high as 1×10^{12} cm^{-3} at argon pressures around 1 Pa with a simultaneous achievement of the suppression of the electrostatic coupling [20].

Furthermore, the lowering of the electrostatic RF voltage via a reduction in the antenna inductance for sustaining ICPs has exhibited additional favorable features for low-damage plasma processes via low-voltage operations of ICPs. The ion energy distribution function (IEDF) attained in an ICP sustained with LIA at Ar at a pressure of 13 Pa and with 13.56-MHz RF power of 1 kW is shown in Fig. 14.4, together with a typical IEDF for conventional RF plasma source (CCP mode with

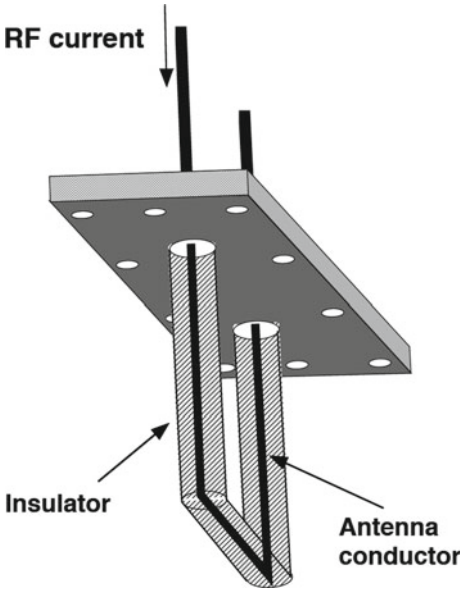

Fig. 14.3 Schematic illustration of low-inductance antenna

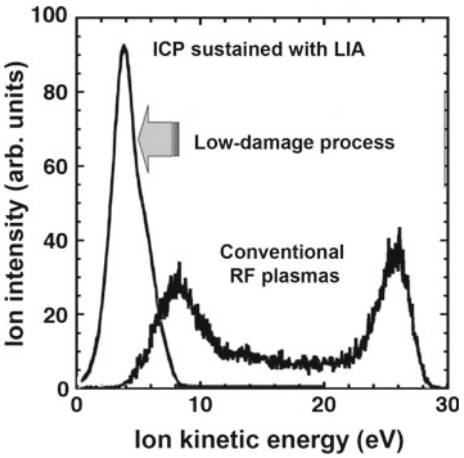

Fig. 14.4 Ion energy distribution function (IEDF) measured in an ICP sustained with LIA modules in Ar gas at a pressure of 13 Pa and with 13.56-MHz RF power of 1 kW with typical IEDF for conventional RF plasma source (CCP mode with large potential fluctuation) for comparison

larger potential fluctuation) for comparison. The peak ion energy in the IEDF for the ICP sustained with the LIAs shows significantly lowered as being equivalent to or less than 5 eV in comparison with conventional RF plasma sources. Moreover, the IEDF for the ICP sustained with the LIA showed a very narrow energy width of about 2 eV, which is significantly narrower than that for the conventional RF plasma sources.

14.3 Plasma Interactions with Organic Materials

In this section, the effects of argon plasma exposure onto the surface of soft materials are described on the basis of chemical bonding states analysis via conventional X-ray photoelectron spectroscopy (XPS) [19]. Polyethylene terephthalate (PET) film has been selected as a test material for investigations in the present study not because of its specific applications, such as a substrate material, but because PET is one of the well-defined organic materials containing a variety of major components in a variety of functional soft materials; C–C main chain, CH bond, oxygen functionalities (O=C–O bond and C–O bond), and phenyl group. Especially, changes in the phenyl group due to argon plasma exposures have been investigated in the present article in order to examine plasma interactions with π-conjugated component, which is in charge of electronic functions in many of the π-conjugated electronic organic materials to be utilized as a functional layer for advanced flexible device applications.

Argon plasmas for this investigation were generated in a plasma chamber with a 500-mm inner diameter and 200-mm height, which was connected to a diffusion chamber with a 500 mm inner diameter and a 400 mm height, as previously reported elsewhere [19–21]. The LIA modules consisted of a U-shaped antenna conductor, which was fully covered with dielectric tubing for complete isolation

from the plasma. Eight LIA modules with a 70 mm width and a 160 mm height were mounted on the top flange of the chamber and were coupled to an RF power generator at 13.56 MHz via a matching network. A water-cooled substrate holder was placed at a distance of 297 mm from the top flange. The base pressure of the chamber evacuated with a turbo-molecular pump was 3×10^{-4} Pa.

Ion energy distribution function (IEDF) of the ions impinging onto the ground potential from the plasmas was measured using a mass-separated ion energy analyzer (Hiden, EQP500), which was mounted beside the substrate holder [27].

For investigations of the plasma–polymer interactions, PET films (0.1 mm thick) were exposed to argon plasmas sustained at an RF power of 1000 W at Ar pressures of 0.67–26 Pa. Here, it is noted that the PET films were set on water-cooled substrate holder when they were exposed to the plasmas.

Chemical bonding states at nanosurface layer of the PET films exposed to argon plasmas were analyzed using conventional XPS. The XPS analysis was performed using AXIS-165x spectrometer (SHIMADZU Corp., JAPAN) with non-monochromatized MgKa radiation (photon energy of 1253.6 eV). The conventional XPS analyses were carried out directly after plasma exposure without the formation of any additional conductive coating on the sample surface due to charging suppression function of the spectrometer. Here, it is also noted that the PET samples were taken out to the air after the plasma exposure before the XPS measurements.

Before the plasma exposure experiment, the IEDF of the argon ions impinging to the ground potential through the sheath edge of the argon plasmas were measured using the mass-separated ion energy analyzer. Peak values of ion energy distributions decreased from 15 eV to 6 eV with increasing Ar pressure from 0.67 Pa to 26.6 Pa (15 eV at 0.67 Pa, 13 eV at 1.3 Pa, 9 eV at 6.5 Pa, 7 eV at 13 Pa, and 6 eV at 26 Pa) [29]. Furthermore, the ion bombardment energy onto nonconductive substrate (the PET film in the present investigation) is almost equivalent to the potential drop from plasma potential to the floating potential. As reported in the previous work, the potential drop of argon plasma was in the range of 3–15 eV for Ar pressures of 0.26–13 Pa (15 eV at 0.26 Pa, 8 eV at 1.3 Pa, and 3 eV at 13 Pa) [29].

Chemical bonding states of the PET films exposed to argon plasmas were examined via conventional XPS. The PET films were exposed to argon plasmas sustained at an RF power of 1000 W and argon pressures of 0.67 Pa–26 Pa with an ion dose of 4.3 x 10^{18} ions/cm^2. The photoelectron C1s spectra for PET films without and with exposure to argon plasmas with a variation of argon pressures are shown in Fig. 14.5. The C1s spectra of the PET samples can be deconvoluted into following components; C–C bond at 284.6 eV, C–O bond at 286.1 eV, C=O bond at 287.4 eV, O=C–O bond at 288.6 eV, and π–π* shake-up satellite at 291.2 eV [19].

The C1s XPS spectra show that the exposure with the argon plasmas tended to degrade the O=C–O bond and the C–O bond with a slight increase of the C=O bond with decreasing argon pressure (i.e., increasing ion energy) [19, 29]. These tendencies of the variation of the chemical bonding states indicate that the scissions of the O=C–O bond and the C–O bond are significantly enhanced by increasing energy of the ion bombardment and the scission of the O=C–O bond may result in

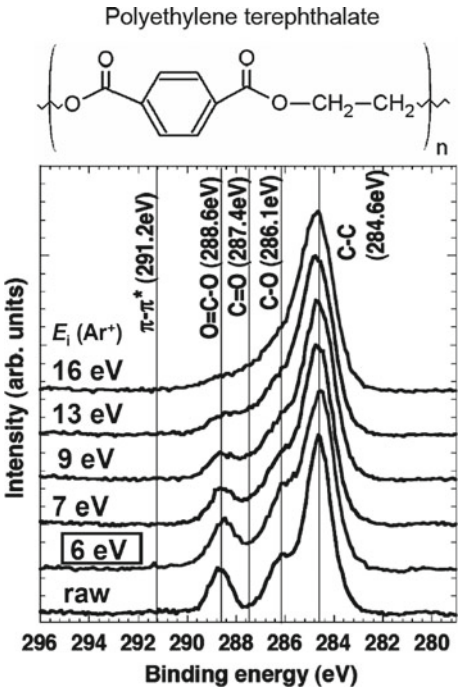

Fig. 14.5 Photoelectron C1s spectra for PET films before and after exposure to argon plasmas with a variation of argon pressures (or ion bombardment energy)

formation of the C=O bond. Here, it is noted that the raw PET sample before the plasma exposure shows that the photoelectron component corresponding to the C=O bond is insignificant because the carbon atom with an oxygen double bond (C=O) is bonded also with another neighbor oxygen atom via single bond and a carbon atom in the pristine molecule of the PET material, thus the photoelectron corresponding to the C=O bond is not present in the pristine PET. Thus, the slight increase in the C=O bond component with increasing ion energy is considered to be due to the bond scission of O=C–O structure to form the C=O bond with a dangling bond.

Additionally, it is remarkable to stress here that the degradation of the oxygen functionalities (the O=C–O bond and the C–O bond) during the plasma exposure at 26 Pa was insignificant, indicating that the suppression of the plasma process damage may be feasible via controlling the ion bombardment energy below $\sim$6 eV during plasma processing of polymers as previously reported elsewhere [19, 29].

Furthermore, in order to examine the effect of the argon plasma exposure on the phenyl group, which is considered to be one of the essential components in a variety of functional organic molecules especially for electronic functions, the C1s XPS spectra to highlight the phenyl group ($\pi \rightarrow \pi^*$ shake-up satellite peak) are shown in Fig. 14.6, in which the spectra in Fig. 14.5 are expanded vertically in the intensities with the C-C bond intensity normalized. Peak–area ratio of $\pi \rightarrow \pi^*$ shake-up satellite peak to C-C bond ($I_{\pi\rightarrow\pi^*}/I_{C-C}$) evaluated from the XPS C1s spectra are summarized in Fig. 14.7 as a function of the peak ion energy measured

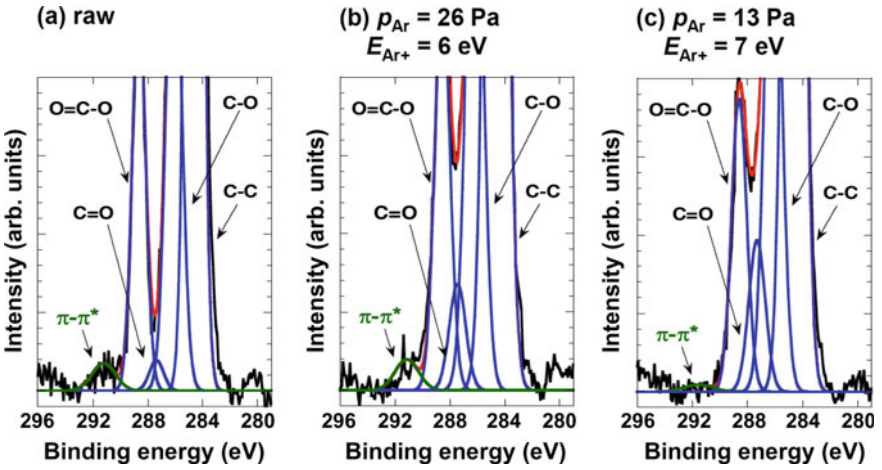

Fig. 14.6 XPS C1s spectra to highlight the phenyl group for PET films; **a** without plasma exposure and with exposure to argon plasmas sustained at an RF 1000 W at argon pressure of **b** 26 Pa and **c** 13 Pa

with the mass-separated ion energy analyzer. The π → π* shake-up satellite peak intensity clearly decreased after the plasma exposure with ion bombardment energy above 6–7 eV.

These results indicate that it is possible to prevent the degradation of C–O bond, O=C–O bond and phenyl group via controlling argon pressure to suppress the ion energy less than 6 eV as previously reported elsewhere [19, 29]. Furthermore, Here it should be stressed that exhibition of the remarkable variation in the peak–area ratio of π → π* shake-up satellite peak to C–C bond as shown in Fig. 14.7 is considered to be due to extremely narrow energy width in the IEDF of approximately 2 eV in the present plasmas sustained with the LIAs. This means that significantly fine control of bond dissociation can be feasible with the present plasma technology, which can control the IEDF with very narrow width due to low-voltage operation of ICPs.

These findings described above indicate that it is significant to control the ion bombardment energy or the ion energy distributions sufficiently below the threshold

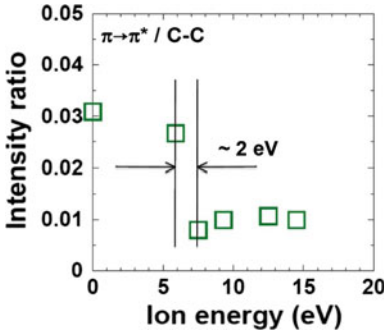

Fig. 14.7 Variation of the peak–area ratio of π → π* shake-up satellite peak to C–C bond ($I_{\pi\rightarrow\pi^*}/I_{C-C}$) evaluated from the XPS C1s spectra

value, which may provide advanced process technology to realize "bond engineering" of the organic molecules of interest for the development of advanced flexible devices.

14.4 Summary

In this chapter, plasma-process technologies for low-damage processing of materials were described on the basis of plasma production with low-inductance antenna (LIA) modules to sustain ICPs. The design issues and basic background involved in the plasma sources were briefly reviewed and feasibility of low-damage plasma sources were shown for the ICPs sustained with the LIAs. The interactions between argon plasmas and the PET films were examined for investigations of physical damages induced by plasma exposures to the organic material via chemical bonding-state analyses via conventional XPS. The results indicate that it is significant to control the ion bombardment energy or the ion energy distributions sufficiently below the threshold value of interest, for development of successful processing of soft materials, especially for development of advanced flexible devices via formation of the structure with inorganic functional layers and/or electrodes to be stacked on organic functional materials as functional layers.

References

1. H. Conrads, M. Schmidt, Plasma Sources Sci. Technol. **9**, 441 (2000)
2. T. CzerwiecU, N. Renevier, H. Michel, Surf. Coatings Technol. **131**, 267 (2000)
3. P.H. Mayrhofer, C. Mitterer, L. Hultman, H. Clemens, Progress in Materials Sci. **51**, 1032 (2006)
4. J. Robertson, Surf. Coatings Technol. **50**, 185 (1992)
5. B. Bhushan, Diam. Relat. Mater. **8**, 1985 (1999)
6. Y. Kuo, J. Electrochem. Soc. **142**, 2486 (1995)
7. A. Goetzbergera, C. Heblinga, H.-W. Schock, Mat. Sci. Eng. R **40**, 1 (2003)
8. P.K. Chua, J.Y. Chena, L.P. Wanga, N. Huang, Mat. Sci. Eng. R **36**, 143 (2002)
9. C.J. Mogab, A.C. Adams, D.L. Flamm, J. Appl. Phys. **49**, 3796 (1978)
10. M.A. Lieberman, A.J. Lichtenberg, *Principles of Plasma Discharges and Materials Processing* (Wiley, New York, 1994)
11. M.-C. Choi, Y. Kim, C.-S. Ha, Prog. Polym. Sci. **33**, 581 (2008)
12. International Technology Roadmap for Semiconductors, 2007 edition, Executive Summary
13. I. Gancarz, G. Pozniak, M. Bryjak, Eur. Polym. J. **35**, 1419 (1999)
14. Y. Setsuhara, K. Cho, M. Shiratani, M. Sekine, M. Hori, E. Ikenaga, S. Zaima, Thin Sold Films **518**, 3555 (2010)
15. T. Steckenreiter, E. Balanzat, H. Fuess, C. Trautmann, Nucl. Instr. Meth. Phys. Res. B **131**, 159 (1997)
16. M. Day, D.M. Willes, J. Appl. Polymer Sci. **16**, 203 (1972)
17. S. Masseya, P. Cloutierb, L. Sancheb, D. Roy, Rad. Phys. Chem. **77**, 889 (2008)
18. S.I. Stoliarov, P.R. Westmoreland, M.R. Nyden, G.P. Forney, Polym. **44**, 883 (2003)

19. Y. Setsuhara, K. Cho, K. Takenaka, M. Shiratani, M. Sekine, M. Hori, Thin Solid Films **519**, 6721 (2011)
20. Y. Setsuhara, T. Shoji, A. Ebe, S. Baba, N. Yamamoto, K. Takahashi, K. Ono, S. Miyake, Surf. Coat. Technol. **174–175**, 33 (2003)
21. K. Takenaka, Y. Setsuhara, K. Nishisaka, A. Ebe, Jpn. J. Appl. Phys. **45**, 8046 (2006)
22. O. Tsuda, M. Ishihara, Y. Koga, S. Fujiwara, Y. Setsuhara, N. Sato, J. Phys. Chem. B **109**, 4917 (2005)
23. H. Deguchi, H. Yoneda, K. Kato, K. Kubota, T. Hayashi, K. Ogata, A. Ebe, K. Takenaka, Y. Setsuhara, Jpn. J. Appl. Phys. **45**, 8042 (2006)
24. Y. Setsuhara, K. Takenaka, A. Ebe, K. Nishisaka, Solid State Phenom. **127**, 239 (2007)
25. Y. Setsuhara, K. Takenaka, A. Ebe, K. Nishisaka, Plasma Process. Polym. **4**, S628 (2007)
26. Y. Setsuhara, K. Takenaka, A. Ebe, J.G. Han, Surf. Coat. Technol. **202**, 5230 (2008)
27. K. Takenaka, Y. Setsuhara, K. Nishisaka, A. Ebe, Jpn. J. Appl. Phys. **47**, 6900 (2008)
28. E. Takahashi, Y. Nishigami, A. Tomyo, M. Fujiwara, H. Kaki, K. Kubota, T. Hayashi, K. Ogata, A. Ebe, Y. Setsuhara, Jpn. J. Appl. Phys. **46**, 1280 (2007)
29. Y. Setsuhara, K. Cho, M. Shiratani, M. Sekine, M. Hori, Thin Sold Films **518**, 6492 (2010)
30. K. Nomura, H. Ohta, A. Takagi, T. Kamiya, M. Hirano, H. Hosono, Nature **432**, 488 (2004)
31. K. Nomura, T. Kamiya, H. Ohta, M. Hirano, H. Hosono, Appl. Phys. Lett. **93**, 192107 (2008)
32. H. Hosono, K. Nomura, Y. Ogo, T. Uruga, T. Kamiya, J. Non-Cryst, Sol. **354**, 2796 (2008)
33. T. Kamiya, K. Nomura, H. Hosono, Sci. Technol. Adv. Mater. **11**, 044305 (2010)
34. K. Takenaka, K. Nakata, H. Otani, S. Osaki, G. Uchida, Y. Setsuhara, Jpn. J. Appl. Phys. **55**, 01AA18 (2016)

Chapter 15
Laser-Induced Processes for Functionalization of Materials Surface

Masahiro Tsukamoto

Abstract Femtosecond laser-induced process, periodic nanostructures formation, for the creation of new functions on a titanium dioxide (TiO_2) film is reviewed in this chapter. It has recently been reported that coating a TiO_2 film on Ti plates may improve the biocompatibility of Ti. The periodic nanostructures have useful effects on the control of cell spreading. The scanning of femtosecond laser at wavelengths of 388 and 775 nm successfully produces periodic nanostructures on TiO_2 film through the laser ablation process. The periodicity of nanostructures formed with those wavelengths are calculated using the surface plasmon polariton (SPP) model. The experimental results with those wavelengths were in the ranges of the calculated period, respectively. This suggests that the mechanism for the formation of periodic nanostructures on TiO_2 film by femtosecond laser irradiation is due to the excitation of SPPs.

Keywords Femtosecond laser · Periodic nanostructures · Cell spreading · Surface plasmon polariton

15.1 Introduction

15.1.1 Materials Surface for Cell Spreading

Titanium (Ti) is an attractive biomaterial because of its excellent chemical resistance and high strength. However, Ti has problems for long-term applications and biofunction [1]; therefore, its biocompatibility must be improved. It has recently been suggested that coating a titanium dioxide (TiO_2) film on Ti plates may improve the biocompatibility of Ti [2–4]. A method for coating a TiO_2 film on Ti plate using an aerosol beam has been developed [5, 6]. The beam is composed

M. Tsukamoto (✉)
Joining and Welding Research Institute, Osaka University, 11-1 Mihogaoka, Ibaraki, Osaka 567-0047, Japan
e-mail: tukamoto@jwri.osaka-u.ac.jp

Y. Setsuhara et al. (eds.), *Novel Structured Metallic and Inorganic Materials*, https://doi.org/10.1007/978-981-13-7611-5_15

of submicron-sized functional ceramic particles and helium gas. The thickness of the film can be controlled to approximately several micrometers.

Controlling the cell spreading on biomaterials is another useful method to improve the biocompatibility of Ti plates [7]. Increasing endothelial cell functions [7], anisotropic morphogenesis of bone tissue [8] and control of differentiation [9] have been achieved for biomaterials by the control of cell spreading. Thus, the control of cell spreading on biomaterials is important for the development of advanced biomaterials. The formation of periodic nanostructures on biomaterials is a useful method for the control of cell spreading [7, 9, 10].

15.1.2 Periodic Nanostructures Formation with Femtosecond Lasers

Femtosecond lasers can be used to form periodic nanostructures on metals [11–14], semiconductors [15–24], and inside transparent materials [25, 26]. Periodic nanostructures are self-organized on the laser focal spot. The nanostructure period is dependent on the wavelength of the femtosecond laser. The directions of the grooves of periodic nanostructures lie perpendicular to the laser electric polarization vector. It has already been reported that periodic nanostructures perpendicular to the laser electric polarization vector were formed on TiO_2 films with a femtosecond laser using the fundamental wavelength of 775 nm [21]. The period of these nanostructures was approximately 230 nm, which is much shorter than the laser wavelength. Cell testing revealed that cells spread along the grooves of the periodic (230 nm) nanostructures, whereas cell spreading did not have a definite direction on a film without periodic nanostructures [21]. The effect of the nanostructure period on cell spreading has been investigated [27].

15.1.3 Mechanism Proposed for Periodic Nanostructures Formation

The mechanism for the formation of periodic nanostructures on the film should be investigated. Various mechanisms have been proposed for the formation of periodic nanostructures, such as second-harmonic generation [15, 17], self-organization due to nonequilibrium surface [22], formation of nanoplasma [23], and a refractive index change during femtosecond laser irradiation [24]. For semiconductors, the period of the nanostructures is much shorter than the laser wavelength. However, there is no mechanism applicable to the formation of periodic nanostructures comprised of different materials. Recently, it was reported that the formation of periodic nanostructures with a femtosecond laser can be attributed to the excitation of surface plasmon polaritons (SPPs) in the glassy carbon layer formed on a diamond-like carbon (DLC) surface [18]. Calculations using the SPP model

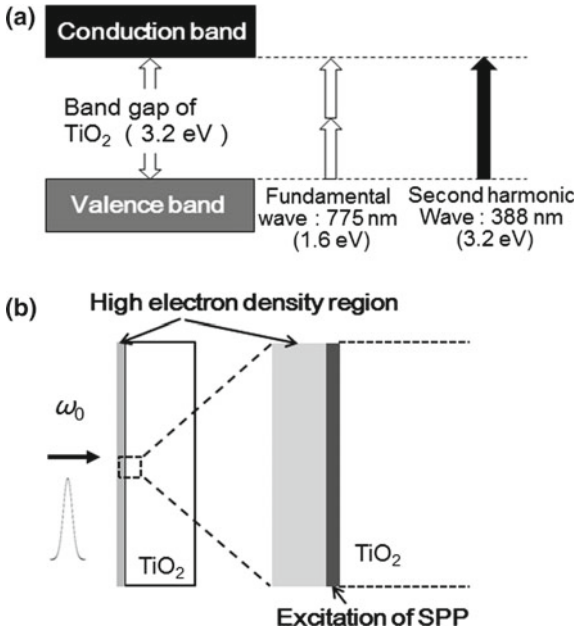

Fig. 15.1 **a** Multiphoton process in a TiO_2 film with femtosecond lasers with wavelengths of 775 and 388 nm, respectively. **b** Formation of high electron density region on the film surface and excitation of SPP interface between high electron density region and the film

reproduced the observed nanosize periodicity. The SPP model can also be applied for periodic nanostructures formed on Si [19] and GaN [20]. It was suggested that a multiphoton process may occur on a TiO_2 film (TiO_2 band gap of 3.2 eV) during femtosecond laser irradiation with a wavelength of 775 nm (photon energy of 1.6 eV) [28, 29], as shown in Fig. 15.1a. Thus, a high electron density region could be formed in the film, as shown in Fig. 15.1b. SPPs may be excited at the interface between the high electron density region and the film, as shown in Fig. 15.1b. SPPs may also be excited by femtosecond laser irradiation with a wavelength of 388 nm (photon energy is 3.2 eV) because electrons could be excited by a one-photon process, as shown in Fig. 15.1a. Hence, periodic nanostructures could also be formed on a film using a femtosecond laser with a wavelength of 388 nm. Calculation of the periods with different laser wavelengths, 775 and 388 nm, using the SPP model has been investigated as Sect. 15.2 shows.

15.2 Surface Plasmon Polaritons Model

Multi- or one-photon processes may occur in the film by femtosecond laser irradiation at wavelengths of 775 and 388 nm, respectively (Fig. 15.1a). The incident femtosecond laser pulse produces a high electron density region in the film, as shown in Fig. 15.1b. Using the Drude model for electrical conduction, the relative refractive index of the high electron density region in the film is calculated as

$$\varepsilon_{\text{high}} = \varepsilon_{\text{TiO2}} - \frac{\omega_{\text{pb}}^2}{\omega_0^2 + i\omega_0/\tau}, \tag{16.1}$$

where $\varepsilon_{\text{high}}$ is the relative dielectric constant of the high electron density region in the film, $\varepsilon_{\text{TiO2}}$ is the relative dielectric constant of TiO_2, ω_{pb} is the plasma frequency with the dielectric constant of a vacuum, ω_0 is the incident light frequency in a vacuum, and τ is the Drude damping time for free electrons. The plasma frequency ω_{pb} is calculated using

$$\omega_{\text{pb}}^2 = \frac{\text{Ne}^2}{\varepsilon_0 \text{m} * \text{m}}, \tag{16.2}$$

where N is the electron density, ε_0 is the dielectric constant of a vacuum, e is the electron charge, m is the electron mass, and m^* is the optical effective mass for carriers [30].

When the dispersion relation is satisfied [31], the SPPs can be excited at the interface between the high electron density region and the film:

$$\text{k}_{\text{SPP}} = \text{k}_0 \left(\frac{\varepsilon_{\text{high}} \varepsilon_{\text{TiO2}}}{\varepsilon_{\text{high}} + \varepsilon_{\text{TiO2}}} \right)^{1/2}, \tag{16.3}$$

where k_{SPP} is the plasmon wave number, k_0 is the wavenumber of the incident light in a vacuum. The optical near-field in the interface is enhanced along the laser polarization direction, at the half SPP wavelength, due to the spatial standing wave of SPPs [18–20]. The nanostructure period may thus correspond to half of the SPP wavelength [18–20]. The SPP wavelength is calculated as

$$\lambda_{\text{SPP}} = \frac{2\pi}{\text{Re}\{\text{k}_{\text{SPP}}\}}, \tag{16.4}$$

where $\text{Re}\{k_{SPP}\}$ is the real part of k_{SPP}. The nanostructure periodicity in the film, d_{TiO2}, is calculated as $d_{TiO2} = \lambda_{SPP}/2$. The relative dielectric constant of TiO_2 for a wavelength of 775 nm, ε_{TiO2} (775 nm) = 7.83 + 0.45i [32] and the relative dielectric constant of TiO_2 for a wavelength of 388 nm, ε_{TiO2} (388 nm) = 12.18 [32], were used in the calculation of k_{SPP}. In addition, m^* = 0.8 [33] and τ = 1 fs [30] were used for both wavelengths of 775 and 388 nm.

Figure 15.2a shows the period $d_{TiO2} = \lambda_{SPP}/2$ of the nanostructures produced by femtosecond laser irradiation at 775 nm and the real part of the relative dielectric constant of the high electron density region $\text{Re}\{\varepsilon_{\text{high}}\}$ calculated as a function of electron density. The condition of $\text{Re}\{\varepsilon_{\text{high}}\} < 0$ must be satisfied for the excitation of SPPs [31], which is indicated by the shaded region of $N > 1.4 \times 10^{22}$ cm^{-3} shown in Fig. 15.2a. The calculated periods with the wavelength of 775 nm are in the range from 120 to 260 nm, as shown in Fig. 15.2a. For the wavelength of 338 nm, the period and the real part of relative dielectric constant of the high

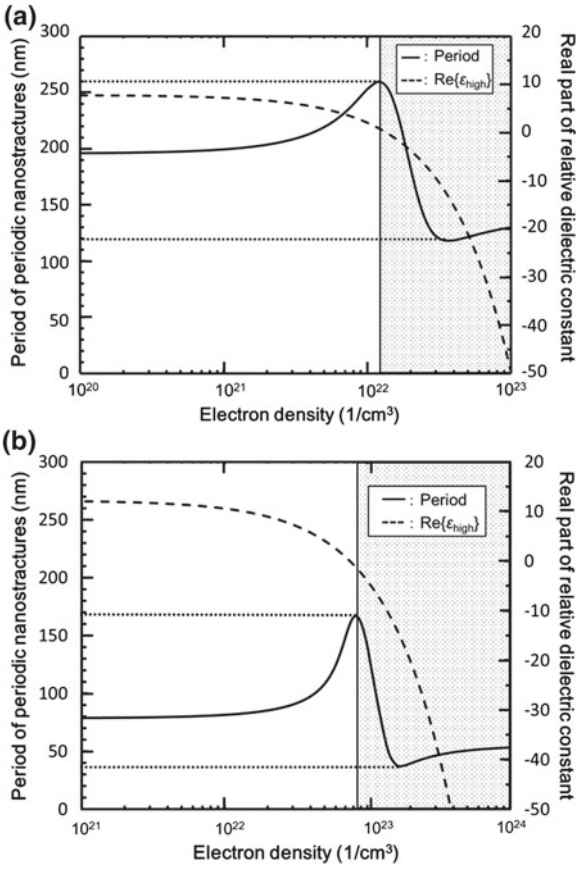

Fig. 15.2 **a** Periods of the periodic nanostructures with the femtosecond laser whose wavelength of 775 nm and real part of the relative dielectric constant of high electron density region ε_{high} calculated as a function of N electron density. **b** Periods of the periodic nanostructures with the femtosecond laser whose wavelength of 388 nm and real part of the relative dielectric constant of high electron density region ε_{high} calculated as a function of N electron density

electron density region were also calculated as a function of electron density, and are shown in Fig. 15.2b. The condition of $\mathrm{Re}\{\varepsilon_{high}\} < 0$ must be satisfied for the excitation of SPPs, which is indicated by the shaded region of $N > 7.6 \times 10^{22}$ cm^{-3} shown in Fig. 15.2b. The calculated periods for a wavelength of 388 nm are in the range from 40 to 170 nm, as shown in Fig. 15.2b.

15.3 Femtosecond Laser-Induced Periodic Nanostructures on TiO_2 Film

Periodic nanostructures were produced on a TiO_2 film by irradiation with a femtosecond laser at wavelengths of 388 and 775 nm. The irradiated area was then observed using scanning electron microscopy (SEM) and the periodicity of the nanostructures was examined. The period was calculated for the different wavelengths using the SPP model described above to assess the validity of the SPP model for the formation of periodic nanostructures on TiO_2 films.

15.3.1 Methods for Formation of Periodic Nanostructures on TiO_2 Film

The TiO_2 film was produced on a pure Ti plate by aerosol beam irradiation [5, 6]. An aerosol beam was formed by mixing TiO_2 particles and helium gas. The diameters of the TiO_2 particles were between 100 and 1000 nm. The particles were accelerated by the helium gas flow to velocities of several hundred meters per second. Impact of the particles with the substrate resulted in film deposition on the substrate. The thickness of the resultant film was approximately 5 μm.

Schematic diagrams of femtosecond laser irradiation and the scanning direction are shown in Fig. 15.3a and b, respectively. A commercial femtosecond Ti:sapphire laser system was employed and is based on the chirped pulse amplification technique. The wavelength, pulse duration, repetition rate and beam diameter for the femtosecond laser were 775 nm, 150 fs, 1 kHz, and about 5 mm, respectively. The laser wavelength of 388 nm was obtained with a harmonic generator. The laser beam was focused on the film surface using a lens with a focal length of 100 mm. The Gaussian laser beam had a diameter of 60 μm (at the $1/e^2$ intensity points) on the film surface. The femtosecond laser focal spot was scanned over the film surface using an XY stage to form periodic nanostructures, as shown in Fig. 15.3b. The scanning speed was fixed at 0.1 mm/s. Laser fluences with wavelengths of 388 and 775 nm were 0.25 and 0.35 J/cm^2, respectively. The periodicities of the nanostructures formed on the film were examined using SEM. The periodicity was calculated according to the SPP model.

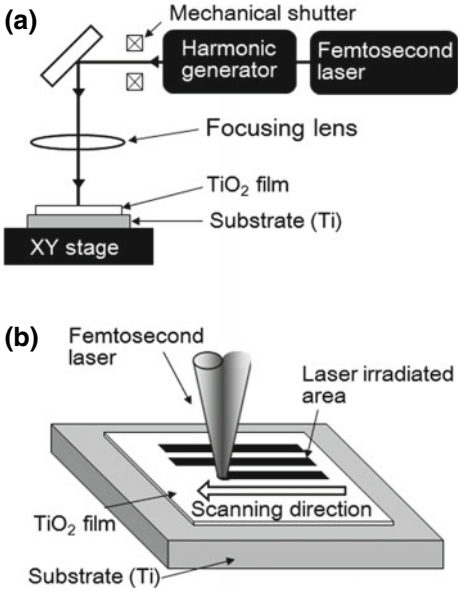

Fig. 15.3 **a** Schematic diagram of the experimental setup for femtosecond laser irradiation and **b** scanning direction of the femtosecond laser focusing spot

15.3.2 Periodic Nanostructures Formation on TiO_2 Films

Figure 15.4a shows an SEM image of the bare film surface (no laser irradiation). SEM images of the film surface after scanning of the femtosecond laser spot at wavelengths of 388 and 775 nm are shown in Fig. 15.4b and c, respectively. Figure 15.4b, c show laser irradiated area in the center region. No periodic nanostructures were observed on the nonirradiated film surface, whereas periodic nanostructures lying perpendicular to the laser electric polarization vector E, were formed on the area irradiated with the laser at a wavelength of 388 nm (Fig. 15.4b). Periodic nanostructures were also formed on the area irradiated at a wavelength of 775 nm (Fig. 15.4c).

The periodicity of the nanostructures shown in Fig. 15.4b, c were examined as a function of the laser wavelengths and the results are shown in Fig. 15.5. The period of the nanostructures on the film was increased from 130 to 230 nm as the laser wavelength was increased from 388 and 775 nm. These periods with 130 and 230 nm were average values from SEM measurement. The standard deviation of the period with approximately 130 and 230 nm is about 10 and 10 nm, respectively. Thus, the nanostructure period on the film was 30% of the femtosecond laser wavelength. Figures 15.2a and 15.5 show that the experimental result of approximately 230 nm is in the range of the calculated period for a wavelength of 775 nm. The experimental result of approximately 130 nm is in the range of the calculated period for a wavelength of 388 nm, as shown in Figs. 15.2b and 15.5. These results suggest that the mechanism for the formation of periodic nanostructures on TiO_2 film by irradiation with a femtosecond laser is due to the excitation of SPPs.

S. K. Das et al. reported that periodic nanostructures were formed on rutile type TiO_2 single crystals [15]. They observed periods of 170 nm with the laser wavelength of 800 nm on TiO_2 single crystals in which explained by interference relation $d = \lambda/(2n \sin\theta)$, where d is period of the periodic nanostructures, λ is the wavelength of the incident radiation, n is the corresponding refractive index of the material, and θ is the half angle between two interfering partial beams. From interference relation $d = \lambda/(2n \sin\theta)$, calculated periods were in the range from 140 to 160 nm ($n = 2.78$ or 2.52), which is slightly shorter than that of the experimental result of the period with 170 nm [15]. In this section, periodic

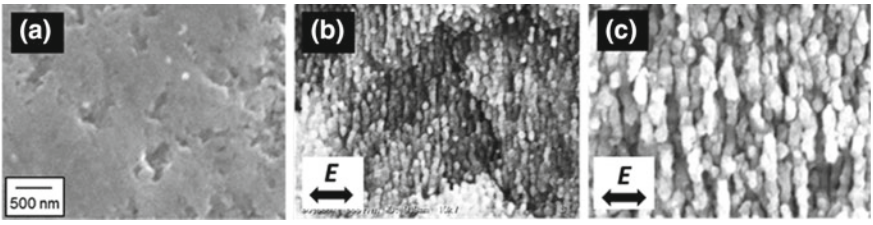

Fig. 15.4 **a** SEM images of the bare film surface. **b** Film with periodic nanostructures formed by femtosecond laser irradiation with the wavelength of 388 nm and **c** 775 nm, respectively. Arrows indicate laser electric field polarization vector

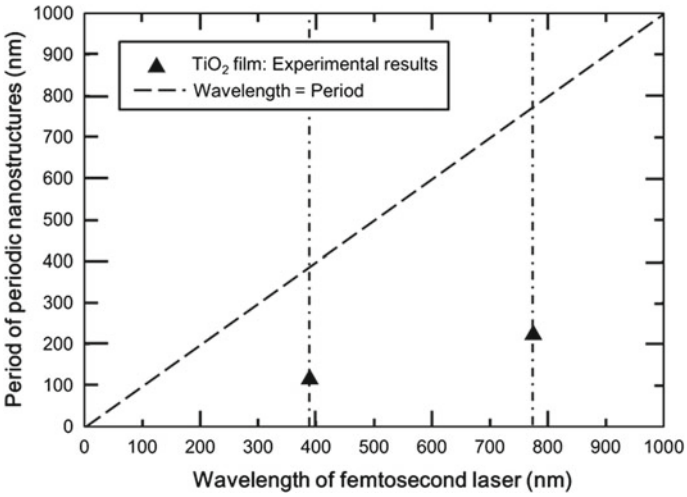

Fig. 15.5 Periods of the periodic nanostructures as a function of the wavelength of femtosecond laser

nanostructures were formed on anatase-type TiO_2 films. Period with the laser wavelength of 775 nm on the film was about 230 nm. From equation $d = \lambda/(2n \sin\theta)$, calculated periods were in the range from 140 to 150 nm (n = 2.80 or 2.52), which is shorter than that of the experimental result of the period with 230 nm. These results suggest that another factor except for interference relation is necessary to clarify the mechanism of the periodic nanostructures formation on TiO_2 film. Excitation of SPP during the femtosecond laser irradiation is one of the possibilities for the mechanism of the periodic nanostructures formation on TiO_2 film.

15.4 Summary

In this chapter, laser-induced process, periodic nanostructures formation, for the creation of new functions has been reviewed. Periodic nanostructures can be formed on a TiO_2 film surface using a femtosecond laser at wavelengths of 388 and 775 nm. The periodicity of nanostructures formed with those wavelengths are calculated using the SPP model. Since the experimental results were in the range of the calculated periods, it is suggested that the mechanism for the formation of periodic nanostructures on TiO_2 film by femtosecond laser irradiation is due to the excitation of SPPs. The nanostructures have useful effects on the control of cell spreading as shown in Chap. 32.

References

1. T. Hanawa, Biofunctionalization of titanium for dental implant. Jpn. Dent. Sci. Rev. **46**(2), 93–101 (2010)
2. L.H. Li, Y.M. Kong, H.W. Kim, Y.W. Kim, H.E. Kim, S.J. Heo, J.Y. Koak, Improved biological performance of Ti implants due to surface modification by micro-arc oxidation. Biomaterials **25**(14), 2867–2875 (2004)
3. X. Liu, P.K. Chub, C. Ding, Surface modification of titanium, titanium alloy sand related materials for biomedical applications. Mater. Sci. Eng. Rep. **47**(3–4), 49–121 (2004)
4. Y. Tsutsumi, M. Niinomi, M. Nakai, H. Tsutsumi, H. Doi, N. Nomura, T. Hanawa, Micro-arc oxidation treatment to improve the hard-tissue compatibility of Ti-29Nb-13Ta-4.6Zr alloy. Appl. Surf. Sci. **262**, 34–38 (2012)
5. J. Akedo, M. Ichiki, K. Kikuchi, R. Maeda, Jet molding system for realization of three-dimensional microstructures. Sens. Actuators A Phys. **69**(1), 106–112 (1998)
6. M. Tsukamoto, T. Fujihara, N. Abe, S. Miyake, M. Katto, T. Nakayama, J. Akedo, Hydroxyapatite coating on titanium plate with an ultrafine particle beam. Jpn. J. Appl. Phys. **42**(2A), L120–L122 (2003)
7. J. Lu, M.P. Rao, N.C. MacDonald, D. Khang, T.J. Webster, Improved endothelial cell adhesion and proliferation on patterned titanium surfaces with rationally designed, micrometer to nanometer features. Acta Biomater. **4**(1), 192–201 (2008)
8. A. Matsugaki, G. Aramoto, T. Nakano, The alignment of MC3T3-E1 osteoblasts on steps of slip traces introduced by dislocation motion. Biomaterials **33**(30), 7327–7335 (2012)
9. S. Fujita, M. Ohshima, H. Iwata, Time-lapse observation of cell alignment on nanogrooved patterns. J. R. Soc. Interface **6**(Suppl. 3), S269–S277 (2009)
10. K. Matsuzaka, X.F. Walboomers, J.E. de Ruijter, J.A. Jansen, The effect of poly-L-lactic acid with parallel surface micro groove on osteoblast-like cells in vitro. Biomaterials **20**(14), 1293–1301 (1999)
11. M. Tsukamoto, K. Asuka, H. Nakano, M. Hashida, M. Katto, N. Abe, M. Fujita, Periodic microstructures produced by femtosecond laser irradiation on titanium plate. Vacuum **80**(11–12), 1346–1350 (2006)
12. M. Tsukamoto, T. Kayahara, H. Nakano, M. Hashida, M. Katto, M. Fujita, M. Tanaka, N. Abe, Microstructures formation on titanium plate by femtosecond laser ablation. J. Phys: Conf. Ser. **59**, 666–669 (2007)
13. K. Okamuro, M. Hashida, Y. Miyasaka, Y. Ikuta, S. Tokita, S. Sakabe, Laser fluence dependence of periodic grating structures formed on metal surfaces under femtosecond laser pulse irradiation. Phys. Rev. B **82**(16), 165417 (2010)
14. S. Sakabe, M. Hashida, S. Tokita, S. Namba, K. Okamuro, Mechanism for self-formation of periodic grating structures on a metal surface by a femtosecond laser pulse. Phys. Rev. B **79** (3), 033409 (2009)
15. S.K. Das, D. Dufft, A. Rosenfeld, J. Bonse, M. Bock, R. Grunwald, Femtosecond laser induced quasiperiodic nanostructures on TiO_2 surfaces. J. Appl. Phys. **105**(8), 084912 (2009)
16. N. Yasumaru, K. Miyazaki, J. Kiuchi, Femtosecond-laser-induced nanostructure formed on hard thin films of TiN and DLC. Appl. Phys. A Mater. Sci. Proc. **76**, 983–985 (2003)
17. D. Dufft, A. Rosenfeld, S.K. Das, R. Grunwald, J. Bonse, Femtosecond laser-induced periodic surface structures revisited: a comparative study on ZnO. J. Appl. Phys. **105**(3), 034908 (2009)
18. G. Miyaji, K. Miyazaki, Origin of periodicity in nanostructuring on thin film surfaces ablated with femtosecond laser pulses. Opt. Express **16**(20), 16265–16271 (2008)
19. G. Miyaji, K. Miyazaki, K. Zhang, T. Yoshifuji, J. Fujita, Mechanism of femtosecond-laser-induced periodic nanostructure formation on crystalline silicon surface immersed in water. Opt. Express **20**(14), 14848–14856 (2012)
20. K. Miyazaki, G. Miyaji, Nanograting formation through surface plasmon fields induced by femtosecond laser pulses. J. Appl. Phys. **114**(15), 153108 (2013)

21. T. Shinonaga, M. Tsukamoto, A. Nagai, K. Yamashita, T. Hanawa, N. Matsushita, G. Xie, N. Abe, Cell spreading on titanium dioxide film formed and modified with aerosol beam and femtosecond laser. Appl. Surf. Sci. **288**, 649–653 (2014)
22. J. Reif, F. Costache, M. Henyk, S.V. Pandelov, Ripples revisited: non-classical morphology at the bottom of femtosecond laser ablation craters in transparent dielectrics. Appl. Surf. Sci. **197–198**, 891–895 (2002)
23. R. Buividas, L. Rosa, R. Sliupas, T. Kudrius, G. Slekys, V. Datsyuk, S. Juodkazis, Mechanism of fine ripple formation on surfaces of (semi) transparent materials via a half-wavelength cavity feedback. Nanotechnology **22**(5), 055304 (2011)
24. C. Wang, H. Huo, M. Johnson, M. Shen, E. Mazur, The thresholds of surface nano-/micro-morphology modifications with femtosecond laser pulse irradiations. Nanotechnology **21**(7), 075304 (2010)
25. Y. Shimotsuma, P.G. Kazansky, J. Qiu, K. Hirao, Self-organized nanogratings in glass irradiated by ultrashort light pulses. Phys. Rev. Lett. **91**(24), 247405 (2003)
26. F.A. Umran, Y. Liao, M.M. Elias, K. Sugioka, R. Stoian, G. Cheng, Y. Cheng, Formation of nanogratings in a transparent material with tunable ionization property by femtosecond laser irradiation. Opt. Express **21**(13), 15259–15267 (2013)
27. M. Tsukamoto, T. Kawa, T. Shinonaga, P. Chen, A. Nagai, T. Hanawa, Cell spreading on titanium periodic nanostructures with periods of 200, 300 and 600 nm produced by femtosecond laser irradiation. Appl. Phys. A Mater. Sci. Process. **122** (2016)
28. M. Tsukamoto, N. Abe, Y. Soga, M. Yoshida, H. Nakano, M. Fujita, J. Akedo, Control of electrical resistance of TiO_2 films by short-pulse laser irradiation. Appl. Phys. A Mater. Sci. Proc. **93**, 193–196 (2008)
29. M. Tsukamoto, T. Shinonaga, M. Takahashi, M. Fujita, N. Abe, Photoconductive properties of titanium dioxide film modified by femtosecond laser irradiation. Appl. Phys. A Mater. Sci. Proc. **110**, 679–682 (2013)
30. K. Sokolowski-Tinten, D. von der Linde, Generation of dense electron-hole plasmas in silicon. Phys. Rev. B **61**(4), 2643–2650 (2000)
31. H. Raether, *Surface Plasmons on Smooth and Rough Surfaces and on Gratings* (Springer, 1988)
32. E.D. Palik, *Handbook of Optical Constants of Solids* (Academic, 1997)
33. B. Enright, D. Fitzmaurice, Spectroscopic determination of electron and hole effective masses in a nanocrystalline semiconductor film. J. Phys. Chem. **100**(3), 1027–1035 (1996)

Chapter 16
Powder Metallurgy Processes for Composite–Materials Integration

Katsuyoshi Kondoh, Chen Biao and Junko Umeda

Abstract Uniform dispersion of unbundled carbon nanotubes (CNTs) was the bottleneck to convert their attractive properties to CNTs-reinforced composites. In this study, a solution ball milling (SBM) approach was developed to homogeneously disperse CNTs in Al matrix composites (AMCs). The process integrated strategies of solution coating, mechanical ball milling, and Al flake producing into a simple organic unity. The dispersion quality, crystal structure, and strengthening effect of CNTs in AMCs processed by SBM were investigated through scanning electron microscopy, transmission electron microscopy, Raman analysis, and tensile tests. Compared with previous methods, the SBM process was simple and effective to obtain a homogeneous CNT dispersion with a large aspect ratio and small CNT damages. The tensile strength of Al matrix was noticeably enhanced by CNT additions agreeing with the potential strengthening effect predicted by the load transfer mechanism. Shortened carbon nanotubes (CNT) were completely transformed to in situ Al_4C_3 nanorods by template reaction of CNT with Al matrix via powder metallurgy. Strong Al–Al_4C_3 interface, good distribution and complete single-crystal structure of Al_4C_3 nanorods, resulted in a remarkably improved strengthening effect in Al matrix composites. It concluded that in situ formed Al_4C_3 nanorod was a novel promising reinforcement for designing high-performance Al nanocomposites.

Keywords Powder metallurgy · Composites · Carbon nanotubes · Aluminum · Sintering

K. Kondoh (✉) · C. Biao · J. Umeda
Joining and Welding Research Institute, Osaka University, Ibaragi, Japan
e-mail: kondoh@jwri.osaka-u.ac.jp

Y. Setsuhara et al. (eds.), *Novel Structured Metallic and Inorganic Materials*, https://doi.org/10.1007/978-981-13-7611-5_16

16.1 Introduction

A metal matrix composite (MMC) is one of the representative materials with high strength due to a dispersion strengthening effect [1, 2]. In the materials design of MMCs, the suitable selection of their reinforcements is significantly important to improve mechanical properties. The material's performance of the composites strongly depends on both the reinforcement properties and interfacial coherence between the matrix and the second phase reinforcement. It is obviously known that the use of reinforcements with superior mechanical properties such as hardness, strength, and Young's modulus causes the improvement of the mechanical performance of the composite itself [3–5]. However, the agglomerated reinforcements could be materials defects, and result in the decrease of its property [6]. Regarding the interfacial coherence, it is related to the load transfer between the matrix and second-phase reinforcements in tensile. Powder metallurgy (PM) process [7] is suitable for the preparation of the MMCs because the powder milling process is available to uniformly mix and disperse the reinforcing particles with metal powders even if there is a large difference in density between them. In addition, the agglomeration of nanoparticles caused by Van del Waals force [5] is successfully reduced by the ball milling process, and the individual particle uniformly dispersed with the metal matrix powders. On the other hand, the interfacial coherence depends on the wettability of the reinforcements to the matrix. In general, the conventional casting process is superior in the improvement of the wettability at the interface compared to PM process in solid-state because the molten metal matrix is much activated and has a high wettability [8]. However, the compounds formation via reaction of matrix powder and reinforcements at the interface during solid-state sintering is effective for a load transfer at the interface due to a metallurgically strong bonding of the compounds to both the matrix and the reinforcements of PM MMCs.

In this chapter, aluminum (Al) and multi-walled carbon nanotube (MWCNT) are selected as a matrix material and reinforcement of MMCs. This is because Al with a low density ($\sim$2.7 g/cc) is one of the environmentally benign materials [9], for example, weight reduction of the components by using light metals is effective both to improve a fuel efficiency for saving energy and to reduce CO_2 gas emission in the transportation industries. On the other hand, MWCNTs [10] have excellent mechanical properties such as high Young's modulus and high tensile strength, and good thermal and electrical conductivity [11] compared to the oxides, nitrides, and carbides used as reinforcements of the conventional MMCs. First of all, two types of uniform CNTs dispersion process to prepare CNTs/Al composite powders; wet process using zwitterionic surfactant solution [12] and dry process using high-energy milling [13], are introduced. After consolidation of these composite powders by solid-state sintering and hot extrusion, the microstructures and mechanical responses are evaluated in detail. In particular, from a load transfer efficiency point of view, the interfacial coherence between CNTs and Al matrix was investigated by SEM and TEM analysis. The fractured surface analysis on tensile

test specimens was also carried out to understand the fracturing behavior of CNTs. Furthermore, to completely obstruct the peeling phenomenon of CNTs due to bridge graphene walls, in situ formation of aluminum carbide (Al_4C_3) nanorods and their uniform dispersion in the Al matrix were applied. According to the above results, the strengthening mechanism of CNTs reinforced Al composites was explained, and the remarkable improvement of mechanical properties of advanced Al nanocomposites by PM route was introduced in this chapter.

16.2 Advanced Mixing Process of Unbundled CNTs with Metal Powders

A homogeneous dispersion of unbundled CNTs is basically essential for achieving the full strengthening potential of CNTs, which were strongly required to carry high load transfer via a suitable CNT-Al contacting interface. Although many attempts [6–10] have been made to deal with CNT dispersion in composites, it is still a great challenge to uniformly disperse CNTs into AMCs with small structure damages. It is due to the multiple problems in CNT-Al system. First of all, there is a strong attractive force between CNTs due to a high van der Waals (vdW) attraction energy of tube–tube interaction. In the previous studies, the chemical methods, or solution-based surface modification of CNTs, were used to enhance their chemical compatibility to medium aqueous [14], organic solutions [15, 16], or polymers [16]. Homogeneously CNT-dispersed solution could be obtained without much difficulty. However, the following problem arises that dispersed CNTs in solution are difficult to be absorbed on Al powder surface due to the weak attractive force between CNTs and Al, resulted from their incompatibility of zeta potential [17]. Moreover, weak CNT–Al bonding might result in reaggregation of CNTs during dispersing, post drying or consolidating processes [18]. For example, the zwitterionic surfactant solution containing CNTs is prepared, and metal powders are dipped into this solution. Then, the metal powder surface is completely coated with individual unbundled CNTs after pulling up the powders from the solution as shown in Fig. 16.1.

This problem was resolved in mechanical ball milling process by strongly attaching CNTs on Al powder under external mechanical force. However, severe CNT structure damages, such as CNT shortening and crystal structure change, seemed evitable at the sacrifice of good CNT dispersion [19]. The final problem is that the size of commonly used Al powder particles (1–200 μm) is about 3 magnitude larger than CNTs (2–100 nm), resulting in a small specific surface area for absorbing CNTs. Flaky Al particles with greatly improved surface areas have been reported in high-energy ball milling (HEBM) processes by preventing cold welding of Al powders [14, 20]. However, due to the ignorance of the strong attractive force between CNTs, HEBM process also confronted the severe CNT damages for dispersing CNTs [21]. Accordingly, homogeneous CNT dispersion with minor or small structure change in composites is difficult to obtain from the conventional methods

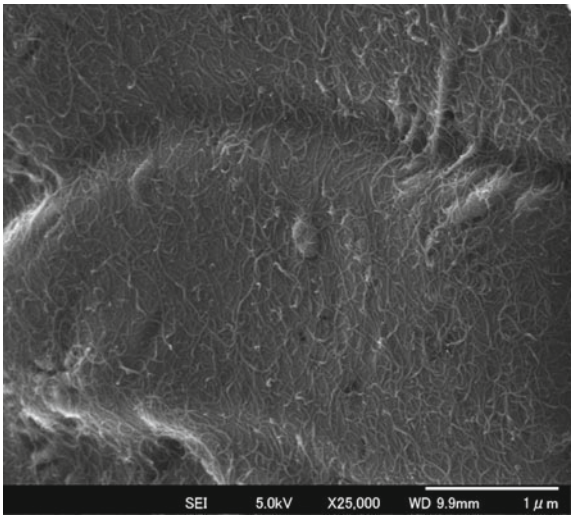

Fig. 16.1 SEM observation on Al powder surface coated with individual unbundled CNTs prepared by using zwitterionic surfactant solution I wet process

based on a single-aspect strategy. From an integrative methodology point of view, a simple but effective solution ball milling (SBM) process integrating present strategies into an organic unity is put forward to simultaneously resolve the problems in CNT dispersion. In order to better understand the SBM process, the CNT dispersion quality was compared with those of the conventional approaches in CNT–Al composite system using the same starting materials and similar milling conditions. The characteristics of present CNT dispersion methods, including the conventional and some newly developed processes, were compared with the SBM process.

The detail example of CNTs/Al composite powder preparation is introduced by using a schematic (Fig. 16.2) of the SBM process developed in this study [22]. The process mainly includes two steps. First is to prepare CNT-dispersed solution. Various solutions [23] have been reported to effectively disperse CNTs. In this study, isopropyl alcohol (IPA) based solution with ~1 wt.% zwitterionic surfactants [12] was used to obtain 1 wt.% CNT solution. The surfactants had both

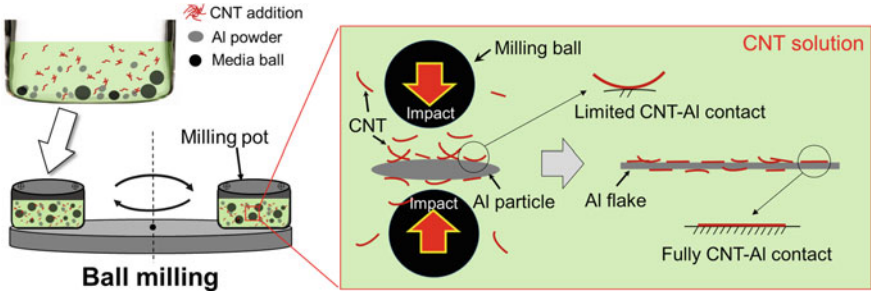

Fig. 16.2 Schematic of solution ball milling (SBM) process for CNTs dispersion

hydrophobic and hydrophilic groups to disperse individual CNTs in the IPA based solution. Multi-walled CNT (Baytubes C150P, Bayer Material Science Co., Japan) was used in this study. The detailed description of the working mechanism of surfactants for CNT debinding could be found elsewhere [24]. In the second step, the slurry of 160 g prepared CNT solution and 160 g Al powders (Kojundo Chemical Laboratory Co., Japan) were mixed using a planetary ball milling machine. Al slurry containing 1 wt.% CNTs was sealed in a ZrO_2 jar together with ZrO_2 milling balls (640 g in diameter of 10 mm and 160 g in diameter of 5 mm). The revolution speed was 200 rpm. The ball milling time was 60 min with an interim period of 10 min for every 10 min in order to prevent the overheating behavior. During ball milling, flaky Al was gradually produced under the impact between the high-energy balls. Simultaneously, dispersed CNTs in the solution was impacted on the flaky powder surface, as shown in Fig. 16.2. Due to the mechanical impact, CNTs were strongly plastically attached on Al surface with a fully CNT–Al contact from the limited contact before impact. After milling, the slurry was transferred to a beaker and stand for ~15 min to settle CNT–Al powders down. The following procedure is to pour out the upper solution containing surfactants and free CNTs. Finally the powder was dried in an oven at 353 K for 30 min. Al slurries containing 0.5 wt.% CNTs and containing no CNT were also processed under the same SBM conditions. Alcohol (99.5% purity) was used to make up IPA to a same solution volume with 1 wt.% CNTs.

For more understanding of the dispersion effect in SBM, conventional methods of HEBM, solution coating (SC) and solution coating on Al flakes (SCF) were also applied with 1 wt.% CNTs. During HEBM process, 2 wt.% stearic acid was added as the process control agent (PCA) to prevent the cold welding of Al particles. HEBM was manipulated for 60–720 min. Flaky Al powder was produced through HEBM of raw Al for 60 min and post heat treatment held at 723 K for 60 min under vacuum of ~100 Pa. SC and SCF process were done by bathing Al powders (raw Al and flaky Al respectively) in the CNT solution on a table rolling machine for 60 min. CNT powder, CNT solution, raw Al powder, and other HEBM conditions are kept the same with SBM process.

The morphologies of raw Al and CNT powders were shown in Fig. 16.3. Raw Al powder had a near-spherical shape with diameter of 5–50 μm (a). The raw CNTs were agglomerated into particles with diameter of ~500 μm under the strong vdW force (b). Large surface area, large aspect ratio (length to diameter ratio), combined with high flexibilities of CNTs, greatly increase the possibilities of nanotube entanglement and close packing (c). From the combination of SEM (c) and TEM observations (d), the average diameter and length of raw CNTs were measured as 12.4 nm and 722 nm from 50 CNTs, respectively. The values of diameter, length and aspect ratio (58) basically agreed with those reported in a previous study [25] using the same type CNT with an aspect ratio of 53. It is also clear to observe the CNT walls and the axial hollow channel under the high-resolution TEM image (inset of Fig. 16.3d).

Figure 16.4 shows the CNT dispersion effect on Al powder surface through the conventional HEBM, SC and SCF processes. After HEBM for 60 min, Al powders

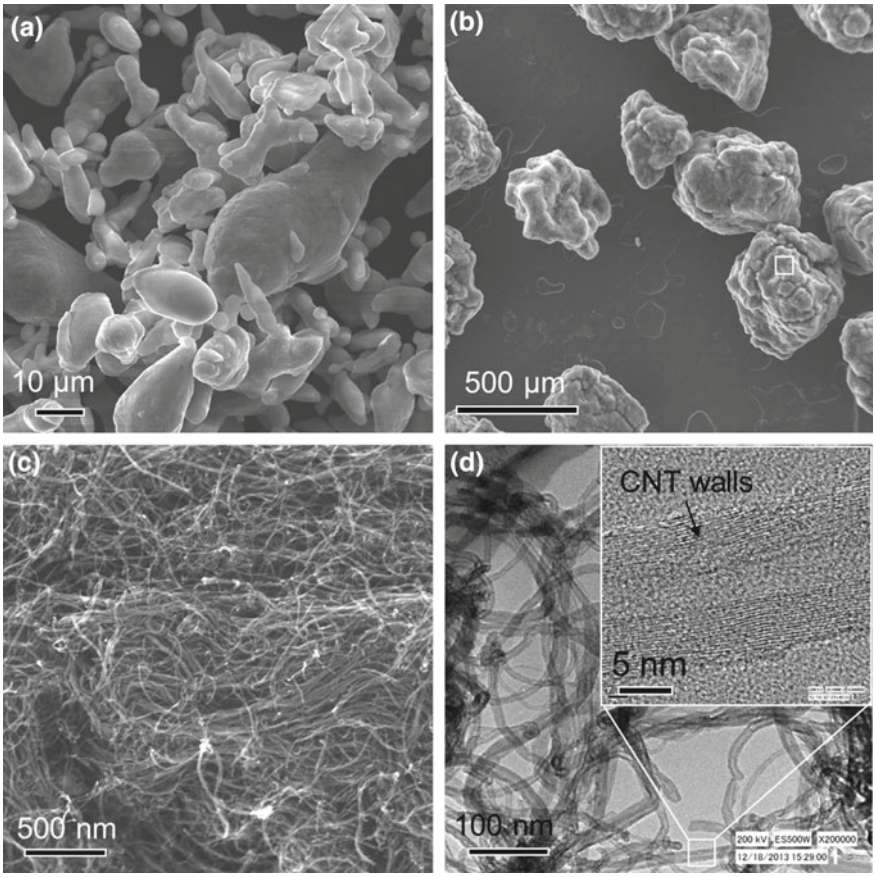

Fig. 16.3 Morphologies of raw materials: **a** Al powder observed by SEM, **b**, **c** agglomerated CNT powder by SEM, **d** CNTs by TEM. **c** is a local view in (**b**). Reprinted from Ref. [22]. Copyright 2015, with permission from Elsevier

changed to flaky morphology (a). CNT dispersion was greatly improved but CNTs still existed in flattened clusters under impact of milling balls (inset of Fig. 16.4a). After a long time milling (720 min), CNT clusters were completely broken up and individual CNTs distributed on the powder surface (b). However, it is clearly observed that CNTs became shortened fragments with an average length of ~100 nm. Figure 16.4c shows CNT clusters on the Al powder surface by the SC process. A few individual CNTs were occasionally observed. It suggested the ineffective absorbing of CNTs by raw Al powder through SC process. Figure 16.4d shows the CNT distribution on flaky Al surface by SCF process. Compared with the SC process, CNT dispersion quality was improved, as one thin CNT layer covered the Al surface. However, CNTs still overlapped and entangled together with the remained surfactant as shown in Fig. 16.4e. The EDS analysis (f) with a strong oxygen K peak provided evidence of the remained surfactant. Figure 16.5 shows

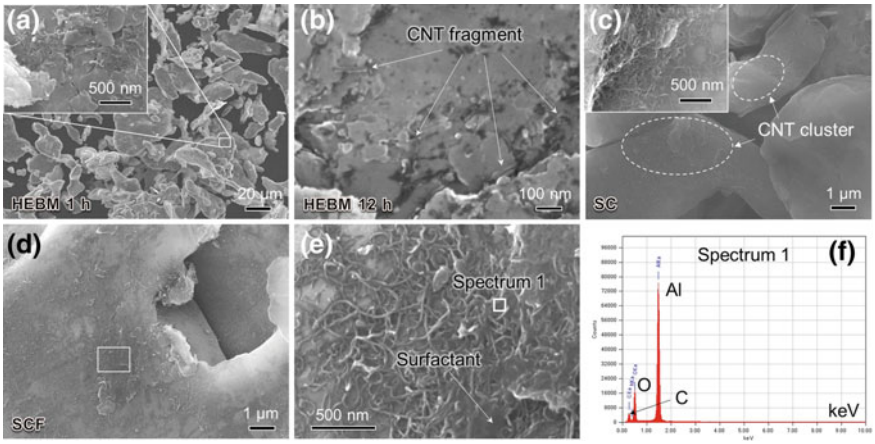

Fig. 16.4 Morphologies of CNT existing on Al powder surface after high-energy ball milling (HEBM) for 1 h (**a**), HEBM for 12 h (**b**), solution coating (SC) (**c**), and solution coating on Al flakes (SCF) (**d**, **e**). **e** is a local view in (**d**), and **f** shows EDS analysis of area in (**e**). Reprinted from Ref. [22] Copyright 2015, with permission from Elsevier

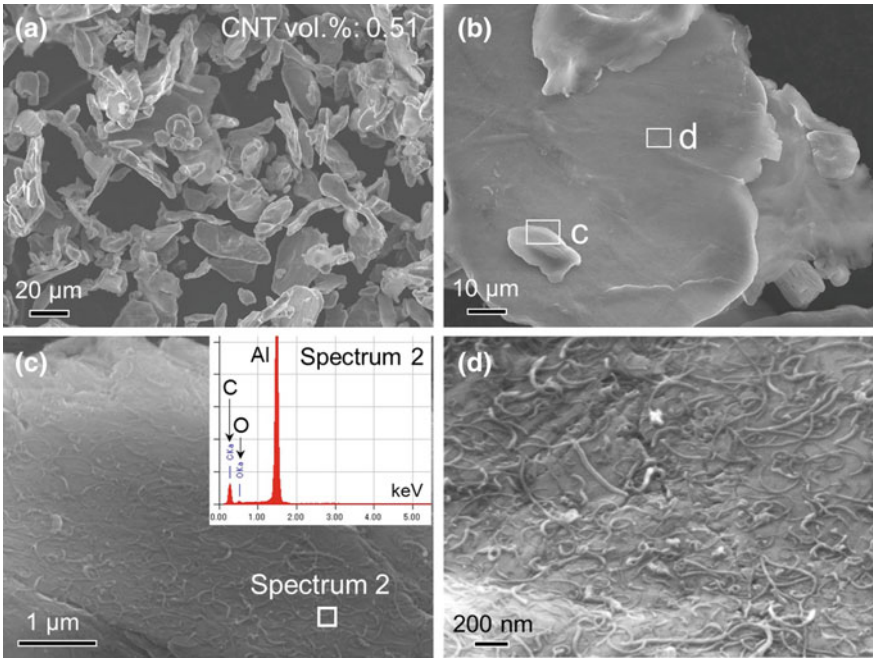

Fig. 16.5 CNT distribution on Al powder surface by solution ball milling (SBM) with 0.5 wt.% starting CNT solution. **a** Low-magnification view shows Al flakes. **b** Local view of a typical Al flake. **c**, **d** High-magnification views in (**b**). Note that CNT surface is completely attached to Al surface, and little surfactant was remained on surface. Reprinted from Ref. [22] Copyright 2015, with permission from Elsevier

the morphology of Al-CNT powder mixture dispersed by SBM process as starting CNT content is 0.51 wt.%. Similar to HEBM, SBM process also produced flaky Al (a and b), because the solution acted as the PCA to prevent cold welding of Al powders. From the local views, it is observed that CNTs are homogeneously dispersed on all flaky Al surfaces, including the surfaces of small flakes (c) and large flakes (d). It can be seen that CNTs were strongly attached to the Al surface or underlying CNTs under the mechanical force of milling balls, as schematically suggested in Fig. 16.2. Moreover, little surfactant was observed on the Al surface due to the observed weak O K peak in the EDS analysis (inset of Fig. 16.5c). Therefore, the absorbed CNT weight content (ω_{CNT}) could be regarded equal to the measured carbon element concentration of 0.39 wt.%. The volume content of CNTs (V_{CNT}) could then be estimated as 0.51 vol.% based on the rule of mixture ($V_{CNT} = \sim 1.3\omega_{CNT}$) [4] using CNT density of 2.0 g cm^{-3} and Al of 2.7 g cm^{-3}.

16.3 Consolidation of CNTs/Al Composite Powder and Mechanical Properties of Nanocomposite

CNTs-reinforced Al composites were fabricated by consolidating the above powder mixture to investigate the strengthening effect of dispersed CNTs. The role of CNTs addition in the strengthening of the nanocomposites was examined and discussed based on tensile properties. The detail conditions in powder mixture consolidation are as follows; the CNT-Al powder mixture from SBM process was consolidated by sparking plasma sintering (SPS) and following hot extrusion. SPS is conducted on a SPS system (SPS-1030S, SPS Syntex) at sintering temperature of 823 K with a heating rate of 20 K/min, and held at 873 K for 30 min by applying a pressure of 30 MPa under vacuum of 5 Pa. Before hot extrusion, CNTs/Al-sintered billet was preheated to 773 K and kept for 180 s under an argon gas atmosphere. And then, it was immediately extruded using a 2000 kN hydraulic press machine. The extrusion ratio and the ram speed were 37:1 and 3 mm/s, respectively. A pure Al powder was also processed under the same RBM, SPS, and hot extrusion process as a reference material.

Mechanical properties of composites were greatly dependent on CNT dispersion. Therefore, the strengthening effect of CNT addition in AMCs was also investigated, as shown in Fig. 16.6. It was observed that a little increase of tensile strength (UTS) of Al happened from 149 MPa of pure Al to 157 MPa of SBM-Al, because of the work hardening of Al in SBM process. Compared with the reference SBM-Al, the composites consolidated from 0.51CNT and 0.88CNT powders were noticeably increased (a) to 180 MPa and 192 MPa, respectively. Moreover, the CNT/Al composites still had a good plasticity with elongation of ~20%. The matrix could be strengthened by CNTs in possible mechanisms of grain refining and load transfer strengthening [26]. The average grain size of SBM-Al, 0.51CNT/Al and 0.88CNT/Al materials were measured as similar values of 2.26 μm,

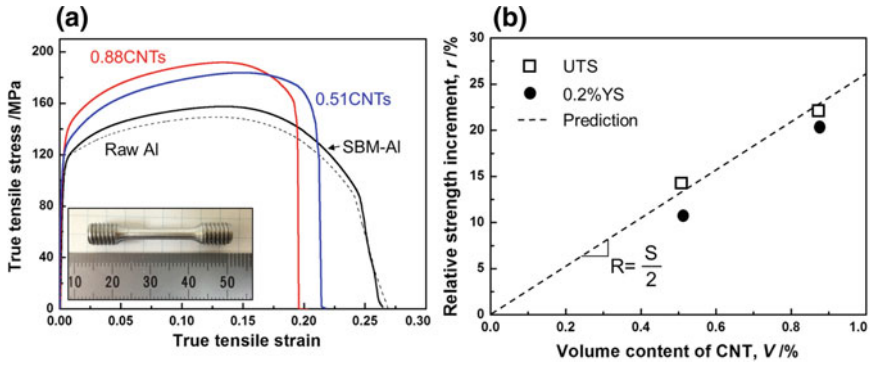

Fig. 16.6 Tensile properties of CNT/Al composites by SBM. **a** True tensile stress–strain curves of CNT/Al composites by SBM, as well as reference Al materials. **b** Strength increment of CNT/Al composites as a function of CNT volume content. Reprinted from Ref. [22] Copyright 2015, with permission from Elsevier

2.19 μm, and 2.03 μm, respectively. It suggested that the grain refining contributed little (~1 MPa) to the strength improvement in AMCs according to Hall–Petch formula [27]. Considering the load transfer strengthening of CNTs, the composite strength (σ_c) can be obtained from the generalized shear-lag model [28] and expressed as

$$\sigma_c = \sigma_m + s/2\, V_{CNT}\sigma_m \tag{16.1}$$

where σ_m was the matrix strength, and V_{CNT} and S are the volume fraction and aspect ratio of CNTs, respectively. The reinforcing effect (r) of CNTs, or the relative strength improvement of CNT/Al composites, can be expressed as

$$r = (\sigma_c - \sigma_m)/\sigma_m \tag{16.2}$$

By introducing Eqs. (16.1)–(16.2), r can be expressed as

$$r = s/2V_{CNT} \tag{16.3}$$

Since S was estimated as 53 for CNTs in SBM process from Fig. 16.5, the relation between predicted r from Eq. (16.3) and the CNT volume of predicted values and from Eq. (16.3) are shown in Fig. 16.6b. The strengthening efficiency (R), or the slope of r-V_{CNT} line, was half of S of CNTs, which was 26.5 for SBM composites. It can be seen that both yield strength (0.2%YS) and UTS of CNT/Al composites agreed well with the predictions (Fig. 16.6b). It suggested that the high strengthening potential of CNTs has been almost achieved through the load transfer mechanism by SBM process. R of CNT/Al composites processed by SBM showed the similar value of Flake PM, and it was far larger than R of 7.5 by HEBM, which was reasonably due to the small S of CNT fragments in HEBM [29]. However, UTS of the present 0.88CNT/Al composite (192 MPa) was still low compared with

the CNT/Al composites processed by HEBM (345–366 MPa) [17]. It was because σ_c was proportional to σ_m (Eq. 16.1), and σ_m of CNT/Al composites by SBM (157 MPa) was far lower than that by HEBM (284–377 MPa) [17]. CNT/Al composites with excellent mechanical properties could be expected by applying strong Al matrix with ultra-fined grains or alloy strengthening elements in the present SBM process. High load transfer during tensile processes in CNT/Al composites were resulted from a strong interfacial strength between CNTs and Al matrix [30]. The breaking and pulling out of CNTs observed on fracture surface shown in Fig. 16.7a confirmed the strong interface in CNT/Al composites. It resulted from the effective physical contact between CNTs and Al matrix. From the TEM observation results (b), dispersed CNTs were effectively incorporated into Al matrix through a clean interface.

Moreover, it is interesting to detect some monocrystal rod-like Al_4C_3 as confirmed by the SAD pattern (inset of Fig. 16.7b). The fully physical contact between dispersed CNTs and Al in SBM process (Fig. 16.4) might be helpful to achieve an ideal reactive interface combined with SPS and hot extrusion. Therefore, the chemical reaction between Al matrix and CNTs, especially damaged CNTs [31], was then greatly promoted, and resulted in the formation of Al_4C_3 nanorods. The in situ Al_4C_3 nanorods were reported helpful to increase the strength of CNT/Al composites [29], probably due to the load transfer enhancement from damaged CNTs to the monocrystal nanorods.

TEM observation results of the in situ Al_4C_3/Al composite are shown in Fig. 16.8. From the low-magnification image (a), many rod-like materials were dispersed in the Al matrix, as black arrow indicated. These structures shared a similar shape with CNT segments (Fig. 16.3c) and generally aligned along the extrusion direction (Fig. 16.8a). From the bright field TEM images and corresponding selected area diffraction (SAD) patterns in Fig. 16.8b and c, these nanorods were identified as single-crystal Al_4C_3. Interestingly, the in situ formed Al_4C_3 nanorods had basal planes (001) of the hexagonal crystal paralleled to the

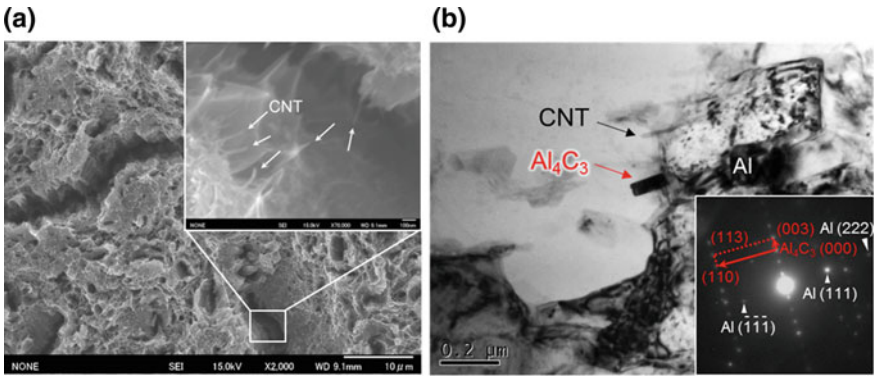

Fig. 16.7 Morphology of fracture surface after tensile test (**a**) and TEM observation (**b**) of Al composite reinforced with 0.88% CNT

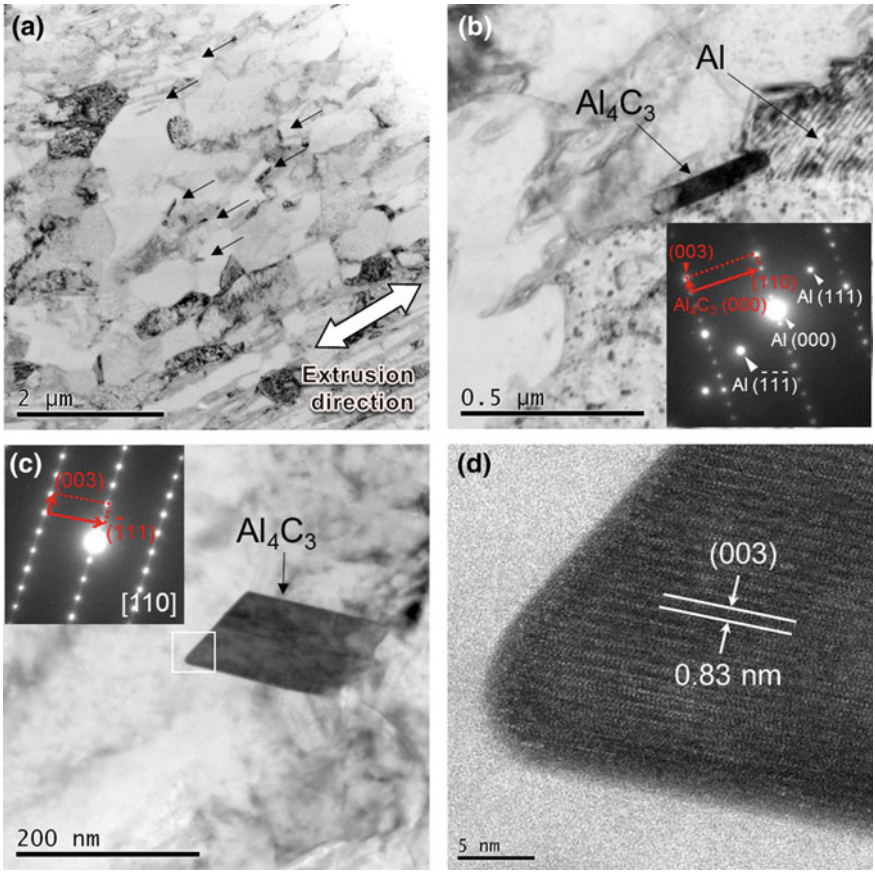

Fig. 16.8 TEM observation on in situ Al_4C_3 nanorods/Al composites. **a** Low-magnification image shows well dispersed and aligned Al_4C_3 nanorods as black arrows indicated. **b**, **c** Local images of two typical Al_4C_3 nanorods. **d** High-resolution TEM image shows atoms in the Al_4C_3 nanorod and Al-Al_4C_3 interface in (**c**). Insets of (**b**) and (**c**) show corresponding SAD patterns

axis direction (b–d). This observation is well coincident with that of the gallium nitride nanorods synthesized using CNT as a template [19]. Since CNT has the same crystal characteristic, it suggested that Al_4C_3 was in situ formed by the template reaction of CNT. Moreover, the hollow structure of CNT transformed to complete and solid Al_4C_3 structure (Fig. 16.8b–d). A clean chemical interface was formed between in situ Al_4C_3 nanorods and Al matrix (d). Due to the good dispersion, strong interfacial bonding and complete single-crystal structure, in situ Al_4C_3 naonorods could be expected to perform an excellent strengthening effect during the mechanical response of the composite.

16.4 Conclusions

An advanced powder mixing technique by SBM process was developed to fabricate Al matrix nanocomposites reinforced by homogeneously dispersed CNTs with a large aspect ratio and small damages. The combining use of the solution coating and HEBM in the SBM process provided a simple and effective approach to obtain unbundled CNTs on the Al powders. The experimental strengthening effect of dispersed CNTs agreed with the strengthening potential predicted by the load transfer mechanism. The present results suggested that the SBM process was promising for producing high-performance metal matrix nanocomposites reinforced with CNTs.

References

1. W.D. Callister Jr, *Materials Science and Engineering, An Introduction*. 7th edn. (Wiley and sons publishing Inc, New Jersey, 2007)
2. J.W. Kaczmar, K. Pietrzak, W. Włosiński, J. Mater. Proc. Tech. **106**, 58 (2007)
3. M. Gupta, M.O. Lai, D. Saravanaranganathan, J. Mater. Sci. **35**, 2155 (2000)
4. Z. Zhang, D.L. Chen, Scr. Mater. **54**, 1321 (2006)
5. F. Shehata, A. Fathy, M. Abdelhameed, S.F. Mustafa, Mater. Des. **30**, 2756 (2009)
6. I. Montealegre Melendez, E. Neubauer, P. Angerer, H. Danninger, J.M. Torralba, Comp. Sci. Tech. **71**, 1154 (2011)
7. M. Randall, *German, Powder Metallurgy Science* (Metal Powder Industries Federation, New Jersey, 1994)
8. P.A. Hartley, G.D. Parfitt, L.B. Pollack, Powder Tech. **42**, 35 (1985)
9. I.J. Polmear, *Light Alloys: Metallurgy of the Light Metals (Metallurgy & Materials Science)*, 3rd edn. (Wiley, New Jersey, 1995)
10. S. Iijima, Nature **354**, 56 (1991)
11. A. Moisala, Q. Li, I.A. Kinloch, A.H. Windle, Comp. Sci. Tech. **66**, 1285 (2006)
12. K. Kondoh, T. Threrujirapapong, H. Imai, J. Umeda, B. Fugetsu, Comp. Sci. Tech. **69**, 1077 (2009)
13. Z.Y. Liu, S.J. Xu, B.L. Xiao, P. Xue, W.G. Wang, Z.Y. Ma, Comp. A. **43**, 2161 (2012)
14. M.F. Islam, E. Rojas, D.M. Bergey, A.T. Johnson, A.G. Yodh, Nano Lett. **3**, 269 (2000)
15. N.C. Jonathan, Adv. Func. Mater. **19**, 3680 (2009)
16. S.W. Kim, T. Kim, Y.S. Kim, H.S. Choi, H.J. Lim, S.J. Yang, Carbon **50**, 3 (2012)
17. Z. Sun, V. Nicolosi, D. Rickard, S.D. Bergin, D. Aherne, J.N. Coleman, J. Phys. Chem. **112**, 10692 (2008)
18. K. Kondoh, H. Fukuda, J. Umeda, H. Imai, B. Fugetsu, Carbon **72**, 15 (2014)
19. D. Poirier, R. Gauvin, R.A.L. Drew, Comp. A. **40**, 1482 (2009)
20. K. Morsi, A. Esawi, J. Mater. Sci. **42**, 4954 (2007)
21. H.J. Choi, J.H. Shin, D.H. Bae, J. Mater. Res. **24**, 2610 (2009)
22. B. Chen, S. Li, H. Imai, L. Jia, J. Umeda, M. Takahashi, K. Kondoh, Mater. Des. **72**, 1 (2015)
23. C. He, N. Zhao, C. Shi, X. Du, J. Li, H. Li, Adv. Mater. **19**, 1128 (2007)
24. B. Fugetsu, W. Han, N. Endo, Y. Kamiya, T. Okuhara, Chem. Lett. **34**, 1218 (2005)
25. L. Jiang, Z. Li, G. Fan, L. Cao, D. Zhang, Carbon **50**, 1993 (2012)
26. D.H. Nam, S.I. Cha, B.K. Lim, H.M. Park, D.S. Han, S.H. Hong, Carbon **50**, 2417 (2012)
27. A.S. Khana, B. Farrokh, L. Takacs, Mater. Sci. Eng. A. **489**, 77 (2008)
28. H.J. Ryu, J. Mater. Res. **18**, 2851 (2003)

29. B. Chen, L. Jia, S. Li, H. Imai, M. Takahashi, K. Kondoh, Adv. Eng. Mater. **16**, 972 (2014)
30. A. Kelly, W.R. Tyson, J. Mech. Phy. Sol. **13**, 329 (1965)
31. L. Ci, Z. Ryu, J. Phillipp, M. Rühle, Acta Mater. **54**, 5367 (2006)

Chapter 17
Dry Nanoparticle Processes for Functional Materials Integration

Takahiro Kozawa and Makio Naito

Abstract Powder processing technique supports the development of next-generation materials and products and thus plays an important role on numerous industries such as life science, energy, environment, and information. Drugs, cosmetics, electronic and magnetic materials, and phosphors as the application materials are widely used in our lives. Powder processing is located in the center of such advanced technologies. Here, we introduce the fabrication of functional materials by dry nanoparticle processing. The mechanically assisted particle bonding becomes a fundamental technique on the design and fabrication of functional materials. The particle bonding is achieved through the enhanced surface reactivity induced by mechanical energy, in addition to the intrinsic high surface reactivity of nanoparticles. Since this process does not require additional heat treatments, it is an environmentally friendly technique. Its applications for high-performance thermal insulation materials and electrodes of lithium-ion batteries and solid oxide fuel cells will be explained.

Keywords Dry powder processing · Nanoparticle bonding · Mechanical process · Material design

17.1 Introduction

Powder, which is an assemblage of small solid particles, is widely used in a variety of industries because of its convenient properties. The typical advantages of powders are as follows: specific change of solid-state characteristics associated with a particle size reduction, a huge specific surface area, and a dynamic behavior like liquid and gas by a function of proper external forces. In order to develop functional materials, it is important to optimize these powder properties. Recently, particle bonding technology between each fine particle that makes up powders has been

T. Kozawa · M. Naito (✉)
Joining and Welding Research Institute, Osaka University, Suita, Japan
e-mail: m-naito@jwri.osaka-u.ac.jp

Y. Setsuhara et al. (eds.), *Novel Structured Metallic and Inorganic Materials*, https://doi.org/10.1007/978-981-13-7611-5_17

attracting much attention to increase the functionality. This chapter explains the direct bonding between nanoparticles without any heat treatment or binders and then introduces the application cases for the fabrication of advanced composites by using this dry powder processing.

17.2 Material Design by Nanoparticle Bonding Processes

The various fabrication methods for preparing composite particles have been proposed in solution- and gas-based processes. Here, we introduce the dry nanoparticle bonding process by mechanical method. This method employs the grinding process of particles as a mechanical principle. The surface activity on particles increases with the decrease of particle size by mechanical grinding. Therefore, the preparation of composite particles can be achieved via direct bonding between nanoparticles by using this enhanced surface activity. Figure 17.1 shows the strategy of the material design by mechanical processing based on nanoparticle bonding technology. The mechanical functions such as compression, shearing, and frictional forces that are locally acted at the surface of nanoparticles lead to a creating of functional materials. By a combination of heterogeneous particles, composite particles with a covering form and an inner-dispersed form can be obtained via particle bonding [1–3]. The particle synthesis occurs by adding a forceful mechanical energy [4–7]. Both of these approaches can be realized in the same treatment. The buildup of these particles leads to a control of microstructure of powders. Meanwhile, this mechanical method can expand to the bonding between particle and substrate. The porous powder layer is directly formed on the substrate [8].

An important factor to consider for the preparation of composite particles is the powder properties of raw materials and the operating conditions in mechanical treatment. The former factor includes particle size, morphology, surface condition,

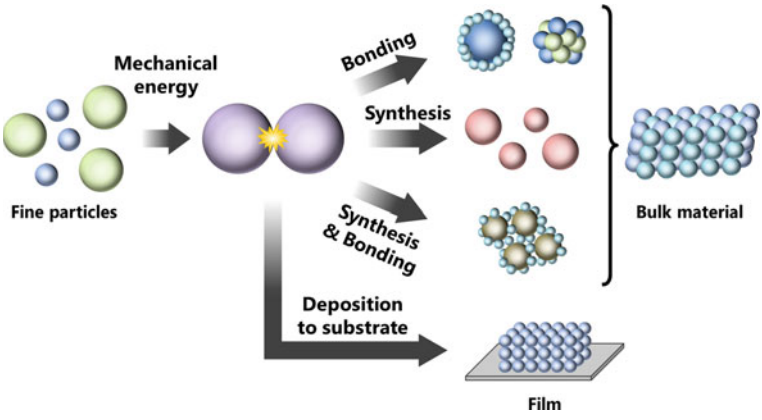

Fig. 17.1 Material design by mechanical processing based on nanoparticle bonding technology

mechanical strength, mixing ratio, and so on. For example, in the case of the preparation of covering-type composite particles, the particle size of the core material is preferable to use as large as possible against that of shell material. The bonding mechanism depends on the combination of particles. The processing conditions on the latter factor include mechanical action, treatment time, average or local temperature, atmosphere, and so on. In addition, types of grinding mills such as ball mill, jet mill, vibration mill, and pin mill vary depending on the intended use. Some fabrication cases of advanced composites by using the dry powder processing are described in the following sections.

17.3 Fabrication of High-Performance Thermal Insulation Boards

Figure 17.2 shows the fabrication scheme of ultra-low thermal insulation board through the particle bonding process [9]. Nanoparticles with the primary particle size until several tens of nanometers tend to form a chain-like aggregated structure. Such nanoparticles can transform to aggregates with pores of the size under 100 nm by mechanical treatment. When the pore diameter reaches to several tens of nanometers, a specific nature appears at the pore as well as particles. The porous materials possessing nanopores suppress a heat transfer, so they are useful as high-performance thermal insulation materials. However, it is extremely difficult to fabricate its bulk materials by pressing from the powder consisting of nanoparticles. We have reported that the aggregates of silica nanoparticles with nanopores were deposited on glass fibers via mechanical bonding and then the composite bulk material was fabricated by a uniaxial pressing [9, 10]. The obtained board is a lightweight and excels in machinability.

Table 17.1 summarizes the thermal conductivities and some characteristics of composite materials fabricated from silica nanoparticles and glass fibers. The obtained composite compacts are lightweight materials with an ultra-low thermal conductivity. The thermal conductivity and fracture strength of composite compacts

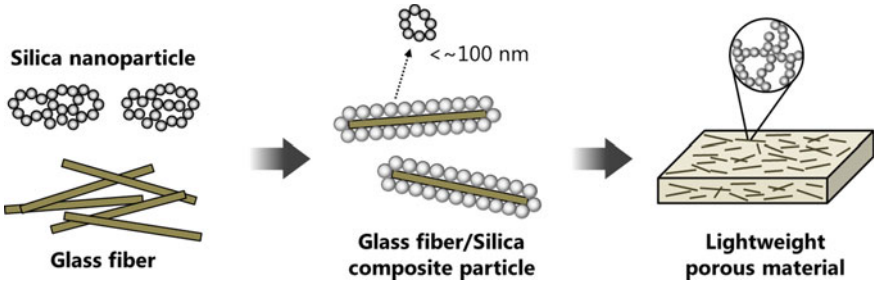

Fig. 17.2 Fabrication process of lightweight porous material with an ultra-low thermal conductivity

Table 17.1 Properties of fibrous fumed silica compacts prepared in this study

Composite compacts	Density (kg/m^3)	Porosity (%)	Fracture strength (MPa)	Thermal conductivity (W/mK@300 °C)
Hydrophilic silica	405	85.5	0.30	0.031
Hydrophobic silica	395	85.9	0.03	0.018

vary by changing the surface property of the used silica nanoparticles [10]. At a high-temperature region, a thermal radiation effect is not negligible. We have fabricated the composite compacts that hold the low thermal conductivity up to 800 °C, by adding silicon carbide fine particles. Based on this powder processing technology, high-performance thermal insulation boards have already been practically used.

17.4 Preparation of Cathode Materials for Lithium-Ion Batteries

17.4.1 Direct Synthesis of $LiFePO_4$/C Composite Granules

Development of cathode active materials for lithium-ion batteries plays a key role in their performance advances. Among cathode materials, lithium iron phosphate ($LiFePO_4$) has attracted much attention because of high thermal stability and environmentally friendliness. From a viewpoint of its low ionic and electronic conductivities, the primary particle size of $LiFePO_4$ is preferred to be as small as possible, as shown in Fig. 17.3 [11]. However, such nano-sized powder tends to form a high porous structure, so it is difficult to fabricate the cathode with a high packing density. The granulation step of nano-sized particles is usually accepted in cathode fabrication process. Additionally, the fine dispersion and the

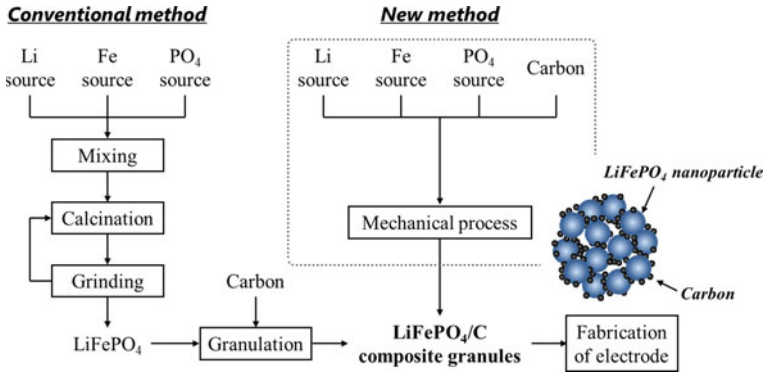

Fig. 17.3 Comparison between the conventional method and the new mechanical method for preparing nano-sized $LiFePO_4$/C composite granules

interconnection of carbon nanoparticles in the $LiFePO_4$ granule is an effective attempt to improve the electronic conductivity. Moreover, the sufficient pores to penetrate liquid electrolyte are necessary in the composite granule [12].

As shown in Fig. 17.3, the preparation of the nano-sized $LiFePO_4$/C composite granules is multistep processes and usually needs an atmosphere control to prevent an iron oxidation. As lithium, iron, and phosphate sources, Li_2CO_3, $FeC_2O_4 \cdot 2H_2O$, and $NH_4H_2PO_4$ are commonly used. In contrast, the proposed mechanical method can directly prepare these composite granules. $LiFePO_4$/C composite granules have been synthesized by one-pot process from raw materials of $LiFePO_4$ and carbon nanoparticles without any heat treatment and atmosphere control. Figure 17.4 shows SEM and TEM images of the mechanically prepared $LiFePO_4$/C composite granules [11]. The overall SEM image indicated the granule with the size ranging from several micrometers to tens of micrometers. According to the XRD analysis, the crystalline phase of the product was mainly $LiFePO_4$. The mechanical synthesis of $LiFePO_4$ was achieved in air without any oxidation of iron. The TEM image of the inside of granules revealed that $LiFePO_4$ nanoparticles coated by carbon have been assembled [11]. The composite granules consisted of $LiFePO_4$ nanoparticles. Such granule structure led to the formation of an electrode with a high packing density [13].

The sufficient penetration of electrolytes into granules is essential for deriving the performance of active materials. By changing the raw materials in mechanical synthesis, the microstructure of granules can be controlled. When Li_3PO_4 was used as lithium and phosphate sources, $LiFePO_4$/C composite granules with porous structure have been prepared. Figure 17.5 shows the SEM image of the fracture surface and the pore size distribution of the prepared granules [12]. The small pores and nano-sized particles existed in the product. The pore size distribution in the granule was estimated from a nitrogen adsorption measurement. The average pore size was 20–30 nm. Owing to these nanopores, the electrochemical performances of the cathode made from $LiFePO_4$/C composite granules were improved along with the cycle number [12]. This is due to the gradual penetration of electrolyte into granules. The formation mechanism of porous composite granules can be proposed as follows: The raw materials are uniformly ground and mixed by mechanical

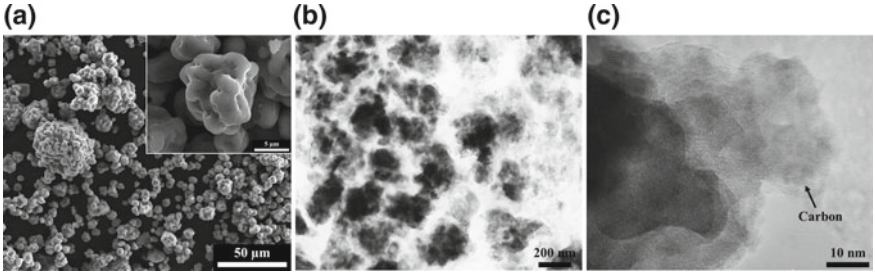

Fig. 17.4 **a** SEM and **b**, **c** TEM images of $LiFePO_4$/C composite granules obtained by the mechanical method. Reprinted from Ref. [11], Copyright 2014, with permission from Elsevier

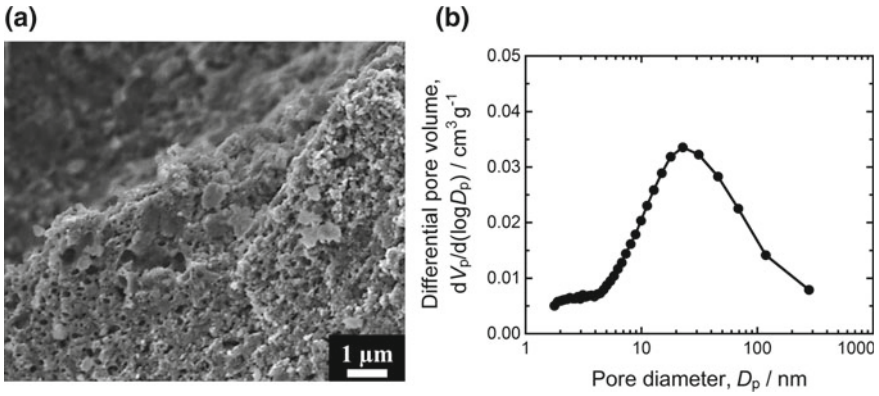

Fig. 17.5 **a** SEM image of the fracture surface and **b** pore size distribution for the porous $LiFePO_4$/C composite granules. Reprinted from Ref. [12], Copyright 2014, with permission from Elsevier

treatment. The synthesis of $LiFePO_4$ nanoparticles mainly occurs by the reaction between Li_3PO_4 and iron oxalate. The Li_3PO_4 particle acts as a seed material for the formation of $LiFePO_4$ because it has a crystal framework of PO_4^{3-}. The gaseous products generated from iron oxalate are trapped in the granulation step of nano-sized $LiFePO_4$/C particles. The resultant granules have a porous structure [12]. The granule structures such as size, morphology, and porosity can be controlled by changing raw materials and treatment conditions [14, 15].

17.4.2 Core–Shell and Concentration-Gradient Cathode Particles

Recently, the particle design for cathode materials has become a hot topic in the field of lithium-ion batteries. Since the improvement of battery performances from solo active material has limitations, the particle composed of two or more different active materials has been synthesized. A core–shell structure, for example, which has the synergistic effects of the core and shell, has attracted much attention. As the further advancement, the cathode particles with a gradient composition have been prepared by heating of core–shell particles. The concentration-gradient particles can be avoided a structural mismatch and volume change that occurs at the interface between core and shell particles. The preparation of these advanced particles is usually conducted by a precisely controlled coprecipitation method. Although the tailored synthesis of the particle with high quality and a uniform size is successfully conducted through the coprecipitation method, the reaction conditions (pH and concentration of the solutions, temperature, aging time, etc.) should be carefully controlled. In the mechanical method, mechanically activated nanoparticles can be

deposited on the surface of core particle [1] and thus core–shell particles can be prepared in one-step dry processing.

The mechanical treatment of Li_2CO_3, NiO, and MnO_2 as raw materials provides $LiNi_{0.5}Mn_{1.5}O_4$ particles, which is one of the high-voltage cathode materials [16]. When the micrometer-sized MnO_2 particles and fine Li_2CO_3 and NiO particles were used as a starting powder, $Li(Ni, Mn)_2O_4$ particles were formed and coated on the MnO_2 particle. Figure 17.6 shows the cross-sectional SEM images and EDX elemental maps of the prepared particles [17]. A cross-sectional observation of the product revealed the deposition of nanoparticles onto the core particle. The EDX maps of oxygen, nickel, and manganese clearly exhibited that the mechanically treated product had a core–shell structure and its shell part was constructed by the deposited nanoparticles. Nickel was detected in the shell part, while oxygen and manganese were homogeneously distributed in the entire particle. Thus, the core is attributed to a MnO_2 phase. The XRD pattern of this product indicated a $Li(Ni, Mn)_2O_4$ spinel phase. Consequently, the MnO_2–$Li(Ni, Mn)_2O_4$ core–shell particles could be prepared by the simple mechanical process without external heating [17].

The mechanically prepared MnO_2–$Li(Ni, Mn)_2O_4$ core–shell particles were converted to the concentration-gradient spinel particle by heating at 700 °C for 2 h [17]. Figure 17.7 shows the superimposed EDX maps and elemental profiles of the

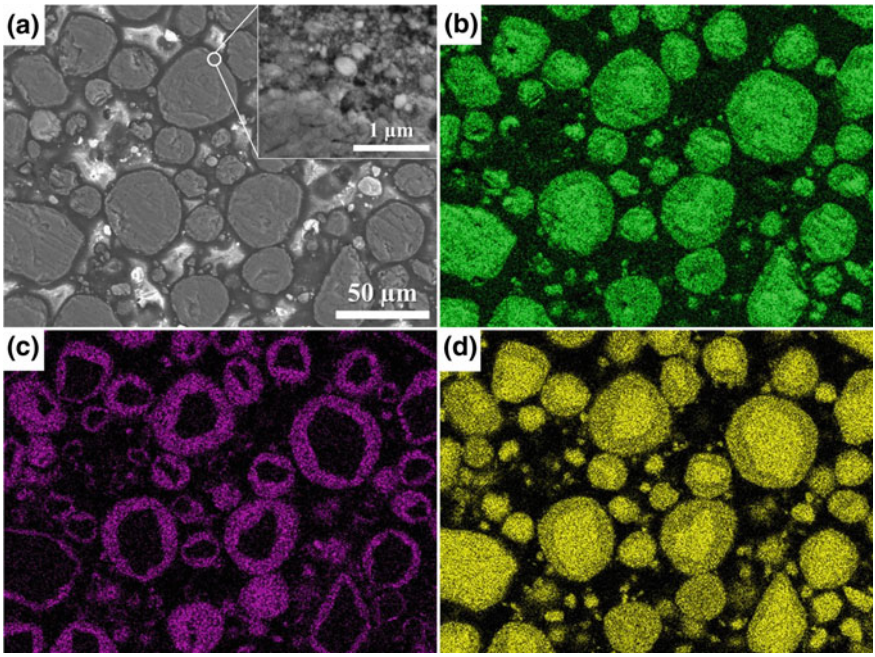

Fig. 17.6 **a** Cross-sectional SEM images and **b–d** EDX elemental maps of the mechanically prepared MnO_2–$Li(Ni, Mn)_2O_4$ core–shell particles. Elemental maps of oxygen, nickel, and manganese are shown in green, purple, and yellow, respectively. Reproduced from Ref. [17], Copyright © 2015 by National Institute for Materials Science, IOP Publishing Ltd.

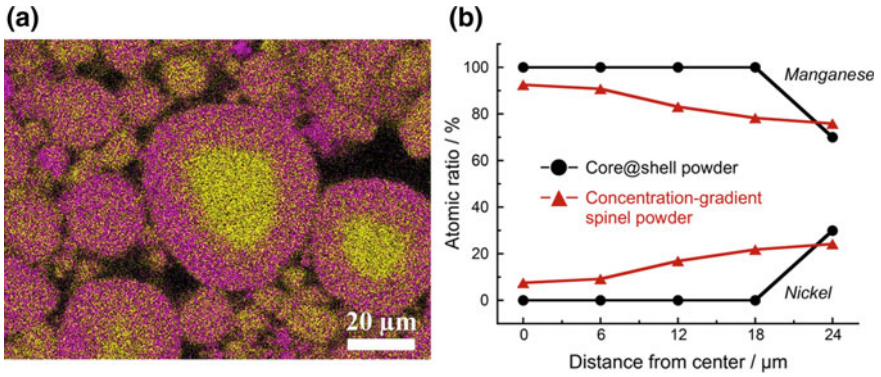

Fig. 17.7 **a** Cross-sectional EDX elemental maps of Ni (purple) and Mn (yellow) for the concentration-gradient powders prepared at 700 °C for 2 h. **b** Atomic ratio of transition metals as a function of the distance from the center to the surface for the core–shell and concentration-gradient powders. Reproduced from Ref. [17], Copyright © 2015 by National Institute for Materials Science, IOP Publishing Ltd.

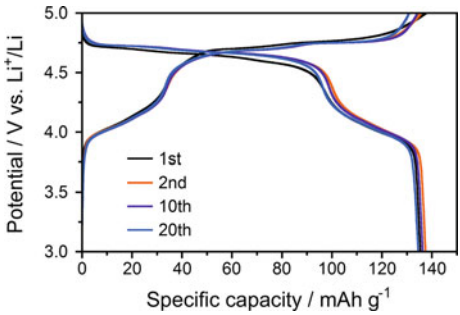

Fig. 17.8 Charge and discharge curves of the concentration-gradient cathode. Reproduced from Ref. [17], Copyright © 2015 by National Institute for Materials Science, IOP Publishing Ltd.

cross-sectional view for the obtained particles. By heating, the distribution of nickel, which existed in the shell part, gradually spread into the core. The heated product possessed a concentration gradient of manganese and nickel in the entire particle. The electrochemical performance of the prepared concentration-gradient spinel cathode exhibited the high discharge capacity, the wide-range plateau at a high voltage, and the good cycle capability. Figure 17.8 shows the charge and discharge curves of the concentration-gradient spinel cathode. A simple preparation route of core–shell and concentration-gradient particles was achieved by dry powder processing [17].

17.5 Direct Fabrication of Electrode for Solid Oxide Fuel Cells

As shown in Fig. 17.1, the particle bonding by mechanical energy is applicable for the deposition onto a substrate. The particle deposition on the substrate by mechanical method was demonstrated by using the apparatus depicted in Fig. 17.9 [8]. When the inside rotor rotates at a high speed, the aggregate of nanoparticles breaks down to fine particles and its particle surface is activated by mechanical energy. These activated nanoparticles are directly deposited on the substrate and stacked.

In this study, the composite particles consisting of NiO and Y_2O_3-stabilized ZrO_2 (YSZ) have deposited onto a dense YSZ substrate to fabricate the anode for solid oxide fuel cells. Figure 17.10 shows the SEM image of the as-deposited film and the thickness of NiO–YSZ films against the processing time [8]. After mechanical processing for 10 min, NiO–YSZ composite particles were deposited. Afterward, the deposition rate was roughly estimated to be $\sim$6 μm/min. The porosity of the formed film was measured to be approximately 80%. The porous film was directly fabricated on the YSZ substrate. The prepared film was sintered at 1200 °C for 2 h to evaluate its anode performance. The polarization of this anode at a current density of 0.5 A/cm^2 was 70 mV and 20 mV at 700 °C and 800 °C, respectively [8]. These values were significantly lower than those reported in the literatures. Figure 17.11 shows the SEM image of the Ni-YSZ anode after the electrochemical performance testing [8]. By the treatment in a reducing atmosphere, NiO was transformed into Ni. The anode with a homogeneous porous structure consisting of dispersed Ni and YSZ grains with the size of $\sim$200 nm was successfully fabricated. Consequently, the mechanical method has promised as a simple fabrication process of electrodes for solid oxide fuel cells.

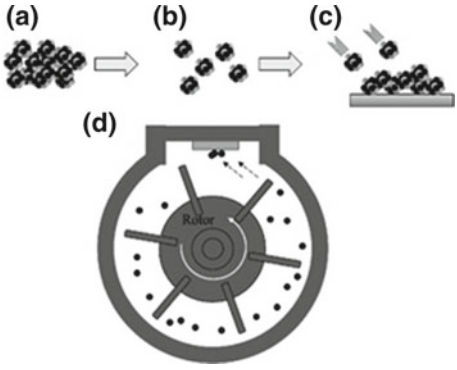

Fig. 17.9 Schematic illustration of mechanically assisted deposition of nanoparticles on the substrate: **a–c** processing steps of the deposition and **d** schematic illustration of an attrition-type milling device. Reproduced from Ref. [8] by permission of Wiley Ltd.

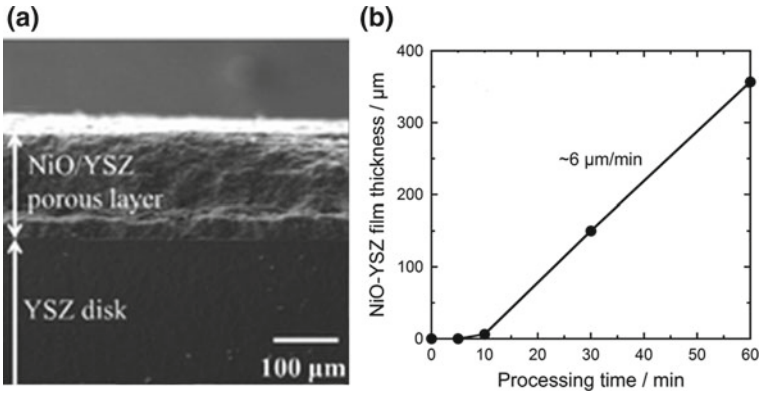

Fig. 17.10 **a** Cross-sectional SEM image of the as-deposited NiO–YSZ film. **b** Relationship between film thickness and processing time. Reproduced from Ref. [8] by permission of Wiley Ltd.

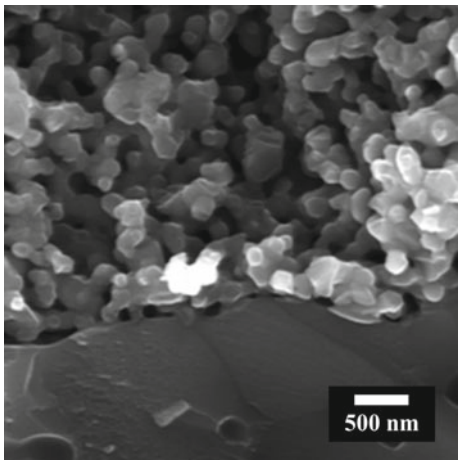

Fig. 17.11 Cross-sectional SEM image of the Ni–YSZ porous film after the electrochemical testing. Reproduced from Ref. [8] by permission of Wiley Ltd.

References

1. M. Naito, A. Kondo, T. Yokoyama, Applications of comminution techniques for the surface modification of powder materials. ISIJ Int. **33**, 915–924 (1993)
2. T. Fukui, K. Murata, S. Ohara, H. Abe, M. Naito, K. Nogi, Morphology control of Ni-YSZ cermet anode for lower temperature operation of SOFCs. J. Power Sources **125**, 17–21 (2004)
3. T. Misono, K. Murata, T. Fukui, J. Chaichanawong, K. Sato, H. Abe, M. Naito, Ni-SDC cermet anode fabricated from NiO-SDC composite powder for intermediate temperature SOFC. J. Power Sources **157**, 754–757 (2006)
4. K. Sato, J. Chaichanawong, H. Abe, M. Naito, Mechanochemical synthesis of $LaMnO_3$ fine powder assisted with water vapor. Mater. Lett. **60**, 1399–1402 (2006)

5. A. Kondo, K. Sato, H. Abe, M. Naito, H. Shimoda, Mechanochemical synthesis of barium titanate from nanocrystalline $BaCO_3$ and TiO_2. Ceram. Trans. **198**, 375–380 (2007)
6. S. Ohara, A. Kondo, H. Shimoda, K. Sato, H. Abe, M. Naito, Rapid mechanochemical synthesis of fine barium titanate. Mater. Lett. **62**, 2957–2959 (2008)
7. X. Xi, A. Kondo, M. Naito, A simple mechanical process to synthesize $La_{0.6}Sr_{0.4}Co_{0.2}Fe_{0.8}O_3$ perovskite for solid oxide fuel cells cathode. Mater. Lett. **145**, 212–215 (2015)
8. H. Abe, M. Naito, K. Sato, Mechanically assisted deposition of nickel oxide-yttria stabilized zirconia nanocomposite film and its microstructure evolution for solid oxide fuel cells anode application. Int. J. Appl. Ceram. Technol. **9**, 928–935 (2012)
9. H. Abe, I. Abe, K. Sato, M. Naito, Dry powder processing of fibrous fumed silica compacts for thermal insulation. J. Am. Ceram. Soc. **88**, 1359–1361 (2005)
10. T.-W. Lian, A. Kondo, T. Kozawa, T. Ohmura, W.-H. Tuan, M. Naito, Effect of fumed silica properties on the thermal insulation performance of fibrous compact. Ceram. Int. **41**, 9966–9971 (2015)
11. T. Kozawa, N. Kataoka, A. Kondo, E. Nakamura, H. Abe, M. Naito, One-step mechanical synthesis of $LiFePO_4$/C composite granule under ambient atmosphere. Ceram. Int. **40**, 13131–16127 (2014)
12. T. Kozawa, N. Kataoka, A. Kondo, E. Nakamura, H. Abe, M. Naito, Facile preparation of porous $LiFePO_4$/C composite granules by mechanical process. Mater. Chem. Phys. **155**, 246–251 (2015)
13. J. Yoshida, S. Nakanishi, H. Iba, A. Kondo, H. Abe, M. Naito, One-step mechanical synthesis of the nanocomposite granule of $LiMnPO_4$ nanoparticles and carbon. Adv. Powder Technol. **24**, 829–832 (2013)
14. A. Kondo, E. Nakamura, T. Kozawa, H. Abe, M. Naito, J. Yoshida, S. Nakanishi, H. Iba, One-pot mechanical synthesis of the nanocomposite granule of $LiCoO_2$ nanoparticles. Adv. Powder Technol. **25**, 1280–1284 (2014)
15. E. Nakamura, A. Kondo, T. Kozawa, H. Abe, M. Naito, J. Yoshida, S. Nakanishi, H. Iba, One-pot mechanical synthesis of $LiCoO_2$ from Li_2O powder. J. Soc. Powder Technol. Japan **51**, 131–135 (2014)
16. T. Kozawa, A. Kondo, E. Nakamura, H. Abe, M. Naito, H. Koga, S. Nakanishi, H. Iba, Rapid synthesis of $LiNi_{0.5}Mn_{1.5}O_4$ by mechanical process and post-annealing. Mater. Lett. **132**, 218–220 (2014)
17. T. Kozawa, M. Naito, Facile preparation of core@shell and concentration-gradient spinel particles for Li-ion battery cathode materials. Sci. Technol. Adv. Mater. **16**, 015006, 8 (2015)

Chapter 18
Three-Dimensional Printing Process

Soshu Kirihara

Abstract Stereolithographic additive manufacturing was developed to create metal and ceramic components with functionally modulated geometry using a computer-aided design, manufacturing, and evaluation. Micrometer-scale ceramic lattices are propagated spatially in the computer graphic space. Photosensitive liquid resins with ceramic nanoparticles are spread on a glass substrate using a mechanical knife edge, and two-dimensional (2D) images are drawn by fine pattern exposure or fast laser scanning to create a cross-sectional solid layer. After these layers are stacked, the obtained three-dimensional (3D) structures of the composite precursors are dewaxed and sintered. Ceramic and metallic glass photonic crystals with dendritic and magnetic micro-lattices can be fabricated to control electromagnetic waves over the terahertz frequency range. Subsequently, solid electrolyte dendrites of yttria-stabilized zirconia with spatially ordered porous structures could be processed for fuel cell miniaturization. Moreover, artificial bones of calcium phosphate with dendritic scaffold structures can be modeled to achieve excellent biological compatibilities.

Keywords Additive manufacturing · Stereolithography · Photonic crystal · Solid oxide fuel cell · Artificial bone

18.1 Stereolithography of Additive Manufacturing

Centimeter-scale components were fabricated by laser scanning stereolithography. 3D geometric patterns in three-dimensional models are modeled by a computer-aided design application. These graphic models are converted automatically into the stereolithography format and sliced into a series of 2D cross-sectional planes of 50 μm in uniform layer thickness. The numerical data are transferred automatically into the stereolithography equipment and raster patterns for laser

S. Kirihara (✉)
Joining and Welding Research Institute, Osaka University, Ibaraki, Japan
e-mail: kirihara@jwri.osaka-u.ac.jp

Y. Setsuhara et al. (eds.), *Novel Structured Metallic and Inorganic Materials*, https://doi.org/10.1007/978-981-13-7611-5_18

scanning are created automatically. Figure 18.1a shows the schematic illustrations of the fabrication process [1]. The photosensitive acrylic resin that contains ceramic particles 200 nm in diameter at 40% volume fraction is spread on a flat metal stage using a mechanical knife edge. The thickness is controlled automatically at the same value of 50 μm in the model slicing pitch. An ultraviolet laser of wavelength 355 nm is scanned on the ceramics slurry in order to create cross-sectional planes with 5 μm edge accuracy. The laser beam is adjusted to a 100 μm spot size and 100 mW power. After the formation of the solid pattern, the elevator stage moved downward 50 μm in layer thickness, and then, the next cross section is stacked. Three-dimensional structures were fabricated by stacking all two-dimensional layers. The accuracy of the part for the green bodies can be measured and observed using a digital optical microscope. The formed models are dewaxed at 600 °C for 2 h with a heating rate of 1.0 °C/min in air and the full ceramic components are obtained after sintering. Microstructures of the sintered components can be observed using a scanning electron microscope (SEM). Relative densities of these ceramic components can be measured by the Archimedes' method.

Micrometer-scale patterns were created by micro-patterning stereolithography. 3D patterns are designed using computer graphic software. The designed models are converted into the stereolithography file format and sliced into the series of two-dimensional cross-sectional data of 10 μm in layer thickness. These data are automatically transferred into the micro stereolithography equipment to create bit map images for micro-pattering. Figure 18.2b shows a schematic illustration of the micro stereolithography system [2]. Photosensitive acrylic resins that include ceramic nanoparticles of 200 nm average diameters at 40 vol.% are placed on a glass substrate from a dispenser nozzle using air pressure. This paste is spread uniformly using a mechanically controlled knife edge. The thickness of each layer was set at 10 μm. Two-dimensional solid patterns are obtained on the slurry surface by light-induced photopolymerization. High-resolution images were obtained using a digital micromirror device. In this optical device, 1024 × 768 μ aluminum mirrors of 14 μm edge length were assembled. Each mirror can be tilted independently by piezoelectric actuation. The ultraviolet lay of 405 nm is introduced into the digital micromirror device, and the cross-sectional image is reduced by 1/5 using an

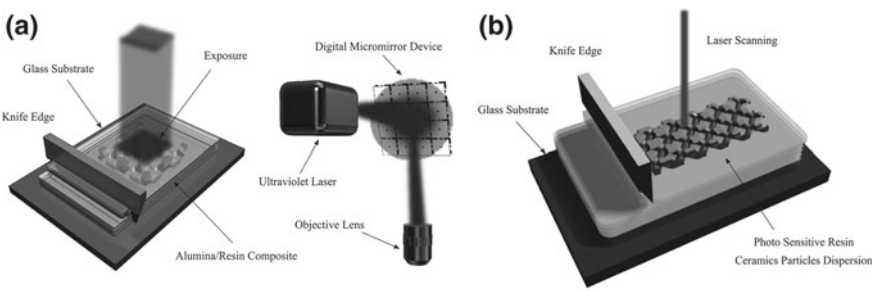

Fig. 18.1 Schematic illustration of **a** fine pattern exposure and **b** fast laser scanning stereolithography of additive manufacturing

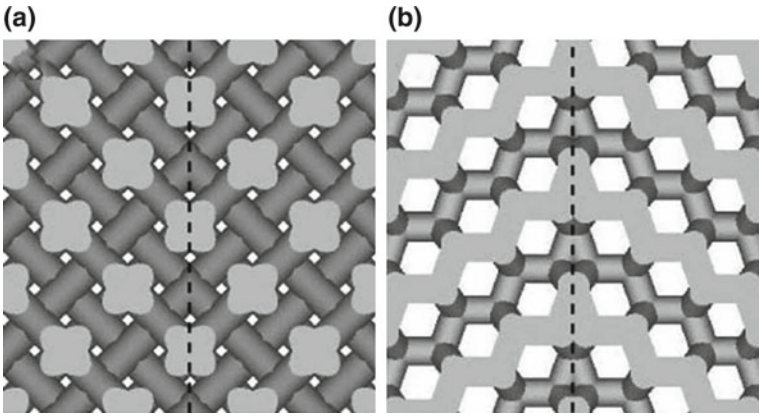

Fig. 18.2 Computer graphic models of twinned photonic crystals with diamond structures. Defect interfaces parallel to the (100) and (111) planes indicated by dotted lines were sandwiched between mirror symmetric lattice domains, as shown in (**a**) and (**b**), respectively

objective lens set and concentrated into an exposure area of 1.3 mm × 1.7 mm. Through layer stacking, which is controlled by a computer, the acrylic resin component with the ceramics particles dispersion is obtained. The composite precursor is dewaxed at 600 °C for 2 h in air. The complete ceramic micro-components are obtained through the sintering heat treatment. The part accuracy and ceramic microstructures of the sintered components can be observed using SEM.

18.2 Photonic Crystals with Dielectric Lattice

Novel electromagnetic devices using photonic crystals have been fabricated by stereolithographic techniques. The artificial crystals with a periodic arrangement of dielectric media can reflect the electromagnetic wave perfectly and can exhibit forbidden gaps in the transmission spectra by Bragg diffraction [3–6]. By introduction of air cavities into the periodic lattices, electromagnetic waves of specific wavelengths can resonate with the structural defects and localized modes of transmission peaks appear in the band gap [7–11]. Alumina microlattices with diamond structures were fabricated to control the terahertz waves [12]. The terahertz waves are expected to detect micro-cracks in the material surfaces and structural defects in electric circuits by fine wave interferences, and to analyze cancer cells in human skins and toxic bacteria in natural foods through the higher frequency excitations [13–17]. A theoretical electromagnetic band diagram of the diamond photonic crystal was graphed through a plane wave expansion (PWE) application [18]. Intensity profiles of the structural defects in the presence of electric fields were simulated at localized mode frequencies using a transmission line modeling (TLM) simulator.

Photonic crystals with diamond lattices with structural defects were designed using a computer graphics application as shown in Figs. 18.2 and 18.3. Twinned defect interfaces between mirror symmetric lattices were formed parallel to the (100) and (111) planes, as shown in Fig. 18.2a, b, respectively. Double-cavity defects, consisting of hollowed unit cells, are arranged with center intervals of 1.5 and 2.0, as shown in Fig. 18.3a and b, respectively. Dielectric rods with an aspect ratio of 1.5 are connected with a coordination number of four to create a diamond structure with a 500 μm lattice constant. Acrylic photonic crystals with dispersed alumina particles of 200 nm average diameter at 40 vol.% were successfully created using micro-stereolithography, as shown in Fig. 18.4a. The part tolerances were measured to be within ±5 μm by DOM. The homogenized dispersions of the alumina particles in the acrylic resin matrix were observed by SEM, as shown in Fig. 18.4b. The complete ceramic micro-lattices of the alumina photonic crystals, after dewaxing and sintering, are shown in Fig. 18.5a. The stereolithography samples were dewaxed at 600 °C for 2 h, and then, sintered at 1500 °C for 2 h in air. The heating rates were 1.0 and 8.0 °C/min in the dewaxing and sintering processes, respectively. The lattice constant and the linear shrinkage were measured by DOM to be 375 μm and 25%, respectively. An alumina microstructure of 99% relative density was observed by SEM, as shown in Fig. 18.5b. The forbidden bands exhibited in the transmission spectra for the <111>, <100>, and <110> crystal directions were analyzed, and the dielectric constant of the alumina lattice was measured to be 9.8 using terahertz time-domain spectroscopy (THz-TDS). The higher and lower edges of the gap regions were plotted in the PWE calculated band diagram. The measured results were in good agreement with the calculated results, and a perfect photonic band gap was created over the 0.4–0.47 THz range. The isotropic propagation of dense alumina lattices with a coordination number of four was verified. These results are evidence that the lattice

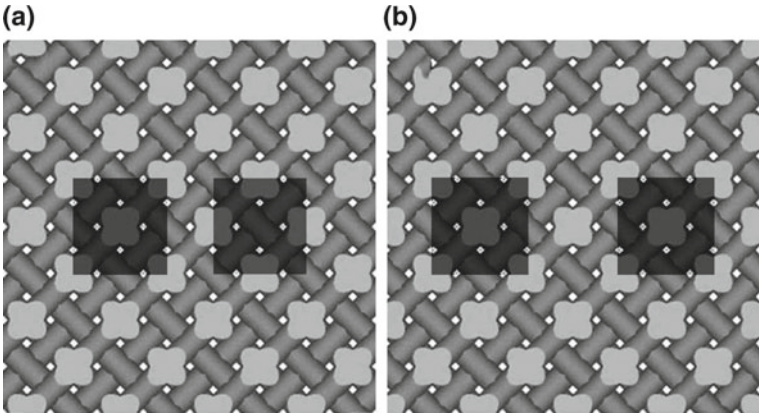

Fig. 18.3 Graphic models of diamond photonic crystals, with cubic defects indicated by dark areas. Unit cells were hollowed from the lattice structures in order to create double-cavity defects with 1.5 and 2.0 periods at center intervals, as shown in (**a**) and (**b**), respectively

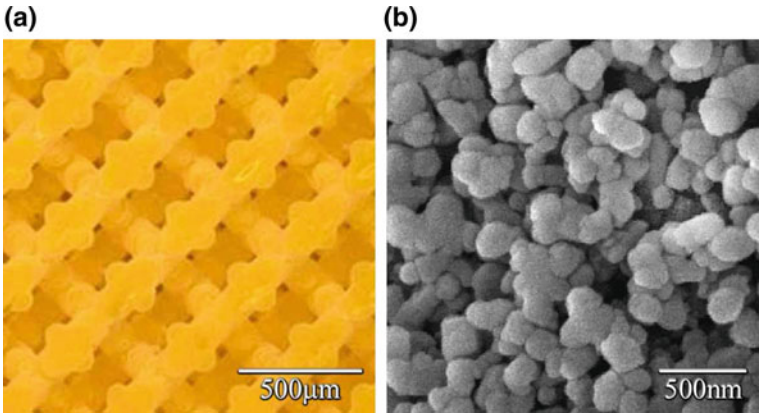

Fig. 18.4 Precursor model of the photonic crystal fabricated using the microstereolithographic 3D printer: **a** Acryl microrods propagating with a coordination number of four and **b** homogenized dispersion of nanometer-sized alumina particles

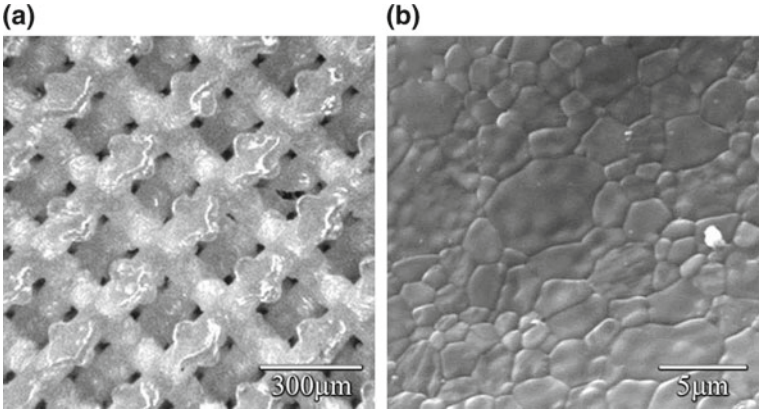

Fig. 18.5 Full ceramic component of the photonic crystal processed through the dewaxing and sintering treatments of the composite precursor. **a** Alumina micro-lattices with **b** fine microstructure were formed successfully

structures had shrunk equally in all crystal directions without any dimensional deviations during the controlled dewaxing and sintering.

Alumina photonic crystals with twinned diamond lattices can be formed successfully through micro stereolithography and powder sintering. As shown in Fig. 18.6a, b, the defect interfaces of the (100) and (111) planes are sandwiched between the mirror symmetric domains with four and three periods, respectively. These period numbers can be optimized to exhibit the clear localized modes of sharp transmission peaks in the band gaps using TLM. The transmission spectra through the twinned crystals can be analyzed by the THz-TDS. As shown in

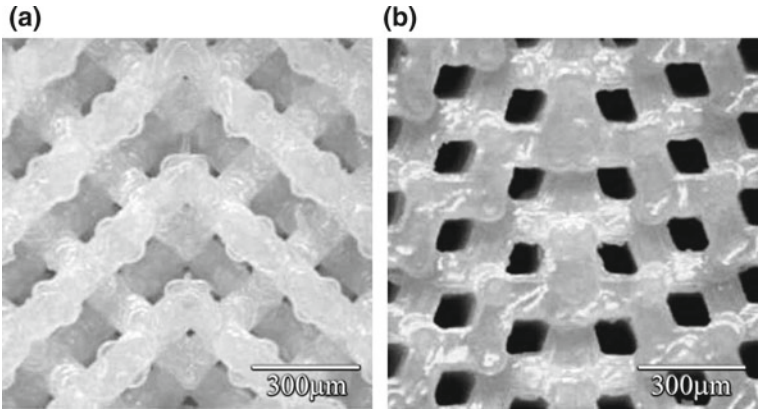

Fig. 18.6 Twinned photonic crystals composed of the sintered alumina lattices. The defect interfaces were formed between the diamond lattice domains parallel to the (100) and (111) planes, as shown in (**a**) and (**b**), respectively

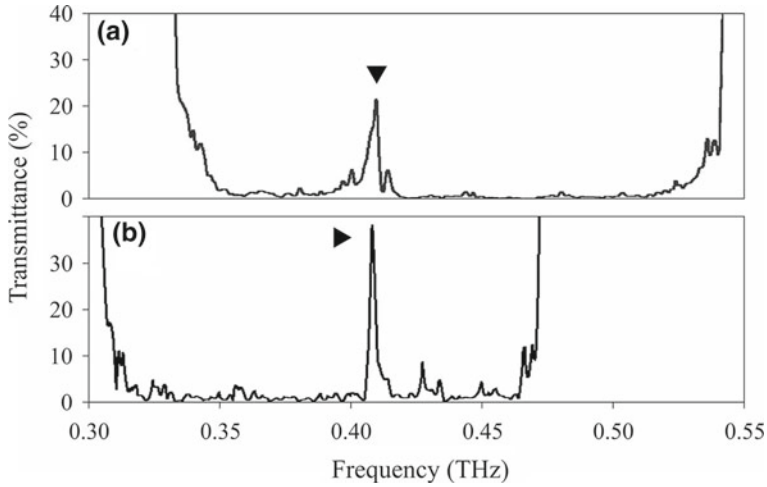

Fig. 18.7 Transmission spectra through the twinned photonic crystals measured by terahertz time-domain spectroscopy (THz-TDS). The localized modes of the transmission peaks, indicated as solid triangles, were formed in the band gaps by the introduction of defect interfaces into the alumina lattices parallel to the (100) and (111) planes, as shown in (**a**) and (**b**), respectively

Fig. 18.7a, b, the localized mode peaks with transmission intensities of 22% and 38% are formed at 0.414 and 0.409 THz through the (100) and (111) defect interfaces, respectively. These localized modes are included in the perfect photonic band gap. Figure 18.8 shows the cross-sectional images of the electric field intensity simulated at the localized frequencies by TLM. The incident electromagnetic waves resonate and are localized strongly through the multiple reflections

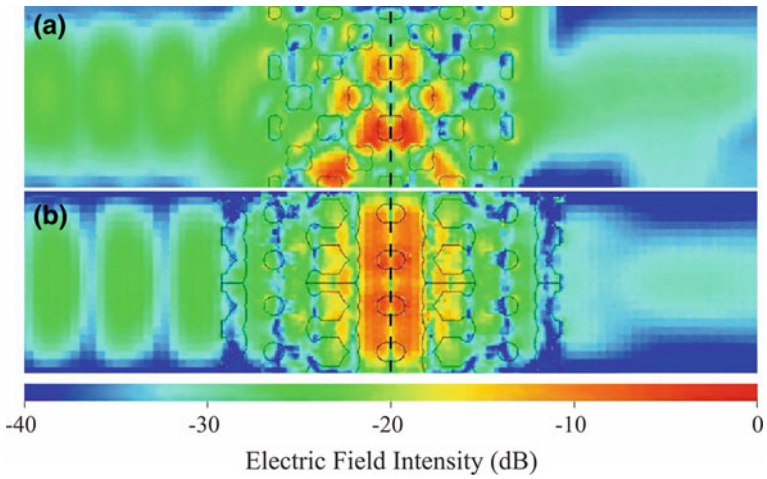

Fig. 18.8 Intensity profiles of electric fields in the twinned photonic crystal visualized by TLM. The strong localized modes were formed in the defect interfaces, indicated as dotted lines, through multiple reflections between the (100) and (111) plane arrangements, as shown in (**a**) and (**b**), respectively

in the twinned defect interfaces between the mirror symmetric diffraction lattices. The amplified electromagnetic waves can propagate to the opposite side, and transmission peaks should be formed in the band gaps. The electromagnetic wave energy can be concentrated strongly near the (111) defect interfaces as compared to the (100) plane. These simulated results conform to the disparity in the measured peak intensities of the localized modes, as shown in Fig. 18.8.

Double-cavity defects are introduced into the alumina photonic crystals by hollowing the unit cells of the diamond lattices, as shown in Fig. 18.9. As shown in

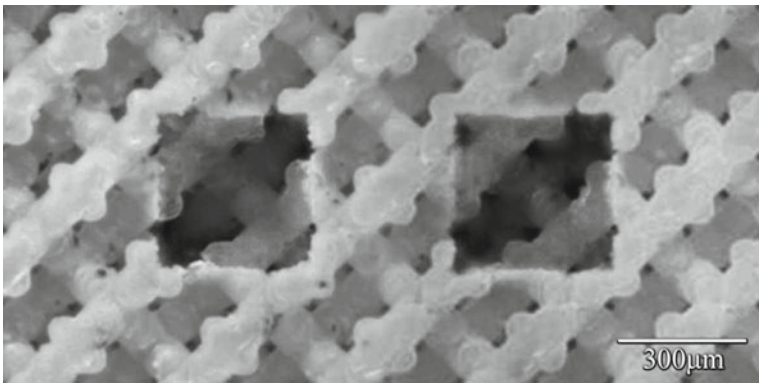

Fig. 18.9 Sintered alumina lattices with double-defect cavities. The unit cells were hollowed from the diamond structure. The cubic cavities were separated by one period of the lattice arrangement

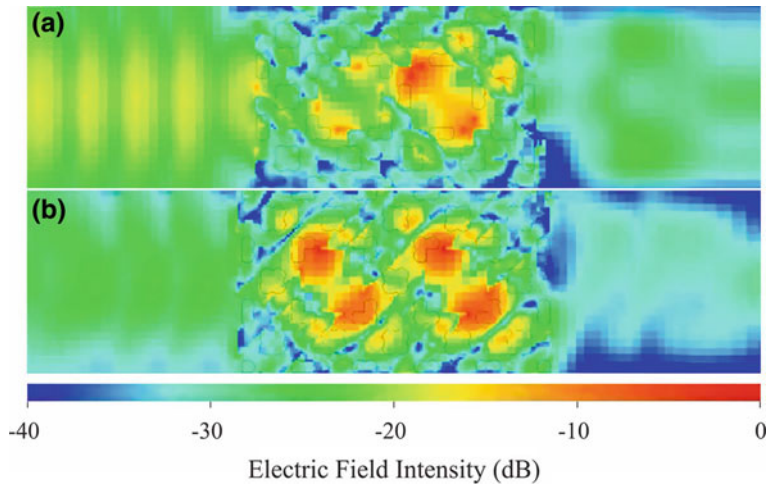

Fig. 18.10 Intensity profiles of electric fields in the double-defect cavities simulated by TLM. The double localized modes were formed in the cubic cavities arranged with 1.5 and 2.0 periods at center intervals, as shown in (**a**) and (**b**), respectively

Fig. 18.10a and b, the intensity profiles of the electric fields in the vicinity of the double-cavity defects arranged with 1.5 and 2.0 periods in center intervals, respectively, can be simulated by TLM. The electromagnetic waves resonated and were localized in the cubic cavities. The single resonance mode spread near closed cavities, and the coupled mode is localized strongly in the separated dual cavity. The transmission spectra, including the photonic band gaps and localized modes, can be analyzed by the THz-TDS. As shown in Fig. 18.11a, b, localized mode peaks with transmission intensities of 5% and 27% form at 0.45 and 0.56 THz, respectively, through the double-cavity defects separated by the 1.5 period lattice structures. The spread mode should form a small resonance peak at the longer wavelength of the lower frequency. The concentrated mode can achieve a sharp and clear peak formation with the higher transmission intensity.

18.3 Photonic Crystal with Magnetic Lattice

Micrometer-scale magnetic photonic crystals with the diamond structure can exhibit forbidden gaps over the terahertz frequency range according to the diffraction theories of electromagnetic waves, and the introduced defects cavities can form the localized modes of the transmission peaks in the photonic band gaps [19]. Micromagnetic lattices composed of metallic glass dispersed oxide glass can be fabricated by the fine pattern exposure stereolithography to control the terahertz waves effectively. The device is schematically illustrated in Fig. 18.12.

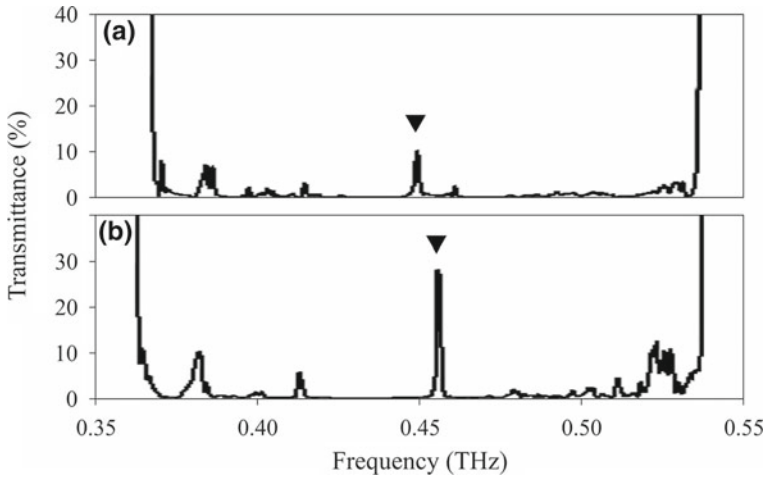

Fig. 18.11 Transmission amplitude of the terahertz waves through the photonic crystal with defect cavities measured by the THz-TDS. The transmission peaks, indicated by solid triangles, were formed in the band gaps through resonance and localization into double-defect cavities separated by the 1.5 period of the diamond structures, as shown in (**a**) and (**b**), respectively

The artificial crystal with a cylindrical structural defect can resonate with the specific terahertz wave of wavelength comparable to the cylinder diameter, and the localized mode of transmission peak appears in the band gap [20–23]. When various aqueous solvents were flown into the microtube, the localized modes will be shifted in the gap according to the dielectric constants of the liquid materials. If the resonant wave can harmonize with the collective vibration mode of the introduced aqueous solvents, the transmission peak will disappear through electromagnetic absorptions. Moreover, the profiles and frequency ranges of the band gaps can be modulated by the permeability control of the diffraction lattices by applying a static magnetic field. The magnetic photonic crystal sensors can be used in various scientific and engineering fields by utilizing the terahertz wave spectroscopic database.

The magnetic photonic crystal with the diamond lattices fabricated by fine pattern exposure stereolithography is shown in Fig. 18.13a [24]. The size tolerance between the designed model and the formed sample converges to within ±3 μm. The rod diameter and length are 144 and 217 μm, respectively, and the lattice constant of the diamond structure is 500 μm. The entire structure is 5 mm × 5 mm × 0.5 mm in size comprising 10 × 10 × 1 unit cells. Photosensitive acrylic resins dispersed with magnetic metallic glass (Fe72B14.4Si9.6Nb4) and dielectric oxide glass (B2O3·Bi2O3) particles of 2.6 μm and 1.0 μm diameter, respectively, were applied on a substrate and spread uniformly using a mechanical knife edge. The metallic glass and oxide glass particles were dispersed in the acrylic resin at 40 vol.%, and these two kinds of particles were mixed at 16:24, 17:23, and 18:22 volume ratios. The iron-based metallic glass is a soft magnetic amorphous alloy with high glass forming ability and magnetic permeability [25]. In the optimization of the

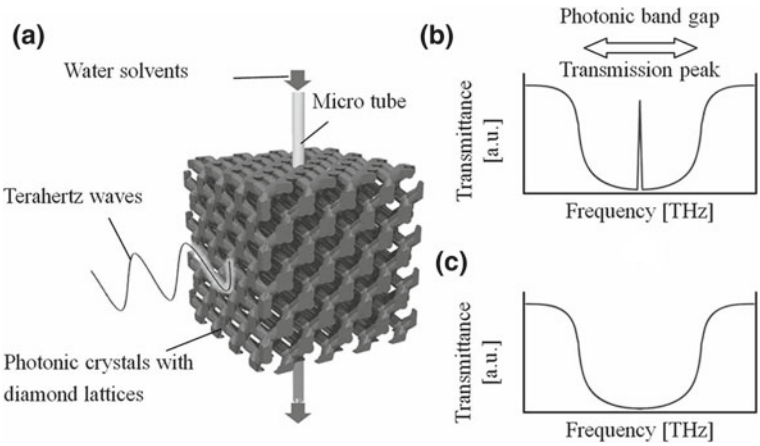

Fig. 18.12 **a** A schematic illustration of a magnetophotonic crystal sensor device and transmission spectra of terahertz waves including various water solvents **b** without or **c** with absorption properties

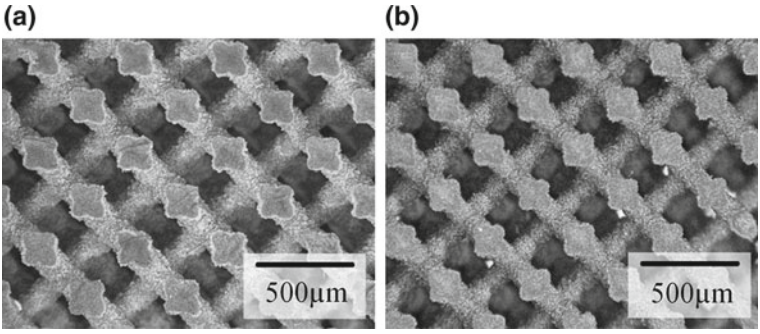

Fig. 18.13 **a** An acryl diamond lattice with metallic glass ($Fe_{72}B_{14.4}Si_{9.6}Nb_4$) and oxide glass ($B_2O_3{\cdot}Bi_2O_3$) particle dispersion fabricated by stereolithography and **b** a magnetophotonic crystal after dewaxing and sintering

stereolithographic parameters, the exposure power influences the layer thicknesses, and size tolerances should be compared and investigated systematically in the formed acrylic objects with the different mixing ratios of the metallic and oxide glasses. When the micropattern was exposed to a light intensity of 700 mJ/cm^2 on the acrylic resin including the metallic and oxide glass particles at 17 and 23 vol.%, the layer thickness and size tolerance were measured as 14.5 μm and ±3 μm, respectively. The photopolymerization depth should be greater than 10 μm of the stacking layer thickness with restraining the exposure right scatters.

The sintered diamond lattice structure with a 500 μm lattice constant is shown in Fig. 18.13b. The formed precursor was dewaxed at 420 °C for 8 h at a heating rate

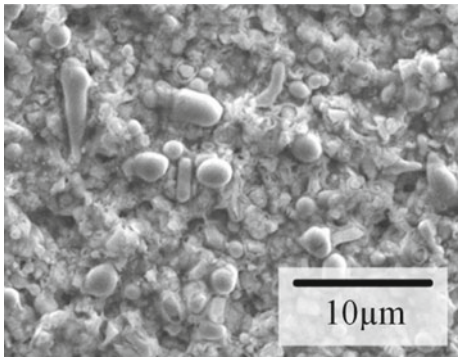

Fig. 18.14 A microstructure of the oxide glass lattice with the metallic glass particles dispersion observed by scanning electron microscopy

of 1.0 °C/min, and sintered at 460 °C, which is below the glass transition temperature of 552 °C of the selected metallic glass, for 0.5 h at a heating rate of 2.0 °C/min in argon atmosphere. The diamond lattice model can be corrected and redesigned according to the linear shrinkage ratios. The linear shrinkage ratios of the horizontal and vertical axes were 10.2% and 12.5%, respectively. These results can be fed back successfully to the computer graphic design to achieve an isotropic arrangement of the diamond lattice. Figure 18.14 shows the microstructure of the sintered metallic glass and the oxide glass composite lattice. The metallic glass particles were dispersed homogeneously in the oxide glass matrix. The X-ray diffraction patterns of metallic glass particles before and after the heat treatments were analyzed. The metallic glass did not crystallize during the dewaxing and sintering heat treatments. The measured terahertz wave transmission spectrum for the magnetic photonic crystal is shown in Fig. 18.15. The black and gray lines show the measured and calculated results, respectively, and there is good agreement between them. The theoretical visualization of the electromagnetic wave propagation could verify the presence of the forbidden gap due to wave diffraction. The electromagnetic bandgap is formed from 0.2 to 1.0 THz. Between the lower and higher bandgap edges, the electromagnetic waves from 300 to 1500 μm wavelengths create standing vibrations in the periodic arrangements of magnetic lattices and achieve total reflection for the incident direction through the Bragg diffractions.

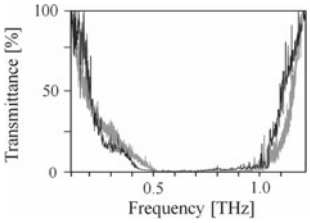

Fig. 18.15 An electromagnetic bandgap formation in the transmission spectrum of the terahertz wave through the magnetophotonic crystal with the diamond lattice structure. The black and gray lines show the measured and calculated results, respectively

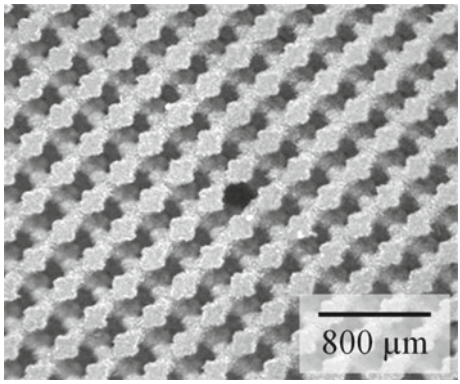

Fig. 18.16 The magnetophotonic crystal with a structural defect in the periodic lattice of the diamond structure. The round hole was created as the defect cavity in the perpendicular direction toward the crystal face

A magnetic photonic crystal with a structural defect fabricated by stereolithography and low-temperature sintering is shown in Fig. 18.16. A round hole of 200 μm diameter is created as the defect cavity exactly into the diamond lattice structure perpendicular to the crystal face. The terahertz wave propagated in a direction parallel to the created hole, and the transmission spectrum is obtained as shown in Fig. 18.17. The black and gray denote the measured and calculated spectra, respectively. The localized modes of the transmission peaks are formed in the band gaps. At peak frequencies of 0.72, 0.75, and 0.79 THz, the half wavelengths of 208, 200, and 189 are comparable to the cavity diameter of the defect hole, and standing waves should be formed by multiple reflections between the diffraction lattices. The amplified terahertz waves can be transmitted selectively toward the opposite side of the magnetophotonic crystal. Because the created hole has an uneven surface, similar wavelengths could resonate in the cavity, and the three localized modes are considered to be formed in the band gap as shown in Fig. 18.17. The electromagnetic field profiles of these localized modes were calculated and visualized in the cylindrical cavity. Moreover, the intentional shifts of the bandgap frequency and localized mode peaks could be simulated through the lattice permeability modulations assuming the application of the static magnetic field toward the magnetophotonic crystal.

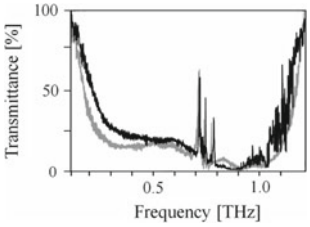

Fig. 18.17 Formation of localized modes in the electromagnetic bandgap. The terahertz waves with the selected wavelengths can resonate with the defect cavity and transmit through the crystal. The black and gray lines show the measured and calculated results, respectively

18.4 Porous Electrode with Ordered Structure

For sustainable development and emission reduction of carbon oxides, solid oxide fuel cells (SOFCs) have been investigated as novel electric power generation systems with high efficiencies in energy conversion devices. Yttria-stabilized zirconia (YSZ) with high ion conductivities of incident oxygen is widely adopted as a material for solid electrolyte anodes in SOFC [26–30]. To increase the surface areas of the reaction interfaces and gap volumes of the stream paths, porous network structures of micrometer or nanometer sizes have been introduced into the YSZ electrodes. By using additive manufacturing of the stereolithography process, solid electrolyte dendrites composed of YSZ spatial lattice structures with various coordination numbers can be fabricated successfully. In the lattice dendrites, fluid flow velocities and pressure stress distributions are simulated and visualized by a finite volume method (FVM) application.

The solid electrolyte dendrites with spatial lattice structures were designed using a computer graphic application. These surface areas of the reaction interfaces and the gap volume of the stream paths are calculated geometrically for the dendrite lattice with four coordination numbers as shown in Fig. 18.18. The dendritic lattices of 1.16 aspect ratio are considered to exhibit higher reaction efficiencies and gas transmittances according to the Nernst equation. In the optimized dendrite structure, the diameter and length of the YSZ rods were 92 μm and 107 μm, respectively. The lattice constant was 250 μm.

Acrylic micro-lattices with YSZ particles of 60 and 100 nm first and second diameters, respectively, at 30 vol.% can be fabricated by the fine pattern exposure stereolithography as shown in Fig. 18.19 [31]. The formed precursors with dendrite structures were heated at various temperatures from 100 to 600 °C at a heating rate of 1.0 °C/min. The dewaxing process was examined with respect to weight and color changes. The YSZ particles could be sintered at 1500 °C for 2 h. The heating rate was 8.0 °C/min. The sintered solid electrolyte dendrite with the YSZ micro-lattice structure is shown in Fig. 18.20. Deformation and cracking were not observed. The volume fraction of the air gaps is 50% because of the open paths. When the porous electrodes were formed by sintering the YSZ surly with polystyrene particles as foaming materials, it was difficult to achieve perfectly formed pore structures with a high porosity of over 40% volume fraction. In the dense

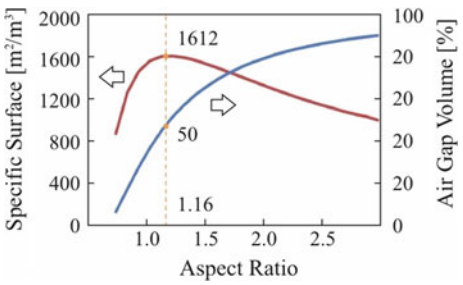

Fig. 18.18 Optimization of the aspect ratio to obtain the widest specific surface and higher air gap volume. The aspect ratio was determined as 1.16 for designing

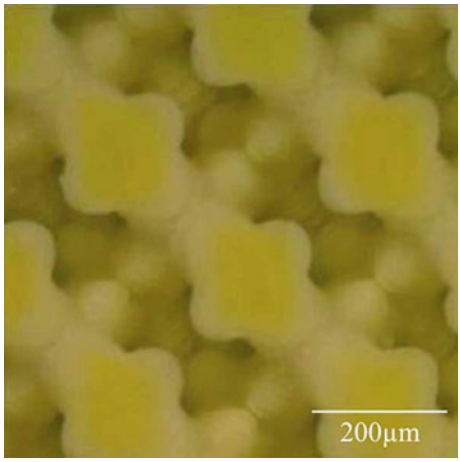

Fig. 18.19 Acryl dendrite lattice with YSZ particle dispersion fabricated using stereolithography

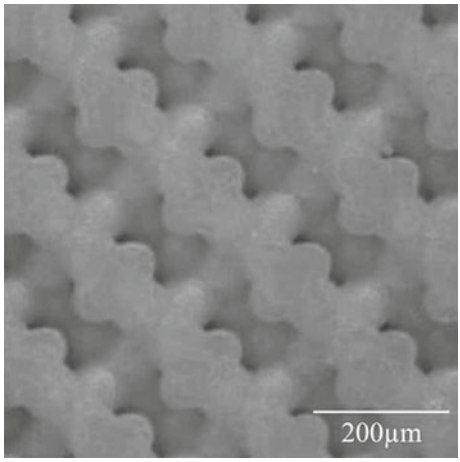

Fig. 18.20 The sintered dendrite lattices of YSZ solid electrolyte. The part accuracy of the lattice is 2 μm

microstructure of the YSZ lattice, the average grain size was approximately 4 μm. The density of the sintered sample was measured using the Archimedes' method. The relative density achieved was 95%. Micrometer-sized cracks or pores were not observed. The obtained dense YSZ lattice structure exhibits higher mechanical properties when used as porous electrodes of the solid electrolyte dendrites.

The fluid flow velocities were visualized using the FVM method as shown in Fig. 18.21. All air paths were open to the outside and connected with each other in the YSZ dendrite lattice structures. The fluid flows can transmit the one direction smoothly. The pressure stress distributions in the dendrite are visualized as shown in Fig. 18.22. The fluid pressures are gradually distributed for the flow direction, and localization of stress is not observed. The fabricated solid electrolyte dendrites with YSZ lattices are considered to have higher performance as novel ceramic electrodes.

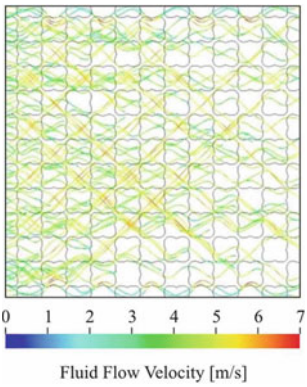

Fig. 18.21 A distribution of the fluid flow velocities in the dendrite lattice structure simulated and visualized using the FVM method. The curved lines show the fluid flow paths according to the velocity vectors

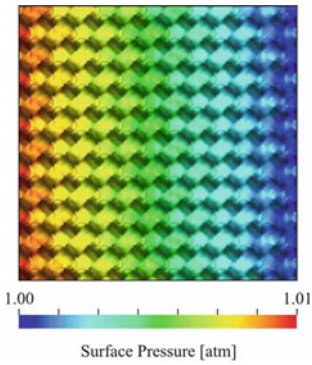

Fig. 18.22 Distribution of the surface pressure on the ceramic lattice of the dendrite structure. The red and blue areas show the higher and lower gas pressures on the reaction interfaces, respectively

18.5 Biological Scaffolds with Graded Lattice

Artificial bones composed of hydroxyapatite (HAP) and beta-tricalcium phosphate (β-TCP) scaffolds with dendritic lattice structures should be designed and formed systematically to achieve osteoconductivity and tissue regeneration successfully [32]. Prosthetic bones with ordered porous structures considering biological fluid flow behaviors can be processed using fast laser scanning stereolithography. The micro-ceramic rods are arranged periodically to create lattice patterns with various coordination numbers, and these aspect ratios should be modulated continuously to achieve biomimetic graded structures. In the dendritic structures, stress distributions and fluid flows can be simulated and visualized using finite element methods (FEM). The successfully manufactured bone substitutes and the strictly designed scaffold structures can be used to promote appropriate biochemical reactions and body fluid circulation in tissue engineering.

The dendritic lattice structures of biological scaffold models with 4 coordination numbers can be controlled from 50 to 90% by adjusting the aspect ratios of the rod length to diameter, as shown in Fig. 18.23a. The porosity variation of skeletal structures is defined at 75% as the same porosity value of a human bone [33–35].

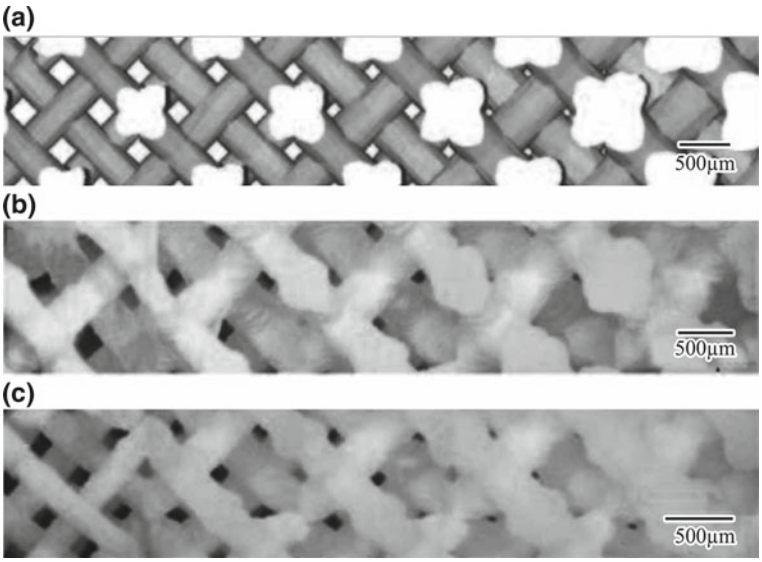

Fig. 18.23 Four-coordinate lattices with graded porous structures: **a** designed computer graphic model, **b** acrylic lattices that include hydroxyapatite particles fabricated by stereolithography, and **c** sintered ceramic scaffold

The composite lattice precursor can be fabricated precisely following the designed model using the fast laser scanning stereolithography as shown in Fig. 18.23b. Photosensitive acrylic resin comprising hydroxyapatite particles of 10 μm diameter at 45 vol.% was used. The part accuracy of the lattices was measured below 50 μm. The hydroxyapatite particles were dispersed homogeneously in the acrylic resin matrix. The formed precursor was dewaxed at 600 °C for 2 h at a heating rate of 1.0 °C/min and sintered at 1250 °C for 2 h at 5 °C/min in air. A dense biological ceramic structure was formed successfully, as shown in Fig. 18.23c. The relative density of the sintered hydroxyapatite lattice was measured as 98% by the Archimedes' method. The linear shrinkage along the horizontal and vertical axes was 23% and 25%, respectively.

Fluid circulation in the perfect interconnected pores was simulated and visualized by fluid dynamic solver as shown in Fig. 18.24. Flow velocities in the spatial grids in the scaffold models were calculated through the FEM. The fluid phase was represented as an incompressible Newtonian fluid with a viscosity of 1.45×10^{-3} Pa s [36]. The inlet velocity at the scaffolds was constant at 0.235 mm/s, and the pressure is zero at the outlet [37]. No-slip surface conditions were assumed. The relation between the fluid velocity and cell deformation has been reported, and the high fluid velocity area in the scaffold is subjected to shear stress, which was assumed to be caused by the difficulty in cell attachment. An isotropic distribution of flow rates was observed in the formed scaffold and this structure is not susceptible to shear stress.

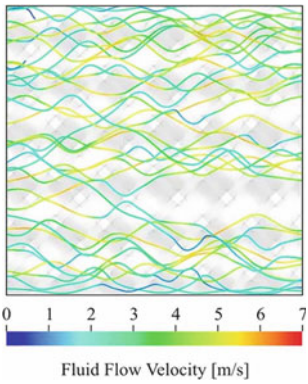

Fig. 18.24 Fluid flow behaviors in the dendrite scaffolds visualized using the finite element method

Homogeneous tissue regeneration will be promoted through geometrical modification of the scaffold models. Hence, this is an invaluable simulation for tissue engineering before confirming osteoconduction in vivo.

References

1. M. Suwa, S. Kirihara, T. Soumura, Fabrication of alumina dental crowns using stereolithography. Ceram. Trans. **219**, 331–336 (2009)
2. S. Kirihara, M. Kaneko, T. Niki, Terahertz wave control using ceramic photonic crystals with a diamond structure including plane defects fabricated by microstereolithography. Int. J. Appl. Ceram. Technol. **6**(1), 41–44 (2009)
3. K. Ohtaka, Energy band of photons and low-energy photon diffraction. Phys. Rev. B **19**(10), 5057–5067 (1979)
4. E. Yablonvitch, Inhibited spontaneous emission in solid-state physics and electronics. Phys. Rev. Lett. **58**(20), 2059–2062 (1987)
5. S. John, Strong localization of photons in certain disordered dielectric superlattices. Phys. Rev. Lett. **58**(23), 2486–2489 (1987)
6. J.D. Jonopoulos, P. Villeneuve, S. Fan, Photonic crystals: putting a new twist on light. Nat. **386**(143), 143–149 (1997)
7. B. Temelkuran, M. Bayindir, E. Ozbay, R. Biswas, M.M. Sigalas, G. Tuttle, K.M. Ho, Photonic crystal-based resonant antenna with a very high directivity. J. Appl. Phys. **87**(1), 603–605 (2000)
8. S. Noda, K. Tomoda, N. Yamamoto, A. Chutinan, Full three-dimensional photonic bandgap crystals at near-infrared wavelengths. Sci. **289**(5479), 604–606 (2000)
9. S. Noda, Three-dimensional photonic crystals operating at optical wavelength region. Phys. B **279**(1–3), 142–149 (2000)
10. Y. Akahane, T. Asano, B. Song, S. Noda, High-Q photonic nanocavity in a two-dimensional photonic crystal. Nat. **425**(6961), 944–947 (2003)
11. H. Takano, B.S. Song, T. Asano, S. Noda, Highly efficient in-plane channel drop filter in a two-dimensional heterophotonic crystal. Appl. Phys. Lett. **86**(24), 241101-1–3 (2005)
12. W. Chen, S. Kirihara, Y. Miyamoto, Three-dimensional microphotonic crystals of ZrO_2 toughened Al_2O_3 for terahertz wave applications. Appl. Phys. Lett. **91**, 153507-1–3 (2007)
13. M. Yamaguchi, F. Miyamaru, K. Yamamoto, M. Tani, M. Hangyo, Terahertz absorption spectra of L-, D-, and DL-alanine and their application to determination of enantiometric composition. Appl. Phys. Lett. **86**, 053903-1–3 (2005)

14. B.M. Fischer, M. Walther, P. Uhd Jepsen, Far-infrared vibrational modes of DNA components studied by terahertz time-domain spectroscopy. Phys. Med. Biol. **47**, 3807–3814 (2002)
15. Y. Oyama, L. Zhen, T. Tanabe, M. Kagaya, Sub-terahertz imaging of defects in building blocks. NDT&E Int. **42**, 28–33 (2009)
16. V.P. Wallace, A.J. Fitzgerald, S. Shankar, N. Flanagan et al., Terahertz pulsed imaging of basal cell carcinoma ex vivo and in vivo. Br. J. Dermatol. **151**, 424–432 (2004)
17. M. Hineno, H. Yoshinaga, Far-infrared spectra of mono-, di- and tri-saccharides in 50-16 cm-1 at liquid helium temperature. Spectrochim. Acta **30A**, 411–446 (1974)
18. K.M. Ho, C.T. Chen, C.M. Soukoulis, Existence of a photonic gap in periodic dielectric structures. Phys. Rev. Lett. **65**, 3152–3155 (1990)
19. E. Yablonobitch, Inhibited spontaneous emission in solid-state physics and electronics. Phys. Rev. Lett. **58**, 2059–2062 (1987)
20. M. Inoue, Magnetophotonic crystals. J. Phys. D Appl. Phys. **39**, R151–R161 (2006)
21. S.M. Angel, T.J. Kulp, T.M. Vess, Remote-Raman spectroscopy at intermediate ranges using low-power CW lasers. Appl. Spectrosc. **46**, 1085–1091 (1992)
22. H. Wang, Q. Wang, Spectrum characteristics of nitrofen by terahertz time-domain spectroscopy. Phys. Conf. Ser. **276**, 012209–012214 (2011)
23. M.R. Kutteruf, C.M. Brown, L.K. Iwaki, M.B. Campbell, T.M. Korter, E.J. Heilwail, Terahertz spectroscopy of short-chain polypeptides. Chem. Phys. Lett. **375**, 337–343 (2003)
24. S. Kirihara, M. Nakano, Freeform fabrication of magnetophotonic crystals with diamond lattices of oxide and metallic glasses for terahertz wave control by micro patterning stereolithography and low temperature sintering. Micromachines, **4**(2), 149–156 (2013)
25. A. Makino, in *New Functional Materials, Fundamentals of Metallic Glasses and their Applications to Industry*, ed. by A. Inoue (Technosystem, Japan, 2009), pp. 322–345
26. Y. Li, Y. Xie, J. Gong, Y. Chen, Z. Zhang, Preparation of Ni/YSZ materials for SOFC anodes by buffer-solution method. Mater. Sci. Eng. B **86**, 119–122 (2001)
27. J.-H. Lee, H. Moon, H.-W. Lee, J. Kim, J.-D. Kim, K.-H. Yoon, Quantitative analysis of microstructure and its related electrical property of SOFC anode, Ni-YSZ cermet. Solid State Ion. **148**, 15–26 (2002)
28. K.-R. Lee, S.H. Choi, J. Kim, H.-W. Lee, J.-H. Lee, Viable image analyzing method to characterize the microstructure and the properties of the Ni/YSZ cermet anode of SOFC. J. Power Sources **140**, 226–234 (2005)
29. H. Koide, Y. Someya, T. Yoshida, T. Maruyama, Properties of Ni/YSZ cermet as anode for SOFC. Solid State Ion. **132**, 253–260 (2000)
30. T. Fukui, S. Ohara, M. Naito, K, Nogi, Performance and stability of SOFC anode fabricated from NiO-YSZ composite particles. J. Power Sources **110,** 91–95 (2002)
31. N. Komori, S. Tasaki, S. Kirihara, Fabrication of dendritic electrodes for solid oxide fuel cells by using micro stereolithography, in *Proceedings of the 36th International Conference and Exposition on Advanced Ceramics and Composites*, vol. 33 (2012), pp. 0813-1–6
32. C. Maeda, S. Tasaki, S. Kirihara, Accurate fabrication of hydroxyapatite bone models with porous scaffold structures by using stereolithography. Mater. Sci. Eng. **18**(7), 072017-1–4 (2011)
33. S. Cai, J. Xi, Comput. Aided Des. **40**, 1040–1050 (2008)
34. S. Itoh, S. Nakamura, M. Nakamura, K. Shinomiya, K. Yamashita, Biomater. **27**, 5572–5579 (2006)
35. I. Sopyan, M. Mel, S. Ramesh, K.A. Khalid, Sci. Technol. Adv. Mater. **8**, 116–123 (2007)
36. A.L. Olivares, E. Marsal, J.A. Planell, D. Lacroix, Finite element study of scaffold architecture design and culture conditions for tissue engineering. Biomater. **30**, 6142–6149 (2009)
37. A.J.F. Stops, K.B. Heraty, M. Browne, F.J. O'Brien, P.E. McHugh, A prediction of cell differentiation and proliferation within a collagen-glycosaminoglycan scaffold subjected to mechanical strain and persuasive fluid flow. J. Biomech. **43**, 618–626 (2010)

Part IV
Novel Structured Materials for Environmental Protection and Advanced Energy

Chapter 19
Current and Future Nanostructured Metals

Toshinobu Yogo

Abstract Nanoporous metals (NPMs) consist of an interconnected backbone and nanosized pores. NPMs were prepared from parent alloys by chemical and electrochemical etching. The interconnected ligaments and nanostructured pores of NPMs are the origins of their novel properties. NP Au and NP Pd exhibited remarkable catalytic reactions compared with nanoparticle-based and supported catalysts. NP Au showed prominent optical properties in plasmonics and surface-enhanced Raman scattering (SERS).

Keywords Nanoporous metal · Dealloying · Heterogeneous catalyst · Plasmon · Surface-enhanced raman scattering

19.1 Introduction

Porous materials are classified into three groups by International Union of Pure and Applied Chemistry (IUPAC) as follows: microporous with pore sizes less than 2 nm in diameter, mesoporous with pore sizes between 2 and 50 nm, and macroporous with pore sizes larger than 50 nm [1]. No definition is included for nanoporous materials in the IUPAC nomenclature. However, the term nanoporous material is usually used for the materials with pore size ranging from several nm to hundreds nm as shown in Fig. 19.1. Nanoporous metals (NPMs) are characterized by interconnected skeleton (ligaments) and nanosized pores. The pore size is tunable from a few nanometers to micron depending on the fabrication conditions. NPMs have a large surface-to-volume ratio, which can be used for further functionalization by surface chemistry, extending their application to a wide range of scientific and engineering fields. NPMs have various remarkable properties, such as electrical and thermal, magnetic, optical, surface-enhanced Raman scattering (SERS), mechanical, catalytic, and electrocatalytic properties, which result from

T. Yogo (✉)
Institute of Materials and Systems for Sustainability, Nagoya University, Nagoya, Japan
e-mail: yogo@imass.nagoya-u.ac.jp

Y. Setsuhara et al. (eds.), *Novel Structured Metallic and Inorganic Materials*, https://doi.org/10.1007/978-981-13-7611-5_19

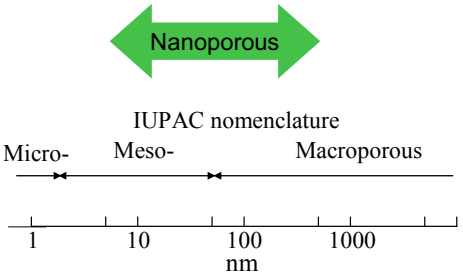

Fig. 19.1 Length scale of nanoporous and other porous materials

their characteristic nanosized structure [2, 3]. Various applications are expected in chemical, physical, and mechanical fields based on the unique properties.

Figure 19.2 shows representative photographs of NP Cu and NP Pd fabricated from CuMn and NiPdP alloys, respectively. The former and the latter were prepared by chemical etching and electrochemical etching, respectively. NP Cu has an interconnected and random 3D morphology. The morphological relation between solid ligaments and empty pore channels is quite similar to that formed by spinodal decomposition. The size of nanopores of NP Pd is smaller than that of NP Cu, although NP Pd has a similar interconnected 3D nanostructure. Hence, the sizes of nanopore and ligament depend on various factors, such as the kind of alloys, original grains, dealloying method, and dealloying conditions.

This paper focuses on the preparation, catalytic and optical properties of NPMs, although a wide range of application in science and engineering is now exploring for NPMs. NPMs are attractive materials not only for heterogeneous catalyst but also for surface plasmon because of their characteristic nanostructure.

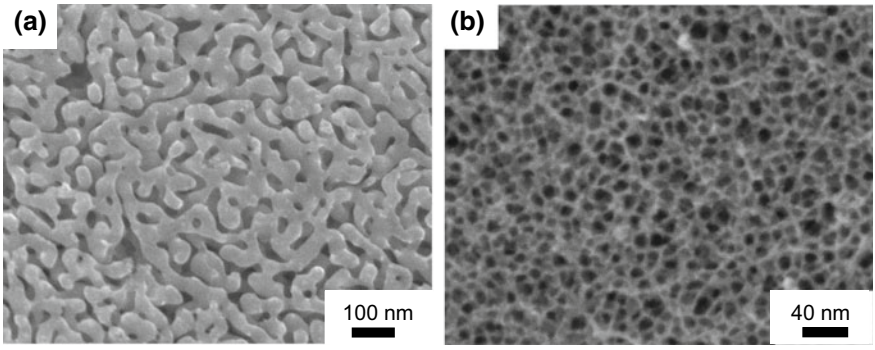

Fig. 19.2 Microstructures of **a** NP Cu prepared from MnCu alloy and **b** NP Pd from NiPPd alloy

19.2 Preparation of NP Metals

The most common methods used for the fabrication of NP metal are chemical and electrochemical dealloying, although many methods have been developed to fabricate NP metallic materials, such as dealloying [4], templating [5], anodization [6], laser etching [7], combustion synthesis [8], sol–gel [8], and thermal decomposition [9]. Among these methods, dealloying is described here as a representative method for the preparation of NPMs. Many nanoporous pure metals have been prepared by chemical etching from various alloys such as Ag–Au [4, 10], Al–Au [11], Cu–Au [12], Al–Cu [13], Zn–Cu [13], Mn–Cu [13], Ni–Cu [13], Cu–Pt [14] and Mg–Cd [15]. When a binary alloy consists of a more noble element and a less noble element, the less noble element is selectively etched away and the more noble element remains in the parent alloy during dealloying.

Various model have been proposed for the formation mechanism of NPMs. In 2001, Erlebacher et al. [16] proposed a continuum model for dealloying. The continuum model explains that nanopore formation is attributed to an intrinsic dynamical pattern formation process because the more noble atoms are moved to aggregate into two-dimensional clusters through a phase separation process (spinodal decomposition) at the solid/electrolyte interface. Figure 19.3 illustrates the dealloying process of a binary alloy. Initially, a less noble metal is dissolved from the surface of the alloy. As the isolated more noble atom is unstable and insoluble to the electrolyte, the more noble atoms diffuse on the electrolyte/alloy interface, accumulating on the surface. During diffusion, the less noble elements can appear on the top surface of alloy because the locally blocking more noble metal moves away. Less noble metal thus appears on the top surface of alloy can dissolve in the electrolyte.

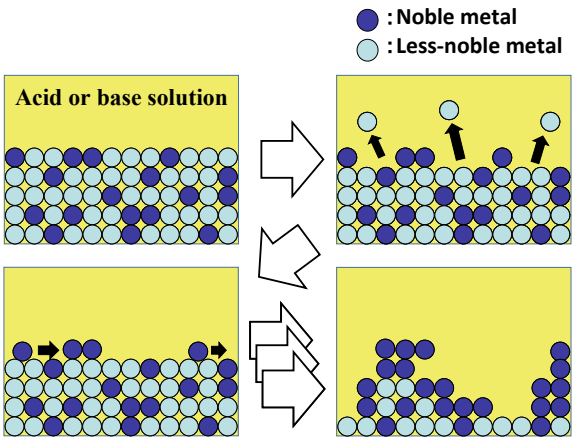

Fig. 19.3 Scheme for the dealloying of binary alloy

19.3 Nanoporous Metals in Heterogeneous Catalysis

NPM catalysts hold several advantages such as simple preparation, easy recovery, repeated use, excellent electric conductivity, and integration into device platforms. In addition, these unsupported nanocatalysts have much simpler structures than supported ones. Therefore, unsupported NPM is a model for the discussion of key parameters, such as size, strain, and electronic effects. Moreover, the catalytic activity of NPMs is different from that of supported nanoparticles for certain reactions because of their different nanostructures.

The important and successful example of dealloying catalyst is "Raney nickel", which is used in the hydrogenation of alkenes and aromatics, ammonolysis, reductive alkylations, and dehydrogenation [17]. Raney nickel is a nanoporous form of Ni produced by leaching Al out of Ni–Al alloys using sodium hydroxide. The resulting alloy includes approximately 85 wt% Ni and exhibits a high specific surface area of approximately 70–100 $m^2\ g^{-1}$ [18]. Hence, Raney nickel is called "skeletal catalysts" or "sponge metal catalysts".

Gold has been known as an inert metal and thus is not regarded as a good catalyst. However, the remarkable catalytic properties of nanoparticle Au has been disclosed from the late 1980s [19]. Unsupported NP Au shows remarkable catalytic activity for CO oxidation, even at temperatures as low as −30 °C [20, 21]. In NP Au system, CO adsorption is considered to be the rate-limiting step [22], whereas the surface oxidation of CO is rate-determining step in the supported gold nanoparticles [23]. The use of NP Au for the long time results in the coarsening of the NP Au catalyst even at temperatures below room temperature, leading to the irreversible catalyst deactivation.

During dealloying, a small amount of Ag remains within the texture of NP Au, as the NP Au was prepared from Ag–Au alloy by chemical etching. For the CO oxidation, therefore, the Ag residues can segregate to the surface and may contribute to the catalytic activities. Wittstock et al. [24] reported CO oxidation reaction over chemically dealloyed NP Au, and suggested that the segregated metallic Ag on the gold ligaments is the dissociation and activation site of O_2, which is the key step of CO oxidation. Pre-activation to of NP Au catalysts was required to achieve decent activity for CO oxidation [24]. However, NP Au dealloyed by an electrochemical method with much smaller ligament sizes is quite active for CO oxidation at low temperature (<0 °C) without any pre-activation [20, 21]. From these deferent results, the catalytic activity appears to depend on the characteristic nanostructure of NP Au, not on the presence of metallic Ag. The high catalytic activity of NP Au is attributed to the high density of the low-coordinated surface Au atoms in NP Au, which cover the high surface area of the gold ligaments. The interconnected short and curved Au ligaments in NP Au have a high radius of curvature. Thus, these low-coordinated step edges and kinks act as the active sites for catalytic reactions.

NP Au has been utilized for liquid phase heterogeneous catalyst [25]. Although unsupported Au colloids is reported to be quite active catalyst for the oxidation of

D-glucose to D-gluconic acid, they lose the catalytic activity after several minutes owing to rapid particle aggregation. On the other hand, dealloyed NP Au also is very active for this reaction and has better structure stability. The high reactivity was observed for NP Au up to the ligament sizes as large as 60 nm [25]. NP Au with small ligament sizes has higher catalytic activity than those with larger ligament sizes. Similar to the gaseous catalytic reactions by NP Au, Au atoms on the step edges and kinks are the active sites for the selective oxidation reaction in the liquid phase.

1-Phenylethanol **1** was reacted with O_2 in MeOH at 60°C for 10 h in the presence of NP Au, affording acetophenone **2** in 88% yield (Scheme 19.1) [26]. Various allylic and heteroaromatic alcohols were oxidized to corresponding ketones from 80 to 98% yield. Aliphatic secondary alcohols were oxidized in high yields by increasing the loading amount of NP Au.

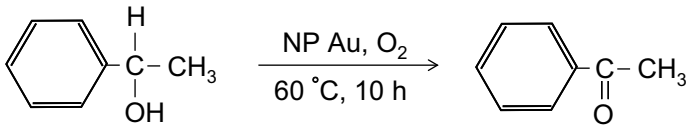

1 **2**

Scheme 19.1 Oxidation of 1-phenylethanol **1** to acetophenone **2** with NP Au

Organosilanol is usually synthesized from organosilane via oxidation with water using metal particles as catalysts. In addition to the decrease of catalytic activity due to the agglomeration, the condensation of silanols proceeds, yielding disiloxanes as by-products. On the contrary, the NP Au catalyzes the oxidation of various organosilanes, affording corresponding silanols in high yields under mild conditions. The rapid evolution of hydrogen gas during reaction was confirmed (Scheme 19.2) [27]. The oxidation of dimethylphenylsilane ($(C_6H_5)(CH_3)_2SiH$) **3** with H_2O using NP Au catalyst undergoes oxidation smoothly at room temperature, yielding dimethylphenylsilanol **4** quantitatively. No disiloxane, 1,1,3,3-tetramethyl-1,3-diphenyldisiloxane, was formed as a by-product of the reaction. The turnover number is up to 10,700. Under the reaction conditions, no grain growth was observed for Au ligaments of NP Au after repeated use. A variety of

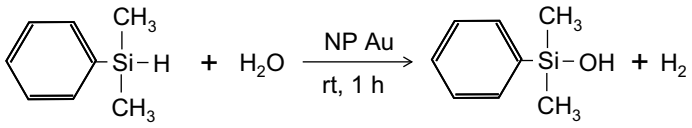

3 **4**

Scheme 19.2 Oxidation of dimethylphenylsilane **3** to dimethylphenylsilanol **4** with NP Au

organosilanes were found to undergo the catalytic oxidation with NP Au [27]. Aromatic silanes and sterically hindered trialkylsilanes were oxidized effectively. In addition, tri-, di-, and mono-phenylsilanes can be oxidized to the corresponding oxygenated products in high yields. Alkenyl- and alkynyl-substituted silanes derivatives were oxidized smoothly. No hydrogenation of their multiple bonds occurred during reaction, although H_2 gas was generated from the Si–H bond of starting silane.

NP Pd was also used for the Suzuki–Miyaura coupling reaction [28]. Iodobenzene **5** was reacted with p-tolylboronic acid **6** using NP Pd catalyst in KOH-MeOH at 50 °C for 3 h, producing the corresponding biphenyl product **7** almost quantitatively (Scheme 19.3) [29]. Although Pd nanoparticles can be used for the Suzuki–Miyaura coupling, this catalyst undergoes agglomeration under the reaction conditions, resulting in deactivation of the catalyst. In contrast, NP Pd exhibited an excellent catalytic activity under the same conditions without any additives, such as supporter, ligand, or stabilizer. Recovery and reuse of NP Pd are extremely easy. High yield of the products was maintained after the repeated use of the catalyst. The Suzuki-coupling reactions with NP Pd was successfully applied to various combination of aryl iodides, aryl bromide, and arylboronic acids, affording the coupling product in high yields [29].

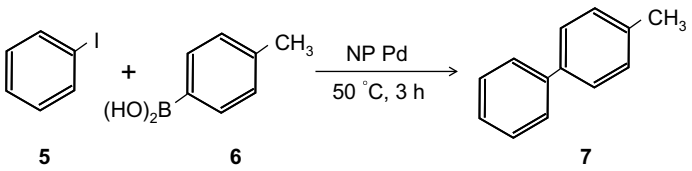

Scheme 19.3 Suzuki–Miyaura coupling reaction between iodobenzene **5** and p-tolylboronic acid **6** using NP Pd

Heck reaction is the palladium catalyzed coupling reaction between aryl halides or vinyl halides and activated alkenes. Iodobenzene was reacted with acrylic acid in the presence of NP Pd in KOH-MeOH gave cinnamic acid in 84% yield [30]. The reaction was applied to the coupling between less reactive arylbromides and alkene. 4-Bromoacetophenone **8** was treated with styrene **9** in the presence of NP Pd in N, N-dimethylacetamide at 140 °C for 12 h, affording the coupling product **10** quantitatively (Scheme 19.4). The repeated use of NP Pd was confirmed for the coupling reaction. The product was obtained quantitatively at least five times after the repeated use of NP Pd.

NPM catalysts are characterized by high surface area, bicontinuous interconnected 3D ligaments, and surfaces enriched of low-coordinated metal atoms on the step edges. Furthermore, the recovery and recycle of NP ribbon is easy, as the nanostructure undergoes no agglomeration. Further surface modification of NPMs by other metals is expected for the development of novel catalytic reaction.

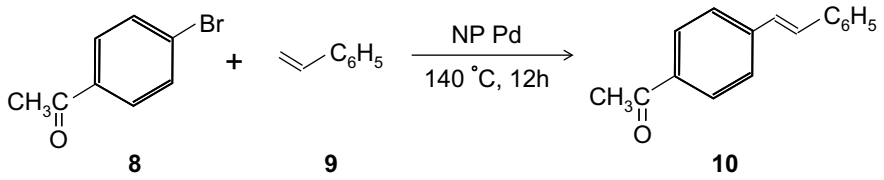

Scheme 19.4 Heck coupling reaction between 4-bromoacetophenone **8** and styrene **9** with NP Pd

19.4 Optical Applications of NPMs

Nanostructured metals exhibit surface plasmon resonance (SPR), which is a dramatically different property from bulk metals [31]. SPR is the collective oscillation of the free conduction electrons excited by visible light when the structural feature of metals is far smaller than the wavelength of light. Two types of SPR, propagating SPR (p-SPR) and localized SPR (l-SPR), are known as the optical resonances of nanostructured metals. Metal ligaments and pore channels in dealloyed NPMs possess much smaller sizes than those of the wavelength of visible light (400–700 nm). Therefore, similar to the cases of grating, nanoparticle, and nanorod, significant SPR is expected for NPMs within the visible wavelength.

The planar gold skeletons consisting of nanopores simultaneously support both p- and l-SPR. NP Au membranes exhibit simultaneous excitation of p-SPR in planar metal films and l-SPR [32, 33]. Propagating SPR of NP Au depends on the wavelength. The increase in the sharpness of the p-SPR dip and the decrease in the dip angle were observed when the laser wavelength increases [32]. As NP Au consists of hollow channels and metal ligaments, its huge metal/dielectric interfaces can be used for application in plasmonic sensing to detect biomolecules.

The optical properties of NP Au are varied with Ag shell on the gold core. Localized SPR spectra of NP Au usually have a wide plateau with two characteristic peaks from ~350 to ~470 nm, corresponding to transverse and longitudinal plasmon absorptions of Au ligaments [34]. The two peaks have different plasmonic responses when the thickness of the Ag shell increased to 10 nm. The peak at the low wavelength of ~350 nm did not shift with Ag plating. This result indicates that this SPR band may derive from the resonant absorption of the gold film. In contrast, the SPR band at the long wavelength of ~470 nm undergoes a significant blue shift to 450 nm with increasing the thickness of the Ag shell larger than 10 nm. This is the characteristic of the continuous gold 3D skeleton covered with Ag film.

NP Au is a highly active substrate with biocompatibility for surface-enhanced Raman scattering (SERS) [33, 35]. The SERS effect of NP Au and NP Au-based composites are reported [35]. The Raman scattering intensities of rhodamine 6G (R6G) molecules adsorbed on the nanopore of NP Au films increase with decreasing in nanopore size from ~700 to ~5 nm. The SERS of NP Au is enhanced by the characteristic lengths of the nanoporosity. The maximum SERS

enhancement of NP Au is observed for the sample with nanopores ~5 nm in size. Similar enhancement of SERS is reported for other organic molecules on nanoporous copper [35, 36]. Therefore, the increase in SERS intensity from smaller nanopore size is recognized as an intrinsic property of NPMs.

Chemical enhancement from the interaction between adsorbed molecules and NP Au substrates causes the SERS effect of NP Au. Moreover, electromagnetic enhancements from the coupling between localized SPR and incident laser contribute to the SERS phenomenon. The small pore size provides large internal surfaces for the adsorption of target molecules, resulting in the generation of the strong Raman signals. In addition, the SERS effect of NP Au mainly results from the electromagnetic field enhancement owing to plasmon excitation of NP Au by the incident laser light.

The SPR of NPMs can be tailored with controlled nanopore and ligament sizes, yielding the tunable optical properties, leading to promising applications of NPMs in optical devices and biochemical detectors and sensors.

19.5 Future Remarks

Catalysis based on extended NPMs is in a preliminary stage of development. It is expected other NPMs based on catalytically active metals will be reported with this dealloying method, which can exhibit favorable properties for important applications ranging from chemical processing to environmental technologies. As NPMs possess the properties of both metals and nanostructured materials, NPMs are expected for application in advanced energy technologies, such as fuel cells, lithium-ion batteries (LIBs), and supercapacitors.

NPMs combine properties of high electronic conductivity of metal ligament, fast diffusion of fuel molecules through open nanopores, higher corrosion resistance than carbon, and strong bonding between Pt catalyst and NPM substrate, exhibiting remarkable candidates for electrode materials of hydrogen fuel cells [37]. The Pt stabilized with other metals on NP Au was found to increase the tolerance to CO poisoning, and was successfully used for the direct formic acid fuel cell [38].

The electrode materials of Li-ion batteries and Li–air batteries require the electrodes properties of high electronic conductivity with large surface area and porous structure for Li-ion diffusion. In addition, the electrode should possess the space to accommodate large volume expansion during charge–discharge process of Li. The bicontinuous structure of NPMs has high tolerance to volume change during charge–discharge cycle, prolonging the cycle stability and life of LIBs. A high and reversible capacity was observed for Sn-based NP Au electrode system based on the porous and good conductive NP Au [39]. The LIBs constructed with SnO_2 deposited NP Cu electrodes kept the almost 96% initial charge capacity after repeated cycle test [40]. MnO_2 decorated NP Cu composite electrode of LIBs exhibited high charge–discharge energies with extremely high rates [41].

The high conductivity, large interfacial surface, and open porosity of NPMs are quite favorable properties for electrochemical double layer capacitor and framework of the supercapacitor. MnO_2 and poly(aniline) on NP Au exhibited a high energy density [42]. All-solid-state ultrathin supercapacitor was fabricated using polypyrrole modified NP Au membrane [43]. Self-grown oxyhydroxide on NP Ni–Mn alloy had a strong chemical bond to the 3D framework, leading to the high cyclic stability of the capacitor up to 4000 cycles [44]. MnO_2/NP Au/MnO_2 sandwich-type capacitor was fabricated to increase MnO_2 loading [45]. The sandwich-type electrode had a very small charge transfer resistance at the three-phase interface of MnO_2, electrode and NP Au, which is attributed to full utilization of redox reaction with high charge storage efficiency.

In the electrochemical systems of fuel cell, LIBs, and supercapacitor, not only the phase boundary at the electrode/electrolyte interface, but also the separation of electron and ion transfer play an important role for their highly efficient operation. As NPMs and modified NPM composites are the suitable scaffolds for three electrochemical systems, NPMs are expected for further progress in advanced energy materials.

19.6 Conclusions

The porosity tuning of NPMs is possible over a wide range of length scales via simple postprocessing at room temperature by immersion in electrolytes or thermal annealing at moderate temperatures. The mechanical rigidity, chemically stability, and often biocompatibility of NPMs can be immediately utilized for applications in catalysis or sensing, as well as supplying a conductive scaffold for the construction of new nanomaterials. Properly designed multifunctional nanostructures offers the fascinating future of NPMs for a broad range application in catalysis, biotechnology, optics, sensing, and energy-generating technologies.

References

1. J. Erlebacher, R. Seshadri, MRS Bull. **34**(08), 561 (2009)
2. A. Wittstock, A. Wichmann, M. Bäumer, ACS Catal. **2**, 2199 (2012)
3. X. Zhang, Y. Ding, Catal. Sci. Technol. **3**, 2862 (2013)
4. A. Forty, Nature **282**, 597 (1979)
5. P. Hyeji, A. Changui, J. Hyungyung, C. Myounggeun, K. Dong Seok, K. Do Kyung et al., Mater. Lett. **129**, 174 (2014)
6. K. Nishio, H. Masuda, Angew. Chem. Int. Ed. **50**, 1603 (2011)
7. O. Näth, A. Stephen, J. Rösler, F. Vollertsen, J. Mater. Process. Technol. **209**, 4739 (2009)
8. B.C. Tappan, S.A. Steiner, E.P. Luther, Angew. Chem. Int. Ed. **49**, 4544 (2010)
9. X. Zhang, P. Guan, L. Malic, M. Trudeau, F. Rosei, T. Veres, J. Mater. Chem. A **3**, 2050 (2015)
10. A.J. Forty, P. Durkin, Philos. Mag. A **42**, 295 (1980)

11. M.B. Cortie, A.I. Maaroof, G.B. Smith, Gold Bull **38**, 14 (2005)
12. T.P. Moffat, F.R.F. Fan, A.J. Bard, J. Electrochem. Soc. **138**, 3224 (1991)
13. M.J. Pryor, J.C. Fister, J. Electrochem. Soc. **131**, 1230 (1984)
14. D.V. Pugh, A. Dursun, S.G. Corcoran, J. Mater. Res. **18**, 216 (2003)
15. J.I. Gardiazabal, J.R. Galvele, J. Electrochem. Soc. **127**, 255 (1980)
16. J. Erlebacher, M.J. Aziz, A. Karma, N. Dimitrov, K. Sieradzki, Nature **410**, 450 (2001)
17. M. Raney, U.S. Patent 1,628,190, 1927
18. R.J. Kokes, P.H. Emmett, J. Am. Chem. Soc. **81**, 5032 (1959)
19. M. Haruta, T. Kobayashi, H. Sano, N. Yamada, Chem. Lett. **16**, 405 (1987)
20. V. Zielasek, B. Jürgens, C. Schulz, J. Biener, M.M. Biener, A.V. Hamza, M. Bäumer, Angew. Chem. Int. Ed. **45**, 8241 (2006)
21. C. Xu, J. Su, X. Xu, P. Liu, H. Zhao, F. Tian, Y. Ding, J. Am. Chem. Soc. **129**, 42 (2007)
22. C. Xu, X. Xu, J. Su, Y. Ding, J. Catal. **252**, 243 (2007)
23. M. Haruta, S. Tsubota, T. Kobayashi, H. Kageyama, M.J. Genet, B. Delmon, J. Catal. **144**, 175 (1993)
24. A. Wittstock, B. Neumann, A. Schaefer, K. Dumbuya, C. Kübel, M.M. Biener, V. Zielasek, H.P. Steinrück, J.M. Gottfried, J. Biener, A. Hamza, M. Bäumer, J. Phys. Chem. C **113**, 5593 (2009)
25. H. Yin, C. Zhou, C. Xu, P. Liu, X. Xu, Y. Ding, J. Phys. Chem. C **112**, 9673 (2008)
26. N. Asao, N. Hatakeyama, Menggenbateer, T. Minato, E. Ito, M. Hara, Y. Kim, Y. Yamamoto, M. Chen, W. Zhang, A. Inoue (2012) Chem. Commun. **48**, 4540
27. N. Asao, Y. Ishikawa, N. Hatakeyama, Menggenbateer, Y. Yamamoto, M. Chen, W. Zhang, A. Inoue (2010) Angew. Chem. Int. Ed. **49**, 10093
28. N. Miyaura, A. Suzuki, Chem. Rev. **95**, 2457 (1995)
29. S. Tanaka, T. Kaneko, N. Asao, Y. Yamamoto, M. Chen, W. Zhang, A. Inoue, Chem. Commun. **47**, 5985 (2011)
30. T. Kaneko, S. Tanaka, N. Asao, Y. Yamamoto, M. Chen, W. Zhang, A. Inoue, Adv. Synth. Catal. **353**, 2927 (2011)
31. N.J. Halas, S. Lal, W.S. Chang, S. Link, P. Nordlander, Chem. Rev. **111**, 3913 (2011)
32. F. Yu, S. Ahl, A.M. Caminade, J.P. Majoral, W. Knoll, J. Erlbacher, Anal. Chem. **78**, 7346 (2006)
33. M.C. Dixon, T.A. Daniel, M. Hieda, D.M. Smilgies, M.H.W. Chan, D.L. Allara, Langmuir **23**, 2414 (2007)
34. L.H. Qian, Y. Ding, T. Fujita, M.W. Chen, Langmuir **24**, 4426 (2008)
35. L.H. Qian, X.Q. Yan, T. Fujita, M.W. Chen, Appl. Phys. Lett. **90**, 153120 (2007)
36. L.Y. Chen, J.S. Yu, T. Fujita, M.W. Chen, Adv. Funct. Mater. **19**, 1221 (2009)
37. R. Zeis, A. Mathur, G. Fritz, J. Lee, J. Erlebacher, J. Power Sources **165**, 65 (2007)
38. R. Wang, J. Liu, P. Liu, X. Bi, X. Yan, W. Wang, Y. Meng, X. Ge, M. Chen, Y. Ding, Nano Res. **7**, 1569 (2014)
39. Y. Yu, L. Gu, X. Lang, C. Zhu, T. Fujita, M.W. Chen, J. Maier, Adv. Mater. **23**, 2443 (2011)
40. C. Hou, X.-M. Shi, C.-X. Zhao, X.-Y. Lang, L.-L. Zhao, Z. Wen, Y.F. Zhu, M. Zhao, J.C. Li, Q. Jiang, J. Mater. Chem. A **2**, 15519 (2014)
41. C. Hou, X.Y. Lang, G.F. Han, Y.Q. Li, L. Zhao, Z. Wen, Y.F. Zhu, M. Zhao, J.C. Li, J.S. Lian, Q. Jiang, Sci. Rep. **3**, 2878 (2013)
42. X.Y. Lang, A. Hirata, T. Fujita, M.W. Chen, Nanoporous metal/oxide hybrid electrodes for electrochemical supercapacitors. Nat. Nanotechnol. **6**(4), 232–236 (2011)
43. F.H. Meng, Y. Ding, Sub-micrometer-thick all-solid-state supercapacitors with high power and energy densities. Adv. Mater. **23**(35), 4098–4102 (2011)
44. J.L. Kang, L.Y. Chen, Y. Hou, C. Li, T. Fujita, X.Y. Lang, A. Hirata, M.W. Chen, Adv. Energy Mater. **3**, 857 (2013)
45. J.L. Kang, A. Hirata, H.J. Qiu, L.Y. Chen, X.B. Ge, T. Fujita, M.W. Chen, Adv. Mater. **26**, 269 (2014)

Chapter 20
Amorphous Alloy Membranes for Hydrogen Separation and Purification

Shin-ichi Yamaura

Abstract Studies on hydrogen permeation of Ni–Nb–Zr amorphous alloys conducted by the author's research group are overviewed. In the early stage of these studies, it was found that the hydrogen permeation coefficients of Pd-coated $(Ni_{0.6}Nb_{0.4})_{70}Zr_{30}$ amorphous alloys were 1.3×10^{-8} mol m^{-1} s^{-1} $Pa^{-1/2}$ at 673 K and that its crystallization temperature was 794 K. Furthermore, the mechanism of hydrogen permeation was discussed based on radial distribution function analysis. Hydrogen extraction and purification from methanol steam reformed gas were successfully conducted by using a Ni–Nb–Zr-based amorphous alloy membrane. The Nb content was then increased to increase the crystallization temperature of the Ni–Nb–Zr-based amorphous alloys. The crystallization temperatures of the $Nb_{42}Ni_{40}Co_{18}$ and $Nb_{42}Ni_{32}Co_6Zr_{20}$ amorphous alloys were 913 K and 859 K, respectively. The hydrogen permeation coefficient of the Pd-coated $Nb_{42}Ni_{32}Co_6Zr_{20}$ amorphous alloy was found to be 1.14×10^{-8} mol m^{-1} s^{-1} $Pa^{-1/2}$. This value is as high as that of the traditionally used Pd-based alloys. The possibility and challenges for applying amorphous alloys for hydrogen permeable membranes are discussed in this chapter.

Keywords Hydrogen production · Methanol steam reforming · Amorphous alloy · Membrane · Hydrogen permeation

S. Yamaura (✉)
Institute for Materials Research, Tohoku University, 2-1-1 Katahira, Aoba, Sendai, Miyagi 980-8577, Japan

Present Address:
The Polytechnic University of Japan, 2-32-1 Ogawanishi-machi, Kodaira, Tokyo 187-0035, Japan
e-mail: s-yamaura@uitec.ac.jp

Y. Setsuhara et al. (eds.), *Novel Structured Metallic and Inorganic Materials*, https://doi.org/10.1007/978-981-13-7611-5_20

20.1 Introduction

Recently, demand for conversion of the present fossil fuel consuming society to a hydrogen-powered society has been greatly increasing worldwide due to the recognition of the need to suppress global warming and to solve pollution and energy problems. A large number of researchers and engineers have made great efforts to develop new fuel cells with higher performance. It is important to not only improve fuel cell technologies but also to establish mass-production techniques of pure hydrogen, so that fuel cells can be practically employed in the coming hydrogen-powered society. The present author has studied hydrogen permeation of amorphous alloy membranes and reported that Pd-coated Ni–Nb–Zr amorphous alloys possess excellent hydrogen permeability, as high as that of Pd metal [1]. Thus, in this chapter, investigations on amorphous alloys for hydrogen permeable membranes by the author's research group will be briefly reviewed from the viewpoint of material development and its application for hydrogen production.

20.2 Hydrogen Permeable Membrane for Hydrogen Production

These days, there are many methods for the production of pure hydrogen [2–4]. For example, pure hydrogen can be obtained by reforming fossil or bio-derived fuels and by water electrolysis. In the case of reformation to produce hydrogen, a purification process using a hydrogen permeable membrane is necessary at the final step because reformed gas contains a large amount of by-product contamination gases such as CO, which degrade fuel cell performance [5]. The mechanism of the purification process using a hydrogen permeable membrane is simple and cost-efficient, as well as being suitable for continuous production [6]. Moreover, phase transformation does not occur in the membrane process, which is also regarded as an energy-saving process in general. Therefore, if a mass-production technique to obtain pure hydrogen using a membrane process were to be established, it would be possible to produce a large amount of pure hydrogen in a cost- and energy-efficient manner.

Recently, three different types of hydrogen permeable membranes have been studied and developed: a polymer membrane [7], a porous ceramic membrane [8] and a metallic membrane [9]. Of these membranes, the metallic membrane is thought to be the most excellent one because it shows the best hydrogen selectivity and, at the same time, possesses high thermal stability. Indeed, the Pd–Ag alloy membrane has been employed for hydrogen purification for decades in the semiconductor engineering field and also in the nuclear engineering field [10]. However, the Pd metal is a noble metal and its availability is limited, so the wide use of Pd–Ag alloy membranes for hydrogen production systems at low cost is obviously difficult. Thus, non-Pd-based alloys that can substitute for Pd-based alloy

membranes have been widely studied by many researchers. For example, the V and Nb metals with a bcc (body-centered crystal) structure can show high diffusivity of hydrogen, and they have been adopted as a base metal for development of a non-Pd-based alloy membrane. It has been reported that the V–Ni alloy showed high hydrogen permeability [11].

20.3 Hydrogen Permeability of Amorphous Alloys

Hydrogen permeability of various amorphous alloys has been reported by many research groups [12], for example, Fe–Ni–P–B amorphous alloy thin ribbons [13], $LaNi_5$ amorphous alloy thin films [14, 15], Fe–Ti amorphous alloy thin films [16], Ni–P amorphous alloy thin films [17], Ni–Zr amorphous alloy thin ribbons [18], Fe–Ni–B–Mo amorphous alloy thin films [19], and so on. The advantages of applying amorphous alloys for hydrogen permeable membranes are as follows: (1) Distinct hydrides may not be formed even after absorbing hydrogen in an amorphous alloy, probably leading to relatively high immunity against hydrogen embrittlement. (2) Amorphous alloys can show higher hydrogen solubility and diffusivity than their crystalline counterparts depending on the chemical compositions. (3) A thin membrane (20–50 μm in thickness) of amorphous alloy having intrinsically high mechanical strength can be easily produced by melt-spinning depending on the chemical composition. So far, the author's group has also attempted to develop amorphous alloys having high hydrogen permeability, looking into in a wide composition range of binary, ternary and quaternary alloy systems. Recently, Inoue et al. found that Ni–Nb–Ti–Zr glassy alloys having a wide supercooled liquid region ΔT_x (= $T_x - T_g$, T_x: crystallization temperature, T_g: glass transition temperature) could be formed in a wide quaternary composition range [20]. Subsequently, Kimura et al. reported that Ni–Nb–Zr alloys could be formed in an amorphous state or in a glassy state depending on the chemical compositions in a wide ternary composition range [21]. We therefore commenced study of hydrogen permeability of the Ni–Nb–Zr-based amorphous alloys prepared by melt spinning.

20.4 Hydrogen Permeability of the Ni–Nb–Zr Amorphous Alloys

First, $(Ni_{0.6}Nb_{0.4})_{100-x}Zr_x$ (x = 0, 20, 30, 40, 50 at.%) mother alloy ingots having nominal chemical compositions were prepared by arc-melting raw materials of Ni, Nb and Zr in a dilute Ar atmosphere. Those mother alloy ingots were crushed and the pieces were placed in a quartz nozzle. The crushed alloy pieces were heated in the quartz nozzle by using a high frequency induction coil and then the molten alloy was injected from the nozzle slit onto a rotating Cu wheel in a dilute Ar atmosphere.

Consequently, a thin alloy ribbon was obtained. The obtained melt-spun ribbons were about 10–100 mm in width and 40 μm in thickness.

Figure 20.1 shows examples of melt-spun amorphous alloys [22, 23]. Indeed, the 100 mm wide amorphous alloy ribbon shown in Fig. 20.1b was successfully produced as part of collaboration with a materials company [23]. The amorphicity and the crystallization temperature, T_x, of the melt-spun ribbon specimens were examined by using X-ray diffractometry (XRD, Cu-Kα, 40 kV, 40 mA) and differential scanning calorimetry (DSC, heating ratio: 0.67 K/s), respectively. The membrane specimens were then polished with emery paper by hand to remove the surface oxide layer and a palladium thin layer was deposited on both sides of all the specimens by RF magnetron sputtering as an active catalyst for promoting hydrogen dissociation and recombination during permeation. The thickness of the deposited Pd layer was about 0.1 μm. These Pd-coated membranes were used for all the subsequent permeation tests.

Figure 20.2 shows schematics of (a) a sample holder [22] and (b) an apparatus for permeation measurement [24]. The membrane specimen was mounted in the sample holder using Al gaskets. As clearly shown in the figure, the upper stream gas was introduced into the holder and then permeated hydrogen was exhausted from the lower stream side. Hydrogen permeation measurements were conducted with the conventional gas permeation technique shown in Fig. 20.2b. A leak check was carefully done by using helium gas to confirm that the membrane specimen had no pinhole before starting the measurement. At first, the apparatus and sample holder were evacuated by using a rotary pump and then argon gas was introduced into the apparatus. This operation was repeated several times before heating the sample holder. After that, the sample holder was again evacuated and heated up to

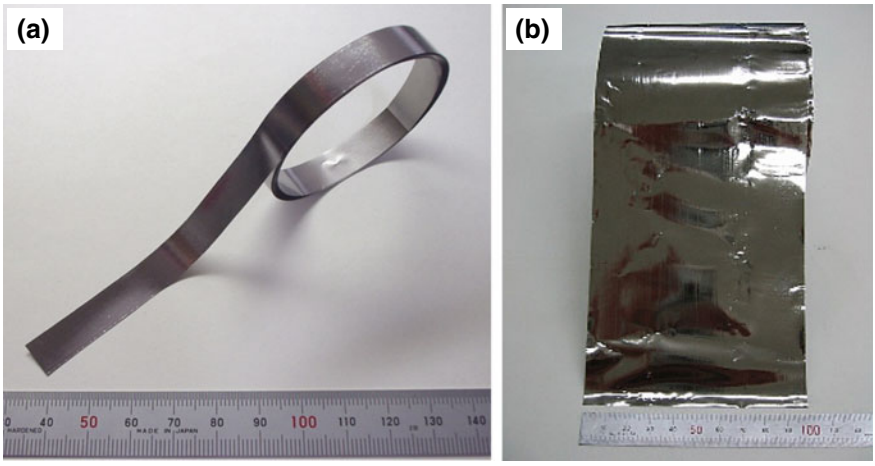

Fig. 20.1 Photographs of the melt-spun (**a**) $Ni_{60}Nb_{20}Zr_{20}$ amorphous alloy, 10 mm in width [22] and (**b**) $(Ni_{0.6}Nb_{0.4})_{45}Zr_{50}Co_5$ amorphous alloy, 100 mm in width. Reprinted from Ref. [23], Copyright 2006, with permission from Elsevier

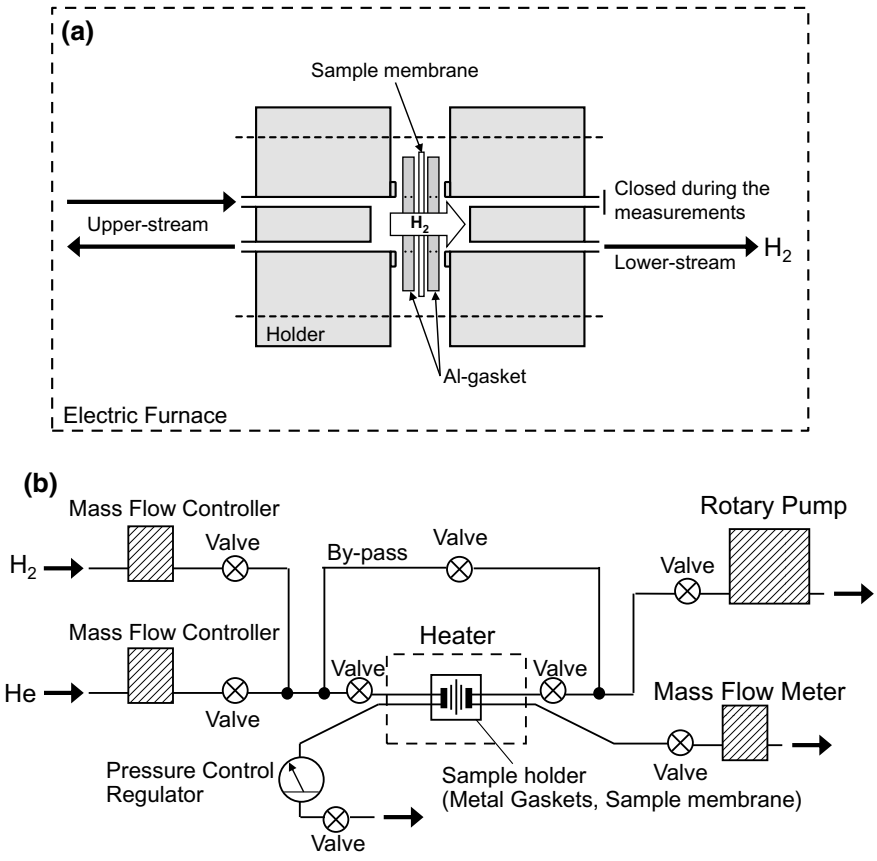

Fig. 20.2 Schematics of **a** sample holder [22] and **b** apparatus for hydrogen permeation measurement after [24]

the test temperature of 573–673 K. Hydrogen gas was introduced to both sides of the membrane specimen. The gas pressure in the lower stream side was fixed to atmospheric pressure and that in the upper stream side was controlled to a pressure higher than the atmosphere, making a pressure difference of about $\Delta P = 0$–0.3 MPa.

In general, the permeation of hydrogen through a membrane is thought to occur through the following three steps [22]; (i) the dissociation of hydrogen gaseous molecules into hydrogen atoms on the upper side surface of the membrane, (ii) the diffusion of hydrogen atoms through the membrane, and (iii) the recombination of hydrogen atoms on the lower side surface and then evolution of hydrogen gas.

Hydrogen permeation rate J [mol s^{-1}] can be calculated by the following equation:

$$J = \frac{P \cdot S}{t}\left(\sqrt{p_{upper}} - \sqrt{p_{lower}}\right), \tag{21.1}$$

where P is the hydrogen permeation coefficient [mol m^{-1} s^{-1} $Pa^{-1/2}$], S is the permeation area [m^2], and t is the membrane thickness [m]. The hydrogen pressures of the upper side and of the lower side are p_{upper} [Pa] and p_{lower} [Pa], respectively. The hydrogen permeation coefficient P is the inherent value of the material, so the increase in the P value is one of the important requirements for the development of good hydrogen permeable membranes.

Figure 20.3 shows the XRD patterns of melt-spun Ni–Nb–Zr alloy ribbons [25]. As you can see in the figure, no sharp peaks but only a broad halo peak appeared, indicating that all the melt-spun alloys possess a single amorphous phase.

Figure 20.4 shows the results of the hydrogen permeation measurements of these alloys summarized in an Arrhenius plot [25]. The permeation coefficients of the Pd-23 mass%Ag alloy and Pd metal are included in the figure. As observed in the figure, the hydrogen permeation coefficient increased with increasing Zr content and also with increasing test temperature. The hydrogen coefficient of the alloy with Zr content of 30 at.% or larger is higher than that of the Pd metal. The hydrogen permeation coefficients were 1.3×10^{-8} and 1.59×10^{-8} [mol m^{-1} s^{-1} $Pa^{-1/2}$] at 673 K for the $(Ni_{0.6}Nb_{0.4})_{70}Zr_{30}$ and the $(Ni_{0.6}Nb_{0.4})_{50}Zr_{50}$ amorphous alloys. As can also be observed in Fig. 20.3, the broad halo peak position shifted to the lower angle side with higher content of Zr addition, leading to an increase in atomic distance. From these observations, it was concluded that the amorphous alloy

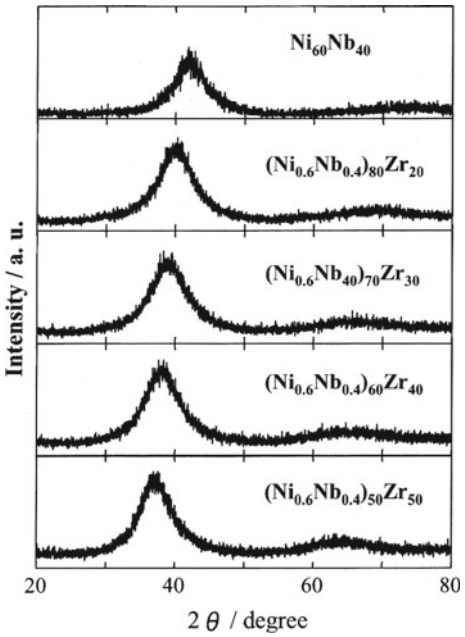

Fig. 20.3 XRD patterns of the Ni–Nb–Zr melt-spun alloys. Reprinted from Ref. [25], Copyright 2005, with permission from Elsevier

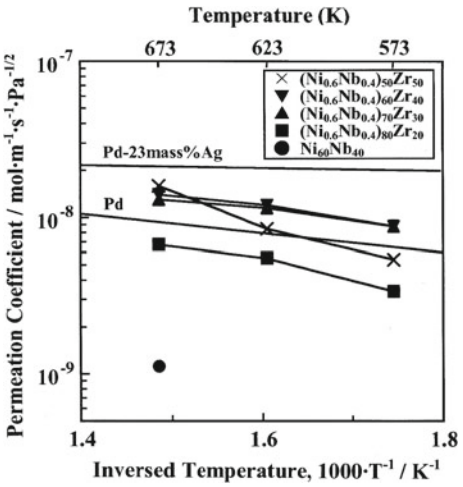

Fig. 20.4 Arrhenius plot of hydrogen permeability of the Ni–Nb–Zr amorphous alloys. Reprinted from Ref. [25], Copyright 2005, with permission from Elsevier

having a larger atomic distance possessed higher hydrogen permeability in this alloy system. In order to investigate the local atomic configuration of the alloys more precisely, radial distribution function (RDF) analysis was conducted for these alloys.

20.5 Local Atomic Configuration of the Ni–Nb–Zr Amorphous Alloys

Figure 20.5 shows the ordinary pair distribution functions in the melt-spun Ni–Nb–Zr alloys before and after heat treatment in the hydrogen atmosphere, calculated by the Fourier transformation of the ordinary interference functions obtained from the XRD data [25]. The solid and dotted lines correspond to the curves for the as-spun and hydrogenated samples. The $(Ni_{0.6}Nb_{0.4})_{70}Zr_{30}$ and the $(Ni_{0.6}Nb_{0.4})_{50}Zr_{50}$ amorphous alloys absorbed hydrogen up to 33.7 at.% and 48.9 at.%, respectively, while the $Ni_{60}Nb_{40}$ amorphous alloy absorbed hydrogen only 1.5 at.%. As a result, it was found that there was no difference between the curves of the $Ni_{60}Nb_{40}$ amorphous alloy which hardly absorbed hydrogen before and after hydrogenation. On the contrary, a distinct peak corresponding to the presence of Zr–Zr pairs appeared drastically by Zr addition and the atomic distance between the Zr atoms increased with absorbed hydrogen content. However, the distance of the other atomic pairs such as Ni–Zr and Ni–Ni and Ni–Nb changed only slightly even after hydrogenation.

The mixing enthalpy (heat of mixing) between the constituent atoms may also play an important role in the formation of a distinctive amorphous structure. Actually, amorphous alloys can be synthesized in a wide range of the Ni–Nb–Zr ternary alloy compositions. The mixing enthalpies of Ni–Nb and Ni–Zr pairs are

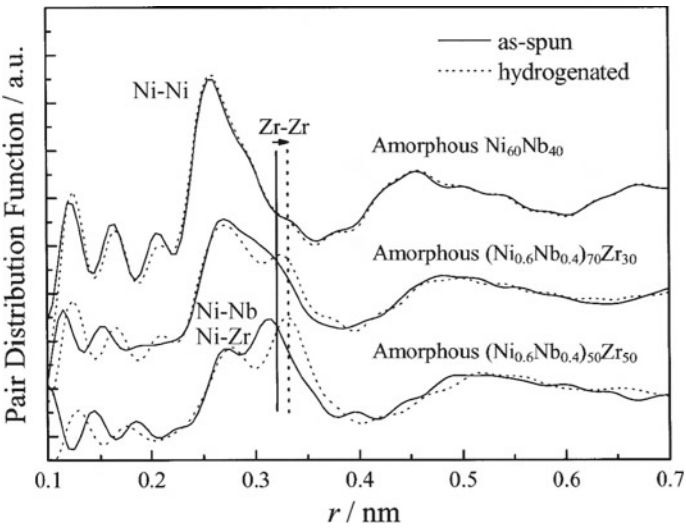

Fig. 20.5 Ordinary radial distribution functions in the melt-spun alloys before and after heat treatment in the hydrogen atmosphere. Reprinted from Ref. [25], Copyright 2005, with permission from Elsevier

large negative values where those binary amorphous alloys can also be formed easily by melt-spinning. On the contrary, that of Nb–Zr pair is positive. So, in the author's opinion, the Nb-slightly-condensed area and the Zr-slightly-condensed area may exist very locally, even in a macroscopically homogeneous amorphous structure of the Ni–Nb–Zr ternary amorphous alloy and hydrogen atoms can permeate through such a Zr-rich area having a relatively large interatomic distance.

From these observations, it was concluded that hydrogen may easily permeate through the expanded free volume around the Zr–Zr pairs where the distance between the Zr atoms increases after hydrogenation, with the result that the excellent hydrogen permeation is achieved in the $(Ni_{0.6}Nb_{0.4})_{70}Zr_{30}$ and the $(Ni_{0.6}Nb_{0.4})_{50}Zr_{50}$ amorphous alloys.

Figure 20.6 shows the results of hydrogen permeation measurement of $(Ni_{0.6}Nb_{0.4})_{100-x}Zr_x$ (x = 0, 20, 30, 40, and 50 at.%), $(Ni_{0.5}Nb_{0.5})_{100-x}Zr_x$ (x = 0, 10, 20, and 30 at.%) and $Ni_{70-x/2}Nb_{30-x/2}Zr_x$ (x = 10, 20, 30, 50, and 60 at.%) ternary alloys superimposed on a triangle map of the glass-forming ability (GFA) [21]. Melt-spun specimens having a certain chemical compositions show a transformation from a solid state to a supercooled liquid state in the heating process and are recognized as glassy alloys, indicated by double circles in the map. The open circles indicate the amorphous alloys. The solid circles indicate crystalline alloys having alloy compositions we cannot produce amorphous alloys by melt-spinning. As seen in the figure, a tendency for hydrogen permeation to increase with increasing Zr content was observed. Also, the Nb addition seems to be effective to increase hydrogen permeation. The composition region in which it is

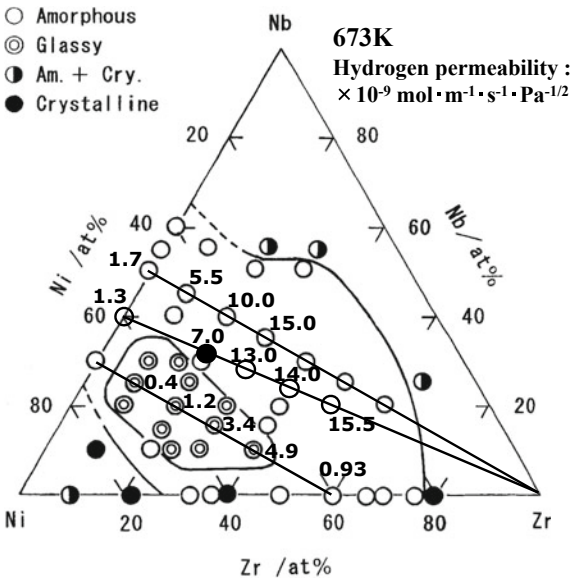

Fig. 20.6 Hydrogen permeability map superimposed on glass formability

possible to synthesize glassy alloys does not always correspond to the composition region in which the alloys can show the highest hydrogen permeation. This is an important point when we develop amorphous alloys and glassy alloys as practical functional materials.

20.6 Long-Time Durability Tests

Figure 20.7 shows the results of long-time durability tests conducted at 573 K for 100 h, indicating the time-dependent change of the hydrogen permeabilities of the melt-spun $(Ni_{0.6}Nb_{0.4})_{55}Zr_{40}Co_5$ and $(Ni_{0.6}Nb_{0.4})_{45}Zr_{50}Co_5$ amorphous alloys (re-calculated after [23]). Co was added to the Ni–Nb–Zr ternary amorphous alloys with the expectation that it would mitigate hydrogen embrittlement. These alloys did not show a significant decrease in hydrogen permeation at 573 K during the long-time tests, but both alloys showed a tendency for the gradual decrease of hydrogen permeation.

Figure 20.8 shows the XRD patterns of the alloys after the tests [23]. As can be seen in the figure, the $(Ni_{0.6}Nb_{0.4})_{55}Zr_{40}Co_5$ alloy possessed a single amorphous phase even after being tested for 100 h, whereas the crystalline peak that came from the crystalline Nb metal appeared in the $(Ni_{0.6}Nb_{0.4})_{45}Zr_{50}Co_5$ alloy. Crystallization causes severe embrittlement of amorphous alloys because of the precipitation of intermetallic compounds of major constituent elements, so optimization of chemical

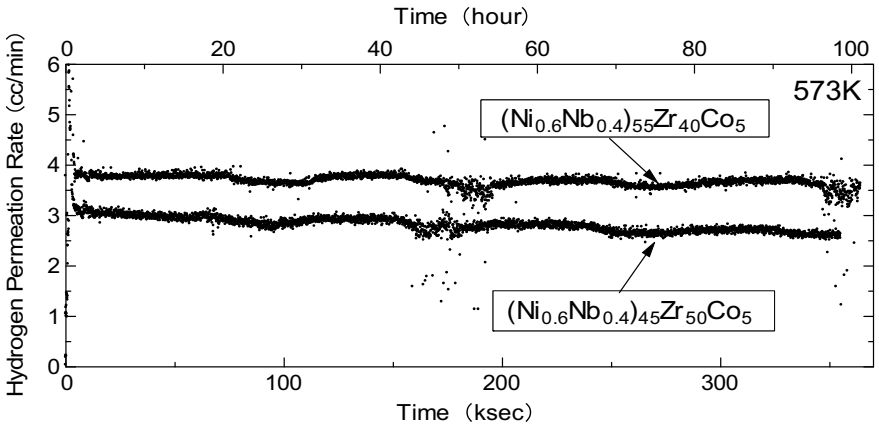

Fig. 20.7 Time-dependent change of the hydrogen permeabilities of the melt-spun $(Ni_{0.6}Nb_{0.4})_{55}Zr_{40}Co_5$ and $(Ni_{0.6}Nb_{0.4})_{45}Zr_{50}Co_5$ amorphous alloys at 573 K (recalculated after [23])

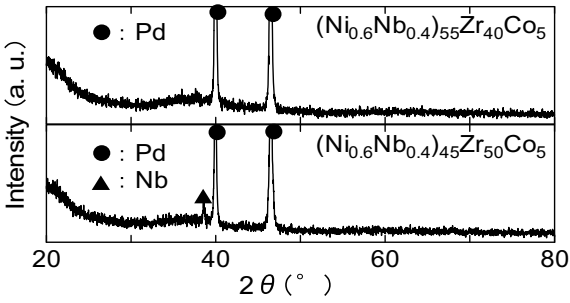

Fig. 20.8 XRD patterns of the $(Ni_{0.6}Nb_{0.4})_{55}Zr_{40}Co_5$ and $(Ni_{0.6}Nb_{0.4})_{45}Zr_{50}Co_5$ samples after permeation test at 573 K. Reprinted from Ref. [23], Copyright 2006, with permission from Elsevier

compositions of amorphous alloys is necessary to avoid crystallization. In this case, it seems that due to its lower Zr content, the $(Ni_{0.6}Nb_{0.4})_{55}Zr_{40}Co_5$ alloy is preferable to the $(Ni_{0.6}Nb_{0.4})_{45}Zr_{50}Co_5$ alloy from the viewpoint of stabilizing the amorphous structure (those crystallization temperatures and the amount of hydrogen absorption in those alloys). Amorphous alloys are thermally more unstable than ordinary crystalline alloys because of their random atomic arrangement, like being frozen in a nonequilibrium liquid state. Therefore, it is preferable to increase the crystallization temperature, T_x, as high as possible even if the amorphous alloy is used at 573 K. Also, it is preferable to decrease the test temperature in order to avoid not only crystallization but also internal diffusion and disappearance of the Pd surface layer.

20.7 Hydrogen Production by Methanol Steam Reforming Using a Melt-Spun Ni–Nb–Ta–Zr–Co Amorphous Alloy Membrane

In this section, the result of an experiment of hydrogen purification from the reformed gas of methanol steam reforming using the melt-spun $Ni_{40}Nb_{20}Ta_5Zr_{30}Co_5$ amorphous alloy is introduced. Ta was added to the Ni–Nb–Zr–Co quaternary alloy to increase its thermal stability (crystallization temperature, T_x) [26]. In this work, the reformed gas containing steam (H_2O), methanol (CH_3OH), carbon monoxide (CO), carbon dioxide (CO_2), and hydrogen (H_2) was produced by using a catalyst (Cu-based compounds), and then pure hydrogen was extracted by using the amorphous alloy membrane.

Figure 20.9 shows schematics of (a) the sample holder [26] and (b) the experiment system used in this work. The Cu-based catalyst (Sued-Chemie Catalysts Japan, Inc., MDC-3, CuO/ZnO type) was filled inside the upper side chamber of the sample holder and then the reformed gas was introduced into the upper side chamber. The reformed gas was produced by the following reactions:

$$CH_3OH \rightarrow CO + 2H_2 \tag{21.2}$$

$$CO + H_2O \rightarrow CO_2 + H_2 \tag{21.3}$$

The total reaction formula is as follows:

$$CH_3OH + H_2O \rightarrow 3H_2 + CO_2 \tag{21.4}$$

In this reaction, a mixed solution of 1 mol CH_3OH and 1 mol H_2O is heated up to 473–573 K and introduced into the upper side chamber of the sample holder, then 3 mol H_2 and 1 mol CO_2 are produced from the methanol steam by the catalyst. The hydrogen partial pressure in the upper side chamber is ideally 0.075 MPa. The hydrogen partial pressure in the lower side chamber is kept almost constant to zero because Ar carrier gas is introduced into the lower side chamber to sweep permeated hydrogen out of the chamber. The driving force for hydrogen in the reformed gas to permeate through the membrane from the upper side chamber to the lower side chamber is the partial pressure difference between the upper side and lower side chambers mentioned above. Gas samples were obtained from the reformed gas in the upper stream and from the sweep gas containing the permeated hydrogen in the lower stream, and were subsequently compared with each other by TCD-type gas chromatography. The detailed conditions are summarized in Fig. 20.10.

Figure 20.10 shows a summary of the experimental conditions and the results [26]. Figure 20.10a indicates the XRD pattern having a broad halo peak and no sharp peaks observed from the melt-spun $Ni_{40}Nb_{20}Ta_5Zr_{30}Co_5$ alloy, confirming that this sample membrane was successfully produced as an amorphous alloy.

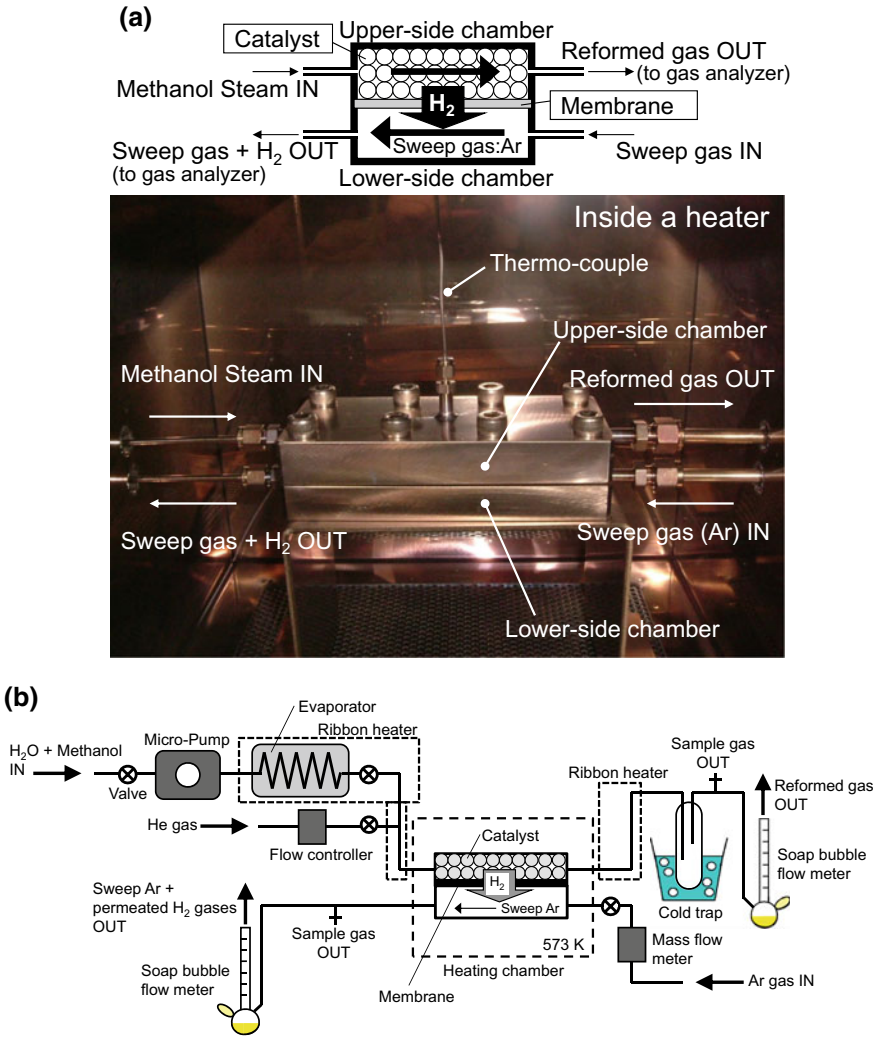

Fig. 20.9 **a** Schematic and photograph of the reactor for methanol steam reforming. Reprinted from Ref. [26], Copyright 2008, with permission from the Society of Materials Science, Japan. **b** Schematic of apparatus for hydrogen purification from methanol steam reforming gas

Conventional hydrogen permeable membranes are used at 573–773 K. Figure 20.10b shows the DSC curve of the amorphous alloy membrane. A large exothermic peak appeared at around 850 K, and the crystallization temperature T_x was about 825 K. The crystallization temperature of the previously reported $(Ni_{0.6}Nb_{0.4})_{70}Zr_{30}$ amorphous alloy was T_x = 794 K [1, 25]. It was found that the addition of Ta and Co to the Ni–Nb–Zr alloy increased T_x by more than 30 K. The temperature in this test of hydrogen purification from methanol steam reforming gas

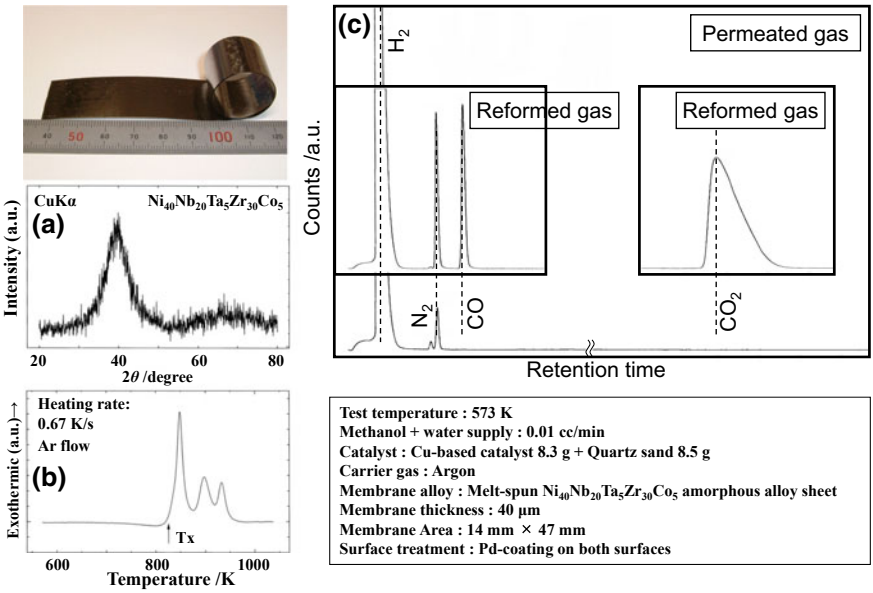

Fig. 20.10 Hydrogen purification test from methanol steam reformed gases by using the $Ni_{40}Nb_{20}Ta_5Zr_{30}Co_5$ amorphous alloy membrane. Reprinted from Ref. [26], Copyright 2008, with permission from the Society of Materials Science, Japan

was fixed at 573 K. Figure 20.10c shows the results of the gas chromatograph analysis of the reformed gas extracted from the upper side chamber and of the permeated gas from the lower side chamber. As you can see in the abovementioned reactions (21.2)–(21.4), the reformed gas contains not only H_2 and CO_2 but also CO because the reaction rate of the catalyst did not always reach 100%. In the permeated gas, Ar gas was used for sweeping the permeated H_2 out of the chamber and was used for the carrier gas inside the gas chromatograph, so Ar gas was masked so as not to appear in the spectrum of the permeated gas. Also, the N_2 peak which originated from the slight amount of air remaining inside the chamber was detected because we did not use a vacuum pump before introducing methanol steam into the upper side chamber and introducing Ar sweep gas into the lower side chamber. Moreover, N_2 gas may be a contamination caused by taking gas samples from the gas flows by an injection-type syringe. A small amount of air is inevitably mixed into the gas sample in the needle of a syringe. Thus, we can ignore those N_2 peaks in the gas chromatograms. Therefore, from these observations, it was clearly shown that the reformed gas contained H_2, CO, CO_2, and N_2 gases and that the permeated gas contained H_2 and N_2 gases only. By comparing the permeated gas with the reformed gas, it can be concluded that the CO and CO_2 gases were completely removed from the reformed gas. Consequently, only hydrogen gas was extracted

from the reformed gas by using the amorphous alloy membrane. The possibility of the application of amorphous alloy membranes for hydrogen purification was successfully demonstrated in this work.

20.8 Amorphous Alloys with Higher Nb Content

Recently, our research group has attempted to produce amorphous alloys with higher crystallization temperatures by increasing Nb content in the Ni–Nb–Zr ternary amorphous alloys. Because Nb is a refractory metal, its significant addition is expected to drastically increase the crystallization temperature of amorphous alloys. Thus, Nb-based amorphous alloys were produced by melt spinning.

Figure 20.11 shows (a) the XRD patterns and (b) the DSC curves of melt-spun $Nb_{42}Ni_{40}Co_{18-x}Zr_x$ (x = 0, 4, 12 at.%) and $Nb_{42}Ni_{32}Co_6Zr_{12}M_8$ (M = Ta, Ti, Zr) alloys [27]. Only broad halo peaks appeared without any sharp peaks in Fig. 20.11a, meaning that all the alloys were produced in a single amorphous phase. The position of the halo peaks shifted to the lower angle side with increasing Zr content, perhaps indicating a possible increase of hydrogen permeation, analogues to the findings of the study of Ni–Nb–Zr amorphous alloys. Figure 20.11b shows the DSC curves of these alloys. None of the specimens showed a supercooled liquid region. Two exothermic peaks appeared in each curve, indicating that the alloys crystallized in two-stage crystallization. The onset of the first crystallization peak corresponds to the crystallization temperature, T_x, of the alloy. The T_x of the $Nb_{42}Ni_{40}Co_{18}$ amorphous alloy is 913 K. In a series of these quaternary alloys, T_x decreased with increasing Zr content. The T_x of the $Nb_{42}Ni_{32}Co_6Zr_{30}$ amorphous alloy is 859 K. The addition of Ti and Ta to the quaternary alloys seemed to be effective to increase the T_x. From these observations, it was clearly shown that the

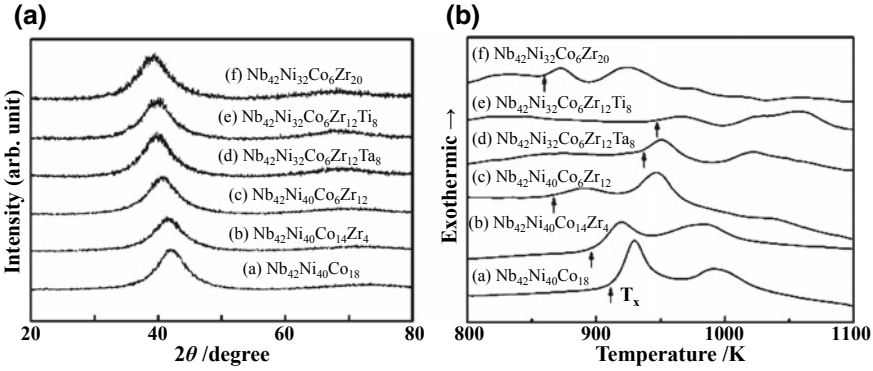

Fig. 20.11 XRD spectra (**a**) and DSC curves (**b**) of the $Ni_{42}Nb_{40}Co_{18-x}Zr_x$ (x = 0, 4, 12) and $Ni_{42}Ni_{32}Co_6Zr_{12}M_8$ (M = Ta, Ti, Zr) alloy ribbons. Reprinted from Ref. [27], Copyright 2013, with permission from the Japan Institute of Metals and Materials

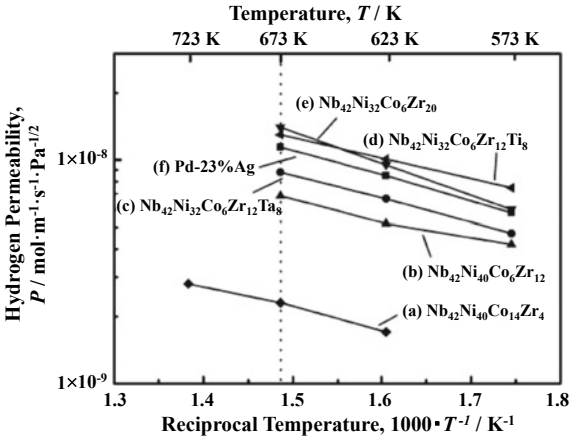

Fig. 20.12 Arrhenius plots of the Nb–Ni–Co–Zr and Nb–Ni–Co–Zr–M amorphous alloys and the Pd-23%Ag alloy. Reprinted from Ref. [27], Copyright 2013, with permission from the Japan Institute of Metals and Materials

Nb-based amorphous alloys produced in this study had higher T_x than the previously prepared alloys.

Figure 20.12 shows the hydrogen permeation coefficients of the Nb-based amorphous alloys produced in this work [27]. The hydrogen permeation coefficients of the $Nb_{42}Ni_{40}Co_{18}$, $Nb_{42}Ni_{40}Co_{14}Zr_4$, $Nb_{42}Ni_{40}Co_6Zr_{12}$, $Nb_{42}Ni_{32}Co_6Zr_{12}Ta_8$, $Nb_{42}Ni_{32}Co_6Zr_{12}Ti_8$, $Nb_{42}Ni_{32}Co_6Zr_{20}$ amorphous alloys and the Pd-23%Ag alloy at 673 K were 0.03×10^{-8}, 0.23×10^{-8}, 0.69×10^{-8}, 0.88×10^{-8}, 1.30×10^{-8}, 1.40×10^{-8}, and 1.14×10^{-8} mol m^{-1} s^{-1} $Pa^{-1/2}$, respectively. The alloys with Zr content higher than 12 at.% possessed a sufficiently high permeation coefficient for practical applications.

Figure 20.13 indicates (a) the XRD patterns of the $Nb_{42}Ni_{32}Co_6Zr_{20}$ amorphous alloy before and after the permeation test at 673 K for 24 h and (b) the depth profiles of the alloy after the 24 h permeation test obtained by Auger Electron

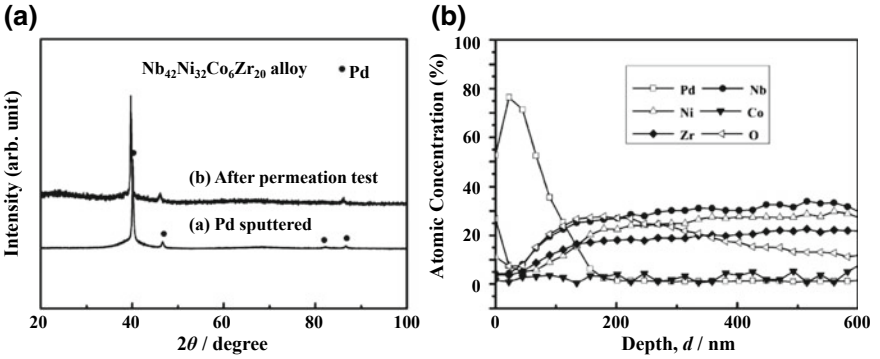

Fig. 20.13 XRD spectra (**a**) and AES depth profile (**b**) of Pd-coated $Nb_{42}Ni_{32}Co_6Zr_{20}$ alloy membrane after 24 h permeation test. Reprinted from Ref. [27], Copyright 2013, with permission from the Japan Institute of Metals and Materials

Spectroscopy analysis [27]. In Fig. 20.13a, it is shown that the amorphous phase was maintained after the permeation test. The peak positions of the Pd surface layer shifted to the lower angle side after the permeation test because the lattice of Pd expanded by hydrogen absorption. In Fig. 20.13b, it can be seen that the composition ratio of Nb, Ni, Co, and Zr remained unchanged compared with the nominal compositions, whereas the total amount decreased due to the presence of oxygen. The authors concluded that an oxide layer formed and that Pd interdiffusion could lead to a gradual decrease in hydrogen permeation during the long-time test.

20.9 Summary

In this chapter, studies on hydrogen permeation of the Ni–Nb–Zr-based amorphous alloys by the author's research group were overviewed. In the early stage of the series of the studies, the $(Ni_{0.4}Nb_{0.6})_{70}Zr_{30}$ and $(Ni_{0.4}Nb_{0.6})_{50}Zr_{50}$ amorphous alloys were prepared by melt-spinning and their hydrogen permeabilities were measured at 573–673 K. Results showed that the hydrogen permeation coefficients were 1.3×10^{-8} and 1.59×10^{-8} mol m^{-1} s^{-1} $Pa^{-1/2}$ at 673 K for the $(Ni_{0.6}Nb_{0.4})_{70}Zr_{30}$ and the $(Ni_{0.6}Nb_{0.4})_{50}Zr_{50}$ amorphous alloys. Those values are equal to or a little higher than that of the Pd metal.

The hydrogen permeability of those Ni–Nb–Zr ternary amorphous alloys in a wide range of chemical compositions was described on a ternary composition diagram superimposed on a contour map of amorphous/glass formability. A tendency for hydrogen permeation to increase with increasing Zr and Nb contents was observed. As can be clearly seen in this ternary composition diagram, the alloy composition area in which the hydrogen permeability reached the maximum value does not correspond to the composition area in which the alloys possess a glassy phase showing a supercooled liquid state. In the case of the development of amorphous/glassy alloys, the alloy compositions in which the functional property you focused on reaches the most suitable value may not always correspond to the alloy compositions in which the alloy can be produced in an amorphous/glassy state. Thus, if we give priority to the most suitable functional property, the alloy may not be able to be produced in an amorphous/glassy state. This is one of the most difficult points in developing amorphous/glassy functional alloys.

The hydrogen purification test was then conducted by using the $Ni_{40}Nb_{20}Ta_5Zr_{30}Co_5$ amorphous alloy and pure hydrogen was extracted from the methanol steam reformed gas.

Finally, the Nb-rich amorphous alloys were prepared and their thermal stability and hydrogen permeability were investigated. As a result, it was found that the addition of Ti and Ta seemed to be effective in increasing the crystallization temperature, T_x, in this alloy system. The T_x values of the $Nb_{42}Ni_{40}Co_{18}$ and $Nb_{42}Ni_{32}Co_6Zr_{20}$ amorphous alloys were 913 K and 859 K, respectively. The hydrogen permeation coefficient of the $Nb_{42}Ni_{32}Co_6Zr_{20}$ amorphous alloy was 1.14×10^{-8} mol m^{-1} s^{-1} $Pa^{-1/2}$.

The potential of amorphous alloy membranes for hydrogen production was successfully demonstrated in these studies, although there are many challenges to overcome in developing amorphous alloy membranes for hydrogen production. In the development of hydrogen permeable membranes, not only high hydrogen permeability but also high resistivity against hydrogen embrittlement are important. The hydrogen embrittlement of metallic materials has been a significant problem for decades. Therefore, hydrogen embrittlement is one of the most important problems to resolve in development of hydrogen permeable metallic membranes. The author hopes the problem of hydrogen embrittlement [28] will be solved and consequently hydrogen permeable amorphous alloy membranes having high hydrogen permeability, high thermal stability and high resistance to hydrogen embrittlement will be developed and put into practice in the future.

References

1. S. Yamaura, Y. Shimpo, H. Okouchi, M. Nishida, O. Kajita, H.M. Kimura, A. Inoue, Mater. Trans. **44**, 1885 (2003)
2. W. Balthasar, Int. J. Hydrogen Energy **9**, 649 (1984)
3. M. Steinberg, H.C. Cheng, Int. J. Hydrogen Energy **14**, 797 (1989)
4. H. Wendt, G. Imarisio, J. Appl. Electrochem. **18**, 1 (1988)
5. M. Amano, C. Nishimura, M. Komaki, Mater. Trans., JIM **31**, 404 (1990)
6. E. Kikuchi, Catal. Today **56**, 97 (2000)
7. R.M. Barrer, Faraday Soc. **35**, 628 (1939)
8. S. Miachon, J.A. Dalmon, *Proceedings of 2002 Materials Research Society Fall Meeting* 581, 2–6 Dec 2002, Boston, USA (2003)
9. N. Itoh, W.C. Xu, K. Haraya, J. Membr. Sci. **66**, 149 (1992)
10. S. Uemiya, N. Sato, H. Ando, Y. Kude, T. Matsuda, E. Kikuchi, J. Membr. Sci. **56**, 303 (1991)
11. C. Nishimura, M. Komaki, S. Hwang, M. Amano, J. Alloy Comp. **330–332**, 902 (2002)
12. M.D. Dolan, N.C. Dave, A.Y. Ilyushechkin, L.D. Morpeth, K.G. McLennan, J. Membr. Sci. **285**, 30 (2006)
13. R.W. Lin, H.H. Johnson, J. Non-Cryst. Solids **51**, 45 (1982)
14. G. Adachi, H. Nagai, J. Shiokawa, J. Less-Common Metals **97**, L9 (1984)
15. H. Sakaguchi, H. Seri, G. Adachi, J. Phys. Chem. **94**, 5313 (1990)
16. M. Amano, Y. Sasaki, K. Nakamura, C. Nishimura, M. Komaki, M. Shibata, *Annual Report of National Research Institute for Metals*, vol. 11 (1990), p. 277 (in Japanese)
17. B.S. Liu, H. Li, Y. Cao, J.Y. Deng, C. Sheng, S. Zhou, J. Membr. Sci. **135**, 33 (1997)
18. S. Hara, K. Sakai, N. Itoh, H.M. Kimura, K. Asami, A. Inoue, J. Membr. Sci. **164**, 289 (2000)
19. W.C. Chian, W.D. Yeh, J.K. Wu, Mater. Lett. **59**, 2542 (2005)
20. A. Inoue, W. Zhang, T. Zhang, Mater. Trans. **43**, 1952 (2002)
21. H.M. Kimura, A. Inoue, S. Yamaura, K. Sasamori, M. Nishida, Y. Shimpo, H. Okouchi, Mater. Trans. **44**, 1167 (2003)
22. S. Yamaura, A. Inoue, in *Membranes for Membrane Reactors: Preparation, Optimization and Selection*, ed. by A. Basile, F. Gallucci (Wiley, UK, 2011)
23. Y. Shimpo, S. Yamaura, M. Nishida, H.M. Kimura, A. Inoue, J. Membr. Sci. **286**, 170 (2006)
24. S. Yamaura, S. Nakata, H.M. Kimura, A. Inoue, J. Membr. Sci. **291**, 126 (2007)
25. S. Yamaura, M. Sakurai, M. Hasegawa, K. Wakoh, Y. Shimpo, M. Nishida, H.M. Kimura, E. Matsubara, A. Inoue, Acta Mater. **53**, 3703 (2005)

26. S. Yamaura, H.M. Kimura, A. Inoue, Y. Shimpo, M. Nishida, S. Uemiya, J. Soc. Mater. Sci. Jpn. **57**, 1031 (2008). (in Japanese)
27. H.Y. Ding, W. Zhang, S.I. Yamaura, K.F. Yao, Mater. Trans. **54**, 1330 (2013)
28. S. Jayalakshmi, S.O. Park, K.B. Kim, E. Fleury, D.H. Kim, Mater. Sci. Eng. **A449–451**, 920 (2007)

Chapter 21
Syntheses of Composite Porous Materials for Solid Oxide Fuel Cells

Hiroya Abe and Kazuyoshi Sato

Abstract This section focuses on the syntheses and characterization of composite porous materials for solid oxide fuel cell (SOFC) electrodes. Considerable efforts have been made to enlarge the triple phase boundary (TPB) where electrode, electrolyte, and pore phases meet, for reducing polarization loss in SOFC. Composite particles, which consist of electrode and electrolyte materials, have been prepared for this purpose, because their utilization is to improve the homogeneity of electrode and electrolyte particle distribution in SOFC electrodes. Among several wet-chemical routes for syntheses of the composite particles, coprecipitation method has been found a particular interest because of its simplicity, cost-effective, and easy scale-up capability. The emphasis will be therefore placed on the development of coprecipitation methods for enlarged TPB in SOFC electrodes.

Keywords Solid oxide fuel cells · Triple phase boundary · Coprecipitation · Composite particle · Structural control

21.1 Introduction

Fuel cells are considered highly efficient devices to convert chemical energy directly into electrical energy with low emission of pollutants [1]. Among the several types of fuel cells, solid oxide fuel cells (SOFCs) can achieve highest efficiency, due to their high operation temperature such as 1000 °C. In the past several decades, the development of SOFCs has been made significant progress, resulting in an increase of power density [1].

H. Abe (✉)
Joining and Welding Research Institute, Osaka University,
11-1 Mihogaoka, Ibaraki, Osaka 567-0047, Japan
e-mail: h-abe@jwri.osaka-u.ac.jp

K. Sato
Graduate School of Science & Technology, Gunma University,
1-5-1 Tenjin-cho, Kiryu, Gunma 376-8515, Japan

Y. Setsuhara et al. (eds.), *Novel Structured Metallic and Inorganic Materials*, https://doi.org/10.1007/978-981-13-7611-5_21

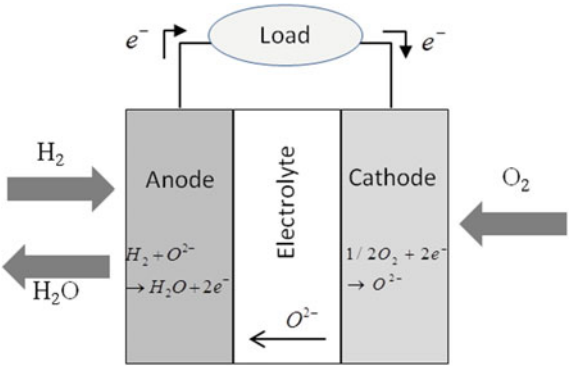

Fig. 21.1 Operation principle of an SOFC

SOFCs are composed of a porous cermet anode and a porous oxide cathode, with a dense electrolyte sandwiched by them (see Fig. 21.1). Typically, air is fed to the cathode as an oxygen source, and fuel including H_2, CO, and CH_4 is fed to the anode. When oxygen gas contacts the cathode/electrolyte interface, the oxygen molecules are electrochemically reduced to form oxygen ions (O^{2-}). These oxygen ions are moved through the electrolyte to the anode, where they electrochemically oxidize the fuel. As the fuel is oxidized, the electrons are released with a higher potential to an external circuit, thus providing power [2]. State-of-the-art SOFCs are composed of yttria-stabilized zirconia (YSZ) electrolyte, Ni–YSZ cermet anode, and a lanthanum–strontium–manganite (LSM) cathode [3].

Recent development on SOFCs have been paid much attention to reduce the operating temperature into the so-called intermediate range (600–800 °C), with the aim of cost reduction and durability enhancement of the cells and the system [4]. However, when the temperature decreases, a significant increase in not only electrolyte ohmic resistance but also polarization resistances of both electrodes is observed [1, 3].

To reduce the electrolyte ohmic resistance at the temperature range, a thin-film electrolyte configuration has been proposed since the resistance is proportional to the thickness [5]. As shown in Fig. 21.2, conventional ceramics powder processing such as tape casting and screen printing has been applied in the fabrication of the thin-film electrolyte SOFCs, i.e., anode or cathode supported SOFCs. The thicknesses down to 10 μm have been successfully achieved and probed to exhibit excellent electrochemical performance [5]. Another significant contribution is the polarization resistance of the electrodes. In case of Ni–YSZ cermet anode [6], the reaction rate for electrochemical oxidation of hydrogen is correlated with the length of the triple phase boundary (TPB) where Ni, YSZ, and pore phases meet as shown in Fig. 21.3. In case of LSM–YSZ cathode, it has been also reported that the oxygen reduction reaction occurs in the vicinity of TPB [7]. These indicate that making extension of the TPB is a technological aim for the reduction of polarization loss.

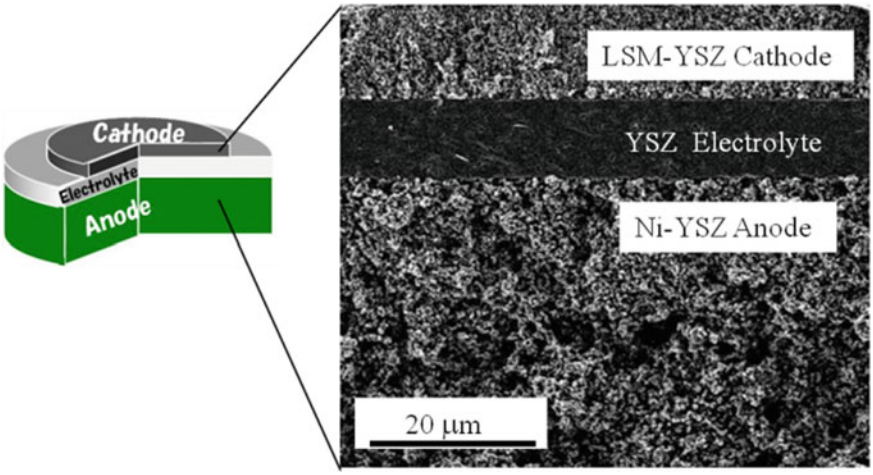

Fig. 21.2 Cross sectional view of an anode-supported SOFC

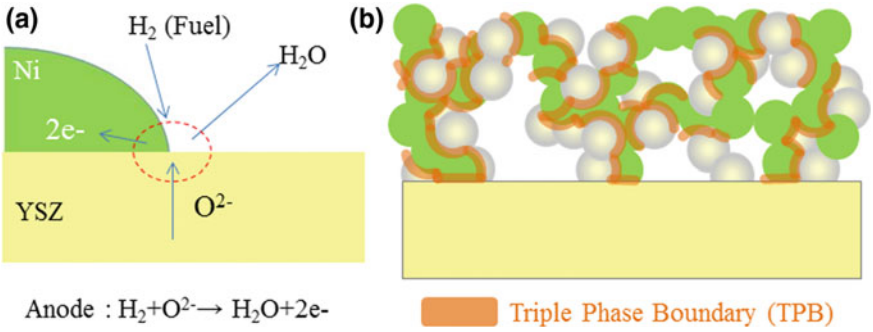

Fig. 21.3 Schematic diagrams of **a** electrochemical reaction at Ni–YSZ anode and **b** triple phase boundary formed in Ni–YSZ composite porous layer

Considerable efforts have been made to enlarge the TPB by controlling the composite microstructure of SOFC electrodes [8, 9]. The previous studies have used the ball-milling technique and determined that the important parameters are the particle diameter, powder size distribution, electrode/electrolyte particles compounding ratio and the degree of calcinations. These control parameters, however, have complicated optimization of the electrode microstructure.

In addition to the conventional mechanical mixing of the electrode (NiO or LSM) and the electrolyte (YSZ) particles, their composite particles can be directly synthesized by wet chemical routes. The purpose of the direct synthesis is primarily to improve the homogeneity of electrode and electrolyte phase distribution and thereby to increase electrode performances. Polymeric complexing [10–12], spray pyrolysis [13–15], and coprecipitation methods [16–18] have been proved to be a

good synthesize route for the preparation of composite particles. Among these routes, the coprecipitation method has been found particular interest because of its simplicity, cost-effective, and easy scale-up capability. In this section, therefore, the emphasis will be placed on the development of coprecipitation methods for SOFC electrodes.

21.2 Precipitation of Metal Hydroxides

The most common method used to collect soluble metal ions from a solution is to precipitate the species as a metal hydroxide. By raising the pH value of the solution, the corresponding metal hydroxides become insoluble and precipitate from solution. First, it is important to understand the precipitation behavior of the metal hydroxides from the solubility curves [19]. The precipitation of metal hydroxide $M(OH)_n$ can be described as

$$M^{n+} + n(OH)^- \rightarrow M(OH)_n \tag{21.1}$$

where n is the valence of metal ion in the solution. The solubility product K_{SP} of $M(OH)_n$ is

$$K_{SP} = [M^{n+}][OH^-]^n \tag{21.2}$$

$$\log K_{SP} = \log [M^{n+}] + n \cdot \log [OH^-] \tag{21.3}$$

$[M^{n+}]$ and $[OH^-]$ were the mole concentration of M^{n+} and OH^- in the solution, respectively. The ionic product of water at 25 °C under the ambient pressure is 10^{-14} M^2.

$$-\log [H^+] - \log [OH] = pH + pOH = 14 \tag{21.4}$$

Therefore Eq. (21.3) can be described as follows:

$$\log K_{SP} = \log [M^{n+}] - 14n - n \log [H^+] \tag{21.5}$$

$$\log [M^{n+}] = -\log K_{SP} + 14n - npH \tag{21.6}$$

K_{sp} can be obtained from the literature [20, 21]. For example, Fig. 21.4 shows the solubility curves of $Zr(OH)_4$, $Y(OH)_3$ and $Ni(OH)_2$ as a function of pH. Metal ion (M^{n+}) is stable (unsaturated state) in the left side of the curve, while metal hydroxide $M(OH)_n$ is stable (supersaturated state) in the right side.

The pH value of a solution is controlled using an alkaline solution such as NaOH or NH_3. Typically, the alkaline solution is dropped into the acid solution of the component cations to obtain the precipitates, which is called as “normal sequence”.

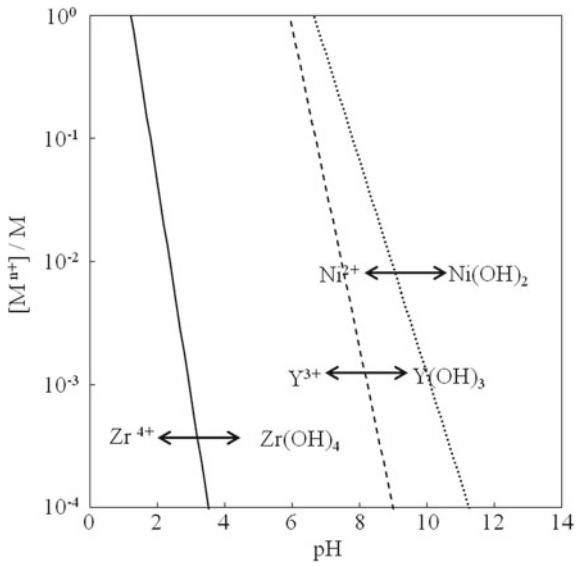

Fig. 21.4 Solubility of Zr $(OH)_4$, $Y(OH)_3$, and $Ni(OH)_2$ as a function of pH at 25 °C. Reprinted from Ref. [19], Copyright 2009 with permission from Elsevier

When the normal sequence is used for the solution dissolved with Zr^{4+}, Y^{3+}, and Ni^{2+}, $Zr(OH)_4$ precipitates first, then $Y(OH)_3$ and $Ni(OH)_2$ precipitate from the solubility curves as shown in Fig. 21.4. As a result, the precipitates would be not homogenous.

21.3 Coprecipitation Under Reverse Sequence

There is an alternative sequence. The mixed cation solution is dropped into the alkaline solution (reservoir). The reservoir pH can be kept constant by adding the extra alkaline solution. The pH in the local region undergoes a change near the droplet, presenting the smaller precipitation system compared to the normal sequence.

The coprecipitation under the reverse sequence has been investigated by the authors for synthesizing NiO–YSZ composite particles [19]. Figure 21.5 shows the effect of reservoir pH on the morphology of the composite particles. The samples synthesized at pH 10 and pH 11 contained very large NiO grains (see Fig. 21.5b, c). On the other hand, the nanocomposite particles were synthesized at pH 13 (see Fig. 21.5d). The clear difference of the microstructure depending on the reservoir pH can be attributed to the difference of nucleation density and growth of the hydroxides. When the reservoir pH was the highest, the number density of nuclei increases and the difference of precipitation rate among $Zr(OH)_4$, $Y(OH)_3$ and Ni $(OH)_2$ decreases. As a consequence, the fine hydroxide phases with uniform distribution could be obtained at pH 13. The uniformly distributed NiO and YSZ

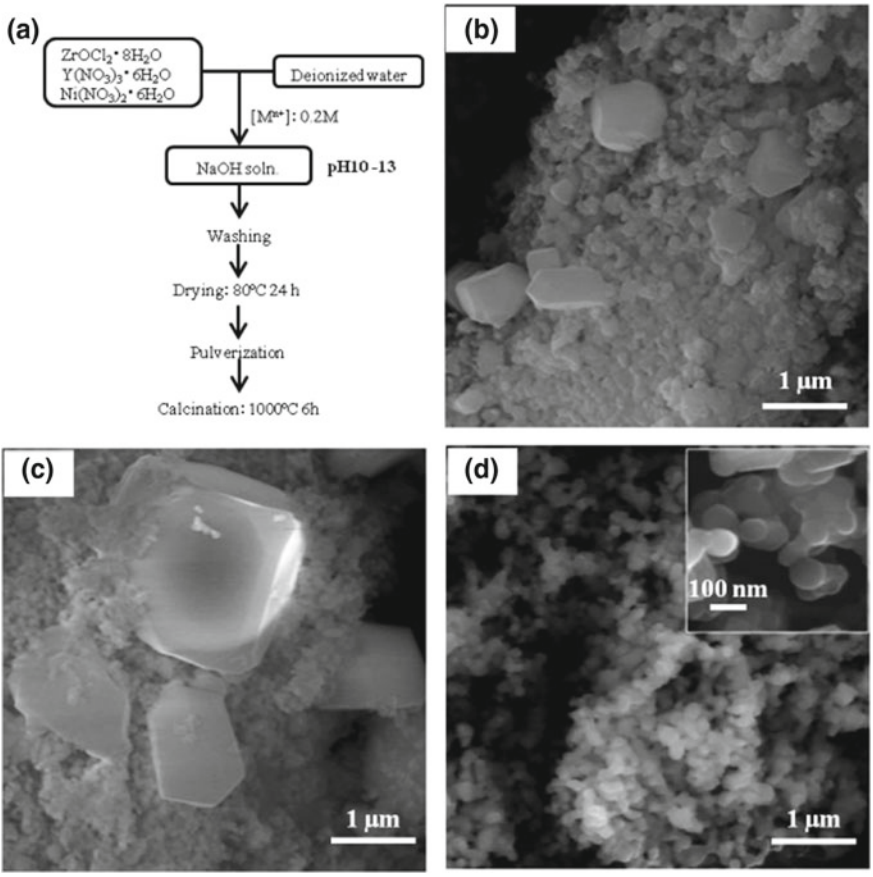

Fig. 21.5 **a** Synthetic flowchart and scanning electron microscopy (SEM) images of the NiO/YSZ composite particles synthesized at **b** pH 10, **c** pH 11, and **d** pH 13. Modified from Ref. [19], Copyright 2009 with permission from Elsevier

phases suppressed the grain growth each other during the subsequent calcination step, resulting in a successful synthesis of the NiO/YSZ nanocomposite particles at pH 13.

The anode was fabricated by screen printing of the paste consisting of the NiO/YSZ composite particles and polyethylene glycol followed by sintering at 1300 °C for 2 h. Finally, the Ni–YSZ cermet anode was obtained by reducing with H_2 + 3% H_2O at 800 °C. The composite particles synthesized at pH 10 resulted in coarse and inhomogeneous anode microstructure and moderate area specific resistance (ASR) as 0.57 Ω cm^2 at 800 °C under open-circuit voltage (OCV). Contrarily, the nanocomposite particles synthesized at pH 13 provided fine as well as homogeneous porous microstructure with the grain size in the range 200–400 nm and the lower ASR as 0.36 Ω cm^2 at 800 °C under OCV.

The nanocomposite particles with sodium contamination may reduce the long-term stability of the anode [22]. Tetramethylammonium hydroxide (TMAH, $(CH_3)_4NOH$) is another choice to keep the high pH in the reverse titration method.

21.4 Coprecipitation in YSZ Nanocrystal Sol

Recently, reliable and reproducible methods have been developed for preparing large quantities of inorganic nanocrystals. Aqueous sols containing the inorganic nanocrystals have been also available. Here, a unique coprecipitation method using an aqueous sol of YSZ nanocrystal is shown for the synthesis of NiO–YSZ nanocomposite particles [23].

The aqueous sol used in our experiment was the colloid containing YSZ nanocrystals (Sumitomo Osaka Cement Co. Ltd., Japan). The sol has a highly transparent appearance due to superior dispersion (almost no agglomeration) as shown in the left of Fig. 21.6a. The dynamic light scattering revealed that the nanocrystals had a narrow size distribution with an average diameter of 3 nm (Fig. 21.6b), showing good agreement with that observed in transmission electron microscopy (TEM) image.

The specific feature of the YSZ sol is its well-dispersed ability even in the highly concentrated metal salts (nitrate and chloride) solution. In the present case, a Ni $(NO_3)_2{\cdot}6H_2O$ was dissolved to be the total concentration of YSZ and Ni $(NO_3)_2{\cdot}6H_2O$ is 0.2 M. After the dissolving, the sol maintained transparency, indicating that the YSZ nanoparticles preserved their well-dispersed state as shown in the right of Fig. 21.6a. Although the origin of YSZ nanocrystal dispersion in a relatively high salt has not been clarified yet, it would be probably hydration force (non-DLVO force [24]).

The YSZ–Ni^{2+} mixed solution was dropped into NH_4HCO_3 solution at room temperature. During the coprecipitation, NH_3 solution (Wako Chemicals, Japan) was added simultaneously into NH_4HCO_3 solution to keep the pH at 8. The corresponding Ni compound (approximately $Ni(CO_3)_{2/3}(OH)_{2/3}{\cdot}nH_2O$), was deposited on YSZ nanocrystals and coprecipitated. The crystalline YSZ nanoparticles (in the circles) were uniformly distributed entire the noncrystalline Ni compound phase (Fig. 21.6c) in the precipitates. Organic bases such as tetramethylammonium hydrogen carbonate solution (TMAC, $(CH_3)_4NHCO_3$) and TMAH is available as the alkaline solutions. Since Ni ion does not form any soluble complexes with them, more precise control of NiO–YSZ mixing ratio can be possible.

Both YSZ and NiO phases were identified in the X-ray diffraction profile for the sample calcined at 600 °C. Their average crystalline sizes, estimated by Scherrer's formula, were about 6 and 4 nm, respectively. Also, the HRTEM image evidenced the successful fabrication of the NiO/YSZ nanocomposite particles with the size of about 5 nm (Fig. 21.6d).

Then the anode layer was fabricated on the sintered YSZ disk from the NiO/YSZ nanocomposite particles, through screen printing followed by sintering at 1300 °C

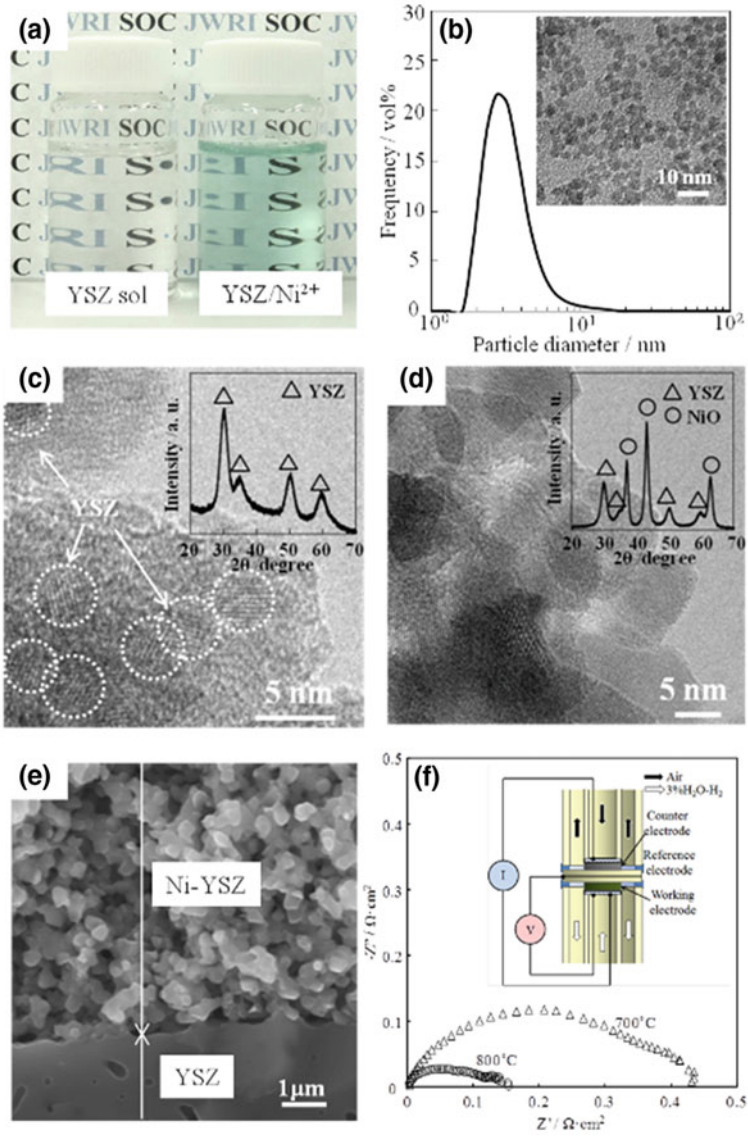

Fig. 21.6 **a** Appearance of aqueous sol of YSZ nanocrystals, **b** its size distribution (*inset* TEM image of the YSZ nanocrystals), **c** HRTEM image and XRD pattern of the coprecipitated sample, **d** HRTEM image XRD pattern of the NiO/YSZ nanocomposite particles calcined at 600 °C, **e** cross-sectional SEM image of the Ni/YSZ anode, **f** electrochemical impedance spectra of the Ni/YSZ anode measured at 700 and 800 °C under OCV. Modified with permission from Ref. [23], Copyright 2010 Wiley

for 2 h. Finally, the Ni–YSZ cermet anode was obtained as mentioned above. The microstructural examination reveals that the anode consisted of fine grains with the size of 200–300 nm (Fig. 21.6e). The grain size is one order of magnitude smaller than that of conventional anodes. Fine and well percolating solid and pore phases can be attributed to the homogeneous arrangement of NiO and YSZ phases in the nanocomposite particles. ASR of the anode was 0.43 and 0.15 Ω cm^2 at 700 and 800 °C, respectively (Fig. 21.6f). These values were significantly lower than those reported in the literatures on Ni/YSZ anodes [23]. It is clearly attributable to the fine composite microstructure, leading to extended adsorption sites and reduced diffusion length of hydrogen, in addition to the significantly enlarged TPB. The formation of the fine grains surely resulted from prevention of abnormal grain growth due to the homogeneously distributed two particle phases.

To estimate TBP length, the three-dimensional microstructure of an SOFC anode has been characterized using a focused ion beam–scanning electron microscope (FIB-SEM). The Ni–YSZ anode was fabricated from NiO–YSZ composite layer sintered at 1350 °C followed by reduction. The volume ratio was Ni:YSZ = 50:50. The microstructure of the anode is virtually reconstructed in a computational field using a series of acquired two dimensional SEM images (Fig. 21.7a, b). The TPB density is estimated to be $\sim$8 μm/μm^3 (Fig. 21.7c), which is longer than that obtained by a mechanical mixing method [25].

The LSM/YSZ nanocomposite powder was also synthesized with the similar manner [26]. Then, the fine-structured LSM/YSZ porous film has been fabricated for a cathode electrode, and it was demonstrated that the ASR was significantly reduced due to the enlarged TPB formed in the fine composite microstructure [27]. The anode-supported cell of Ni–YSZ/YSZ/LSM–YSZ was fabricated using the LSM–YSZ nanocomposite particles. The cells exhibited the high power density of 0.20, 0.40, 0.69, and 0.85 W/cm^2 at 650, 700, 750, and 800 °C, respectively, under the cell voltage of 0.7 V [27]. This high performance indicates that the anode-supported cell with the nanostructured cathode has potential to be operated at the intermediate temperature range with an acceptable power density.

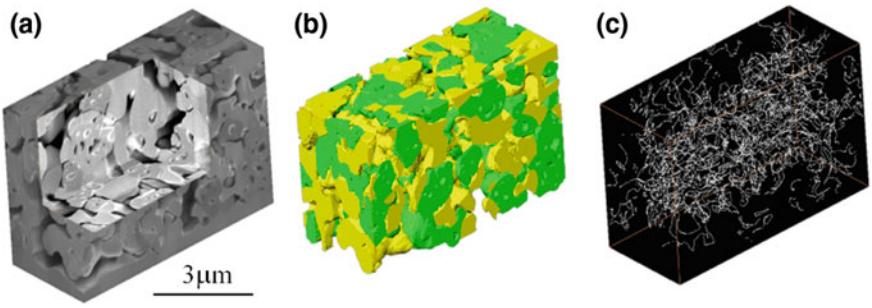

Fig. 21.7 **a** FIB-SEM image of Ni–YSZ anode from the reduction of NiO–YSZ sintered at 1350 °C, **b** 3D Ni–YSZ anode reconstruction, Ni(green) and YSZ(yellow), **c** 3D map of three-phase boundaries in the anode

21.5 Coprecipitation with Anionic Zr(IV) Complex Solution

Zr^{4+} forms soluble anionic complexes with hydroxide and carbonate ions in aqueous solution [28]. Karlysheva et al. predicted the generation of $[Zr(OH)_2(CO_3)_2]^{2-}$ in a mixed solution of $ZrOCl_2$ and Na_2CO_3 at pH > 7 [29]. Malinko et al. demonstrated the presence of $[Zr(OH)_2(CO_3)_2]^{2-}$, $[Zr(OH)(CO_3)_3]^{3-}$, and $[Zr(CO_3)_4]^{4-}$, depending on the concentration of carbonate in a mixed solution of Na_2CO_3 and $Zr(SO_4)^2$ [30]. Veyland et al. revealed a variation in the number of carbonate ions coordinating to zirconium depending on the chemical composition of a mixed solution of K_2CO_3–$KHCO_3$–$ZrOCl_2$ [31]. The authors have simply prepared a transparent solution of anionic Zr complex, $[Zr(OH)_2(CO_3)_2]^{2-}$, by mixing $ZrOCl_2$ and TMAC ($(CH_3)_4NHCO_3$) solutions (Fig. 21.8). The anionic Zr complex is stable in pH 7–10 at temperatures below about 80 °C.

It has been reported that the soluble anionic Zr complex can be used as the precursor for the synthesis of Zr-based materials. Afanasiev has synthesized the mesoporous ZrO_2 though reaction with cetyltrimethylammonium bromide (CTAB) [32]. The authors have synthesized monoclinic ZrO_2 [33] and YSZ nanocrystals

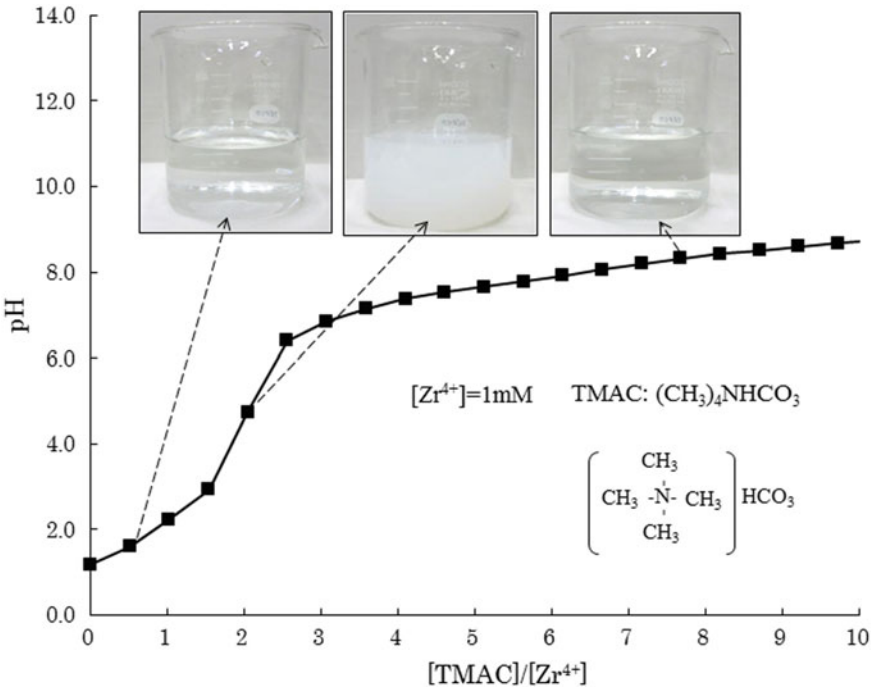

Fig. 21.8 pH titration curve for 1 mM solution of $ZrOCl_2$ under TMAC ($(CH_3)_4NHCO_3$)) addition

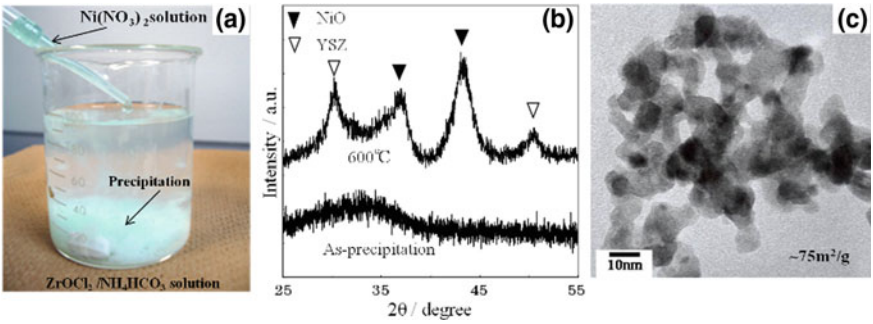

Fig. 21.9 **a** precipitation phenomenon by dropping of $Ni(NO_3)_2$ solution into the Zr complex solution ($ZrOCl_2/NH_4HCO_3$), **b** XRD patterns for the precipitate calcined at 600 °C, **c** TEM image of the sample (**b**)

[34] under hydrothermal condition with tetramethylammonium ion as capping agent. Also, an interesting coprecipitation phenomenon has been found in the soluble anionic Zr complex. Recently, highly dispersive nanocomposite particles have been synthesized based on this interesting coprecipitation [35].

Here, the synthesis of NiO–YSZ nanocomposite particles using anionic Zr complex is briefly shown. The soluble anionic Zr complex was prepared by mixing $ZrOCl_2$ and NH_4HCO_3 solutions. When Ni nitrate solution was dropped in the soluble anionic Zr complex solution, a mint-green precipitate was obtained (Fig. 21.9a). Concentrations of Ni and Zr ions in the supernatant solution were measured to be less than 5% of initial concentrations, indicating that the precipitates contained both Ni and Zr. Supplementary experiments suggested that aqua ligands in $[Ni(H_2O)_6]^{2+}$ complex play an important role on the reaction with anionic Zr complex. Similarly, a precipitation was observed when $Y(NO_3)_3$ aqueous solution is dropped, too. Therefore, when the solution of Ni and Y nitrates was dropped, the compound containing Ni, Y and Zr was easily coprecipitated. The thermal decomposition of the precipitates accompanying with the evolution of H_2O and CO_2 was almost completed until 450 °C, and no significant weight loss was observed during further increase of temperature. The XRD and TEM revealed that the products calcined at 600 °C consisted of nanosized NiO and YSZ grains (Fig. 21.9b, c), which were surely highly homogeneous.

21.6 Conclusion

Advanced coprecipitation routes have been developed to synthesize nanocomposite particles suitable for application in SOFC electrodes. The reverse sequence coprecipitation with the strong alkaline solution is a promising approach to obtain the hydroxides including $Zr(OH)_4$, $Y(OH)_3$, and $Ni(OH)_2$ with homogeneous phase

distributions, compared to conventional normal sequence. In addition, the coprecipitation with YSZ nanocrystal can produce the homogeneous precipitate for the synthesis of NiO–YSZ and LSM–YSZ nanocomposite particles. Furthermore, it is demonstrated that coprecipitation through reaction of Ni^{2+} and aqueous anionic Zr (IV) complex is another way for homogeneous NiO–YSZ nanocomposites. It is expected that there are opportunities of these facile synthetic routes for not only SOFC electrodes but also advanced composite materials.

References

1. B.C.H. Steele, A. Heinsel, Nature **414**, 345 (2001)
2. T.A. Adams, J. Nease, D. Tucker, P.I. Barton, Ind. Eng. Chem. Res. **52**, 3089 (2013)
3. S.M. Haile, Acta Mater. **51**, 5981 (2003)
4. Z. Shao, W. Zhou, Z. Zho, Prog. Mater. Sci. **57**, 804 (2012)
5. J. Will, A. Mitterdorfer, C. Kleinlogel, D. Perednis, L.J. Gaucker, Solid State Ionics **131**, 79 (2000)
6. A. Bieberle, L.P. Meier, L.J. Gauckler, J. Electrochem. Soc. **148**, A646 (2001)
7. K. Sasaki, J.P. Wurth, R. Gschwend, M. Gödickemeier, L.J. Gauckler, J. Electrochem. Soc. **143**, 530 (1996)
8. S.P. Jiang, S.H. Chan, J. Mater. Sci. **39**, 4405 (2004)
9. S.P. Jiang, J. Mater. Sci. **43**, 6799 (2008)
10. J. Martynczuk, M. Arnold, H. Wang, J. Caro, A. Feldhoff, Adv. Mater. **19**, 2134 (2007)
11. S.D. Kim, H. Moon, S.H. Hyun, J. Moon, J. Kim, H.W. Lee, Solid State Ionics **178**, 1304 (2007)
12. J.X. Wang, Y.K. Tao, J. Shao, W.G. Wang, J. Power Sources **186**, 344 (2009)
13. T. Fukui, T. Oobuchi, Y. Ikuhara, S. Ohara, K. Kodera, J. Am. Ceram. Soc. **80**, 261 (1997)
14. T. Fukui, S. Ohara, K. Mukai, Electrochem. Solid-State Lett. **1**, 120 (1998)
15. A. Hagiwara, N. Hobara, K. Takizawa, K. Sato, H. Abe, M. Naito, Solid State Ionics **178**, 1552 (2007)
16. G.M. Grgicak, R.G. Green, W.F. Du, J.B. Giorgi, J. Am. Ceram. Soc. **88**, 3081 (2005)
17. Y. Li, Y. Xie, J. Gong, Y. Chen, Z. Zhang, Mater. Sci. Eng. **B86**, 119 (2001)
18. X. Fang, G. Zhu, C. Xia, X. Liu, G. Meng, Solid State Ionics **168**, 31 (2004)
19. K. Sato, G. Okamoto, M. Naito, H. Abe, J. Power Sources **193**, 185 (2009)
20. L.G. Sillen, A.E. Martell, in *Stability Constants of Metal-Ion Complexes*, No. 17 and No. 25 (Chemical Society, London, 1964 and 1971)
21. W. Feitknecht, P. Scindler, Pure Appl. Chem. **6**, 130 (1963)
22. Y.L. Liu, S. Primdahl, M. Morgensen, Solid Sate Ionics **161**, 1 (2003)
23. K. Sato, T. Kinoshita, H. Abe, Fuel Cells **10**, 320 (2010)
24. J. Israelachvili, in *Intermolecular and Surface Forces*, 2nd edn. (Academic Press, 1991), pp. 260–282
25. J.R. Wilson, S.A. Barnett, Electrochem. Solid-State Lett. **11**, B181 (2008)
26. K. Sato, T. Kinoshita, H. Abe, M. Naito, J. Ceram. Soc. Jpn. **117**, 1186 (2009)
27. K. Sato, T. Kinoshita, H. Abe, J. Power Sources **195**, 4144 (2009)
28. F. Takahashi, K. Fujiwara, Y. Nakajima, T. Nishikawa, H. Masu, M. Imanari, Y. Hidaka, N. Ogawa, Dalton Trans. **44**, 645
29. K.F. Karlysheva, L.S. Chumakova, L.A. Malinko, I.A. Sheka, Russ. J. Inorg. Chem. **27**, 1582 (1982)
30. L.A. Malinko, L.S.C. Chumakova, K.I. Arsenin, K.F. Karlysheva, I.A. Sheka, Russ. J. Inorg. Chem. **25**, 1184 (1980)

31. A. Veyland, L. Dupont, J. Rimbault, J.C. Pierrard, M. Aplincourt, Helv. Chim. Acta **83**, 414 (2000)
32. P. Afanasiev, Mater. Res. Bull. **37**, 1933 (2002)
33. K. Sato, H. Abe, S. Ohara, J. Am. Chem. Soc. **132**, 2538 (2009)
34. K. Sato, K. Horiguchi, T. Nishikawa, S. Yagishita, K. Kuruma, T. Murakami, H. Abe, Inorg. Chem. **54**, 7976 (2015)
35. X. Xi, H. Abe, K. Kuruma, R. Harada, A. Shui, M. Naito, Adv. Powder Technol. **25**, 490 (2014)

Chapter 22
Hybrid Membrane-Type Fuel Cells for Intermediate Temperatures

Toshinobu Yogo

Abstract This chapter describes the syntheses and characterization of proton-conductive hybrid membranes for the use at intermediate temperatures from 100 to 150 °C. The inorganic–organic hybrid membranes were synthesized from an unsaturated organoalkoxysilane and a vinylphosphonic acid derivative via copolymerization and acidic hydrolysis. The hybrid membranes were characterized by infrared spectroscopy, thermogravimetry, and indentation test. The proton conductivity was measured for various compositions of the membranes. The current–voltage curves for the membrane electrode assembly consisting of the hybrid membrane were evaluated.

Keywords PEFC · Inorganic–organic hybrid · Sol–gel process · Copolymerization · Conductivity · Fuel cells

22.1 Introduction

Polymer electrolyte fuel cells (PEFCs) are characterized by their high energy-conversion efficiency and clean exhaust gas [1, 2]. Perfluorosulfonic polymers are the representatives of PEFCs, and have high proton conductivity, high mechanical strength, and good chemical stability. However, these membranes exhibit the maximum performance at around 80 °C and 100% relative humidity (RH). Perfluorosulfonic polymers require a complicated water management system in order to maintain high relative humidity and pure hydrogen gas with low inclusion of CO less than 20 ppm to avoid the poisoning of Pt anode catalysts [3]. When the operation temperature of PEFCs is raised to higher temperatures around 130 °C, the greatest advantages, such as a decrease in catalyst poisoning, higher efficiency, and a simple management system, are achieved [4, 5]. Therefore,

T. Yogo (✉)
Institute of Materials and Systems for Sustainability, Nagoya University, Nagoya, Japan
e-mail: yogo@imass.nagoya-u.ac.jp

Y. Setsuhara et al. (eds.), *Novel Structured Metallic and Inorganic Materials*, https://doi.org/10.1007/978-981-13-7611-5_22

proton-conducting materials with high conductivity at intermediate temperatures from 100 to 150 °C are required.

Inorganic–organic hybrid materials are nanocomposites between organics and inorganics. Organic materials have merits of flexibility and chemical functionality, whereas inorganic materials have advantages of high mechanical strength, chemical, and thermal stability. Thus, the demerits of organic materials, such as low thermal and mechanical stability, can be improved by the incorporation of inorganic materials. As silica and/or organosiloxane form a network structure, silica-based inorganic–organic hybrids are appropriate materials for the proton-conductive membranes at intermediate temperatures [6–19]. Only mixing and doping of proton carriers in silica and/or organosiloxane matrix is not desirable for the synthesis of proton-conductive membranes. As the proton carriers, such as sulfonic acid, phosphonic acid, are quite soluble in water, which is generated during fuel cell reaction, the proton carriers are leached out from the membrane during use [20]. The leach-out of the carriers results in the decrease in conductivity and degradation of cell performance. Therefore, the proton carriers should be bound to the matrix polymer via covalent bonds.

22.2 Proton Conduction in the PEFC Membranes

Figure 22.1 shows the schematic principle of the H_2–O_2 fuel cell. The fuel cell consists of membrane sandwiched with two electrodes, anode and cathode. The membrane should have a very high proton conductivity but is not permeable to gas.

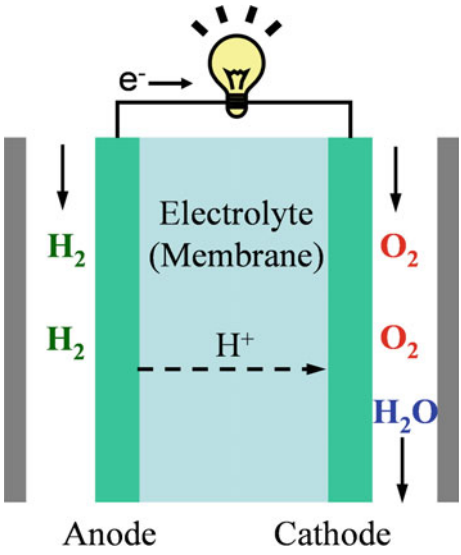

Fig. 22.1 Basic principle of H_2–O_2 fuel cell

At the anode, hydrogen is reduced electrochemically to protons according to Eq. (22.1).

$$H_2 \rightarrow 2H^+ + 2e^- \tag{22.1}$$

The generated protons enter the membrane and move to the cathode, whereas the generated electrons collected by the metallic electrode. At the cathode, the protons are electrochemically reacted with oxygen, producing water (Eq. (22.2)).

$$\frac{1}{2}O + 2H^+ + 2e^- \rightarrow H_2O \tag{22.2}$$

Thus, the overall reaction is the formation of water from 1 mol of hydrogen and a half mole of oxygen (Eq. (22.3)).

$$H_2 + \frac{1}{2}O_2 \rightarrow H_2O \tag{22.3}$$

The electromotive force or reversible potential E° at the standard state generated by Eq. (22.3) is represented by the following equation:

$$E^\circ = -\Delta G^\circ / nF \tag{22.4}$$

where ΔG° is the standard free energy change, n is the number of moles of electrons involved, and F is Faraday's constant. The value of ΔG accompanied by Eq. (22.3) is −229 kJ/mole, n = 2, F = 96,500 C/g mole electron, and therefore the value of E is 1.23 V.

Although fuel cells consist of various parts, such as membrane, electrodes, catalyst, H_2, and O_2 gas supplies, the membrane is a key material for the successful operation of cells at intermediate temperatures. The membranes are required to have high proton conductivity, unpermeability to hydrogen and oxygen, non-electronic conductivity, high chemical and electrochemical stability, high mechanical strength, and high thermal stability.

22.3 Synthesis of Siloxane-Based Hybrid Materials

The present hybrid material is composed of an organic main chain and inorganic Si–O linkage. The organic chain is formed via radical polymerization of the unsaturated double bond, while the Si–O linkage is constructed via sol–gel condensation of silicon alkoxide.

The hydrolysis of silicon alkoxide is a typical sol–gel reaction, and proceeds under both acidic and basic conditions [21]. Base-catalyzed reactions occur by nucleophilic substitution. Not only the electron density around the central silicon atom, but also the steric effects derived from the size of substituent groups influence

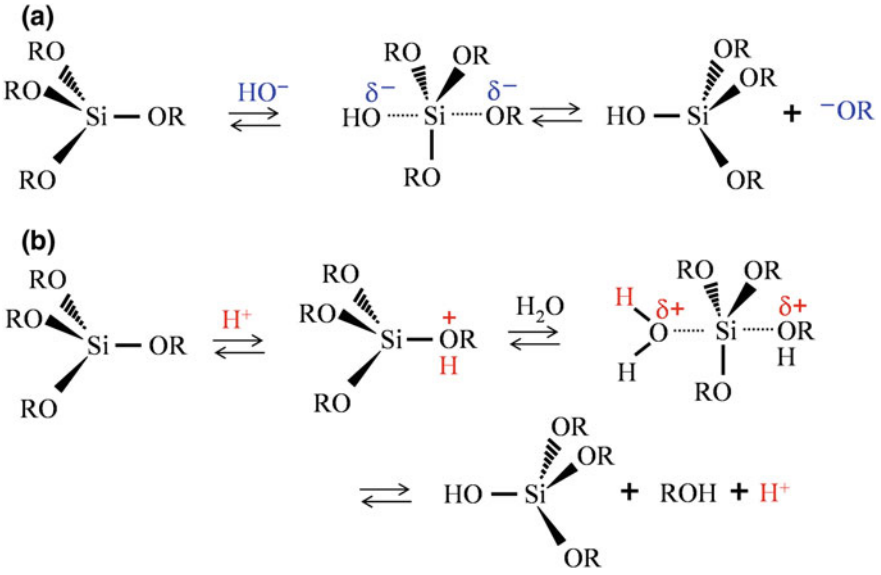

Fig. 22.2 Hydrolysis of silicon alkoxide, **a** hydrolysis under basic conditions, **b** hydrolysis under acidic conditions

the easiness of the nucleophilic attack by HO^-. As the reaction rate decreases with an increase in bulk and basic alkoxy groups around the central silicon atom, the basic hydrolysis undergoes through S_N2 mechanism with inversion of the silicon tetrahedron as shown in Fig. 22.2a. On the other hand, under acidic conditions, an alkoxy group is protonated, withdrawing electron density from silicon (Fig. 22.2b). Thus, the central silicon is more susceptible to electrophilic attack by H_2O. The backside attack of water to the central silicon inverts the silicon tetrahedron. Hence, the less sterically crowding substituent around silicon enhances the acidic hydrolysis rate.

The hydrolysis of the Si–OR bond results in the formation of unstable silanols (Si–OH) that condensate yielding the Si–O–Si linkage. On the other hand, Si–C bond is stable to hydrolysis, and intact during sol–gel reaction. These reactions are shown in the following Eqs. (22.5) and (22.6). As the Si–C bond is stable during sol–gel condensation, T linkage is formed from $RSi(OR')_3$.

$$RSi(OR')_3 + 3H_2O \rightarrow RSi(OH)_3 + 3R'OH \tag{22.5}$$

$$nRSi\,(OH)_3 \rightarrow RSi(O-)_3 \tag{22.6}$$

In T^n notation, T corresponds to a silicon atom bonded to three oxygen atoms forming tetrahedron. The superscript n indicates the number of other T unit attached to the $RSiO_3$ tetrahedron as shown in Fig. 22.3.

The organic–inorganic hybrid for fuel cells consist of the building blocks of inorganic Si–O–Si linkage covalently bonded to the organic polymer chain.

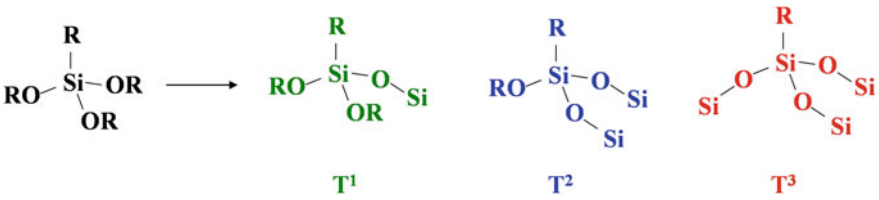

Fig. 22.3 T^3 notation of $RSiO_3$ tetrahedra

Generally, inorganic–organic hybrid is classified into two groups according to the character of the chemical bonds between organic and inorganic phase [22]. Figure 22.4 shows the schematic structures of Class I type and Class II type hybrids. The tetrahedron and the flat hexagon correspond to an inorganic and an organic unit, respectively. The Class I type hybrids consist of organic and inorganic phases, which are linked together through weak bonds, such as van der Waals force, hydrogen bonding, and weak electrostatic interactions. On the other hand, in Class II-type hybrids, an inorganic component is bound with an organic component through strong covalent chemical bonds. Therefore, Class II-type hybrids are much more appropriate for the membranes, in which proton carriers are fixed firmly to the stable inorganic–organic hybrid matrices via chemical bonds, leading to the prevention of the leach-out problem.

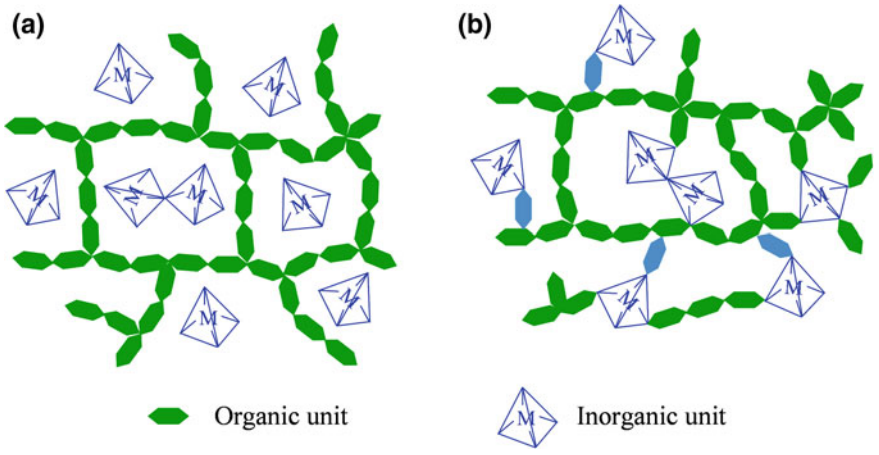

Fig. 22.4 Schematic structures of the hybrid material, **a** Class I-type hybrid, **b** Class II-type hybrid

22.4 Synthesis of Inorganic–Organic Hybrid Membrane

Figure 22.5 shows the starting materials and the reaction scheme for the synthesis of hybrid membrane. 4-fluorophenylvinylphosphonic acid (FC_6H_4PVA) consists of a vinyl group for radical polymerization and a phosphonic acid as a proton carrier. (Trimethoxysilylmethyl)styrene (TMSMS) includes a vinyl group for polymerization and trimethoxysilyl groups for hydrolysis and condensation. TMSMS was copolymerized with FC_6H_4PVA in dimethylformamide (DMF) with various monomer ratios in the presence of AIBN initiator. The samples were named as x/y = TMSMS/FC_6H_4VPA, more specifically, Si/P, according to their molar ratios. After the sealed glass capsule was heated at 85 °C for 8 h, a viscous solid copolymer was separated by centrifuging. The TMSMS–FC_6H_4VPA copolymer was dissolved in anhydrous DMF again immediately after separation. Then, 1.0 N hydrochloric acid solution was added dropwise to the copolymer solution to hydrolyze silicon alkoxide. The solution was stirred at room temperature for 24 h, yielding a sol, and the sol obtained was casted onto a Teflon plate. The casted film was heated in a dry oven at a stepwise heat treatment from 100 to 140 °C. The synthesized hybrid is classified to Class II hybrid, because the organic polymer chain is covalently bound to the Si–O linkages. The representative photographs of the hybrid membrane are shown in Fig. 22.6. The membranes are transparent and flexible. The optical transparency indicates that the membrane includes no

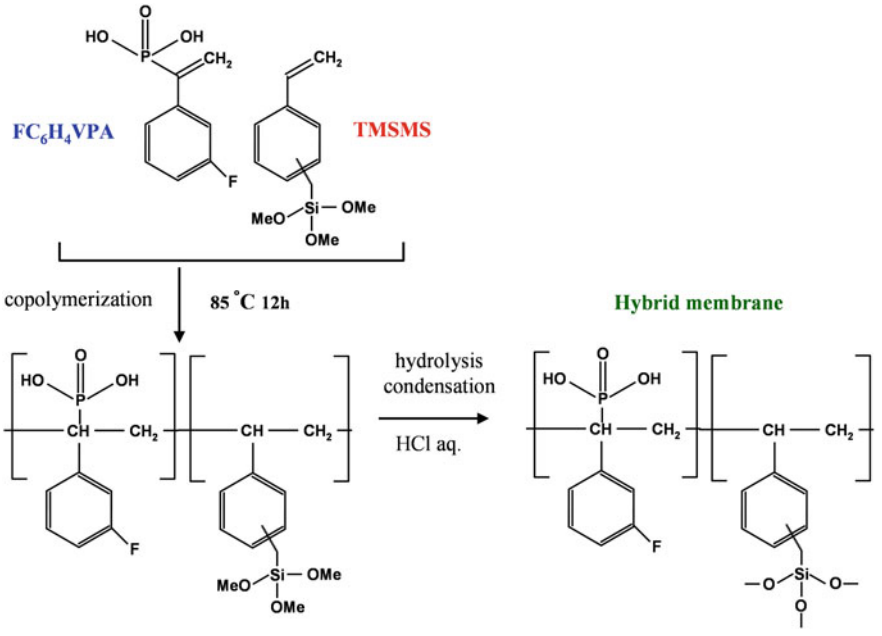

Fig. 22.5 Reaction procedure for the synthesis of hybrid membrane

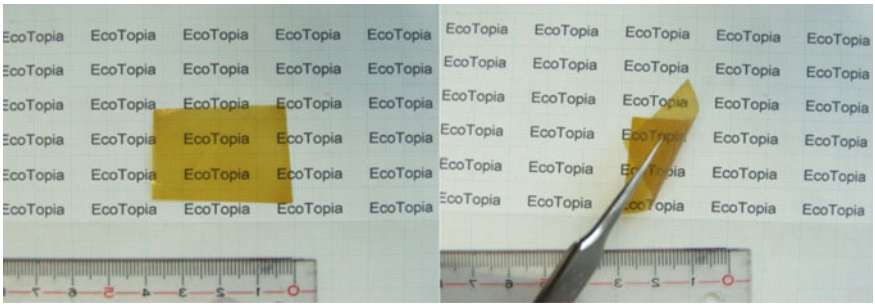

Fig. 22.6 Photographs of the hybrid membranes (Si/P = 1/6)

micron-sized region as the origin of light scattering. The flexibility is required for the construction of membrane electrode assembly (MEA) for fuel cell measurement.

TMSMS, FC_6H_4VPA, and the hybrid membrane with Si/P ratios of 1/2, 1/4, and 1/6 were analyzed by IR spectroscopy. TMSMS exhibited a C=C stretching band at 1630 cm^{-1}, aromatic bands at 1590, and 1490 cm^{-1}, and a Si–OCH_3 band at 827 cm^{-1} [23]. The P–OH bands were observed for FC_6H_4VPA as broad absorption bands from 2300 to 2800 cm^{-1}. Moreover, FC_6H_4VPA showed the absorption bands at 1583 and 1490 cm^{-1} attributed to the aromatic ring, the C=C and C–F stretching absorptions at 1620 and 1200 cm^{-1}, respectively. After copolymerization between TMSMS and FC_6H_4VPA followed by hydrolysis, the C=C absorption disappeared. In addition, the Si–OCH_3 band of TMSMS at 827 cm^{-1} disappeared in the spectra of all of the hybrid membranes, and a new absorption band for the Si–O–Si bond appeared at 1110 cm^{-1}. From these results, the hybrid was synthesized via the copolymerization of C=C bonds and the hydrolysis condensation of Si–OCH_3 groups.

Figure 22.7 shows the ^{29}Si CP-MAS NMR spectra of the hybrid membranes with Si/P ratios of 1/2, 1/4, and 1/6. Two signals were observed at −60 and −71 ppm in the T region which are assigned to T^2 and T^3, respectively [24]. Three-dimensional Si–O–Si cross-linkage is formed in the hybrid membranes through the hydrolysis and condensation of the Si–OCH_3 groups. Moreover, when the Si/P ratio decreases from 1/2 to 1/6, the intensity of the T^2 signal decreases. These results indicate that three-dimensional cross-links form more easily in the membranes with high P contents. Hence, the Si–OCH_3 groups of TMSMS undergo more rapid and complete hydrolysis, leading to the exclusive formation of T^3 cross-linkages, when the FC_6H_4VPA content is high. As phosphonic acid promotes the effective acidic condensation of the Si–OCH_3 bonds, the formation of T^3 linkages is more favorable than that of T^2 linkages.

The thermogravimetric curves were measured for the TMSMS/FC_6H_4VPA hybrid membranes with Si/P ratios of 1/2, 1/4, and 1/6 under an O_2 flow from room temperature to 800 °C. The gradual weight losses below 8 wt% were observed for all the membranes up to 180 °C. The weight loss was ascribed to the desorption of physically absorbed water. No other weight change was observed for the

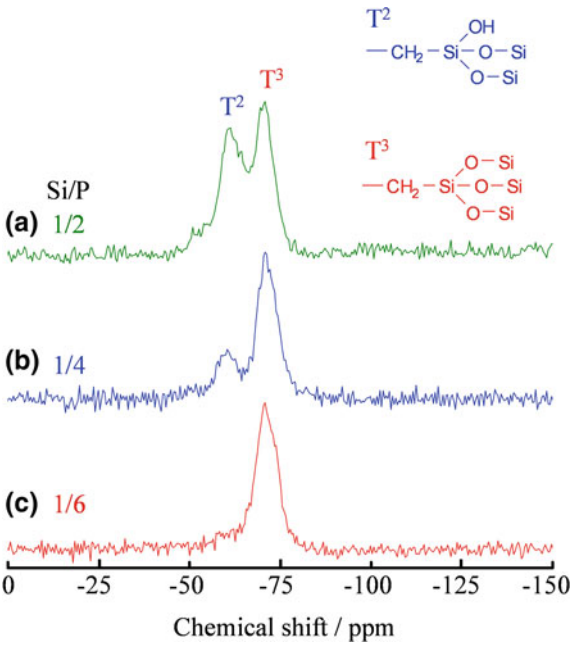

Fig. 22.7 ^{29}Si NMR spectra of hybrid membranes with the ratios of Si/P = **a** 1/2, **b** 1/4, **c** 1/6. Reprinted from Ref. [18]. Copyright 2015, with permission from Elsevier

membranes up to 180 °C. Therefore, the hybrid membranes were found to be thermally stable up to 180 °C, which is the higher temperature than the targeted temperature from 100 to 150 °C.

The oxidative stability of the TMSMS/FC_6H_4VPA membranes was examined using Fenton's reagent [8]. After treatment in Fenton's reagent at 80 °C for 24 h, the membranes with Si/P ratios of 1/4 and 1/6 maintained their outer shapes with no visible cracks. Usually, all organic polymer membranes dissolved in Fenton's reagent under the same conditions [25, 26]. Therefore, the chemical stability of the hybrid membranes is confirmed for fuel cell applications.

The mechanical properties of the TMSMS/FC_6H_4VPA membranes were measured using a Knoop indentation test. The Knoop microhardness (μHK) were 0.18, 0.12, and 0.088 GPa for the TMSMS/FC_6H_4VPA membranes of 1/2, 1/4, and 1/6, respectively. The μHK value decreases with increasing FC_6H_4VPA amount from 1/2 to 1/6. This result indicates that the Si–O linkage contributes to the hardness of hybrid membranes. The elastic modulus (E) were 1.9, 1.8, and 1.9 GPa for the TMSMS/FC_6H_4VPA membranes of 1/2, 1/4, and 1/6, respectively. The μHK and E values for the membranes with TMSMS/FC_6H_4VPA = 1/2 and 1/4 were comparable to those for the polycarbonate (μHK (micro-Vickers hardness): 0.14 GPa; E: 2.3 GPa) [27]. The TMSMS/FC_6H_4VPA membrane with a Si/P ratio of 1/6 had a μHK value of 0.088 GPa and an E value of 1.9 GPa due to the high organic polymer content and large number of T^3 Si–O–Si linkages. The organic polymer chain does not contribute to the hardness, but to the E value. The Si NMR spectra (Fig. 22.7) revealed that the TMSMS/FC_6H_4VPA = 1/6 membrane includes the

highest amount of T^3 linkage, indicating that T^3-type linkages were more favorable than T^2-type linkages for strengthening the hybrids. The TMSMS/FC_6H_4VPA = 1/6 membrane consisting of only T^3 Si–O–Si linkages has the optimum flexibility, which is useful for the construction of MEAs, as shown Fig. 22.10.

22.5 Proton Conductivity and Fuel Cell Properties of the Membrane

Figure 22.8 shows the temperature dependence of the proton conductivity for the hybrid membranes synthesized with TMSMS/FC_6H_4VPA ratios of 1/2, 1/4, and 1/6 at various RH. The open and solid symbols represent the conductivities of the membranes at 100% RH and low humidities from 19.3% to 27.0% RH, respectively. The conductivity at each humidity level increased with increasing temperature up to 130 °C. In addition, the conductivity depends on the Si/P ratio, and the highest conductivity was observed for the membranes with the Si/P ratio of 1/6 at all humidities. The maximum conductivity of 6.4×10^{-2} S cm^{-1} was observed for the membrane with Si/P = 1/6 ratio at 130 °C and 100% RH. This result indicates that the conductivity increased with increasing phosphonic acid, which acts as the proton carrier. At a low humidity of ~20% RH, the conductivity of the present membrane at 80 °C (5.0×10^{-5} S cm^{-1}) is much higher than that of an alkoxyphenylsilane-phosphonic acid system (~1×10^{-6} S cm^{-1}) [28].

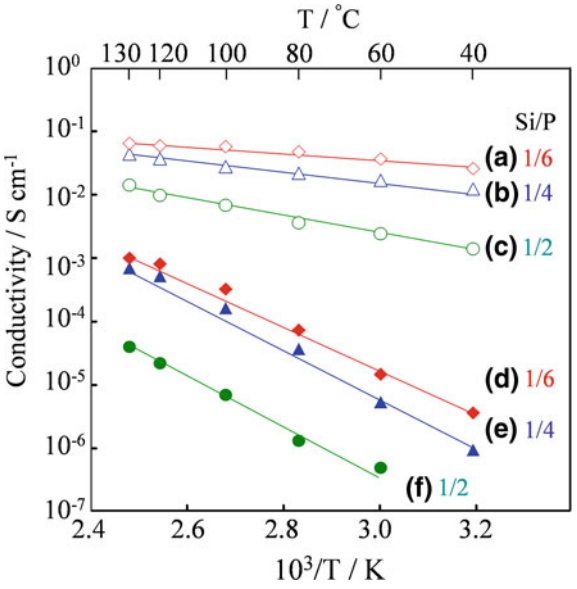

Fig. 22.8 Temperature dependences of the proton conductivities of hybrid membranes of TMSMS/FC_6H_4VPA with the ratios of 1/2, 1/4, and 1/6, **a** 1/6 at 100% RH, **b** 1/4 at 100% RH, **c** 1/2 at 100% RH, **d** 1/6 from 27.0 to 19.2% RH, **e** 1/4 from 27.0 to 19.2% RH, **f** 1/2 from 24.0 to 19.2% RH. Reprinted from Ref. [18]. Copyright 2015, with permission from Elsevier

As the proton conductivity increase with temperature, the conduction is thermally stimulated process. Therefore, the activation energies (Ea) for the proton conductivities at each humidity were calculated using the Arrhenius Eq. (22.7)

$$\ln \sigma = \ln A - Ea/kT \tag{22.7}$$

where A is the pre-exponential term, Ea is activation energy, and k is the Boltzmann constant. At 100% RH, the Ea values for the hybrid membranes with Si/P ratios of 1/2, 1/4, and 1/6 were determined to be 28, 15, and 11 kJ/mol, respectively. The Ea values for the membranes with Si/P ratios of 1/4 and 1/6 Si/P ratios were nearly the same as that of Nafion (9–13 kJ/mol) [29] Furthermore, at low RH, the Ea values for the membranes with Si/P ratio of 1/2, 1/4, and 1/6 were calculated to be 81, 75, and 57 kJ/mol, respectively. Nafion has high conductivity via both the Grotthuss and vehicle mechanisms at 100% RH. At 100% RH, proton transfer in the present hybrid membrane occurs via water-cooperative conduction mechanism through the hydrophilic nanochannels. At low humidities, however, the proton transfer decreases due to the depletion of water in the nanochannels. The decrease in the water content necessary for water-assisted proton conduction is considered to increase the energy barrier for proton transfer.

Figure 22.9 shows the hybrid membrane with Si/P = 1/6 composition attached with black catalyst layers, a carbon separator, and an assembled MEA. The catalyst layer was prepared on the membrane by decal transfer method. A catalyst ink was prepared from 5% Nafion solution, Pt/C powder, and methanol. After ultrasonication, a catalyst ink was uniformly casted on a Teflon film. The catalyst layer on the Teflon film was cut into a desired size, and then hot pressed on the hybrid membrane, yielding the laminated composite film consisting of the membrane, the catalyst layer, and the Teflon film. After hot press, the Teflon film was peeled off

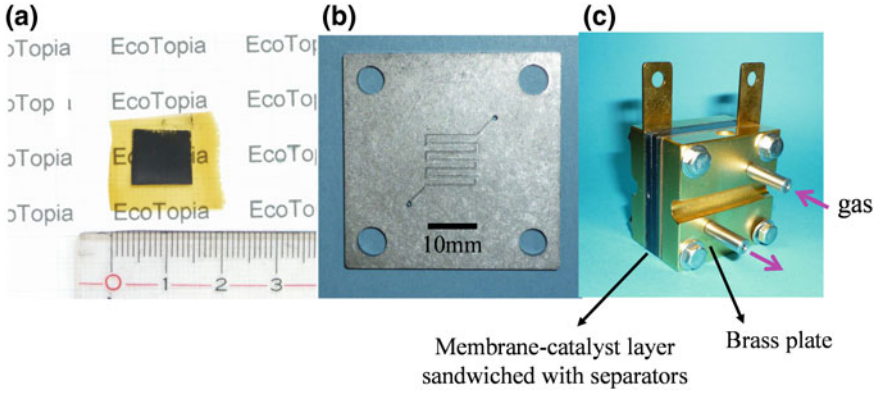

Fig. 22.9 Photographs of hybrid membrane with catalyst layers, carbon separator, and assembled MEA, **a** hybrid membrane (Si/P = 1/6) with catalyst layers, **b** carbon separator, **c** assembled MEA

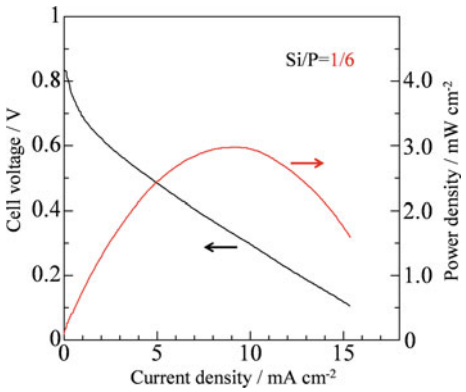

Fig. 22.10 I–V properties of the hybrid membrane of TMSMS/FC_6H_4VPA (Si/P = 1/6) measured at 140 °C and 30% RH. Reprinted from Ref. [18]. Copyright 2015, with permission from Elsevier

from the membrane–catalyst layer composite, resulting in the preparation of a membrane with catalyst layers as shown in Fig. 22.9a. The carbon separator has a serpentine flow channel for hydrated gases, such as oxygen and hydrogen (Fig. 22.9b). Hydrogen or oxygen gas is supplied to the flow channel through the tubing shown in Fig. 22.9c. The MEA was constructed from the membrane with catalyst layers sandwiched with a pair of carbon separators as shown in Fig. 22.9c. The brass plates are used as heat transfer elements from a flexible heater (not shown in Fig. 22.9c).

Figure 22.10 shows the power densities for an MEA fabricated using the hybrid membrane with Si/P = 1/6 at 30% RH. The peak power density was 3.0 mW/cm^2 at 140 °C with an open-circuit voltages (OCVs) of 0.85 V. The initial lower OCV may be due to gas cross-over or an internal micro short-circuit as the result of a reduction of the mechanical strength of the membrane at 140 °C. Although many examples of I–V properties at 100% RH below 100 °C have been reported for various membranes, not many papers deal with the cell properties at temperatures above 120 °C and low RH. The reported power densities for siloxane-based membranes are as follows: a silylmethylstyrene derivative–phosphoryl acrylate system, ~3 mW/cm^2 at 120 °C and 51% RH [11], and silylmethylmethoxystyrene derivative–methacryl phosphonic acid membrane, 4.8 mW/cm^2 at 140 °C and 30% RH [19]. The cell fabricated from the prepared hybrid membrane showed an I–V performance at an intermediate temperature and low humidity, although further investigation is required to improve the cell properties.

22.6 Conclusions

Proton-conductive inorganic–organic hybrid membranes of Class II type were synthesized from a mixture of TMSMS and FC_6H_4VPA. The formation of the inorganic–organic membranes consisting of Si–O networks and aliphatic polymer chains bound with phosphonic acid groups was confirmed based on IR and ^{29}Si

NMR. These membranes were self-standing, homogeneous, and exhibited high formability, and high thermal stability up to 180 °C. F substitution in the aromatic ring of phenylphosphonic acid was effective for the increase of the T^3 unit of the silica linkages, resulting in the increased Young's modulus of the membranes. The proton conductivities of the hybrid membranes were dependent on the phosphonic acid content, and increased with temperature up to 130 °C. MEAs were fabricated using the membranes with improved strengths. The peak power density for the MEA prepared from the TMSMS/FC_6H_4VPA membrane with a Si/P ratio of 1/6 was 3.0 mW/cm^2 at 140 °C and 30% RH. Chemical design of the monomers was found to be useful for the synthesis of hybrid membranes that work over a broad range of operating conditions from low to 100% RH at intermediate temperatures.

References

1. B.G. Pollet, I. Staffell, J.L. Shang, Electrochim. Acta **84**, 235 (2012)
2. U. Winter, H. Weidner, Fuel Cells **3**, 76 (2003)
3. M. Aparicio, A. Duran, J. Sol-Gel. Sci. Technol. **31**, 103 (2004)
4. Q. Li, R. He, J.O. Jensen, N.J. Bjerrum, Chem. Mater. **15**, 4896 (2003)
5. M.S.F. Schuster, W.H. Meyer, M. Schuster, K.D. Kreuer, Chem. Mater. **16**, 329 (2004)
6. H.W. Zhang, P.K. Shen, Chem. Rev. **112**, 2780 (2012)
7. C.L. Robert, K. Vallé, F. Pereira, C. Sanchez, Chem. Soc. Rev. **40**, 961 (2011)
8. M. Kato, S. Katayama, W. Sakamoto, T. Yogo, Electrochim. Acta **52**, 5924 (2007)
9. M. Kato, W. Sakamoto, T. Yogo, J. Membr. Sci. **303**, 43 (2007)
10. M. Kato, W. Sakamoto, T. Yogo, J. Membr. Sci. **311**, 182 (2008)
11. J. Umeda, M. Suzuki, M. Kato, M. Moriya, W. Sakamoto, T. Yogo, J. Power Source **195**, 5882 (2009)
12. Y. Xue, R. Fu, C. Wu, J.Y. Lee, T. Xu, J. Membr. Sci. **350**, 148 (2010)
13. Y. Tokuda, T. Yamada, M. Takahashi, T. Yoko, H. Kitagawa, Y. Ueda, J. Mater. Res. **26**, 796 (2011)
14. O. Sel, T. Azais, M. Maréchal, G. Gébel, C.L. Robert, C. Sanchez, Chem. Asian J. **6**, 2992 (2011)
15. U. Thanganathan, D. Dixon, S.L. Ghatty, B. Rambabu, Int. J. Hydrogen Energy **37**, 17180 (2012)
16. L. Wang, S.G. Advani, A.K. Prasad, Electrochim. Acta **105**, 530 (2013)
17. E.A. Mistri, S. Banerjee, RSC Adv. **4**, 22398 (2014)
18. M. Hattori, S. Yamaura, W. Zhang, W. Sakamoto, T. Yogo, J. Membr. Sci. **488**, 166 (2015)
19. T. Hoshino, K. Hayashi, W. Sakamoto, T. Yogo, J. Membr. Sci. **502**, 133 (2016)
20. J.F. Brinker, J. Non-Cryst. Solid **100**, 31 (1988)
21. P. Judeinstein, C. Sanchez, J. Mater. Chem. **6**, 511 (2004)
22. R.M. Silverstein, F.X. Webster, D.J. Kiemle, D.L. Bryce, in *Spectrometric Identification of Organic Compounds*, 8th edn. (Wiley, New York, 2014), p. 71
23. Y. Sugahara, S. Okada, S. Sato, K. Kuroda, C. Kato, J. Non-Cryst. Solid **167**, 21 (1994)
24. K. Miyatake, H. Zhou, T. Matsuo, H. Uchida, M. Watanabe, Macromolecules **37**, 4961 (2004)
25. X. Zhang, S. Liu, J. Yin, J. Polym. Sci. B: Polym. Phys. **44**, 665 (2006)
26. P. Innocenzi, M. Esposto, A. Maddalena, J. Sol-Gel. Sci. Technol. **20**, 293 (2001)

27. Y. Hamano, K. Yasuda, T. Yazawa, K. Kuraoka, J. Mater. Sci. **39**, 7097 (2004)
28. M. Saito, K. Hayamizu, T. Okada, J. Phys. Chem. B **109**, 3112 (2005)
29. T. Tezuka, K. Tadanaga, A. Matsuda, A. Hayashi, M. Tatsumisago, Solid State Ionics **176**, 3001 (2005)

Chapter 23
Synthesis of Nanomaterials Using Solution Plasma Process

Nagahiro Saito, Tomonaga Ueno, Maria Antoaneta Bratescu and Junko Hieda

Abstract This chapter introduces the synthesis of nanomaterials by solution plasma process (SPP). The SPP was used as a simple method for metal nanoparticles (NPs) synthesis, bimetallic NPs, and NPs incorporated in mesoporous silica. The SPP, which is a non-equilibrium plasma, can provide an extremely rapid reduction of a metal ion to the neutral form without using a reducing agent. Preferential oxidation (PROX) of CO is an important practical process to purify H_2 for use in polymer electrolyte fuel cells. Pt NPs in mesoporous silica synthesized by the SPP give a high conversion rate at a lower temperature. Recently, we focused on developing the SPP for producing carbon materials containing heteroatom as oxygen reduction reaction (ORR) catalyst. The SPP method can produce low-cost carbon materials, in one-step process, with controllable structure.

Keywords Solution plasma · Plasma in liquid · Metal nanoparticles · Mesoporous silica · Carbon

23.1 Introduction

In this chapter, we present the application of solution plasma process (SPP) in the synthesis of nanomaterials. The SPP is a discharge in a liquid environment at atmospheric pressure and usually at room temperature. Plasma in water has been known since 1899 when different pairs of metal electrodes were used to generate the discharge, and the optical emission spectra were collected to explain various features of spectral lines observed in astronomy [1, 2]. In our group, the SPP was

N. Saito (✉) · T. Ueno · J. Hieda
Department of Chemical System Engineering, Graduate School of Engineering, Nagoya University, Nagoya, Japan
e-mail: hiro@rd.numse.nagoya-u.ac.jp

N. Saito · M. A. Bratescu
Institute of Innovation for Future Society, Nagoya University, Furo-cho, Chikusa-ku, Nagoya 464-8603, Japan

Y. Setsuhara et al. (eds.), *Novel Structured Metallic and Inorganic Materials*, https://doi.org/10.1007/978-981-13-7611-5_23

used as a simple method for metal nanoparticles (NPs) synthesis, since this non-equilibrium plasma can provide an extremely rapid reduction of a metal ion to the neutral form without using a reducing agent. The SPP offers the possibility to control the NPs size by controlling the surrounding chemistry of the solution and operates in normal temperature and pressure conditions [3–5].

We have also demonstrated another merit of the SPP method for the fabrication of bimetallic NPs using a combination of the reduction reaction of the metal (M) ion to the neutral state, while simultaneously eroding the electrodes during the discharge, which generates the second metal in the structure of the bimetallic NPs. This combination of processes makes SPP a more useful method since no reducing agent or gold precursor is required in the reaction mixture, thus offering an ecologically friendly procedure for nanostructure synthesis. The electron transfer effect between the gold bimetallic nanoparticles and graphene was studied as a possible application in a solar cell [6].

The plasma discharge in aqueous solution was applied to template removal in mesoporous silica synthesis. Highly dispersed spherical mesoporous silica particles were synthesized by the ternary surfactant system containing the Pluronic P123 copolymer (EO20PO69EO20), sodium dodecylbenzene sulfonate, and 1,1,2,2,3,3,4,4,4-nonafluoro-1-butane sulfonate, via the sol–gel method in acid solutions. The SPP was used to remove the template during mesoporous silica fabrication instead of conventional thermal calculations [7].

Recently, our group has focused on developing the SPP for producing different catalysts to be used in fuel cell and batteries. Until now, although platinum (Pt) based catalysts have demonstrated the best performance as catalysts, some limiting factors remain such as the bottleneck of the oxygen reduction reaction (ORR) at the cathode of the fuel cell, the scarcity, and the high cost of Pt. Recently, in the field of energy storage and battery, new materials containing heteroatom (as nitrogen and boron) doped carbon are intensively researched to replace and reduce the noble metals [8]. The SPP method can produce low-cost carbon materials, in one-step process, with controllable structure [9].

23.2 One-Step Synthesis of Gold Bimetallic Nanoparticles with Various Metal Compositions

The gold bimetallic nanoparticles with different compositions (Fig. 23.1) were synthesized in the SPP as schematically is shown in Fig. 23.2. First, gold is produced in plasma by electrode erosion. There are various processes by which the metal electrodes can erode or wear away. First, there is the obvious process of a chemical reaction, such as oxidation or corrosion. This process in SPP has a small contribution to the production of gold in the solution because gold is hard to oxidize and the solution pH value does not fall below 3 for most of the metal salts used in the experiment. Another process is the disintegration of the electrode structure

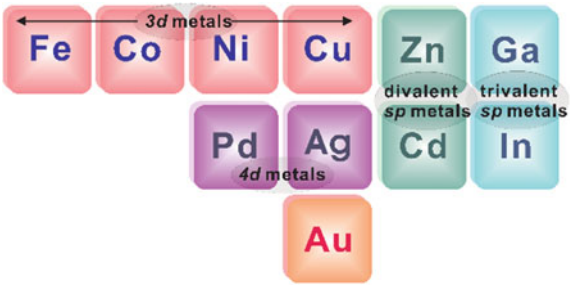

Fig. 23.1 Schematics of metals which were alloyed with gold in the nanostructures. Reprinted from Ref. [14], Copyright 2013, with permission from Elsevier

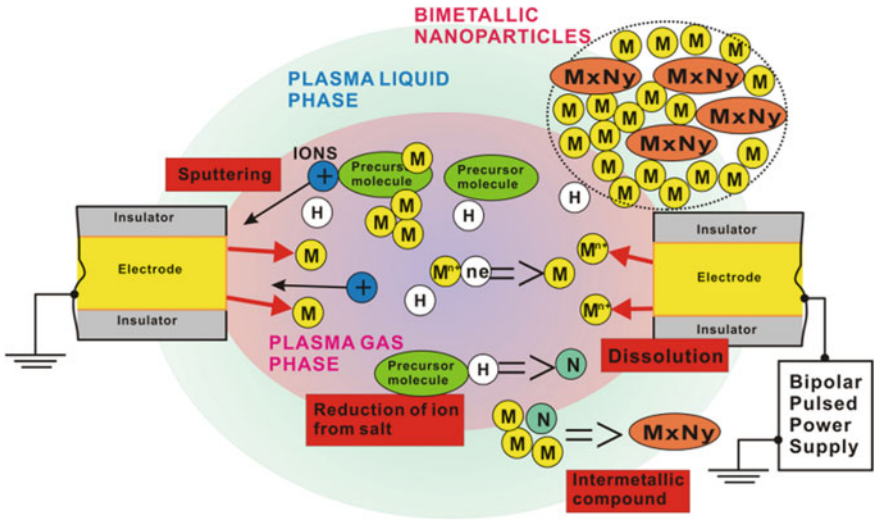

Fig. 23.2 The synthesis method of gold bimetallic NPs in the SPP. Mechanism of formation of the bimetallic structure is explained by the reduction of metal M simultaneously with the erosion of electrode. Reprinted from Ref. [14], Copyright 2013, with permission from Elsevier

under atomic or ionic bombardment. This process, which is, in fact, the cathode sputtering, leads to the highest amount of gold released into the solution. Moreover, thirdly, electrode erosion occurs by the action of an electrical discharge. It is well known that at local regions on an electrode surface during discharge, hot spots at very high temperature can be produced, from where the metal of the electrode can be released into the solution [10, 11].

The anode undergoes bombardment by electrons, which are not so efficient to produce a high rate sputtering, while the cathode suffers bombardment by positive

ions, leading to a higher sputtering and evaporation rate than that at the anode surface.

Another process which occurs in SPP, at the anode surface is the anodic dissolution, which happens when the electrode surface is covered with a solution, and the current flows between the electrodes. Due to the instabilities of the solution plasma system, it happens that the electrode surfaces are shortly covered with solution. In this case, the electrode metal is released from the anode as ions, which are rapidly neutralized by electrons from the plasma gas phase. Anodic dissolution can also produce free gold atoms which can nucleate and generate clusters or gold NPs [12, 13]. The sputtered gold from the cathode, or eroded from both electrodes, is present in solution plasma as free atoms, which agglomerate as clusters or NPs, or directly as NPs.

At the same time, in the SPP, the hydrogen radicals ($H^{\cdot}$), which are formed from water dissociation, move into the solution phase from the plasma gas phase and produce the reduction reaction of the metal ion (M^{x+}) to the neutral form (M^0): $M(NO_3)_x + xH^{\cdot} \rightarrow xHNO_3 + M^0$, where $M(NO_3)_x$ represents the metal nitrate, and x is the valence [5, 14].

The morphology, composition, and crystal structure were characterized by transmission electron microscope (TEM), energy dispersion spectroscopy (EDS), and X-ray diffraction (XRD) measurements. Figure 23.3 represents some characteristics of the bimetallic NPs.

For the interaction of free radicals with gold NPs, it was found that the electron spin resonance (ESR) signal decreases after the adsorption of nitroxyl free radicals

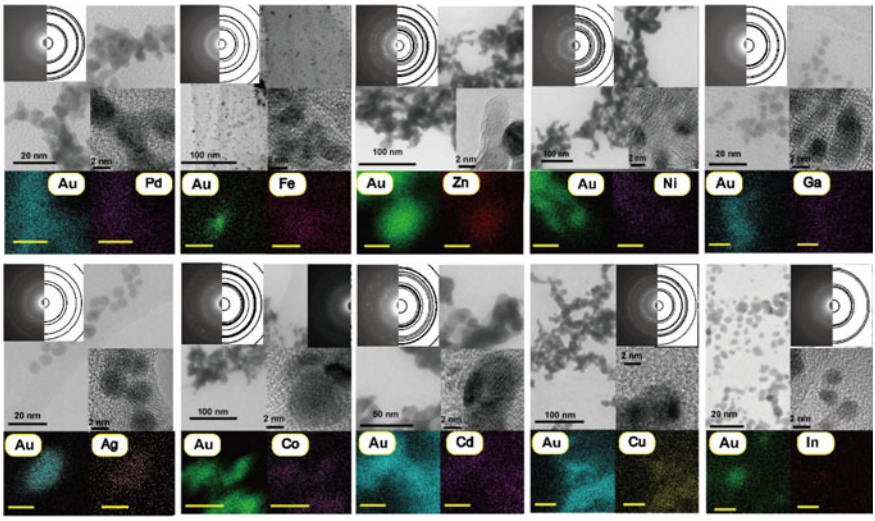

Fig. 23.3 TEM and EDS characterization of the bimetallic AuM NPs, where the metal M is Pd, Ag, Zn, Cd, Ga, In, Fe, Co, Ni, and Cu. Reprinted from Ref. [14], Copyright 2013, with permission from Elsevier

on the surface of gold NPs [15]. Nitroxyl free radicals, like TEMPOL and its derivative, are used in ESR as spin labels, spin traps, and antioxidant in biological applications. The interaction was stronger for 2.5 nm diameter gold NPs than for 15 nm diameter particles. It was suggested that the interaction of gold NPs with free radicals might be due by the exchange interaction of unpaired electrons of the free radical with the conduction band electrons of the gold NPs. We studied the interaction of gold bimetallic NPs with TEMPOL free radicals in 1 mM solution in benzene (Fig. 23.4). The strongest interaction between the gold bimetallic NPs with the unpaired electrons of the TEMPOL molecule was measured in the case of bimetallic NPs composed of Au and a *3d* metal. We observed that the composition of the Au-Co and Au-Fe bimetallic NPs does not influence the relative decrease in the number of spins, and that, in the case of the Au-Ni and Au-Cu NPs, the highest decrease of the ESR signal corresponds to those NPs synthesized from a starting solution with 1 mM initial concentration. A weak interaction was found in the case of the divalent *sp* metals and *4d* metals, especially in the case of the Au-Pd NPs, where R_S was the smallest. In the case of trivalent *sp* metals, we could not obtain results due to the small quantity of powder NPs (the Au-Ga and Au-In NPs are highly water-soluble nanoparticles). The results suggest that the decreasing of the ESR signal of TEMPOL due to the interaction with the gold bimetallic NPs might be because of the electron exchange between the free radical and the conduction band of the bimetallic NPs. Except for Au-Pd NPs, all the other gold bimetallic NPs show an SPR absorption band; that is the excitation by the visible light of the free electrons within the conduction band.

23.3 Synthesis of Mesoporous Silica

SPP plays a major role in template removal after the synthesis of the mesoporous silica particles. The ternary surfactant system containing Pluronic P123 copolymer (EO20PO69EO20), sodium dodecylbenzene sulfonate (SDBS), and 1,1,2,2,3,3,4,4,4-nonafluoro-1-butane sulfonate (NFBS) was successfully used to prepare spherical mesoporous silica particles via a simple sol–gel method under various acid concentrations using 1, 2, and 3 M hydrochloric acid (HCl) solutions, hereafter denoted PFS1 M, PFS2 M, and PFS3 M (PFSaM), respectively, where PFS is the mesoporous silica synthesized using the surfactant system of the P123 copolymer, fluorinated surfactant (NFBS), and sodium dodecylbenzene sulfonate (SDBS), and a M is the acid concentration of the synthesized solution. For instance 1 M means that 1 M HCl solution was used. Subsequently, SPP, instead of conventional processes, was employed under controlled plasma conditions to remove the surfactant template. The pH of the SPP solutions in the range of 3–11 was evaluated as a function of the acid concentration of the solutions during synthesis. The overall reaction of mesoporous silica in this present study is shown in Fig. 23.5.

TEM images of PFS3 M, PFS2 M, and PFS1 M are revealed in Fig. 23.6, which directly provide evidence of the mesoporous structure; the images are in good

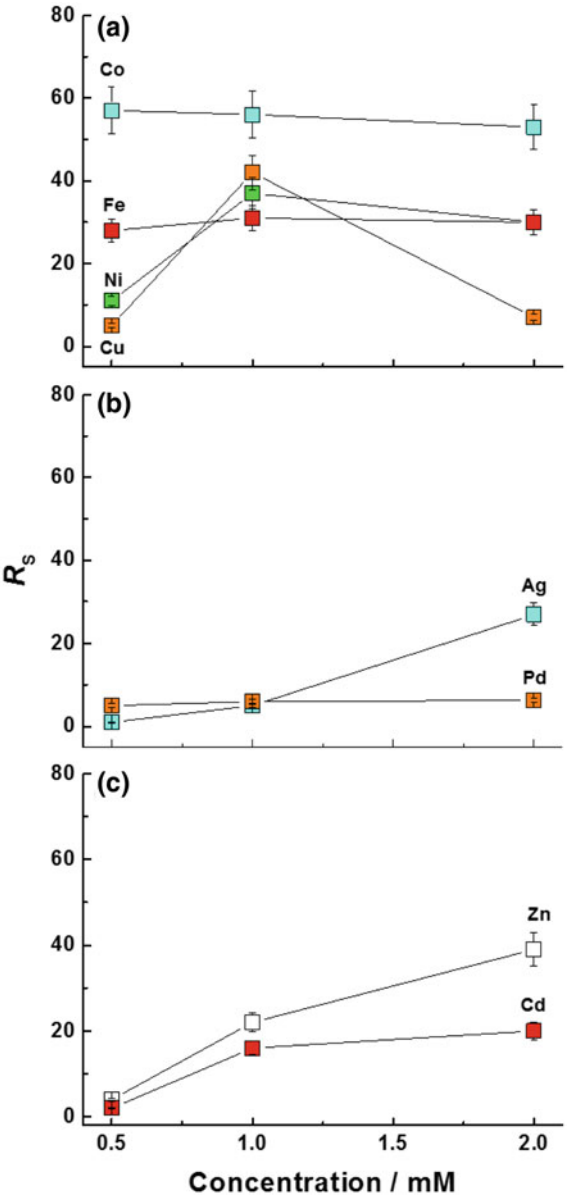

Fig. 23.4 Dependence of the relative decrease in the number of spins of TEMPOL in benzene solution with 1 mM concentration, due to the interaction with the gold bimetallic NPs with 10 mg mL^{-1} concentration, in the case of gold alloying with **a** *3d*, **b** *4d*, and **c** divalent *sp*. Reprinted from Ref. [14], Copyright 2013, with permission from Elsevier

agreement with the XRD results. Disordered wormlike mesoporous structures are observed in the cases of PFS3 M and PFS2 M (Figs. 23.6a, b) and ordered 2D hexagonal structures (Fig. 23.6c) are observed in PFS1 M. It is, therefore, valid to conclude that the characteristics of mesoporous structures are dependent on the

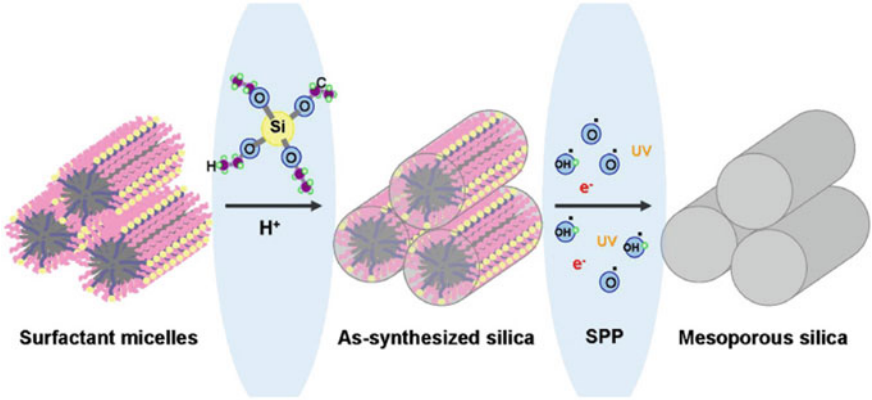

Fig. 23.5 Schematic representation of overall reaction in mesoporous silica synthesis using ternary surfactant system as a template, TEOS as silica precursor, and calcination by SPP [7]. Copyright (2010) The Japan Society of Applied Physics

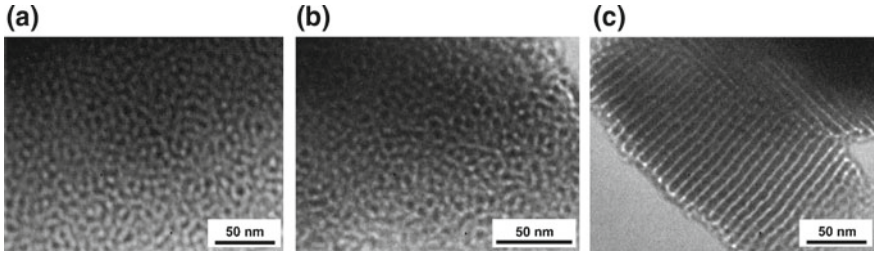

Fig. 23.6 TEM images of mesoporous silica after SPP for 15 min in pH 3 solution: **a** PFS3 M, **b** PFS2 M, and **c** PFS1 M [7]. Copyright (2010) The Japan Society of Applied Physics

acidity of the synthesized solution, which is strongly affected by structural micelle formation.

Spherical mesoporous silica materials have been successfully synthesized via the sol–gel method using a ternary surfactant system as the organic template. The acidity of the synthesized solutions significantly influenced the mesoporous structure of mesoporous silica, as have been determined by the XRD and TEM analysis, which shows the transformation of the structure from a disordered wormlike structure to an ordered 2D hexagonal structure. Almost, all the surfactant template was discarded by SPP in acid and base solutions, as confirmed by FTIR and thermal analyses. Compared with thermal calcination, the discharge in the acid solution had no effect on the mesoporous size. Moreover, SPP in acid solution resulted in the highest BET surface area and mean pore diameter for mesoporous silica. Thus, the SPP for 15 min in acid solution (pH 3) was highly efficient for template removal in mesoporous silica [7].

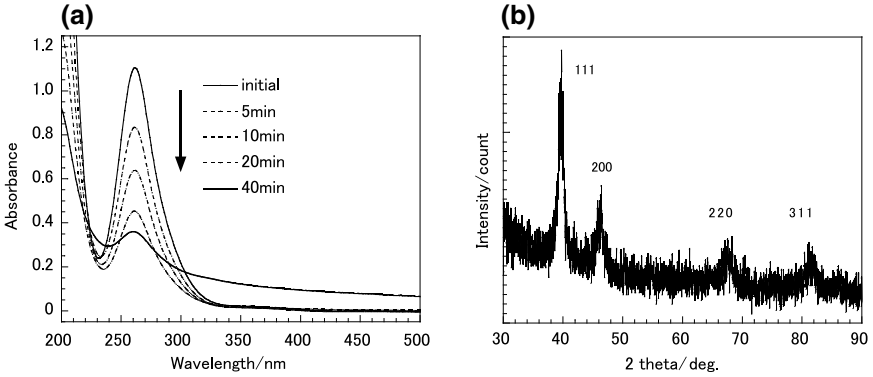

Fig. 23.7 **a** The changes in the UV-vis spectra of the aqueous solution with 1.37 mM Chloroplatinic acid as a function of SPP time; **b** XRD pattern of NPs synthesized in 40 min [17]. Reproduced by permission of the Surface Finishing Society of Japan

23.4 SPP Synthesis of Platinum Nanoparticles in Mesoporous Silica and Characterization of Their Catalytic Properties in the Selective Oxidation Reaction of CO

Preferential oxidation (PROX) of CO is an important practical process to purify H_2 for use in polymer electrolyte fuel cells. Although many supported noble metal catalysts have been reported so far, their catalytic performances remain insufficient for operation at low temperature. It was reported that Pt nanoparticles in mesoporous silica give unprecedented activity, selectivity, and durability in the PROX reaction below 353 K [16].

The SPP have been applied to synthesize Pt NPs during 40 min (Fig. 23.7) and Pt NPs incorporated in mesoporous silica (Fig. 23.8) [17]. The PROX reaction depends on of the size and location of the Pt NPs inside the mesoporous silica. We determined that a high conversion rate, at lower temperature was obtained in the case of Pt NPs inside the mesoporous silica (Fig. 23.9). A successful reaction conversion was obtained starting from 140 °C.

23.5 Carbon Catalyst for Fuel Cells

Fuel cells have been paid attention because they can generate efficiently electric energy from hydrogen and do not emit pollution to the environment. Polymer electrolyte fuel cells (PEFC), which consists of proton-conducting polymer electrolytes, is widely used for fuel cell vehicle. In PEFC, the operating temperature is low, so the ORR at the cathode of the fuel cells influences the performance of

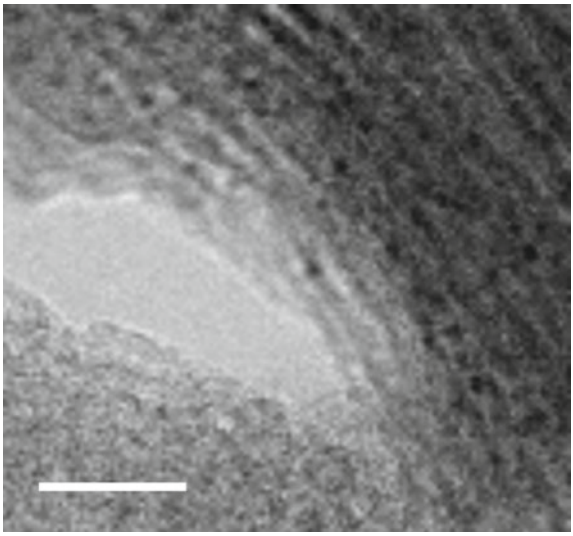

Fig. 23.8 HRTEM image of Pt NPs incorporated in mesoporous silica (Pt/FSM-16 catalyst). The bar scale represents 50 nm [17]. Reproduced by permission of the Surface Finishing Society of Japan

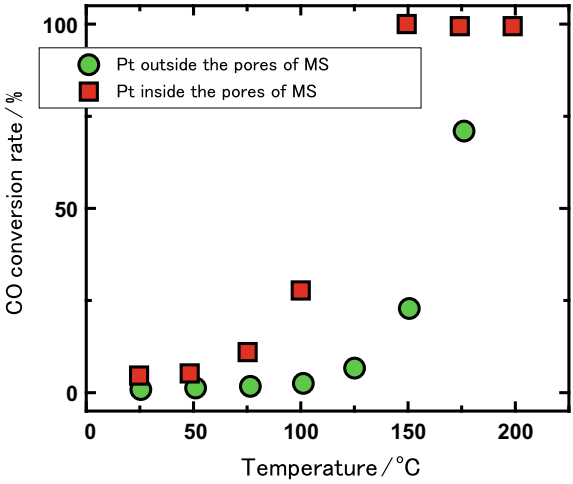

Fig. 23.9 CO conversion rate in dependence with temperature when Pt NPs were outside the pores of MS and inside of the pores of MS [17]. Reproduced by permission of the Surface Finishing Society of Japan

PEFC. It is well known that the rate of ORR is low, so far, Pt and its alloys are used as the most active catalysts for ORR and resistant materials in acidic condition. However, Pt is limited in nature and expensive, which is a hurdle for the commercialization of PEFC. In recent years, enormous research has been done on developing an alternative non-precious metal ORR catalyst to fully replace the Pt/C catalysts. However, the materials are limited in acidic condition. Among non-precious metal catalysts, a family of transition metal–N_4 macrocyclic complexes or composites has been considered to be potential candidates for

next-generation ORR catalysts due to their comparable ORR activity and lower cost compared with Pt/C catalysts.

Carbon materials have been synthesized by SPP. Figure 23.10a–d shows the process of carbon materials synthesis from the benzene solution. Plasma is generated between two electrodes inserted into the solution by applying a bipolar pulse voltage. Black carbons are produced from benzene decomposition in the solution surrounding plasma. Figure 23.10e–g shows the morphology images of the synthesized carbon materials observed by SEM and TEM. It can be seen that the spherical carbons with a diameter of ~20 nm were obtained [9]. In the solution plasma, the benzene is decomposed mainly to active species such as C_2 and CH radicals. These radicals react with each other and form carbon. It is believed that carbon compounds are mostly produced by the reaction of benzene rings at the gas–liquid interface. So, the properties of the synthesized carbon materials depend on the structure of the precursors.

When N-methyl pyrrolidone (NMP) is used as a precursor, the sheet-like carbon materials are synthesized as shown in Fig. 23.11a. From the Raman spectroscopy, 2D peak (2720 cm^{-1}) appears, which indicates that the crystallinity of the domain structure is developed. Regarding the conductivity, the sheet-like carbon obtained from NMP has a conductivity comparable to other conductive carbons [18]. Furthermore, the use of the nitrogen-containing compound introduces nitrogen into the carbon material, and the catalytic performance for ORR is better than the material without nitrogen.

When carbon materials are synthesized in an organic solvent including phthalocyanines, phthalocyanines are embedded into the synthesized carbon materials. The cyclic voltammetry curves of the carbon materials with Fe-phthalocyanine

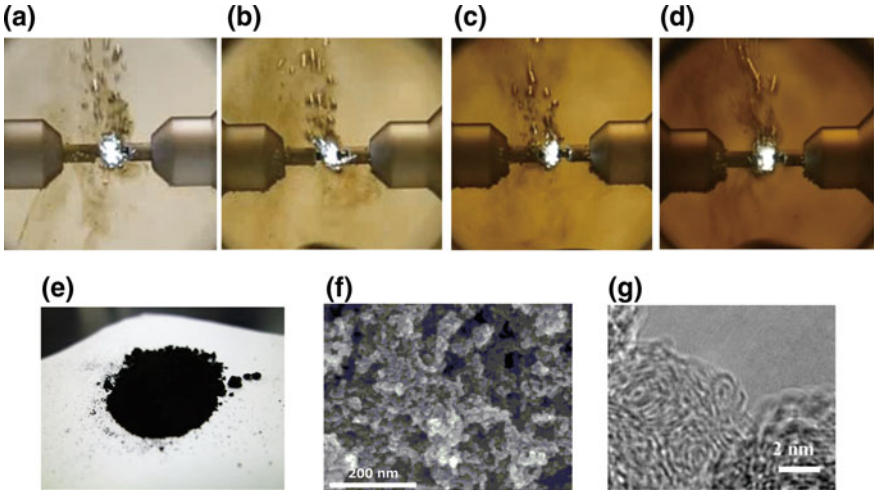

Fig. 23.10 **a–d** Images of carbon synthesis during discharge, **e** synthesized carbon materials, **f** SEM image, **g** TEM image

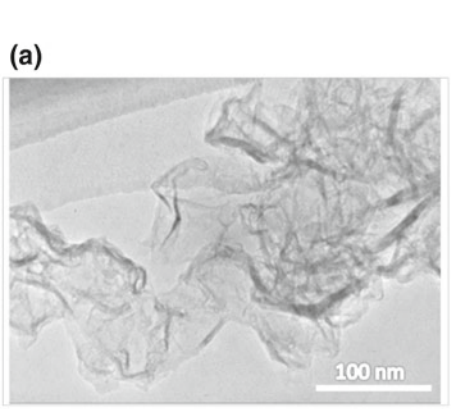

(c)

Carbon materials	Resistivity Ω·cm
Nitrogen-doped CNFs	0.065
Nitrogen-doped CNTs	~0.04
SP-synthesized Carbon	0.065

Fig. 23.11 **a** Morphology image of carbon materials synthesized from N-methylpyrrolidone, **b** Raman spectroscopy, **c** Resistivity [19]. Reproduced by permission of the PCCP Owner Societies

(Fe-Pht) complex are shown in Fig. 23.12a [19]. The oxygen reduction reaction (ORR) was evaluated in acidic condition. In the case of N_2 gas bubbling, the ORR is not observed. In the case of bubbling with O_2 gas, the ORR appears at a potential of 0.5 V (vs. Ag/AgCl). To compare the catalytic performance of the carbon materials with and without Fe-Pht, the linear sweep voltammetry curve was measured and as shown in Fig. 23.12b. The ORR potential of carbons with Fe-Pht is higher than that

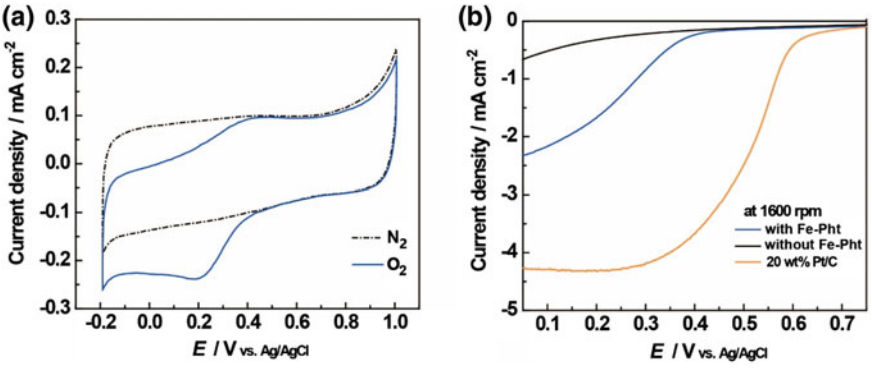

Fig. 23.12 **a** Cyclic voltammetry of the carbon materials with Fe-Pht in 0.5 M H_2SO_4 with N_2 and O_2 bubbling. **b** Linear sweep voltammetry of carbon materials with Fe-Pht and without Fe-Pht, as well as 20 wt% Pt/C in 0.5 M H_2SO_4 at 1600 rpm [19]. Reproduced by permission of the PCCP Owner Societies

without Fe-Pht, which means that the catalytic performance was improved by adding Fe-Pht. These results show that Fe-Pht was incorporated into the carbon material without decomposition of the molecular structure of Fe-Pht by SPP.

23.6 Conclusions

In all the experiments, SPP shows to be a useful and straightforward method for materials synthesis with various applications in nanotechnology. The SPP method proves particular merits in the metal NP synthesis since this non-equilibrium plasma can provide an extremely rapid reduction of a metal ion to the neutral form without using a reducing agent, and offers the possibility to control the size by controlling the surrounding chemistry. Furthermore, the operation at room temperature and normal pressure makes SPP a cheap method. We also demonstrate another merit of the SPP method for the fabrication of bimetallic NPs using a combination of the reduction reaction of the metal (M) ion to the neutral state, while simultaneously eroding the electrodes during the discharge, which generates the second metal in the structure of the bimetallic NPs. This combination of processes makes SPP a more useful method since no reducing agent or gold precursor is required in the reaction mixture, thus offering an ecologically friendly procedure for nanostructure synthesis.

The synthesis of carbon-based catalyst for applications in fuel cell and battery confirms that the SPP method can be used in the production of new materials through the chemical reactions particularly at the interface between liquid and plasma.

Acknowledgements The authors would like to express their gratitude to the researchers and professors, Prof. Nobuyuki Zettsu from Shinshu Univ., Dr. Pootawang, Panuphong from Kamnoetvidya Science Academy, and Dr. Koangyong Hyun from Shinshu Univ. The research was supported in part by *Inter-University Collaboration of 6 Research Institutes* of Ministry of Education, Culture, Sports, Science and Technology, Japan.

References

1. J. Wilsing, On the interpretation of the typical spectrum of new stars. Astrophys. J. **10**, 113–125 (1899)
2. N. Sir Lockyer, On the spark discharge from metallic poles in water. Astrophys. J. **15**, 190–198 (1902)
3. N. Saito, J. Hieda, O. Takai, Synthesis process of gold nanoparticles in solution plasma. Thin Solid Films **518**, 912–917 (2009)
4. S.P. Cho, M.A. Bratescu, N. Saito, O. Takai, Microstructural characterization of gold nanoparticles synthesized by solution plasma processing. Nanotechnology **22**, 455701–455707 (2011)

5. M.A. Bratescu, S.P. Cho, O. Takai, N. Saito, Size-controlled gold nanoparticles synthesized in solution plasma. J. Phys. Chem. C **115**, 24569–24576 (2011)
6. M.A. Bratescu, N. Saito, Charge doping of large-area graphene by gold alloy nanoparticles. J. Phys. Chem. C **117**, 26804 (2013)
7. P. Pootawang, N. Saito, O. Takai, Solution plasma process for template removal in mesoporous silica synthesis. Jpn. J. Appl. Phys. **49**, 126202 (2010)
8. L. Dai et al., Nitrogen-doped carbon nanotube arrays with high electrocatalytic activity for oxygen reduction. Science **323**, 760–764 (2009)
9. J. Kang, O.L. Li, N. Saito, Synthesis of structure-controlled carbon nano spheres by solution plasma process. Carbon **60**, 292–298 (2013)
10. F. Llewellyn-Jones, Electrode evaporation and the electric spark. Nature **157**, 298–299 (1946)
11. F. Llewellyn-Jones, The mechanism of electrode erosion in electrical discharges platinum. Metals Rev. **7**, 58–65 (1963)
12. M.T. Reetz, W. Helbig, S.A. Quaiser, Electrochemical preparation of nanostructural bimetallic clusters. Chem. Mater. **7**, 2227–2228 (1995)
13. C. Richmonds, R.M. Sankaran, Plasma-liquid electrochemistry: rapid synthesis of colloidal metal nanoparticles by microplasma reduction of aqueous cations. Appl. Phys. Lett. **93**, 131501–131503 (2008)
14. M.A. Bratescu, N. Saito, O. Takai, One-step synthesis of gold bimetallic nanoparticles with various metal-compositions. J. Alloys Compd. **562**, 74–83 (2013)
15. Z. Zhang, A. Breg, H. Levanon, R.W. Fessenden, D. Meisel, On the interactions of free radicals with gold nanoparticles. J. Am. Chem. Soc. **125**, 7959–7963 (2003)
16. A. Fukuoka, J. Kimura, T. Oshio, Y. Sakamoto, M. Ichikawa, Preferential oxidation of carbon monoxide catalyzed by platinum nanoparticles in mesoporous silica. J. Am. Chem. Soc. **129** (33), 10120–10125 (2007)
17. Y. Aoki, N. Zettsu, T. Yamamoto, H. Nanbu, N. Saito, Solution plasma synthesis of platinum nanoparticles in mesoporous silica and characterization of their catalytic property in selective oxidation reaction of CO. J. Surf. Finish. Soc. Jpn. **66**, 70–72 (2015)
18. K. Hyun, T. Ueno, O.L. Lun, N. Saito, Synthesis of heteroatom-carbon nanosheets by solution plasma processing using N-methyl-2-pyrrolidone as precursor. RSC Adv. **6**(9), 6990–6996 (2016)
19. K. Hyun, T. Ueno, G. Panomsuwan, O.L. Li, N. Saito, Heterocarbon nanosheets incorporating iron phthalocyanine for oxygen reduction reaction in both alkaline and acidic media. Phys. Chem. Chem. Phys. **18**(16), 10856–10863 (2016)

Chapter 24
Metal Oxide Materials for Automotive Catalysts

Masakuni Ozawa

Abstract Nanostructured metals and metal oxides are combined to produce advanced automobile catalysts for exhaust pollutant control. Catalytic emissions control was introduced in the form of noble metal-based three catalysts for the removal of exhaust gas pollutants of hydrocarbons (HC), carbon monoxide, and nitrogen oxides (NOx). Alumina as wash coat components provides a high and stable surface area for dispersion of the precious metals. Cerium oxides (ceria, CeO_2) and ceria-zirconia (CeO_2–ZrO_2) as oxygen storage capacity components are typical non-metallic functional materials in the automotive catalysts. The catalysts component layer is some hundreds of micrometers thick and loaded on the substrate, usually made from cordierite ceramic and metallic alloys, which is called coat layer with alumina-based and precious metal and ceria-based ceramic composite. This section deals with developed metal oxide materials controlled with nanometer scale, their structures, and some current advances including the author's achievement.

Keywords Three-way catalyst (TWC) · Noble metals · Al_2O_3 · CeO_2 · ZrO_2 · Nanoparticle · Oxygen storage capacity

24.1 Catalysts and Metal Oxide Nanomaterials

Automotive catalysts for the exhaust depollution were first applied to US and Japan vehicles manufacture industry in 1975 [1–6]. They are the principal emission control tools and typical model as an application of environmental materials to devices, proving their usefulness on environmental improvement. The environmentally functional materials have made catalytic devices which contain practical nanomaterials, and the catalytic methods for exhaust gas treatment have established

M. Ozawa (✉)
Materials Division, Institute of Materials and Systems for Sustainability, Nagoya University, Nagoya 464-8603, Japan
e-mail: ozawa@imass.nagoya-u.ac.jp

Y. Setsuhara et al. (eds.), *Novel Structured Metallic and Inorganic Materials*, https://doi.org/10.1007/978-981-13-7611-5_24

now and most of the automobiles have equipped the catalysts for emission control. Thus, these environmental materials have both large industrial market and requirement of improvement for pollution control around citizen life. Figure 24.1 shows an example of a catalyst converter part which is usually both attached near engine exhaust manifold and underbody in a car.

When a driver first starts the automobile both the engine and the catalyst are cold, and it reaches a temperature high enough to initiate the catalytic reactions after the exhaust gradually warms. This is referred to as the light-off performance of catalyst and it depends on the nanomaterials combination of catalyst and its chemistry since all the transport reactions must be fast and complete. The three-way catalysts (TWCs) in gasoline engine are the most widely used and effective system for the exhaust gas pollutants including hydrocarbons (HC), carbon monoxide, and nitrogen oxides (NOx). The chemically pollutant-purifying reaction rates are enhanced through pore diffusion and/or bulk mass transfer controlling the overall conversion in honeycomb substrate with capillary pores, followed by coating catalytic wash coat layer (Fig. 24.2). The TWC is the fundamental, however, leading technology, consisting of precious nanometals (Pt, Rh, and Pd) dispersed on an alumina support

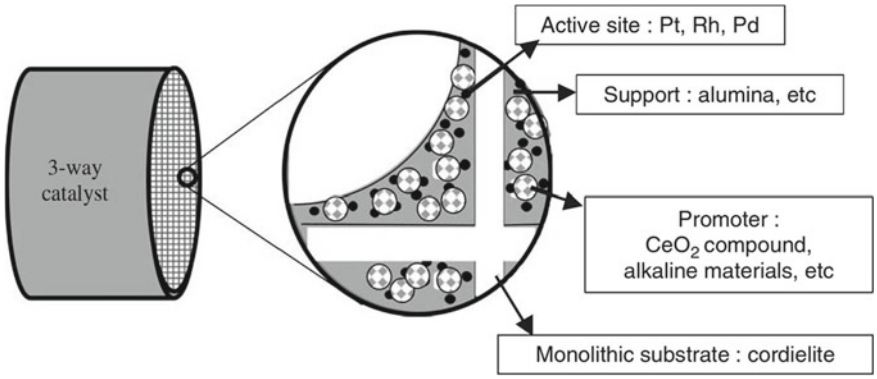

Fig. 24.1 Schematic catalytic monolith with carious composition-containing coat layer for exhaust treatment. Reproduced from [4] with permission from Elsevier Science

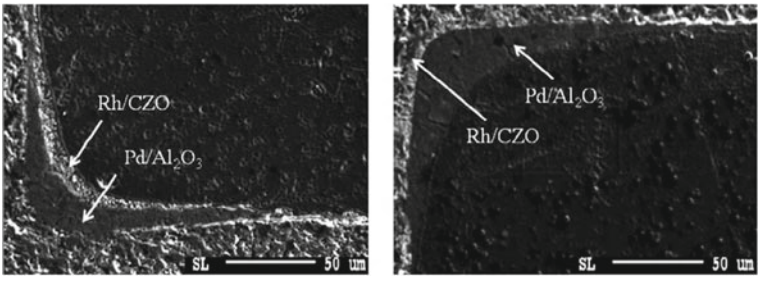

Fig. 24.2 Examples of composite coat layers of Pd–Rh–CeO_2–ZrO_2–Al_2O_3 catalysts for TWC performance. Reproduced from [5] with permission from Elsevier Science

coated on cordierite monolith, oxygen storage catalyst such as ceria or ceria-zirconia, and other functional promoters. Such inexpensive materials have been examined through more advanced technology, and their effective application has resulted in both better properties and lower cost level for advanced automotive catalyst converters including gasoline, diesel and hybrid engine systems.

Regarding materials design in the practical use of catalysts, essential factors is the control in the state of catalysts from the aspect of nanometer-scaled composite of several catalytic compositions. Also, fabrication of catalysts was required with nanometer and micron scale, for example, bimetallic combination between precious metals and their controlled interaction between ceria and alumina as the supporting phase in uniform wash coat layer on the substrate. This chapter touches on the development and scientific and technological effort about catalytic materials, especially metal oxides nanoparticulate compounds such as alumina and ceria-zirconia.

24.2 Alumina Support and Its Modification

Nanoparticle alumina (Al_2O_3) as wash coat components on honeycombs provides a dispersion of the precious metals due to its high and stable surface area even at high temperatures [6]. Since the temperature in the catalyst can rise to over 1000 °C in engine combustion, the thermal stabilization of catalysts is important. In general, the surface area of starting alumina support with ca. 100 $m^2\ g^{-1}$ decreases to below 30 $m^2\ g^{-1}$ after heat treatment over 1100 °C, because phase transition in metastable gamma alumina induces large sintering with the formation of alpha alumina. The performance of surface area stabilization is strongly influenced by the purity and morphology of alumina, as well as additive elements modification and their optimization in processing. Lanthanum (La) is actually the most industrial modifier to alumina supports, which are prepared by several methods, in automotive catalysts. The additive of La species greatly improves the thermal stability to inhibit the sintering and phase transformations of alumina [7–9], and the method of adding La is important to the practical fabrication of catalysts. Besides the direct fabrication of alumina support in industrial large scale, both surface and bulk modification using some precipitation agent can be possibly applied to prepare catalytic alumina. The content of a modifier should be selected if the surface area versus concentration is optimized for heat condition used. The relationship of surface area versus modifier content after heat treatment at 1200 °C for comparison of several high surface area alumina powders shows that any alumina has the optimum content with relatively low concentration if they are used at 1000–1200 °C. The other factor is the interaction between nanoparticles in agglomeration, as well as particles and water, which is the same as in oxides, such as silica with hydroxyl group on the surface. The surface coverage and/or bulk doping of lanthanum oxide as a final form affect the surface area of alumina and other stabilizing factors. Figure 24.3 shows an example of surface area stabilization in developed alumina with La, where the best performance appears in limited dopant contents depending starting alumina purities.

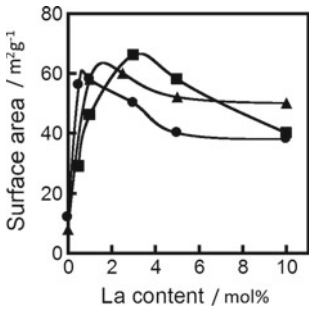

Fig. 24.3 Relationship of surface area versus La content for several alumina catalytic support (powder) after heat treatment at 1200 °C. Rreproduced from [9] with permission from Elsevier Science

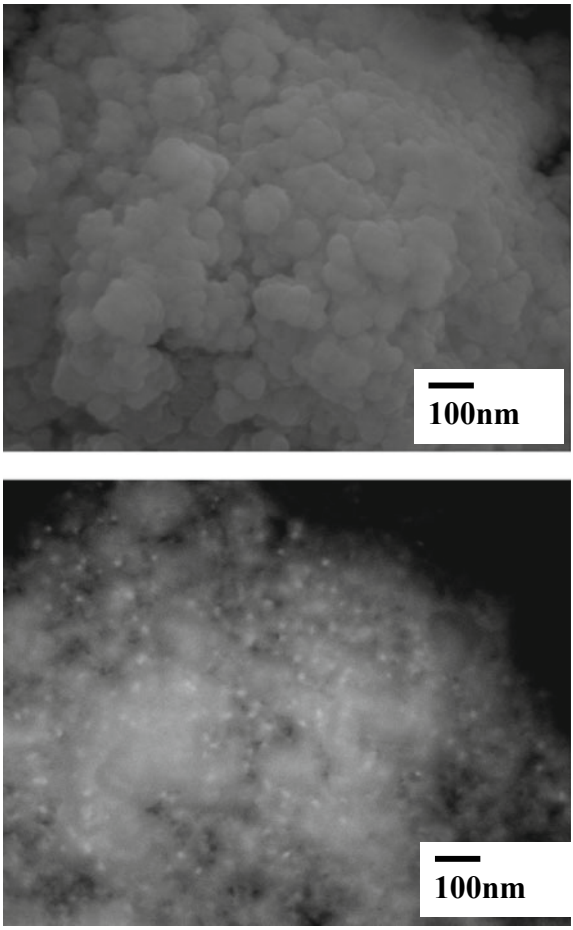

Fig. 24.4 Electron microscopic image of 5 mol% La-modified alumina support heated at 1200 °C: secondary (upper) and reflection (lower) electron microscopy image in the same area

The author has provided a new concept of the nanocomposite of complex oxide/alumina system [10]. Figure 24.4 shows an example of the TEM image, where a 10 nm-size $LaAlO_3$ (as a dark-contrast particle) has nucleated in alumina nanoparticulate aggregate matrix when overloaded La content exits. In the simple

impregnation, the La and nitrate species both remains on alumina surface during the drying process, so that an attractive force by the bridging La species should be active, leading the hard agglomerates of alumina. Such starting state of agglomeration should induce the difference about sintering, phase transformation and solid-state reactions in heat treatment. Although $LaAlO_3$ is believed as one of the stabilizing form on alumina with mono-unit layer on the surface [7], it is generally difficult to detect such crystallites in practical materials. In industrial-stabilized alumina products, La species is combined with metastable alumina in nanoscaled dispersion state.

Concerning morphology stabilization of alumina coat layer in practical catalytic converters, an aspect of ceramics is important to make a thermal stable wash coat layer. The sintering of catalyst layers was related to neck growth, grain growth and phase evolution in alumina support on the substrate. The so-called "sintering" of ceramics, in this case, has finally resulted in the fracture of wash coat layers as well as grain growth in catalysts. A larger shrinkage of porous alumina than that of the honeycomb substrate in the automotive catalyst is induced by high-temperature exhaust, leading to a local stress to form cracks. Figure 24.5 shows the scanning

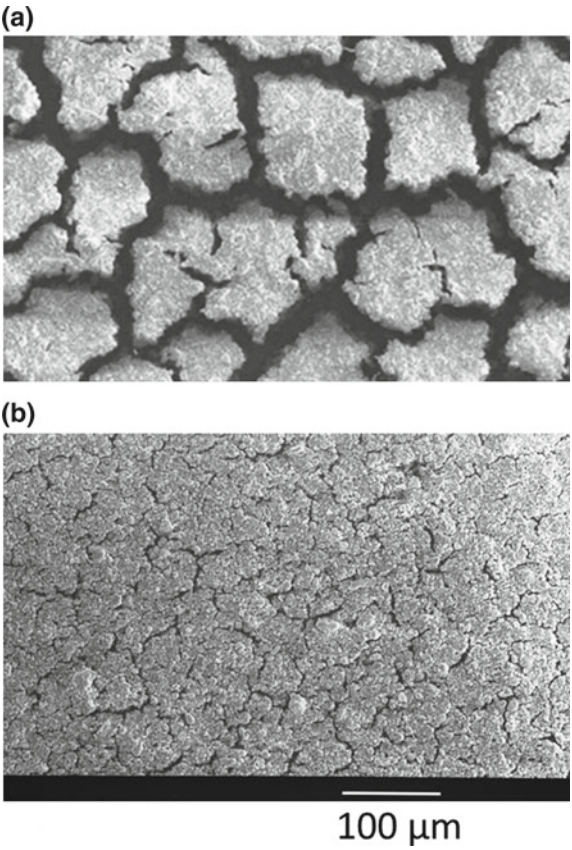

Fig. 24.5 Surface morphologies of alumina coat layer on FeCrAl alloy substrate, heated at 1100 °C for 3 h in air. **a** γ-Al_2O_3 and **b** La-stabilized γ-Al_2O_3. See Ref. [11] in details, reproduced from [11] with permission from Elsevier Science

electron microscopy (SEM) image of compared pure Al_2O_3 and La-stabilized Al_2O_3, which were coated on an Fe–Cr–Al foil (general metal substrate in TWC), followed by heating at 1100 °C for 3 h in air [11]. No critical fracture was found when alumina has been stabilized with La, although some fair cracks are observed. In practical fabrication processing, the rheology of alumina suspension must be controlled during the coating process of the porous, stable and homogeneous thick coat layer in the capillary pore of alloy or ceramic substrates. After then, the La-modified composite alumina will become stable support (as wash coat layer) on an automotive honeycomb bed even subjected to high heat environment. The strength of agglomerates in powders often prepared by a chemical route is controlled by the extent of particle–particle interaction.

24.3 Ceria-Zirconia for Oxygen Storage Capacity (OSC)

The TWCs has characteristic properties that the operation under a certain air/fuel ratio (A/F) of around 14.5 (stoichiometric point, $\lambda = 1$) results in highest performance about removal efficiencies [1–5]. The performance of TWC rapidly decreases as illustrated in Fig. 24.6 in both conditions out of $\lambda = 1$. In a series of reactions, CO, H_2, and HC are oxidized and NOx are reduced simultaneously into CO_2, H_2O, and N_2. At stoichiometric condition, the right balance of CO, H_2, and HC to reduce NOx and O_2 can be achieved. In general, A/F occasionally fluctuates in actual vehicle engine operation. For example, NOx emissions increase during acceleration in actual driving conditions, since the A/F fluctuates out of the stoichiometric point to lean (excess oxygen) condition.

Oxygen storage capacity (OSC) has been a key function in automotive catalysts for precisely controlling the variation of A/F in exhaust [1–5, 14]. The optimization of atmosphere in nanometer-sized space around catalyst particles leads better

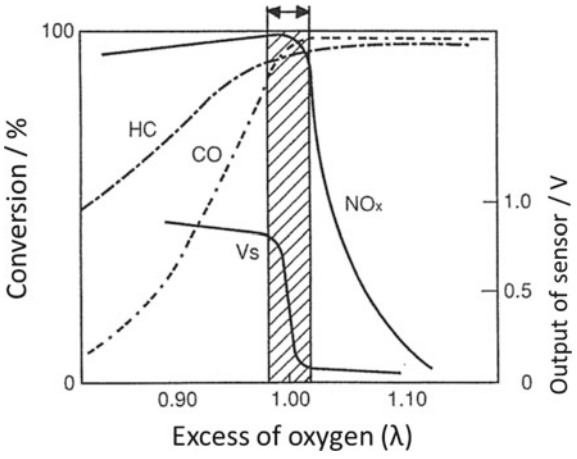

Fig. 24.6 Hydrocarbons (HC), CO, and NOx conversions versus excess oxygen condition in TWC. Oxygen sensor output is also illustrated

efficiencies to remove CO, HC, and NOx. Also, the oxidation performance may possibly be used for the design of the advanced catalyst for combustion, for example, cold starting condition. Now, ceria-zirconia system has been a standard composition of OSC in high-performance automotive catalyst including TWC and diesel exhaust systems. The composite (solid solution) subcatalyst is widely applied to practical TWCs that must have excellent catalytic OSC performance, high durability, and thermal stability. Such ceria-zirconia (CeO_2–ZrO_2) catalytic components for TWCs was invented by Ozawa et al. in 1987, and during the 1990s, the OSC material has been one of the main targets as improvement method of a series of automotive catalysts [12–16], and then this material has recently been applied to the research and development of various catalysis including other air pollution catalysts, hydrogen production, reforming, and so on. The fundamental dynamic performance of Pt catalyst was given by comparing the model examples of TWCs; Pt/Al_2O_3 and Pt/CeO_2–ZrO_2/Al_2O_3 [17]. The light-off TWC activity of catalysts was tested during temperature-arising condition by using the simulated mixture of gases (CO, NO, C_3H_6, CO_2, H_2, H_2O, O_2, N_2 balance) with the variation of O_2/CO ratio. These observations (Figs. 24.7 and 24.8) indicated that the activities of Pt catalyst under the condition corresponding to A/F modulation (CO–O_2) were enhanced by CeO_2–ZrO_2. The experiment of the model catalysts directly shows the effect of the mixed oxides themselves on the activities under A/F modulation. The behavior of oxygen evolution and/or uptake originates from the nonstoichiometry and oxygen diffusion at the surface and in lattice in $Ce_{1-x}Zr_xO_2$. The OSC promoter should satisfy both factors; the wide-range operation for redox between Ce^{3+} and Ce^{4+} in the reducing and oxidizing atmosphere, and the essentially high reaction rate for oxygen evolution and storage over the modified catalysts. Catalytic reaction for OSC is essentially the phenomenon between a reactant such as gaseous hydrogen and CO and oxygen at a surface active site of CeO_2 based materials. The enhanced oxygen diffusion is an important factor to improve and find OSC promoters for TWCs.

There appears the cubic solid solution of $Ce_{1-x}Zr_xO_2$ in Ce-rich region, while tetragonal and monoclinic solid solutions form in the tight regions of Zr-rich side. In the central region, there are several structures such as $Ce_2Zr_2O_7$ as well as another metastable mixed oxide [15]. However, the compounds or mixed oxides in CeO_2–ZrO_2 are often obtained as their metastable states, which are also useful for the catalytic application. Also, a strong requirement for OSC materials is their thermal stability and durability for hot exhaust at around or above 1000 °C. Usual CeO_2 powder easily sinters at elevated temperatures, although it is one of the good refractory oxides with high melting point. The addition of zirconium, especially the formation of CeO_2–ZrO_2 solid solution is effective to the inhibition of the sintering of ceria. The simple experiments indicated that the Zr modification of CeO_2 powder, followed by solid-state reactions, had the effects to the improvement of the thermal stability of CeO_2 promoter [13]. The chemical synthesis processes, as well as an impregnation are expected to lead to more excellent inhibition to the thermal deactivation (sintering) of CeO_2. The system of CeO_2–ZrO_2/Al_2O_3 (ACZ) composite powder brings a larger effect on surface area stabilization compared with

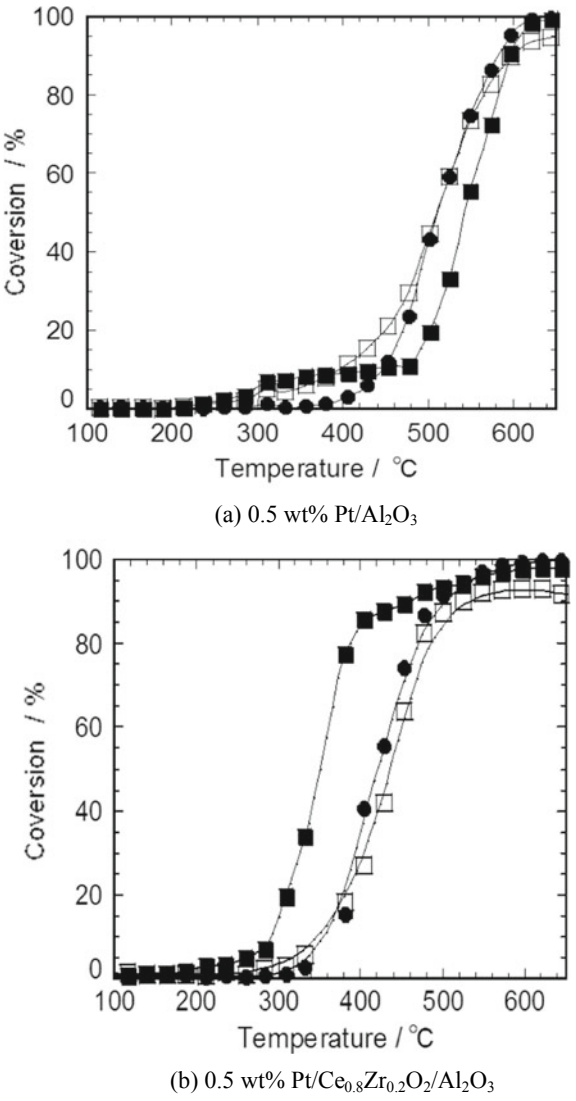

(a) 0.5 wt% Pt/Al_2O_3

(b) 0.5 wt% $Pt/Ce_{0.8}Zr_{0.2}O_2/Al_2O_3$

Fig. 24.7 Light-off three-way catalytic performance of 0.5 wt% Pt/Al_2O_3 (**a**), and 0.5 wt% $Pt/_{Ce_{0.8}}Zr_{0.2}O_2/Al_2O_3$ (**b**) after aging test at 1000 C. Symbols: ■: CO, ●: C_3H_6, □: NO. Reproduced from [16] with permission from Elsevier Science

ordinary CeO_2–ZrO_2 subcatalyst. Since the influence of stabilized nanoparticulate alumina is the same as the figure effect, the interaction between CeO_2, ZrO_2 and Al_2O_3 is found to has specially induced inhibition behavior on sintering (Fig. 24.9). There is often the trade-off relationship between an atomically structured crystal and practical nanoparticulate heterogeneous catalyst with high surface area.

As a matter of fact, the state of precious metals are very important to design overall three-way removal performance as well as OSC. Thus, the interaction of precious metals with CeO_2–ZrO_2 subcatalysts and Al_2O_3 support should be

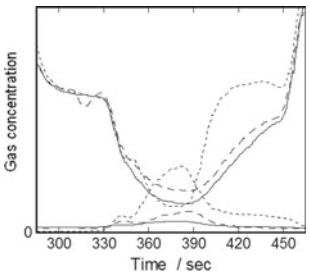

Fig. 24.8 Rich-lean transient conversion behavior of CO and NOx concentrations at 600 °C over 0.5 wt% Pt/Al_2O_3 (·····), 0.5 wt% $Pt/CeO_2/Al_2O_3$ (- - - -), and 0.5 wt% $Pt/Ce_{0.8}Zr_{0.2}O_2/Al_2O_3$ (–). Full scales are 400 ppm for NO and 800 ppm for CO. Reproduced from [16] with permission from Elsevier Science

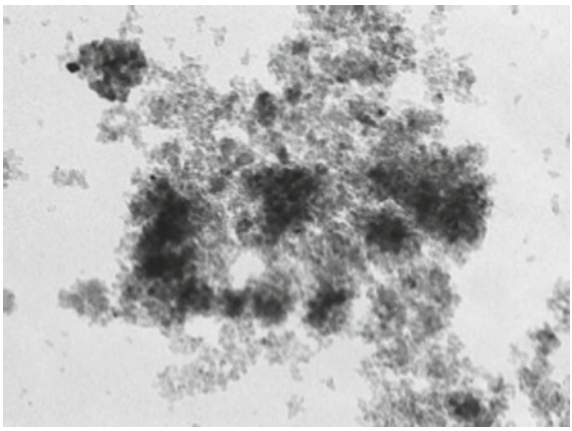

Fig. 24.9 Transmission electron microscopy images of $Al_2O_3/CeO_2–ZrO_2$ (ACZ) OSC subcatalyst

examined more with respects to SMSI (strong metal support interaction) in oxidizing and reducing atmosphere [17–21]. Recent technologies provide a strong method to examine the interaction by using X-ray and electrons, for example XAFS and environmental electron microscopy. Figure 24.10 shows a transmission electron microscopy (TEM) image observed in order to reveal the morphology and state of palladium species in $Pd/CeO_2–ZrO_2$ catalysts [19]. In general, the XRD peaks assigned as Pd or PdO were not identified due to the strong diffraction of support, and TEM image suggests an amorphous state of Pd or PdO with two or three atomic layers on $CeO_2–ZrO_2$. Thus, it is confirmed that the palladium species were highly dispersed on OSC support, and the strong interaction between palladium and $CeO_2–ZrO_2$ seems to inhibit the particle growth of palladium.

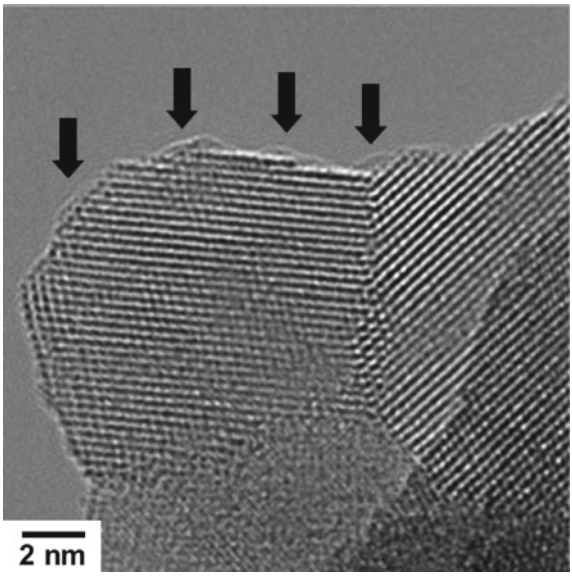

Fig. 24.10 Transmission electron microscopy images of 1 wt% Pd/CeO_2–ZrO_2 catalyst. Allows indicate PdOx nanophase. Reproduced from [15] with permission from Elsevier Science

24.4 Summary

Catalytic nanomaterials are considered to be important inorganic such as catalytic aluminas, ceria, and zirconia or ceramic products. They are very much in demand, because they are widely used as components in environmental pollution control and automotive exhaust treatment. Concerning surface area and morphology stabilization of alumina coat layer, an aspect of nanocomposite is important to make a thermal stable and smooth wash coat. CeO_2–ZrO_2 and modified CeO_2 promoters like ACZ have been applied in practice so far, and there are extensive researches and development of oxides themselves as catalytic materials. Research using more advanced fabrication techniques should be enhanced toward nanoparticles which are well dispersed and with high surface area as the original single and/or mixed oxides. An advanced approach to such catalytic nanomaterials is believed to play a more important role toward future development of novel ecosystem. Of course, the detailed studies of catalytic reactions and mechanism of catalysis regarding with chemistry will be strongly required, and the author suggests that the materials research and development to find novel environmental catalyst is promising to research and industrial field for various depollution requirements.

References

1. M. Shelef, Catal. Rev. Sci. Eng. **11**, 1 (1975)
2. P. Nortier, M. Soustelle, *Catalysis and Automotive Pollution Control*, ed. by Crucq, A. Frennet (Elsevier Science Publisher B.V., Amsterdam, 1987) pp. 275–300
3. H.S. Gandhi, G.W. Graham, R.W. McCabe, J. Catal. **216**, 433 (2003)
4. S. Matsumoto, H. Shinjoh, Adv. Chem. Eng. **33**, 1 (2008)
5. S. Kang, Seok, J. Han, I.-S. Nam, B. Cho, C. Kim, S. Oh, Chem. Engin. J. **241**, 273 (2014)
6. N. Miyoshi, S. Matsumoto, M. Ozawa, M. Kimura, *SAE Paper Series 89190* (1989), p. 1
7. M. Ozawa, M. Kimura, A. Isogai, J. Less-Common Met. **162**, 297 (1990)
8. M. Ozawa, Y. Nishio, J. Alloy Compds. **374**, 397 (2004)
9. M. Ozawa, J. Alloy Compds. **408–412**, 1090 (2006)
10. M. Ozawa, Y. Nishio, Appl. Surf. Sci. **380**, 288 (2016)
11. M. Ozawa, K. Araki, Surf. Coat. Technol. **271**, 80–86 (2015)
12. M. Ozawa, M. Kimura, A. Isogai, J. Alloy Compds. **193**, 73 (1993)
13. M. Ozawa, J. Alloy Compds. **257–277**, 886 (1998)
14. M. Ozawa, K. Matuda, S. Suzuki, J. Alloy Compds. **303–304**, 56 (2000)
15. M. Sugiura, M. Ozawa, A. Suda, T. Suzuki, T. Kanazawa, Bull. Chem. Soc. Jpn. **78**, 752 (2005)
16. M. Ozawa, T. Okouchi, M. Haneda, Catal. Today B **242**, 329–337 (2015)
17. M. Ozawa, M. Takahashi-Morita, K. Kobayashia, M. Haneda, Catal. Today **281**, 482 (2017)
18. M. Ozawa, C.-K. Loong, Catal. Today **50**, 329 (1999)
19. N. Kamiuchi, M. Haneda, M. Ozawa, Catal. Today A **241**, 100 (2015)
20. M. Haneda, T. Kaneko, M. Ozawa, Catal. Sci. Technol. **5**, 1792 (2015)
21. M. Ozawa, S. Kato, K. Kobayashi, T. Yogo, S. Yamaura, Jpn. J. Appl. Phy. **55**, 01AG05 (2016)

Part V
Novel Structured Materials for Bio-Medical Applications

Chapter 25
Current and Future Hard Materials for Biomedical Field

Takao Hanawa

Abstract Many materials are used in the field of medicine and dentistry. In this section, current metallic, ceramic, and polymer materials in medicine and problems of them are explained and future materials to solve the problems are prospected. A hard biomaterial is defined first against soft biomaterial and the necessity of biosis–abiosis intelligent interface between hard materials and living tissue is demonstrated. Tissue compatibility of titanium and surface treatment for hard tissue compatibility including its current problems, basis of materials research sometimes left behind, and hard materials for regenerative medicine, are discussed. In addition, medical use of metals, ceramics, and polymers are finally explained.

Keywords Hard materials · Metals · Ceramics · Polymers · Biomaterials · Surface treatment

25.1 Hard Biomaterials

Biomaterials consist of metals, ceramics, and polymers, as well as biomolecules such as proteins, lipids, nucleic acids, etc. Near recently, some cells and tissues are also employed as biomaterial. Constituents of the human body are basically polymers such as biomolecules, cells, and tissues, therefore, polymers designed based on these structures usually show biofunctions. In fact, major research techniques of polymers in biomedical filed are proceeded as bio-mimic design and synthesis of materials and the evaluation of them with cell culture and animal implantation. Also in ceramics, bioactive ceramics such as hydroxyapatite and calcium phosphate are investigated with the same techniques. On the other hand, metallic materials do not exist in the human body, while metal elements exist there.

T. Hanawa (✉)
Institute of Biomaterials and Bioengineering, Tokyo Medical and Dental University, Tokyo, Japan
e-mail: hanawa.met@tmd.ac.jp

Y. Setsuhara et al. (eds.), *Novel Structured Metallic and Inorganic Materials*, https://doi.org/10.1007/978-981-13-7611-5_25

Therefore, nobody knows how to make biofunctional metals and alloys because there is no model of them in the nature.

In the field of biopolymers, researches on so-called "soft materials" such as carrier of drug delivery system (DDS) gel and polymers similar to cell membrane are active. The interface between the soft materials and living tissues is called "soft interface." Soft materials function basically in aqueous solutions. On the contrary, a term "hard materials" represents metals, crystalline ceramics, glasses, and solid polymers, as shown in Fig, 25.1. Here, calcium phosphate ceramics dissolved and changed to bone in the human body may be categorized intermediate between soft and hard materials.

Major required property for hard materials is unchanged dimension in solid state: (1) non-deformation, (2) non-fracture, and (3) maintaining solid-state long term. In other words, high strength, fracture toughness, fatigue strength, and corrosion resistance are required. When hard materials are used as biomaterials, namely in hard biomaterials, the solid surface contacts living tissues and its function appears in the solid state. The function contains not only interfacial and chemical functions but also mechanical functions. Biosis–abiosis interface between living tissue and solid surface is usually clear, prevents mass transfer, and works as a barrier to conduct biofunctions (Fig. 25.2a). Therefore, tremendous studies are conducted to convert this clear interface to an intelligent interface: The intelligent interface is unclear, graded, mass transferable, and conducting biofunction (Fig. 25.2b). Hence, the additional following properties are required for hard biomaterials: (4) biofunction and tissue compatibility such as bone formation and bonding, prevention of bone assimilation, soft tissue bonding, prevention of thrombus, and prevention of biofilm formation, (5) significant stiffness to prevent loading to tissue during healing and the same deformation as living tissue after healing, and (6) no damage to living tissue with friction wear. The properties (4) are chemical and possibly performed with surface treatment and modification; the properties (5) and (6) are mechanical and possibly performed with material development: Alloy design and manufacturing process in metals, composition design, synthesis and sintering in ceramics, and molecular design and synthesis in polymers.

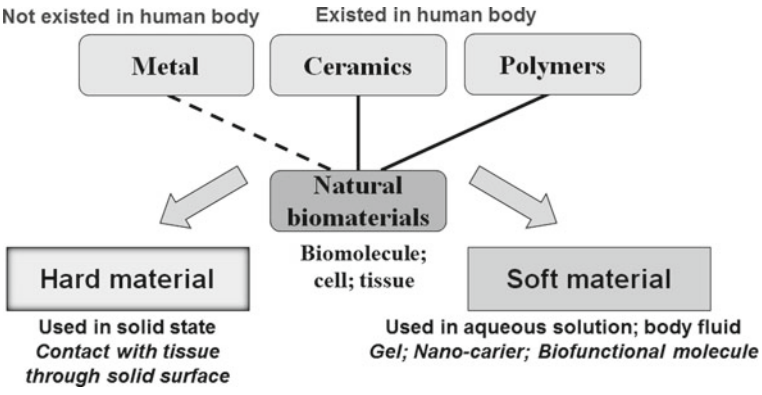

Fig. 25.1 Concept of hard biomaterials and soft biomaterials

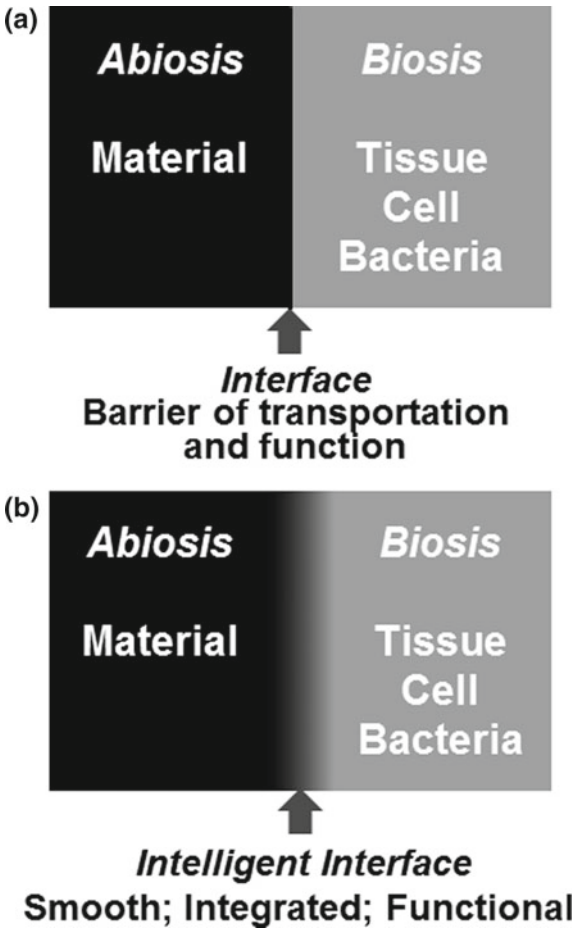

Fig. 25.2 Clear interface against cell, bacterial, and tissue: the interface works as a barrier for the transportation of molecules and conduction of biofunction (**a**). Unclear and graded interface at which smooth transportation of molecules occurs, both material and tissue are integrated together, and biofunctions are conducted (**b**)

25.2 Metals

Metallic materials are generally multi-crystal body consisting of metal bonds. For example, metal oxide, metal salt, metal complex, etc., contains metal elements, however, these are compounds consisting of ionic bond or covalent bond; these properties are completely different from those of metals consisting of the metal bond. Therefore, in the field of materials engineering, ceramics and metals are clearly distinguished, in spite of these are categorized in inorganic compounds together. Each material has its own advantages and disadvantages and the application is determined according to its property.

Metals are utilized for dental restoration and bone fixation since 2500 years ago; they have a long history as biomaterials. Advantages of metals as biomaterials are listed as follows. These properties are caused by the metal bond.

(a) Large strength.
(b) Large ductility; easy working.
(c) Large fracture toughness.
(d) Equipment of both elasticity and stiffness.
(e) Electroconductivity.

Metals and alloys are widely used as biomedical materials and are indispensable in the medical field. The advantages of metals compared with ceramics and polymers are large strength and difficulty to fracture. In particular, toughness, elasticity, rigidity, and electrical conductivity are essential properties for metals used in medical devices.

The use of metals as raw materials has a long history and it can be said that the present "materials science and engineering" has been developed based on research into metals. However, metals are sometimes thought of as "unfavourite materials" for biomaterials because of memories of the environmental and human damage caused by heavy metals. Since an improvement in the safety of metals for medical use is vital, strenuous efforts have been made to improve corrosion resistance and mechanical durability. In addition, metals are typically artificial materials and have no biofunctions, which makes them fairly unattractive as biomaterials. On the other hand, the fast technological evolution of ceramics and polymers has made it possible to apply these materials to medical devices over the last three decades. In particular, because of their excellent biocompatibility and biofunctions, ceramics and polymers are expected to show excellent properties for use as biomaterials; in fact, many devices made from metals have been replaced by others made from ceramics and polymers. In spite of this fact, over 70% of implant devices are still made from metals and this percentage remains unchanged because of their high strength, toughness, and durability. Metallic biomaterials cannot be replaced with ceramics or polymers at present. In addition, research into their use in regenerative medicine will not be completed for at least another few decades. In other words, artificial materials such as metals will continue to be used as biomaterials in the future.

Medical devices consist of metals and their materials are summarized in Table 25.1. About over 70% of implant devices and over 95% of orthopedic implants consist of metals: Metals are still the main materials for implant devices [1]. Conventionally, metals are essential for orthopedic implants: Bone fixators, artificial joints, external fixators, etc., since they can substitute for the mechanical function of hard tissues in orthopedics. Stents and stent grafts are placed at angusty in blood vessels for dilatation. Therefore, elasticity or plasticity for expansion and rigidity for maintaining dilatation are required for the devices. In dentistry, metals are used for restorations, orthodontic wire, and dental implants. In noble metals and alloys, gold (Au) marker for the imaging of stent, platinum (Pt) for embolization wire, and Au alloys and silver (Ag) alloys for dental restoratives are utilized. In base metals and alloys, austenitic stainless steels, cobalt–chromium (Co–Cr) alloys,

Table 25.1 Metals used for medical devices

Clinical division	Medical device	Material
Orthopedic surgery	Spina fixation	316L stainless steel; Ti; Ti–6Al–4V; Ti–6Al–7Nb
	Bone fixation (bone plate, screw, wire, bone nail, mini plate, etc.)	316L stainless steel; Ti; Ti–6Al–4V; Ti–6Al–7Nb
	Artificial joint; bone head	Co–Cr–Mo; Ti–6Al–4V; Ti–6Al–7Nb
	Spina spacer	316L stainless steel; Ti–6Al–4; Ti–6Al–7Nb
Cardiovascular medicine and surgery	Implant-type artificial heart (housing)	Ti
	Pacemaker (case) (electric wire) (electrode) (terminal)	Ti; Ti–6Al–4V Ni–Co Ti; Pt–Ir Ti; 316L stainless steel; Pt
	Artificial valve (frame)	Ti–6Al–4V
	Stent	316L stainless steel; Ti–N; Ta; Co–Cr–Mo
	Guide wire	316L stainless steel; Ti–Ni; Co–Cr
	Embolization wire	Pt
	Clip	Ti–6Al–4V; 630 stainless steel; Co–Cr
Otolaryngology	Artificial inner year (electrode)	Pt
	Artificial eardrum	316L stainless steel
Dentistry	Filling	Au foil; Ag–Sn(–Cu) amalgam
	Inlay, crown; bridge; clasp; denture base	Au–Cu–Ag; Au–Cu–Ag–Pt–Pd; Ti; Ti–6Al–7Nb; Co–Cr; 304 stainless steel; 316L stainless steel
	Thermosetting resin facing crown; porcelain-fused-to-metal	Au–Pt–Pd; Ni–Cr
	Solder	Au–Cu–Ag; Au–Pt–Pd
	Dental implant	Ti; Ti–6Al–4V; Ti–6Al–7Nb; Au
	Orthodontic wire	316L stainless steel; Co–Cr; Ti–Ni; Ti–Mo
	Magnetic attachment	Sm–C; Nd–Fe–B; Pt–Fe–Nb; 444 stainless steel; 447J1 stainless steel; 316L stainless steel
	Treatment device (bar, scaler, periodontal probe, dental tweezers, raspatory, etc.)	304 stainless steel
General surgery	Needle of syringe	304 stainless steel
	Scalpel	420J1 stainless steel
	Cathetel	Ni–Ti; 304 stainless steel; 316L stainless steel; Co–Cr; Au; Pt–In
	Staple	630 stainless steel

commercially pure titanium (CP Ti) and Ti alloys, whose corrosion resistance is maintained with surface oxide film as s passive film, are utilized for implant materials. On the other hand, wear resistance is required to decrease the generation of wear debris. Co–Cr–molybdenum (Mo) alloys have good wear resistance and are used for sliding part of artificial joints.

Safety to the human body is essential in biomaterials; no toxic material is used for biomaterials. Metals implanted in tissues do not show any toxicity without metal ion dissolution by corrosion and/or generation of wear debris by wear. Therefore, corrosion resistance is absolutely necessary for metals in biomedical use, causing the uses of noble or corrosion-resistant metals and alloys for medicine and dentistry.

25.3 Ceramics

The advantages of ceramics are high strength, high wear resistance, and high heat resistance, as well as esthetic white color for dental restorations. Hydroxyapatite (HA) and tricalcium phosphate (TCP) are mainly used for hard tissue substituting materials such as bone substituting materials gradually transit to natural bone and artificial bone, because inorganic constitution in human hard tissue is mainly HA. On the other hand, other types of ceramics such as zirconia show high chemical stability and high wear resistance. Therefore, ceramics occupy important positions among biomaterials. Bioceramics are categorized three groups: bioinert ceramics unreacted with human tissue, bioactive ceramics integrated with bone, and biodegradable ceramics absorbed in the human tissue.

The disadvantages of ceramics are low fracture toughness, especially low notch toughness, inducing sudden and rapid fracture. Therefore, ceramics are not employed where large load and frequent loads are applied and stress is concentrated.

Medical devices consist of ceramics and their materials are summarized in Table 25.2. In orthopedics, restorations of relatively small bone defect, spinal spacers, artificial joints, and coating of stem of artificial stems. In dentistry, porcelain and artificial teeth mainly consisting of alumina (Al_2O_3), silica (SiO_2), and leucite, yettria-stabilized zirconia (YSZ) for crown and bridge formed by CAD/CAM, and powder of dental cements. In the process of dental technology, plaster and dental stone for model materials and plaster and silica for the investment of dental casting are used. In dental implants, calcium phosphate for filler of periodontal pocket, titania (TiO_2) and HA for coating of the fixture, and YSZ for abutment. For scaffold materials in regenerative medicine, HA-collagen, HA-chitosan, HA-chitin, and HA-hyaluronic acid composites are used. In addition, HA nanoparticle is attempted to use for nanocareer in gene therapy.

Table 25.2 Ceramics used for medical devices

Clinical division	Medical device	Material
Orthopedic surgery	Artificial joint	Alumina, zirconia; HA; bioactive glass; bioactive ceramics
	Artificial bone	
	Bone extending agent	β-tricalcium phosphate (β-TCP), alumina, HA, bioactive glass
	Fixator	Poly(lactic acid) (PLA) + carbon fiber (CF), PLA + glass fiber + calcium phosphate
	Artificial tendon, Artificial ligament	PLA + CF
Otolaryngology	Artificial auditory ossicles	Alumina, glass, HA
Dentistry	Dental implant (fixture)	Alumina, HA, bioactive glass
	Dental implant (abutment)	Zirconia
	Periodontal pocket filler	HA, HA + PLA, β-TCP, Calcium phosphate salt, Bioactive glass
	Dental cement powder	Zinc oxide, alumina silicate glass
	Dental porcelain	Leucite + quartz, leucite + alumina
	Crown, bridge	Zirconia
	Artificial teeth	Feldspar + quartz + clay

25.4 Polymers

Polymers are used for various medical devices because of their high degree of flexibility, lightweight, and plasticity. Also, it is relatively easy to design biofunctional polymers based on biomimetic technique, because biofunctional polymers exist in the human body as parts of biomolecules, cells, tissues, and organs. Therefore, some of the polymeric materials are widely known as biocompatible and biofunctional materials. Proper polymeric materials could be employed according to the purpose because they cover a large range of mechanical property such as strength, hardness, and elongation. However, over 90% of medical polymers are used outside the human body; less than 10% of them are used in the human body.

As a disadvantage, polymers are hardly used under large load because of their low strength and limited sterilization techniques are feasible because of low thermal resistance. In addition, after long uses, polymers gradually decrease their molecular weight due to crystallization and fragmentation. In the human body, polymers degrade due to the decrease of local pH with enzyme, infection, and inflammation.

Medical devices consist of polymers and their materials are summarized in Table 25.3. Natural polymers used for biomaterials are proteins such as collagen and fibrin and polysaccharide such as cellulose and chitin. Natural polymers are mainly used for suture, hemostat, adhesive, scaffold for regenerative medicine and careers for DDS.

On the other hand, in synthesized polymers, poly(methyl methacrylate) (PMMA) is employed when transparence and quick cure are requested, silicone and polytetrafluoroethylene (PTFE) is employed when flexibility is requested, polyester is

Table 25.3 Polymers used for medical devices

Clinical division	Medical device	Material
Orthopedic surgery	Artificial ligament	PTFE; polyester; polypropylene (PP)
	Bone substitute; ointment; substitute tendon	Silicone
	Artificial hip joint; artificial knee joint	UHMWPE, MPC polymer
	Artificial knuckle	Silicone
	Spinal cage and spacer	PEEK
	Bone cement	PMMA
	Hernia patch	PTFE
Plastic surgery	Artificial skin	Collagen
	Artificial breast	Silicone
	Facial prostheses	Silicone
	Nose prostheses	Silicone
Internal medicine and urology	Blood purification membrane	PMMA; cellulose; nylon; polysulfone (PSF); polyacrylonitrile
	Ascites filtration membrane	Cellulose
	Hemodialysis circuit	Polyvinyl chloride (PVC)
	Artificial kidney	Cellulose; cellulose acetate; polyethylene vinyl alcohol; PMMA; PSF; MPC polymer
Cardiovascular medicine and surgery	Artificial heart	Polyurethane; MPC polymer
	Artificial valve	Silicone
	Pacemaker electric wire	Silicone; polyurethane
	Vascular graft	PTFE; polyester; MPC polymer
	Balloon catheter	Polyurethane
	Stent graft	Polyester; polyurethane; PTFE
	Heart patch; vascular patch	PTFE
	Cardiopulmonary bypass circuit	PVC
	Pericardial sheet	PTFE
Otolaryngology	Artificial pinna	Silicone

(continued)

Table 25.3 (continued)

Clinical division	Medical device	Material
Respiratory medicine	Artificial lung	MPC polymer
Ophthalmology	Contact lens	PMMA; poly(2-hydroxyethyl methacrylate)
	Intraocular lens	PMMA
	Haptics	PP
Dentistry	Denture base	PMMA; polycarbonate (PC); PSF
	Artificial teeth	PMMA
	Filler	Methacrylic acid-derived polymers
Surgery	Artificial lever	Activated carbon; porous polymer beads
	Membrane oxygenator	Silicone; PP
	Artificial esophagus	PE + natural rubber
General surgery	Disposable supplies	PP
	Suture	Polyester; PP; nylon; PTFE; collagen; fibroin
	Catheter	Silicone; PVC
	Nonwoven fabric	Cellulose
	Hemostatic material	Collagen; gelatin; fibrin; cellulose
	Synechia preventive film	Silicone; PTFE
	Wound dressing	Chitin
	Adhesive	Fibrin
	Embolus	Gelatin
Others	Transfusion set	PVC
	Infusion bag; blood bag	PVC
	Drug-eluting carrier	Collagen

employed when strength is requested, and ultra-high molecular weight polyethylene (UHMWPE) is employed when the wear resistance is requested. 2-(methacryloyloxy)ethyl phosphorylcholine (MPC) polymer similar to cell membrane structure is used for contact lens, artificial heart, artificial lung, artificial blood vessel, artificial kidney, surface modification of artificial joint, utilizing to its lubrication, antithrombogenicity, and water retention characteristics properties [2]. Polyetherketoneketone (PEEK) as an engineering plastic is applied to spinal cage and spacer and the evaluation is high because of their small artifact under MRI. The tensile strength of PEEK is 100–130 MPa that is sufficiently large as a polymer, while it is about one-fourth that of CP Ti (ISO grade 2) that is 345–510 MPa.

25.5 Surface Treatment

25.5.1 Necessity

The disadvantage of metals as biomaterials is that they are typically artificial materials and have no biofunction. Therefore, additional properties are required for the metals. Requests to metals for biomedical use are summarized in Table 25.4. To respond to these requests, a new design of alloys and many techniques for surface treatment of metals have been attempted on a research stage and some of them are commercialized. Surface treatment is necessary, because biofunction could not be added during manufacturing processes of metals such as melting, casting, forging, and heat treatment, to add biofunction to metals. Surface treatment is a process that changes a material's surface composition, structure, and morphology, leaving the bulk mechanical properties intact. With surface treatment, the tissue compatibility of the surface layer can be improved, as shown in Fig. 25.3. Surface treatment techniques by both dry and wet processes used in research and industry are summarized in Fig. 25.4. Surface treatment techniques are reviewed elsewhere [3, 4].

Table 25.4 Requests to metals for medical devices

Required property	Target medical devices	Effect
Elongation to fracture	Spinal fixation; maxillofacial plate	Improvement of durability
Elastic modulus	Bone fixation; spinal fixation	Prevention of bone absorption by stress shielding
Superelasticity shape memory effect	Multipurpose	Improvement of mechanical compatibility
Wear resistance	Artificial joint	Prevention of generation of wear debris; improvement of durability
Biodegradability	Stent; artificial bone; bone fixation	Elimination of materials after healing; unnecessity of retrieval
Bone formation Bone bonding	Stem and cup of artificial hip joint; dental implant	Fixation of devices in bone
Prevention of bone formation	Bone screw; bone nail	Prevention of assimilation
Adhesion of soft tissue	Dental implant; trans skin device; external fixation; pacemaker housing	Fixation in soft tissue; prevention of inflectional disease
Inhibition of platelet adhesion	Devices contacting blood	Prevention of thrombus
Inhibition of biofilm formation	All implant devices; treatment tools and apparatus	Prevention of infectious disease
Low magnetic susceptibility	All implant devices; treatment tools and apparatus	No artifact in MRI

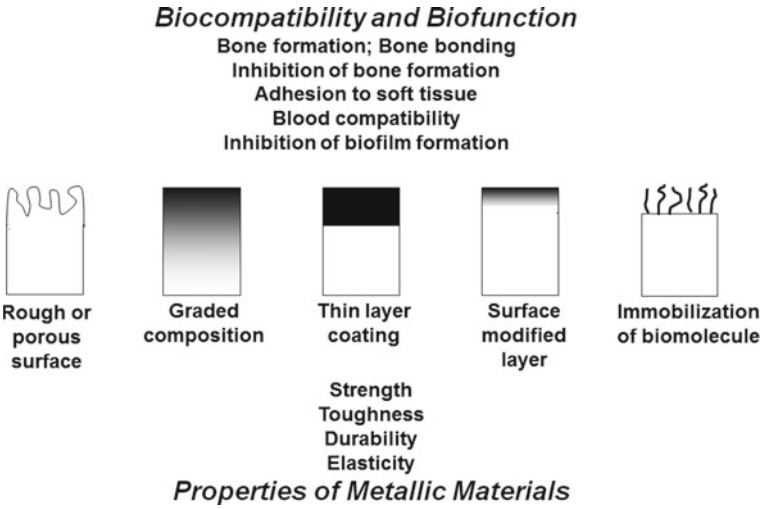

Fig. 25.3 Category of surface treatment of metallic materials to add biocompatibility and biofunctions remaining good mechanical property

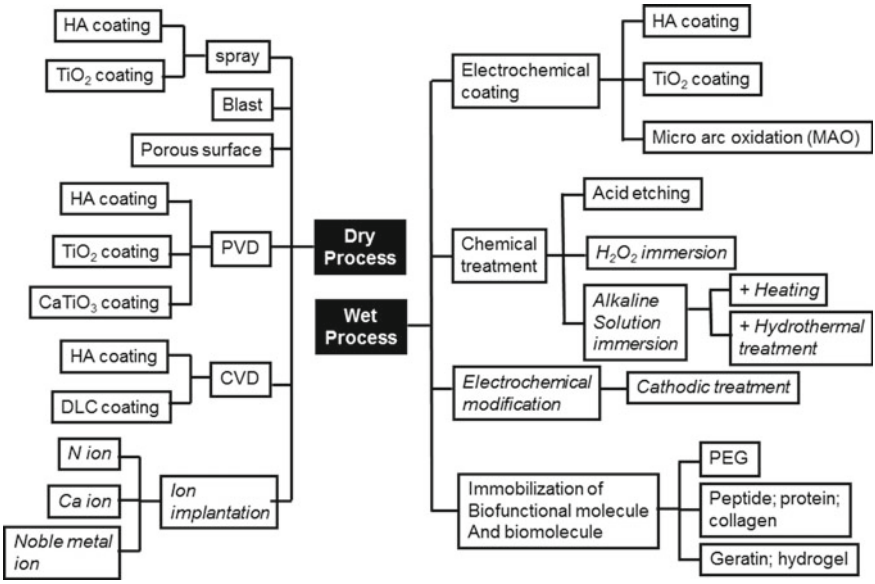

Fig. 25.4 Surface treatment techniques by dry and wet processes. Mechanical anchoring is expected b hatched processes

25.5.2 Surface Treatment for Bone Formation

Ti and its alloys, which show good hard tissue compatibility, are used for dental implants and artificial hip joints. However, the hard tissue compatibility of these materials is lower than that of bioactive ceramics, such as HA and bioactive glasses. Therefore, numerous surface treatment techniques to improve the hard tissue compatibility of Ti have been developed, and some have been commercialized.

In the stems of artificial hip joints and dental implants, the chemical bonding of metal surfaces with bone is not expected. In other words, it is impossible for metals as typical artificial materials to chemically and naturally bond with bone as living tissue, especially in the human body with body fluid. Therefore, the surface morphology is sometimes controlled, and rough and porous surface is formed in titanium. Living tissue, such as bone, is expected to grow into the rough porous surface, and the materials and bone are strongly connected as a result of the so-called anchoring effect.

25.5.3 Evolution of Surface Treatment for Bone Formation

Figure 25.5 shows the evolution of surface treatment techniques to improve hard tissue compatibility at the research level:

First generation: Grind machining of the surface.
Second generation: Grooving, blast, acid etching, anodic oxidation, and laser abrasion.
Third generation: Chemical treatment and hydroxyapatite coating.
Fourth generation: Immobilization of biofunctional molecules (collagen, bone morphogenetic protein, and peptide).
Fifth generation: Coating of stem cells and tissues?

The bone formation of the material surface is accelerated when biomolecules concerning bone formation are immobilized on the material surface, such as in the

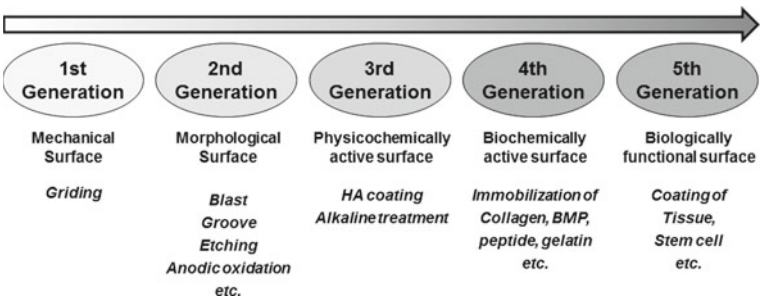

Fig. 25.5 The evolution of surface treatment techniques to improve hard tissue compatibility at the research level

fourth generation in Fig. 25.5. Therefore, many studies have achieved good results in this direction. However, to increase the popularity of the immobilization of biofunctional molecules, it is necessary to ensure the safety, quality maintenance during storage, and dry-conditioned durability of the immobilized layer. Therefore, it is difficult for manufacturers to commercialize those research results. Most of commercialized goods are categorized into the second generation, a few belong to the third generation. The commercialization went faster for the second than third generation possibly because materials employing mechanical anchoring are more practical than materials employing chemical bonding with bone.

25.6 Conclusions

Researches on surface treatment techniques to add biocompatibility and bifunction sometimes leave mechanical properties out of account. This matter may delay commercialization of the techniques. Most of the researchers make the best effort to evaluate biological effects with cell culture and animal test; they hesitate to conduct the evaluation of durability. They sometimes do not remind "materials engineering", while reminding only materials chemistry and biological evaluation. To rapidly utilize and commercialize a material successfully investigated in the stage of basic researches, the disadvantage and limit of the material should be clear and known.

References

1. T. Hanawa, Sci. Technol. Adv. Mater. **13**, 064102 (2012)
2. Y. Iwasaki, K. Ishihara, Sci. Technol. Adv. Mater. **13**, 064101 (2012)
3. T. Hanawa, J. Royal Soc. Interface **6**, S361 (2009)
4. T. Hanawa, Jpn. J. Dent. Sci. Rev. **46**, 93 (2010)

Chapter 26
Mechanical Property of Biomedical Materials

Masaaki Nakai and Mitsuo Niinomi

Abstract Metallic materials are mainly employed for the orthopaedic and dental implants because of high strength and appropriate ductility. Further, the implants are used for long term so that high fatigue strength is one of the most important properties in practical use. In addition, these implants are exposed to human body fluid, which is composed of corrosive liquid for metallic materials. In the case of metallic materials, corrosion sometimes accelerates the fatigue failure, that is, corrosion fatigue. Therefore, the effect of testing environment on fatigue strength should be also considered. In this chapter, the mechanical properties such as tensile properties and fatigue properties of the representative metallic materials for biomedical applications such as stainless steels, cobalt–chromium alloys, and titanium alloys in air and simulated body fluid are reviewed.

26.1 Introduction

Implants such as artificial hip joints, bone plates, dental roots, etc., are usually used under loading conditions in the human body. Therefore, metallic materials are mainly employed for these implants because of high mechanical reliability.

High mechanical reliability of metallic materials is generally caused by their high strength and ductility. Further, these implants are used for long term so that

M. Nakai (✉)
Faculty of Science and Engineering, Kindai University, Osaka, Japan
e-mail: nakai@mech.kindai.ac.jp

M. Nakai · M. Niinomi
Institute for Materials Research, Tohoku University, Sendai, Japan

M. Niinomi
Tohoku University, Sendai, Japan

Graduate School of Science and Technology, Meijyo University, Nagoya, Japan

Graduate School of Engineering, Osaka University, Osaka, Japan

Institute of Materials and Systems for Sustainability, Nagoya University, Nagoya, Japan

Y. Setsuhara et al. (eds.), *Novel Structured Metallic and Inorganic Materials*, https://doi.org/10.1007/978-981-13-7611-5_26

high fatigue strength is one of the most important properties in practical use in order to increase the mechanical reliability of the implant. In addition, these implants are exposed to human body fluid, which is composed of corrosive liquid for metallic materials. In the case of metallic materials, corrosion sometimes accelerates the fatigue failure, that is, corrosion fatigue. Therefore, the effect of testing environment on fatigue strength should be also considered.

Currently, the main metallic materials for the implants are stainless steels, cobalt–chromium alloys, and titanium alloys. Therefore, in this chapter, the mechanical properties such as tensile properties and fatigue properties of stainless steels, cobalt–chromium alloys, and titanium alloys in air and simulated body fluid are reviewed.

26.2 Tensile Properties in Air

Figure 26.1 shows the tensile properties of representative metallic materials for biomedical applications [1]. In general, stainless steels tend to show high ductility, while cobalt–chromium alloys tend to show high strengths among these materials. However, the strengths of these materials are markedly increased by a combination of fabrication processes and heat treatments. In particular, the tensile strength of the 20% cold-worked CP Ti grade 4 is close to that of Ti–6Al–4V, while that of

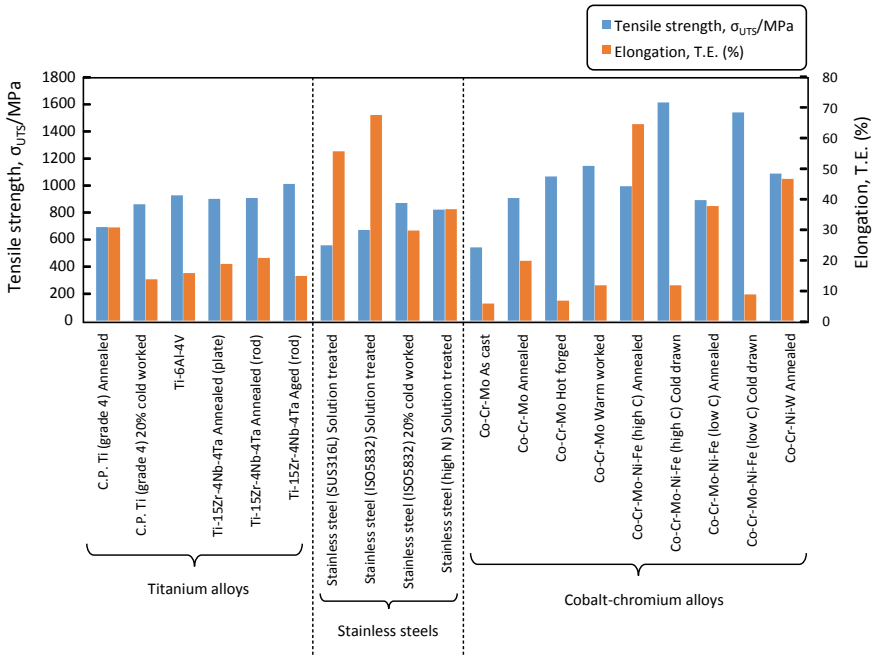

Fig. 26.1 Tensile properties of representative titanium alloys, stainless steels, and cobalt–chromium alloys for biomedical applications

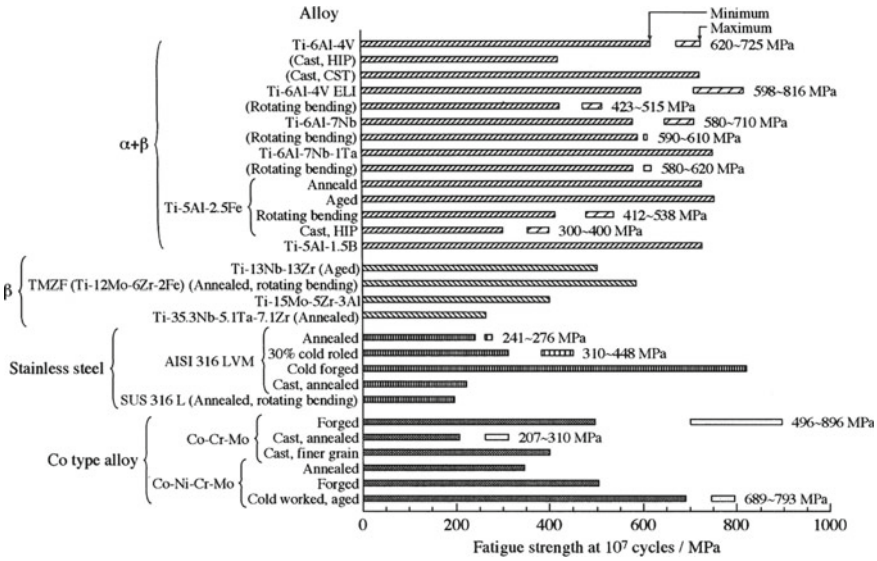

Fig. 26.2 Fatigue strengths of representative titanium alloys, stainless steels, and cobalt–chromium alloys for biomedical applications tested in air

annealed CP Ti grade 4 is lower. The tensile strengths of the 20% cold-worked stainless steel, hot-forged and warm-worked Co–Cr–Mo, cold-drawn Co–Cr–Mo–Ni–Fe, and aged Ti–15Zr–4Nb–4Ta alloys are markedly higher than those under the solution treated and annealed conditions. On the other hand, the elongation values of the same materials decrease with an increase in their strengths.

26.3 Fatigue Properties in Air

Fatigue strengths of biomedical metallic materials including stainless steels, cobalt–chromium alloys, and titanium alloys at 10^7 cycles tested in the air are shown in Fig. 26.2 [2]. The fatigue strengths are scattered depending on factors such as the fabrication process, microstructure type, and testing method. The fatigue strength of bovine bone is around 30 MPa [3], and thus those of metallic materials tested in the air are higher than that of bone. The fatigue strength of any metallic materials fabricated by casting is generally lower than those fabricated by melting, and then thermomechanical treatment. Among the titanium alloys, the fatigue strength of α + β-type titanium alloys are higher than those of β-type titanium alloys. However, the fatigue strength of β-type titanium alloys is drastically changed by heat treatment, namely it is increased by aging. With regard to stainless steels and cobalt–chromium alloys, cold working is effective to increase their fatigue strengths.

26.4 Fatigue Crack Propagation in Air

In order to understand the fatigue behavior, it is necessary to make clear each fatigue initiation and fatigue crack propagation. However, it is usually difficult to detect the crack initiation experimentally. Therefore, the fatigue crack propagation should be examined, and then estimate the fatigue initiation of the materials. When the fatigue crack propagation is evaluated, both short and long crack propagation should be considered because the trends in propagation rates of short and long crack are not always similar.

With regards to short crack propagation, Fig. 26.3 shows the relationship between the surface fatigue crack length, 2a, and the ratio of the number of cycles to the number of cycles to failure, N/N_f, in Ti–6Al–7Nb and Ti–6Al–4V ELI with equiaxed α structure [4]. The number of cycles required for the first observation of an initial fatigue crack by optical microscopy is defined as the short fatigue crack initiation life, $2a < 10$ μm. The fraction of fatigue crack initiation life in the total fatigue life that is equal to the number of failures is around 5% in Ti–6Al–7Nb and around 20% in Ti–6Al–4V ELI. Assuming that the short fatigue crack initiation and propagation life is the period for the surface crack to grow a length five times or less than the size of primary α grain, they are around 50% of the total fatigue life in Ti–6Al–7Nb and around 70% of it in Ti–6Al–4V ELI.

Figure 26.4 reveals the fatigue crack initiation site and propagation path in Ti–6Al–7Nb with equiaxed α structure [4]. The fatigue crack in the equiaxed α structure tends to initiate mainly at the primary α grain boundaries, while the crack tends to propagate preferentially along the interface between the primary α and β regions. On the other hand, Fig. 26.5 reveals the fatigue crack initiation site and propagation path in Ti–6Al–4V ELI with Widmanstätten α structure [5]. In the

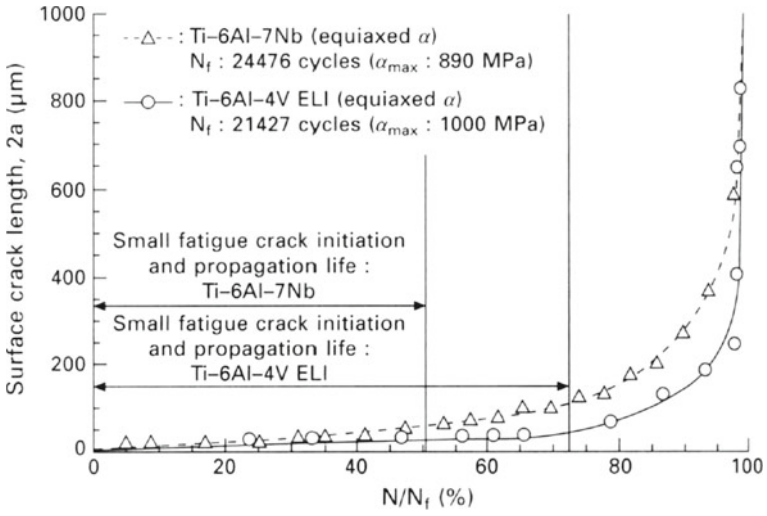

Fig. 26.3 Surface crack lengths in Ti–6Al–7Nb and Ti–6Al–4V ELI with equiaxed α structure

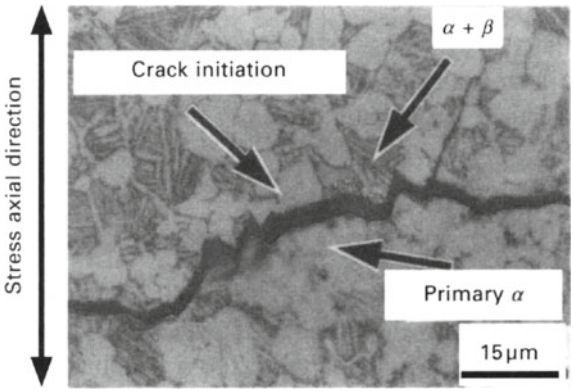

Fig. 26.4 Fatigue crack initiation site and propagation path in Ti–6Al–7Nb with equiaxed α structure

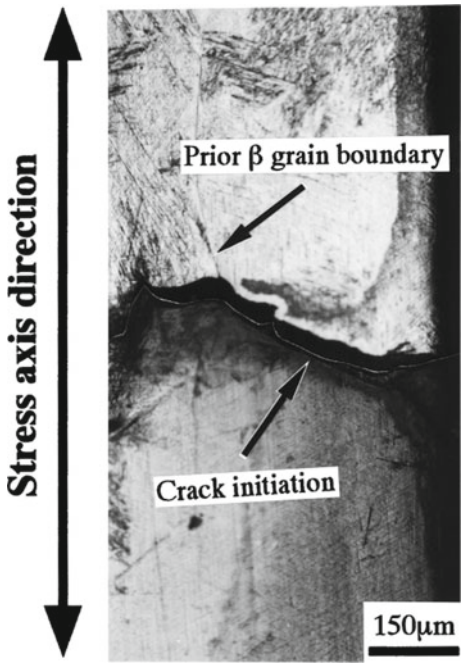

Fig. 26.5 Fatuge crack initiation site and propagation path in Ti–6Al–4V ELI with Widmanstätten α structure

Widmanstätten α structure of both alloys, the fatigue crack initiates at the very early stage of the fatigue. After a few hundred cycles, the crack initiates and grows to a length equal to the size of the α colony in the prior β grain and the crack propagation is retarded at the colony boundary or at the prior β grain boundary. However, the crack propagates in an unstable manner soon after passing through these boundaries, and this ultimately results in specimen fracture. The arresting period of the crack blocked at the α colony or β grain boundaries occupies more than 90% of the total fatigue life in both alloys. Namely, the short fatigue crack propagation rate of Widmanstätten α structure is generally higher than that in equiaxed α structure.

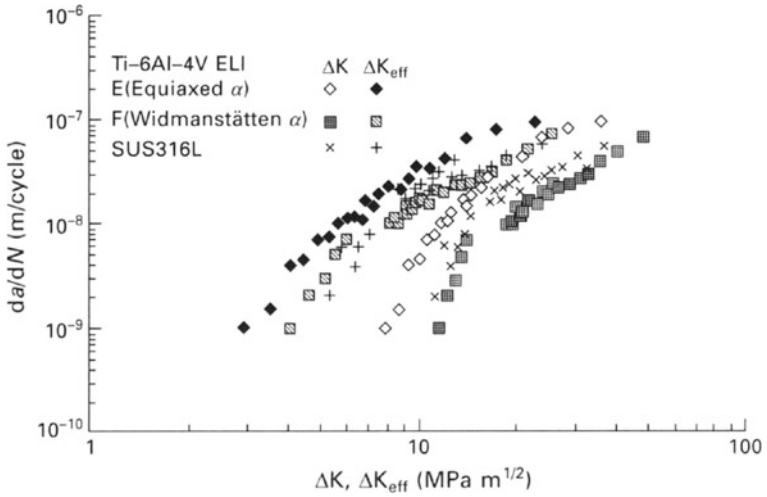

Fig. 26.6 Fatigue crack propagation rate as a function of nominal cyclic stress intensity factor range or effective cyclic stress intensity factor for long cracks in Ti–6Al–4V ELI with equiaxed α and Widmanstätten α structures and SUS316L in air

With regards to long crack propagation, Fig. 26.6 shows the relationship between the fatigue crack propagation rate, da/dN, and the nominal cyclic stress intensity factor, ΔK, or the effective cyclic stress intensity factor, ΔK_{eff}, for Ti–6Al–4V ELI with equiaxed α and Widmanstätten α structures and SUS316L obtained in the air [6]. The da/dN is plotted against ΔK in the following order, Ti–6Al–4V ELI with Widmanstätten α structure ≤ SUS316L ≤ Ti–6Al–4V ELI with equiaxed α structure. On the other hand, when da/dN is plotted against ΔK_{eff}, the da/dN of Ti-6Al–4V ELI with Widmanstätten α structure is still similar to that of SUS316L, and further that of Ti–6Al–4V ELI with equiaxed α structure is the highest. However, in this case, the differences in the long crack propagation rates among these materials are relatively small. Therefore, the crack closure effect in Ti–6Al–4V ELI with Widmanstätten α structure is greater than that in Ti–6Al–4V ELI with equiaxed α structure. The main reason for this phenomenon is the large crack deflection in Widmanstätten α structure [7]. Namely, the long fatigue crack propagation rate of Widmanstätten α structure is generally lower than that in equiaxed α structure. This fact is the opposite trend of short fatigue crack propagation rate of these materials.

26.5 Surface Substructure with Cyclic Loading in Physiological Environment

The surface substructure of metallic materials in body fluid is composed of three distinct layers; (1) a molecular absorbed layer, (2) the passive oxide film, and (3) the deformed layer, as shown in Fig. 26.7 [8]. The molecular absorbed layer consists of

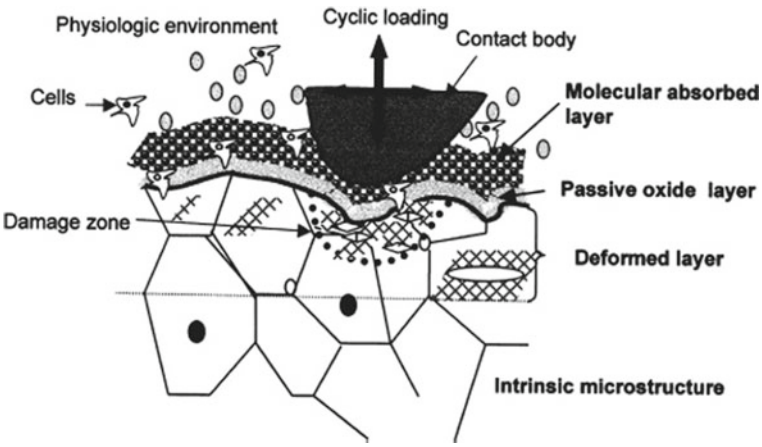

Fig. 26.7 Schematic drawing of the surface substructure of metallic materials in the physiological environment

growing tissue (cells) in contact with the physiological environment and the passive layer on the surface of the metallic materials. The deformed layer arises from the cyclic loadings that cause localized plastic deformation, forming the damage zone in the microstructure of the metallic materials. Therefore, it is important to make clear the effect of intrinsic microstructure of the metallic materials on an ability to withstand cyclic loadings without fatigue failure and the stability of passive film in contact with the physiological environment during cyclic loading.

26.6 Fatigue Properties in Simulated Body Fluid

S–N curves of titanium alloy, Ti–6Al–4V ELI with equiaxed and Widmanstätten α structures, and stainless steel, annealed SUS316L, tested in the air and Ringer's solution obtained from rotating bending fatigue is shown in Fig. 26.8 [9]. The rotating bending fatigue strength of Ti–6Al–4V ELI with both structure in the air and Ringer's solution are equivalent. However, the fatigue strength of SUS316L decreases in Ringer's solution at relatively greater number of cycles to failure compared to that in the air. It has been reported that the fatigue strength of Co–Cr–Mo is also lower in Ringer's solution compared to that in air, as shown in Fig. 26.9 [10].

The concentration of oxygen in the body fluid or muscle tissue except blood is rather small. The fatigue strength of Ti–5Al–2.5Fe in Ringer's solution with N_2 gas, leading to lower oxygen concentration in the solution, has been reported as shown in Fig. 26.10 [9]. The fatigue strength of Ti–5Al–2.5Fe above 10^6 cycles decreases in the Ringer's solution with N_2 than in usual Ringer's solution.

Titanium alloys have greater corrosion resistance because the titanium oxide film formed on the surface of alloys acts as an electrochemically passive film. The

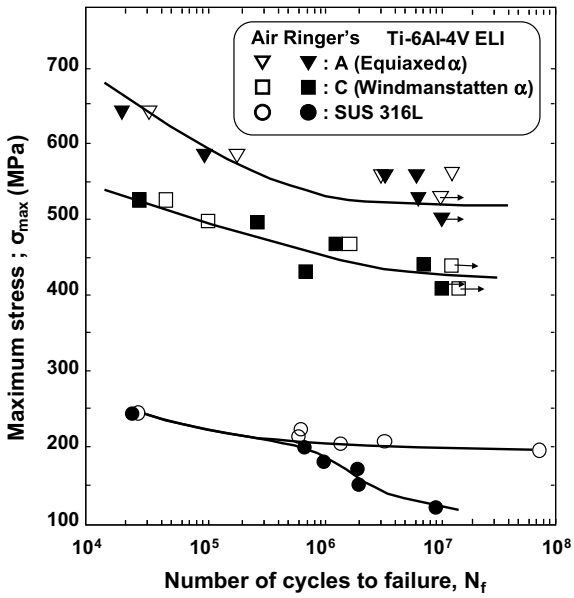

Fig. 26.8 S–N curves of Ti–6Al–4V ELI and SUS316L in air and Ringer's solution

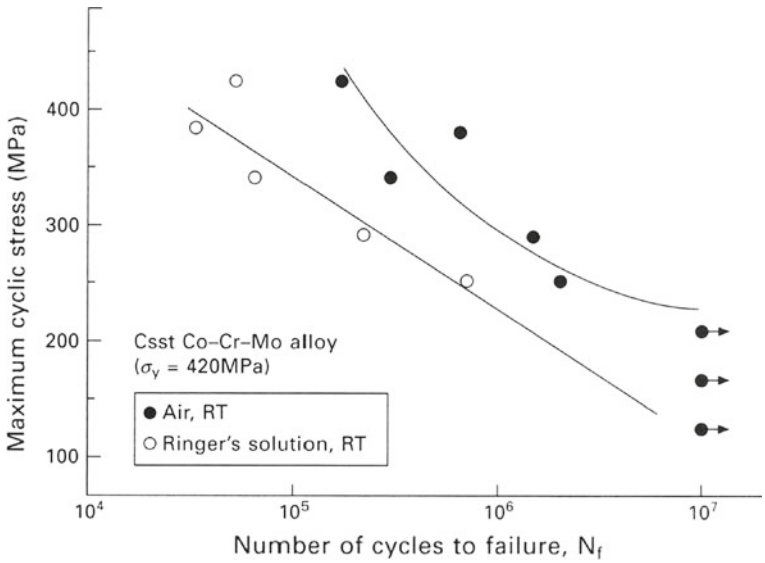

Fig. 26.9 S–N curves of Co–Cr–Mo in air and Ringer's solution

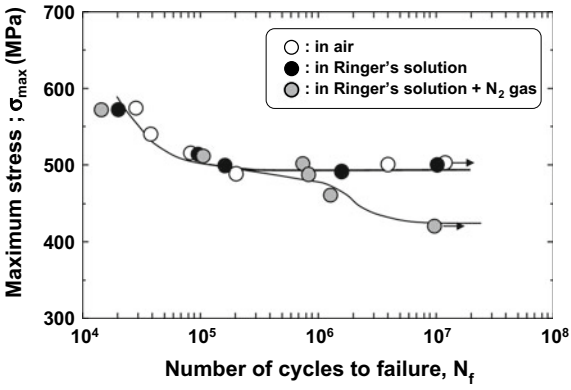

Fig. 26.10 S–N curves of Ti–5Al–2.5Fe in air and Ringer's solution with N_2 gas

fracture of the passive film is highly possible when the bending stress is loaded on the specimen, even if the specimen itself is not fractured. The fracture of the specimen by corrosion fatigue is accelerated in the Ringer's solution with lower oxygen content by N_2 gas because the fractured oxide film is difficult to be formed again under such the low oxygen concentration condition. The corrosion fatigue is likely to occur in such an environment when the immersing time of the specimen in the Ringer's solution is longer (a greater number of cycles).

26.7 Fatigue Crack Propagation in Simulated Body Fluid

Figure 26.11 shows the relationship between da/dN and ΔK for Ti–6Al–4V ELI with Widmanstätten α structures and Ti–5Al–2.5Fe with (equiaxed α + fine precipitated α) structure in air and Ringer's solution [11]. The long fatigue crack propagation rates of both materials in Ringer's solution are higher than those in the air. However, it has been reported that, when da/dN was plotted against ΔK_{eff}, the long fatigue crack propagation rates of these materials in Ringer's solution is similar to that in the air. It reveals that the clack closure effect reduces in Ringer's solution because the number of secondary cracks and the roughness of fatigue fracture surface in Ringer's solution are smaller than those in the air, suggesting that the fatigue fracture surface corrodes and dissolves in Ringer's solution.

Figure 26.12 shows the relationship between da/dN and ΔK for SUS316L in air and Ringer's solution [12]. The decrease in da/dN with increasing ΔK may be related to the secondary cracking that occurred along striations. The authors found that above ΔK = 30 MPa $m^{1/2}$ a fully developed striation appearance formed across the fracture surface and the striation spacing increased with stress intensity. Consequently, the opening up of a fatigue crack along the base of striations suggests that changes took place during the reversed plastic flow. As a result, the shape

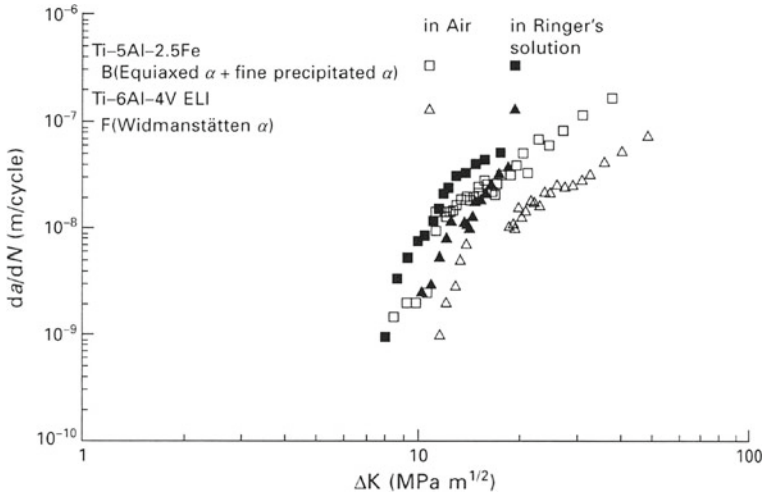

Fig. 26.11 Fatigue crack propagation rate as a function of nominal cyclic stress intensity factor range for long cracks in Ti–6Al–4V ELI with Widmanstätten α structure and Ti–5Al–2.5Fe with (equiaxed α + fine precipitated α) structure in air and Ringer's solution

of the fatigue cracks was altered, as was the morphology of the striations, leading to a decrease in the crack growth rate. This analysis was supported by SEM images of the fractured surfaces.

26.8 Fatigue Properties of Medical Device

Recently, newly developed β-type titanium alloys are tried to be utilized for actual medical devices. For example, Ti–29Nb–13Ta–4.6Zr (TNTZ) is applied to spinal fixation devices. Testing of the spinal fixation device assemblies was based on a simulated vertebrectomy model using a large gap between two UHMWPE test blocks based on ASTM-F1717 as shown in Fig. 26.13 [13]. The ASTM-F1717 specification is the standard testing method used to evaluate the mechanical performance of spinal fixation devices. The UHMWPE test blocks are designed to minimize the effects of the variability of bone properties and morphometry. In this case, the ASTM-F1717 fatigue tests were conducted with rods made of Ti–29Nb–13Ta–4.6Zr (TNTZ) with oxygen contents of 0.06 mass% (06O) and 0.89 mass% (89O) and Ti–6Al–4V ELI (Ti64) as comparison in both air and saline solution. There is almost no difference in fatigue strength between in air and saline solution for both alloys, and further the fatigue strength increases in the order of 06O < 89O < Ti64 in both air and saline solution as shown in Fig. 26.14 [13]. These results

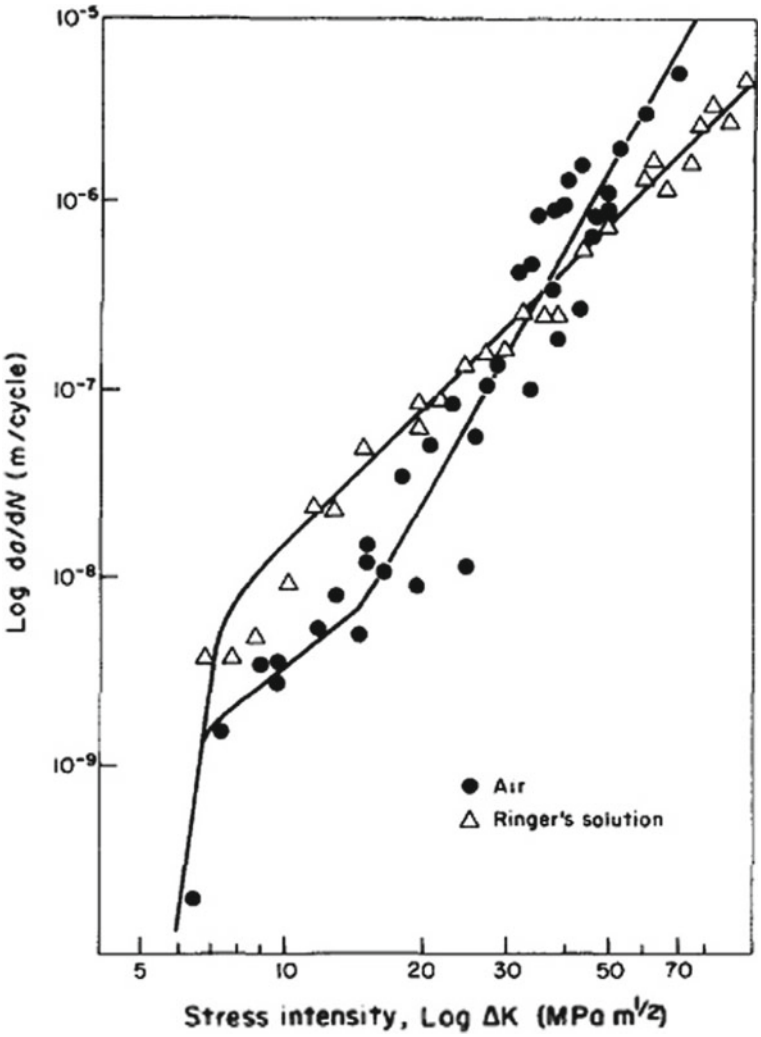

Fig. 26.12 Fatigue crack propagation rate as a function of nominal cyclic stress intensity factor range for long cracks in SUS316L in air and Ringer's solution

indicate that effect of saline solution on the fatigue strength of both titanium alloys can be ignored for this device, and then the solid solution strengthening by oxygen addition is effective to improve the mechanical reliability of the device made of TNTZ.

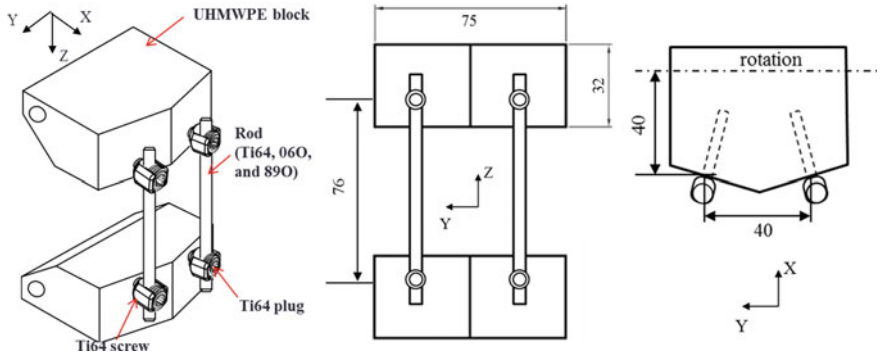

Fig. 26.13 Specification of experimental setup according to ASTM-F1717 model

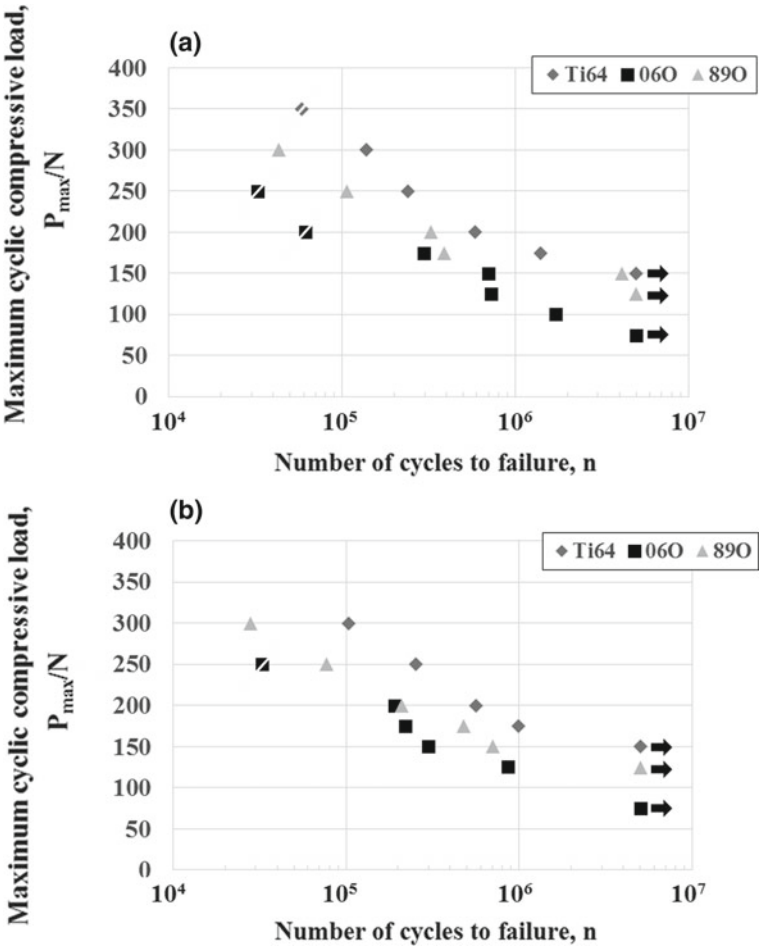

Fig. 26.14 Compressive fatigue test results for Ti-based spinal constructs containing Ti64, 06O, and 89O rods using an ASTM-F1717 model, in **a** air and **b** saline solution

References

1. Y. Okazaki, Comparison of fatigue properties and fatigue crack growth rates of various implantable metals. Materials **5**(12), 2981–3005 (2012)
2. M. Niinomi, Mechanical properties of biomedical titanium alloys. Mater. Sci. Eng. A **243** (1–2), 231–236 (1998)
3. J.H. Kim, M. Niinomi, T. Akahori, J. Takeda, H. Toda, Effect of microstructure on fatigue strength of bovine compact bones. JSME Int. J. Ser. A-Solid Mech. Mater. Eng. **48**(4), 472–480 (2005)
4. T. Akahori, M. Niinomi, K. Fukunaga, I. Inagaki, Effects of microstructure on the short fatigue crack initiation and propagation characteristics of biomedical alpha/beta titanium alloys. Metall. Mater. Trans. A **31**(8), 1949–1958 (2000)
5. T. Akahori, M. Niinomi, K.I. Fukunaga, An investigation of the effect of fatigue deformation on the residual mechanical properties of Ti–6Al–4V ELI. Metall. Mater. Trans. A **31**(8), 1937–1948 (2000)
6. M. Niinomi, Fatigue characteristics of metallic biomaterials. Int. J. Fatigue **29**(6), 992–1000 (2007)
7. M. Niinomi, T. Kobayashi, A. Akmoulin, Mechanical properties of titanium alloys. J. JILM **42**(11), 605–613 (1992)
8. R.A. Antunes, M.C.L. de Oliveira, Corrosion fatigue of biomedical metallic alloys: mechanisms and mitigation. Acta Biomater. **8**(3), 937–962 (2012)
9. M. Niinomi, T. Kobayashi, O. Toriyama, N. Kawakami, Y. Ishida, Y. Matsuyama, Fracture characteristics, microstructure, and tissue reaction of Ti–5Al–2.5Fe for orthopedic surgery. Metall. Mater. Trans. A **27**(12), 3925–3935 (1996)
10. P. Kumar, A.J. Hickl, A.I. Asphahani, A. Lawley, Properties and characteristics of cast wrought and powder metallurgy (P/M) processed cobalt-chromium-molybdenum implant materials. ASTM STP **859**, 30–56 (1985)
11. M. Niinomi, A. Saga, K. Fukunaga, Long crack growth behavior of implant material Ti–5Al–2.5Fe in air and simulated body environment related to microstructure. Int. J. Fatigue **22**(10), 887–897 (2000)
12. J.D. Bolton, M.L. Redington, The effects of saline aqueous corrosion on fatigue crack growth rates in 316 grade stainless steels. Int. J. Fatigue **5**(3), 155–163 (1983)
13. Y.-S. Lee, M. Niinomi, M. Nakai, K. Narita, H.H. Liu, Effect of solute oxygen on compressive fatigue strength of spinal fixation rods made of Ti–29Nb–13Ta–4.6Zr alloys. Mater Trans. **57**(12), 1993–1997 (2016)

Chapter 27
Chemical Properties of Bio-medical Materials

Yusuke Tsutsumi

Abstract In biomedical materials, chemical properties are as important as mechanical properties. None of these materials can avoid deterioration by chemical reaction in a living body owing to various physiological factors. In this chapter, corrosion reaction, which is a primary process of deterioration in metallic biomaterials, is discussed. First, several important factors that influence the corrosion reactions of metallic biomaterials in actual environments are introduced. In the latter part of this chapter, representative methods for evaluating corrosion reactions of metallic biomaterials that are frequently used in the biomedical material research field are introduced. The principles, procedures, and examples of experimental results of these testing methods based on both electrochemical and non-electrochemical systems are explained.

Keywords Corrosion · Biosafety · Metal allergy · Electrochemical measurements · Corrosion resistance

27.1 Introduction

When designing biomedical materials, we must be careful about not only their mechanical properties but also their chemical properties. The deterioration of biomedical materials is one of the most important factors in the living body. None of these materials can avoid deteriorating under severe practical conditions. Implant materials are often used for a long time in vivo, and the problems owing to deterioration reactions often cause serious problems. Although there are exceptions of biodegradable materials such as poly-L-lactic acid, magnesium, and magnesium alloys, most biomedical materials are designed to avoid reacting with the physiological environment.

Y. Tsutsumi (✉)
Research Center for Structural Materials, National Institute for Materials Science (NIMS), 1-2-1 Sengen, Tsukuba, Ibaraki 305-0047, Japan
e-mail: TSUTSUMI.Yusuke@nims.go.jp

Y. Setsuhara et al. (eds.), *Novel Structured Metallic and Inorganic Materials*, https://doi.org/10.1007/978-981-13-7611-5_27

However, problems owing to the deterioration of implant devices have not been completely solved. For example, Tomizawa et al. reported on the deterioration of stainless steel sternal wires at 22 and 30 years after implantation [1]. Akazawa et al. reported on the apparent volume loss in posterior instrumentation rods made of 316L stainless steel [2]. Heintz et al. reported on severe corrosion pits and partial fractures in Ni–Ti alloy in an aortic stent graft [3]. Dobbs et al. reported on fractures of an artificial hip joint made of Ti alloy [4]. These cases are caused by deterioration reactions during the implantation period. In the case of metallic materials, the problem was caused by corrosion reactions. Corrosion reactions are unavoidable for metallic biomaterials. They finally cause not only degradation or fractures in devices, but they also cause serious harm to living tissue. In particular, the release of metal ions as a result of a corrosion reaction is known to cause metal allergies [5–7].

Nevertheless, metallic biomaterials are still commonly used as biomedical materials in the fields of orthopedics, cardiovascular, and dentistry because of their superior mechanical properties: an excellent combination of strength and ductility, resulting in high fracture toughness that cannot be replicated by using other materials.

This chapter focuses on the corrosion reaction of metallic biomaterials. Typical evaluation methods of electrochemical and non-electrochemical techniques are introduced.

27.2 Evaluation of Corrosion Behavior

27.2.1 Testing Environment

An actual body is a complicated environment with many factors that influence corrosion reactions in metallic biomaterials. Each factor must be carefully considered to precisely predict the corrosion reaction. If the critical factors that influence corrosion reactions in an actual environment are not accurately reproduced under testing conditions, unexpected corrosion and metal-ion release may occur. Table 27.1 shows typical testing solutions for corrosion evaluation. The following sections introduce some important factors that influence the corrosion behavior of metallic biomaterials in a living body.

27.2.1.1 Temperature and pH

Most living organisms have homeostasis. In the case of human, body temperature is maintained at approximately 310 K. The pH of body fluid is also kept near neutral by the buffering functions of phosphoric acid, carbonic acid, and some types of amino acids and proteins. However, the pH near the material surface exhibits a

Table 27.1 Typical testing solutions for corrosion-resistant evaluation of metallic biomaterials

Generic term	Characteristics
Physiological saline	The simplest composition (0.9% NaCl aq.) Isotonic for extracellular fluid
Phosphate buffered saline (PBS)	Relatively strong buffering capacity (pH: around 7.4)
Ringer solution	NaCl with K^+ and Ca^{2+} Isotonic for extracellular fluid
Hanks' solution/Hanks' balanced salt solution (HBSS)	NaCl with K^+, Mg^{2+}, Ca^{2+}, PO_4^{3-}, CO_2^{2-}, and glucose simulating extracellular fluid
(Kokubo's) simulated body fluid (SBF) [8]	NaCl with K^+, Mg^{2+}, Ca^{2+}, PO_4^{3-}, CO_2^{2-} Relatively higher concentration of Ca^{2+} simulating blood plasma
Artificial saliva	NaCl with other inorganic ions, organic components several types with different compositions (Typical composition: Fusayama et al. [9])
Cell culturing media: minimum essential medium (MEM)	NaCl with other inorganic ions, organic components several types with different compositions
Cell culturing media: MEM with serum	Serum: blood without hemocytes or clotting factors abundant nutrients

weak acidic condition owing to an inflammatory reaction after the implantation of a device. This can continue for a maximum of several months [10]. In addition, both temperature and pH and conditions in the oral cavity are easily changed by the intake of foods and beverages. The oral bacterial metabolism also causes acidification [11, 12].

27.2.1.2 Concentration of Dissolved Oxygen

The concentration of dissolved oxygen in the solution directly influences the following cathodic reaction:

$$O_2 + 2H_2O + 4e^- \rightarrow 4OH^-$$

Furthermore, dissolved oxygen is used in the formation, breakdown, and repair of passive film. In the case of general corrosion testing, open-air (7–9 ppm) or completely deaerated (0 ppm) conditions are often used. However, the dissolved oxygen concentration in vivo is reported to be approximately one-fourth to one-twentieth of the open-air condition [13]. To reproduce this low-oxygen environment, exact control over the deaeration time or adjustments to the deaerating gas composition are required. When the testing solution includes carbonate or bicarbonate ions, the drifting of the pH by deaeration should be also considered.

27.2.1.3 Inorganic Components

Chloride ions make up approximately 0.1 mol L^{-1} of body fluids. The chloride ion is well-known as a major factor that promotes corrosion reactions in various metallic materials. Generally, in corrosion protection, it is effective to prevent corrosion by interrupting any contact with a solution that includes chloride ions or other aggressive components. However, this environmental corrosion control is not applicable to biomedical materials.

When a testing solution contains both calcium ions and phosphorous ions, a spontaneous reaction of calcium phosphate precipitation on a metal surface may influence the corrosion reaction. Figure 27.1 shows differences in the corrosion behavior of Ti immersed in two types of testing solutions: Hanks' solution (which contains calcium and phosphorous ions) and physiological saline (0.9% NaCl aq.). The increase in the impedance at the lowest frequency of 10 mHz indicates a suppression of the corrosion reaction. This derives from calcium phosphate precipitation on the Ti surface during immersion in Hanks' solution.

27.2.1.4 Organic Components

Amino acids and proteins included in body fluids also react with metal surfaces. These organic components contain carboxyl, amino, and thiol groups, and they influence corrosion reactions by adsorption on the metal surface or by metal-ion complexing [14, 15]. The organic components that adsorb to a metal surface fluctuate as a result of substitution reactions. The adsorption period depends on the molecular size: small molecules adsorb earlier than large ones (Vroman effect) [16]. Thus, time dependence should be a concern when corrosion tests are performed with solutions that contain multiple organic components.

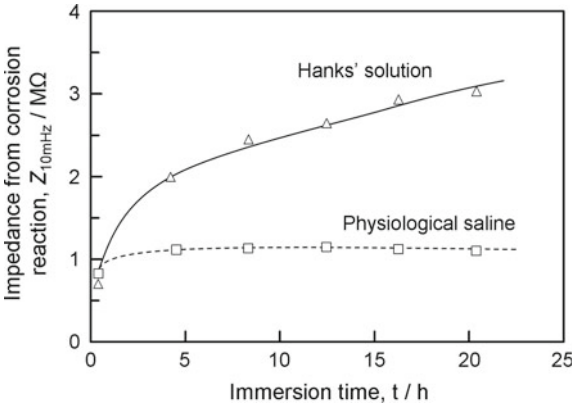

Fig. 27.1 Difference in corrosion behavior of Ti immersed in Hanks' solution and physiological saline. electrochemical impedance spectroscopy (EIS) was performed to monitor the corrosion rates of Ti in different simulated body fluids

27.2.2 Corrosion Evaluation Techniques

27.2.2.1 Dissolution Test

In general metallic materials, corrosion resistance is often evaluated by surface observation or weight-loss measurement after exposing the material in the testing environment for a certain period. However, these methods are not applicable to metallic biomaterials because all of them, except for biodegradable materials, show excellent corrosion resistance even in severe biological environments. Therefore, it is necessary to use high-sensitivity equipment to detect the signatures of slight corrosion reactions. With regard to the abovementioned simple corrosion testing methods, a dissolution test is performed by exposing the material to a testing environment for a certain period. The metal ions released into the testing solution are detected. Inductively coupled plasma spectroscopy (ICP-AES, ICP-MS) or atomic absorption spectroscopy (AAS) are used for this test.

Before starting a dissolution test, the following elaborate preparation step is necessary. All apparatus and glassware for preparation of the specimens and solutions should be thoroughly washed in acid or alkali to completely remove any contaminants. The testing container should be chemical resistant, airtight, and of the proper shape to minimize the area of contact points with the specimen. Glass containers should not be used because released metal ions may adsorb on the internal wall of the container and result in the underestimation of the corrosion degree. A testing solution of a constant volume is poured into the container together with the specimen. A testing container filled with only the testing solution is also prepared as a control. By using this control, measurement errors derived from the contaminants in the container or from impurity elements included in the reagents can be balanced out. After the immersion period, the specimen is carefully removed from the container to avoid contaminating the solution. The concentrations of the released metal ions are measured with ICP or AAS. The mean corrosion rate r during the immersion period can be calculated by the following equation:

$$r = V(C - C_0) \,/\, At$$

where V is the solution volume, C is the concentration of metal ions in the testing solution, C_0 is the concentration of metal ions in the control solution, A is the entire area of the specimen surface, and t is the immersion period.

An example of a dissolution test is shown in Fig. 27.2 [17]. One of the advantages of dissolution tests among other corrosion tests is the differential analysis for each element. From this figure, the amounts of released metal ions strongly depend on the alloy composition. The metal ion concentrations are often too small to detect even when ICP or AAS are used for corrosion-resistant alloys. In that case, the application of accelerated body fluid for rapid testing [18] may be useful. This fluid has higher concentrations of chloride ions or a lower pH than those in typical fluids.

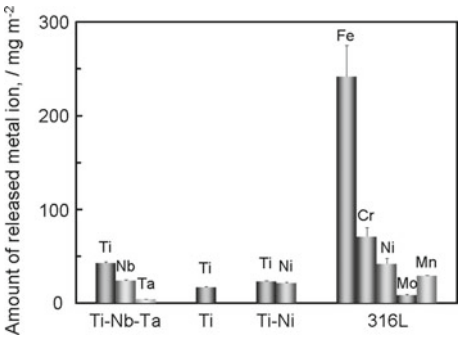

Fig. 27.2 Amounts of released metal ions from Ti-33.5Nb-5.7Ta alloy, commercially pure Ti (Grade 2), Ti-50.8at.%Ni superelastic alloy, and type-316L stainless steel after immersion in accelerated body fluid for rapid testing (5.85 gL^{-1} NaCl and 10.0 gL^{-1} lactic acid, pH: 2.3, aerated) at 310 K for 7 d (N = 3). Reprinted with permission from Ref. [17]. Copyright 2012 The Electrochemical Society

27.2.2.2 Open-Circuit Potential and Anodic Polarization Tests

Before explaining the testing methods used in this section, a fundamental electrochemical subtopic should be introduced. All corrosion reactions of metals can be represented by the following simple electrochemical reaction:

$$\mathrm{M} \rightarrow \mathrm{M}^{n+} + ne^{-}$$

where M is the type of metal, and n is the valence of the metal ion. A metal atom loses several electrons to form a metal ion. This electrochemical reaction to release electrons results in an anode. Unlike chemical reactions which have no involvement in electron transfer, electrochemical reactions can be controlled by externally applied electric fields. The application of a positive potential accelerates the corrosion reaction, while the application of negative potential inhibits the corrosion reaction.

An anodic polarization test, which is also called linear sweep voltammetry or potentiodynamic polarization test, is an electrochemical method that applies a positive potential to the testing metals. Information in the form of potential and current from an anodic polarization test can be utilized in a polarization curve to clarify the differences between the corrosion behaviors of metallic biomaterials that have high corrosion resistance.

Figure 27.3 shows a schematic of an experimental setup for electrochemical measurement, including an anodic polarization test. A working electrode (W.E.) is a testing specimen connected with a lead wire. The working electrode should be insulated except for the part of the specimen surface that is exposed to the testing environment. A counter electrode (C.E.) is used for current loop formation to control the corrosion reaction by an external potential. However, this electrode reaction should not be concerned with the focused corrosion reaction that takes

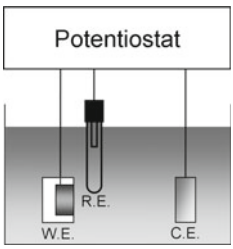

Fig. 27.3 Schematic of three-electrode electrochemical measurement system. Reference electrode sometimes separated by a salt bridge or porous ceramic plate to avoid contamination of chloride ions into the testing solution

Table 27.2 Typical reference electrodes for practical usage

Name	Electrochemical constitution	Potential/V versus SHE (at 25 °C)	Abbreviation
Standard hydrogen electrode	Pt–Pt|H_2|HCl (Standard condition)	0.000	SHE
Standard silver–silver chloride electrode	Ag|AgCl|KCl (Saturated)	0.196	Ag/AgCl
	Ag|AgCl|KCl (3.33 mol L^{-1})	0.206	
Saturated calomel electrode	Hg|Hg_2Cl_2|KCl (Saturated)	0.244	SCE
	Hg|Hg_2Cl_2|KCl (1.00 mol L^{-1})	0.280	

place on the W.E. Therefore, highly stable and electroconductive materials such as platinum or carbon are often used as a C.E. A reference electrode (R.E.) is used as an absolute indicator to show the net potential applied to the W.E. A standard electrode potential of zero is defined by the following equilibrium reaction under standard conditions:

$$H^+ + e^- \rightleftarrows 1/2H_2$$

The electrode that maintains the above reaction is called a standard hydrogen electrode (SHE). Unfortunately, this electrode has disadvantages in safety, cost, and handling. Therefore, alternative electrodes are used as R.E.s. Table 27.2 shows typical electrodes and their potential differences with regard to the SHE.

Although different types of R.E. are used, it is possible to compare them under the same conditions by converting the measured potential to a calculated potential and comparing this to the SHE. It should be noted that the potential of an R.E. shifts according to the concentration of solution inside the electrode. If an R.E. seems to be aging, its internal solution should be refreshed, followed by a potential check using a reliable R.E.

An anodic polarization test will be often performed after three electrodes are immersed in a test solution, followed by an open-circuit potential (OCP) measurement with a potentiostat. OCP, also called the corrosion potential, natural potential, or rest potential, is simply measured as the potential between the

W.E. and R.E. On the other hand, the C.E. is disconnected from a current circuit that can apply an external potential. Therefore, in this situation, the corrosion system is completely undisturbed because the electrometer for monitoring the OCP has an extremely high impedance.

The OCP value represents the condition of the corrosion reaction that took place on the W.E., which shifts as a result of both anodic and cathodic reactions. If there is no change in the exposed environment over time—in other words, the cathodic reaction does not change during the measurement period—the potential shift toward a positive value indicates the suppression of the corrosion reaction, and vice versa. For corrosion-resistant alloys such as metallic biomaterials, monitoring the OCP during a long-term immersion may be possible. This allows for the evaluation of the stabilization process of the passive film, or the occurrence of localized corrosion on the tested specimen [18, 19].

After the OCP is measured for a sufficient period, an anodic polarization test can be started from the initial potential, which is often set to be the same as the final value of the OCP or negative potential than that. A gradient anodic potential is applied at a constant sweep rate that is as small as possible because interference current unrelated to the corrosion reaction is not ignorable at a larger sweep rate. Generally, 20-mV min^{-1} or 1-mV s^{-1} (60-mV min^{-1}) conditions are preferred.

Polarization curves that plot the potential and the logarithmic absolute current density as a result of the anodic polarization test are shown in Fig. 27.4. Unlike common cases shown in other textbooks, a current peak just after the positive overpotential is rarely observed for most of the metallic biomaterials because they spontaneously form passive film and have already finished passivation before the test is conducted. Thus, only the current plateau is observed from the initial stage of the test. The value of the current density at this stage is called a passive current density, which represents the difficulty of mass transfer through the passive film. A small passive current density means that the passive film on the tested metal is

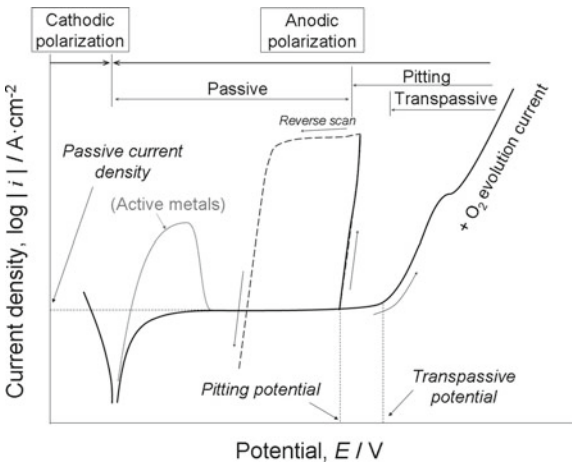

Fig. 27.4 Model of polarization curves of metallic biomaterials in simulated body fluids

protective and that few resulting metal ions are released. When the applied potential increases, the electrochemical driving force for the corrosion reaction drastically increases at an exponential rate. If part of the passive film is broken down, an abrupt increase in the current density is observed. This phenomenon is defined as localized corrosion.

Localized corrosion is a generic term that includes pitting corrosion and crevice corrosion. Alternatively, a relatively sedate but inevasible increase in the current density may be observed, indicating that the entire passive film may be dissolving. This phenomenon is defined as transpassive state caused by active dissolution of the main component of the passive film. This occurs because the potential borderline between oxide/hydroxide and an ion in a Pourbaix diagram has been exceeded [20]. Current from a following O_2 gas evolution,

$$H_2O \rightarrow 1/2O_2 + 2H^+ + 2e^-,$$

which is independent from the corrosion reaction, may be overlapped around a higher applied potential range. Observation of the specimen surface by the naked eye during the test is valuable for recognizing the evolution of O_2 gas. Microscopic observation after the test is recommended to distinguish the type of corrosion as either localized corrosion or transpassive corrosion. A reverse potential scan in the negative direction after a sufficient current increase can be also useful. An apparent histolysis loop in the resulting polarization curve is derived from the localized corrosion because the reaction is not immediately suppressed until repassivation occurs at a certain potential drop. A higher pitting potential or transpassive potential indicates that the passive film on the tested metal is stable and reliable against unexpected corrosion.

Typical examples of polarization curves for metallic biomaterials are shown in Fig. 27.5 [17]. Ti and Ti alloys maintain a passive state. On the other hand, a Ti–Ni alloy exhibits transpassive corrosion from 1.4 V_{SCE} owing to the selective dissolution of Ni. Type-316L stainless steel suffers from localized corrosion at an early stage of the test. It can be concluded that Ti and its alloys have excellent resistance against localized corrosion because they have little sensitivity to chloride ions [21].

Thus, the anodic polarization test is quite useful in evaluating corrosion resistance, especially in passive metals such as metallic biomaterials. It should be noted that anodic polarization is a type of stress test that promotes corrosion reactions by electrical bias. The tested specimen should be replaced for each measurement.

27.2.2.3 Electrochemical Impedance Spectroscopy

Electrochemical Impedance Spectroscopy (EIS) is an electrochemical test method that enables the monitoring of corrosion behavior. Several electrical parameters involved in a corrosion reaction, including the corrosion rate, can be determined by analyzing the data from an EIS measurement. EIS has another advantage: it is a nondestructive technique and can measure continuously. Its experimental setup is

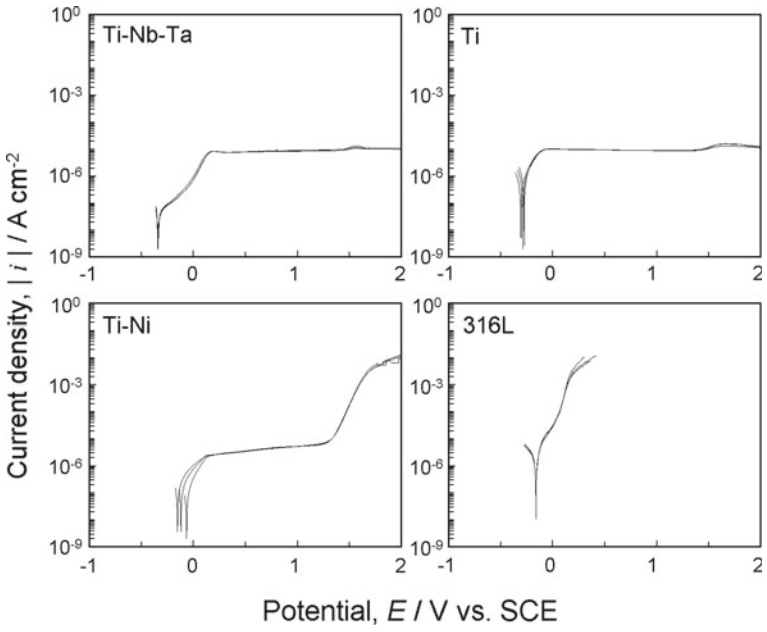

Fig. 27.5 Polarization curves of Ti-33.5Nb-5.7Ta alloy, commercially pure Ti (Grade 2), Ti-50.8at.%Ni superelastic alloy, and type-316L stainless steel in an accelerated body fluid for rapid testing (5.85 gL^{-1} NaCl and 10.0 gL^{-1} lactic acid, aerated, pH: 2.3, aerated) at 310 K. Reprinted with permission from Ref. [17]. Copyright 2012 The Electrochemical Society

almost the same as the common one for an anodic polarization test, as shown in Fig. 27.3, except for an additional piece of equipment: a frequency response analyzer (FRA). An alternating potential with a tiny amplitude is applied to the W.E., and the impedance and phase shift of the current signal as a response are analyzed by the FRA.

The frequency of the applied potential is widely modulated on the order of megahertz to millihertz. After creating an equivalent circuit model that properly represents the tested corrosion system, each parameter is calculated by a curve-fitting process. Figure 27.6 shows the simplest equivalent circuit model of a corrosion system composed of a charge-transfer resistance R_{ct}, electric double-layer capacitance C_{dl}, and solution resistance R_{sol}. The corrosion rate is proportional to the reciprocal of R_{ct}. Thus, continuous corrosion-rate monitoring is achieved by EIS. Figure 27.7 shows an example of a long-term EIS measurement of a Ti alloy in accelerated body fluid for rapid testing [17]. The corrosion rate of the Ti alloy keeps decreasing over a period of 15 d after immersion in the test solution. This is mainly a result of the growth and reconstruction of the passive film.

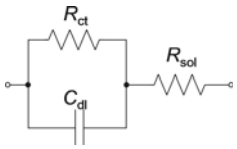

Fig. 27.6 Simplest equivalent circuit model of corrosion system for curve fitting of EIS analysis. Other electrical parameters are added in accordance with actual conditions

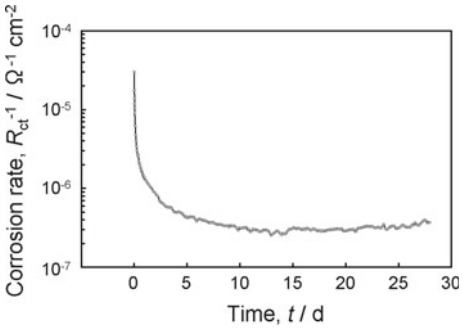

Fig. 27.7 Change in corrosion rate of Ti-33.5Nb-5.7Ta alloy during immersion in accelerated body fluid for rapid testing (5.85 gL^{-1} NaCl and 10.0 gL^{-1} lactic acid, pH: 2.3, aerated) at 310 K. Reprinted with permission from Ref. [17]. Copyright 2012 The Electrochemical Society

27.3 Summary

The term "corrosion resistance" is ambiguous because it is often used without defining the environment in which the materials are exposed. Corrosion behavior is determined not only by the testing materials involved but also by the exposure environment, including any lapses in the time period. Experimental results among various testing methods may exhibit different tendencies because specific corrosion events are also different. The result of an anodic polarization test mainly indicates the stability and reliability of the passive state under a condition of electrical stress. On the other hand, the result from a dissolution test indicates the total amount of released metal ions as a result of overall corrosion reactions. In this sense, investigating the corrosion resistance of metallic biomaterials by using only a single testing method must be insufficient. To ensure the biosafety of the testing materials, a multifaceted investigation of corrosion behavior, based on the results from several testing methods in properly simulated environments, is necessary.

References

1. Y. Tomizawa, T. Hanawa, D. Kuroda, H. Nishida, M. Endo, J. Artif. Organ **9**, 61 (2006)
2. T. Akazawa, S. Minami, K. Takahashi, T. Kotani, T. Hanawa, J. Orthop. Res. **10**, 200 (2005)
3. C. Heintz, G. Riepe, L. Birken, E. Kaiser, N. Chakfe, M. Morlock, G. Delling, H. Imig, J. Endovasc. Ther. **8**, 248 (2001)
4. H.S. Dobbs, J.T. Scales, *Titanium Alloys in Surgical Implants, ASTM STP 796* (American Society for Testing and Materials, Philadelphia, 1983), pp. 173–186
5. T. Hanawa, Mater. Sci. Eng. C **24**, 745 (2004)
6. N.H. Nielsen, T. Menne, Acta Dermato. Venereol. **72**, 456 (1992)
7. C. Liden, S. Carter, Contact Dermatitis **44**, 160 (2001)
8. T. Kokubo, H. Takadama, Biomaterials **27**, 2907 (2006)
9. T. Fusayama, T. Katayori, S. Nomoto, J. Dent. Res. **42**, 1183 (1963)
10. L.L. Hench, E.C. Ethridge, Adv. Biomed. Eng. **5**, 35 (1975)
11. R.M. Stephan, B.F. Miller, J. Dent. Res. **22**, 45 (1943)
12. R.M. Stephan, B.F. Miller, J. Dent. Res. **22**, 53 (1943)
13. J. Black, *Biological Performance of Materials* (Plenum, New York, 1984), pp. 10–12
14. R.L. Williams, S.A. Brown, K. Merritt, Biomaterials **9**, 181 (1988)
15. R.L. Williams, D.F. Williams, Biomaterials **9**, 206 (1988)
16. L. Vroman, A.L. Adams, Surf. Sci. **16**, 438 (1969)
17. Y. Tsutsumi, S. Bartakova, P. Prachar, S. Suyalatu, H. Migita, N. Doi, T.Hanawa Nomura, J. Electrochem. Soc. **159**, C435 (2012)
18. ISO 10271, *Dental metallic materials—corrosion test methods* (International Organization for Standardization, Geneva, 2011)
19. M. Nakagawa, Y. Matono, S. Matsuya, K. Udoh, K. Ishikawa, Biomaterials **26**, 2239 (2005)
20. M. Pourbaix, *Atlas of Electrochemical Equilibria in Aqueous Solutions* (National Association of Corrosion Engineers, Houston, 1974)
21. M.G. Fontana, *Corrosion Engineering* (McGraw-Hill, New York, 1985)

Chapter 28
Biological Properties of Biomedical Materials

Miho Nakamura

Abstract Biocompatibility and cytocompatibility are explained in the beginning of this section. This section provides a clear presentation of practical methods for in vitro biological evaluations of medical devices. Also, this section takes into consideration the mechanisms of cell behaviors including cell adhesion, proliferation, and differentiation on biomaterial surfaces.

Keywords Biocompatibility · Cytocompatibility · Cell adhesion · Cell proliferation · Cell differentiation · Surface characteristics of biomaterials

28.1 Biocompatibility

Biomaterials are used in contact with biological molecules, cells, tissues, and organs in the human body. The implantation of the biomaterials into living body induces biological reactions such as foreign body and toxic responses. The former is triggered by the interactions between biomaterials and surrounding tissues. Complement activation, blood coagulation, platelet thrombosis, and phagocytosis are categorized as the early stage of foreign body response. Encapsulation, hyperplastic scar tissue, and ectopic calcification are categorized as the late stage of foreign body response. The latter occurred with the release of metallic ions and toxic components. Fever, inflammation, hemolysis, tumor, and necrosis are categorized as toxic response. Biomaterials should not be toxic. Since the nontoxic requirement is the norm, toxicology for biomaterials has evolved into a sophisticated science.

Biocompatibility is defined with "the ability of a material to perform with an appropriate host response in a specific application" (1986, European Society of

M. Nakamura (✉)
Tokyo Medical and Dental University, Tokyo, Japan
e-mail: miho.bcr@tmd.ac.jp

M. Nakamura
University of Turku, Turku, Finland

Y. Setsuhara et al. (eds.), *Novel Structured Metallic and Inorganic Materials*, https://doi.org/10.1007/978-981-13-7611-5_28

Biomaterials Consensus Conference). The purpose of biocompatibility evaluation is to determine the fitness and adequacy of devices for human use and to see whether the use of the device can have any potentially harmful biological reactions. Since the material should be nontoxic to perform with an appropriate host response, which having a biomaterial interface with human body are required to perform particular physiological functions. An understanding of how a foreign object alters the normal inflammatory reaction sequence remains an important concern.

Biocompatibility examination and evaluation of medical devices are performed to determine the potential toxicity resulting from contact of the device with body. The device materials should not either directly or through the release of their material constituents profuse any local or systemic adverse effects, be carcinogenic, produce adverse reproductive and/or developmental effects.

To percent inadequate biomaterials from coming on the market, most nations of the world have medical device regulatory bodies. In addition, the international standards organization (ISO) has introduced international standards for the world community. The starting point for understanding biocompatibility requirements is ISO standard 10993, biological evaluation of medical devices. According to the ISO website (https://www.iso.org/obp/ui/#iso:std:44908:en), ISO 10993 consists of the following parts, under the general title "biological evaluation of medical devices":

- Part 1: Evaluation and testing within a risk management process
- Part 2: Animal welfare requirements
- Part 3: Tests for genotoxicity, carcinogenicity and reproductive toxicity
- Part 4: Selection of tests for interactions with blood
- Part 5: Tests for in vitro cytotoxicity
- Part 6: Tests for local effects after implantation
- Part 7: Ethylene oxide sterilization residuals
- Part 8: Selection and qualification of reference materials for biological tests
- Part 9: Framework for identification and quantification of potential degradation products
- Part 10: Tests for irritation and skin sensitization
- Part 11: Tests for systemic toxicity
- Part 12: Sample preparation and reference materials
- Part 13: Identification and quantification of degradation products from polymeric medical devices
- Part 14: Identification and quantification of degradation products from ceramics
- Part 15: Identification and quantification of degradation products from metals and alloys
- Part 16: Toxicokinetic study design for degradation products and leachables
- Part 17: Establishment of allowable limits for leachable substances
- Part 18: Chemical characterization of materials
- Part 19: Physicochemical, morphological and topographical characterization of materials (Technical Specification)
- Part 20: Principles and methods for immunotoxicology testing of medical devices (Technical Specification).

Part 1 of the standard is the guidance on selection of tests, part 2 covers animal welfare requirements, and part 3 through 20 are guidelines for specific test procedures or other testing related issues.

28.2 Cytocompatibility

Cytocompatibility evaluations are required in all types of medical devices. Cytocompatibility tests involve the exposure of substances extracted from test material to cell culture lines. Cell cultures are extremely sensitive to minute quantities of leachable chemicals and readily display characteristic signs of toxicity in the presence of potentially harmful leachables. The tests are frequently used during product planning stages to qualify the use of a material and as a periodic check for routinely used materials to ensure that no shift in quality has occurred.

Typical cytocompatibility testing programs will utilize the ISO test method to meet international regulatory requirements. The screening test method can be performed to characterize materials or to evaluate new materials against established ones. There are three cytocompatibility evaluation tests commonly used for medical devices.

(a) Direct contact

In the direct contact method, a piece of test material is placed directly onto cells growing on culture medium. The cells are then incubated. During incubation, leachable chemicals in the test material can diffuse into the culture medium and contact the cell layer. Reactivity of the test sample is indicated by malformation, degeneration, and lysis of cells around the test material.

(b) Indirect contact

In the indirect contact method, a thin layer of nutrient-supplemented agar is placed over the cultured cells. The test material (or an extract of the test material dried on filter paper) is placed on top of the agar layer, and the cells are incubated. A zone of malformed, degenerative or lysed cells under and around the test material indicates cytotoxicity.

(c) Test on extract

Extracts can be titrated to yield a semiquantitative measurement of cytotoxicity. After preparation, the extracts are transferred onto a layer of cells and incubated. Following incubation, the cells are examined microscopically for malformation, degeneration, and lysis of the cells.

There also exists specific quantitative tests. The following two quantitative cytocompatibility evaluation tests have been internationally recognized for chemicals and medical devices:

(d) MTT assay

The MTT cytocompatibility test measures the viability of cells by spectrophotometric methods. This measures the reduction of the yellow, water-soluble MTT (3-4,5 dimethyl-thiazol-2-yl)-(2,5-diphenyl tetrazolium bromide) by mitochondrial succinate dehydrogenase. A minimum of four concentrations of the test material is tested. This biochemical reaction is only catalyzed by living cells.

(e) Cell adhesion test

The colony formation cytocompatibility test enumerates the number of colonies formed after exposing them to the test material at different concentrations. This is a very sensitive test since the colony formation is assessed while the cells are in a state of proliferation (logarithmic phase), and thus more susceptible to toxic effects. A concentration dependence curve evaluating the induced inhibition of the test material can be created, and the IC50 value (concentration of the test material that provides 50% inhibition) can be calculated. The quantitative tests can be performed on extracts and by direct contact.

28.3 Mechanisms of Cell Behaviors on Biomaterials

In general, cells were affected by (1) contact with cells and antibodies, (2) growth factors, (3) hormone and (4) contact with extracellular matrix (ECM) (Fig. 28.1). These signals make cells responses; proliferation, differentiation, quiescence (G_0 phase in cell cycle), aging or apoptosis (Fig. 28.2). Contact with biomaterial surfaces is one of the signals to affect cell behaviors. In general understanding (Fig. 28.3), cells migrate to the surface of the biomaterials, attach and adhere. If the biomaterial surface is compatible and not toxic, cells spread and changes the morphology to a flat shape. Then cells migrate and make some colonies, proliferate and differentiate to mature cells to make extracellular matrix.

Adhesion of cells to biomaterial surfaces plays an important role in the regulation of the subsequent differentiation following spreading and migration. Cell

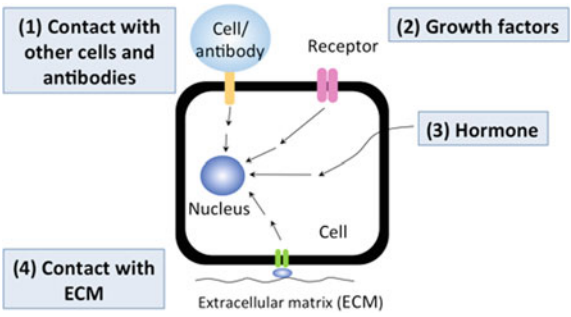

Fig. 28.1 Signals that can have effects on cell behaviors; (1) contact with cells and antibodies, (2) growth factors, (3) hormone and (4) contact with extracellular matrix (ECM)

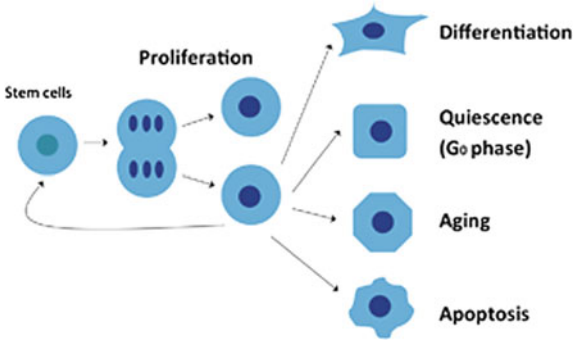

Fig. 28.2 Responces of the cells to signals

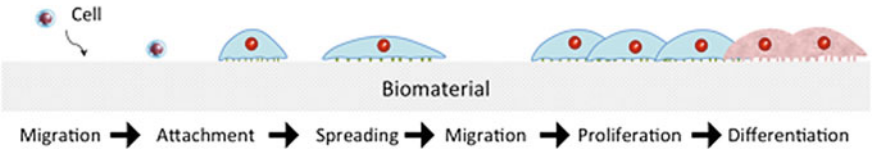

Fig. 28.3 Cell behaviors on biomaterial surface. Cells migrate to the surface of the biomaterials, attach and adhere. If the biomaterial surface is compatible and not toxic, cells spread, and changes the morphology to a flat shape. Then cells migrate and make some colonies, proliferate and differentiate to mature cells to make extracellular matrix

attachment and adhesion are affected by the surface characteristics, including the topography, constituent elements, functional group, wettability, surface free energy, surface roughness, and surface crystallinity (Fig. 28.4).

The effects of surface characteristics of biomaterials can be evaluated by cell morphology (Fig. 28.5). During the process of cell adhesion, a cell undergoes attachment, spreading and then formation of stress fibers and focal adhesions. The adhesive strength increases with each stage of cell adhesion. Cells adhere to the biomaterial surfaces through focal adhesion, which is large and dynamic protein

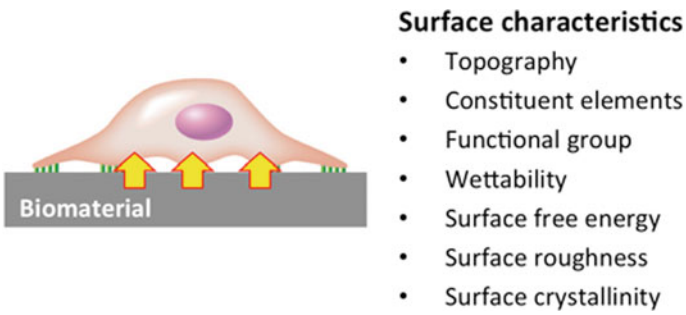

Fig. 28.4 Effective factors on cell behaviors. Cell attachment and adhesion are affected by the surface characteristics, including the topography, constituent elements, functional group, wettability, surface free energy, surface roughness, and surface crystallinity

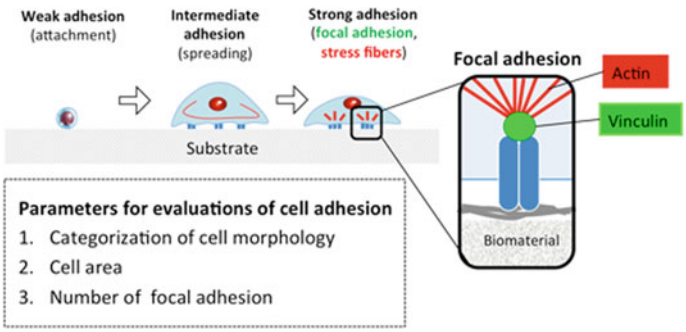

Fig. 28.5 During the process of cell adhesion, a cell undergoes attachment, spreading, and then formation of stress fibers and focal adhesions. The adhesive strength increases with each stage of cell adhesion. Cells adhere to the biomaterial surfaces through focal adhesion, which is large and dynamic protein complexes

complexes. Focal adhesions connect of cellular cytoskeleton and extracellular matrix and include some proteins such as vinculin and actin. Based on the cell morphology, the parameters for the evaluation of cell adhesion are proposed; categorization of the cell morphology, the cell area and the number of focal adhesions.

From fluorescent photographs of actin staining, the cell morphology was categorized into three types; round, semi-spread and well-spread cells (Fig. 28.6b). Round cells show the cells just attached with spherical shape. Semi-spread cells

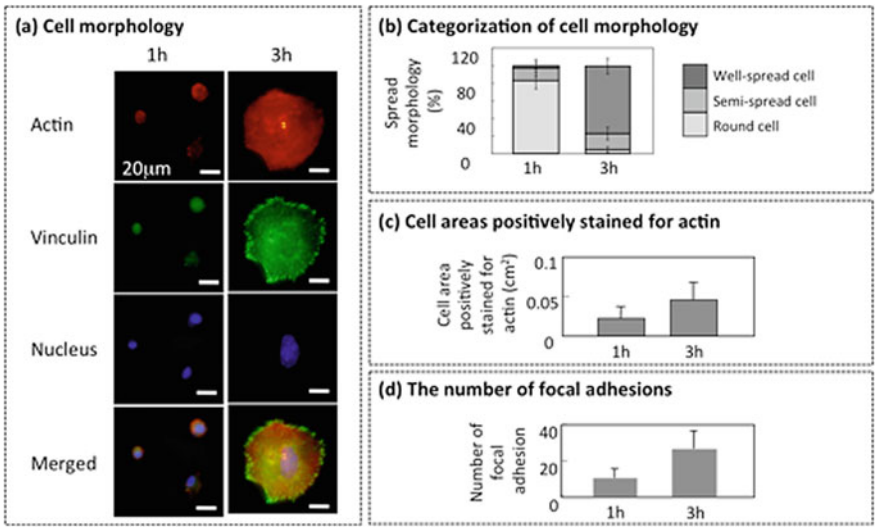

Fig. 28.6 **a** Cell evaluations based on the cell morphology. The parameters for the evaluation of cell adhesion are proposed; **b** categorization of the cell morphology, **c** the cell area and **d** the number of focal adhesions

show the cells slightly spread with no stress fiber. Well-spread cells show the cells with stress fiber. Second parameter, cell area is shown by the measurement of actin-positive areas (Fig. 28.6c). The bigger actin area shows the surface is compatible for the cells. From the fluorescent photographs of actin staining, the cell areas are measured to quantify how the cells spread. Third parameter, the number of focal adhesions is shown by the count of vinculin positive dots structure in cytoplasm (Fig. 28.6d). More vinculin dots show the surface is compatible for the cells. From the photographs of vinculin staining, the number of focal adhesions is counted to quantify how many focal adhesions are there at the contact points between cells and biomaterial surfaces.

Cell proliferation depends on cell adhesion. Eukaryotic cells except for hematocytes can proliferate through mitotic phase in cell cycle when they adhere and spread on substrates. For instance, the cells cultured in agarose gels can not proliferate because they have no receptors for agarose. The cells cultured in collagen gels can proliferate with growth factors because they make connections of integrin with collagen fibrils. In another example, the rate of the cells to start S phase (DNA synthesis) in cell cycle increase with increasing the area of cell adhesion (Fig. 28.7). The rate to start DNA synthesis was 8% in the cells cultured in agarose, 30% in the cells cultured on smaller adhesive areas and 90% in the cells cultured on larger adhesive areas.

Cells have sensors for mechano-stimulation in extracellular matrix. Discher DE et al. found that fibroblasts cultured on polyacrylamide gels showed round shape on soft gels and made stress fibers on solid gels [1]. Engler A et al. found that mesenchymal stem cells (MSCs) derived from mouse bone marrow specify lineage and commit to phenotypes with extreme sensitivity to tissue level elasticity [2]. MSCs cultured on polyacrylamide gels differentiated into neurogenic cells on the soft gels, myogenic cells on the moderately stiff matrices and osteogenic cells on the stiffest matrices.

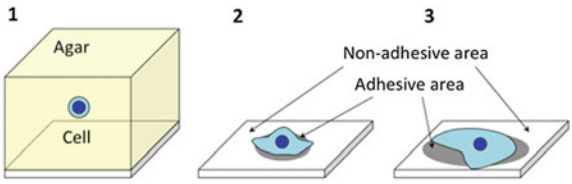

Cell cycle	1	2	3
S phase (DNA synthesis)	8%	30%	90%

Fig. 28.7 The rate of the cells to start S phase (DNA synthesis) in cell cycle increase with increasing the area of cell adhesion. The rate to start DNA synthesis was 8% in the cells cultured in agarose, 30% in the cells cultured on smaller adhesive areas and 90% in the cells cultured on larger adhesive areas

28.4 Evaluations of Cellular Functions

The in vitro methods were established to evaluate the cell functions of each cell type such as cell migration, cytotoxicity, and differentiation. Cell migration is initiated by a stimulation that activates a set of signaling pathways leading to cellular polarization and a rapid reorganization of cytoskeleton molecules such as actin filaments. Cell migration is evaluated by wound healing assay and chemotaxis/boyden chamber/transwell assay using transwell membrane filter. In wound healing assay (Fig. 28.8), the basic steps involve creating a "wound" in a cell monolayer, capturing the images at the beginning and at regular intervals during cell migration to close the wound, and comparing the image to quantify the migration rate of the cells. In transwell membrane assay (Fig. 28.9), cells are placed in the upper compartment and are allowed to migrate through the pores of the membrane into the lower compartment. After an appropriate incubation time, the membrane between the two compartments is fixed and stained, and the number of cells that have migrated to the lower side of the membrane is counted.

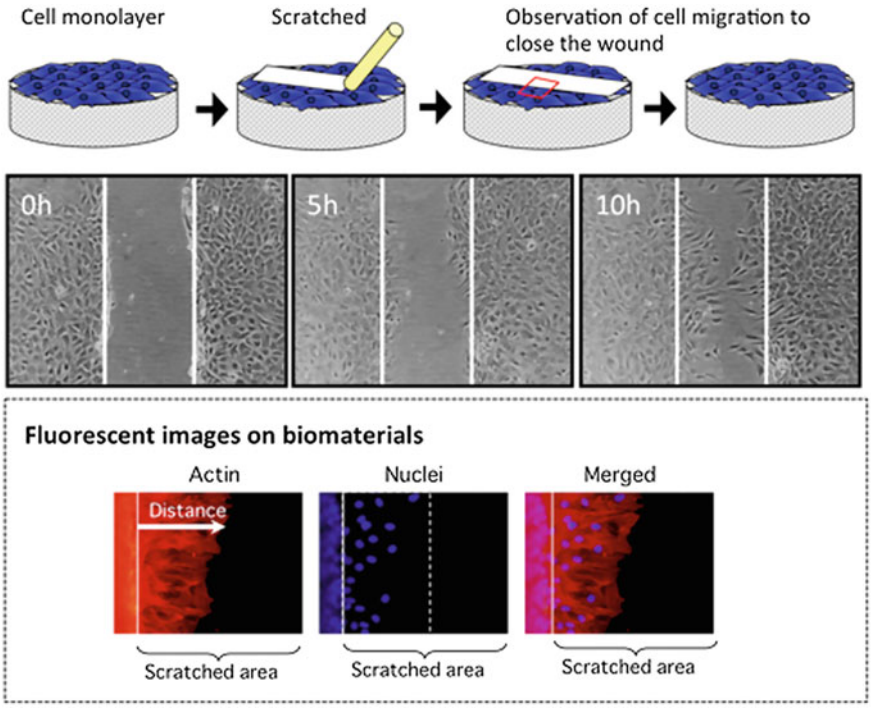

Fig. 28.8 Illustration of wound healing assay to evaluate cell migration

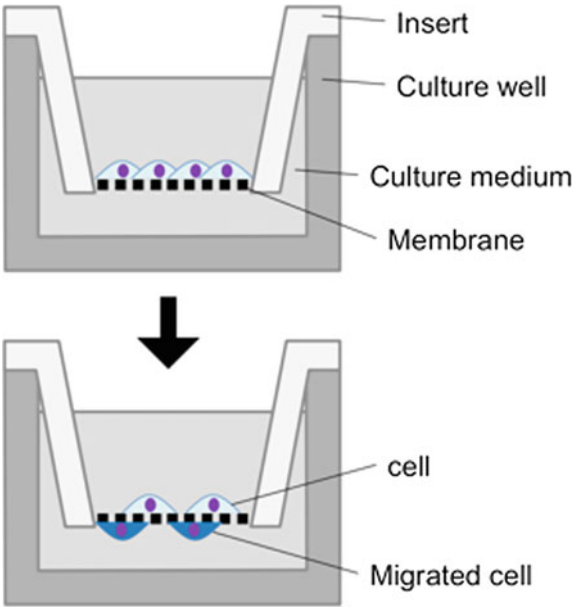

Fig. 28.9 Illustration of transwell assay to evaluate cell migration

Cytotoxicity assays are widely used in vitro toxicology studies. LDH leakage assay, neutral red assay, and MTT (3-[4,5-dimethylthiazol-2-yl]-2,5-diphenyltetrazolium bromide) (or MTS, WST) assay are the most commonly employed for the evaluation of cell viability following exposure to biomaterials. LDH assay is based on the measurement of lactate dehydrogenase activity in the conditioned medium. To loss of intracellular LDH and its release into the culture medium is an indicator or irreversible cell death due to cell membrane damage. MTT assay is another cell viability assay often used to determine cytotoxicity following exposure to biomaterials. MTT is a water-soluble tetrazolium salt, which is converted to an insoluble purple formazan by cleavage of the tetrazolium ring by succinate dehydrogenase in the mitochondria. The formazan product is impermeable to the cell membranes and therefore it accumulates in healthy cells. Neutral red assay is also used to measure cell viability. Living cells take up the neutral red, which is concentrated in the lysosomes of cells.

The choice of cell type and the maturity of the cells depends on the objective of the differentiation study. However, not all cell types are capable of differentiation in vitro. Especially, there are some differences between primary cells and cell lines. Primary cells have a finite life span and die after a certain period of time in culture. They have a variety of types depending on donors whereas cancer cell lines often come from a single patient. Primary cells are finicky to culture and can change in culture after some passages.

For instance, mesenchymal stem cells (MSCc) (Fig. 28.10a) derived from mouse bone marrow differentiate into osteoblasts and mature to make mineralized extracellular matrix (ECM) (Fig. 28.10b). MSCc cultured with differentiation factors

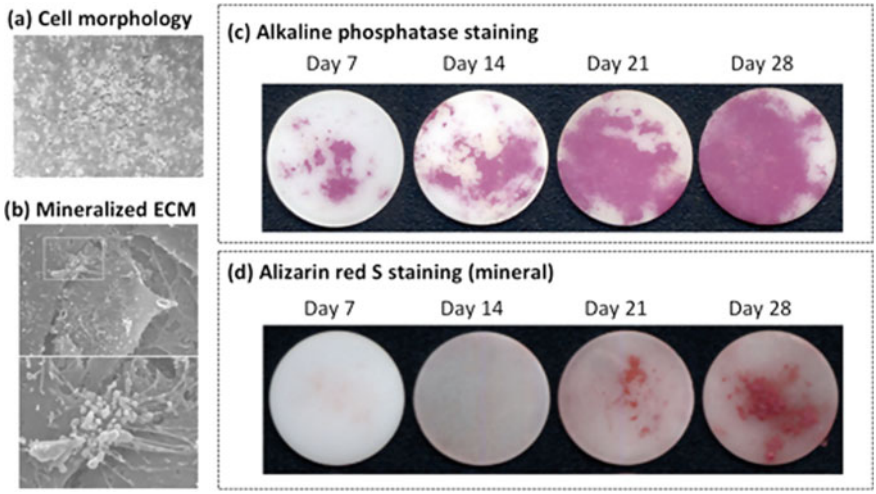

Fig. 28.10 **a** Cell morphology of mesenchymal stem cells (MSCs) derived from mouse bone marrow. **b** MSCs differentiate into mature osteoblasts to make mineralized extracellular matrix ECM). **c** MSCs cultured on biomaterials with differentiation factors differentiate into osteoblasts. They can be visualized using the staining methods of **c** alkaline phosphatase (ALP) and **d** alizarin red S

differentiate into mature osteoblasts. The osteoblasts differentiation can be characterized by staining and gene expression of molecular markers such as alkaline phosphatase (ALP), type I collagen, osteocalcin, osteopontin, bone sialoprotein, and etc. ALP (Fig. 28.10c) and calcium deposition (Fig. 28.10d) can be visualized using adequate staining methods.

References

1. D.E. Discher, P. Janmey, Y.L. Wang, Tissue cells feel and respond to the stiffness of their substrate. Science **310**, 1139 (2005)
2. J.A. Engler, S. Sen, H.L. Sweeney, D.E. Discher, Matrix elasticity directs stem cell lineage specification. Cell **126**, 677 (2006)

Chapter 29
Metallic Glasses for Biomedical Applications

Guoqiang Xie and Xingmin Wang

Abstract Bulk metallic glasses (BMGs) are promising materials for biomedical applications due to their high corrosion resistance, excellent mechanical properties, and good biocompatibility. In this chapter, recent progress in the biocompatibility evaluations of the biomedical BMGs, in particular to biomedical Ti-based BMGs and Mg-based BMGs, are summarized. Some examples about the BMGs for applications to biomedical fields such as biomedical tools, biomedical devices, and biomedical implants are described in detail.

Keywords Bulk metallic glasses · Biomedical applications · Biocompatibility · Biomedical implants · Stent · Biomedical devices

29.1 Introduction

Metallic materials owing to their high strength, high hardness, superior fracture and fatigue resistances, demonstrate a much more favorable mechanical response to biological systems than ceramic or polymer materials and are presently regarded as the materials of choice for load-bearing implant applications. To assure long life-time of the load-bearing orthopedic implants, biomaterials need to satisfy the following requirements [1, 2]: (1) They should not contain toxic or non-biocompatible elements (e.g., Ni or Be), and this places stringent restriction to the choice of alloying elements. (2) Their long service life coupled with the variety

G. Xie (✉)
School of Materials Science and Engineering, Harbin Institute of Technology (Shenzhen), Shenzhen 518055, China
e-mail: xieguoqiang@hit.edu.cn

G. Xie
Institute for Materials Research, Tohoku University, Sendai 980-8577, Japan

X. Wang
Ningbo Institute of Materials Technology & Engineering, Chinese Academy of Sciences, Ningbo 315201, Zhejiang, China

Y. Setsuhara et al. (eds.), *Novel Structured Metallic and Inorganic Materials*, https://doi.org/10.1007/978-981-13-7611-5_29

of human activity demands excellent mechanical properties, primarily high strength, and high fatigue resistance, but low elastic modulus. This is a big challenge because for crystalline materials their strength and elastic modulus tend to increase or decrease simultaneously. (3) Wear resistance is important because wear causes not only implant loosening but also harmful reactions if the wear debris is deposited in the tissue. (4) Biochemical compatibility requires the implanted materials to possess superior corrosion resistance in body environment and be bioactive. Presently, the metallic materials used for these applications are pure Ti and Ti alloys, pure Zr and Zr alloys, stainless steel and cobalt chromium alloys. Unfortunately, these materials have exhibited tendencies to fail after long-term use due to various reasons [2, 3].

Besides the joint replacements that need permanent prosthesis implantation in the human body, there are many other clinical cases, such as bone fracture, cardiovascular diseases, in which the temporary implant materials are needed. In this case, biodegradable materials are the optimal choice. Pure Mg and Mg alloys, pure Zn and Zn alloys have been studied and developed as biodegradable materials [4]. However, these conventional crystalline metals and alloys have disadvantages such as low strength, low wear resistance, poor corrosion resistance, which cause various problems in clinical application [2].

Bulk metallic glasses (BMGs) have been rapidly developed in the past two decades in many alloy systems because of their unique excellent physical, chemical, and mechanical properties compared with their conventional crystalline alloys. This is because BMGs exhibit no long-range atomic order, appearing instead as an atomically frozen liquid. The lack of atomic order yields some remarkable properties. These novel properties include superior strength, high elastic strain limit, low Young's modulus, excellent corrosion resistance, high wear resistance, excellent formability in the supercooled liquid region, and so on [5–7]. Because of these unique properties, BMGs exhibit promising potential to be applied as biomaterials and biomedical materials.

Based on the conventional crystalline biomedical metals and alloys, such as Ti alloys, Zr alloys, stainless steels, Mg alloys, Zn alloys as references, many potential biomedical BMGs have been developed. These developed biomedical BMGs can be divided into two categories, namely, bioinert group and biodegradable group. The bioinert BMGs include Ti-based BMGs, Zr-based BMGs, Fe-based BMGs (which are also known as amorphous stainless steels), and so on. The biodegradable BMGs include Mg-based BMGs, Ca-based BMGs, Zn-based BMGs, Sr-based BMGs, and so on. The alloy compositions, fabrication methods and mechanical properties of the biomedical BMGs have been described in Chap. 2 (Sect. 2.3). In this Chapter, recent progress in the biocompatibility evaluations of the biomedical BMGs are summarized. Some examples about the BMGs for applications as biomedical tools, biomedical devices, and biomedical implants are described in detail.

29.2 Biocompatibility of Biomedical Bulk Metallic Glasses

The biocompatibility is regarded as the ability of a material to perform with an appropriate biological response [8]. For a candidate biomaterial to be used in clinical applications, excellent biocompatibility is an essential property in order to avoid any adverse effect in human body. To date, our understanding of material biocompatibility has evolved mainly through empirical testing, observing the interaction of materials with cells and host tissue in vitro and in vivo. Materials can induce host responses varying from local and systemic inflammation, hypersensitivity, toxicity, and even tumorogenesis, meaning that thorough evidence of material safety is required before regulatory approval and clinical application. In this section, some results of the biocompatibility evaluations about the Ti-based BMGs and the Mg-based BMGs are summarized. The recent progress of other biomedical BMGs such as Zr-based BMGs, Fe-based BMGs, Ca-based BMGs, Zn-based BMGs and Sr-based BMGs can be referred to a recent publication [9].

29.2.1 Biocompatibility of Ti-Based Bulk Metallic Glasses

Ni- and Be-free Ti-based BMGs exhibited large glass-forming ability, high strength, high thermal stability, low-stress-corrosion cracking (SCC) susceptibility in Hanks' solution and good bioactivity [10, 11]. It makes the Ti-based BMGs become a competent candidate for application as biomaterials.

The success of an implant is determined by its integration into the tissue surrounding the material. Cell adhesion and cell spreading is an important parameter for implant engineering. Oak et al. [12] performed a series of studies about the corrosion behavior and biocompatibility of the $Ti_{45}Zr_{10}Cu_{31}Pd_{10}Sn_4$ metallic glass, and the results demonstrated that the Ti-based metallic glass exhibited good corrosion resistance and excellent biocompatibility in osteoblast culture test. Nagai et al. [13] investigated cellular behaviors responding to the Ti-based ($Ti_{40}Zr_{10}Cu_{36}Pd_{14}$) metallic glass surface irradiated with a femtosecond laser [14], which can form periodic nanostructures on the Ti-based BMG surface [15]. The results demonstrated that numbers of osteoblasts attached to the modified Ti-based metallic glass surfaces after 3 h of incubation. Li et al. [16] prepared different roughness surfaces by sandblasting using corundum with various grit sizes and investigated the effect of the surface roughness of Ti-based BMGs on the osteoblast responses. The results demonstrated that the corundum sand blasting surfaces significantly increased the surface wettability and cell attachment, cell proliferation, and alkaline phosphatase (ALP) activity. The sample surface treated by large grit corundum was more favorable for cell attachment, proliferation, and differentiation than samples treated by small grit corundum.

By implanting the Ti-based ($Ti_{40}Zr_{10}Cu_{34}Pd_{14}Sn_2$) BMG rods in the back subcutaneously and in the femoral bone of rats, followed up local tissue reaction as

well as its component ions' diffusion in local area and whole body, the biocompatibility has been in vivo evaluated [17]. There was no obvious inflammatory reaction or foreign-body response occurred around the implanted Ti-based BMG rods. No hyperemia or edema was found in either subcutaneous or bone tissue. The subcutaneous samples showed mild capsule reaction of fibroblasts without inflammatory cells invasion. The bone implanted samples of the Ti-based BMG at 12 weeks after implantation demonstrated that inflammatory reaction was totally not observed, implant dislocation or loosing is not observed in all cases, indicating excellent biocompatibility and integration to bone tissue. Histological images (Fig. 29.1) reveal that both BMG sample and Ti sample are well covered by surrounding bone tissue, and there are no abnormal findings in surrounding bone tissue. The average value of bone attachment ratio, bone formation area on surface, and bonding strength with bone in BMG group were same level with those in Ti group. No significant difference was found between the two groups. EDX elemental analysis of implant border area demonstrates no diffusion of any metallic ions in the BMG sample (Fig. 29.2). Assay of serum Cu level showed same level of serum copper which is just normal. The Ti-based BMGs displayed excellent biocompatibility in both soft tissue and hard tissue, it also showed excellent osteoconductivity when implanted in bone tissue and no metal ion diffusion was found up to 12 weeks after operation. The Ti-based BMGs should be a strong candidate for the clinic applications that require mechanical strength highly.

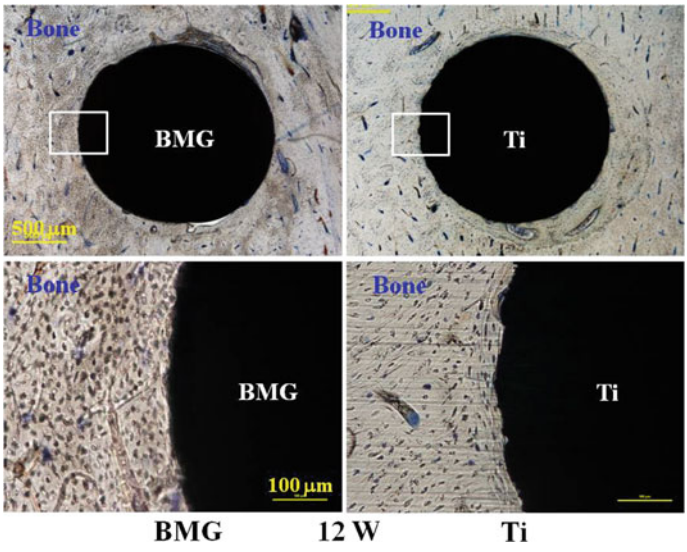

Fig. 29.1 Histological views of Ti-based BMG implant and Ti implant [17]. Both samples are well covered by surrounding bone tissue. There are no abnormal findings in surrounding bone tissue. Objective magnification of upper images is ×4 and lower images are ×20

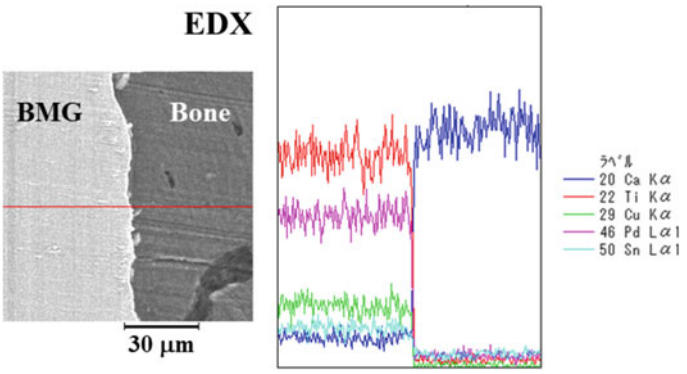

Fig. 29.2 EDX elemental analysis of implant border area [17]. No diffusion of any metallic ions in the BMG sample is found

29.2.2 Biocompatibility of Mg-Based Bulk Metallic Glasses

There are clinical advantages for certain metallic medical implants to dissolve in a controlled fashion in vivo following surgery, provided the corrosion products are not harmful, thus obviating the need for further surgery to extract the implant after it has served its function, reducing both the burden on the health system, and the associated risks toward the patient [18]. Mg and its alloys have recently attracted much interesting in applications as biodegradable materials due to their low toxicity, degradability, low density, and proper mechanical property. Series crystalline Mg alloys, such as Mg–Zn, Mg–Ca, Mg–RE systems have been designed and developed for biomedical applications [9, 18]. However, the development and deployment of biodegradable Mg alloys faces some practical challenges. First, a much higher inherent strength would be required of such an alloy since an implant's strength would naturally deteriorate gradually during the corrosion/degradation process. Next, pitting corrosion, resulting in surface defects, would likewise lead to the quick loss of the Mg alloy's strength. Third, most current Mg alloys have fast degradation rates, exceeding rates for bone healing. Finally, too-rapid corrosion can lead to implant failure before healing can complete, and the same corrosion often leads to catastrophic H_2 evolution in patient areas with poor transport mechanisms [19, 20].

On the other hand, recent studies have found that Mg-based BMGs have higher strength and lower elastic moduli than pure Mg and conventional Mg alloys. A number of Mg-based BMGs exhibited high strength, often exceeding 1000 MPa, greater than stainless steel biomedical alloys, and, in some cases, even titanium and cobalt–chrome alloys. Studies of the corrosion behavior, cellular response and tissue response of Mg–Zn–Ca BMGs demonstrated that the Mg–Zn–Ca BMGs presented more uniform corrosion morphology than conventional crystalline Mg alloys, had much lower corrosion rates, and showed higher cell viability than

conventional crystalline pure Mg [21–23]. For example, a Mg-based ($Mg_{66}Zn_{30}Ca_4$) metallic glass corroded in physiologically relevant solutions at less than half the rate of WE43 [23], a particularly corrosion resistant crystalline alloy, and at less than 20% the rate of other common Mg alloys, as shown in Fig. 29.3. Exhibiting a strength of roughly 800 MPa in both tension and compression, a high elastic strain up to 2%, and high facture toughness, the BMG alloy showed significantly improved mechanical properties over conventional Mg alloys. An elastic modulus of 45 GPa also reveals a stiffness close to that of cortical bone [24, 25]. Minor silver (Ag) or strontium (Sr) additions further enhanced the corrosion properties and strength of the alloy, as well as improving the antibacterial effect (Ag) and osteogenesis (Sr) [23, 26, 27]. Cytotoxicity testing revealed that alloy samples were able to support significant cellular activity to a high degree against a control, with increased cell viabilities up to 90%, (compared to 60% for crystalline Mg alloys), while a stimulatory effect on the rate of bone growth was also reported [22, 28–30].

In addition, animal studies were carried out in the abdominal walls and cavities (two tissue types apiece) of domestic pigs to evaluate the tissue reactions of the Mg–Zn–Ca BMGs during degradation and the hydrogen evolution in vivo. Figure 29.4 shows the evaluated results of Mg-based glass (a, c) in comparison with a crystalline Mg alloy reference sample (b, d). As shown in Fig. 29.4, results from animal studies indicate that all samples show a typical fibrous capsule foreign-body reaction (indicated by white arrows), while only the crystalline samples (implanted discs indicated by dashed lines) show pronounced hydrogen evolution (area between discs and fibrous capsules indicated by black arrows). And no tissue-imprinted hydrogen gas cavities had formed in the histological preparations of the Mg–Zn–Ca BMG samples and no inflammatory reactions were observed [21].

Despite such promising characteristics, the BMG alloys must overcome some critical stumbling blocks to be seriously considered for clinical purposes. Critical casting diameters of the initial MgZnCa BMG alloys were capped at about 5 mm, potentially restricting use to small pins and screws. Using a spark plasma sintering

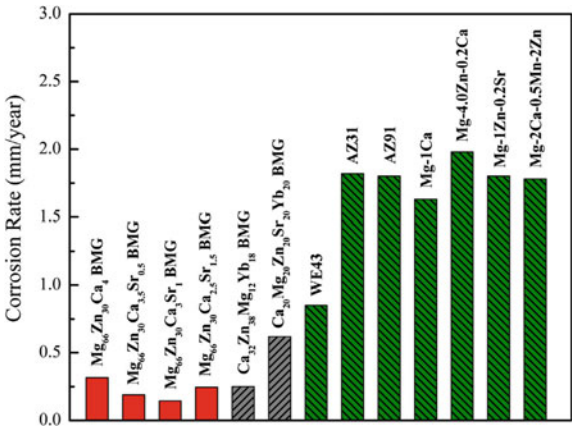

Fig. 29.3 Corrosion rates of Mg-based BMGs and Mg alloys in physiologically relevant solutions [23]

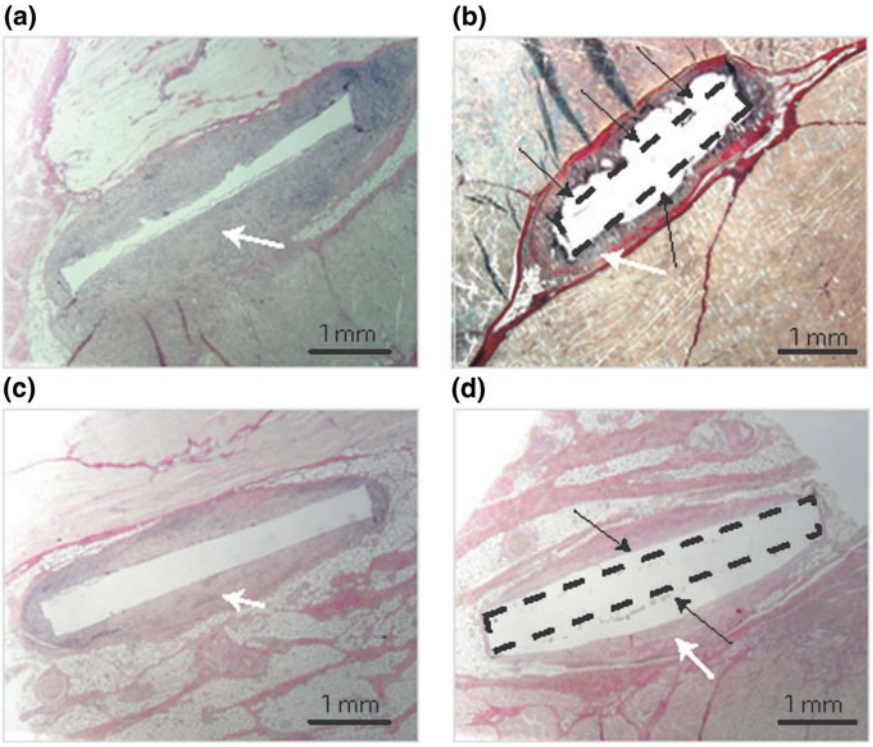

Fig. 29.4 Animal studies of Mg-based glass in comparison with a crystalline Mg alloy reference sample. Glassy $Mg_{60}Zn_{35}Ca_5$ (**a**, **c**) and crystalline Mg alloy reference (WZ21) (**b**, **d**) in two types of porcine abdominal tissue (muscle after 27 days (**a**, **b**) and subcutis after 91 days (**c**, **d**) of implantation) [21]

(SPS) technique, large sized Mg-based (Mg–Zn–Ca) BMGs and the composites with a diameter of over 15 mm have been developed [31]. The consolidated Mg-based BMGs exhibited high strength of over 450 MPa. The corrosion resistance of sintered Mg-based BMGs and the composites was evaluated to be higher than that of pure Mg and commercial Mg alloy (AZ31) in Hanks' solution.

29.3 Applications of Biomedical Bulk Metallic Glasses

Compared with conventional crystalline metals and alloys, BMGs have unique properties including superior strength, high elasticity, low Young's modulus, and excellent wear and corrosion resistances, which are attributed to the lack of grain boundaries and crystal defects that usually lead to weakening of material strength, intergranular corrosion and stress-corrosion cracking in biological environments. They have attracted increasing attention in recent years, and present great potential

in biomedical applications. Many efforts and attempts have been carried out ranging from orthopedic, cardiovascular to dental implants and fillers. As the bioinert BMGs, Ti-based, Zr-based and Fe-based BMGs with combined excellent mechanical properties and corrosion resistance have been attempted to use as biomedical devices, such as surgical blades, pacemakers, medical stapling anvils, and minimally invasive surgical devices; and biomedical implants, such as articulating surfaces, artificial prostheses and dental implants, which are needed to serve a long time in the severe human body environments. On the other hand, for the biodegradable BMGs, Mg-based, Ca-based, Zn-based and Sr-based BMGs have great potential as fracture repair materials (such as intramedullary needles, bone plates and bone screws), as well as cardiovascular stent materials, absorbable sutures, fillers around dental implants, and fillings of bone after cyst/tumor removal in arthroplasty; as they will degrade gradually in human body after completing their temporary mission (would dissolve completely upon fulfilling the mission of fixing or supporting) during which arterial/bone remodeling and healing would occur [9].

29.3.1 Surgical Tools

Due to the lack of any grain-size limitations on feature size, very sharp edges are possible to produce using BMGs. Sharpness improvement on surgical blades by using BMG and metallic glass coatings has been reported, as shown in Fig. 29.5a [9]. Low values of blade sharpness index (BSI) indicate sharper edges. The BSI on a produced ZrCuAlAgSi BMG blade was 0.24, a value of 0.23 was achieved for a martensitic steel blade coated with a thin film of the same glassy alloy, whereas the uncoated steel blade value was 0.34 [32]. A surgical blade coated with an Fe-based

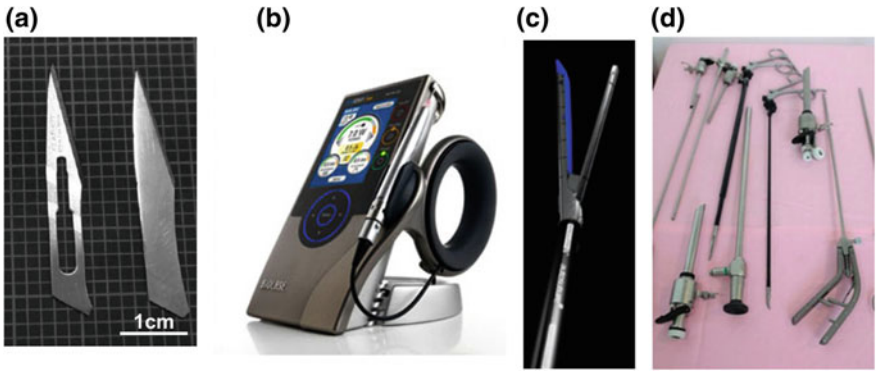

Fig. 29.5 Illustrations of biomedical devices made of BMGs [9]. **a** Commercial martensitic steel surgical blade coated with ZrCuAlAgSi metallic glass film (left) and ZrCuAlAgSi BMG surgical blade (right). **b** The ezlase diode dental laser system, from Biolase Technology, uses Liquidmetal in its housing. **c** BMG medical stapling anvils. **d** Liquidmetal alloys in minimally invasive medical devices

metallic glass thin film, demonstrated a BSI value of 0.28, while also displaying a significant increase (65%) in blade durability, due to its extreme hardness (1200 Hv) [33]. The local roughness of all coated blades was extremely low (<5 nm). Figure 29.5b shows an ezlase diode dental laser system using metallic glass as its housing, which is a handheld pen laser for dental procedures, attracted by the unique strength, ability to be molded to a thin wall thickness, and ornamental finish of metallic glass. Figure 29.5c is a medical stapling anvil, which considers the top 4 advantages BMGs providing: (1) Superior as-cast surface finishes; (2) Pocket-to-pocket dimensional accuracy; (3) Molded-in camber for proper alignment to staple cartridge when clamped to tissue; (4) Lot-to-lot variability limited to mold cavity-to-cavity variability. Figure 29.5d shows some minimally invasive medical devices, with enhanced precision, durability, repeatability and more convenient manufacturing processing [9].

When cells stick to medical devices they can cause potentially lethal problems like bacterial infections, cancer metastases, and blood clots. To prevent cells of all kinds from hanging out in medical equipment, a novel anti-adhesive coating, which is a zirconium-based thin film metallic glass (TFMG), have recently developed [34]. The coating can be easily sputtered onto a variety of medical tools. As shown in Fig. 29.6a, the TFMG-coated needle shows a nonsticky characteristic with muscles tissue, whereas the muscle tissue is shown to stick on titanium or titanium-nitride coated needles and bare needles [34].

Utilizing high wear resistance of the metallic glass, high strength medical scissor was also fabricated, as shown in Fig. 29.6b [35].

Like other glassy materials, such as oxide glasses and amorphous polymers, BMGs have a wide supercooled liquid range when heated from room temperature. Within this temperature range, BMGs transform into a viscous supercooled liquid with significant softening and, thus, can be shaped by Newtonian viscous flow under very small applied forces. The is unique property of glassy materials endows BMGs with extraordinary formability and superplasticity, comparable to those of polymers and window glasses. BMGs are quite stable in the supercooled state and, after thermal processing, can be slowly cooled back to the strong glassy state with negligible volume shrinkage [36]. The is outstanding thermal formability of BMGs has been utilized to fabricate biomedical devices. Figure 29.7 shows the fabricated medical bipolars [35]. BMGs were used in the tip portion of the bipolars. Utilizing the excellent superplasticity of metal glass, a complex pattern was made at the tip portion of the bipolars, which can prevent effectively cells slip.

29.3.2 Stents

Besides the above mentioned biomedical surgical tools and devices, BMGs are promising candidates as biomedical implants. It has been reported that BMGs could increase the strength, corrosion resistance, biocompatibility and longevity of

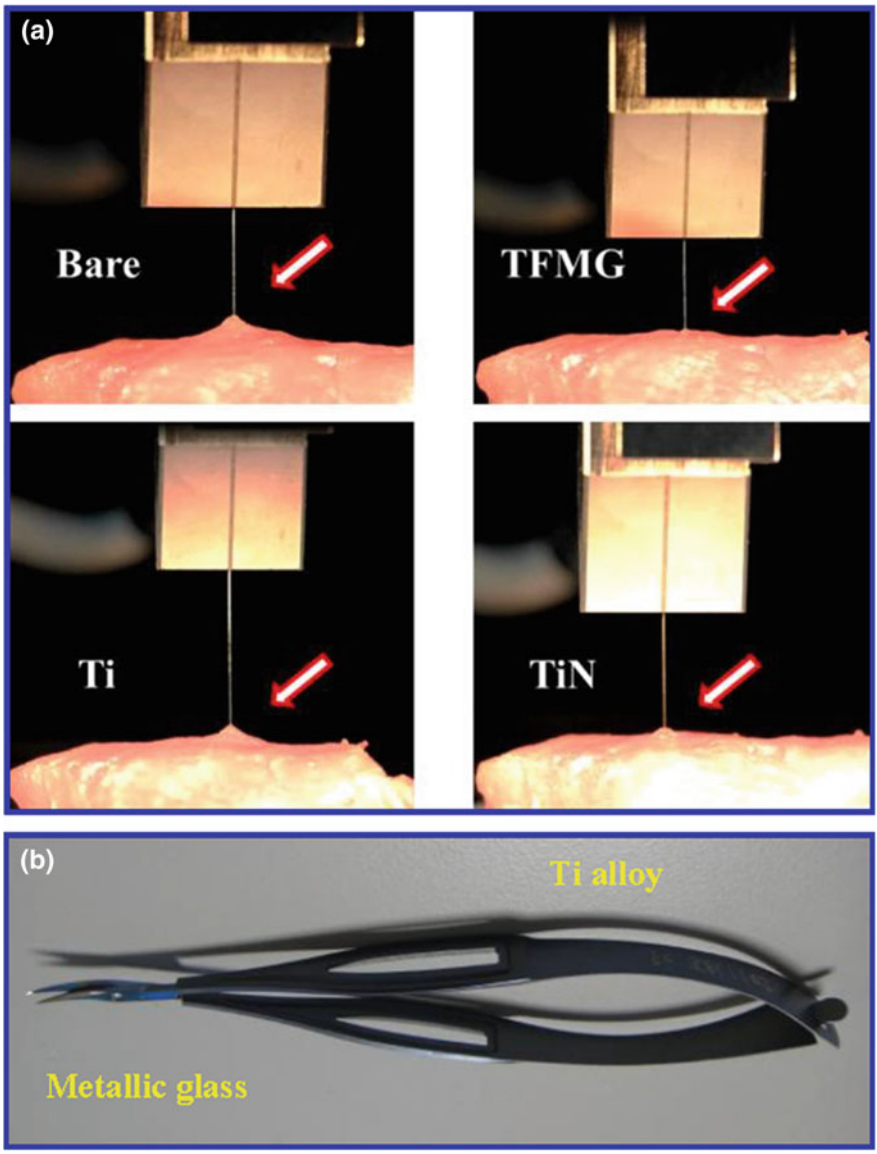

Fig. 29.6 Illustrations of biomedical devices made of metallic glasses. **a** Medical syringe coated with thin film metallic glass (TFMG). These images show an experiment testing the retraction of a needle from porcine tissues. The TFMG-coated needle shows a nonsticky characteristic with muscles tissue, whereas the muscle tissue is shown to stick on titanium or titanium-nitride coated needles and bare needles [34]. **b** Medical scissor using metallic glass in the tip portion [35]

biomedical implants, which are aimed to be used as cardiovascular stents [37] and orthopedic implants (such as bone plates, bone screws, articulating surfaces, artificial prostheses, absorbable sutures, dental implants, and fillers) [38].

Fig. 29.7 Medical bipolars made of BMGs in the tip portion with a complex pattern [35]

The material creating the stent must be flexible, supportive, capable of expansion, biocompatible, and easily producible. The vast majority of stents are made of a stainless steel framework, which is not completely biocompatible and is

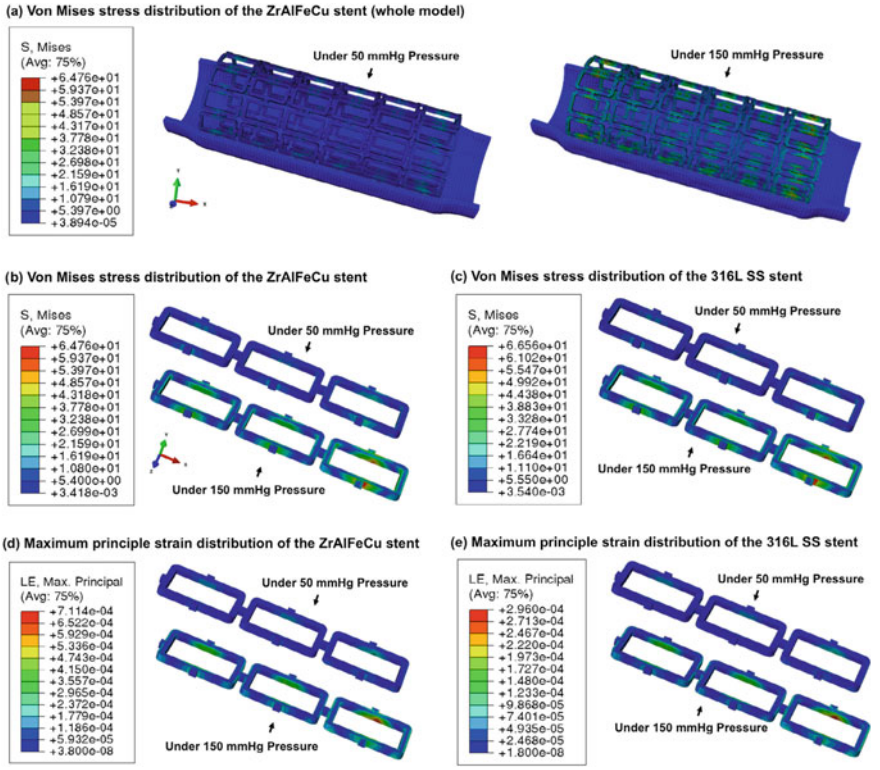

Fig. 29.8 Finite element stress analysis of a Zr-based BMG (**a**, **b**, **d**) and 316L stainless steel (**c**, **e**) stent under pressure. Note significantly increased strain values in BMG members, when compared with stainless steel members at the same applied stresses (**d**) versus (**e**) [37]

associated with high occurrence of restenosis. Ideally, stents should induce minimal injury to vessels following deployment and should not activate coagulation and thrombosis. In addition, it is desirable that they are compliant with the blood vessel biomechanics. BMGs are 3–4 times more flexible than materials currently used for stent applications, suggesting enhanced compliance [39]. A finite element modeling has been used to predict the relevant mechanical behavior of a ZrAlFeCu BMG in vivo [37]. The BMG alloy, developed to avoid Ni and Be, has shown improved hardness and strength [37] over 316L SS (roughly twice, in both cases), which allows for stent struts to be markedly thinner-shown to significantly reduce restenosis [40] and improve the deliverability of the device. The finite element results (as shown in Fig. 29.8) show that the high elastic limit and low modulus allow a stent to flex more (facilitated by the thinner members) and deform during heartbeats. Comparisons of the mechanical properties between stented and unstented arteries showed a better match over a 316L stent—compliance mismatch has been shown to be correlated with intimal hyperplasia, which also leads to restenosis [41].

29.4 Summary

Bulk metallic glasses (BMGs) have become candidate materials for biomedical applications. Two types of the BMGs for medical applications have emerged, in which some BMGs such as Ti-based, Zr-based and Fe-based BMGs are being developed for permanent devices, while another such as Mg-based, Ca-based, Zn-based and Sr-based BMGs are showing promise in biodegradable implants. These BMGs have presented excellent biocompatibility. The bioinert BMGs have been attempted to use as biomedical devices, such as surgical blades, pacemakers, medical stapling anvils, and minimally invasive surgical devices; and biomedical implants, such as articulating surfaces, artificial prostheses and dental implants. On the other hand, the biodegradable BMGs show great potential as fracture repair materials (such as intramedullary needles, bone plates and bone screws), as well as cardiovascular stent materials, absorbable sutures, fillers around dental implants, and fillings of bone after cyst/tumor removal in arthroplasty.

References

1. M. Long, H.J. Rack, Biomaterials **19**, 1621 (1998)
2. M. Geetha, A.K. Singh, R. Asokamani, A.K. Gogia, Prog. Mater. Sci. **54**, 397 (2009)
3. M. Niinomi, Metall. Mater. Trans. A **33**, 477 (2002)
4. Y.F. Zheng, X.N. Gu, F. Witte, Mater. Sci. Eng., R **77**, 1 (2014)
5. A. Inoue, A. Takeuchi, Acta Mater. **59**, 2243 (2011)
6. A. Inoue, Acta Mater. **48**, 279 (2000)
7. W.L. Johnson, MRS Bull. **24**, 42 (1999)

8. J. Black, *Biological Performance of Materials: Fundamentals of Biocompatibility* (CRC Press, Taylor & Francis, New York, 2006)
9. H.F. Li, Y.F. Zheng, Acta Biomater. **36**, 1 (2016)
10. G.Q. Xie, F.X. Qin, S.L. Zhu, Mater. Trans. **54**, 1314 (2013)
11. F.X. Qin, S.L. Zhu, Z.H. Dan, A. Kawashima, G.Q. Xie, J. Alloys Compd. **615**, S123 (2014)
12. J.J. Oak, G.W. Hwang, Y.H. Park, H. Kimura, S.Y. Yoon, A. Inoue, J. Biomed. Sci. Eng. **4**, 384 (2009)
13. A. Nagai, K. Yamashita, S. Murayama, N. Matsushita, K. Okada, N. Abe, M. Tsukamoto, K. S. Son, X.M. Wang, G.Q. Xie, A. Inoue, Trans. JWRI **39**, 306 (2010)
14. M. Tsukamoto, K. Asuka, H. Nakano, M. Hashida, M. Katto, N. Abe, M. Fujita, Vacuum **80**, 1346 (2006)
15. K.S. Son, E.S. Park, G.Q. Xie, X.M. Wang, M. Tsukamoto, A. Inoue, in *Proceedings of the Visual-JW2010*, ed. by Joining and Welding Research Institute, Osaka University (2010), p. 336
16. H.F. Li, Y.B. Wang, Y.F. Zheng, J.P. Lin, J. Biomed. Mater. Res. B **100**, 1721 (2012)
17. R. Kokubun, W. Wang, S.L. Zhu, G.Q. Xie, S. Ichinose, S. Itoh, K. Takakuda, Bio-med. Mater. Eng. **26**, 9 (2015)
18. H. Waizy, J.M. Seitz, J. Reifenrath, A. Weizbauer, F.W. Bach, A. Meyer-Lindenberg, B. Denkena, H. Windhagen, J. Mater. Sci. **48**, 39 (2013)
19. F. Witte, V. Kaese, H. Haferkamp, E. Switzer, A. Meyer-Lindenberg, C.J. Wirth, H. Windhagen, Biomaterials **26**, 3557 (2005)
20. M.P. Staiger, A.M. Pietak, J. Huadmai, G. Dias, Biomaterials **27**, 1728 (2006)
21. B. Zberg, P.J. Uggowitzer, J.F. Löffler, Nat. Mater. **8**, 887 (2009)
22. X.N. Gu, Y.F. Zheng, S.P. Zhong, T.F. Xi, J.Q. Wang, W.H. Wang, Biomaterials **31**, 1093 (2010)
23. H. Li, S. Pang, Y. Liu, L. Sun, P.K. Liaw, T. Zhang, Mater. Des. **67**, 9 (2015)
24. Y.Y. Zhao, E. Ma, J. Xu, Scr. Mater. **58**, 496 (2008)
25. B. Zberg, E.R. Arata, P.J. Uggowitzer, J.F. Löffler, Acta Mater. **57**, 3223 (2009)
26. F.X. Qin, G.Q. Xie, Z.H. Dan, S.L. Zhu, I. Seki, Intermetallics **42**, 9 (2013)
27. H. Li, S. Pang, Y. Liu, P.K. Liaw, T. Zhang, J. Non-Cryst. Solids **427**, 134 (2013)
28. J.D. Cao, P. Martens, K.J. Laws, P. Boughton, M. Ferry, J. Biomed. Mater. Res. B **101**, 43 (2013)
29. Z. Li, X. Gu, S. Lou, Y. Zheng, Biomaterials **29**, 1329 (2008)
30. Y.B. Wang, X.H. Xie, H.F. Li, X.L. Wang, M.Z. Zhao, E.W. Zhang, Y.J. Bai, Y.F. Zheng, L. Qin, Acta Biomater. **7**, 3196 (2011)
31. F.X. Qin, Z.H. Dan, G.Q. Xie, Mater. Sci. Forum **783–786**, 1931 (2014)
32. P.H. Tsai, Y.Z. Lin, J.B. Li, S.R. Jian, J.S.C. Jang, C. Li, J.P. Chu, J.C. Huang, Intermetallics **31**, 127 (2012)
33. J.S.C. Jang, P.H. Tsai, A.Z. Shiao, T.H. Li, C.Y. Chen, J.P. Chu, J.G. Duh, M.J. Chen, S.H. Chang, W.C. Huang, Intermetallics **65**, 56 (2015)
34. http://www.newswise.com/articles/cleaner-safer-medical-equipment-with-metallic-glass-coatings
35. http://amdi-pro.imr.tohoku.ac.jp/achievements4.html
36. M.W. Chen, NPG Asia Mater. **3**, 82 (2011)
37. L. Huang, C. Pu, R.K. Fisher, D.J.H. Mountain, Y. Gao, P.K. Liaw, W. Zhang, W. He, Acta Biomater. **25**, 356 (2015)
38. J.A. Joseph Jr., D.E. Parsell, Bulk metallic glass medical instruments, implants, and methods of using same. US Patent 20,020,162,605 (2002)
39. J. Schroers, G. Kumar, T.M. Hodges, S. Chan, T.R. Kyriakides, JOM **61**, 21 (2009)
40. B. O'Brien, W. Carroll, Acta Biomater. **5**, 945 (2009)
41. J.L. Berry, E. Manoach, C. Mekkaoui, P.H. Rolland, J.E. Moore Jr., A. Rachev, J. Vasc. Interv. Radiol. **13**, 97 (2002)

Chapter 30
Low-Young's-Modulus Materials for Biomedical Applications

Mitsuo Niinomi and Masaaki Nakai

30.1 Introduction

Young's moduli of metallic biomaterials for implant devices such as artificial hip joints, bone plates, intramedullary rods, and rods for spinal fixation devices should be similar to that of cortical bone to prevent stress shielding [1]. Titanium alloys are advantageous because of their low Young's modulus, which is close to that of bone. Titanium alloys are classified based on the dominant phase or phases present: α, (α + β) and β. The crystal structures of α- and β-phases are hexagonal closed packed (hcp) and body centered cubic (bcc). Since the atomic density of the bcc structure is smaller than that of the hcp structure, Young's modulus is expected to be lower in the β-type titanium alloy than in the α- and (α + β)-type titanium alloys. Recently, many low-Young's-modulus β-type titanium alloys for biomedical applications have been developed or are under study [2].

In light of this, the design, manufacturing process, mechanical properties, chemical properties, biological properties, and surface modification of new titanium alloys with low Young's modulus intended to prevent stress shielding are reviewed.

M. Niinomi (✉)
Institute for Materials Research, Tohoku University, Sendai, Japan
e-mail: niinomi@imr.tohoku.ac.jp

Graduate School of Science and Technology, Meijyo University, Nagoya, Japan

Graduate School of Engineering, Division of Materials and Manufacturing Science, Osaka University, Osaka, Japan

Institue of Materials and Systems for Sustainability, Nagoya University, Nagoya, Japan

M. Nakai
Faculty of Science and Technology, Kindai University, Osaka, Japan

Y. Setsuhara et al. (eds.), *Novel Structured Metallic and Inorganic Materials*, https://doi.org/10.1007/978-981-13-7611-5_30

30.2 Selection of Alloying Elements

Ti-6Al-4V (Ti64) ELI is the most widely used orthopedic titanium alloy because of its excellent corrosion resistance and good mechanical properties. In the case of Ti64 ELI, the toxic vanadium (V) ions released from metal implants severely affect the long-term biocompatibility of these alloys [3]. In addition, it has been reported that aluminum (Al) ions are neurotoxic and inhibit bone mineralization [4]. Steinemann [5] has reported on the cytotoxicity of pure metals and the relationship between biocompatibility and polarization resistance of typical pure metals and surgical implant materials. Results of this study are summarized in Fig. 30.1. Ti, Nb, Ta, and Zr exhibit excellent biocompatibility and belong to the loose connective vascularized (vital) group in the type of tissue reaction. Kawahara [6] and Okazaki et al. [7] has reported that Ti, Nb, Ta, Zr, Sn, Cr, Pd, In, Au, and Si exhibit low cytotoxicity as shown in Fig. 30.2. The allergy problem should also be taken into account. Figure 30.3 [8] shows the rate of metallic allergy for each pure metal. Hg, Ni, Co, Sn, Pd, and Cr are high-risk elements from the viewpoint of allergy problems. Ni, in particular, is a high-risk element for allergy problems. Adding Si to

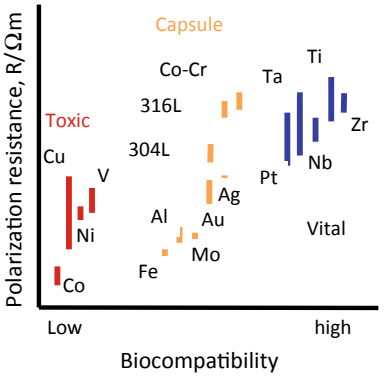

Fig. 30.1 Corrosion resistance and biocompatibility of representative pure metals and metallic biomaterials

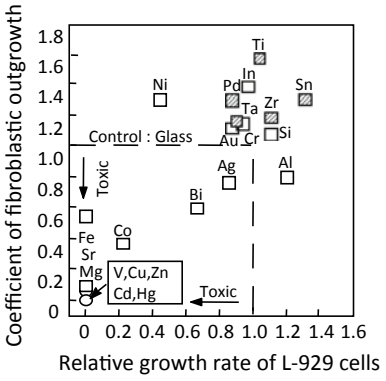

Fig. 30.2 Cyto-toxicity of pure metals

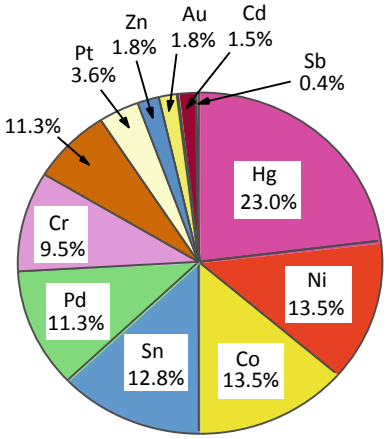

Fig. 30.3 Rate of metallic allergy of each pure metal

titanium results in a brittle alloy. Finally, Nb, Ta, and Zr are judged to be nontoxic and allergy-free elements. Consequently, these elements are selected for designing β-type titanium alloys with lower Young's moduli, greater strength, and greater corrosion resistance.

30.3 Design of Low-Young's-Modulus Titanium Alloys for Biomedical Applications

Employing a molecular orbital method, electronic structures were calculated for bcc Ti alloyed with a variety of elements [9]. Two alloying parameters were determined theoretically. One is the bond order (hereafter referred to as *Bo*), which is a measure of the covalent bond strength between Ti and the alloying element. The other is the metal d-orbital energy level (*Md*), which correlates with the electronegativity and the metallic radius of elements. For alloys, the average values of *Bo* and *Md* are defined by taking the compositional averages of the parameters and are denoted as $\bar{Bo}$ and $\bar{Md}$, respectively. By plotting the calculated values of $\bar{Bo}$ and $\bar{Md}$ for practical titanium alloys, the areas of α-, (α + β)- and β-type titanium alloys are separated clearly on the $\bar{Bo}$ and $\bar{Md}$ map, as shown in Fig. 30.4 [9, 10]. The values of Young's moduli of practical titanium alloys are also plotted, and the direction for lowering Young's modulus is defined by the arrow shown in the map. The alloy position moves in the $\bar{Bo}$–$\bar{Md}$ map as the content of Nb, Ta or Zr varies as also shown in Fig. 30.4. The target values of $\bar{Bo}$ and $\bar{Md}$ are in the dotted area on the map. As a result, the composition of the target alloy is Ti-29Nb-13Ta-4.6Zr (hereafter TNTZ).

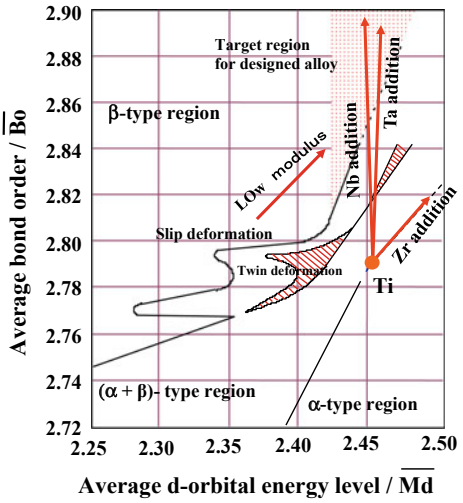

Fig. 30.4 Phase stability index diagram based on *Bo* and *Md* parameters, and low Young's modulus direction

30.4 Manufacturing Process of Designed Alloy

An ingot of TNTZ, approximately 20 kg in mass, can be fabricated by the levitation casting (Levicast) method, which is schematically shown in Fig. 30.5 [11].

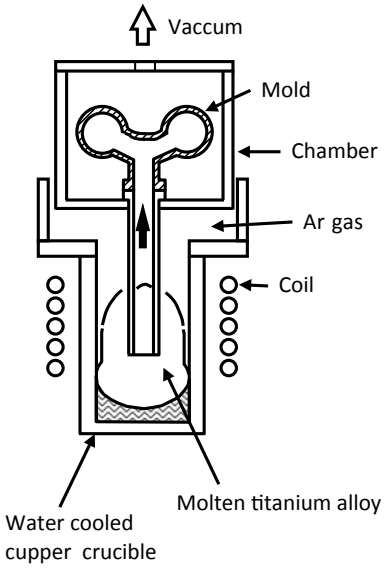

Fig. 30.5 Schematic illustration of Levicast method

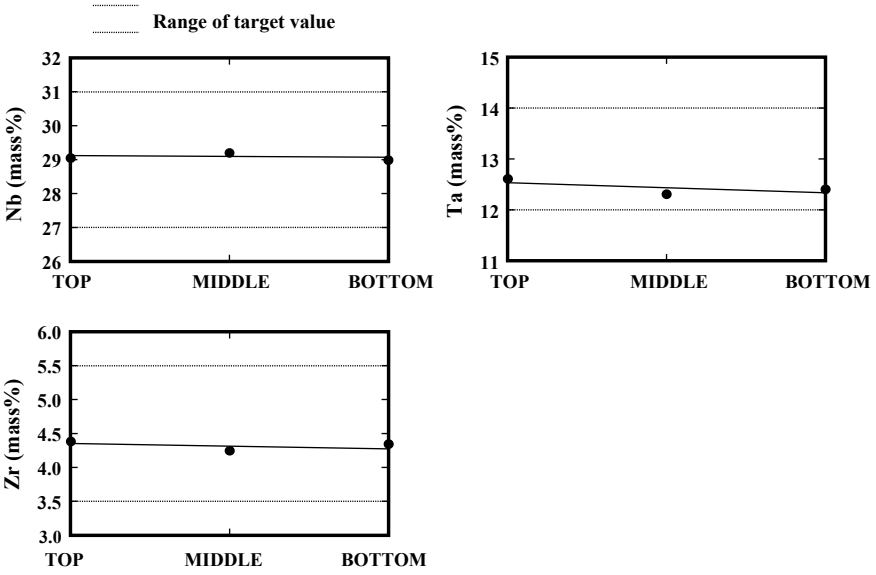

Fig. 30.6 Distribution of Nb, Ta or Zr from top through bottom of ingot of Ti-29Nb-13Ta-4.6Zr

30.5 Distribution of Alloying Elements in Ingot

The alloy contains elements Ta and Nb that have greater specific gravity and higher melting points than those of Ti. Therefore, there is a possibility for the elements to segregate. The distribution of each element should be checked. The distribution of each element from the top through the bottom of the ingot is shown in Fig. 30.6 [12]. It is clear that each element is distributed homogeneously from the top of the ingot to the bottom, and is in the range of target content value.

30.6 Mechanical Properties

30.6.1 Young's Modulus

The Young's modulus of TNTZ samples subjected to various heat treatments and thermomechanical treatments are compared with those of Ti-6Al-4V ELI and bone in Table 30.1 [13]. The Young's modulus of TNTZ is approximately 60 GPa when it is subjected to solution treatment (ST) followed by water quenching, but it is approximately 100 GPa close to that of Ti-6Al-4V ELI, which has Young's modulus of approximately 110 GPa when the sample is subjected to aging treatment. The lowest Young's modulus of approximately 55 GPa is obtained for TNTZ samples subjected to cold working after ST followed by water quenching, but it is

Table 30.1 Young's moduli of (α + β)-type Ti-6Al-4V ELI, β-type Ti-29Nb-13Ta-4.6Zr (TNTZ), and cortical bone

Material	Young's modulus (GPa)
Ti-6Al-4V ELI (ST)	110
Ti-29Nb-13Ta-4.6Zr	
ST	63
ST + aged at 673 K for 3.6 ks	97
ST + CW	55–60
Cortical bne	10–30

ST Solution treatment followed by water quenching
AC Air cooling after solution treatment
CW Cold working

still higher than that of the bone (approximately 10–30 GPa). Further reduction of Young's modulus is required.

30.6.2 Static Strength and Ductility

The lowest Young's modulus of the β-type titanium alloy is obtained under solution-treated conditions. Therefore, its strength is generally poor, and an increase in strength is required while maintaining a low Young's modulus. Static strength characteristics, such as the tensile strength, can be improved by mechanisms such as work hardening, grain refinement strengthening, precipitation strengthening, and distribution strengthening. One of the best ways to increase tensile strength while maintaining a low value for Young's modulus is by introducing numerous dislocations by ordinal severe cold working, such as cold rolling and cold swaging, and special severe cold working such as high-pressure torsion (HPT), accumulated rolling bonding (ARB), and equal channel angular pressing (ECAP) [14].

The relationships between tensile properties and working ratio of TNTZ subjected to cold working by general cold swaging are shown in Fig. 30.7 [15]. The relationships between Young's modulus and working ratio of TNTZ subjected to cold working by general cold swaging are also shown in Fig. 30.7 [15]. The tensile strength and the 0.2% proof strength increase with increasing working ratio. They reach the levels of those of Ti-6Al-4V ELI (tensile strength of approximately 800 MPa) with good elongation for TNTZ subjected to cold swaging. Nearly the same trend has been reported for TNTZ in the case of general cold rolling, but, in that case, the sample elongation decreases with increasing cold working ratio. The Young's modulus of TNTZ subjected to cold swaging is almost constant with increasing working ratio. In the case of cold rolling, Young's modulus of TNTZ decreases at high working ratios (as shown in Fig. 30.8 [16]) because of the formation of texture.

Figure 30.9 [17] shows the tensile properties of TNTZ subjected to HPT ($TNTZ_{HPT}$) as a function of the rotation number N, along with those of TNTZ subjected to solution treatment and severe cold rolling ($TNTZ_{CR}$). The tensile

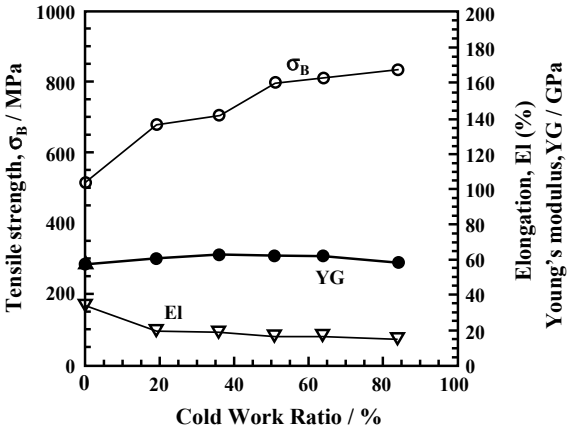

Fig. 30.7 Tensile properties of cold swaged bar as a function of cold working ratio

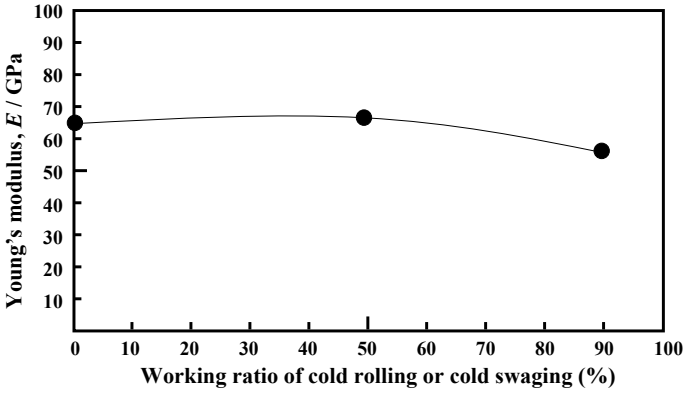

Fig. 30.8 Young's modulus of TNTZ subjected to cold rolling as a function of working ratio

strength of TNTZ subjected to HPT increases significantly with increasing rotation number, but the elongation decreases with increasing. The Young's modulus is almost constant with increasing rotation number, decreasing only marginally as shown in Fig. 30.10 [17].

30.6.3 Dynamic Strength and Ductility

The dynamic strength, i.e., the fatigue strength, of the severe cold-worked TNTZ did not improve as compared to that of the TNTZ subjected to solution treatment [18]. However, the fatigue strength improved considerably when aging treatment was provided after the solution treatment or after thermomechanical processing

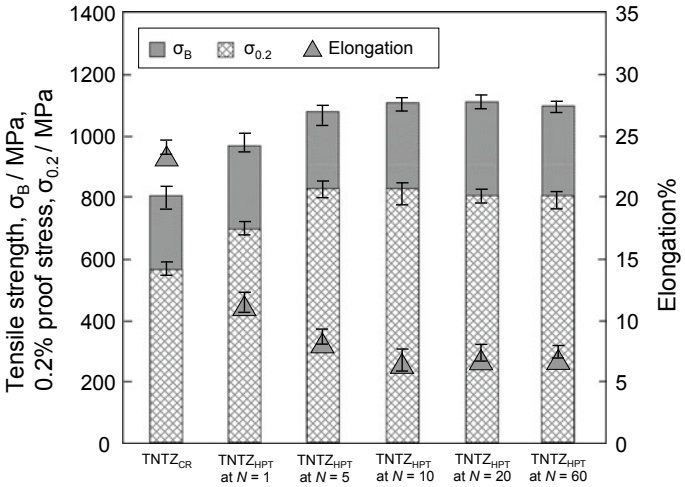

Fig. 30.9 Tensile properties of $TNTZ_{CR}$ and $TNTZ_{HPT}$ at N = 1–60

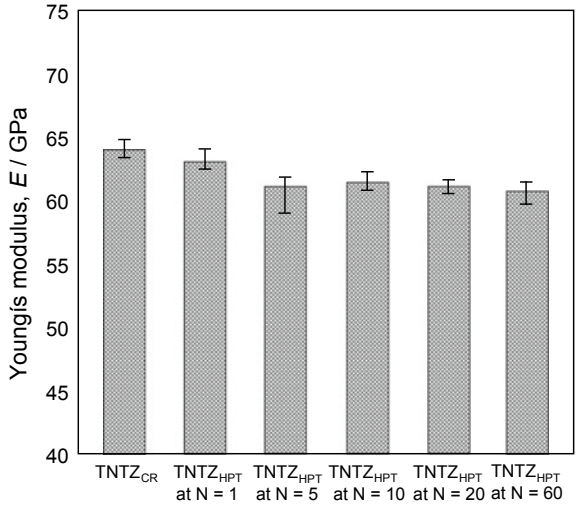

Fig. 30.10 Young's moduli of $TNTZ_{ST}$, $TNTZ_{CR}$ and TNT_{HPT} at N = 1–60

including severe cold working and aging treatment. The α phase or ω phase precipitates in the β-matrix phase because of the aging treatment.

The ω-phase precipitation significantly increases the strength and Young's modulus as compared to α-phase precipitation, although the ω phase enhances the brittleness of the alloy. Therefore, a small amount of the ω-phase precipitation is expected to improve the fatigue strength of TNTZ while maintaining a low Young's modulus. For this purpose, short-time aging at fairly low temperatures, which enhances a small amount of the ω-phase precipitation, is effective. Figure 30.11

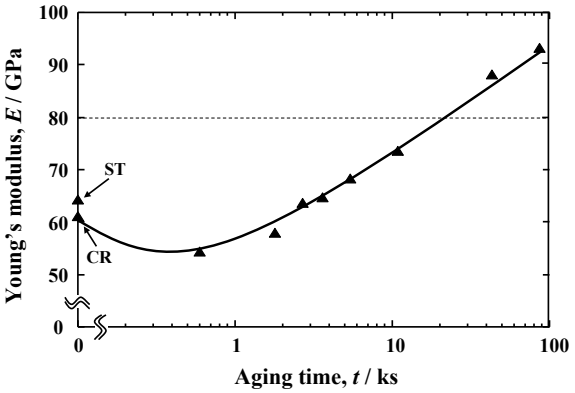

Fig. 30.11 Young's moduli of ST, CR, and AT samples as a function of aging time

[19] shows Young's moduli of TNTZ subjected to ST, severe cold rolling (CR), and aging after cold rolling at 573 K as a function of aging time (AT). For up to approximately 10.8 ks of aging time, Young's modulus is below 80 GPa, which is a tentative target value for a low Young's modulus. Figure 30.12 [19] shows fatigue properties in the form of S-N curves for TNTZ subjected to ST, severe cold rolling (CR), and aging for 3.6 ks and 10.8 ks at 573 K. The fatigue strength of TNTZ is improved by aging treatment for 10.8 ks, while Young's modulus remains lower than 80 GPa. The TEM micrograph of a sample with an AT of 10.8 ks shows the ω-phase distribution. We conclude that it is possible to effectively exploit a small amount ω phase precipitation; short-time aging at relatively low temperatures improves the fatigue strength of TNTZ while maintaining a low Young's modulus.

The addition of a small amount of ceramics particles in the matrix is also expected to improve the fatigue strength of β-type titanium alloys while maintaining a low Young's modulus. Figure 30.13 [20] shows Young's modulus of TNTZ with TiB_2 or Y_2O_3 additions subjected to severe cold rolling (TNTZ-B_{CR} or TNTZ-Y_{CR}); data are shown as a function of B or Y concentration. Young's

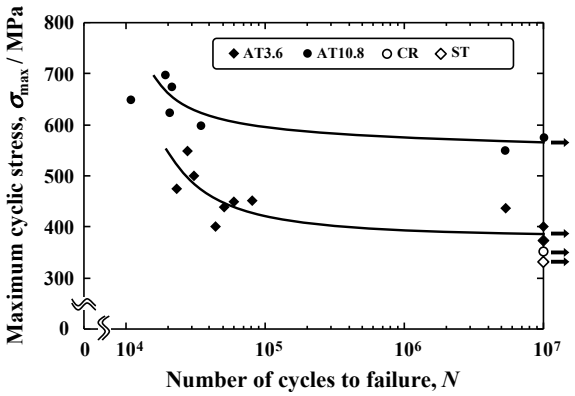

Fig. 30.12 Fatigue properties of AT3.6 and AT10.8 samples obtained in this study and those of ST and CR samples reported previously

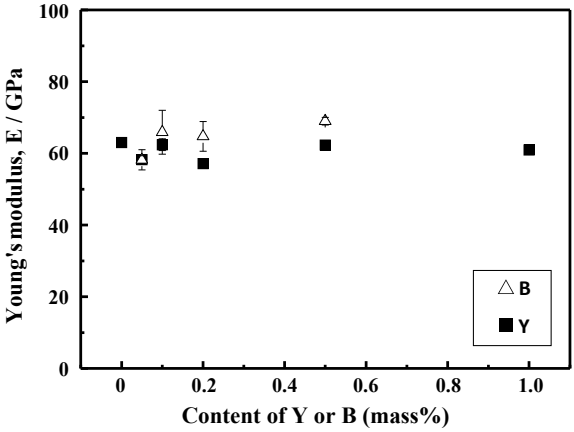

Fig. 30.13 Young's modulus as a function of Y or B concentration in TNTZ-B_{CR} or TNTZ-Y_{CR}

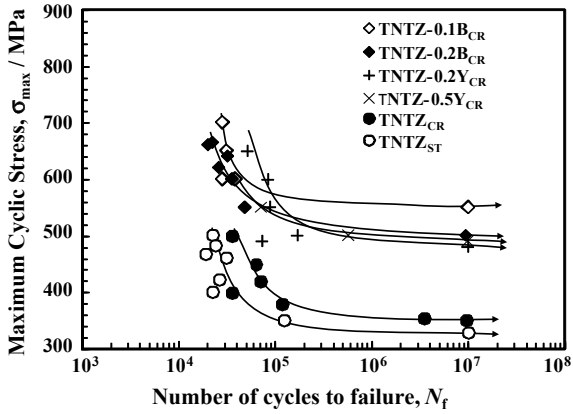

Fig. 30.14 S-N curves of TNTZ with TiB_2 or Y_2O_3 additions subjected to cold rolling after solution treatment along with those of TNTZ subjected to solution treatment or cold rolling after solution treatment

modulus is nearly constant with increasing B or Y concentration and is around 60 GPa. Figure 30.14 [20] shows the S-N curves for TNTZ with 0.1 and 0.2% B concentration or 0.2 and 0.5% Y concentrations subjected to cold rolling after solution treatment (TNTZ-0.1B_{CR} and TNTZ-0.2B_{CR} or TNTZ-0.2Y_{CR} and TNTZ-0.5Y_{CR}, respectively) along with those of TNTZ subjected to solution treatment ($TNTZ_{ST}$) or cold rolling after solution treatment ($TNTZ_{CR}$). The fatigue strength of TNTZ is improved by adding TiB_2 or Y_2O_3.

30.7 Titanium Alloys with Low and Adjustable Young's Modulus

The amount of springback is small for alloys with high Young's modulus as compared to that of alloys with low Young's modulus (Fig. 30.15 [21]). A solution has been found to address the problem of high springback in the form of a β-type

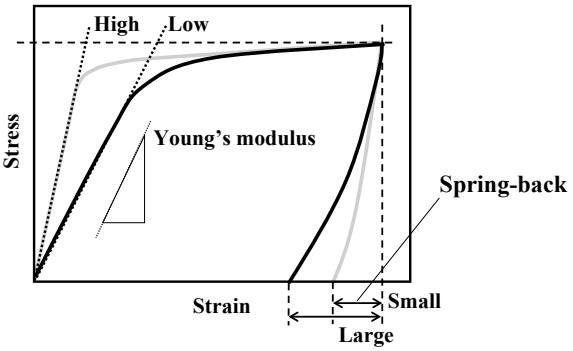

Fig. 30.15 Schematic explanation of relationship between Young's modulus and springback

titanium alloy having a low Young's modulus that increases in value only at the deformed part. This will reduce springback and fully satisfy the low Young's modulus requirement. This is called a self-adjustable Young's modulus. In general, Young's modulus of metals and alloys is not drastically changed by deformation. However, in the case of certain metastable β-type titanium alloys, nonequilibrium phases, such as α′, α″, and ω phases appear in the β matrix during deformation. If Young's modulus of the deformation-induced phase is higher than that of the original β phase, Young's modulus of only the deformed part of the implant rod increases but that of the nondeformed part remains low as schematically shown in Fig. 30.16 [21]. In orthopedic surgical procedures on the spine, the implant rod is bent by the surgeons so that it corresponds with the curvature of the spine. Therefore, if a suitable titanium alloy is employed as the implant rod material, springback can be suppressed by the deformation-induced phase transformation that

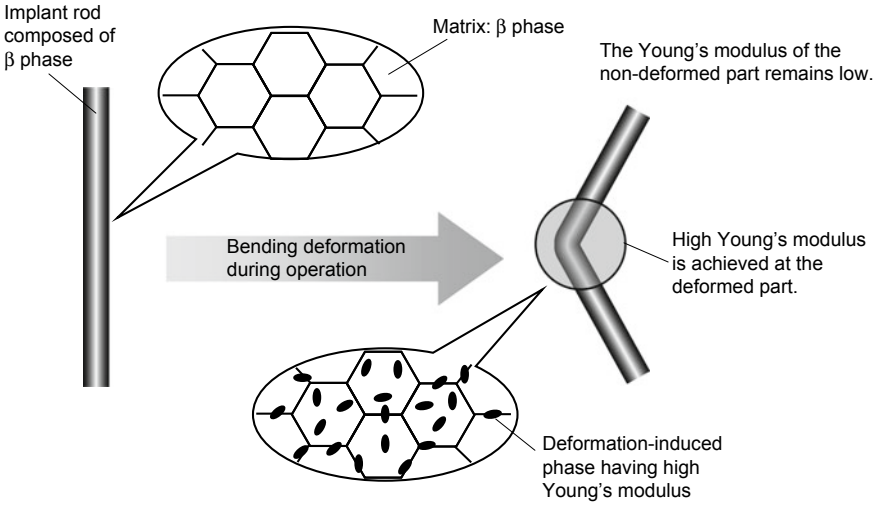

Fig. 30.16 Concept of self-adjustment of Young's modulus in implant rod

occurs during bending in the course of the operation. Here, a low Young's modulus can be retained for the patients. In general, Young's modulus of the ω phase is much greater than those of the α, α′, α″, and β phases. Among these phases, the ω, α′, and α″ phases can be induced by deformation in β-type titanium alloys with certain chemical compositions.

One possible alloy is reported to be Ti-12Cr. Figure 30.17 [21] shows Young's moduli of Ti-12Cr samples subjected to solution treatment (Ti-12Cr-ST) and samples subjected to 10% reduction cold rolling (Ti-12Cr-CR). It also shows data from those TNTZ alloys subjected to solution treatment (TNTZ-ST) and 10% reduction cold rolling (TNTZ-CR). Ti-12Cr-ST exhibits a low Young's modulus of the order of 60 GPa; this value is comparable to that of TNTZ-ST, which has been developed as a biomedical β-type titanium alloy having a low Young's modulus. TNTZ-CR also shows a low Young's modulus almost equal to that of TNTZ-ST. Thus, cold rolling hardly changes Young's modulus of TNTZ. However, in the case of Ti-12Cr, Young's modulus is increased by cold rolling and that of Ti-12Cr-CR is greater than 80 GPa. The deformation-induced ω phase was detected in Ti-12Cr, but no induced phase was detected in TNTZ. Therefore, the increase in Young's modulus of Ti-12Cr is probably derived from the deformation-induced ω phase transformation.

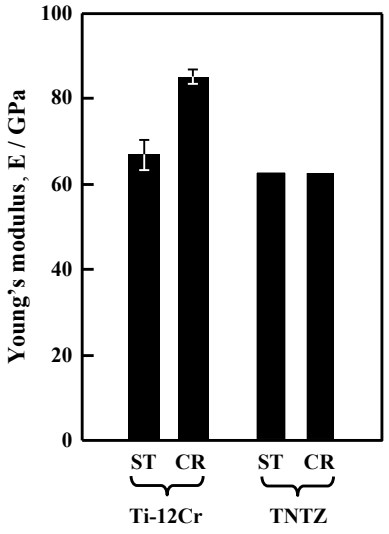

Fig. 30.17 Comparison of Young's moduli of Ti-12Cr-ST, Ti-12Cr-CR, TNTZ-ST, and TNTZ-CR

30.8 Low Young's Modulus and Stress Shielding

Figure 30.18 [16, 22] shows X-ray photographs of the fracture models 24 weeks after implantation with intramedullary rods made of TNTZ and SUS316 stainless steel whose Young's moduli measured by three-point bending tests are 58 GPa and 161 GPa, respectively. Bone atrophy can be observed at the upper back portion of the tibia for the SUS stainless steel intramedullary rod, but no bone atrophy can be

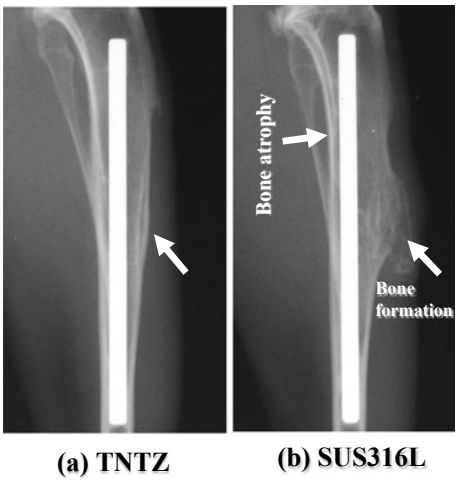

Fig. 30.18 X-ray photographs of intramedulary rods made of **a** TNTZ and **b** SUS 316L stainless steel at 24 weeks after implantation into tibiae of rabbits

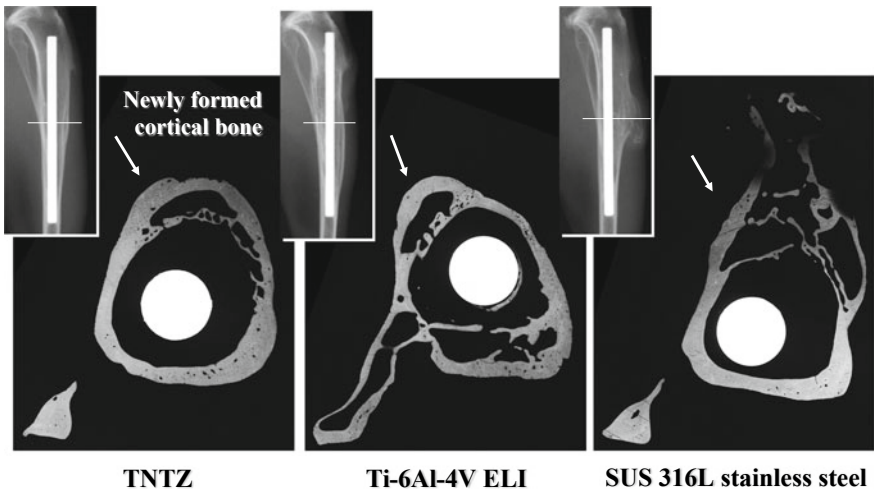

Fig. 30.19 CMR of cross sections of tibias implanted with intramedullary rods made of TNTZ, Ti-6Al-4V ELI and SUS 316L stainless steel at 24 weeks after implantation

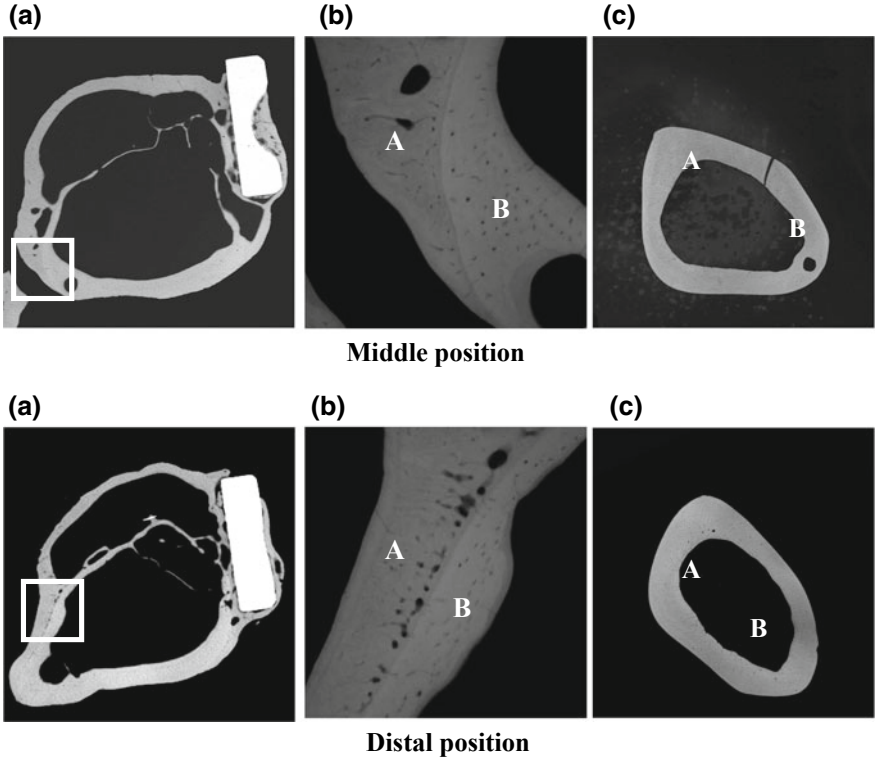

Fig. 30.20 CMRs of cross sections of fracture models implanted with and without bone plates made of TNTZ at middle position and distal position at 48 weeks after implantation: **a** cross-section of fracture model, **b** parts of □ of (**a**), namely high magnification CMR of branched parts of bones formed outer and inner sides of tibiae, and **c** cross sections of unimplanted tibiae

observed for the TNTZ intramedullary rod. The large bone formation can be observed at the frontal portion of the tibia for the SUS 316L stainless steel intramedullary rode, but very small bone formation is observed at the frontal portion of the tibia for the TNTZ intramedullary rod. Figure 30.19 [16, 22] shows the contact micro radiogram (CMR) of the cross-section of a tibia implanted with each rod at 24 weeks after implantation. Among all the cases, the remodeling of bones is evidently the best in the case of TNTZ. It is concluded that low Young's moduli are effective in inhibiting bone atrophy and providing excellent bone remodeling.

Further, studies on the effects of Young's modulus on bone remodeling have been done by implanting bone plates made of TNTZ, Ti-6Al-4V ELI (Young's modulus measured by three-point bending tests of 108 GPa), and SUS 316L stainless steel into the fracture models made in tibiae of rabbits. Only for the case of the bone plate made of TNTZ, the increase in the diameter of the tibia and the double-wall structure in the intramedullary bone tissue have been reported to be

observed as shown in Fig. 30.20 [16, 22]. In Fig. 30.20, the inner wall bone structure is the original (old) cortical bone and the outer wall bone structure is newly formed bone. This is the possible result of bone remodeling with a bone plate having a low Young's modulus.

30.9 Corrosion Resistance

Figures 30.21 and 30.22 [23] shows anodic polarization curves of TNTZ subjected to solution treatment at 1063 K ($TNTZ_{ST}$), $TNTZ_{ST}$ aged at 673 K for 259.2 ks, TNTZ subjected to 5 times (solution treatment and cold rolling) where final cold rolling ratio is 87.5% ($TNTZ_{multi}$) and $TNTZ_{multi}$ aged at 673 K for 259.2 ks obtained in 5%HCl solution with that of hot-swaged Ti-30Nb-10Ta-5Zr fabricated by powder metallurgy process [18], which has 0.2 mass% O and mirror surface produced by buff polishing, fabricated by powder metallurgy processing (hereafter Ti-30-10-5). The current density increases in the low potential region. The passive current density of $TNTZ_{ST}$ is somewhat higher than that of aged $TNTZ_{ST}$, although the critical current density, I_c, of both samples is nearly the same at approximately 0.7 A m^2. However, the corrosion resistance of $TNTZ_{ST}$ and aged $TNTZ_{ST}$ is lower than that of Ti-30-10-5. In general, the corrosion resistance of Ti is expected to improve by alloying with Nb, Zr and Ta [19] However, the behaviors of the anodic polarization curves of $TNTZ_{ST}$ and aged $TNTZ_{ST}$ are significantly different from that of Ti-30-10-5. The critical current density of $TNTZ_{ST}$ and aged $TNTZ_{ST}$ are ten times greater than that of Ti-30-10-5. On the other hand, I_c and passive current density, I_p, at 0.6 V of TNTZ multi and aged $TNTZ_{multi}$ are very similar to that of Ti-30-10-5. This trend was the same in Ringer's solution.

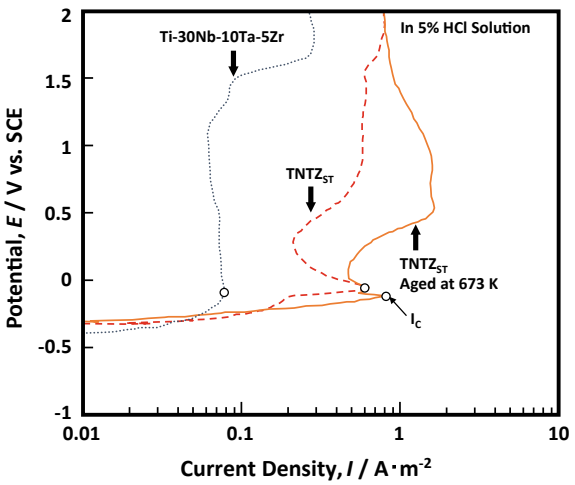

Fig. 30.21 Anodic polarization curves of $TNTZ_{ST}$, $TNTZ_{ST}$ aged at 673 K for 259.2 ks and Ti-30Nb-10Ta-5Zr fabricated by powder metallurgy processing in 5% HCl solution at 310 K

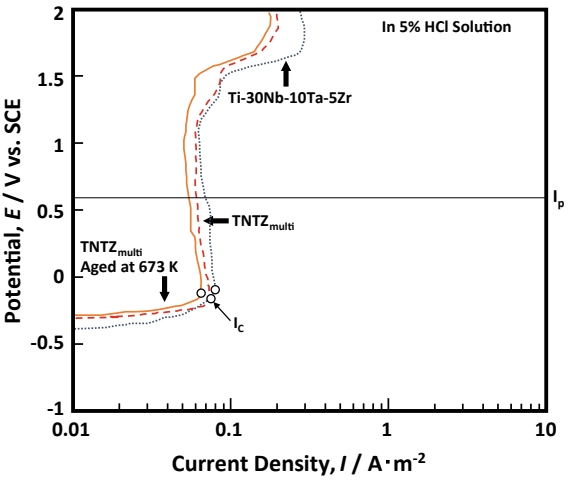

Fig. 30.22 Anodic polarization curves of $TNTZ_{multi}$, $TNTZ_{multi}$ aged at 673 K and Ti-30Nb-10Ta-5Zr fabricated by powder metallurgy processing in 5% HCl solution at 310 K

Figure 30.23 [23] shows SEM micrographs and elemental map of $TNTZ_{ST}$ and $TNTZ_{multi}$. The elemental maps shown in gray scale in Fig. 30.23b, f indicate the change in concentration of the alloying element where the concentration of each element increases with increasing gray level. The stripes on the surface of $TNTZ_{ST}$ parallel to the rolling direction shown in Fig. 30.23b correspond to the change in Ta content (Fig. 30.23c). It is thought that the fluctuation of Ta concentration, which may develop during the melting and hot forging used in processing, is aligned with the rolling direction. The difference between the maximum level and the minimum level of Ta concentration was found to be around 3 mass% by EDX. Fluctuations in Nb or Zr concentration were not observed in this study. It was difficult to eliminate the stripes parallel to rolling direction by solution treatment or aging conducted in this study. In the $TNTZ_{multi}$ surface stripes associated with Ta-content fluctuation in the $TNTZ_{ST}$ sample are completely absent (Fig. 30.23f, g). Therefore, each alloying element including, Ta, is distributed homogeneously. As a result, the corrosion resistance of $TNTZ_{multi}$ is improved remarkably.

Figure 30.24 [23] shows relationship between passive current densities, Ip, in 5%HCl and Ringer's solution of $TNTZ_{ST}$, $TNTZ_{multi}$ and Aged $TNTZ_{mul}$ with those of hot-rolled Ti-6Al-4V ELI subjected to aging, hot-rolled Ti-5Al-2.5Fe subjected to aging and forged Ti-13Mo-5Zr-3Al subjected to annealing. Values of I_p for TNTZ multi and aged $TNTZ_{multi}$ in 0.5%HCl and Ringer's solutions are very low less than 0.1 A m^2 and have a correlation each other, while those of $TNTZ_{ST}$ and aged $TNTZ_{ST}$ are significantly scattered. They are much greater than that of Ti-5Al-2.5Fe, and are a little smaller than that of Ti-15Mo-5Zr-3Al or Ti-6Al-4V ELI.

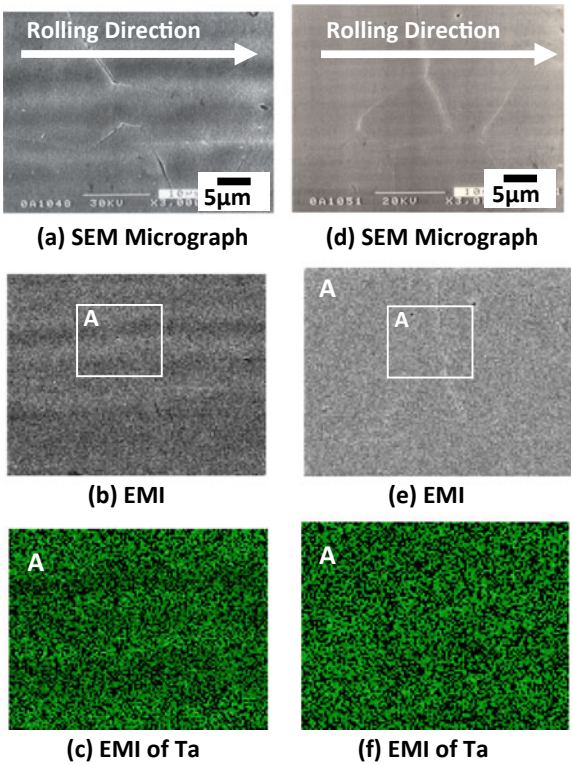

Fig. 30.23 SEM micrographs and elemental mapping images (EMI) of $TNTZ_{ST}$ (left) and $TNTZ_{multi}$ (right)

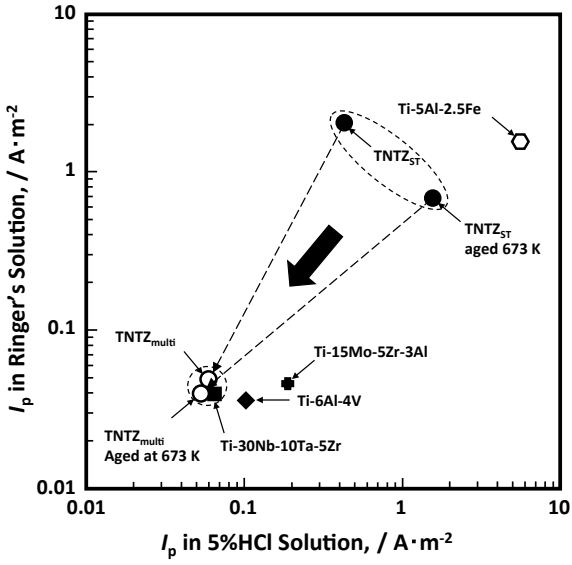

Fig. 30.24 Comparison of passive current density, I_p, of each titanium alloy in 5% HCl and Ringer's solution

30.10 Bioactive Ceramic Surface Modification

Titanium alloys show the best biocompatibility among metallic materials for biomedical applications. However, based on the patterns of osteogenesis, they are grouped under bioinert materials together with ceramics, such as alumina and zirconia. The biocompatibility of titanium alloys is inferior to that of calcium phosphate (CaP) or hydroxyapatite (HAp: Ca $(PO_4)_3OH$), which are grouped under bioactive materials. Therefore, bioactive surface treatment (i.e., bioactive surface modification) is applied to titanium alloys intended for biomedical applications to further improve their biocompatibility. In this case, phosphate calcium-type ceramics, such as calcium phosphate (CaP), TCP (β-$Ca_3(PO_4)_2$), CCP (β-$Ca_2P_2O_7$) and hydroxyapatite are coated on the surface of the titanium alloy. In general, our goal is to form a coating of hydroxyapatite.

There are many bioactive surface treatment processes [24]. These include plasma spray methods, ion plating, RF magnetron sputtering, pulse laser deposition ion beam dynamic mixing, super plastic joining, calcium ion implantation (where calcium ions are implanted into biomedical titanium alloys), calcium ion mixing method (where Ca is sputtered on the surface of biomedical titanium alloys followed by argon ion implantation), and electrochemical treatment. Alkali treatment is also used. In this process, the biomedical titanium alloy is immersed in a NaOH solution and heated. Then, the alloy is immersed into living-body liquid. In yet another method, a powder of calcium phosphate invert glass mixed with distilled water is coated on the surface of the titanium alloy and heated to 1073 K. Then, phosphate calcium-type ceramics such as bioactive β-TCP and β-CCP are precipitated. Furthermore, HAp is formed by immersing these ceramics in simulated body fluid (SBF). The apatite formation resulting from soaking in SBF is enhanced by autoclaving between 393 and 413 K for 1 h after heating. Figure 30.25 [25] shows SEM micrographs of the autoclaved and untreated glass-ceramic coated TNTZ after 10 days of soaking in SBF. The micrographs show that apatite formation in SBF occurs on the coated surfaces. The autoclaved glass-ceramic coated TNTZ is

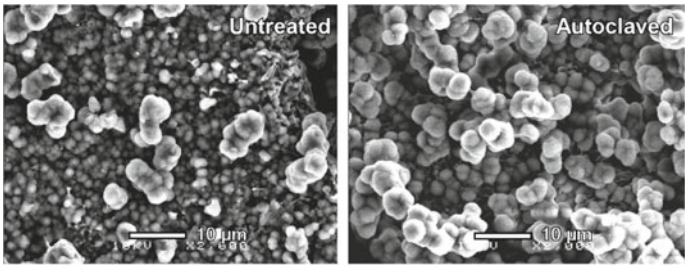

Fig. 30.25 SEM micrographs of the **a** untreated and **b** autoclaved glass-ceramic-coated Ti-29Nb-13Ta-4.6Zr surfaces 10 days after soaking in SBF

completely covered with apatite. In contrast, coverage is incomplete for the untreated one, and the original glass-ceramic surface is seen in some portions.

Figure 30.26 [25] shows contact micro-radiograms (CMR) of TNTZ and the autoclaved glass-ceramic-coated TNTZ after implantation into the femurs of Japanese rabbits. The photographs show new bone formation around TNTZ and the autoclaved glass-ceramic-coated TNTZ four weeks after implantation; the bone tissue shows areas of direct contact with the implants. One year after implantation, the direct contact of bone tissue with TNTZ and the autoclaved glass-ceramic-coated TNTZ can be seen in many regions.

Figure 30.27 [25] shows cross-sectional SEM micrographs one year after implantation. Crack propagation occurs between TNTZ and the bone whereas no crack occurs between the glass-ceramic coating and the bone. The glass-ceramic coating bonds directly with the bone.

Chemical vapor deposition (CVD) is advantageous for fabricating coatings at a high deposition rate with excellent control over microstructure and excellent step coverage. Single phases of HAp having a dense microstructure were fabricated

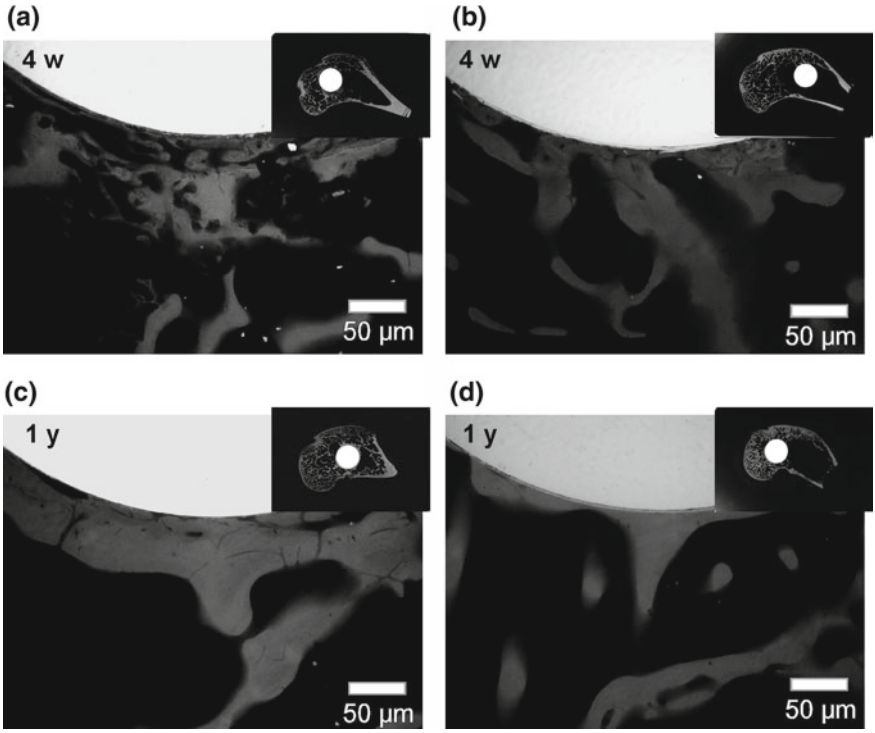

Fig. 30.26 C.M. R photographs of **a**, **c** Ti-29Nb-13Ta-4.6Zr and **b**, **d** the glass-ceramic-coated Ti-29Nb-13Ta-4.6Zr after implantation in the femurs of Japanese rabbits, **a**, **b** 4-week implantation and **c**, **d** 1-year implantation. Diameter of the samples is 5 mm

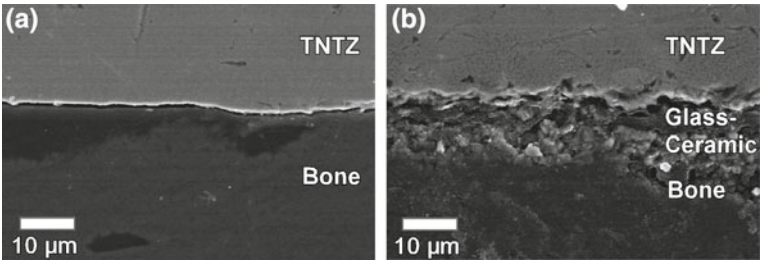

Fig. 30.27 Cross-sectional SEM micrographs of **a** Ti-29Nb-13Ta-4.6Zr and **b** the glass-ceramic coated Ti-29Nb-13Ta-4.6Zr after 1-year implantation

using the metal–organic chemical vapor deposition (MOCVD) technique by changing the deposition conditions, mainly the substrate temperature.

Figure 30.28 [26] shows the surface of TNTZ subjected to solution treatment ($TNTZ_{ST}$) and the surface and cross-sectional morphologies of TNTZ subjected to MOCVD for HAp coating) ($TNTZ_{HAp}$). The HAp film deposited on TNTZ has a dense granular microstructure and its grain size is approximately 2 μm.

During MOCVD treatment, TNTZ is heated up to 973 K. Therefore, the α-phase precipitates in the matrix after MOCVD treatment. Figure 30.29 [26] shows the relationship between the Vickers hardness and the distance from the specimen surfaces of $TNTZ_{ST}$, $TNTZ_{HAp}$, and TNTZ subjected to a simulated MOCVD process where the heating process is similar to that of MOCVD ($TNTZ_{SH}$). The Vickers hardness numbers of $TNTZ_{SH}$ and $TNTZ_{HAp}$ are higher than that of $TNTZ_{ST}$. The Vickers hardness of TNTZ increases because of the precipitation strengthening of the α-phase. In particular, the values of Vickers hardness near the surfaces of $TNTZ_{SH}$ and $TNTZ_{HAp}$ are much higher than that near the surface of $TNTZ_{ST}$. The amount of solute oxygen at the TNTZ surface is much greater than that inside TNTZ. The solute oxygen induces the α-phase precipitation. Therefore, the Vickers hardness near the surface of the TNTZ becomes higher than at the center of the TNTZ. The tensile properties of $TNTZ_{ST}$, $TNTZ_{SH}$, and $TNTZ_{HAp}$ are

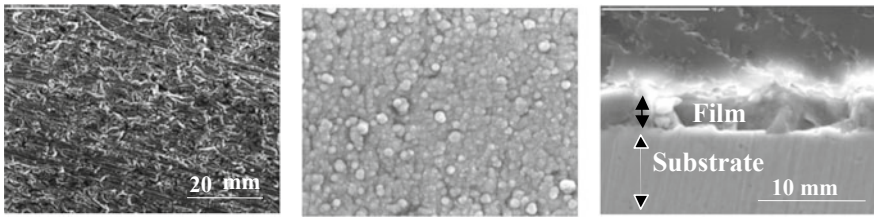

(a) $TNTZ_{ST}$ **(b) $TNTZ_{HAp}$** **(c) $TNTZ_{HAp}$**

Fig. 30.28 SEM images of surfaces of TNTZ subjected to **a** solution treatment ($TNTZ_{ST}$), **b** MOCVD for fabricating HAp film on TNTZ ($TNTZ_{HAp}$), and **c** cross-sectional image of $TNTZ_{HAp}$. Deposition time is 15 min

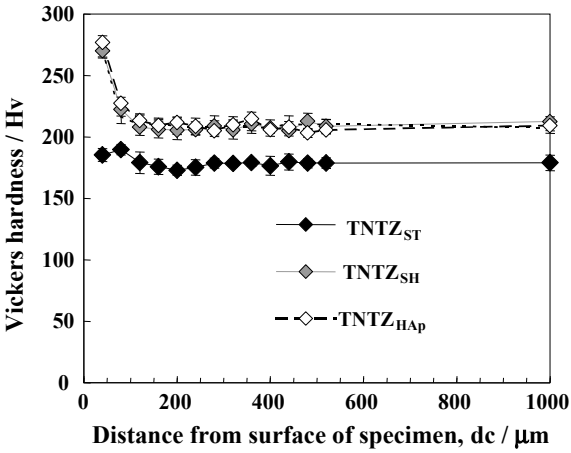

Fig. 30.29 Relationship between Vickers hardness and distance from specimen surface of $TNTZ_{ST}$, $TNTZ_{SH}$, and $TNTZ_{HAp}$

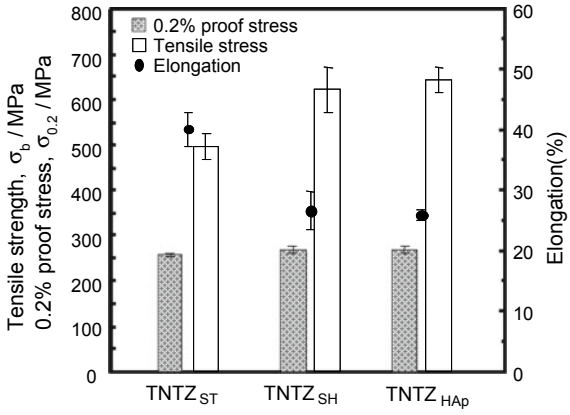

Fig. 30.30 Tensile properties of $TNTZ_{ST}$, $TNTZ_{SH}$, and $TNTZ_{HAp}$

shown in Fig. 30.30 [26]. The tensile strength and 0.2% proof stress increase because of substrate heating during MOCVD and the consequent precipitation strengthening of the α-phase. The elongation of $TNTZ_{SH}$ and $TNTZ_{HAp}$ is maintained at 20% even though the elongation decreases because of substrate heating. In addition, the Young's modulus increases because of substrate heating.

30.11 Summary

Design, manufacturing process, and mechanical, chemical, and biological properties, and surface modification of new titanium alloys with low Young's modulus intended to prevent stress shielding are reviewed with a focus on low-Young's-modulus Ti-29Nb-13Ta-4.6Zr referred to as TNTZ.

TNTZ exhibits a low Young's modulus of approximately 60 GPa under solutionized conditions. Since under solutionized conditions, the strength of TNTZ is poor, the static strength, namely, tensile strength is improved remarkably by conventional severe cold working including cold rolling, swaging and forging, and severe plastic deformation, including high-pressure torsion (HPT). The strength is improved while maintaining good ductility and low Young's modulus. Severe cold working and HPT cannot improve the dynamic strength (for example, fatigue strength) of TNTZ, but the dynamic strength does improve significantly as a result of a short-time aging process, where a small amount of ω-phase precipitates, and the addition of a small amount of ceramics, such as TiB and Y_2O_3, while maintaining a low Young's modulus. Bioactive ceramic coating on TNTZ is successfully achieved using a calcium phosphate invert glass and MOCVD. By implanting intramedullary rods and bone fixation plates made of TNTZ into fracture models made in the femurs of rabbits, low Young's modulus is found to be effective in preventing stress shielding.

References

1. M. Niinomi, M. Nakai, Titanium-based biomaterials for preventing stress shielding between implant devices and bone. Int. J. Biomater. (2011). Article ID 836587
2. M. Niinomi, M, Nakai, J. Hieda, Development of new metallic alloys for biomedical applications. Acta Biomater. **8**, 3888–3903
3. J. Domingo, Vanadium and tungsten derivatives as antidiabetic agents—a review of their toxic effects. Biol. Trace Elem. Res. **88**, 97–112 (2002)
4. B. Boyce, J. Byars, S. McWilliams, M. Mocan, H. Elder, I. Boyle, B. Junor, Histological and electron microprobe studies of mineralisation in aluminium-related osteomalacia. Br. Med. J. **45**, 502–508 (1992)
5. S.G. Steinemann, in *Evaluation of Biomaterials*, ed. by G.D. Winter, J.L. Leray, K. de Goot (Wiley, New York, 1980), pp. 1–34
6. H. Kawahara, Cytotoxicity of implantable metals and alloys. Bull. Jpn. Inst. Metal. Mater. **31**, 1033–1039 (1992)
7. Y. Okazaki, Y. Ito, A. Ito, T. Tateishi, Effect of alloying elements on mechanical properties of titanium alloys for medical implants. J. Jpn. Inst. Metals Mater. **57**, 332–337 (1993)
8. M. Niinomi, Development of high biocompatible titanium alloys. Funct. Mater. **20**(3), 36–44
9. M. Morinaga, M. Kato, T. Kamimura, M. Fukumotom, I. Harada, K. Kubo, Theoretical design of β-type titanium alloys, in *Proceedings of 7th International Conference on Titanium, 1992*, Science and Technology, San Diego, CA, USA, June 29–July 2, 1992, pp. 276–283
10. D. Kuroda, M. Niinomi, M. Morinaga, Y. Kato, T. Yashiro, Design and mechanical properties of new β type titanium alloys for implant materials. Mater. Sci. Eng. A **A243**, 244–249 (1998)
11. A. Suzuki, M. Okabe, T. Kato, Mechanical properties of titanium alloys produced by levitation melting and counter-gravity low-pressure casting process. Electr. Furnace Steel **70** (3), 231–237 (1999)
12. M. Niinomi, T. Hattori, K. Morikawa, T. Kasuga, A. Suzuki, H. Fukui, S. Niwa, Development of low rigidity β-type titanium alloy for biomedical applications. Mater. Trans. **43**(12), 2970–2977 (2002)
13. M. Niinomi, Titanium alloys for medical and dental applications. In: *Medical Devices Materials*, ed. by S. Shrivastava (ASM International, 2004), pp. 417–422

14. H. Yilmazer, M. Niinomi, T. Akahori, M. Nakai, H. Tsutsumi, Effects of severe plastic deformation and thermo-mechanical treatments on microstructures and mechanical properties of β-type titanium alloys for biomedical applications, in *Proceedings of PFAMXIII* (2009), pp. 1401–1410
15. M. Niinomi, H. Fukui, T. Hattori, K. Kyo, A. Suzuki, Development of high biocompatible titanium alloy. Materia Jpn. **41**, 221–223 (2002)
16. M. Niinomi, Tend and present state of titanium alloys with body centered structure for biomedical applications. Bull. Iron Steel Inst. Jpn. **15**(11), 661–670 (2010)
17. H. Yilmazer, M. Niinomi, M. Nakai, J. Hieda, Y. Todaka, T. Miyazaki, Mechanical properties of a medical β-type titanium alloy with specific microstructural evolution through high pressure torsion. Mater. Sci. Eng. C **33**, 2499–2507 (2013)
18. M. Niinomi, T. Akahori, Improvement of fatigue life of titanium alloys for biomedical devices through microstructural control. Expert Rev. Med. Dev. **7**(4), 481–488 (2010)
19. M. Nakai, M. Niinomi, T. Oneda, Improvement in fatigue strength of biomedical β-type Ti–Nb–Ta–Zr alloy while maintaining low Young's modulus through optimizing ω-phase precipitation. Metall. Mater. Trans. A **43**(1), 294–302 (2012)
20. X. Song, M. Niinomi, H. Tsutsumi, T. Akahori, M. Nakai, S. Yonezawa, L. Wang, Effect of Y_2O_3 on mechanical properties of Ti-29Nb-13Ta-4.6Zr for biomedical applications, in *Materials Science Forum*, vol. 654–656 (2010), pp. 2142–2145
21. M. Nakai, M. Niinomi, X.F. Zhao, X. Zhao, Self-adjustment of Young's modulus in biomedical titanium alloys during orthopaedic operation. Mater. Lett. **65**, 688–690 (2011)
22. M. Niinomi, T. Hattori, Effect of Young's modulus in metallic implants on atrophy and bone remodeling, in *Interface Oral Health Science 2009*, ed. by T. Sasano, O. Suzuki, P. Stashenko, K. Sasaki, N. Takahashi, T. Kawai, M.A. Taubman, H.C. Margolis (Springer, 2010), pp. 90–99
23. T. Akahori1, M. Niinomi1, H. Fukui, A. Suzuki, Fatigue, fretting fatigue and corrosion characteristics. Mater. Trans. **45**(5), 1540–1548
24. M. Niinomi, M. Nakai, Mechanically bio-functional titanium alloys for substituting failed hard tissue, in *Proceedings of Fray International Symposium on Metals and Materials Processing in a Clean Environment*, 27 Nov–1 Dec 2011, Cancun, Mexico, appeared in Volume 7: Composites, Ceramics, Nanomaterials & Titanium Processing, ed. by F.K. Flogen (2012), pp. 409–433
25. T. Kasuga, M. Nogami, M. Niinomi, T. Hattori, L.L. Hench, Enhancing effect of autoclaving on bioactivity of β-titanium alloy coated with calcium phosphate glass-ceramic. Key Eng. Mater. **284–286**, 243–246 (2005)
26. H. Tsutsumi, M. Niinomi, M. Nakai, T. Gozawa, T. Akahori, K. Saito, R. Tu, T. Goto, Fabrication of hydroxyapatite film on Ti-29Nb-13Ta-4.6Zr using a MOCVD technique. Mater. Trans. **51**(12), 2277–2283 (2010)

Chapter 31
Electret Ceramics for Biomedical Applications

Naohiro Horiuchi

Abstract An electret is a dielectric material that has quasi-permanently stable polarization and surface charges, and forms electric fields in its neighborhood. In this chapter, the basics of electrets are briefly introduced, and a representative electret for biomedical use is presented. The most important ceramics for biomedical applications, hydroxyapatite, can be polarized and become an electret. The properties of hydroxyapatite electrets and the application, i.e, an ability to promote bone regeneration, are reviewed.

Keywords Polarization · Hydroxyapatite · Proton conduction · Osteoconduction

31.1 Electret

An electret is the electrostatic equivalent of a permanent magnet. The history of "electret" is much younger than that of magnet [1, 2]. The term was coined by Oliver Heaviside at the end of nineteenth century, in order to describe "*a body which is naturally permanently electrized by internal causes*" [3]. The first example of electret was introduced by Mototaro Eguchi in 1919 [4]. In magnetism, magnetic charges are always observed as magnetic dipoles, and magnetic monopole is not found. In electrostatics, electric dipoles also exist, however, electrostatic charges have many forms, and positive and negative charges are easily divided. Therefore, polarized states are easily eliminated or/and covered by opposite charges. This complicates the fabrication and evaluation of electrets, which is a reason for the shorter history of electrets.

An electret is defined as a material that quasi-permanently creates electric fields around the material. The electric fields were caused by quasi-permanent electric

N. Horiuchi (✉)
Department of Inorganic Biomaterials, Institute of Biomaterial & Bioengineering, Tokyo Medical and Dental University, 2-3-10 Kanda-Surugadai, Chiyoda-ku, Tokyo 101-0062, Japan
e-mail: nhori.bcr@tmd.ac.jp

Y. Setsuhara et al. (eds.), *Novel Structured Metallic and Inorganic Materials*, https://doi.org/10.1007/978-981-13-7611-5_31

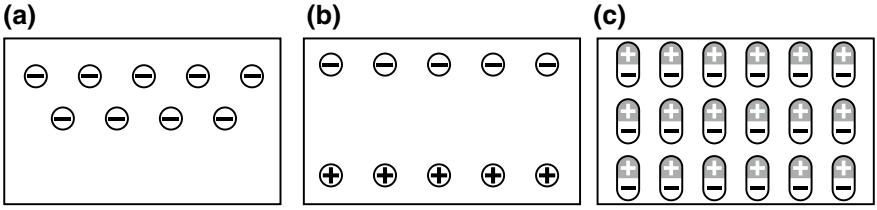

Fig. 31.1 Schematic illustrations of cross sections of typical electret formation. They consist of **a** negative space charges, **b** negative and positive space charge, and **c** dipolar charges

charges. The electret charge consists of monopolar charges, e.g., space charge or surface charge, or/and dipolar (hetero) charges. Examples of electrets are presented in Fig. 31.1. The electrets of Fig. 31.1a, b consist of space charges. The negative charges exist in the electret of Fig. 31.1a. The charges are generally injected from outside of the material through electron or ion beam irradiation. In Fig. 31.1b, the electret is derived from the displacement of negative and positive space charges. The displacement can be caused by an applied external electric field. Figure 31.1c originates from aligned dipolar charges (dipoles).

A wide range of materials has the potential to be an electret. Representative electrets that are practically used are fabricated from polymers, for example, fluoropolymers (e.g, PTFE, PVDF), polyethylene terephthalate, etc. Piezoelectric crystals and ceramics are also electrets. One of the most important ceramics for biomedical applications is hydroxyapatite, which has a similar chemical composition and structural features to the bone. Hydroxyapatite also can be polarized and become an electret.

31.2 Properties of Hydroxyapatite Electret

31.2.1 Crystal Structure of Hydroxyapatite

Hydroxyapatite (HAp) is an apatite which has the general formula $Ca_{10}(PO_4)_6X_2$ where the *X* is, in most case, a halogen ion (F^-, Cl^-, Br^-) or a hydroxide (OH^-) ion [5]. As the name implies, HAp contains OH^- ions in its structure. The crystal structure symmetry is generally expressed by $P6_3/m$ (space group 176) [6], therefore the unit cell is depicted with hexagonal cylinder as shown in Fig. 31.2a, which is a view of the structure projected down the *c*-axis. The structure consists of PO_4 tetrahedra, Ca^{2+} ions, and columns of OH^- ions oriented along the *c* axis. The unit cell formula of the hexagonal HAp is expressed as $Ca_{10}(PO_4)_6(OH)_2$. The Ca^{2+} ions are divided into: Ca^1 and Ca^2. The Ca^1 and Ca^2 have 4 and 6 ions, respectively. The Ca^1 arranges repeatedly along the *c*-axis, which is called columnar calcium ion. The Ca^2 forms triangles on the *ab* plane, and one triangle locates at $\pi/3$ angle with respect to the neighboring triangles. The stacking of the Ca triangles forms a

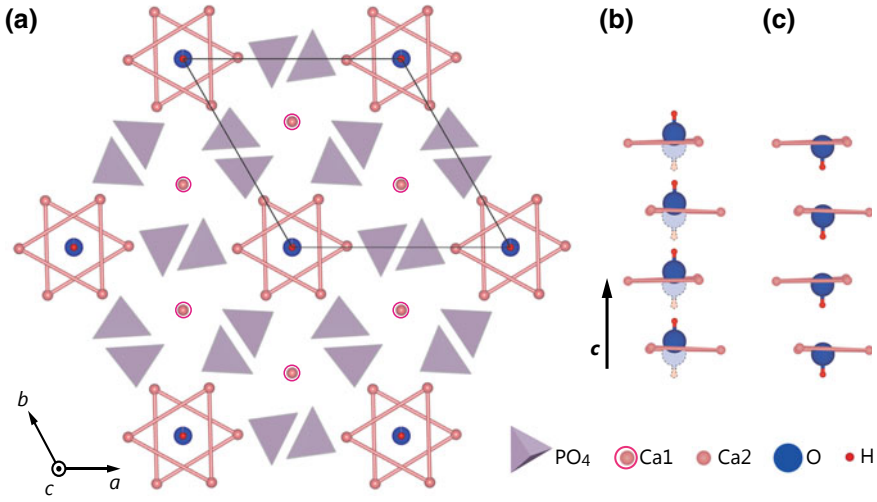

Fig. 31.2 Schematic illustration for crystal structure of hydroxyapatite

column which encloses the OH^- ion column. The existence of the OH columns is important when we discuss and understand the properties of HAp [7].

The crystal structure of the calcium apatite is occasionally described by the word "pseudohexagonal". The reason for "pseudo" is because some ordered alignment of the OH^- ions breaks the hexagonal symmetry $P6_3/m$. The arrangement of OH^- ions has two states as shown in Fig. 31.2b. The OH^- ions can be located above and below the Ca triangles. The OH^- ions are located at both sides of the mirror planes at $z = 0.25$ and 0.75. However, in this case, the OH^- ions do not exist simultaneously at both side of the mirror planes. The OH^- ions are disordered. On average, half of the OH^- ions are located above the plane of the Ca triangles and the other half are below the plane. Generally, HAp has disordered arrangements of the OH^- ions, which is caused by a slight amount of impurities, e.g., F^-, Cl^- or vacancies. In the case of stoichiometric HAp, the arrangement is ordered as presented in Fig. 31.2c. The orientations of OH^- ion in one column aligned in one direction. The crystal structure is known to be monoclinic at room temperature ($P2_1/b$) [8, 9]. This kind of ordering can change the crystal structure and remove the center of symmetry. It is noteworthy because that suggest that piezoelectricity may indeed exist in hydroxyapatite. The polar structure having ordering OH^- ions is expected to be ferroelectric, however, no experimental results that prove ferroelectricity in hydroxyapatite has been reported.

31.2.2 Electric Properties of Hydroxyapatite Electret

HAp is known as a proton conductor. Protons can move in the OH columns path along the *c*-axis. The report of the ionic conductivity of HAp dates back to 1973, and Royce considered conduction of OH^- ions in HAp [10]. Maiti and Freund [11] studied the proton conductivity of HAp and fluorine substituted HAp. Proton conduction with the activation energy of 0.6 (±0.1) eV was observed at a lower F substitution. Yamashita et al. [12] reported a proton conductivity of about 10^{-3} S/cm at 700 °C using sintered ceramic HAp. The ionic transference number was estimated using a hydrogen concentration cell and determined to be unity, suggesting that protons transported the electrical charges in HAp. Proton conduction in HAp is involved with proton defects, which are formed by dehydration as described as the equation: $Ca_{10}(PO_4)_6(OH)_2 \rightarrow Ca_{10}(PO_4)_6(OH)_{2-x}O_x\Upsilon_x + xH_2O$, where the Υ presents a vacancy of OH^- ion and O^{2-} ions at the OH^- lattice sites are converted from the OH^- ions, which contains proton defects. The protons migrate through the proton defects. The defects were easily introduced by Ca^{2+}-substitution with trivalent cations [13]: $Ca_{10-x}M_x(PO_4)_6(OH)_{2-x}O_x$, where M represents Y^{3+} or La^{3+}. Yttrium-doped HAp (Y-HAp) exhibited higher proton conductivity of 10^{-4} S/cm at 800 °C [14]. Aligning the crystallographic axis increases the proton conductivity. Fully dense Y-HAp membranes having aligned crystallographic orientation normal to the electrode substrate had the proton conductivity of 10^{-2} S/cm at 700 °C, and the measured activation energy for proton conduction was 0.73 eV (Fig. 31.3a) [15]. The proton conduction is one-dimensional conduction through OH^- ions along the c-axis. The detailed path was visualized by Yashima et al. [9, 16] using a combined technique of high-temperature neutron diffraction and bond valence sum (BVS) method. The obtained pathway of a complex sinusoidal process is presented in Fig. 31.3b, which consists of the reorientations of OH^- ions and proton migrations to the neighboring proton sites.

As described above, in HAp, protons can move in HAp crystals. These properties can be utilized to prepare electret because an applied external voltage to the HAp can move the protons in HAp. In fact, HAp electrets can be fabricated via a facile poling process as shown in Fig. 31.4. First, place a HAp ceramic pellet between a pair of electrodes. The HAp pellet is heated to a certain temperature (poling temperature: T_p), and a direct current (DC) electric field (poling electric field: E_p) is applied for an arbitrary amount of time (poling time: t_p). After the poling time, cool the pellet to room temperature. The electric field was maintained until the samples cooled to room temperature. In this process, the heating has an important role because the proton conduction in HAp requires a relatively high temperature. Displacement of protons is induced by the applied electric field at the elevated temperature. After the cooling, the protons cannot move at room temperature, thus, the displacement is frozen and maintained quasi-permanently. The displacement is the origin of the electret of HAp.

A method to characterize electrets is TSDC (thermally stimulated depolarization current) measurement [17]. Electrets are quasi-permanent at room temperature

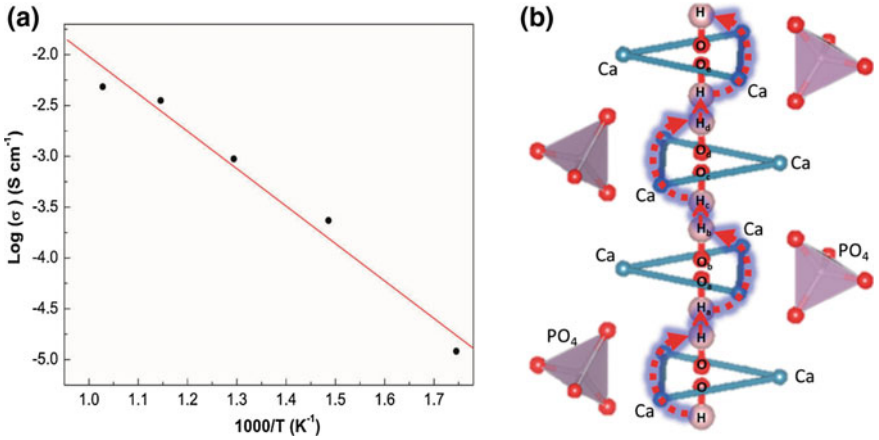

Fig. 31.3 **a** Proton conductivity of Y-HAp membrane on palladium surface. Reprinted with the permission from Ref. [15], Copyright 2012 American Chemical Society. **b** Geometry of the proton conduction path along the *c*-axis. Red arrows and dotted lines indicate the proton migration pathways. Red, blue, and white spheres and purple triangle stand for the oxygen, calcium, and hydrogen atoms and PO_4 tetrahedron, respectively. Reprinted with the permission from Ref. [16] Copyright 2014 American Chemical Society

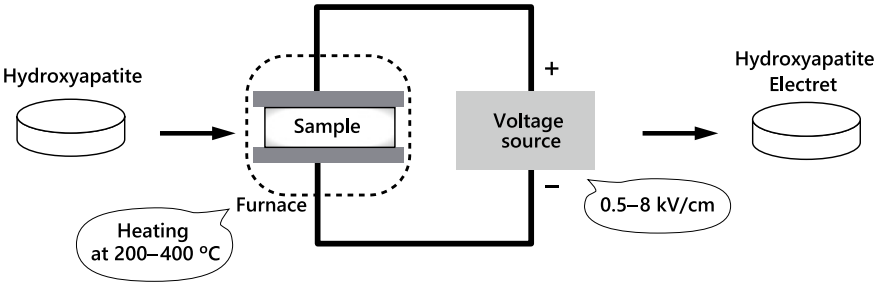

Fig. 31.4 Schematic illustration of the preparation of HAp electret

because the charges are frozen, but, as the temperature increases, the charges increase their mobility. The displacements go back to the thermal equilibrium, which means that thermal stimulation induces relaxations of the charges in the electret. The relaxation process generates depolarization currents, and, therefore the relaxation phenomena can be evaluated by detecting the depolarization currents. A typical procedure of TSDC measurement is as follows. First, prepare an electret via poling procedure with certain conditions (T_p, E_p and t_p). The electret is connected to an ammeter, and the sample is heated at a constant heating rate (e.g, 5 K/min). The depolarization currents are measured as a function of temperature. TSDC curves for HAp electrets were of course measured [18–20]. The results for HAp electrets with different poling electric field (E_p) were presented in Fig. 31.4a. As

shown in the figure, two peaks, located at higher and lower temperature range, were observed, indicating that the polarization comprises at least two elements. The inset of the figure shows the peak current values of the two peaks. The values of peaks located at higher temperature increase exponentially, and the peak position also increases as the E_p increases. The behavior suggests that peak at higher temperature range is caused by space charge polarizations. In contrast, the peak value of lower temperature increases linearly and the positions are independent on the poling electric field (E_p). This result implies that the peak at lower temperature range is attributed to dipolar polarization or polarization involving interface.

Electrets form electric fields around themselves. The electric fields can be evaluated by the Kelvin probe method, which is noncontact measurement of surface potentials of the electrets [21]. In this method, a vibrating electrode is placed over a sample and the electrode detect the potential difference (surface potential; ϕ_{sp}) between the sample surface and the sensing electrode that is placed over the sample. The potential difference can be changed to surface charge density (σ_s) using the following equation: $\sigma_s = \varepsilon_0 \varepsilon_s \phi_{sp}/d$, where ε_s is the relative permittivity of the sample (a value of 20 was used for the relative permittivity of HAp) and d is the sample thickness. Figure 31.5b presents the surface charge density at the sides of the HAp electret with different thicknesses (d) [22]. The surface charge is independent of the thickness, suggesting that the surface charge does not originate from

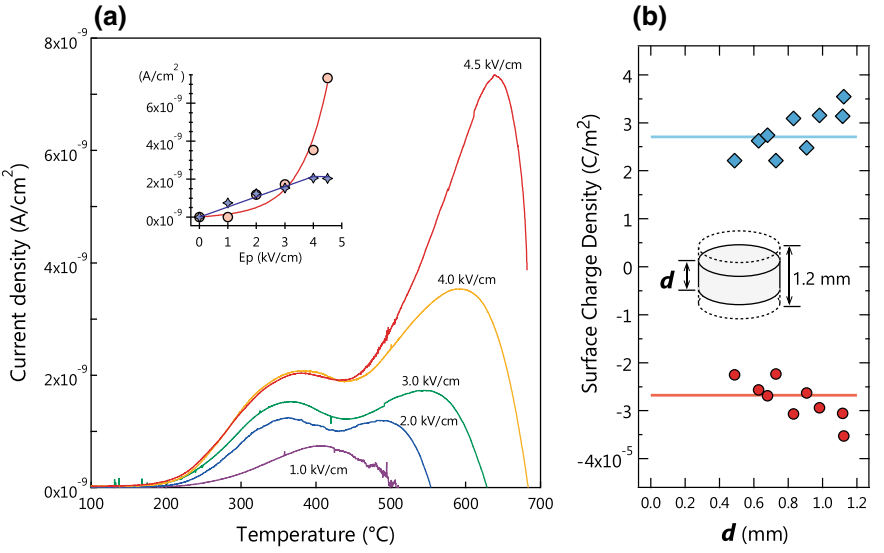

Fig. 31.5 **a** TSDC curves of HAp electrets with various polarization electric fields (E_p). Polarization conditions T_p and t_p, are, respectively, 623 K, 60 min. The inset shows a relation between maximum currents for each peak and polarization electric field E_p. Reprinted with permission from Ref. [20], Copyright 2012, American Institute of Physics. **b** Depth profile of surface charges on HAp electrets. Reprinted with permission from Ref. [22] Copyright 2014, American Institute of Physics

local charge that is inhomogeneously distributed (for example, the interfacial charge near the electrode). The surface charge is believed to be induced by polarization that is uniformly distributed in the HAp samples. Comparing HAp electrets and non-polarized HAp, there is no difference in the surface roughness, crystallinity, and constituent elements, however, the wettability to water is increased on the surface of HAp electret [23].

31.3 Applications of Hydroxyapatite Electret

31.3.1 Cell Behavior on Hydroxyapatite Electret

Surfaces of HAp electrets affect cell adhesion, which was revealed by valuation of osteoblasts (cells that synthesize bone) [23]. While the typical adhered cells on non-polarized HAp have a round or spherical shape, on HAp electret, the cells have a spindle or fanlike spreading configuration. The cell adhesion areas, which indicate the degree of cell spreading, were distinctly larger on the HAp electrets than that on the non-polarized HAp. An important reason for the enhancement of cell spreading is the improved surface wettability on the HAp electrets. In some cases, surface wettability change provides advantages in cellular behaviors such as attachment and spreading [24–28]. Another reason for the enhancement of the initial cell attachment on the HAp electret is considered to be caused by the difference in protein adsorption that stimulates cell adhesion. In fact, increase of protein (fibrin) adsorption on HAp electret surfaces in vivo was reported [29].

31.3.2 New Bone Formation on Hydroxyapatite Electret

Bone has the ability of self-repairing if the fracture is small enough, however, in case that the defect becomes larger, a surgical procedure that refills missing bone, bone grafting, is required. HAp is a material used for bone grafting. The defect of bone is filled with HAp. Materials for bone grafting is required to have osteoconductivity: property of a material that encourages osteoconduction. Osteoconduction is a bone formation process which is carried out on surfaces of implanted materials. When an osteoconductive material is implanted into a lost part of bone, the material serves as a scaffold where bone cells attach, spread, and proliferate. The bone cells reconstruct bone tissue and replace the scaffold with the new bone.

HAp electrets were demonstrated to enhance osteoconductivity and the bone formation processes varied with the polarity of surface charges [30]. Rectangular holes of 1.4×5.0 mm^2 prepared at cortical bone of male beagle dogs, and the holes were filled with HAp electrets. The results of morphologic evaluation of the

samples, which were harvested at 3, 7, 14, and 28 days after the implantation, were presented in Fig. 31.6. Comparison among the three different types of surfaces (negative, positive, non-polarized) suggests the surface charges of HAp electret significantly cooperate with the innate bioactivity of HAp and promote reconstruction of the bone defects. As shown in Fig. 31.6a, new bone (Nb) layers 0.01–0.02 mm thick are in contact with the surface without any inclusion. In contrast, the non-polarized HAp surface (Fig. 31.6g) was still isolated from osteoid tissues by dominant fibrin multilayers.

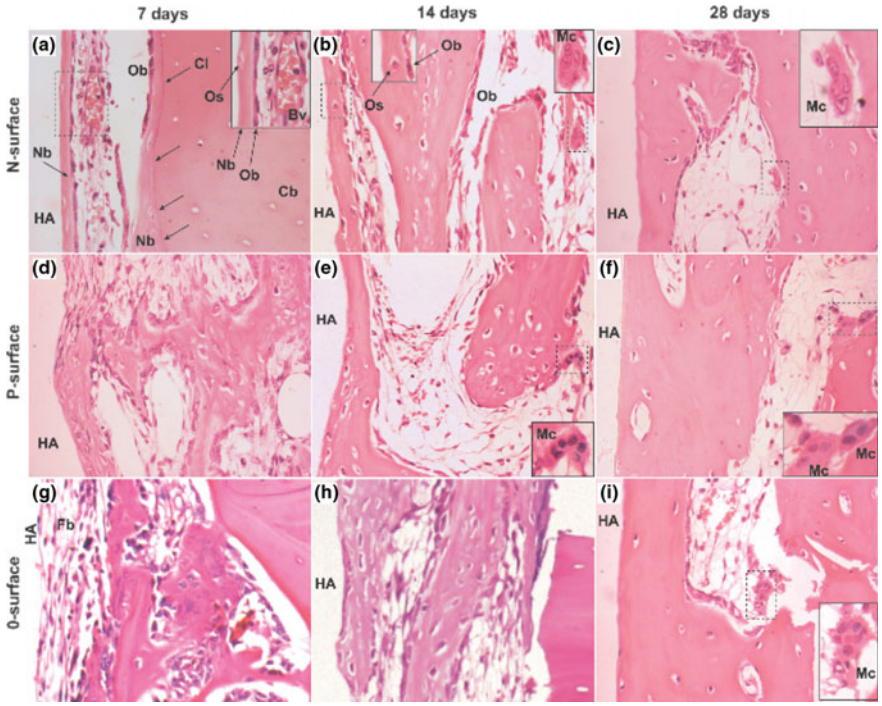

Fig. 31.6 Cell morphologies in wide gap between HAp ceramics (HA) and cortical bones (Cb). Insets are magnified views of rectangular frames of broken lines. **a** Newly formed bone (Nb) layer of 0.01–0.02 mm with osseous cells (Os) and layered osteoblastic cells (Ob) were in direct contact with N-surfaces on day 7. Newly formed bones also were found on cortical bone with cement line. Many blood vessels (Bv) with erythrocytes occupied space among newly formed bones. **b** On days 14 and **c** 28, newly formed bone layers in direct contact with N-surface had gradually grown. A few multinucleated giant cells (Mc) were found in proximity of cortical bones. **d** Osteoid tissues surrounded by osteoblastic cells in the vicinity of P-surface on day 7. **e** On days 14 and **f** 28, newly formed bones derived from osteoid tissues were gradually matured in proximity of P-surface. A few multinucleated giant cells (Mc) were found on osteoids and cortical bones. **g** On days 7 and **h** 14, osteoid tissues were found to be isolated from 0-surface by dominant fibrin layers (Fb). **i** Parts of newly formed bones were in direct contact with 0-surface on day 28. Reproduced from Ref. [30] by permission of John Wiley & Sons Ltd

References

1. G.M. Sessler, *Electrets*, vol. 1, 3rd edn. (Laplacian Press, 1999)
2. K.C. Kao, 5—Electrets, in *Dielectric Phenomena in Solids*, ed. by K.C. Kao (Academic Press, San Diego, 2004), pp. 283–326
3. O. Heaviside, *Electrical Papers* (Macmillan, 1892)
4. M. Eguchi, On dielectric polarisation. Proc. Phys. Math. Soc. Jpn., 3rd Ser. **1**, 326–331 (1919)
5. J.C. Elliott, *Structure and Chemistry of the Apatites and Other Calcium Orthophosphates* (Elsevier, 1994)
6. M.I. Kay, R.A. Young, A.S. Posner, Crystal structure of hydroxyapatite. Nature **204**, 1050–1052 (1964). https://doi.org/10.1038/2041050a0
7. V. Uskoković, The role of hydroxyl channel in defining selected physicochemical peculiarities exhibited by hydroxyapatite. RSC Adv. **5**, 36614–36633 (2015). https://doi.org/10.1039/C4RA17180B
8. J.C. Elliott, P.E. Mackie, R.A. Young, Monoclinic hydroxyapatite. Science **180**, 1055–1057 (1973). https://doi.org/10.1126/science.180.4090.1055
9. M. Yashima, Y. Yonehara, H. Fujimori, Experimental visualization of chemical bonding and structural disorder in hydroxyapatite through charge and nuclear-density analysis. J. Phys. Chem. C **115**, 25077–25087 (2011). https://doi.org/10.1021/jp208746y
10. B.S.H. Royce, The defect structure and ionic transport properties of calcium apatite. J. Phys. Colloq. **34**, 327–332 (1973). https://doi.org/10.1051/jphyscol:1973957
11. G.C. Maiti, F. Freund, Influence of fluorine substitution on the proton conductivity of hydroxyapatite. J. Chem. Soc. Dalton Trans. **949** (1981). https://doi.org/10.1039/dt9810000949
12. K. Yamashita, K. Kitagaki, T. Umegaki, Thermal instability and proton conductivity of ceramic hydroxyapatite at high temperatures. J. Am. Ceram. Soc. **78**, 1191–1197 (1995). https://doi.org/10.1111/j.1151-2916.1995.tb08468.x
13. K. Yamashita, H. Owada, T. Umegaki et al., Ionic conduction in apatite solid solutions. Solid State Ion **28–30**, 660–663 (1988). https://doi.org/10.1016/S0167-2738(88)80121-8
14. K. Yamashita, H. Owada, T. Umegaki et al., Protonic conduction in yttrium-substituted hydroxyapatite ceramics and their applicability to H2-O2 fuel cell. Solid State Ion **40–41**(Part 2), 918–921 (1990). https://doi.org/10.1016/0167-2738(90)90153-i
15. X. Wei, M.Z. Yates, Yttrium-doped hydroxyapatite membranes with high proton conductivity. Chem. Mater. **24**, 1738–1743 (2012). https://doi.org/10.1021/cm203355h
16. M. Yashima, N. Kubo, K. Omoto et al., Diffusion path and conduction mechanism of protons in hydroxyapatite. J. Phys. Chem. C **118**, 5180–5187 (2014). https://doi.org/10.1021/jp412771f
17. P. Braunlich, *Thermally Stimulated Relaxation in Solids* (Springer-Verlag Berlin and Heidelberg GmbH & Co. K, 1979)
18. S. Nakamura, H. Takeda, K. Yamashita, Proton transport polarization and depolarization of hydroxyapatite ceramics. J. Appl. Phys. **89**, 5386–5392 (2001). https://doi.org/10.1063/1.1357783
19. Y. Tanaka, T. Iwasaki, M. Nakamura et al., Polarization and microstructural effects of ceramic hydroxyapatite electrets. J. Appl. Phys. **107**, 014107 (2010). https://doi.org/10.1063/1.3265429
20. N. Horiuchi, M. Nakamura, A. Nagai et al., Proton conduction related electrical dipole and space charge polarization in hydroxyapatite. J. Appl. Phys. **112**, 074901–074901–6 (2012). https://doi.org/10.1063/1.4754298
21. C.W. Reedyk, M.M. Perlman, The measurement of surface charge. J. Electrochem. Soc. **115**, 49–51 (1968). https://doi.org/10.1149/1.2411001
22. N. Horiuchi, S. Nakaguki, N. Wada et al., Polarization-induced surface charges in hydroxyapatite ceramics. J. Appl. Phys. **116**, 014902 (2014). https://doi.org/10.1063/1.4886235

23. M. Nakamura, A. Nagai, T. Hentunen et al., Surface electric fields increase osteoblast adhesion through improved wettability on hydroxyapatite electret. ACS Appl. Mater. Interfaces **1**, 2181–2189 (2009). https://doi.org/10.1021/am900341v
24. K. Webb, V. Hlady, P.A. Tresco, Relative importance of surface wettability and charged functional groups on NIH 3T3 fibroblast attachment, spreading, and cytoskeletal organization. J. Biomed. Mater. Res. **41**, 422–430 (1998)
25. L. Hao, J. Lawrence, K.S. Chian, Osteoblast cell adhesion on a laser modified zirconia based bioceramic. J. Mater. Sci. Mater. Med. **16**, 719–726 (2005). https://doi.org/10.1007/s10856-005-2608-3
26. M.C. Advincula, F.G. Rahemtulla, R.C. Advincula et al., Osteoblast adhesion and matrix mineralization on sol-gel-derived titanium oxide. Biomaterials **27**, 2201–2212 (2006). https://doi.org/10.1016/j.biomaterials.2005.11.014
27. L.-C. Xu, C.A. Siedlecki, Effects of surface wettability and contact time on protein adhesion to biomaterial surfaces. Biomaterials **28**, 3273–3283 (2007). https://doi.org/10.1016/j.biomaterials.2007.03.032
28. K. Das, S. Bose, A. Bandyopadhyay, Surface modifications and cell-materials interactions with anodized Ti. Acta Biomater. **3**, 573–585 (2007). https://doi.org/10.1016/j.actbio.2006.12.003
29. M. Nakamura, Y. Sekijima, S. Nakamura et al., Role of blood coagulation components as intermediators of high osteoconductivity of electrically polarized hydroxyapatite. J. Biomed. Mater. Res. A **79**, 627–634 (2006). https://doi.org/10.1002/jbm.a.30827
30. S. Nakamura, T. Kobayashi, K. Yamashita, Extended bioactivity in the proximity of hydroxyapatite ceramic surfaces induced by polarization charges. J. Biomed. Mater. Res. **61**, 593–599 (2002). https://doi.org/10.1002/jbm.10224

Chapter 32
Surface Modification with Femtosecond Laser

Peng Chen and Masahiro Tsukamoto

Abstract Surface modification of metallic and inorganic materials with femtosecond laser irradiation for biomedical applications is reviewed in this chapter. Titanium (Ti) and titania (TiO_2) were selected as the models for metallic and inorganic substrates, respectively. Femtosecond laser scanning successfully creates unique periodic surface topography on various materials through a one-step process. Present data showed that surface modification with a femtosecond laser had scale-independent effects on the surface chemical properties and biocompatibility. By controlling the unique periodic surface topography, surface wettability could be changed, and cell adhesion, proliferation, differentiation, calcification, and hemocompatibility could be regulated in vitro. A relative in vivo study also showed that this unique hierarchical periodic topography by femtosecond laser surface modification could also be effective regulating the biocompatibility of the metallic and inorganic material with bone tissues. It was revealed that surface modification with a femtosecond laser can be an effective technology to create unique hierarchical periodic surface topography on metallic and inorganic materials. Moreover, the scale of surface topography can be controlled with a one-step modification and has positive effects in controlling the biocompatibility, which is predicted to be very useful for further medical applications.

Keywords Femtosecond laser · Surface topography · Biocompatibility · Bioactivity

P. Chen (✉)
Institute of Biomaterials and Bioengineering, Tokyo Medical and Denial University,
2-3-10, Kanda-surugadai, Chiyida-ku, Tokyo 101-0062, Japan
e-mail: chen.met@tmd.ac.jp

M. Tsukamoto
Joining and Welding Research Institute, Osaka University,
11-1, Mihogaoka, Ibaraki, Osaka 567-0047, Japan
e-mail: tukamoto@jwri.osaka-u.ac.jp

Y. Setsuhara et al. (eds.), *Novel Structured Metallic and Inorganic Materials*, https://doi.org/10.1007/978-981-13-7611-5_32

32.1 Introduction

Metallic and inorganic materials have been widely used for the fabrication of medical devices due to their high strength, toughness, and durability. In particular, about 80% of implant materials in the human body are made of metal [1]. When considering metal implants in a living body, low cytotoxicity and high corrosion resistance are required, for example, metal alloys with high corrosion resistance such as stainless steel, Co-Cr alloy, commercially pure titanium (Ti) and its alloy, and noble metals such as gold and its alloy, are good choices. Clinically, Ti and its alloy have been used for dental implants, bone plates, artificial joints, etc. On the other hand, compared with metallic or polymeric material, inorganic material such as titania (titanium dioxide, TiO_2), which is used as a substitute for hard tissues, shows better durability, biocompatibility, and bioactivity [2].

Both metals and inorganic materials also have negative aspects. For example, compared with metallic or polymeric materials, inorganic material shows dissatisfactory processability which leads to a higher cost and restricts its applications. Compared with ceramic or polymeric biomaterials, metals have no biofunction, which limits their applications in biomedical treatment. To give a biofunction to metals, surface modification is necessary, because routine metal manufacturing processes like melting, casting, or heat treatment cannot lead to inherent biocompatibility. On the other hand, surface properties such as topography, chemical composition, or structure can be modified by a surface treatment. Various modification methods have been explored, like ion implantation, electrochemical coating, immobilization of biofunctional molecules, and biomolecules [3].

Among these surface modification methods, surface modification of a substrate with a femtosecond laser has an important role in improving biocompatibility. A unique periodic surface topography is created by femtosecond laser irradiation [4–6], which affects surface properties of the substrate relevant for medical applications such as initial molecular attachment, cell proliferation and differentiation, and compatibility with surrounding tissue [7–27]. In addition, surface modification with a femtosecond laser was thought to be the second generation of surface modification techniques to improve biocompatibility at the research level, at the same time, it is already the most widely used method in present commercialized goods [3]. Metallic substrates with designed surface topography could show improved surface area, roughness [15], wettability [16–18], and other properties. These physical changes will affect the absorption of small molecules and proteins in a living system and also the cell attachment and adhesion on these modified surfaces [21, 22]. Thereby, the biocompatibility of metals could be improved. Moreover, the femtosecond laser could be also a powerful technology applied to the surface modification and materials processing of inorganic materials [28, 29] and polymeric materials [30–33].

In this chapter, our latest research results and recent published reports on surface modification with a femtosecond laser have been reviewed, in particular, the improved biocompatibility, including the latest in vitro and in vivo results, are discussed. Data on Ti and TiO_2 substrate materials are focused on. These contents could offer important information for improving the biocompatibility of metallic and inorganic biomaterials, while providing a basis for designing novel implant–host interfaces to promote an appropriate host response in specific applications.

32.2 Surface Modification with a Femtosecond Laser

In recent years, femtosecond laser technology has been developed, which is a high-quality cold ablation process. Femtosecond laser irradiation's small beam size allows for machining of very fine surface structures and requires less postprocessing treatment [34]. Because of these advantages, it has been recognized as a next-generation technology for medical treatment, such as ophthalmological surgery [35–39]. On the other hand, the femtosecond laser is also thought to be a hopeful technology to be used in surface modification of biomaterials because of the unique periodic surface topography formed after femtosecond laser irradiation.

The details concerning laser processing for surface functionalization are presented in Chap. 15. In this section, the changes in biocompatibility concerning surface properties of metallic and inorganic materials after surface modification with femtosecond laser are briefly summarized.

32.2.1 Morphology and Surface Roughness

With femtosecond laser irradiation, the substrate surface is modified with a unique periodic topography. By adjusting the irradiation conditions, such as laser fluence (J cm^{-2}) and scanning speed, the periodic topography can be easily changed. In addition, nanoscaled topography could also be designed and formed during periodic micron-topography fabrication. Therefore, a multiscale periodic topography can be curated through one-stage laser irradiation with femtosecond laser scanning.

32.2.2 Surface Chemical Contents

As a cold ablation process, compared with traditional melting processing, femtosecond laser irradiation induces fewer changes in surface chemical content. Slight oxidation could be induced, increasing the amount of metallic oxides, surface water

adsorption, or carbon contamination [40]. However, the present common perception is that the surface modification changes from femtosecond lasers do not have significant effects on the surface properties [5, 40].

32.2.3 Surface Wettability

Surface wettability plays an important role in improving the biocompatibility of biomaterials. Surface modification by femtosecond lasers under different conditions could result in different surface wettability of the material [5, 16, 18, 40–43]. The surface topography created by femtosecond laser irradiation was thought to be the primary cause of surface wettability changes. For example, a superhydrophobic surface can be obtained by modifying a stainless steel substrate with a hierarchical periodic topography [5]. However, the surface composition of stainless steel after surface modification with a femtosecond laser has increased carbon and oxygen and decreased iron (Fe), indicating the formation of iron oxides which are not hydrophobic. In addition, our data further clarifies this standpoint, as changing the surface periodic architecture modified both the hydrophilic and hydrophobic surfaces (Fig. 32.1) [18]. Moreover, this property could also apply to the surface modification of polymeric materials [41, 42].

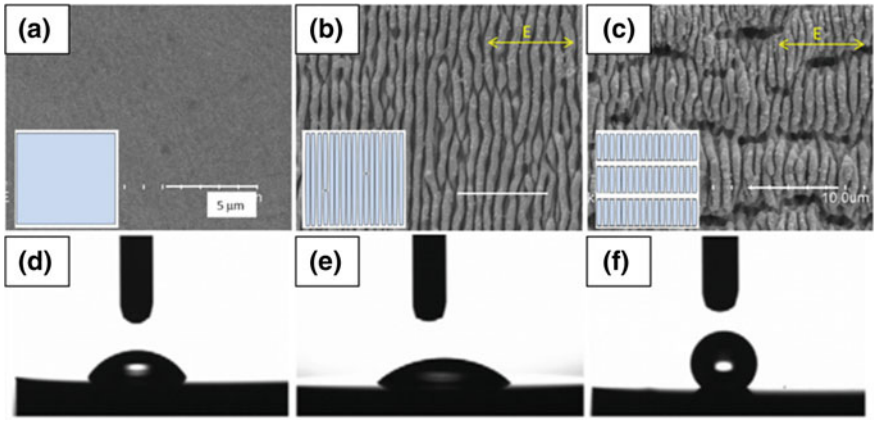

Fig. 32.1 The surface morphology and wettability of nitinol with and without femtosecond laser surface modification. The surface morphologies of specimens were detected by SEM: (**a**) a mirror-polished surface without surface treatment, and the specimens after femtosecond laser scanning with (**b**) periodic nano- and (**c**) hierarchical periodic micro/nano topographies, respectively. Wettability was evaluated by measuring contact angles of 1 μL water dropped onto the nitinol surface, and side view images of the water droplets of (**a**), (**b**), and (**c**) surfaces are shown in (**d**), (**e**), and (**f**), respectively. Reprinted from Ref. [18]. Copyright 2016, with permission from Elsevier

32.3 Bioactivity Evaluation

Generally, there are three commonly used ways to evaluate the bioactivity of biomaterials: soaking in simulation body fluid (SBF), in vitro study, and in vivo study. The easiest way to investigate the biocompatibility of materials is by simply soaking them in a simulation body fluid, which has inorganic chemicals and may also contain a small amount of organic components. In vitro (Latin for "within the glass") study is generally defined as the research activities of biomolecules, cells, tissues, or even organs in a specific controlled artificial environment. On the other hand, the study of biological responses in an intact living organism is termed in vivo (Latin for "within the living") research.

32.3.1 Soaking in Simulation Body Fluid

This chemistry-based method to mimic the human body environment is a simple and easy way for most material scientists or researchers to evaluate their newly prepared materials for biological or medical applications. Potential contaminations or statistical differences among testing groups caused by organic contents and living cells could be avoided. For example, Hanks' solution has been widely used to evaluate osseointegration of materials for dental/bone implant applications [44–46], through comparing the calcium (Ca) and phosphate (P) contents in the calcium phosphate deposits formed after soaking in SBF [44–47]. The determination of Ca/P atomic ratios enables researchers to evaluate the formation of octacalcium phosphate, which is a precursor to hydroxyapatite (HAp) [47]. It was reported that, after soaking in SBF, rapid formation of a Ca/P layer was obtained on a Ti surface with femtosecond laser modification. This phenomenon implies that good bioactivity has been achieved on Ti by surface modification with a femtosecond laser [48].

32.3.2 In Vitro Study

Although soaking in SBF is a simple and effective way to investigate the biocompatibility of materials, studies based on pure chemical contents may lead to results that do not correspond to the circumstances occurring in the environment of a living organism [49]. In addition, compared with a complicated in vivo study, it is simpler and more convenient to study potential mechanisms in vitro. Therefore, to investigate the compatibility of femtosecond laser surface-modified metallic and inorganic materials, in vitro studies are ideal.

32.3.2.1 In Vitro Models

The in vitro models used for evaluating the biocompatibility of substrates after surface modification with femtosecond lasers vary depending on what specific parameters are desired and detected. Usually, two kinds of cell resources have been used: cell lines and primary cells. For example, bone cells (e.g., osteoblastic cell lines) [21, 22, 50] or mesenchymal stem cells (MSCs) [51–53] could be good candidates for evaluating a surface-modified material for bone implant applications, while endothelial cells or blood platelets are suitable models for evaluating the effect of a material on endothelialization or thrombosis, respectively [18]. Cell models are distinguished by their different surface transmembrane proteins and incretion specific proteins, which may activate specific cellular signaling pathways to induce unique target gene(s) expression and protein(s) synthesis.

Moreover, considering the size of surface topography after surface modification, proper in vitro models can be selected. For example, osteoblasts, which are about 10 μm by 2 μm in size, may not be suitable for testing a substrate with a surface topography scale over 10 μm. This is because it is impossible for any individual cell to sense surface topography of a larger scale.

32.3.2.2 Cell Adhesion

Cell adhesion is defined as the cellular process of interacting and attaching to a surface, which is the first step of a cell's response to an artificial substrate during in vitro testing. This cell behavior strongly depends on the interaction between cell adhesion molecules (e.g., integrins, selectins, and cadherins) and the substrate surface [54–60]. Changing substrate surface topographies could select for specific bonding modalities between the substrate and cells to induce different cellular signal transduction pathways [58]. Consequently, cell proliferation and differentiation as well as calcification of osteoblasts can be specifically regulated.

For example, cell alignment on a surface-modified substrate is a challenging issue, because it could promote neurogenesis or also mimic the osteocyte alignment found normally in long bone structure. As we reported, nanostructures with periods of 130 and 230 nm, especially 230 nm, created by a femtosecond laser with a wavelength of 775 nm, were effective for cell spreading [21]. Aligned cell morphologies were observed on both Ti and TiO_2 substrates after femtosecond laser surface modification; fluorescent images depicting this phenomenon are shown in Fig. 32.2.

32.3.2.3 Cell Proliferation

Cell proliferation is regarded as an important way to measure cytotoxicity of an artificial substrate. The inhibition of cell viability by 50% (IC_{50}) has been used to assess the toxicity response induced by artificial substrates or drugs during cell

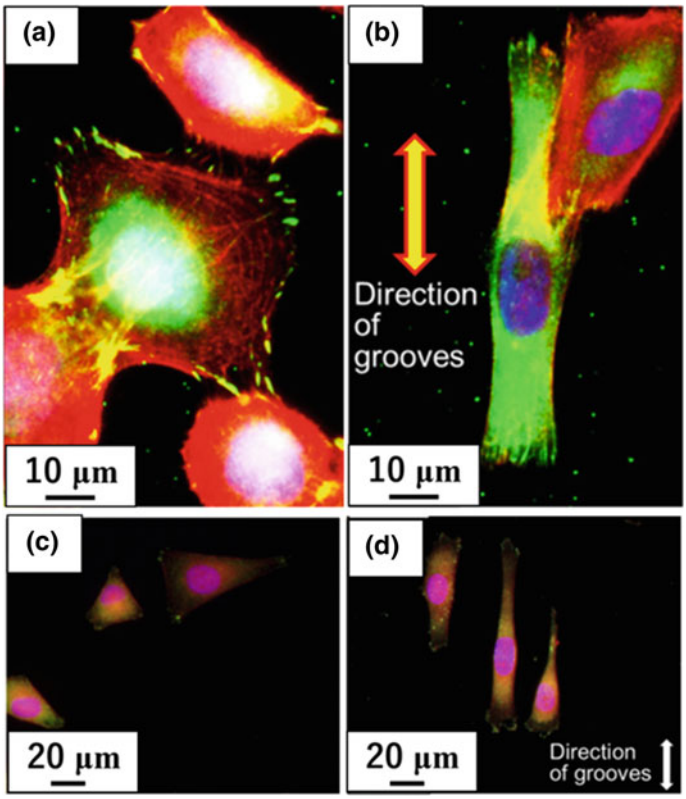

Fig. 32.2 Differences in initial cellular spreading on surfaces with or without femtosecond laser surface modification. Cellular morphology was examined by immunocytochemistry. Nuclei (blue), F-actin cytoskeleton (red), and vinculin (green)-positive adhesion plaques were visualized. Fluorescence microscopy images of osteoblasts cultured on a Ti metal surface with (**b**) or without (**a**) femtosecond laser surface modification (Reprinted from Ref. [21], Springer). Fluorescence microscopy images of osteoblasts cultured on an inorganic TiO_2 surface with (**c**) or without (**d**) femtosecond laser surface modification. Reprinted from Ref. [22]. Copyright 2016, with permission from Elsevier

proliferation [61, 62]. A substrate with high corrosion resistance is thought to have no significant cytotoxic effect if a cell viability over 80% is maintained for 5–7 d. In addition, if the cell number increases with increasing culture time and the doubling time is normal, the material is thought to have no safety concern.

On the other hand, one study reported that micron-scale surface topography has little effect on cell proliferation, while cells cultured on substrates with nanoscale topography show a slowed growth rate [58]. However, it was also reported that mouse osteoblasts (MC3T3-E1) grow faster on a ZA318B magnesium alloy after surface modification with femtosecond laser, especially with the laser fluence of 0.64 J cm^{-2}, compared to their growth on the alloy without surface modification

[23]. This phenomenon may be explained by the intricate mutual effects of novel multiscale periodic topography formed by femtosecond laser irradiation.

32.3.2.4 Cell Differentiation

For primary cells and stem cells, evaluating cell differentiation is another critical criterion for artificial substrates applied toward medical treatment. For example, when a metal implant is implanted in bone tissue, osteocytes and mesenchymal stem cells are exposed to the metallic body of the implant, which could have an effect on cell differentiation. Because surface modification with a femtosecond laser has effects on cellular initial adhesion and proliferation, cell differentiation could also be effected. In addition, different topography scales have different effects on cell adhesion and proliferation as previously mentioned, and cell differentiation could also be affected by topography scale differences. For example, an equiatomic Ni-Ti alloy with hierarchical periodic micro/nanosurface topography ($\sim$2.0 μm width, $\sim$590 nm depth) from femtosecond laser irradiation promoted the endothelialization of porcine endothelial cells [18]. In addition, it has been shown that a femtosecond laser-modified polyimide coating surface promotes different differentiation patterns in MSCs depending on topology: 15 μm periodic topography promoted adipogenic differentiation, 2 μm periodic topography promoted osteogenic differentiation, and 650 nm topography promoted differentiation toward both lineages [63].

32.3.2.5 Calcification

Considering its importance and pervasiveness, calcification of osteocytes cultured on the femtosecond laser-modified surface is examined. Calcification, the accumulation of calcium salts in a tissue occurs during bone formation. Calcium deposition on a substrate surface is used for evaluating calcification of biomaterials in vitro. Alizarin red staining is commonly used to show the calcified area (Fig. 32.3).

It has been reported that the substrate surface modified by femtosecond laser irradiation promotes osteogenic differentiation and maturation of pre-osteoblasts [63]. However, there are still some problems with this evaluation because the calcified surface area only indicates the contact area of newly formed bone tissue on substrate, and the results cannot yield any quantified data on the calcified tissue itself.

32.3.2.6 Hemocompatibility

Metallic materials play important roles in the fabrication of medical devices that need to exist in a hematologic environment chronically, such as stents and

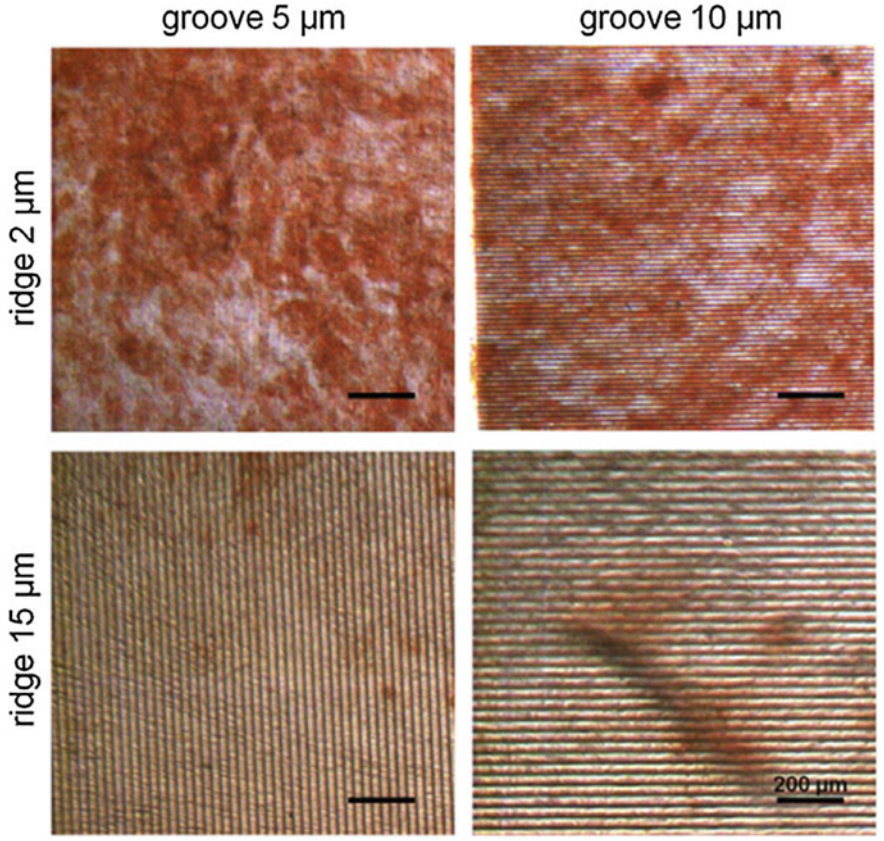

Fig. 32.3 The impact of groove surface topographies created by femtosecond laser scanning on osteogenic differentiation of MSCs cultured on a glass wafer surface with spin-coated polyimide after alizarin red staining. After 2 weeks of differentiation induction, osteoblast calcium deposition on each indicated surface was stained with alizarin red. Reprinted from Ref. [71]. Copyright 2016, with permission from Elsevier

pacemakers, or temporarily, such as surgical clips for aneurysm ruptures. Therefore, the hemocompatibility of metals is crucial. The adsorption of platelets onto a surface can induce thrombus formation, which results in unwanted in-stent restenosis. Thus, to avoid the unwanted formation of thrombus on the metal surface of those artificial medical devices, effective surface modification is important.

Femtosecond laser-formed hierarchical periodic micro/nanosurface topography showed possible anti-thrombosis ability through a platelet adhesion test [18]. It was shown that the number of platelets attached on nitinol specimens with a hierarchical periodic micro/nanostructure surface topography was reduced by half compared to as-polished specimens without surface modification (Fig. 32.4).

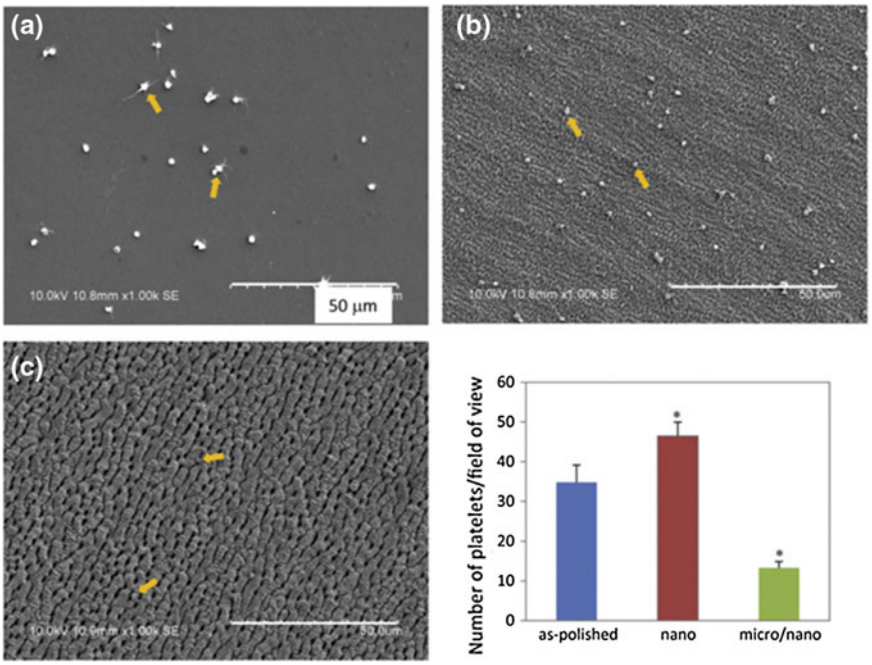

Fig. 32.4 Platelet adhesion onto the different surfaces after 30 min of incubation with platelet-rich plasma: **a** as-polished, **b** nano-, and **c** micro/nanosurface. Scale bars, 50 μm. Platelets are indicated by yellow arrows. The data represent the mean ±SD, * $p < 0.05$ (multiple comparison analysis). Reprinted from Ref. [18]. Copyright 2016, with permission from Elsevier

32.3.3 In Vivo Studies

One of the distinct weaknesses of in vitro study is that it is difficult to replicate precise conditions of living organisms using cell culture. Therefore, in vivo studies are usually employed following in vitro study as the ultimate assessment to offer a conclusive insight about the compatibility of biomaterials and their overall effects in a living organism. In vivo studies have two forms: animal studies and clinical trials.

As the surface modification with femtosecond laser modification is a still-emerging unique technology, information is extremely lacking concerning its in vivo performance. An animal study [64] is presented as one example, where it was reported that zirconia dental implants with 30 μm wide hierarchical periodic surface topography fabricated by femtosecond laser irradiation showed an improved bone-to-implant contact value in dog mandible after 90 days. However, conclusions concerning the potential performance of materials altered by this method are in urgent need of further evidence in vivo.

32.4 Future Developments and Applications

As a cutting-edge technology, femtosecond lasers have been utilized for surface modification of metallic and inorganic materials for biomedical applications. Present research results show that the unique periodic surface topography created by femtosecond laser irradiation affects the biocompatibility of metallic and inorganic materials. This method is thought to be a hopeful surface modification strategy to fabricate materials with novel structures for biomedical applications. However, a systematic comparison of cellular responses to substrates with distinct topographies has not been carried out completely.

The details concerning surface properties and biocompatibility of materials after femtosecond laser irradiation still need to be thoroughly investigated. For example, the data concerning the scale effect on surface wettability and biocompatibility should be investigated in more detail in vitro. More importantly, information about the stability and biocompatibility of specimens with femtosecond laser surface modification should be further studied in vivo.

Knowing that cellular responses depend on the size of a material's surface topography, controlling the scale of surface topography could be a key element to controlling cell function. This could be a proper technology for fabricating specific artificial devices with complicated structure to meet various surface modification demands. For example, dental implants require promotion of osseointegration between the dental implant and surrounding bone tissue, while less cell attachment is necessary for implant abutments, the connectors between the crown and implant. Another example is that artificial joints require better osseointegration for stem (hip implant) and socket (acetabular shell) parts, while less abrasion and tissue attachment are required for the femoral head. Through surface modification with a femtosecond laser, varying surface properties on artificial devices could be fabricated through a one-step treatment.

32.5 Concluding Remarks

In this chapter, surface modification to metallic and inorganic materials by the emerging technology of femtosecond laser irradiation has been reviewed. A unique periodic surface topography through one-step process formed by femtosecond laser scanning is thought to be a hopeful surface modification technology for fabricating metallic and inorganic materials with novel structures, especially for use in biomedical applications.

Ti and TiO_2 were used as model substrates for metallic and inorganic substrate, respectively. Femtosecond laser-treated surfaces have scale-independent effects on surface wettability and cellular behavior. Through controlling the unique periodic surface topography of the material, cell adhesion, proliferation, and differentiation, as well as calcification and hemocompatibility were regulated in vitro. A relative

in vivo study showed that this unique hierarchical periodic topography could also be effective for regulating biocompatibility with bone tissue.

However, because femtosecond lasers are a new technology for surface modification of metallic and inorganic materials, detailed information concerning its effects on biocompatibility and chemical properties like stability is lacking.

Regardless of the lacking information, based on present research results, surface modification with femtosecond laser seems to be an effective technology for creating unique hierarchical periodic surface topography on metallic and inorganic materials. Through this surface treatment, the scale of surface topography can be controlled with a one-step modification and has positive effects on the control of biocompatibility, which should prove very useful in further medical applications.

References

1. T. Hanawa, Biofunctionalization of metals with polymers, in *Advances in Metallic Biomaterials: Processing and Applications*, ed. by M.N. Niinomi, M. Nakai (Springer, Berlin, 2015), pp. 127–142
2. T. Hanawa, T. Yoneyama, Metals in biomaterials, in *Biomaterials*, ed. by T. Hanawa (Corona Publishing Co., LTD, Tokyo, 2007), pp. 3–11
3. T. Hanawa, Research and development of metals for medical devices based on clinical needs. Sci. Tech. Adv. Mater. **13**(6), 064102 (2012)
4. B.K. Nayak, M.C. Gupta, Self-organized micro/nano structures in metal surfaces by ultrafast laser irradiation. Opt. Laser Eng. **48**(10), 940–949 (2010)
5. M.V. Rukosuyev et al., One-step fabrication of superhydrophobic hierarchical structures by femtosecond laser ablation. Appl. Surf. Sci. **313**, 411–417 (2014)
6. H.Y. Tao et al., One-step formation of multifunctional nano- and microscale structures on metal surface by femtosecond laser. Chin. Opt. Lett. **13**(6) (2015)
7. M. Tsukamoto et al., Periodic microstructures produced by femtosecond laser irradiation on titanium plate. Vacuum **80**(11–12), 1346–1350 (2006)
8. H. Nakano et al., Femtosecond laser peening of stainless steel. J. Laser Micro Nanoeng. **4**(1), 35–38 (2009)
9. M. Tsukamoto et al., Rewriting process of lower electrical resistance lines on TiO_2 film using methods of whitening with electric furnace and darkening with femtosecond laser. J. Laser Micro Nanoeng. **6**(2), 164–167 (2011)
10. M. Tsukamoto et al., Photoconductive properties of titanium dioxide film modified by femtosecond laser irradiation. Appl. Phys. A **110**(3), 679–682 (2013)
11. T. Shinonaga et al., Formation of TiO_2 film with lower electrical resistance by aerosol beam and fiber laser irradiation. Appl. Phys. A **112**(1), 57–60 (2013)
12. M. Tsukamoto et al., Rewriting of low electrical resistance lines on TiO_2 film by writing and erasing with femtosecond and CW fiber lasers. Appl. Surf. Sci. **313**, 730–735 (2014)
13. T. Shinonaga, M. Tsukamoto, G. Miyaji, Periodic nanostructures on titanium dioxide film produced using femtosecond laser with wavelengths of 388 nm and 775 nm. Opt. Express **22** (12), 14696–14704 (2014)
14. D.V. Abramov et al., Formation of a system of microcraters on a titanium surface by femtosecond laser radiation under rapid cooling conditions. Tech. Phys. Lett. **39**(8), 719–722 (2013)
15. D. Tanigawa et al., Effect of laser path overlap on surface roughness and hardness of layer in laser cladding. Sci. Technol. Weld Join. **20**(7), 601–606 (2015)

16. P. Bizi-Bandoki et al., Modifications of roughness and wettability properties of metals induced by femtosecond laser treatment. Appl. Surf. Sci. **257**(12), 5213–5218 (2011)
17. Z.J. Bao et al., Modification of wettability of stainless steel by picosecond laser surface microstructuring. Photon. Res. **3**(4), 180–183 (2015)
18. K. Nozaki et al., Hierarchical periodic micro/nano-structures on nitinol and their influence on oriented endothelialization and anti-thrombosis. Mater. Sci. Eng. C Mater. Biol. Appl. **57**, 1–6 (2015)
19. Y.H. Jeong, H.C. Choe, W.A. Brantley, Nanostructured thin film formation on femtosecond laser-textured Ti-35Nb-xZr alloy for biomedical applications. Thin Solid Films **519**(15), 4668–4675 (2011)
20. C.Y. Liang et al., Femtosecond laser-induced micropattern and Ca/P deposition on Ti implant surface and its acceleration on early osseointegration. ACS Appl. Mater. Interfaces **5**(16), 8179–8186 (2013)
21. T. Shinonaga et al., Formation of periodic nanostructures using a femtosecond laser to control cell spreading on titanium. Appl. Phys. B **119**(3), 493–496 (2015)
22. T. Shinonaga et al., Cell spreading on titanium dioxide film formed and modified with aerosol beam and femtosecond laser. Appl. Surf. Sci. **288**, 649–653 (2014)
23. C.Y. Liang et al., Femtosecond lasers induced micropatterns on magnesium alloy to promote cell proliferation. Rare Metal Mater. Eng. **43**, 253–256 (2014)
24. S. Bashir et al., Surface and structural modifications of titanium induced by various pulse energies of a femtosecond laser in liquid and dry environment. Appl. Phys. A **114**(1), 243–251 (2014)
25. C. Symietz et al., Fixation of bioactive calcium alkali phosphate on Ti–6Al–4V implant material with femtosecond laser pulses. Appl. Surf. Sci. **257**(12), 5208–5212 (2011)
26. A.Y. Vorobyev, C. Guo, Femtosecond laser structuring of titanium implants. Appl. Surf. Sci. **253**(17), 7272–7280 (2007)
27. G.C. Wang et al., Enhancing orthopedic implant bioactivity: refining the nanotopography. Nanomedicine **10**(8), 1327–1341 (2015)
28. R.A. Delgado-Ruiz et al., Femtosecond laser microstructuring of zirconia dental implants. J. Biomed. Mater. Res. B Appl. Biomater. **96**(1), 91–100 (2011)
29. M.J. Smith et al., Pressure-induced phase transformations during femtosecond-laser doping of silicon. J. Appl. Phys. **110**(5) (2011)
30. Z.K. Wang et al., Polymer hydrophilicity and hydrophobicity induced by femtosecond laser direct irradiation. Appl. Phys. Lett. **95**(11) (2009)
31. L.N. He et al., Wettability modification of electrospun poly(epsilon-caprolactone) fibers by femtosecond laser irradiation in different gas atmospheres. Appl. Surf. Sci. **257**(8), 3547–3553 (2011)
32. N.E. Stankova et al., fs- and ns-laser processing of polydimethylsiloxane (PDMS) elastomer: comparative study. Appl. Surf. Sci. **336**, 321–328 (2015)
33. L.H. Hofmeister et al., Patterned polymer matrix promotes stemness and cell-cell interaction of adult stem cells. J. Biol. Eng. **9** (2015)
34. S. Hypsh, Femtosecond laser processing overcomes barriers for use in medical device manufacturing. Adv. Mater. Processes **172**(11), 26–29 (2014)
35. H.K. Soong et al., Femtosecond laser-assisted posterior lamellar keratoplasty—initial studies of surgical technique in eye bank eyes. Ophthalmology **112**(1), 44–49 (2005)
36. M.C. Lorenzo et al., In vitro analysis of femtosecond laser as an alternative to acid etching for achieving suitable bond strength of brackets to human enamel. Lasers Med. Sci. **29**(3), 897–905 (2014)
37. R.G. Abell et al., Femtosecond laser-assisted cataract surgery versus standard phacoemulsification cataract surgery: outcomes and safety in more than 4000 cases at a single center. J. Cataract Refract. Surg. **41**(1), 47–52 (2015)
38. R. Antonios, S.A. Mosquera, S.T. Awwad, Hyperopic laser in situ keratomileusis: comparison of femtosecond laser and mechanical microkeratome flap creation. J. Cataract Refract. Surg. **41**(8), 1602–1609 (2015)

39. C. Schweitzer et al., Anterior capsule contraction treated by femtosecond laser capsulotomy. J. Refract. Surg. **31**(3), 202–204 (2015)
40. P. Bizi-Bandoki et al., Time dependency of the hydrophilicity and hydrophobicity of metallic alloys subjected to femtosecond laser irradiations. Appl. Surf. Sci. **273**, 399–407 (2013)
41. Z.K. Wang, H.Y. Zheng, Y.C. Lam, Investigation on femtosecond laser irradiation energy in inducing hydrophobic polymer surfaces. Appl. Surf. Sci. **257**(24), 10427–10433 (2011)
42. Z.K. Wang, H.Y. Zheng, H.M. Xia, Femtosecond laser-induced modification of surface wettability of PMMA for fluid separation in microchannels. Microfluid Nanofluidics **10**(1), 225–229 (2011)
43. A. Cunha et al., Wetting behaviour of femtosecond laser textured Ti–6Al–4V surfaces. Appl. Surf. Sci. **265**, 688–696 (2013)
44. K. Asami et al., Titanium-implanted CaTiO3 films and their changes in Hanks' solution. Surf. Interface Anal. **35**(5), 483–488 (2003)
45. J.Y. Ha et al., Enhancement of calcium phosphate formation on zirconium by micro-arc oxidation and chemical treatments. Surf. Coat. Technol. **205**(21–22), 4948–4955 (2011)
46. Y. Tsutsumi et al., Micro-arc oxidation treatment to improve the hard-tissue compatibility of Ti–29Nb–13Ta–4.6Zr alloy. Appl. Surf. Sci. **262**, 34–38 (2012)
47. N. Eliaz et al., Electrochemical processes of nucleation and growth of calcium phosphate on titanium supported by real-time quartz crystal microbalance measurements and X-ray photoelectron spectroscopy analysis. J. Biomed. Mater. Res. A **89A**(1), 270–280 (2009)
48. C.Y. Liang et al., Surface modification of cp-Ti using femtosecond laser micromachining and the deposition of Ca/P layer. Mater. Lett. **62**(23), 3783–3786 (2008)
49. T. Umezawa et al., Calcification of MC3T3-E1 cells on titanium and zirconium. Dent. Mater. J. **34**(5), 713–718 (2015)
50. C.Y. Liang et al., Biocompatibility of the micro-patterned NiTi surface produced by femtosecond laser. Appl. Surf. Sci. **261**, 337–342 (2012)
51. H. Kenar et al., Femtosecond laser treatment of 316L improves its surface nanoroughness and carbon content and promotes osseointegration: an in vitro evaluation. Colloids Surf. B **108**, 305–312 (2013)
52. C.W. Chan et al., Effect of laser treatment on the attachment and viability of mesenchymal stem cell responses on shape memory NiTi alloy. Mater. Sci. Eng. C Mater. Biol. Appl. **42**, 254–263 (2014)
53. A. Cunha et al., Human mesenchymal stem cell behavior on femtosecond laser-textured Ti–6Al–4V surfaces. Nanomedicine **10**(5), 725–739 (2015)
54. N.J. Fredin et al., Nanoimprinted thin films of reactive, azlactone-containing polymers: combining methods for the topographic patterning of cell substrates with opportunities for facile post-fabrication chemical functionalization. Biomacromolecules **10**(4), 994–1003 (2009)
55. R.E. Waugh, E.B. Lomakina, Active site formation, not bond kinetics, limits adhesion rate between human neutrophils and immobilized vascular cell adhesion molecule 1. Biophys. J. **96**(1), 268–275 (2009)
56. K. von der Mark et al., Nanoscale engineering of biomimetic surfaces: cues from the extracellular matrix. Cell Tissue Res. **339**(1), 131–153 (2010)
57. S. Zhang et al., Biological behavior of osteoblast-like cells on titania and zirconia films deposited by cathodic arc deposition. Biointerphases **7**(1–4), 60 (2012)
58. D. Khang et al., Role of subnano-, nano- and submicron-surface features on osteoblast differentiation of bone marrow mesenchymal stem cells. Biomaterials **33**(26), 5997–6007 (2012)
59. R.K. Das, O.F. Zouani, A review of the effects of the cell environment physicochemical nanoarchitecture on stem cell commitment. Biomaterials **35**(20), 5278–5293 (2014)
60. N. Li et al., Effect of surface topography and bioactive properties on early adhesion and growth behavior of mouse preosteoblast MC3T3-E1 cells. ACS Appl. Mater. Interfaces **6**(19), 17134–17143 (2014)

61. H. Sadeghi-Aliabadi, M. Minaiyan, A. Dabestan, Cytotoxic evaluation of doxorubicin in combination with simvastatin against human cancer cells. Res. Pharm. Sci. **5**(2), 127–133 (2010)
62. B. Braeckman, H. Raes, D. VanHoye, Heavy-metal toxicity in an insect cell line. Effects of cadmium chloride, mercuric chloride and methylmercuric chloride on cell viability and proliferation in Aedes albopictus cells. Cell Biol. Toxicol. **13**(6), 389–397 (1997)
63. G. Abagnale et al., Surface topography enhances differentiation of mesenchymal stem cells towards osteogenic and adipogenic lineages. Biomaterials **61**, 316–326 (2015)
64. J.L. Calvo-Guirado et al., Histological, radiological and histomorphometric evaluation of immediate vs. non-immediate loading of a zirconia implant with surface treatment in a dog model. Clin. Oral Implants Res. **25**(7), 826–830 (2014)

Chapter 33
Surface Modification with Hydrothermal–Electrochemical Technique

Nobuhiro Matsushita

Abstract A sodium-contained amorphous titanium oxide layer having nano size mesh-like structure was fabricated on TiCuZrPd and TNTZ substrates by three different processes using alkaline solution. XPS result suggested that TiCuZrPd samples surface-modified by hydrothermal–electrochemical (HE) process exhibited the much less toxic Cu content than the original substrate composition, which is favorable for implant material. HE-processed TiCuZrPd sample had intermediated layer in which the structure was gradually changed to thickness direction with a widely diffused interface and it caused strong adhesion of hydroxyapatite layer. The nanomesh structure formed on TiCuZrPd substrate by HE process exhibited enough bioactivity in vitro test to form hydroxyapatite on their whole surface after immersing in SBF for 12 days. The surface chemical composition affects the apatite induction ability of TNTZ samples. The surface incorporation of fewer niobium species exhibited hydrophilic condition. The HE treated TNTZ sample at 90 °C for 2 h had a rough surface with fewer Nb content and it exhibited enough high bioactivity without forming any cracks or peeling.

Keywords Solution process · Bio-active surface · Titanium bulk metallic glass · Ti-Nb-Ta-Zr · Hydroxyapatite

33.1 Introduction

Titanium and its alloys have been investigated for long years as bone implant materials due to their superior biocompatibility, high corrosion resistance, and high strength-to-weight ratio. However, their high original Young's modulus exceeding 100 MPa provides cause of the bone resorption and the material exhibiting the Young's modulus closer to the bone have being investigated to date [1–6]. One of the promising candidate for the implant is Ti-based bulk metallic glass families such

N. Matsushita (✉)
Tokyo Institute of Technology, Tokyo, Japan
e-mail: matsushita.n.ab@m.titech.ac.jp

Y. Setsuhara et al. (eds.), *Novel Structured Metallic and Inorganic Materials*, https://doi.org/10.1007/978-981-13-7611-5_33

as Ti-Cu-Ni-Co [7], Ti-Cu-Ni-Zr [8], Ti-Cu-Ni-Zr-Be [9]. However, they contain some toxic elements, Ni and/or Be in order to provide good glass-forming abilities, and thus restrict their practical application in biomedical field. Zhu S.L. et al. invented Ti-36Cu-10Zr-14Pd (TiCuZrPd), which is a toxic element free Ti-based BMG [10]. On the other hand, Niinomi et al. invented the β phase titanium alloy, Ti-29Nb-13Ta-4.6Zr (TNTZ) [11]. Since its Young's modulus of around 70 MPa is closer to that of the cortical bone, it can be also recognized as promising candidates for implant materials in next generation.

These Ti alloys, TiCuZrPd, and TNTZ having both of moderately low Young's modulus and high corrosion resistances are suitable for implant materials. However, despite favorable mechanical properties, these alloys surfaces exhibit low bioactivity and cannot be joined directly to human bone due to their high chemical stability. Therefore, it is essential to attain biocompatibility (such as bone inducing ability) of these materials by means of ceramic coating on their surfaces.

One popular modification process to form ceramic coating on Ti alloys is alkali solution treatment. It enables the fabrication of a bioactive titanate layer by soaking a sample in a highly alkaline solution. There are several articles which reported the fabrication of bioactive surface layer using alkaline solutions [12–14].

In this study, three of alkaline solutions were investigated to fabricate oxide layers having high bioactivity on Ti alloys surfaces. They were conventional hydrothermal (H) and electrochemical (E) process and a novel one of their combination named as Hydrothermal–electrochemical (HE) process [15]. This HE process is environmentally friendly because it can perform below 150 °C without using an energy consuming vacuum system, and this process enables to create bioactive oxide layer on Ti alloys surfaces efficiently.

This technique has the advantage of a processing temperature typically less than 423 K, which is low enough to avoid the crystallization of amorphous TiCuZrPd and the phase change of TNTZ from β to α. This advanced technique is also enabled to control the composition of surface oxide layers to attain better biocompatibility. It was possible to create the oxide layers with less Cu component on TiCuZrPd substrate and that with less Nb component on TNTZ substrate, which would be favorable for less toxic and higher hydrophilic surface which are required for the implant material.

The bioactivities of H, E, and HE treated samples were also evaluated by SBF test. Not only bioactivity but also the structural and compositional characteristics of the modified layer were also compared to each other. The effects of the morphology and chemical composition of the surface layers upon the apatite induction ability were also investigated.

33.2 Surface Modifications on TiCuZrPd and TNTZ Substrates

33.2.1 Pretreatments

A foil of TiCuZrPd 0.07 mm in thickness was fabricated by arc-melting a mixture of pure metal (>99.9%) in an argon atmosphere [16]. Each substrate was cut into 10×40 mm^2 in size and was degreased prior to all treatments. The degreasing was carried out by sonication in acetone for 10 min, rinsing with distilled water (Millipore Milli-Q), and then drying at ambient temperature. Almost the same pretreatment was conducted for a platinum substrate (Tanaka Kikinzoku), $10 \times 50 \times 0.5$ mm^3, and was used as the cathode. These electrodes were immersed in the electrolyte of 1 and 5 M NaOH aqueous solution and hydrothermally treated at 90–150 °C for 2 h. After the treatments, the substrate was rinsed with deionized water and finally dried at 80 °C for 20 min in air. After each treatment, the specimens were washed with distilled water to remove the alkali, and finally dried at 60 °C for 24 h in air.

TNTZ round bar was first hot forged at 1273 K under Ar atmosphere, and hot rolled under the condition of rolling reduction ratio of 80%. After that, TNTZ was subjected to solution heat treatment at 1013 K for 3.6 ks [17]. TNTZ was then formed in disk plates with a diameter of 10 mm and a thickness of 1 mm. The TNTZ disk plates were then polished using rotating polishing machine with emery of a grid of #500 to remove any undesirable contaminations left. It is also degreased prior to the start of the experiment by sonication in acetone for 10 min, rinsing with distilled water, and drying at the ambient temperature.

33.2.2 Solution Processes

The hydrothermal–electrochemical apparatus was used for all H, E and HE processes. The photographic image and schematic illustration of hydrothermal–electrochemical system used in this study are shown in Fig. 33.1a, b. It was composed of the autoclave and electrochemical electrodes.

H process is one of the solution processes which is conducted under high pressure. It is widely known since it can create chemically uniformed component [18]. H process in this study was carried out in 40 ml of NaOH solution at different concentration of 0.2–5 M. The operating temperature was ranged from the room temperature to 200 °C. The pressure inside the container was approximately 1 and 7 Pa/atm for the treatment at 90 and 150 °C, respectively.

The E process was performed in the same solution for the same duration as the H process given above. The aim of this process was to attain a strong adhesive strength between the TiCuZrPd or TNTZ substrates and formed oxide layers. The TiCuZrPd or TNTZ substrates and a platinum plate were suspended as the working

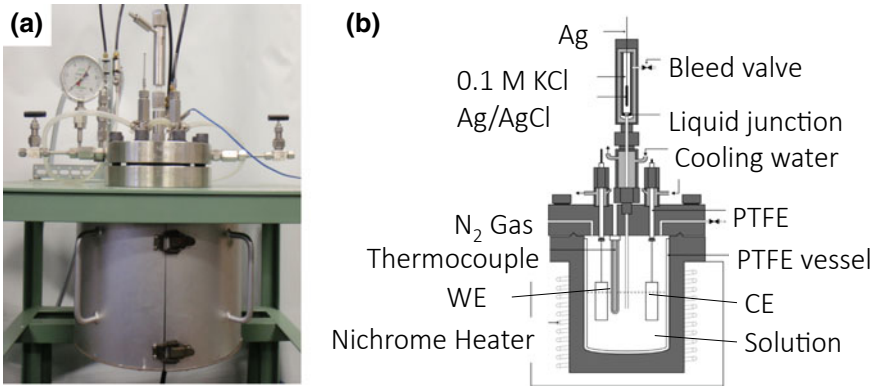

Fig. 33.1 **a** Photographic image and **b** schematic illustration of hydrothermal–electrochemical technique

and the counter electrodes, respectively, maintaining their separation distance at around 40–60 mm constant. The constant dc electric current density of 0–200 mA/cm^2 was applied using the constant current mode of KEITHLEY 2400 Source Meter between the electrodes whose active surface areas immersed in the electrolyte were 3 cm^2.

The HE process was conducted H and E processes simultaneously. In this process, the hydrothermal and electrochemical conditions were the same as the conditions given above for the H and E process except the reaction time. The reaction time varied between 0.5 and 2 h. This novel HE process was proposed by Yoshimura and his group members [19]. The samples treated by this process had a widely diffused intermediate layer at the interface between metallic substrate and formed oxidized layers. They named the structure having this widely diffused intermediate layer as "Growing Integration Layer (GIL)" which works to improve the adhesion performance at the interface between ceramic and metallic materials and to avoid the accumulation of thermal residual stress in the ceramic layer. The GIL is formed from a reactive component of the metallic substrate by chemical and electrochemical reactions. In particular, in the case of titanium alloy, like TiCuZrPd or TNTZ, the hydrothermal–electrochemical technique is one of the most adaptable processes for the formation of the GIL layer, since they contain active component of Ti as the major element. For the treatments of highly corrosive-resistant TNTZ substrates, the 0.17 mass% of NH_4F was added to the solution to create a rough surface and thus provide a large surface area, which is believed to be suitable for apatite induction [20, 21].

33.2.3 Measurements and Evaluations of Samples

X-ray diffraction (XRD) measurements were performed using MXP3VA (MAC Science, Japan) or RINT2100 vertical type (Rigaku, Japan) with monochromatized CuK_{α} radiation at wavelength $\lambda = 1.5418$ Å, an acceleration voltage of 40 V and a current of 20–40 mA.

The SEM images of the specimens were taken with a Hitachi SP 4500 scanning electron microscope operating at 15 kV. The elemental composition of the titanate nanomesh layer was characterized by energy dispersive X-ray spectroscopy (EDS). The sample surface was analyzed with Raman spectroscopy, using a T64000 Jobin-Yvon spectrometer with an Ar laser ($\lambda = 514.5$ nm) operated at 50 mW.

The bioactivity of the surface is easily measured by the simulated body fluid (SBF) test [22]. SBF solution, which is modeled after our body plasma, has been served as a very useful tool to anticipate its bone bonding activity in vitro situation. If samples induce apatite on their surface, it means that these samples have bioactivity since the first step of bone bonding is dependent on apatite induction. Therefore, SBF has been used extensively to examine bioactivity because it is not expensive and also easy to detect bioactivity. In short, SBF test is a very effective way to detect bioactivity before proceeding clinical test.

The SBF was prepared by dissolving reagent grade NaCl, $NaHCO_3$, KCl, $K_2HPO_4{\cdot}3H_2O$, $MgCl_2{\cdot}6H_2O$, $CaCl_2$, and Na_2SO_4 in distilled water, and buffering it at pH 7.4 with tris-aminomethane and hydrochloric acid [23]. The ion concentrations and pH of the solution were almost equal to those of human blood plasma. The solution treated specimens and bare TiCuZrPd and TNTZ substrates were immersed in 30 mL of SBF in a polypropylene vial, and stored in an incubator at 37 °C for 2, 7, and 12 days. The specimen surface was later rinsed with distilled water followed by drying in air. After the SBF immersion test, the samples were gently rinsed with ultrapure water and dried at 40 °C.

33.3 Surface Modifications by Solution Processes

33.3.1 TiCuZrPd Samples

Figure 33.2 shows the SEM micrographs of (a) raw material, treated by (b) H, (c) E and (d) HE process in 5 M NaOH solution. Nanowire arrays have been uniformly formed on a large scale on the substrate. These nanowire arrays with diameters of tens of nanometers were named as “nanomesh layer”. It is interesting to note the similarities in the morphologies of these samples which were treated in high alkaline conditions of 5.0 M. This result suggested that all of these processes enabled to fabricate nanomesh layers on the surface of TiCuZrPd. The crystalline phases of the nanomesh materials were examined using X-ray diffractometer. Figure 33.3 shows X-ray diffraction patterns of H-, E-, and HE-processed samples,

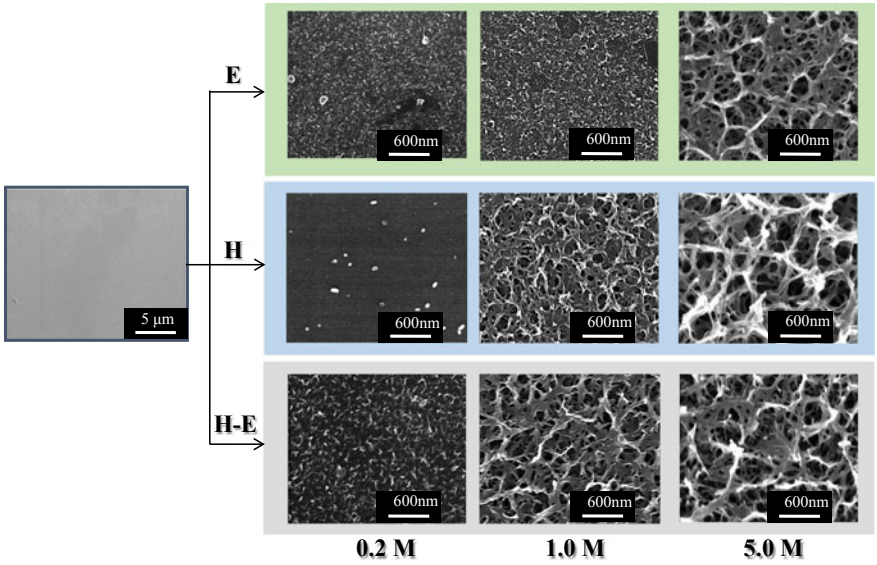

Fig. 33.2 Surface SEM images of raw substrate and the samples treated by H, E and HE processes using different concentrations of alkaline solution of 0.2, 1.0 and 5.0 M

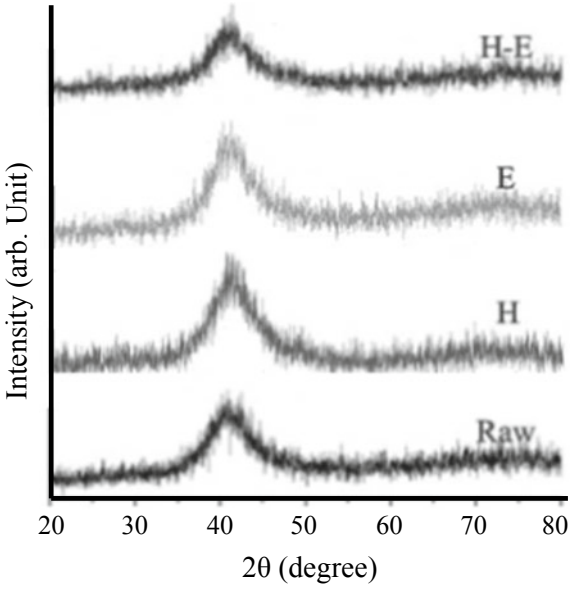

Fig. 33.3 X-ray diffraction patterns for the bare TiZrCuPd substrate, and the samples treated by H, E and HE processes

respectively, in 5.0 M of NaOH solution for 2 h in addition to the bare TiCuZrPd substrate. Only the broad diffraction peak of the substrate at $2\theta = 42°$ was observed and no sharp peak corresponding to a crystalline phase could be detected. This

result suggested that the TiCuZrPd substrate maintained its amorphous structure even after all treatments.

The composition of these nanomesh layers was characterized using Raman spectroscopy and XPS. Figure 33.4 shows Raman spectra of the H-, E- and HE-processed samples. Obvious peaks were observed only for the HE-processed samples. Unlike the other two processes, the HE process may promote the formation of nanomesh layer and thus specific peak was obtained in this case. The peak obtained around 300 cm^{-1} is similar to that of titanate nanowires, which was reported by Zárate et al. [24] and Gao et al. [25].

The XPS results of the E-, H-, and HE-processed samples are listed in Table 33.1. XPS analyses show that large amount of Ti, O_2, and Na suggested the presence of sodium titanate in the nanomesh layer.

There were significant differences in chemical composition among the samples treated by E, H, and HE processes. The Cu is incorporated originally in TiCuZrPd substrate to attain glass-forming ability, but it is an element known for its cytotoxicity. XPS result suggested also that the Cu content was drastically decreased for HE-processed samples. This phenomenon seemed to be closely related to the for-

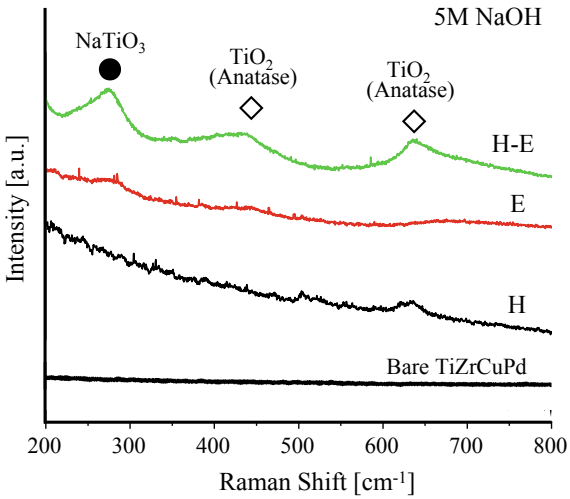

Fig. 33.4 Raman spectra for the sample X-ray diffraction patterns for the bare TiZrCuPd substrate and the samples treated by H, E and HE processes using 5 M NaOK solution

Table 33.1 Results of chemical composition of upmost surface of the treated sample

	Ti	Na	Zr	Cu	O	Pd
Hydrothermal electrochemical	17.78	2.62	0.56	0.49	78.55	Nu
Hydrothermal	18.24	5.05	0.72	8.19	67.81	Nu
Electrochemical	21.01	2.34	0.32	3.93	72.41	Nu

mation mechanism of sodium titanate layer. According to the potential-pH diagrams of pure Ti, Zr, and Cu, they are dissolved in the alkaline solution and exist as anions such as $HTiO^-$, $HZrO^-$, and CuO_2^{2-} [26]. However, only the $HTiO^-$ can form insoluble sodium titanate by reacting with Na^+, followed by the precipitation on the surface of the alloy. In the case of H and E treatment, the formation rate was slower than that of HE one. Therefore, the dissolved Cu ions existing in the vicinity of the surface were incorporated into the surface layer. This mechanism indicates that the combination of H and E process could fabricate low Cu cytotoxicity bioactive nanomesh layer.

Finally, the bioactivity of the surface-modified TiCuZrPd substrate was examined for in vitro test. The titanate nanomesh layer induced the formation of hydroxyapatite when immersed in the SBF, demonstrating that the biologically inert surface of the BMG was converted into a bioactive surface. Figure 33.5 shows SEM images of the samples treated by (a) H, (b) E and (c) HE process and immersed in SBF for 12 days. The hydroxyapatite formation in the network surface was confirmed for all samples. The Ca/P ratio identified by means of energy dispersive X-ray spectroscopy was to be 1.70–1.74 which is nearly equal to the stoichiometric composition 1.72 of hydroxyapatite. These results suggested that the nanomesh layers fabricated by any of the three processes have enough bioactivity to form hydroxyapatite in the network.

However, hydroxyapatite layers produced by H and E process were easily peeled off after drying samples for several days as seen in their surface SEM images in Fig. 33.6a, b. On the contrary, the layer fabricated by HE process exhibited uniform

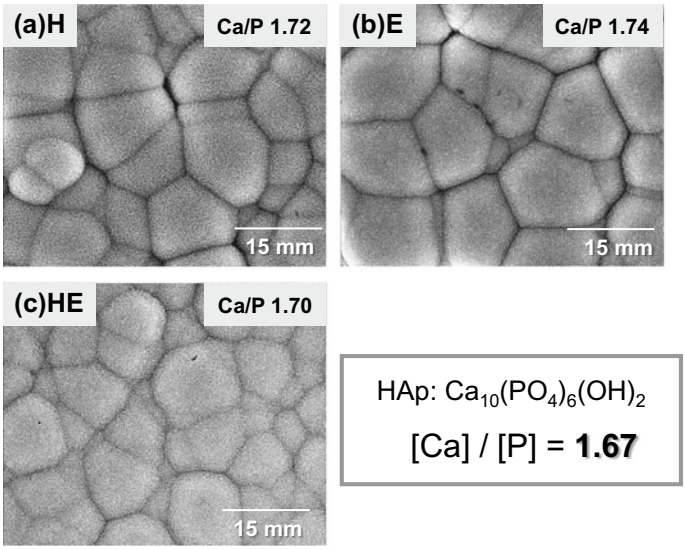

Fig. 33.5 SEM images of the samples treated by **a** hydrothermal, **b** electrochemical and **c** hydrothermal–electrochemical processes and immersed in SBF for 12 days

layer strongly adhered on the substrate and kept its structure as seen in Fig. 33.6c. This can be explained by the presence of interfacial surface diffusion between the TiCuZrPd substrate and the oxidized nanomesh surface layer. The cross-sectional SEM images for the samples show that only the boundary surface has remained for the sample treated by (a) H and (b) E processes, while no boundary was observed between nanomesh layer and the TiZrCuZr substrate in the case in (c) HE process. The HE-processed sample having intermediated layer in which the structure was gradually changed to thickness direction. This "intermediated layer" with a widely diffused interface worked to exhibit strong adhesion of hydroxyapatite layer. The HE process allowed the formation of this unique structure, which Yoshimura et al. named as "growing integration layer (GIL)" [19]. This result indicated that HE process improved the adhesion performance at the interface between ceramics and metallic materials which is a quite important to design implant materials.

XRD patterns of the titanate nanomesh after SBF immersion for 12 days revealed that the formation of the calcium phosphate hydroxide and the peaks at 25.9 and 31.8° correspond to the (002) and (211) planes, respectively, were clearly observed in Fig. 33.7. Figure 33.8 shows the Raman spectra of the HE-processed samples after immersion in the SBF for different durations. After 12 days of SBF immersion, vibration mode peaks were detected at 432, 447, 580, 593, 608, and 962 cm^{-1}, which correspond to the vibration mode of the PO_4^{3-} ion in hydroxyapatite [27–29].

The hydroxyapatites were not formed on the bare TiCuZrPd substrate, indicating that the inertness against the SBF. These results demonstrate that bone-like hydroxyapatites, well known as bioactive materials, were formed on the titanate

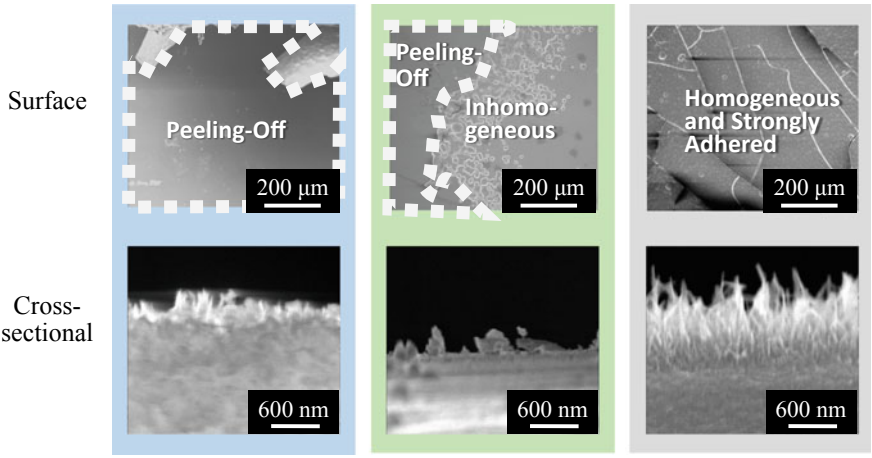

Fig. 33.6 Surface and cross-sectional SEM images of oxide layers fabricated on TiZrCuPd substrate by **a** hydrothermal, **b** electrochemical, **c** hydrothermal–electrochemical processes and left for 3 days in air

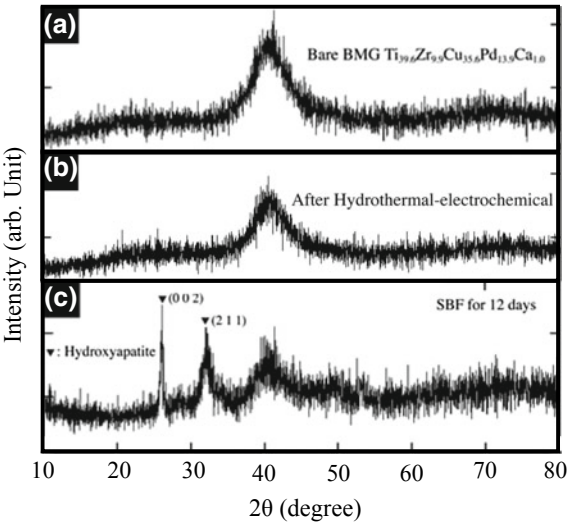

Fig. 33.7 X-ray diffraction patterns of a **a** bare BMG, **b** hydrothermal–electrochemical-treated BMG, and **c** titanate nanomesh layer on BMG after SBF immersion for 12 days

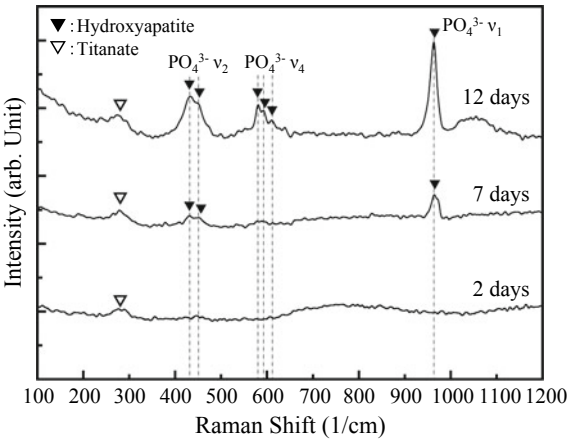

Fig. 33.8 Raman spectra of the HE treated samples after immersion in the SBF for different durations (days)

nanomesh layer [30, 31]. Therefore, titanate nanomesh layers on the TiCuZrPd substrates have a great potential for exhibiting bioactivity.

33.3.2 TNTZ Samples

Figure 33.9 shows the SEM images of surface morphologies of (a) Raw TNTZ substrate and TNTZ samples subjected to each solution process. The samples of (c), (d), (e) and (f), subjected to H and HE process exhibited nanosize mesh-like structures, wherein the sample (b) subjected to the E process does not show

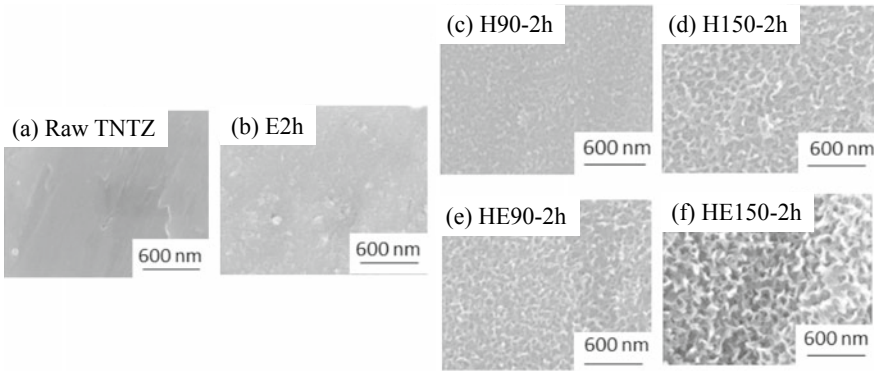

Fig. 33.9 Surface SEM images of raw TNTZ and TNTZ samples subjected to electrochemical (E), hydrothermal (H) and hydrothermal–electrochemical (HE) processes. **a** Raw TNTZ: without any solution treatment, **b** E2h: electrochemically treated sample for 2 h, **c** H90-2h and **d** H150-2h: hydrothermally treated samples at 90 and 150 °C for 2 h, **e** HE90-2h and **f** HE150-2h: hydrothermal–electrochemically treated samples at 90 and 150 °C for 2 h

mesh-like structure. Thus, it can be said that the heating factor in the alkali solution treatment contributes more effectively than an electric factor to form mesh-like structures which seems to be suitable for apatite induction.

The sample (d) H150-2h has a rougher surface morphology than (c) H90-2h. That is because higher temperature proceeded the corrosion of the TNTZ sample surface faster. It was reported that the corrosion rate depends on the reaction temperature and the higher the temperature is the faster the reaction [32]. The same tendency can be seen for the TNTZ samples (e) HE90-2h and (f) HE150-2h. However, even though the processing temperature was the same, the sample (e), which was subjected to HE90-2h, exhibited a rougher surface morphology than that of the sample subjected to H90-2h seen in (c). Therefore, it was shown that not only the hydrothermal reaction but also the electrochemical one corrodes the surface of the TNTZ sample. Electrochemical reaction contributes to attaining the reaction energy higher than the corrosion activation energy [33]. The roughness of the mesh-like structure on sample surfaces was closely related to the process itself in addition to reaction temperature.

X-ray diffraction (XRD) profiles of the TNTZ samples subjected to different alkali solution treatments of E, H, and HE at 200 °C for 2 h were shown in Fig. 33.10. All detected peaks of (110), (200) and (220) peaks were related to the TNTZ substrate of the β-phase [34], and no peaks originated from the formed nanomesh layer were observed for every sample. This X-ray peak trend of solutions treated samples is considered to be due to the amorphous phase of the nanomesh layer formed on TNTZ surface and/or their small amount compared with substrate bulk.

Figure 33.11 shows the Raman spectra of the TNTZ sample subjected to E, H, and HE processes. There was a total of six Raman active mode for the TNTZ

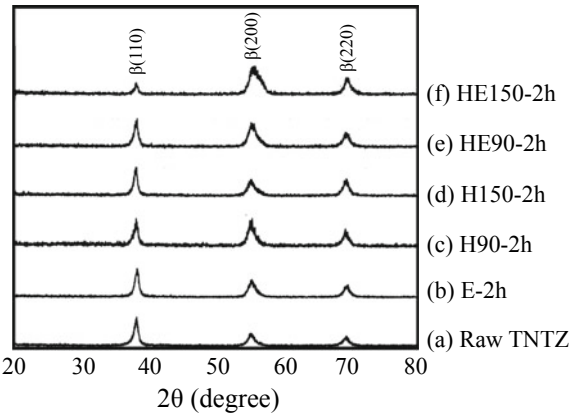

Fig. 33.10 XRD profiles obtained from raw TNTZ, and TNTZ samples subjected to E process for 2 h (E-2h), H processes at 90 and 150 °C for 2 h (H90-2h and H150-2h), and HE process at 90 and 150 °C for 2 h (HE90-2h and HE150-2h)

sample subjected to HE150-2h and four of them were shown in Fig. 33.11. The peak of 278, 439, 645, and 896 cm^{-1} was assigned to a Ti–O–Na^+ stretching vibration, a Ti–O bending vibration involving threefold oxygen, a Nb–O stretching vibration, and a Ti–O stretching vibration involving non-bridging oxygen, respectively. Some of them are coordinated with Na^+ ions [35–37]. Therefore, the surface layer formed on the TNTZ sample subjected to HE150-2h was a sodium-contained amorphous titanium oxide with a small amount of niobium oxide. The Ti–O stretching vibration should appear at 905 cm^{-1} if a crystal phase is present in the sample [35]. The mesh-like structure fabricated on the TNTZ surface exhibited the peak shifted away from 905 cm^{-1}, which indicated that they do not possess crystalline structure, but a distorted structure, probably an amorphous phase. After the consideration of the both results of Raman spectra and XRD profiles, the surface nanomesh structures were recognized to be composed of sodium-contained amorphous titanium oxides. The TNTZ sample subjected to E-2h exhibited only the peak related to the TNTZ sample (507 cm^{-1}) because the surface layer was very thin. Each peak intensity corresponds to sodium titanate and was the strongest for the TNTZ samples subjected to the HE process, followed by those subjected to the H process and then the E process.

The solution-processed TNTZ samples were soaked in SBF for two weeks and their apatite induction abilities were compared with each other. The raw TNTZ and the samples subjected to the E process did not induce apatite as shown in Fig. 33.12a, b. The surfaces of the TNTZ samples subjected to H90-2h formed apatite only sparsely as seen in (c), while H150-2h exhibited enough hydroxyapatite induction ability in (d). On the other hand, a good apatite induction was observed on the whole surfaces of the TNTZ samples subjected to HE90-2h and HE150-2h as seen in Fig. 33.12e, f. The ion ratio between calcium and phosphate Ca/P of all the apatite was also calculated by ICP-AES to confirm the formation of apatite. Average Ca/P ratio of 2.22 was a little bit higher than stoichiometric composition (Ca/P = 1.67). It was indicated that these hydroxyapatites contain CaO phase [38],

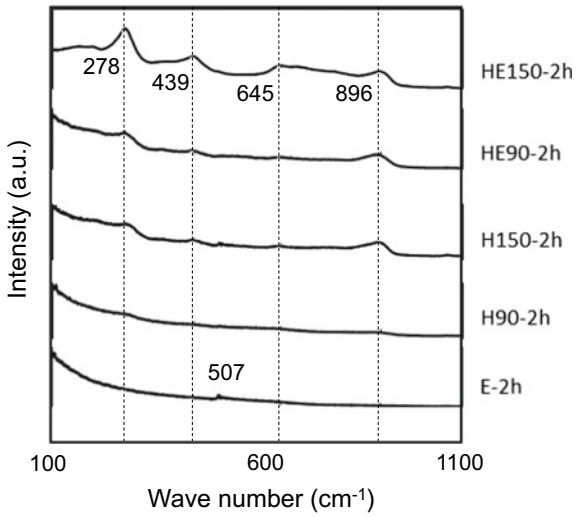

Fig. 33.11 Raman spectra of the TNTZ sample subjected to each alkali treatment

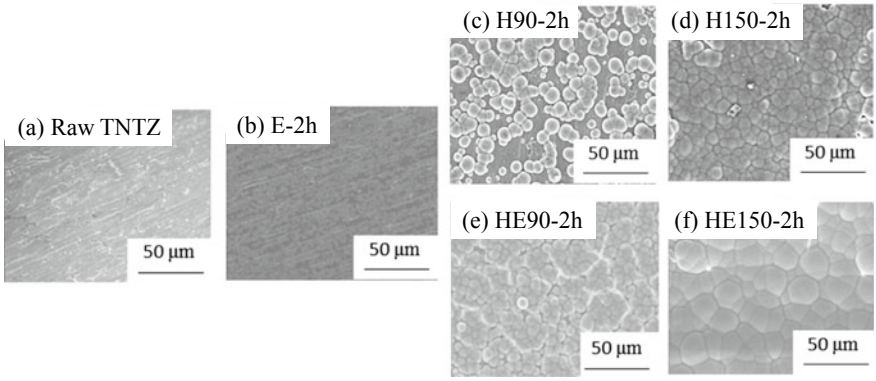

Fig. 33.12 SEM images of surfaces of TNTZ samples subjected to H processes at 90 and 150 °C for 2 h (**a** H90-2h and **b** H150-2h), E process for 2 h (**c** E-2h), and HE process at 90 and 150 °C for 2 h (**e** HE90-2h and **f** HE150-2h) after immersion in SBF for 14 days

and the presence of the CaO phase increased osteoblast NO production and decreases osteoblast viability.

These SBF tests revealed that each TNTZ sample subjected to different solution treatments exhibited different apatite induction ability. There might be two main factors which affect to apatite induction. The first one is the chemical composition of the sample surface. The quantitative composition analysis using an X-ray photoelectron spectroscopy (XPS) was conducted for all solution treated samples and their results are listed in Table 33.2. First, the adverse effect of fluoride ion incorporation into sample was to be investigated since the reaction solution contains NH_4F. However, no fluoride signal was detected on the surface of the TNTZ

Table 33.2 Chemical compositions of the uppermost surface of TNTZ samples subjected to each alkali solution treatment obtained from XPS analysis (atomic%)

	Ti	Nb	Ta	Zr	Na	O	F	Nb/Ti
Raw TNTZ	21.31	7.59	0.58	1.52	0.00	68.99	0.00	0.36
E-2h	17.36	4.11	0.75	0.35	10.75	66.69	0.00	0.24
H90-2h	24.05	3.40	1.39	0.62	19.54	51.20	0.00	0.14
H150-2h	18.42	2.01	0.24	0.41	19.12	59.80	0.00	0.11
HE90-2h	18.60	3.04	0.65	0.79	15.6	61.32	0.00	0.16
H150-2h	18.89	1.88	0.40	0.40	16.33	62.11	0.00	0.10

samples. Second, the Nb/Ti ratio was the highest on the surface of the TNTZ sample subjected to the E process, which matches the report by Gao et al. [25]. According to this previous report, Nb species appear on surfaces of the TNTZ samples which was subjected to anodization, and it made the surfaces of the samples more hydrophobic and lowers its osteoconductivity. Correspondingly, the results obtained from this study show the same tendency as that in the previous report [25]. The water contact angles of the samples treated by each process are shown in Fig. 33.13. Raw TNTZ shows the highest water contact angle of around 70° indicating quite high hydrophobicity. Likewise, the sample treated by E-2h showed higher water contact angle than other processes. It is noted that these samples were also confirmed to have higher amount of Nb species on their surface. It could be suggested that the existence of Nb species on sample surface was not favorable for apatite induction. The reason why Nb species appear only when the TNTZ sample was subjected to the E process had not been made clear, but one possible explanation is a different reaction mechanism between the H and E processes. For the H process, reaction proceeds based on the Gibbs free energy; therefore, the stability of the final product is decided by the standard producing free

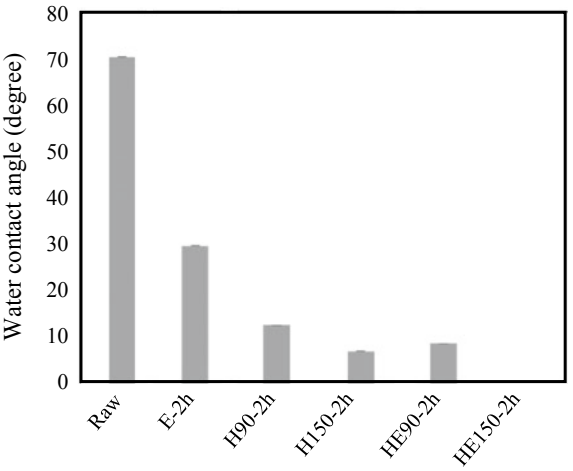

Fig. 33.13 Water contact angles of the samples treated by each process

energy of each oxide. Since the standard producing free energy of titanium dioxide (Ti/TiO_2 = −440 kJ/mol) is lower than that of niobium oxide (Nb/Nb_2O_5 = −350 kJ/mol), titanium oxide is more stable than niobium oxide [26]. Since the most stable oxide exists on the surface of the sample, titanium oxide appears on the outermost surface of the oxide layer. However, for the E process, the reaction proceeds based on the standard electrode potential. Since the standard electrode potential of Ti^{3+}/TiO_2 is −0.66 eV is comparable to that of Nb/Nb_2O_5 of −0.65 eV [27], these two reactions proceed at almost the same time, and the surface of the sample is covered by both of titanium and niobium oxides.

Surface roughness was measured on the surface of the TNTZ sample subjected to each solution treatment to investigate the relationship between roughness and apatite induction. A laser microscopy was used for the measurements, and the results are shown in Table 33.3. The R_a value of the TNTZ sample subjected to H90-2h was 0.155 μm, while that of the TNTZ sample subjected to H150-2h is 0.245 μm. It is speculated that the difference in R_a also affected to the apatite induction ability. In Fig. 33.12, the surface of the TNTZ sample subjected to H90-2h induces apatite sparsely, wherein the surface of the TNTZ subjected to H150-2h apatite on its whole surface. Since low roughness reduces the rate of ion exchange between the surface of the alkali solution treated TNTZ sample and the SBF solution, apatite nucleation is less likely to occur [28]. The TNTZ sample subjected to E-2h exhibits low R_a value and shows no apatite induction, while the TNTZ sample subjected to HE150-2h exhibits relatively high R_a value and shows good apatite induction. Therefore, a relatively higher surface roughness is advantageous for inducing apatite.

On the other hand, XPS measurement revealed that the amount of Nb species might play an important role. Therefore, Nb ratio to the Ti that is the basic alloy's component (Nb/Ti ratio) can be considered as the index of chemical composition. Thus, the relationship between the R_a value and the Nb/Ti ratio for the apatite induction ability is illustrated in Fig. 33.14. When considered along with the results obtained from the SBF tests, it is clear that samples with high apatite induction ability appear at the bottom right of Fig. 33.14, while samples with low apatite induction ability appear on upper left side of the figure. Since the apatite formation is based on ion exchange between the surface of the sample and the SBF solution, a high R_a value corresponding to the large effective surface enhances apatite formation. Therefore, apatite induction is greatly affected by both the surface roughness and chemical composition.

Table 33.3 Measured R_a values for TNTZ sample subjected to each alkali solution treatment ($R_a \pm$ SE)

	H90-2h	H150-2h	E-2h	HE90-0.5h	HE90-1h	HE90-2h	HE150-2h
R_a (μm)	0.155 (±0.0077)	0.245 (±0.03759)	0.068 (±0.0048)	0.083 (±0.0028)	0.102 (±0.00359)	0.206 (±0.0040)	2.141 (±0.1820)

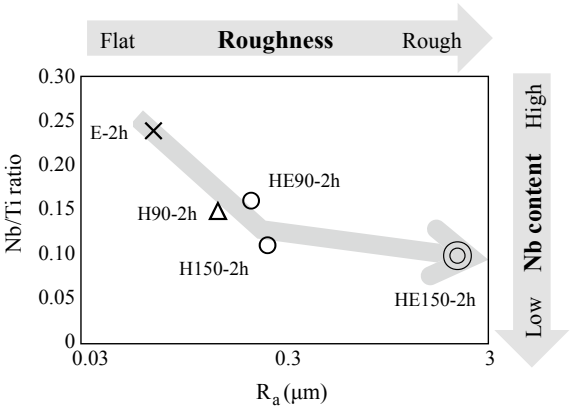

Fig. 33.14 Illustration of the relationship between surface roughness and chemical composition. Relationship between surface roughness (R_a) and chemical composition (Nb/Ti ratio): blue arrows indicate the direction to high apatite induction ability

33.4 Conclusions

A sodium-contained amorphous titanium oxide layer having nanosize mesh-like structure was fabricated on both of TiCuZrPd and TNTZ substrates using three different alkali solution treatments of hydrothermal (H), electrochemical (E), and electrochemical–hydrothermal (HE) processes. Each process creates different surface morphologies and they affect their apatite induction ability and the SBF soaking tests reveal that the rough mesh-like structure is the most likely to induce apatite among all the surface morphologies.

XPS result suggested that HE-processed TiCuZrPd samples exhibited the much less toxic Cu content decreased from the original substrate composition, which is favorable for implant material. HE-processed TiCuZrPd sample having intermediated layer in which the structure was gradually changed to thickness direction with a widely diffused interface worked to exhibit strong adhesion of hydroxyapatite layer. The nanomesh structure formed on TiCuZrPd substrate by HE process exhibited enough high bioactivity in vitro test to form hydroxyapatite on their whole surface after immersing in SBF for 12 days.

The surface chemical composition affects the apatite induction ability of TNTZ samples. The surface incorporation of fewer niobium species exhibited hydrophilic condition. The HE treated TNTZ sample at 90 °C for 2 h having a rough surface with fewer Nb content could exhibit enough high bioactivity without forming any cracks or peeling.

Acknowledgements The author gratefully acknowledges the financial support from the Collaboration Research Project of Advanced Materials Development and Integration of Novel Structured Metallic and Inorganic Materials supported by MEXT, as well as the great support from the collaborative research of the Institute for Materials Research at Tohoku University. The author thanks Prof. Emeritus Masahiro Yoshimura and Prof. Emeritus Kiyoshi Okada of Tokyo Institute of Technology, Prof. Emeritus Mitsuo Niinomi and Prof. Guoqiang Xie of Tohoku University, Prof. Keisuke Kuroda of Nagoya University, and Prof. Masahiro Tsukamoto of Osaka University for their significant suggestions and discussions. The author expresses his thanks to graduates from

his laboratory who investigated biomaterial topics, Ms. Eri Takematsu, Ms. Eriko Fukushima, Ms. Sayaka Maruyama, Ms. Eriko Ito, and Dr. Naota Sugiyama for their contributions to obtain valuable results and fruitful discussions.

References

1. L.E. Tanner, R. Ray, Scr. Metall. **11**, 783–789 (1977)
2. K. Amiya, N. Nishiyama, A. Inoue, T. Masumoto, Mater. Sci. Eng. A **179**, 692 (1994)
3. Y.C. Kim, D.H. Bae, W.T. Kim, D.H. Kim, J. Non-Cryst. Solids **325**(1–3), 242–250 (2003)
4. G.A. Crawford, N. Chawla, K. Das, S. Bosea, A. Bandyopadhyay, Microstructure and deformation behavior of biocompatible TiO_2 nanotubes on titanium substrate. Acta Biomater. **3**, 359–367 (2007)
5. M.L. Morrison, R.A. Buchanan, A. Peker, P.K. Liaw, J.A. Horton, J. Non-Cryst. Solids **353** (22–23), 2115–2124 (2007)
6. S. Fujimoto, V. Raman, H. Tsuchiya, Surface modification of β-type titanium alloy by electrochemical potential pulse polarization. JPCS **165**, 012007 (2009)
7. A. Inoue, N. Nishiyama, K. Amiya, T. Zhang, T. Masumoto, Ti-based amorphous-alloys with a wide supercooled liquid region. Mater. Lett. **19**, 131 (1994)
8. K. Amiya, N. Nishiyama, A. Inoue, T. Masumoto, Mechanical strength and thermal-stability of Ti-based amorphous-alloys with large glass-forming ability. Mater. Sci. Eng. A-Struct. Mater. Prop. Microstruct. Process. **179**, 692 (1994)
9. J.M. Park, Y.C. Kim, W.T. Kim, D.H. Kim, Ti-based bulk metallic glasses with high specific strength. Mater. Trans. **45**, 595 (2004)
10. S.L. Zhu, X.M. Wang, F.X. Qin, A. Inoue, A new Ti-based bulk glassy alloy with potential for biomedical application. Mater. Sci. Eng. A-Struct. Mater. Prop. Microstruct. Process. **459**, 233 (2007)
11. M. Niinomi, T. Hattori, K. Morikawa, T. Kasuga, A. Suzuki, H. Fukui, S. Niwa, Development of low rigidity β-type titanium alloy for biomedical applications. Mater. Trans. **43**, 2970–2977 (2002)
12. R.L.P. Teixeira, G.C.D. Fodoy, M.M. Pereira, Calcium phosphate formation on alkali-treated titanium alloy and stainless steel. Mater. Res. **7**(2), 299–303 (2004)
13. R. Godley, D. Starosvetsky, I. Gotman, Bonelike apatite formation on niobium metal treated in aueous NaOH. J. Mater. Sci. Med. **10**, 1073–1077 (2004)
14. T. Akahori, M. Niinomi, M. Nakai, H. Fukuda, H. Fukui, M. Ogawa, Bioactive ceramic surface modification of β-type Ti-Nb-Ta-Zr system alloy by alkali solution treatment. Mater. Trans. **48**, 293–300 (2007)
15. N. Sugiyama, X. HaiYan, T. Onoki, Y. Hoshikawa, T. Watanabe, N. Matsushita, X. Wang, F. Qin, M. Fukuhara, M. Tsukamoto, N. Abe, Y. Komizo, A. Inoue, M. Yoshimura, Bioactive titanate nanomesh layer on the Ti-based bulk metallic glass by hydrothermal-electrochemical technique. Acta Biomater. **5**, 1367–1373 (2009)
16. A. Inoue, Mater. Trans. JIM **36**(7), 866–875 (1995); Y. Fukushima, K. Katsumata, Z. Shengli, X. Guoqiang, M. Niinomi, K. Okada, N. Matsushita, Solution process for synthesizing bioactive nano-mesh layer on Ti-based bulk metallic glasses. Mater. Trans. **54**(8), 1343–1346 (2013)
17. M. Niinomi, Fatigue performance and cyto-toxicity of low rigidity titanium alloy Ti-29Nb-13Ta-4.6Zr. Biomaterials **24**, 2673–2683 (2003)
18. K. Yanagisawa, Preparation of ceramic powders by hydrothermal method. J. Soc. Inorg. Mater. Jpn. **12**(319), 486–491 (2005)
19. M. Yoshimura, T. Onokia, M. Fukuharab, X. Wangb, K. Nakatac, T. Kurodac, Formation of growing integrated layer [GIL] between ceramics and metallic materials for improved adhesion performance. Mater. Sci. Eng. B **148**, 2–6 (2008)

20. L.V. Taveira, J.M. Macák, H. Tsuchiya, L.F.P. Dick, P. Schmuki, Initiation and growth of self-organized TiO_2 nanotubes anodically formed in $H_4F/(NH_4)_2SO_4$ electrolytes. J. Electrochem. Soc. **152**(10), B405–B410 (2005)
21. H.W. Kim, E.J. Lee, H.E. Kim, V. Salih, J.C. Knowles, Effect of fluoridation of hydroxyapatite in hydroxyapatite-polycaprolactone composites on osteoblast activity. Biomaterials **26**, 4395 (2005)
22. T. Kokubo, H. Takadama, How useful is SBF in predicting in vivo bone bioactivity? Biomaterials **27**, 2907–2915 (2006)
23. S.B. Cho, K. Nakanishi, T. Kokubo, N. Soga, C. Ohtsuki, T. Nakamura, T. Kitsugi, T. Yamamuro, Dependence of apatite formation on silica-gel on its structure—effect of heat-treatment. J. Am. Ceram. Soc. **78**, 1769 (1995)
24. R.A. Zárate, S. Fuentes, J.P. Wiff, V.M. Fuenzalida, A.L. Cabrera, J. Phys. Chem. Solid **68**, 628637 (2007)
25. X. Gao, H. Zhu, G. Pan, S. Ye, Y. Lan, F. Wu, D. Song, J. Phys. Chem. **108**, 28682872 (2004)
26. M. Pouraix, *Atlas of Electrochemical Equilibria in Aqueous Solutions* (Houston, Cebelcor, 1974), p. 215391
27. S. Koutsopoulos, Synthesis and characterization of hydroxyapatite crystals: a review study on the analytical methods. J. Biomed. Mater. Res. **62**, 600 (2002)
28. H. Tsuda, J.L. Arias, P. Gonzalez, B. Leon, J. Arends, Raman spectroscopic analysis of sub- and supragingival calculus. J. Dent. Res. **76**, 1110 (1997)
29. G. Penel, G. Leroy, C. Rey, E. Bres, MicroRaman spectral study of the PO_4 and CO_3 vibrational modes in synthetic and biological apatites. Calcif. Tissue Int. **63**, 475 (1998)
30. B. Ben-Nissan, A. Milev, R. Vago, Morphology of sol-gel derived nano-coated coralline hydroxyapatite. Biomaterials **25**, 4971 (2004)
31. K. Fatehi, F. Moztarzadeh, M. Solati-Hashjin, M. Tahriri, M. Rezvannia, A. Saboori, Biomimetic hydroxyapatite coatings deposited onto at and alkali treated Ti6Al4V surface. Surf. Eng. **25**(8), 583–588 (2009)
32. R. Matsuhashi, S. Ito, E. Sato, Relationship between the apparent activation energy of corrosion reaction and alloy contents of stainless steels **528**, 521–528 (1993)
33. H. Nakano, I.J. Son, H. Ohara, S. Oue, K. Nakamura, H. Fukushima, Effect of continuous rotation evolutional control on the pitting corrosion resistance of anodized aluminum-magnesium alloy **73**(5), 394–400 (2009)
34. T. Akahori, M. Niinomi, M. Nakai, M. Ogawa, Change in fatigue strength of biomedical β-type titanium alloy through heat treatment processes. J. Soc. Mater. Sci., Jpn. **57**(9), 893–898 (2008)
35. H.M. Kim, F. Miyaji, T. Kokubo, T. Nakamura, Effect of heat treatment on apatite-forming ability of Ti metal induced by alkali treatment. J. Mater. Sci. Mater. Med. **8**, 341–347 (1997)
36. R.F. Brandão, R.L. Quirino, V.M. Mello, A.P. Tavares, A.C. Peres, F. Guinhos, J.C. Rubim, P.A.Z. Suarez, Synthesis, characterization and use of Nb_2O_5 based catalysts in producing biofuels by transesterification, esterification and pyrolysis. J. Braz. Chem. Soc. **20**(5), 954–966 (2009)
37. T. Bao-Li, D. Zu-Liang, M. Yan-Mei, L. Xue-Fei, C. Qi-Liang, C. Tian, L. Bing-Bing, Z. Guang-Tian, Raman investigation of sodium titanate nanotubes under hydrostatic pressures up to 26.9 GPa. Chin. Phys. Lett. **27**, 026103 (2010)
38. H. Liu, H. Yazici, C. Ergun, T.J. Webster, H. Bermek, An in vitro evaluation of the Ca/P ratio for the cytocompatibility of nano-to-micron particulate calciu phosphates for bone regeneration. Acta Biomater. **4**(5), 1472–1479 (2008)

Chapter 34
Surface Modification with Hydrophilization

Kensuke Kuroda

Abstract Corrosion-resistant valve metals, such as Ti, Nb, Ta, and Zr, and their alloys have attracted much interest as bone substitutes in dental and orthopedic fields. However, in their pure form, these metals and alloys do not always encourage hard-tissue growth on their surface in living bodies. Surface characteristics always influence the biological response at the interface between the implants and body tissues. Titanium dioxide (TiO_2) is known as an osteoconductive material and it has been shown to exhibit strong physicochemical fixation with living bone. In this paper, our experimental results using anodized TiO_2 coatings are briefly outlined, including their in vivo evaluation. Based on these results, a comprehensive description of the factors that influence osteoconductivity with respect to the surface characteristics of the implants is presented, and a new approach to controlling the osteoconductivity of Ti and other valve metals and their alloys by using hydrothermal treatment is proposed. Furthermore, the hydrophilization of ceramics such as alumina and zirconia, and polymers such as polyetheretherketone (PEEK) and polyethersulfone (PES) is discussed. The protein adsorbability of the surface-treated samples and the osteoconductivity of the protein-adsorbed samples are also discussed.

Keywords Hydrophilicity · Hydrothermal treatment · Osteoconductivity · Protein adsorption

34.1 Introduction

Titanium and its alloys are widely used in dental and orthopedic implants. These materials have high corrosion resistance in saltwater environments and high chemical stability in the body. They have good biocompatibility and long-term

K. Kuroda (✉)
Institute of Materials and Systems for Sustainability, Nagoya University, Furo-cho, Chikusa-Ku, Nagoya 464-8603, Japan
e-mail: kuroda.kensuke@material.nagoya-u.ac.jp

Y. Setsuhara et al. (eds.), *Novel Structured Metallic and Inorganic Materials*, https://doi.org/10.1007/978-981-13-7611-5_34

success rates of implants are well documented [1, 2]. However, Ti in its pure form does not always encourage hard-tissue growth onto its surface in living bodies. Therefore, the development of appropriate surface treatments that encourage bone formation, such as hydroxyapatite (HAp) and other calcium phosphate coatings [3, 4], has been studied extensively. Such approaches include plasma spraying [5, 6], sol-gel methods [7, 8], electron beam sputtering [9], ion beam sputtering [10], cathodic electrolysis [11–13], electrophoretic methods [14, 15], and thermal substrate methods [16–22]. Similarly to HAp, titanium dioxide (TiO_2) is also important as an osteoconductive material because, although it is not a component of natural bone, it has been shown to exhibit strong physicochemical fixation with living bone [23]. There are many types of TiO_2 coating methods for Ti substrates, as discussed later [24–34]. The thin oxide films on Ti, formed by the oxidation of Ti substrates, have high adhesion. Ti has strong affinity with oxygen and it is well known that very thin TiO_2 passivation films are formed under an air atmosphere. Implants with these coatings are typically presterilized and used without any special treatment before surgery. Given that the TiO_2 coating generally has the high resistance to biofouling, the attachment and growth of a biofilm followed by the onset of infectious diseases could be minimized. The surface characteristics of a material usually influence the biological response at the interface between the implant and body tissues [35–40]. Coating materials and coating processes designed to improve osteoconductivity have received special attention; in contrast, while the chemical characteristics of the coatings have been largely overlooked in manufacturing and clinical practice. Specific control of the surface properties of implants leads directly to the control of osteoconductivity. Therefore, it is important that the surface bioactivity of such implants be maintained until the surgical operation. Alternatively, a bioactivation treatment can be performed immediately prior to clinical application.

Herein, the results of our experimental studies on anodized TiO_2 coatings are briefly outlined, including an in vivo evaluation. Based on these results, a comprehensive description of the factors that influence osteoconductivity is provided, and a new approach that can be used to control the osteoconductivity of valve metals and their alloys by using hydrothermal treatment is proposed. The relationship between protein adsorbability (albumin and fibronectin) and the osteoconductivity of the surface-treated samples are also discussed. Moreover, the hydrophilization of ceramics, such as alumina and zirconia, and polymers, such as polyetheretherketone (PEEK) and polyethersulfone (PES), is also described.

34.2 TiO_2 Coating (Anodizing in Aqueous Solution)

TiO_2 has attracted attention as a surface-coating compound because of its high osteoconductivity. On the one hand, many pyroprocessing methods for forming TiO_2 coatings on metallic substrates have been reported, including thermal oxidation [24] and physical vapor deposition [25, 26]. On the other hand, hydrocoating

techniques, such as chemical treatment [27–30] and anodizing [31–34], have also been proposed as alternative approaches to forming thin-film coatings on metallic Ti substrates. Oxidation of Ti or Ti-alloy substrates causes a layer of TiO_2 to form, which generally exhibits substantial adhesion between the substrate and the coating. In this chapter, we focus mainly on anodizing processes for Ti and describe the currently available techniques in detail. Figure 34.1 shows the typical surface of anodized films produced on commercial pure Ti plates; the coating conditions and test results are listed in Table 34.1. All of the samples were evaluated after sterilization in an autoclaving unit (121 °C, 20 min), as preparation for in vivo testing. Mirror-finished Ti plates were prepared by polishing with silicon carbide emery paper and buffing with Al_2O_3 particles. Titanium substrates were used as the working electrode and a platinum coil was used as the counter electrode. Aqueous acid, alkaline, and neutral solutions were used as electrolytic baths, and the anodizing potential was increased slowly (0.1 V s^{-1}) to a target potential (E_{max}) at 25 °C to prevent sparking due to breakdown of the films. The applied potential was selected to obtain anatase films with the same thickness (120 nm). Anodic electrolysis of Ti gave compact and adhesive thin TiO_2 films on Ti substrates in aqueous solutions. The film thickness depended on both the applied potential and the nature of the aqueous solution; applying a higher potential produced thicker films at a given constant temperature in the same type of solution. The thin TiO_2

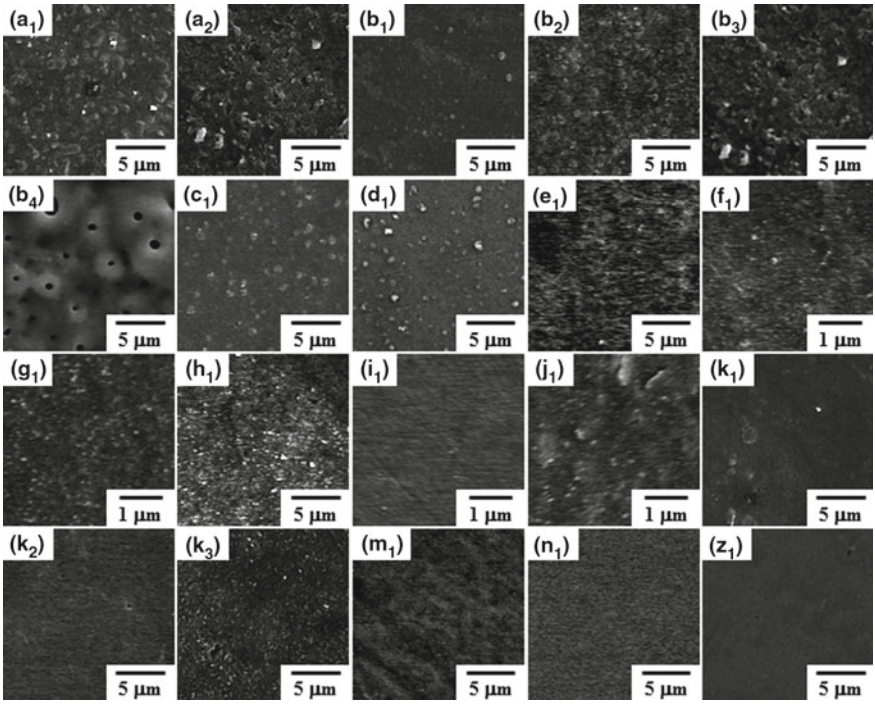

Fig. 34.1 Typical surface of TiO_2 films produced on commercially pure Ti plates

Table 34.1 Coating conditions and test results

	Anodizing		Thermal oxidation	Liquid phase oxidation	Hydrothermal oxidation	Crystal structure A: anatase R: rutile a: amorphous	Film thickness (nm)	Surface roughness (Ra) (μm)
	Solution	E_{max}/V	Solution, temperature, period, atmosphere					
a_1	0.1 M H_2SO_4	100	–	–		A	120	0.08
a_2		200	–	–		A + R	***	0.11
b_1	0.1 M H_3PO_4	100	–	–		A	120	0.08
b_2		70	673 K, 2 h, air	–			***	0.09
b_3	0.1 M H_3PO_4	200	–	–	–	A + R	***	0.11
b_4	5 M H_3PO_4		–	–	–	a	3 μm	0.45
b_5	9 M H_3PO_4						***	0.73
c_1	0.1 M $CH_3CH(OH)COOH$	70	–	–	–	A	120	0.10
d_1	0.1 M CH_3COOH	70	–	–	–			0.11
e_1	0.1 M Na_2SO_4	65	–	–	–			0.08
f_1	0.1 M Na_2HPO_4	70	–	–	–			0.08
g_1	2 mM $Mg(OH)_2$	150	–	–	–			0.08
h_1	0.1 M NH_3aq	80	–	–	–			0.10
i_1	20 mM $Ca(OH)_2$	70	–	–	–			0.10
j_1	0.1 M KOH	80	–	–	–			0.10
k_1	0.1 M NaOH	80	–	–	–			0.09
k_2		50	673 K, 2 h, air	–	–			0.10
k_3		200	–	–	–	A + R	***	0.13

(continued)

Table 34.1 (continued)

	Anodizing		Thermal oxidation	Liquid phase oxidation	Hydrothermal oxidation	Crystal structure A: anatase R: rutile a: amorphous	Film thickness (nm)	Surface roughness (Ra) (μm)
	Solution	E_{max}/V	Solution, temperature, period, atmosphere					
m_1	–	–	–	0.1 M HNO_3 + 4.4 M H_2O_2, 353 K, 20 min	–	A (hydrogel)	0.6 μm	0.10
n_1	–	–	673 K, 2 h, air	–	–	R	120	0.09
o_1	–	–	–	0.1 M HNO_3 + 4.4 M H_2O_2, 353 K, 20 min	1 M NH_3aq, 453 K, 12 h	A	***	0.16
z_1	(as-polished)					–	–	0.06

*** Without measurement

films took on interference coloration, depending on their thickness [41]. The surface roughness of the samples was evaluated by using the arithmetical means of the surface roughness (Ra) [42] and measured with a confocal laser-scanning microscope (contactless probing). The measurement area was 150×112 μm. Anatase-type TiO_2 was obtained without sparking during anodizing at 100 V in several different solutions (listed in Table 34.1), and the value of Ra was then almost identical to that of the initial polished Ti substrates. In addition, the TiO_2 films have solute ions (both anions and cations) in the anodizing solution [43, 44].

34.3 Evaluation of Osteoconductivity

The evaluation methods for bioactivity and/or osteoconductivity of implants are classified into in vitro and in vivo methods. In this chapter, the in vivo evaluation method is described. For in vivo evaluations, many types of animals of different ages have been used previously, and different researchers have used different implantation sites in the animals. Different evaluation methods have also been employed, such as mechanical assessment (pull-out, push-out, torsion and abrasion tests) and biological assessment (histological, CT, MRI and other imaging techniques). However, a unified quantification criterion has not yet been established, and the different criteria used in various studies are incompatible. Therefore, we used the bone implant contact ratio (BIC) as an osteoconductive index, based on the observation of bone tissue on the implants using an optical microscope, to assess samples 14 days after implantation in the tibiae of 8-week-old male rats. The BIC was determined by the linear measurement of bone in direct contact with the implant surface as shown in the following equation.

$$\mathrm{BIC}\,(\%) = \frac{\text{sum of the length of the part of bone formation on the implant surface}}{\text{total implant length}} \times 100$$

The sum of the length of bone formation on the implant surface was measured, and the BIC was expressed as a percentage of the total implant length in the cancellous and cortical bone regions [20–22]. Significant differences in BIC were examined statistically by using the Tukey–Kramer method [45]. The results were considered significant when $p < 0.05$.

34.4 Factors that Influence Osteoconductivity

It is well known that many factors influence the osteoconductivity of implants; these include surface roughness and morphology [36, 39, 46], film thickness [47], crystal structure [48], crystallinity and hydrophilicity. However, many researchers have reached different conclusions based on in vitro evaluations, and have not

reached agreement. Our previous research based on in vivo testing revealed the following points with respect to osteoconductivity:

(i) Differences in the crystal structure of TiO_2 (anatase and rutile) did not influence osteoconductivity (Fig. 34.2) [49].
(ii) The osteoconductivity of thermally oxidized samples (anatase and rutile) was as low as that of as-polished samples (Fig. 34.2) [49]. That is, the use of thermally oxidized TiO_2 did not contribute to an improvement in osteoconductivity.
(iii) The surface roughness of TiO_2 has been reported to influence the osteoconductivity, but this tendency was not seen in samples with *R*a values in the range 0.3–1.5 μm (Fig. 34.3). On the one hand, the BIC within this Ra region was as low as that of as-polished samples [43]. On the other hand, samples with Ra < 0.3 μm had a higher BIC of nearly 40% after anodizing in H_2SO_4 aqueous solution. However, this tendency was not seen in the thermally oxidized and as-polished samples [49].
(iv) There was not always a correlation between the crystallinity of the TiO_2 films and osteoconductivity. However, amorphous anatase films, formed by anodizing in a high content H_3PO_4 aqueous solution, had very high BIC values (Fig. 34.4) [50].
(v) Anions and cations, included in the anodizing bath and evident in the resulting TiO_2 films, did not influence the osteoconductivity [51], as discussed below.

As noted above, there is almost no doubt that many complex and interrelated factors influence osteoconductivity. A broad consensus on the influence of these factors has not been reached because their effects have not always been confirmed. In other words, there is a possibility that other factors that have not yet been noticed may strongly influence osteoconductivity. Figure 34.5 shows the relationship between the BIC and the pH value of the aqueous solution used in anodizing [51]. All samples had an anatase film of a single phase and had almost the same Ra and film thickness to control for the effect of these variables on the osteoconductivity. Anions and cations were included in the anodizing bath and were also present in the

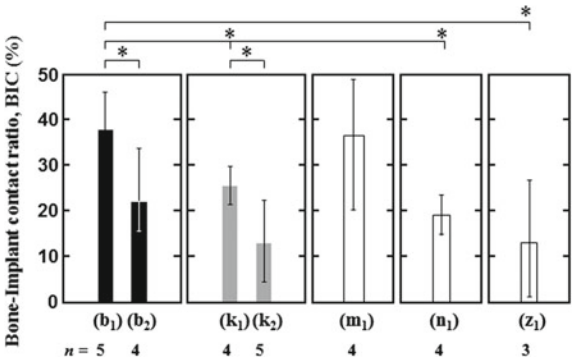

Fig. 34.2 BIC values of TiO_2 films formed by several processings. * $p < 0.05$ (b_1), (b_2), (k_1), (k_2), (m_1), (n_1), and (z_1) correspond to in Table 34.1

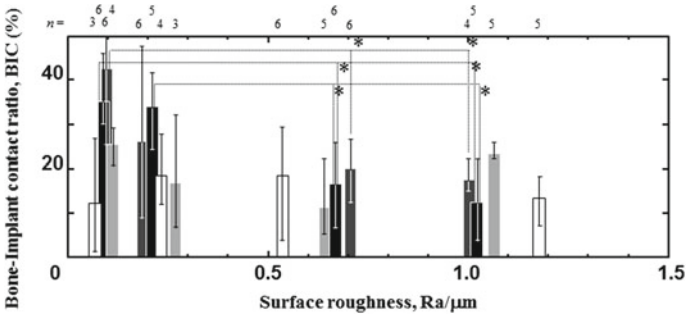

Fig. 34.3 Relationship between the surface roughness, Ra, and BIC of anodized TiO_2. * $p < 0.05$ ■: (a_1) ■: (b_1) ■: (k_1) □: (z_1). (a_1), (b_1), (k_1), and (z_1) correspond to in Table 34.1

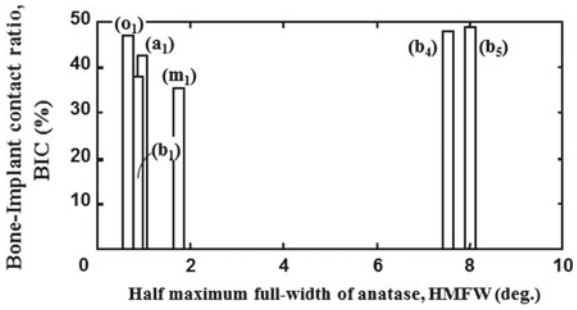

Fig. 34.4 Relationship between the half maximum full-width of anatase, HMFW, and BIC of TiO_2. * $p < 0.05$ (a_1), (b_1), (b_4), (b_5), (m_1), and (o_1) correspond to in Table 34.1

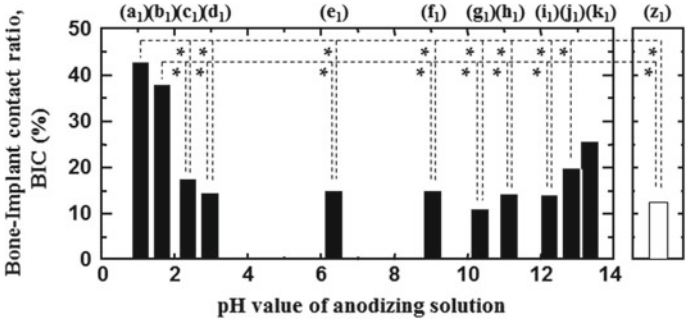

Fig. 34.5 Relationship between the BIC and the pH value of the aqueous solution used in anodizing. * $p < 0.05$ (a_1)–(k_1) and (z_1) correspond to in Table 34.1

anodized TiO_2 films. For example, anodized TiO_2 films generated in H_2SO_4 contained SO_4^{2-}, and films created in NaOH aqueous solution contained both Na^+ and OH^-. A comparison of TiO_2 films anodized in H_2SO_4, Na_2SO_4, and NaOH

solutions demonstrated that the presence of SO_4^{2-} and Na^+ did not influence the BIC. Similarly, a comparison of anodized TiO_2 films formed in H_3PO_4, $NaHPO_4$ and NaOH solutions showed that PO_4^{3-} did not affect the BIC. However, anodized TiO_2 films created in acidic and alkaline solutions had higher BIC values compared with films created in neutral pH solutions. The BIC values of TiO_2 films formed in neutral solutions were as low as that of an as-polished sample, which meant that anodized TiO_2 films that formed in neutral solutions did not improve the osteoconductivity. From these results, it appears that the pH of the aqueous solution used in anodizing does influence osteoconductivity. However, the pH value is one of the coating conditions, and cannot represent the surface characteristics of TiO_2 films by itself. Therefore, we conclude that the pH value does not directly influence the osteoconductivity, and changes in surface properties resulting from different pH values caused the observed changes in osteoconductivity.

34.5 Surface Hydrophilicity

34.5.1 Surface Hydrophilicity of TiO_2 Films [52]

The factors that influence the osteoconductivity of TiO_2 films remain unclear. To examine the surface characteristics of hydrophilicity and hydrophobicity, the BIC in the cortical bone region was plotted against the water contact angle (WCA) of TiO_2 films (Fig. 34.6a). To perform the WCA measurements, a 2 mL droplet of distilled water was used. Samples were submitted to TiO_2 coating and autoclave sterilization (121 °C, 20 min), then left for 24 h in an air atmosphere at room temperature considering the time between coating and implantation. Based on these results, it is clear that the factors discussed in Chap. 4 had almost no relationship with the BIC, and samples with a more hydrophilic surface (smaller value of WCA) were associated with a higher BIC. Therefore, we conclude that the surface characteristics represented by the WCA appear to influence the osteoconductivity.

34.5.2 Osteoconductivity of TiO_2 Films

Given that samples with more hydrophilic surfaces had higher BIC values, we studied the production of superhydrophilic surfaces on TiO_2 coatings and evaluated their osteoconductivity. In general, hydrothermal treatment in distilled water removes adsorbed contaminants (mainly hydrocarbons) from the TiO_2 surface, and this cleaning effect creates superhydrophilic surfaces on the TiO_2 films. Irradiation with ultraviolet light or exposure to atmospheric plasma is one of other potential methods for surface cleaning [53, 54]. In this study, these processes were used to obtain TiO_2 films with superhydrophilic surfaces. The change in WCA over the

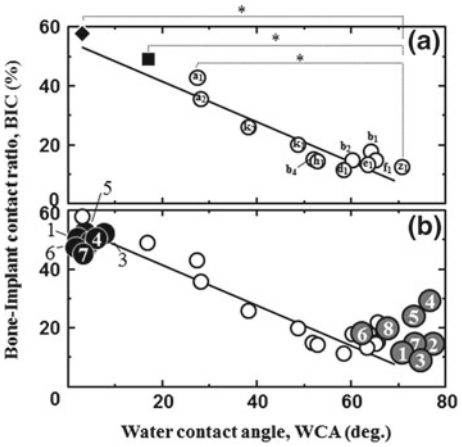

Fig. 34.6 Relationship between the WCA and BIC value of **a** anodized TiO_2 and **b** valve metals and alloys. ■: hydrothermally treated at 180 °C for 180 min in distilled water and then stored in PBS(-) solution, ◆: hydrothermally treated at 180 °C for 180 min in distilled water and then stored in 5 × PBS(-) solution. * $p < 0.05$. (a), (b), (d), (e), (f), (h), (k), and (z) correspond to in Table 34.1. (1) Ti, (2) Nb, (3) Ta, (4) Zr, (5) Ti-29Nb-13Ta-4.6Zr, (6) Ti-13Cr-1Fe-3Al, (7) Ti-6Al-4 V, (8) Ti-6Al-7Nb

processing period is shown in Fig. 34.7. For TiO_2 samples produced by anodizing Ti substrates in 0.1 M H_2SO_4 at 100 V, sterilization by autoclaving, and drying for 24 h in air, the initial WCA was approximately 30°. This value changed to less than 15° after hydrothermal treatment (180 °C), ultraviolet irradiation (Hg–Xe lamp, 250 nm wavelength), and atmospheric plasma irradiation (N_2 operating gas, 500 W), although the rate of change was different for each technique. In particular, atmospheric plasma irradiation rapidly reduced the WCA to less than 10°. X-ray photoelectron spectroscopy (XPS) analysis revealed that, although the amount of adsorbed hydrocarbon decreased in all cases, not every process introduced hydrophilic functional moieties, such as –OH groups. The surface-cleaning effect created the hydrophilic surface. In this study, it was found that hydrothermal treatment could be used to generate uniform hydrophilicity over the entire implant surface, which can have complex shapes and topographies. After superhydrophilic surfaces are prepared, it is important to maintain the surface properties until implantation, because surface hydrophilicity can be lost easily over time, as reported by Att et al. [55]. Therefore, hydrophilic (cleaned) surfaces should be kept in an environment that does not contain hydrocarbons, such as under vacuum or in an aqueous solution. Keeping in mind that the implants are handled in air in surgical operations, samples were kept in an aqueous environment in this research. It can be expected that storage in an aqueous solution containing a high concentration of anions and cations will maintain hydrophilicity, and this also encourages the adsorption of these ions in preference to trace hydrocarbons that may be present. Figure 34.8 shows the effects of different storage environments on the variation in

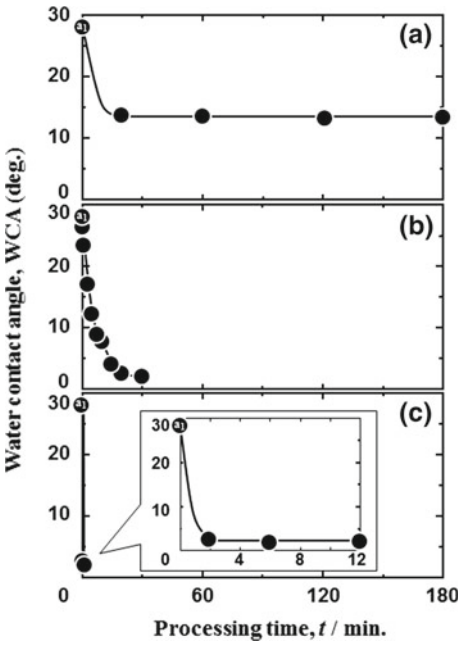

Fig. 34.7 Change in WCA with the processing time of anodized TiO_2 in 0.1 M H_2SO_4. **a** Hydrothermal treatment in distilled water, **b** ultraviolet light irradiation, and **c** atmospheric plasma irradiation

WCA over time for TiO_2 samples that were treated hydrothermally at 180 °C for 180 min. The reasons why processing conditions by hydrothermal treatment were selected for these tests were as follows.

(i) Hydrothermal treatment at more than 150 °C (but less than 210 °C) for less than 180 min resulted in a WCA of 15°.
(ii) Hydrothermal treatment for more than 180 min did not result in any decrease in the WCA. In addition, we confirmed that general sterilization by using an autoclaving unit (121 °C, 20 min) did not achieve these WCA values.

The WCA values of the samples varied greatly according to the storage conditions and the period of storage. Irrespective of whether a sample was hydrothermally treated, storage in air caused a continuous increase in the WCA as the storage period increased, which resulted in similarly high WCA values for all samples after 168 h (Fig. 34.8a). Storage in distilled water also caused the WCA to increase slightly (Fig. 34.8b). However, storage in PBS(-) solution (8 gL^{-1} NaCl, 0.2 gL^{-1} KCl, 1.44 gL^{-1} NaH_2PO_4, 0.24 gL^{-1} KH_2PO_4, pH 7.4), which provides the same wet environment as distilled water, reduced the WCA of the as-anodized Ti (○ in Fig. 34.8c, d). This tendency was enhanced both when the sample was hydrothermally treated and when it was stored in a higher concentration of 5 × PBS (-) solution (● in Fig. 34.8c, d). When samples were stored in solutions containing concentrations higher than 5 × PBS(-), the WCA values did not decrease any further. Na^+ and Cl^- ions, which are the main components of PBS(-), were detected on the surfaces of the samples stored in the PBS(-) solution. All of these solute ions

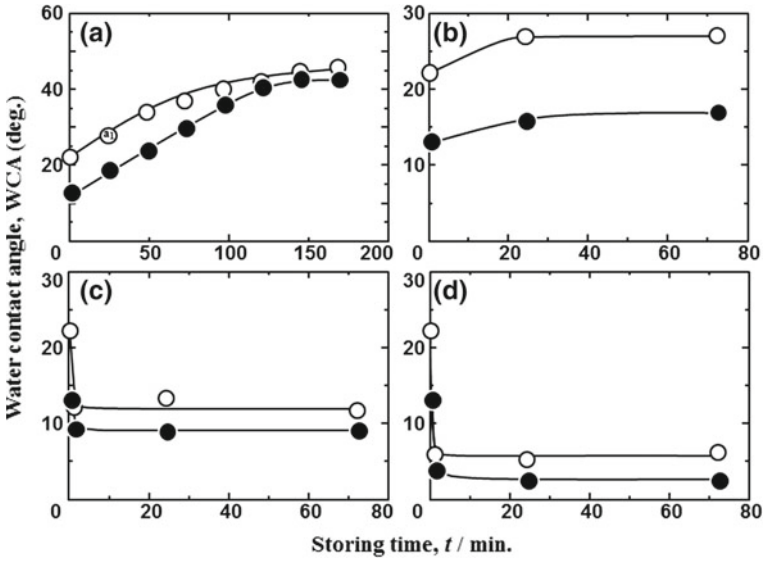

Fig. 34.8 Changes in WCA on the Ti samples processed with different surface modifications (○: as-anodized; ●: hydrothermally treated at 180 °C for 180 min in distilled water) and then stored under different conditions for different periods: **a** in air; **b** in distilled water; **c** in 1 × PBS(-) solution; and **d** in 5 × PBS(-) solution

were adsorbed on the surfaces of the samples, irrespective of the type of ion or the pH of the solution, consequently reducing the WCA values. There were no differences between the types of solute ions with respect to their capacity to reduce the WCA, but when the samples were immersed in 5 × PBS(-) solution, the Na^+ and Cl^- ions were adsorbed more markedly on the surfaces of the samples because their concentrations in the solution were high. In general, it was found that storing samples in 5 × PBS(-) solution effectively maintained the superhydrophilic surface for an extended time. The osteoconductivity of these coatings was then evaluated by using in vivo tests. Before surgery, all of the implants were cleaned in normal saline solution and immediately implanted in the tibiae of 8-week-old male rats. The BIC values are plotted in Fig. 34.6a (■, ◆). These values are on the line extrapolating the BIC values for the as-anodized samples (○). Each of the hydrothermally treated samples showed quite high BIC values, up to 48 and 58%, which were approximately four times higher than the BIC for the as-polished surface. This indicates that the hydrophilic surface had significant osteoconductivity. In particular, the very high BIC in the sample with WCA < 10° is particularly noteworthy.

34.6 Applications

34.6.1 Superhydrophilic or Hydrophobic Surface of Valve Metals

In Sects. 34.5.1 and 34.5.2, hydrophilic surfaces on TiO_2 films were described. In this section, we examine the osteoconductivity of polished valve metals (Ti, Nb, Ta and Zr) and their alloys (Ti-6Al-4V, Ti-6Al-7Nb, Ti-29Nb-13Ta-4.6Zr, Ti-13Cr-1Fe-3Al, and Zr-9Nb-3Sn; mass%) with either hydrophilic or hydrophobic surfaces, in the presence or absence of coating films [56–59]. Hydrothermal treatment in distilled water was again selected to produce the hydrophilic surfaces because anodizing of Nb, Ta, Zr, and Zr alloys did not generate the hydrophilic surface, although the anodized TiO_2 coating displayed hydrophilic characteristics. Hydrothermally treated samples were stored in 5 × PBS(-) solution. Hydrophobic surfaces were obtained by using thermal oxidation at 250 °C or by storing the sample at room temperature after the above hydrothermal treatment. Figure 34.6b shows the correlation between WCA and the osteoconductivity of treated valve metals and alloys. All of the samples had hydrophilic (WCA < 10°) or hydrophobic surfaces, and the WCA value was as low as that of hydrothermally treated TiO_2 films. The BIC values of the hydrophilic samples were also as high as that of hydrophilic TiO_2. These results indicate that the formation of hydrophilic and hydrophobic surfaces leads to higher osteoconductivity, rather than the inclusion of osteoconductive substances such as HAp, TCP (tricalcium phosphate), and TiO_2. The results also show that the hydrothermal treatment can improve the osteoconductivity of valve metals and alloys dramatically.

34.6.2 Protein Adsorbability of Superhydrophilic or Hydrophobic Surface

Protein adsorption is considered to have a strong influence on the biological reactions of bone substitute materials. In this section, we describe the production of protein-adsorbed Ti implants as a demonstration of the application of superhydrophilicity arising from hydrothermal treatment. Fibronectin, which is known to act as a cell adhesive protein, and albumin, which is not adhesive, were selected as test proteins. The proteins were dissolved in distilled water (25 mg mL^{-1} in albumin and 0.5 mg mL^{-1} in fibronectin) and separately adsorbed on the hydrophilic and hydrophobic surfaces for 60 min. The amount of adsorbed protein was evaluated by analyzing the peptide peak in proteins by FT-IR (ATR mode). Figure 34.9 shows the protein adsorbability of surface-treated Ti samples with various WCAs and the osteoconductivity of the protein-adsorbed samples [60]. WCA correlated with the amount of adsorption of the protein, and both hydrophilic and hydrophobic surfaces had significant levels of protein adsorbability. The WCA

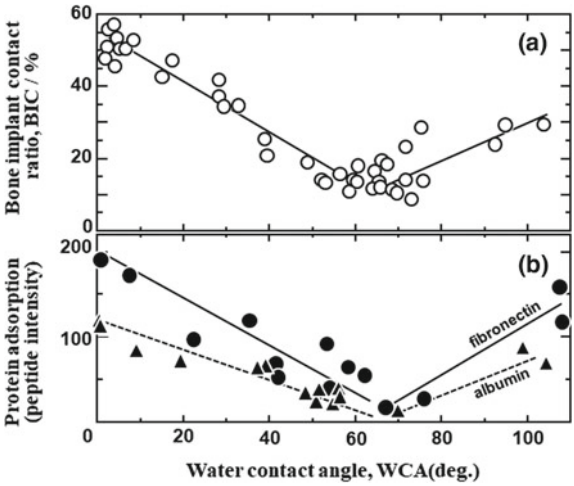

Fig. 34.9 Relationship between the WCA and **a** BIC value of all samples and **b** protein adsorption (peptide intensity). ●: fibronectin and ▲: albumin

of the protein-adsorbed samples was approximately 45° and 65° for fibronectin and albumin, respectively. The protein-adsorbed samples had high BIC values even though they did not possess superhydrophilic surfaces [61]. Therefore, it may be concluded that the hydrophilic and hydrophobic surfaces display high osteoconductivity because they have a higher tendency to adsorb proteins. The high osteoconductivity of the albumin-adsorbed sample is particularly noteworthy [62] because it indicates that the nature of the protein (cell adhesive or not adhesive) may not determine the osteoconductivity.

34.6.3 Superhydrophilic Surface of Ceramics and Polymers

Many kinds of ceramics (Al_2O_3, ZrO_2) and polymers (PTFE, PEEK, PLGA) have been used in dental and orthopedic fields and many of them have hydrophobic surfaces. For ceramics, hydrothermal treatment, irradiation with ultraviolet light (173 nm), or the application of atmospheric plasma have been found to be effective for the hydrophilization of the sintered body of ceramics, such as aluminum oxide (Al_2O_3), zirconium oxide (ZrO_2), and titanium oxide (TiO_2). However, hydrophilization of polymers cannot be achieved by using these processing techniques alone. Polymers acquire superhydrophilicity by applying a two-step treatment, including the disconnection of chemical bonds and immobilization of hydrophilic groups (e.g., –OH and –COOH) that are present. The method selected for the disconnection of the chemical bonds has to overcome chemical reaction barriers. We could generate superhydrophilicity on PEEK, which is known as a superengineering plastic and is used as an intervertebral spacer, by using the combination of immersion in concentrated H_2SO_4 and irradiation with ultraviolet light at 173 nm [63]. The hydrophilicity of the treated ceramics and polymers was

lost upon storage under air in the same manner as hydrothermally treated Ti; therefore, a controlled storage environment was required to maintain their superhydrophilicity. The treated ceramics and polymers with superhydrophilic surfaces acted exactly as described for hydrophilic Ti; e.g., the samples could adsorb proteins and medical agents.

34.7 Conclusion

A comprehensive description of the factors influencing osteoconductivity using TiO_2 coatings has been presented, and a new approach for controlling the osteoconductivity of valve metals and their alloys has been evaluated. However, research in this field has so far been limited to a relatively small number of metallic, ceramic and polymeric materials, and it is clear that further research on this topic needs to be encouraged. For the further development of biomaterials, the correlation between the surface characteristics of implants (metals, ceramics, and polymers) and body tissue must be understood fully. Even when the chemical characteristics of the surface of the implants are controlled, the resulting material may not be optimal. It is thought that nothing can compete with these implants during the progress and development of individual technology. We hope that these important issues can be addressed by developing new bioactive surfaces (organic and inorganic) and surface modification techniques, and by improving alloy designs for the implants and related techniques for their construction and use. We conclude that engineering, especially materials science, has an important role to play in the development of advanced biomaterials that will fulfill a wide variety of medical requirements.

References

1. R. Adell, B. Eriksson, U. Lekholm, P.I. Branemark, T. Jemt, Int. J. Oral Maxillofac. Implants **5**, 347 (1990)
2. D. van Steenberghe, U. Lekholm, C. Bolender, T. Folmer, P. Henry, I. Herrmann, K. Higuchi, W. Laney, U. Linden, P. Astrand, Int. J. Oral Maxillofac. Implants **5**, 272 (1990)
3. L.L. Hench, J. Wilson, in *An Introduction to Bioceramics*, Chap. 1, ed. by L.L. Hench, J. Wilson. Advanced Series in Ceramics, vol. 1 (World Scientific, Singapore, 1993), p. 1
4. K. Kuroda, M. Okido, Bioinorg. Chem. Appl. **2012**, 730693 (2012)
5. R.M. Pilliar, D.A. Deporter, P.A. Watson, M. Pharoah, M. Chipman, N. Valiquette, S. Carter, K. De Groot, J. Dent. Res. **70**, 1338 (1991)
6. S.W.K. Kweh, K.A. Khor, P. Cheang, Biomater. **21**, 1223 (2000)
7. B. Mavis, A.C. Tas, J. Am. Ceram. Soc. **83**, 989 (2000)
8. S. Langstaff, M. Sayer, T.J.N. Smith, S.M. Pugh, S.A.M. Hesp, W.T. Thompson, Biomaterials **20**, 1727 (1999)
9. D.H. Kim, Y.M. Kong, S.H. Lee, I.S. Lee, H.E. Kim, J. Am. Ceram. Soc. **86**, 186 (2003)
10. T.S. Chen, W.R. Lacefield, J. Mater. Res. **9**, 1284 (1994)
11. H. Ishizawa, M. Ogino, J. Mater. Sci. **31**, 6279 (1996)

12. M. Okido, K. Kuroda, M. Ishikawa, R. Ichino, O. Takai, Solid State Ionics **151**, 47 (2002)
13. M. Okido, K. Nishikawa, K. Kuroda, R. Ichino, Z. Zhao, O. Takai, Mater. Trans. **43**, 3010 (2002)
14. X. Nie, A. Leyland, A. Matthews, Surf. Coat. Technol. **125**, 407 (2000)
15. L.A. De Sena, M.C. De Andrade, A.M. Rossi, G.A. De Soares, J. Biomed. Mater. Res. **60**, 1 (2002)
16. K. Kuroda, R. Ichino, M. Okido, O. Takai, J. Biomed. Mater. Res. **59**, 390 (2002)
17. K. Kuroda, R. Ichino, M. Okido, O. Takai, J. Biomed. Mater. Res. **61**, 354 (2002)
18. K. Kuroda, Y. Miyashita, R. Ichino, M. Okido, O. Takai, Mater. Trans. **43**, 3015 (2002)
19. K. Kuroda, S. Nakamoto, R. Ichino, M. Okido, R.M. Pilliar, Mater. Trans. **46**, 1633 (2005)
20. K. Kuroda, S. Nakamoto, Y. Miyashita, R. Ichino, M. Okido, Mater. Trans. **47**, 1391 (2006)
21. K. Kuroda, M. Moriyama, R. Ichino, M. Okido, A. Seki, Mater. Trans. **49**, 1434 (2008)
22. K. Kuroda, M. Moriyama, R. Ichino, M. Okido, A. Seki, Mater. Trans. **50**, 1190 (2009)
23. R. Hazan, R. Brener, U. Oron, Biomaterials **25**, 443 (2004)
24. S. Fujibayashi, M. Neo, H.-M. Kim, T. Kokubo, T. Nakamura, Biomaterials **25**, 443 (2004)
25. K.-R. Wu, C.-H. Ting, W.-C. Lie, C.-H. Lin, J.-K. Wu, Thin Solid Films **500**, 110 (2006)
26. L.S. Hsu, R. Rujkorakarn, J.R. Sites, C.Y. She, J. Appl. Phys. **59**, 3475 (1986)
27. L. Jonasova, F.A. Muller, A. Helebrant, J. Strnad, P. Greil, Biomaterials **25**, 1187 (2004)
28. F. Xiao, K. Tsuru, S. Hayakawa, A. Osaka, Thin Solid Films **441**, 271 (2003)
29. J.-M. Wu, S. Hayakawa, K. Tsuru, A. Osaka, Scr. Mater. **46**, 101 (2002)
30. M. Ueda, M. Ikeda, M. Ogawa, Mater. Sci. Eng. C **C29**, 994 (2009)
31. Y.-T. Sul, C.B. Johansson, S. Petronis, A. Krozer, Y.S. Jeong, A. Wennerberg, T. Albreksson, Biomaterials **23**, 491 (2002)
32. J.P. Schreckenbach, G. Marx, F. Schlotigg, M. Textor, N.D. Spencer, J. Mater. Sci. Mater. Med. **10**, 453 (1999)
33. B. Yang, M. Uchida, H.-M. Kim, X. Zhang, T. Kokubo, Biomaterials **25**, 1003 (2004)
34. L.A. de Sena, N.C.C. Rocha, M.C. Andrade, G.A. Soares, Surf. Coat. Technol. **166**, 254 (2003)
35. D. Buser, N. Broggini, M. Wieland, R.K. Schenk, A.J. Denzer, D.L. Cochran, B. Hoffmann, A. Lussi, S.G. Steinemann, J. Dent. Res. **83**, 529 (2004)
36. D.L. Cochran, D. Buser, C.M. Ten Bruggenkate, D. Weingart, T.M. Taylor, J.P. Bernald, F. Peters, J.P. Simpson, Clin. Oral Implants Res. **13**, 144 (2002)
37. C. Eriksson, H. Nygren, K. Ohlson, Biomaterials **25**, 4759 (2004)
38. J.-W. Park, K.-B. Park, J.-Y. Suh, Biomaterials **28**, 3306 (2007)
39. G.B. Schneider, R. Zaharias, D. Seabold, J. Keller, C. Stanford, J. Biomed. Mater. Res. A **69A**, 462 (2004)
40. G. Zhao, Z. Schwartz, M. Wieland, F. Rupp, J. Geis-Gerstorfer, D.L. Cochran, B.D. Boyan, J. Biomed. Mater. Res. A **74A**, 49 (2005)
41. S.V. Gils, P. Mast, E. Stijns, H. Terryn, Surf. Coat. Technol. **185**, 303 (2004)
42. Japanese Industrial Standards, JIS B 0601
43. D. Yamamoto, I. Kawai, K. Kuroda, R. Ichino M. Okido, A. Seki, Mater. Trans. **52**, 1650 (2011)
44. J.-H. Lee, S.-E. Kim, Y.-J. Kim, C.-S. Chi, H.-J. Oh, Mater. Chem. Phys. **98**, 39 (2006)
45. C.Y. Kramer, Biometrics **12**, 307 (1956)
46. G.-L. Yang, F.-M. He, X.-F. Yang, X.-X. Wang, S.-F. Zhao, Oral Surg. Oral Med. Oral Pathol. Oral Radiol. Endod. **106**, 516 (2008)
47. C. Larsson, P. Thomsen, J. Lausmaa, M. Rodahl, B. Kasemo, L.E. Ericson, Biomaterials **15**, 1062 (1994)
48. X. Cui, H.-M. Kim, M. Kawashita, L. Wang, T. Xiong, T. Kokubo, T. Nakamura, Dent. Mater. **25**, 80 (2009)
49. D. Yamamoto, I. Kawai, K. Kuroda, R. Ichino M. Okido, A. Seki, Bioinorg. Chem. Appl. **2012**, 495218 (2012)
50. D. Yamamoto, T. Iida, K. Kuroda, R. Ichino, M. Okido, A. Sek, Mater. Trans. **53**, 508 (2012)

51. D. Yamamoto, T. Iida, K. Arii, K. Kuroda, R. Ichino M. Okido, A. Seki, Mater. Trans. **53**, 1956 (2012)
52. D. Yamamoto, K. Arii, K. Kuroda, R. Ichino, M. Okido, A. Seki, J. Biomater. Nanobiotech. **4**, 45 (2013)
53. M.E. Simonsen, Z. Li, E.G. Sogaard, Appl. Surf. Sci. **255**, 8054 (2009)
54. K.-X. Zhang, W. Wang, J.-L. Hou, J.-H. Zhao, Y. Zhang, Y.-C. Fang, Vacuum **85**, 990 (2011)
55. W. Att, N. Hori, M. Takeuchi, J. Ouyang, Y. Yang, M. Anpo, T. Ogawa, Biomaterials **30**, 5352 (2009)
56. M. Zuldesmi, A. Waki, K. Kuroda, M. Okido, J. Biomater. Nanobiotechnol. **4**, 284 (2013)
57. M. Zuldesmi, A. Waki, K. Kuroda, M. Okido, Mater. Sci. Eng. C **42**, 405 (2014)
58. M. Zuldesmi, A. Waki, K. Kuroda, M. Okido, Mater. Sci. Eng. C **49**, 430 (2015)
59. M. Zuldesmi, K. Kuroda, M. Okido, M. Ueda, M. Ikeda, J. Biomater. Nanobiotechnol. **6**, 126 (2015)
60. K. Kuroda, M. Okido, Mater. Sci. Forum **879**, 1049 (2017)
61. M. Omori, S. Tsuchiya, K. Hara, K. Kuroda, M. Okido, H. Hibi, M. Ueda, Stem Cell Res. Ther. **6**, 124 (2015)
62. Y. Yamaguchi, K. Kuroda, M. Okido, Abstract, in *JIM Spring Meeting*, Mar 2016
63. K. Kuroda, K. Igarashi, H. Kanetaka, M. Okido, J. Biomater. Nanobiotechnol. **9**, 233 (2018)

Chapter 35
Surface Modification with Micro-arc Oxidation

Akiko Nagai, Yusuke Tsutsumi and Kosuke Nozaki

Abstract Micro-arc oxidation (MAO) is one of the methods of surface modification of metal substrates and is a relatively simple procedure. The MAO surface is suitable for biomaterials because of its rough complex geometry and the ability to incorporate various ions. The conditions of MAO coatings can be optimized using some parameters, such as electrolytes and electrical factors. In this chapter, the principle of MAO is explained in the first section. The applications of MAO to biomedical fields are introduced in subsequent sections. The second section describes the efficacy on bioactivity of metallic biomaterials in vitro. The third section describes the methodology of in vivo evaluation of the osseointegration capability of titanium implants. Because direct integration of titanium implant to bone tissue is closely involved in bone formation around titanium surfaces without fibrous soft tissue, the evaluation of histological and three-dimensional morphology of bone tissue is absolutely imperative. Furthermore, the stability of titanium implants evaluated by mechanical test has an impact on the clinical situation.

Keywords Surface modification · Biocompatibility · Metals · Ceramics · Micro-arc oxidation

A. Nagai (✉)
Department of Anatomy, Aichi Gakuin University, 1-100 Kusumoto, Chikusa, Nagoya 464-8650, Japan
e-mail: aknagai@dpc.agu.ac.jp

Y. Tsutsumi
Research Center for Structural Materials, National Institute of Materials Science (NIMS), 1-2-1 Sengen, Tsukuba, Ibaraki 305-0047, Japan
e-mail: TSUTSUMI.Yusuke@nims.go.jp

K. Nozaki
Department of Fixed Prosthodontics, Grauate School of Medical and Dental Sciences, Tokyo Medical and Dental University (TMDU), 1-5-45 Yushima, Bunkyo-ku, Tokyo 113-8510, Japan
e-mail: k.nozaki.fpro@tmd.ac.jp

Y. Setsuhara et al. (eds.), *Novel Structured Metallic and Inorganic Materials*, https://doi.org/10.1007/978-981-13-7611-5_35

35.1 Introduction—Method and Principals of Micro-arc Oxidation (MAO)

Micro-arc oxidation (MAO), which is also known as plasma electrolytic oxidation, is a high voltage plasma-assisted anodic oxidation process for surface modification of valve metals. Valve metals, such as aluminum, tantalum, niobium, titanium, magnesium, and zirconium, can form an adherent, electrically insulating anodic oxide films after the MAO treatment [1]. The MAO-treated surface obtains excellent adhesive, strength, friction, corrosion, wear, electrical, and thermal properties. The coating layer is uniform, and many open and closed pores are distributed homogenously in the specimen (Fig. 35.1). Because this rough complex geometry is preferred to biomaterials because it improves fixation of metal in bone and cellular entry in the material, it has been used for medical applications such as dental implants.

Because the MAO process includes electrochemical oxidation, plasma chemical reaction, and thermal diffusion in an electrolyte, the components in the MAO setup, illustrated in the schematic representation in Fig. 35.2, are immersed in an aqueous electrolyte. The valve metals serve as anodes, and stainless steel is used as a cathode in the electrolytic bath. A cooling system within the container is highly desired to produce thicker coatings.

The conditions of MAO coatings can be optimized using parameters, such as electrolytes and electrical factors.

(a) Electrolytes. The concentration and compositions of the electrolyte affect the morphology and incorporating ions of the MAO coatings. The base electrolyte is an alkaline solution, usually sodium or potassium hydroxide. Various electrolytes consisting of anions such as phosphate, fluoride, and silicate were reported in previous studies, while oxalate or sulfate solution was unreported [2, 3]. Ionic additives in electrolytes, such as calcium and silver, incorporate

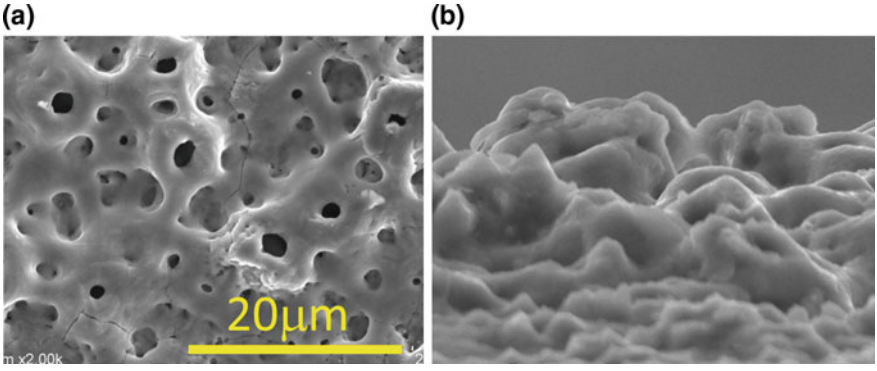

Fig. 35.1 SEM micrographs of **a** a top view and **b** an oblique view of the micro-arc oxidation coatings. Scale bars: 10 μm

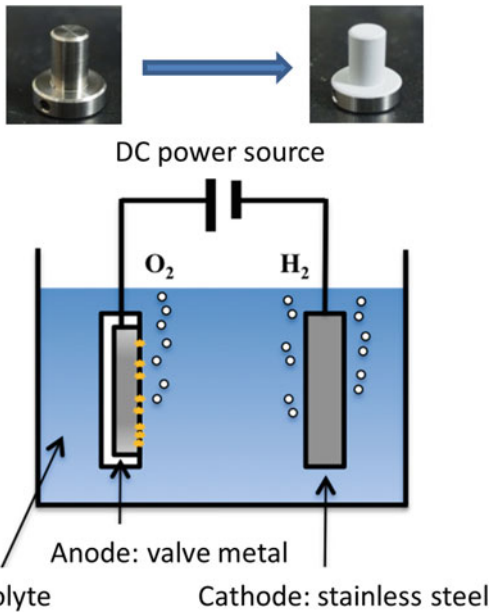

Fig. 35.2 The representative apparatus for the micro-arc oxidation method

into MAO coatings and release the specific ion; they subsequently enhance biological activity or antibacterial properties.

(b) Electrical parameters. The parameters, including voltage, current density, and treatment time, also influence the morphology and thickness of the MAO coatings. The thickness of the coatings increased with increasing voltage (Fig. 35.3a, c). When the current density increased, the pore size increased and the roughness decreased (Fig. 35.3a, b). The constant current density decays in the later stages of the MAO process; the intensity of the spark charges decreases, and smaller sparks are distributed over the entire surface of the coatings. Then, the coatings obtained a relatively smooth and a homogenous microstructure.

Although all of the details of the mechanism of the MAO process have not yet been explained the process can be classified into four stages, as described below, depending on the variation of voltage with time (Fig. 35.4) [4].

(1) Anodizing stage. The voltage increases rapidly and linearly with time to the breakdown voltage. Some oxygen bubbles and an oxide layer are observed on the anode surface. The formed oxide layer subjected to the barrier type anodization is dense and is in an amorphous form.

(2) Dielectric breakdown stage. When the applied voltage exceeds a certain critical value, dielectric breakdown occurs, and spark discharges are observed (Fig. 35.5). An inhomogeneous breakdown, resulting in localized thickening of the oxide coatings, may cause these events.

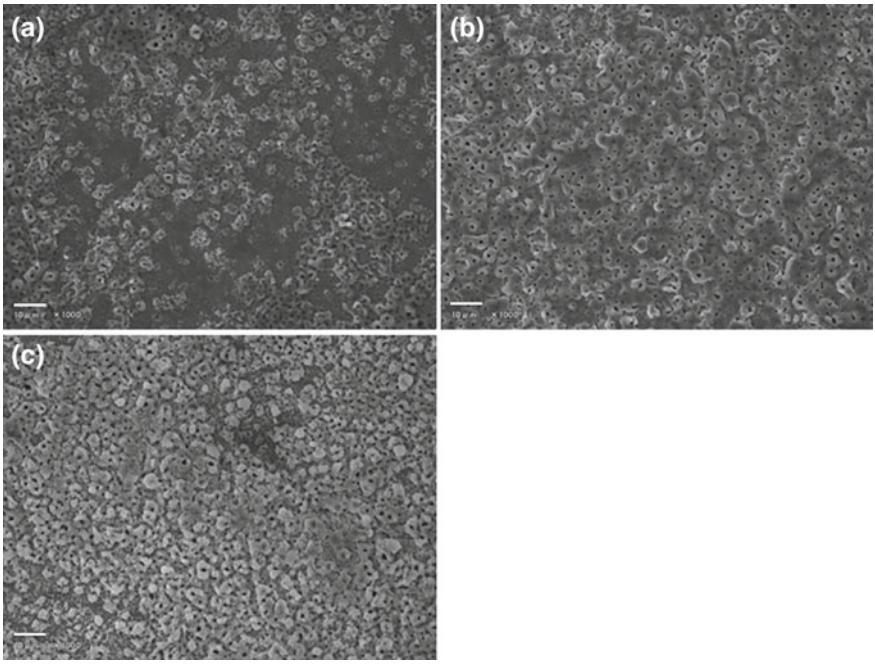

Fig. 35.3 Surface morphologies of MAO coatings on zirconium at various applied voltages and current densities. **a** 450 V, 20 mA; **b** 450 V, 100 mA; **c** 500 V, 20 mA. Scale bars: 10 μm

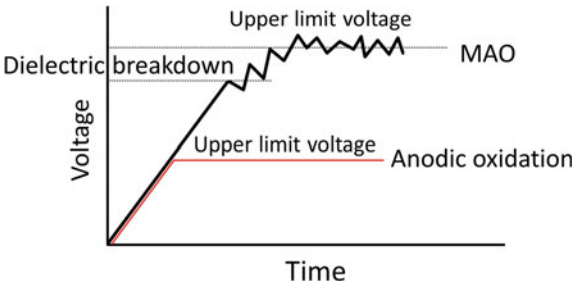

Fig. 35.4 The scheme of variation of voltage with time in the micro-arc oxidation process

(3) MAO surface formation stage. The breakdown and formation of the oxide coatings continue, and the voltage fluctuates. The fluctuation indicates the existence of discontinuous reaction by electric discharges.
(4) The convergence of the process. The intense sparks and gas release trigger the formation of large-sized pores and thermal cracking of the coatings. The voltage decreases rapidly with the disappearance of the surface reactions.

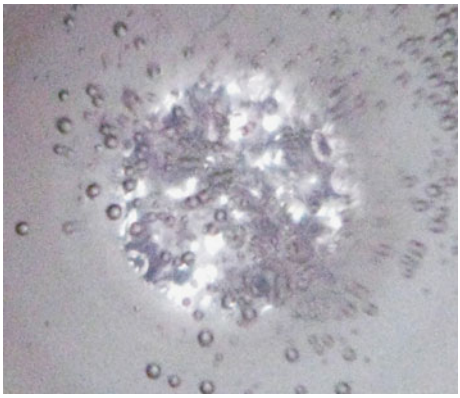

Fig. 35.5 Sparks and gas release from the anode observed in the micro-arc oxidation process

Here, we will introduce several studies of MAO-treated surfaces and evaluate the biological properties in the following section. We focused on the bioactivity of MAO in the in vitro (Sect. 35.2) and the osseointegration ability of MAO in the in vivo assays (Sect. 35.3).

35.2 Bioactivity Evaluation in Vitro

Bioactivity is one of the parameters indicating the reactiveness in a living body environment of the material's surface. Bioactivity can be evaluated by a relatively simple procedure without using cells or animals, thereby enabling many researchers to apply this evaluation as a first step of verification on bone-contacting devices.

The procedure of bioactivity evaluation is composed of two steps: immersion in simulated body fluids for a certain period and surface observation and/or elemental analysis. An SBF solution [5] is recognized as the most common fluid for bioactivity evaluation medium. Hanks' solution can also be used because of more adequate judgment on intricately structured surfaces such as MAO-treated metals [6]. A container made of plastics is desirable for the immersion of the specimens in a simulated body fluid. In the case of a glass container, calcium phosphate might form on the bottle wall as a result of reaction with the fluid. The fluid must be prepared with sufficient volume to the entire surface area of the specimen. In general, the testing temperature and the immersion period are 37 °C and several days, respectively. The simulated body fluid may be changed periodically to simulate circulation of the body fluid. A container may be shaken to prevent the simulated body fluid from accumulating in the gap and forming a local environment.

After the immersion period, the specimen is picked up from the fluid and carefully rinsed with pure water. A scanning electron microscope (SEM) is useful for observation of calcium phosphate formation on the specimen surface. Figure 35.6 shows calcium phosphate formation on Ti alloy after immersion in

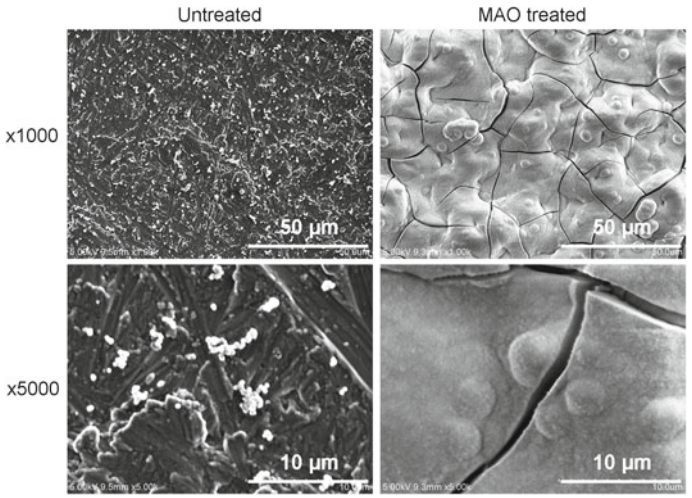

Fig. 35.6 Scanning electron micrographs of Ti alloys after immersion in Hanks' solution for 7 d. Reprinted from Ref. [7], Copyright 2012, with permission from Elsevier

Hanks' solution for 7 d [7]. Calcium phosphate precipitates of less than 1 μm are observed on the surface of the untreated specimen (only ground by abrasive papers). The bare metal surface remained exposed even after a 7 d immersion in Hanks' solution. On the other hand, the MAO-treated specimen was completely covered by the calcium phosphate layer with an apparent thickness of a few micrometers after immersion in Hanks' solution. The cracks in the layer are introduced under the vacuum condition used for SEM observation. The amount of calcium phosphate precipitated on the specimen surface can be determined by some elemental analyses. Figure 35.7 shows the amount of calcium and phosphorous formed on MAO-treated and untreated Ti. The tested specimens are immersed and stirred in the nitric acid solution to completely dissolve the precipitated calcium phosphate. An inductively coupled plasma atomic spectrometer (ICP-AES) or

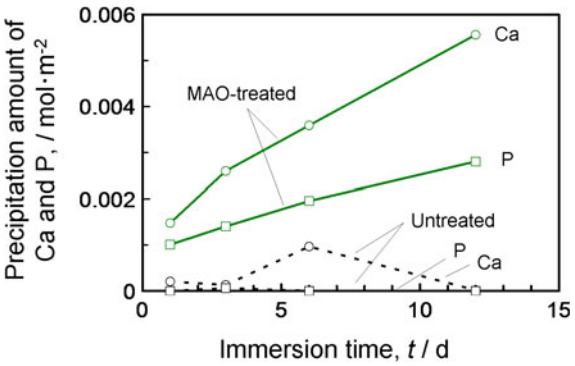

Fig. 35.7 Accelerated calcium phosphate formation on MAO-treated Ti during immersion in Hanks' solution determined by ICP-AES measurement

atomic absorption spectrometer (AAS) can be used to determine the concentrations of both Ca and P ions in the resulting solution. As shown in Fig. 35.7, the amounts of both Ca and P increase during immersion in Hanks' solution. In other words, the calcium phosphate forms spontaneously on MAO-treated Ti and grows to form a thick layer, as shown in Fig. 35.6. The amount of calcium phosphate on untreated Ti seems to be almost negligible. Thus, the specimen surface after MAO treatment is much more reactive to the simulated body fluid than the untreated specimen. Bioactivity evaluation is a useful tool to compare the hard tissue compatibility of the materials because of advantages in cost and time. However, a more detailed investigation is required to confirm that a biological reaction occurs at the interface between material and living cells/tissues.

35.3 In Vivo Evaluation

35.3.1 Animal Testing

The in vitro evaluation shows the characterization of bone-contacting materials to some extent; however, owing to its complex mechanisms of bone modeling and remodeling, an appropriate in vivo model would be used to assess osseointegration capability. The concept of osseointegration was first introduced by Branemark et al. to describe direct contact between bone and titanium implants without fibrous soft tissue at the level of light microscopy [8].

Laboratory animals should be selected according to several factors such as the cost of acquiring and caring for the animals, availability, acceptability to society, tolerance to captivity, and ease of housing [9]. Although the size and number of implanted materials are limited, the rabbit is one of the most commonly used species among musculoskeletal research studies [10, 11]. The rabbit femur and tibia were reportedly shown to have similarities of bone mineral density and fracture toughness to human bone [12]. Because of histological features of cancellous bone, the epicondyle of the femur was widely chosen for the implant location. After placement of a titanium implant, the short-term responses are normally assessed from 1 week up to 4 weeks, and the long-term responses are assessed in tests exceeding 12 weeks (ISO 10993-6:2007 Biological evaluation of medical devices —Part 6: Tests for local effects after implantation).

35.3.2 Histomorphometric Evaluation

Non-decalcified tissue sections were usually selected to evaluate achievement of osseointegration. After anesthesia with an overdose of sodium pentobarbital solution, the implant and surrounding tissues were excised after a certain number of

months postimplantation, fixed in paraformaldehyde, dehydrated in graded ethanol, penetrated with acetone, and then embedded in resin. Thin sections were prepared using microtome and stained with toluidine blue; this procedure was based on the principle of metachromasia. Metachromasia resulted in a stacking of dye cations at the site of high-density anionic groups in the tissues [13].

The bone implant contact (BIC) ratio, which was defined as the percentage of the bone surface border in direct contact with the implant, has been investigated as one of the parameters of osseointegration (Fig. 35.8). Sul et al. compared the BIC ratio of MAO-treated titanium implants to that of machined implants using tuberositas tibiae of rabbit [14]. A MAO-treated surface 6 weeks postimplantation showed enhanced osteoconductivity (BIC ratio: 24%) in comparison with a machined surface (20%).

The surface changes of MAO-treated titanium were previously shown to be controlled through an electrical polarization process and to enhance proliferation and differentiation of osteoblast-like MG63 cells [15, 16]. The application of an electrical polarization method to ceramic biomaterials was first introduced by Yamashita et al. [17]. The dipoles in ceramics were generated with DC voltage under a programmed heat profile and fixed in room temperature. An MAO-treated titanium implant with highly dense surface charges placed in the epicondyle of a rabbit femur resulted in a higher BIC ratio than an MAO-treated titanium surface [18].

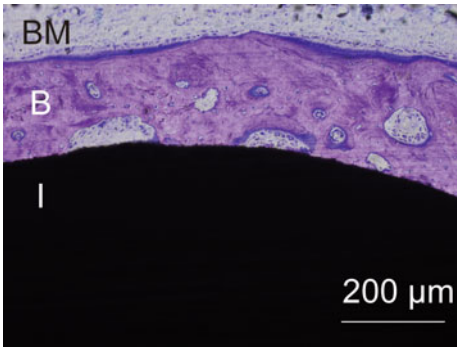

Fig. 35.8 Histological observations of interface between bone and MAO-treated titanium implant 4 weeks postimplantation. Titanium implant was placed at epicondyle of rabbit femur. Resin embedded section was stained with toluidine blue. Trabecular bone directly integrated implant surface at the level of light microscopy. I: Implant, B: Bone, BM: Bone marrow

35.3.3 Mechanical Stability Evaluation

35.3.3.1 Fracture Force Measurement

Implant stability is evaluated by not only the BIC ratio but also mechanical testing, which is usually conducted by removing the implant from bone tissue. Mechanical force, such as pull-out, push-out, and removal torque forces, is applied to the implant, depending on its design. Cylindrical implants inserted in the cortical and cancellous bone of the femur, tibia, or mandible were generally subjected to push-out and pull-out forces, and screw implants were subjected to removal torque force [19].

The anodized screw-type implant inserted in the rabbit tibia appeared to have higher removal torque values and a higher BIC ratio than the machined implant [20]. The moderately rough surface created by MAO can scratch along the walls of the bone during surgery, compared to a machined implant, and result in a smear layer composed of bone and blood, which causes osteoinduction [21]. Choi et al. reported that using an MAO-treated implant with increased surface roughness as a function of applied voltage resulted in a higher removal torque value than an implant with a smoother surface [22].

The mechanical stability test depends on not only the osseointegration but also the mechanical properties of the surrounding bone [23]. Although a cohesive fracture in the bone contributes to bone properties, due to the irregularities of trabecular bones, the failure mode was difficult to assess using an SEM. We previously reported that the fracture occurred at the interface and in the bone tissue after a pull-out test of a cylindrical MAO-treated implant inserted in cancellous bone (Fig. 35.9a) [18].

In order to quantitatively evaluate the fracture mode, bone apposition on the implant surface was stained with alizarin red S, which forms a calcium-alizarin red

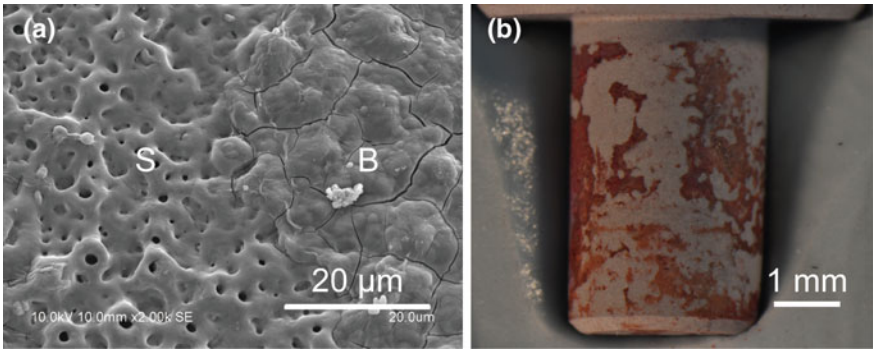

Fig. 35.9 Fracture mode of MAO-treated implant surface after removing from bone. **a** SEM image showed the bone apposition on the implant surface. B: Bone, S: MAO-treated implant surface. **b** Stereomicroscope image of MAO-treated implant stained with alizarin red S

S complex via a chelation process (Fig. 35.9b). Residual bone apposition post-pull-out means that the fracture occurred in bone tissue, and the integration between bone and implant was adequately established.

35.3.3.2 Resonance Frequency Measurement

Resonance frequency analysis (RFA) is a noninvasive test method to measure the implant stability in clinical practice [24]. The transducer, which is attached to the implant fixtures, is triggered to vibrate by means of sinusoidal waves. The resonance frequency value is converted to implant stability quotients (ISQ), ranging from 1 to 100. Although the ISQ is an indicator of implant stability, due to its dependence on the surrounding bone stiffness, the accurate condition of the bone formation is unclear.

Rasmusson et al. reported the superiority of delayed implant placement compared to simultaneous implant placement by measuring the resonance frequencies using a rabbit model [25]. The mean resonance frequency value of delayed implant placement was statistically higher than that of simultaneous implant placement. Nevertheless, the removal torque value and the BIC ratio showed no statistical difference between them. Thus, RFQ is widely used in clinical practice; however, its application to research fields to evaluate bone formation and BIC ratio should be further studied.

35.3.3.3 Three-Dimensional Morphometric Evaluation

Micro-computed tomography (micro-CT) is a nondestructive three-dimensional imaging technique that analyzes trabecular bone morphology and bone mineral density without complicated specimen preparation (Fig. 35.10). Moreover, the

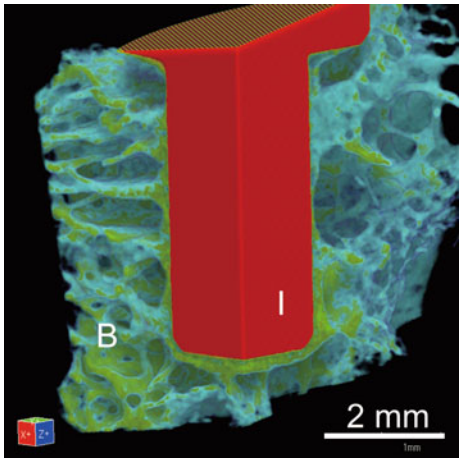

Fig. 35.10 Cross-sectional image of MAO-treated titanium implant 12 weeks postimplantation using micro-computed tomography. Trabecular bone architecture can be observed in three dimensions. Color code indicates bone mineral density (red: high, blue: low). B: Bone, I: Implant

samples used in micro-CT can be subjected to other tests, therefore contributing to the reduction of animals in in vivo testing. Micro-CT imaging was introduced to the preclinical research field in the early 1980s, providing higher quality resolution compared to the computed tomography imaging used in the 1970s. A rising number of publications using micro-CT illustrate the increased importance of three-dimensional analysis of bone architecture [26].

Liu et al. reported the use of osseointegration fraction density (OV/TV) to predict BIC ratio using micro-CT [27]. Owing to the metal artifact, they calculated bone fraction density (BV/TV) in a 3-voxel-thick ring (48 μm) that excluded the 3 voxels immediately adjacent to the implant. Although OV/TV as measured on micro-CT images had no significant correlation to BIC ratio, implant stability estimated from pull-out force measurement had a weak correlation.

We previously reported the OV/TV of an MAO-treated implant with highly dense surface charges in a 100-μm-thick ring, excluding 60 μm, which was equal to 3 voxels [18]. OV/TV showed no correlation with either the BIC ratio or the pull-out force because the newly formed bone on the implant surface was multiple-architecture in an excluded 3-voxel-thick ring and accounted for implant stability. Thus, further study will be needed to evaluate the osseointegration capability of titanium implants using micro-CT, including imaging conditions.

References

1. H. Matsuno, A. Yokoyama, F. Watari, M. Uo, T. Kawasaki, Biomater. **22**, 1253 (2001)
2. S. Abbasi, F. Golestani-Fard, S.M.M. Mirhosseini, A. Ziaee, M. Mehrjoo, Mater. Sci. Eng. C **33**, 2555 (2013)
3. J. Liang, L. Hu, J. Hao, Appl. Surf. Sci. **253**, 4490 (2007)
4. T.S.N. Sankara Narayanan, I.S. Park, M.H. Lee, Prog. Mater Sci. **60**, 1 (2014)
5. T. Kokubo, H. Takadama, Biomater. **27**, 2907 (2006)
6. Y. Tsutsumi, M. Niinomi, M. Nakai, M. Shimabukuro, M. Ashida, P. Chen, H. Doi, T. Hanawa, Metals **6**, 76 (2016)
7. Y. Tsutsumi, M. Niinomi, M. Nakai, M.H. Tsutsumi, H. Doi, T. Hanawa, Appl. Surf. Sci. **262**, 34 (2012)
8. P.I. Branemark, R. Adell, T. Albrektsson, U. Lekholm, S. Lundkvist, B. Rockler, Biomater. **4**, 25 (1983)
9. J.H. Schimandle, S.D. Boden, Spine **19**, 1998 (1994)
10. A.I. Pearce, R.G. Richards, S. Milz, E. Schneider, S.G. Pearce, Eur. Cell. Mater. **13**, 1 (2007)
11. J.G. Neyt, J.A. Buckwalter, N.C. Carroll, Iowa Orthop. J. **18**, 118 (1998)
12. X. Wang, J.D. Mabrey, C.M. Agrawal, Biomed. Mater. Eng. **8**, 1 (1998)
13. G. Sridharan, A.A. Shankar, J. Oral. Maxillofac. Pathol. **16**, 251 (2012)
14. Y.T. Sul, C.B. Johansson, K. Roser, T. Albrektsson, Biomater. **23**, 1809 (2002)
15. C.F. Ma, A. Nagai, Y. Yamazaki, T. Toyama, Y. Tsutsumi, T. Hanawa, W. Wang, K. Yamashita, Acta Biomater. **8**, 860 (2012)
16. A. Nagai, Y. Yamazaki, C.F. Ma, K. Nozaki, T. Toyama, K. Yamashita, J. Eur. Ceram. Soc. **32**, 2647 (2012)
17. K. Yamashita, N. Oikawa, T. Umegaki, Chem. Mater. **8**, 2697 (1996)
18. K. Nozaki, W. Wang, N. Horiuchi, M. Nakamura, K. Takakuda, K. Yamashita, A. Nagai, J. Biomed. Mater. Res. **102**, 3077 (2014)

19. G. Giavaresi, M. Fini, A. Cigada, R. Chiesa, G. Rondelli, L. Rimondini, P. Torricelli, N.N. Aldini, R. Giardino, Biomater. **24**, 1583 (2003)
20. K.H. Park, S.J. Heo, J.Y. Koak, S.K. Kim, J.B. Lee, S.H. Kim, Y.J. Lim, J. Oral Rehabil. **34**, 517 (2007)
21. A. Tabassum, F. Walboomers, J.G.C. Wolke, G.J. Meijer, J.A. Jansen, Clin. Implant Dent. Relat. Res. **13**, 269 (2011)
22. J.W. Choi, S.J. Heo, J.Y. Koak, S.K. Kim, Y.J. Lim, S.H. Kim, J.B. Lee, J. Oral Rehabil. **33**, 889 (2006)
23. M. Soncini, R. Rodriguez y Baena, R. Pietrabissa, V. Quaglini, S. Rizzo, D. Zaffe, Biomater. **23**, 9 (2002)
24. N. Meredith, D. Alleyne, P. Cawley, Clin. Oral Implants Res. **7**, 261 (1996)
25. L. Rasmusson, N. Meredith, I.H. Cho, L. Sennerby, Int. J. Oral Maxillofac. Surg. **28**, 224 (1999)
26. S.J. Schambach, S. Bag, L. Schilling, C. Groden, M.A. Brockmann, Methods **50**, 2 (2010)
27. S. Liu, J. Broucek, A.S. Virdi, D.R. Sumner, J. Microsc. **245**, 34 (2012)

Part VI
Novel Structured Materials for Electronic Devices

Chapter 36
Spin Electronics

Takahide Kubota, Takeshi Seki and Koki Takanashi

36.1 Introduction to Giant Magnetoresistance

Semiconductor electronics has utilized characteristics of electron charge: Transportation of electrons and holes. Although an electron has a spin angular momentum, the electron spin had been ignored in electronic devices until the discovery of giant magnetoresistance (GMR) in 1988. The technology exploiting the characteristics of spin is called "Spin electronics" or "Spintronics". The GMR effect is the most fundamental phenomenon in spin electronics and was first reported by Fert and his collaborators in the experiment of Fe/Cr superlattices [1]. Before the discovery of GMR by Fert et al., Grünberg and coworkers had reported in 1986 antiferromagnetic interlayer exchange coupling of Fe layers through a Cr interlayer in a Fe/Cr/Fe trilayer structure [2]. The antiferromagnetic interlayer exchange coupling is closely related to GMR. Their findings of antiferromagnetic interaction and GMR significantly stimulated interests of many researchers, which led to an enormous amount of studies for magneto-transport properties in various kinds of nanometer-scaled layered structures with ferromagnetic metals.

In only 10 years after the discovery of GMR, the read head of a hard disk drive (HDD) using GMR was commercially available. The GMR-based read head dramatically improved the storage density of HDD. Since GMR was considered 'the first major application of nanotechnology', both Fert and Grünberg were jointly awarded the Nobel prize in physics in 2007. Nowadays, tunnel magnetoresistance (TMR) effect is used for the read head of HDD. In contrast to GMR for all-metallic superlattices, TMR is observed in a magnetic tunnel junction (MTJ) consisting of an ultra-thin insulating layer sandwiched by two ferromagnetic (FM) layers. In a MTJ, its tunneling probability of electrons depends on the relative orientation of magnetization vectors of two FM layers. Because a larger TMR ratio than GMR led

T. Kubota · T. Seki · K. Takanashi (✉)
IMR, Tohoku University, 2-1-1, Katahira, Aoba-ku, Sendai 980-8577, Japan
e-mail: koki@imr.tohoku.ac.jp

Y. Setsuhara et al. (eds.), *Novel Structured Metallic and Inorganic Materials*, https://doi.org/10.1007/978-981-13-7611-5_36

to the further improvement of the storage density of HDD, the TMR-based read head replaced the GMR-based read head. As described later, however, GMR has recently drawn renewed attention for the read head application.

36.1.1 Giant Magnetoresistance (GMR) Effect

When an external magnetic field (H_{ext}) is applied to a material, the electric resistance of the material changes in general, which is known as a magnetoresistance (MR) effect. There are many types of MR effects: All conductive materials, irrespective of magnetic or nonmagnetic, show a MR effect. The electric resistance of a material increases as H_{ext} is increased, i.e., the sign of MR is positive, which originates from the Lorentz force that affects the motion of conduction electrons. This MR effect is called an ordinary magnetoresistance effect. On the other hand, ferromagnetic materials (including ferrimagnetic materials) show a MR effect due to the spontaneous magnetization (M). This MR effect is called an anomalous magnetoresistance effect, which is classified into an anisotropic magnetoresistance (AMR) effect and a forced effect. The AMR effect appears when the relative orientation between M and electric current (I) is changed. The forced effect appears under the high magnetic field application after saturating the magnetization, and a slight increase in M leads to the corresponding decrease in electric resistance. Although the AMR effect is well known as a MR effect in ferromagnetic materials, its magnitude is usually small.

The phenomenon of the GMR effect is different from that of the AMR effect in terms of both quantitative and qualitative characteristics. First, the GMR effect is isotropic irrespective of the relative angle between H_{ext} and I. Second, the resistance decreases remarkably when the magnetization is being saturated, so the sign of MR is negative. A typical GMR curve and the corresponding magnetization curve are shown in Fig. 36.1a and b, respectively. The magnetization vectors in adjacent FM layers show antiparallel alignment at $H_{ext} = 0$. In the process that they are aligned in parallel with increasing H_{ext} up to the saturation field (H_s), the electric resistivity (ρ) decreases significantly. The antiparallel alignment is caused by the antiferromagnetic interlayer exchange coupling between FM layers through a nonmagnetic (NM) layer. The magnitude of interlayer exchange coupling is proportional to the exchange coupling energy per unit area (J), and $J < 0$ is required for the antiparallel alignment of magnetization vectors for FM layers. In addition, the sign and the magnitude of J depend on the NM layer thickness.

The magnitude of GMR is usually defined as the MR ratio ($\Delta\rho/\rho$), and is given by

$$\Delta\rho/\rho = (\rho_o - \rho_s)/\rho_s, \tag{36.1}$$

where ρ_0 is the maximum value of ρ at $H_{ext} = 0$ and ρ_s is that when the magnetization is saturated ($|H_{ext}| > H_s$). GMR was studied using superlattices that are

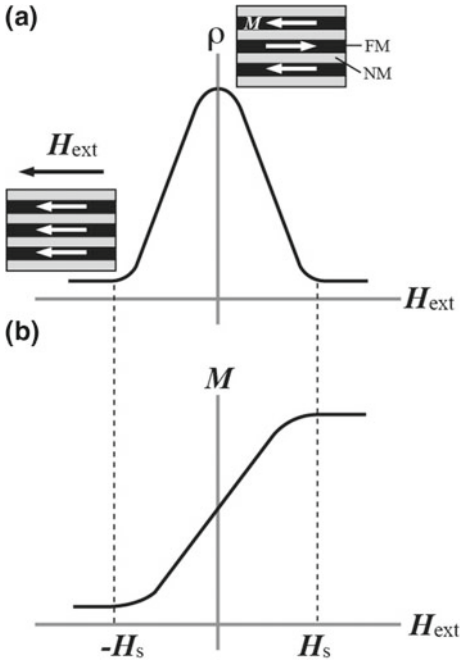

Fig. 36.1 **a** A typical magnetoresistance (MR) curve and **b** a magnetization curve of a superlattice showing giant magnetoresistance (GMR)

composed of two or more different materials alternately deposited in a nanometer scale by film preparation techniques such as molecular beam epitaxy (MBE) and sputtering. A variety of superlattices consisting of FM metals and NM metals were investigated, e.g., Co/Cu [3], Co/Ag [4], Ni/Ag [5], etc.

If the antiferromagnetic interlayer exchange coupling is strong, one needs to apply a high H_{ext} to align the magnetization vectors in parallel, i.e., to obtain GMR. This was a major obstacle for practical applications of GMR. One of the solutions to obtain GMR in a low H_{ext} is to utilize the difference between switching fields for adjacent FM layers without the help of antiferromagnetic interlayer exchange coupling [6]. Another effective way is to make a spin-valve structure [7]. In the spin-valve structure, the magnetization direction in one of FM layers (free layer) is easily changed when a low H_{ext} is applied, whereas the other (fixed layer) has its magnetization pinned by the exchange magnetic anisotropy from the neighboring antiferromagnetic (AFM) layer. Consequently, GMR appears even under the application of a low H_{ext}. The spin-valve structure was used in a central part for a read head of HDD in 1998 and played an important role for the remarkable increase in recording density.

36.1.2 Mechanism of GMR Effect

The spin-dependent scattering of conduction electrons is the key physics to understand the GMR effect. The spin-dependent scattering occurs in FM layers or at FM/NM interfaces. In a two-current model, up-spin (↑) and down-spin (↓) electrons are supposed to pass through two independent channels without taking into account the spin-flip scattering that causes the change of spin orientation. The scattering probability of conduction electrons depends on whether the spin orientation is parallel or antiparallel to the magnetization, which is called spin-dependent scattering. The electric resistivity for spins parallel to the magnetization (ρ_+) is not equal to that for spins antiparallel to the magnetization (ρ_-), i.e., $\rho_+ \neq \rho_-$. Here we assume that the electrons with spins parallel to the magnetization have a scattering possibility lower than that in the case of antiparallel, i.e., $\rho_+ < \rho_-$. Figure 36.2 shows a schematic illustration of the conduction of electrons passing through a superlattice in the current-in-plane (CIP) geometry. Since the thickness of each layer in the superlattice is of the order of nanometer, the electrons flow across the layers even in the case of the electric current flowing in the film plane. If the magnetization vectors of adjacent FM layers are parallel, the electrons with ↑ spins parallel to the magnetizations are not scattered very much, which contributes dominantly to the conduction, leading to a low electric resistance. On the other hand, both ↑ spins and ↓ spins are significantly scattered when the magnetization vectors are antiparallel, leading to a high electric resistance. The electric resistivity ρ is expressed as,

$$\rho = \rho_\uparrow \rho_\downarrow / (\rho_\uparrow + \rho_\downarrow), \tag{36.2}$$

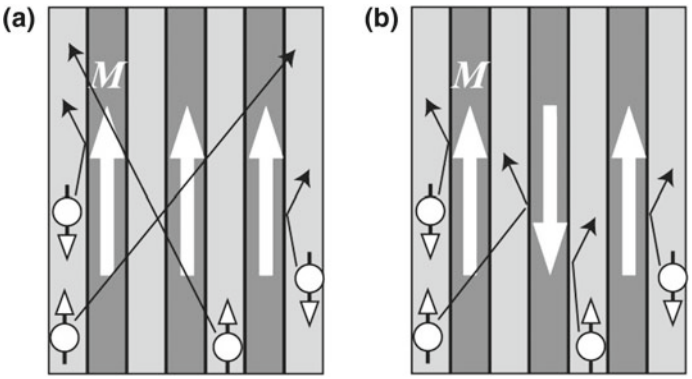

Fig. 36.2 Schematic illustrations of the conduction of electrons in a superlattice with alternatively stacked a ferromagnetic (FM) metal and a nonmagnetic (NM) metal. The cases for **a** parallel and **b** antiparallel alignments of the magnetization vectors are shown

where $\rho_\uparrow$ ($\rho_\downarrow$) is the resistivity for the electrons with ↑ (↓) spin. When all the magnetization vectors are parallel, we consider $\rho_\uparrow \sim \rho_+$ and $\rho_\downarrow \sim \rho_-$ and the total resistance of the parallel state (ρ_P) is expressed as

$$\begin{aligned} \rho_P &= \rho_+ \rho_- / (\rho_+ + \rho_-) \\ &\sim \rho_+ \quad (\text{for} \quad \rho_+ \ll \rho_-) \end{aligned} . \tag{36.3}$$

When the adjacent magnetization vectors are antiparallel, we consider $\rho_\uparrow \sim \rho_\downarrow \sim (\rho_+ + \rho_-)/2$, the total resistance ($\rho_{AP}$) is expressed as

$$\rho_{AP} = (\rho_+ + \rho_-)/4. \tag{36.4}$$

Using Eqs. (36.3) and (36.4), the magnitude of GMR is given by

$$\begin{aligned} (\rho_{AP} + \rho_P)/\rho_p &= (\rho_+ + \rho_-)/4\rho_+\rho_- \\ &= (1 - \alpha^2)/4\alpha \end{aligned} , \tag{36.5}$$

where $\alpha = \rho_-/\rho_+$ that is a parameter representing the spin dependence of electron scattering. One sees that GMR appears when $\alpha \neq 1$, and GMR is larger as $\alpha \gg 1$ or $\alpha \ll 1$. The requirements for the appearance of GMR in the CIP geometry are summarized as follows: (i) Antiparallel alignment of the magnetization vectors in adjacent FM layers through a NM layer, (ii) large spin-dependent scattering of electrons ($\alpha \gg 1$ or $\alpha \ll 1$), and (iii) the multilayer period of the superlattice shorter than the mean free path of conduction electrons.

36.1.3 Applications of GMR Effect

A spin-valve structure with a FM/NM/FM trilayer is suitable for practical applications as mentioned in Sect. 36.1.1 since small H_{ext} is enough to switch the magnetization vector in the free layer. However, the magnitude of GMR depends on the number of layers in a superlattice, meaning that a structure having more layers shows a larger MR ratio and the trilayer structure is unfavorable to obtain a large GMR effect. However, if the electric current flows perpendicularly to the film plane, all the electrons contribute to the conduction through each layer and the magnitude of GMR is expected to become larger. The type of GMR when the electric current flows in the film plane is called CIP-GMR, whereas GMR when the electric current flows perpendicularly to the film plane is called current-perpendicular-to-plane GMR (CPP-GMR). It has experimentally been confirmed that the MR ratio of CPP-GMR is usually larger than that of CIP-GMR [8]. In the case of CPP-GMR, the characteristic length is not the mean free path, but the spin diffusion length that is the distance over which the traveling electron spin keeps the initial orientation. The Valet-Fert model [9] is often used to analyze CPP-GMR, in which the finite

spin diffusion length is taken into account based on the two-current model. The analysis using the Valet-Fert model enables us to evaluate the spin dependence in electron scattering separately for the bulk and the interface, which are represented by the parameters of β and γ, respectively.

CPP-GMR has attracted much attention in terms of practical applications because the miniaturization of device elements leads to an increase in the device resistance. In the case of a TMR device for read heads of ultrahigh-density HDD, the device resistance becomes so high that it will be a hurdle for high-speed operation in near future. On the other hand, a CPP-GMR device has a low device resistance thanks to all-metal structure. That is to say, the CPP-GMR device will be advantageous because of its low resistance. However, CPP-GMR devices based on the typical FM/NM/FM trilayer structure showed only a small MR ratio of the order of 1% because of a large contribution of parasitic resistance. A variety of studies have been done to increase the MR ratio. From the viewpoint of materials development, half-metals such as Heusler alloys are promising materials to improve the MR ratio for CPP-GMR.

36.2 Half-Metallic Heusler Alloys for Spin Electronics

Half-metallic ferromagnets are materials with an electronic structure with 100% spin polarization at the Fermi level, in which one spin channel has metallic nature whereas the other spin channel has a semiconducting band gap. This characteristic band structure generates completely spin-polarized conduction electrons [10, 11]. Schematics of the density of states for a conventional ferromagnet and a half-metallic ferromagnet are shown in Fig. 36.3a and b, respectively.

Heusler alloys [12] are intermetallic compounds with a number of materials that are classified into two types: Half-Heusler alloys and full-Heusler alloys. The chemical formulae of the half- and full-Heusler alloys are expressed as XYZ and X_2YZ, respectively, where X and Y elements are transition metals, and Z is an

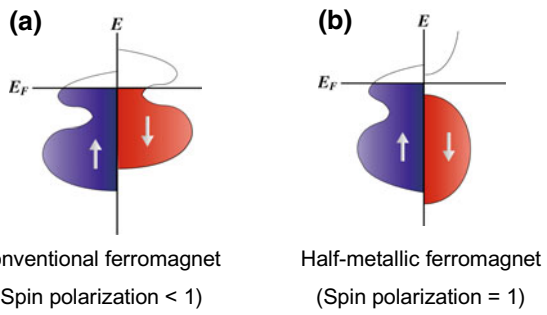

Fig. 36.3 Schematic illustrations of the density of states for **a** a conventional ferromagnet and **b** a half-metallic ferromagnet

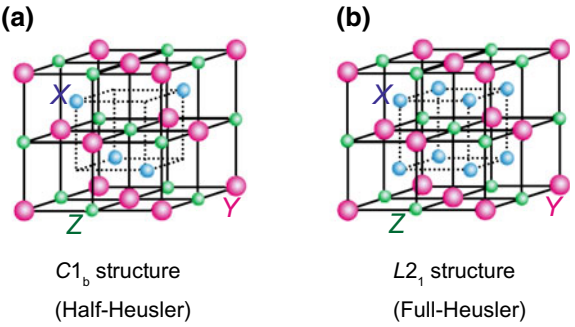

Fig. 36.4 Crystal structures of **a** $C1_b$ (half-Heusler) and **b** $L2_1$ (full-Heusler)

element belonging to the group 13 or 14 of the periodic table. The crystal structure of the half-Heusler alloys is a $C1_b$ phase (MgAgAs-type) having the space group of F-43m (number 216). The unit cell consists of three interpenetrating face-centered-cubic (fcc) cells with site occupancies at 4a (0, 0, 0), 4b (1/2, 1/2, 1/2) and 4c (1/4, 1/4, 1/4) for X, Y, and Z atoms in Wyckoff coordinate (Fig. 36.4a). On the other hand, the crystal structure of the full-Heusler alloys is an $L2_1$ phase (Cu_2MnAl type) having the space group of Fm-3 m (number 225). The unit cell consists of four interpenetrating fcc cells with site occupancies at 8c (1/4, 1/4, 1/4), 4a (0, 0, 0), and 4b (1/2, 1/2, 1/2) for X, Y, and Z atoms in Wyckoff coordinate (Fig. 36.4b) [13]. Some half- and full-Heusler alloys exhibit half-metallic electronic structures, which is an attractive aspect of the material class for the research field of spin electronics. The first prediction of the half-metallicity was reported by Groot et al. for $C1_b$-type NiMnSb and PtMnSb in 1983 [14]. In the case of full-Heusler alloys, the pioneer ab initio studies of half-metallic density of states (DOS) were reported by Kübler et al. [15], and Ishida et al. [16], for cobalt (Co)-based alloys, such as Co_2MnAl and Co_2MnSn. Following those reports, numerous theoretical predictions have been reported both for half- and full-Heusler alloys [17–22]. Those theoretical studies motivated experiments on half-metallic Heusler alloys as materials for spin electronics.

36.3 Magnetoresistance Effects Using Heusler Alloy Thin Films

Half-metallic Heusler alloys enable us to improve the MR ratio because their conduction electrons are theoretically predicted to be fully spin-polarized. In this section, TMR and CPP-GMR effects in the Heusler alloys are surveyed.

36.3.1 Tunnel Magnetoresistance Effect Using Heusler Alloy Thin Films

After the discoveries of TMR effect at low temperature [23] and room temperature [24, 25], in 2003 Inomata et al. reported a pioneering work on MTJ consisting of a polycrystalline $Co_2Cr_{0.6}Fe_{0.4}Al$ Heusler alloy thin film and an Al–oxide barrier prepared by magnetron sputtering, which gave a MR ratio of 19% at room temperature [26]. In 2005, a further large TMR effect was demonstrated by Sakuraba et al. for MTJs with epitaxially grown-Co_2MnSi (CMS) Heusler alloy layers and an Al-oxide barrier prepared by ultrahigh vacuum magnetron sputtering system, showing MR ratios of about 70% [27, 28] and 570% [28] at room temperature and 2 K, respectively. However, the MR ratio at room temperature was comparable with those for the MTJs using conventional 3*d*-transition metal-based ferromagnets and an Al-oxide barrier [29, 30] although the MR ratio at low temperature was much larger than those for the MTJs with conventional ferromagnets [27, 28]. They also discussed the electronic structure of the CMS films by measuring the bias voltage dependence of tunneling conductance for the MTJs and concluded that the giant TMR effects originated from the half-metallic density of states for CMS [28]. The reported MR ratios for some cobalt based-Heusler alloy MTJs with an Al-oxide barrier are summarized in Table 36.1 [26–37].

As described above, many works on the MTJs with Heusler alloys in the early stage used amorphous Al-oxide as a tunneling barrier, which prevented the epitaxial growth of Heusler alloy films onto the barrier layer. The demonstration of giant TMR in MTJs with a MgO tunnel barrier [38–40] led to a significant enhancement in the MR ratio. Following the demonstration using the conventional 3*d*-transition metal-based ferromagnets, MTJs with fully-epitaxial Heusler alloy layers and a (001)-oriented MgO tunneling barrier were reported as shown in Table 36.2 [41–51]. As of the beginning of 2016, the maximum MR ratios are 429% and 2610% at room temperature and 4.2 K, respectively [51].

Table 36.1 A summary of TMR ratio using Heusler alloys electrodes and Al–O tunnel barrier

Material	MTJ stacking structure	TMR ratio	References
Co_2(Cr–Fe)Al	poly-$Co_2Cr_{0.6}Fe_{0.4}Al$/Al–O/Co–Fe	19% (RT), 27% (5 K)	[26]
Co_2MnSi	poly.-Co_2MnSi/Al–O/Co–Fe	33% (RT), 86% (10 K)	[31]
	epi.-Co_2MnSi/Al–O/Co–Fe	70% (RT), 159% (2 K)	[27]
	epi.-Co_2MnSi/Al–O/Co_2MnSi	67% (RT), 570% (2 K)	[28]
Co_2MnAl	poly.-Co_2MnAl/Al–O/Co–Fe	40% (RT), 60% (5 K)	[32]
	epi.-Co_2MnAl/Al–O/Co–Fe	65% (RT), 83% (5 K)	[33]
Co_2FeSi	epi.-Co_2FeSi/Al–O/Co–Fe	41% (RT), 60% (5 K)	[34]
Co_2FeAl	epi.-Co_2FeAl/Al–O/Co–Fe	47% (RT)	[35]
Co_2Fe(Al–Si)	epi.-$Co_2FeAl_{0.5}Si_{0.5}$/Al–O/Co–Fe	76% (RT), 106% (5 K)	[36]
Co_2(Fe–Mn)Si	epi.-$Co_2Fe_{0.4}Mn_{0.6}Si_{0.5}Si$/Al–O/Co–Fe	73% (RT), 164% (2 K)	[37]

Table 36.2 A summary of TMR ratio using epitaxially grown Heusler alloys electrodes and MgO tunnel barrier

Material	MTJ stacking structure	TMR ratio	References
Co_2MnSi	Co_2MnSi/MgO/Co–Fe	90% (RT), 192% (4.2 K)	[41]
	Co_2MnSi/MgO/Co_2MnSi	179% (RT), 683% (4.2 K)	[42]
	Co_2MnSi/MgO/Co–Fe	217% (RT), 753% (2 K)	[43]
	Co–Mn–Si/MgO/Co–Mn–Si	354% (RT), 1995% (4.2 K)	[44]
Co_2MnGe	Co_2MnGe/MgO/Co–Fe	160% (RT), 376% (4.2 K)	[45]
	Co–Mn–Ge/MgO/Co–Mn–Ge	220% (RT), 650% (4.2 K)	[46]
Co_2FeAl	Co_2FeAl/MgO/Co–Fe	330% (RT), 700% (10 K)	[47]
Co_2Fe(Al–Si)	$Co_2FeAl_{0:5}Si_{0:5}$/MgO/ $Co_2FeAl_{0:5}Si_{0:5}$	386% (RT), 832% (9 K)	[48]
Co_2(Cr–Fe)Al	$Co_2Cr_{0:6}Fe_{0:4}Al$/MgO/Co–Fe	109% (RT), 317% (4.2 K)	[49]
	$Co_2Cr_{0:6}Fe_{0:4}Al$/MgO/ $Co_2Cr_{0:6}Fe_{0:4}Al$	60% (RT), 238% (4.2 K)	[50]
Co_2(Fe–Mn)Si	Co_2(Fe–Mn)–Si/MgO/Co_2 (Fe–Mn)–Si	429% (RT), 2610% (4.2 K)	[51]

Extremely large MR ratios have been achieved in MTJs with half-metallic Heusler alloys at low temperature. However, the MR ratios at room temperature are comparable with or smaller than those in MTJs with conventional ferromagnetic materials [52]. Possible origins for the remarkable temperature dependence of TMR with half-metallic Heusler alloys have been discussed [53–57], and the experimental studies have been also performed to improve the temperature dependence [58, 59].

36.3.2 Current-Perpendicular-to-Plane Giant Magnetoresistance Effect Using Heusler Alloy Thin Films

Thanks to large CPP-GMR effects using half-metallic Heusler alloys, CPP-GMR devices have recently drawn renewed attention as a candidate for a read head of future HDD [60]. The reported CPP-GMR ratio and the change of resistance area product (ΔRA) are summarized in Table 36.3 [61–80]. In 2006, Yakushiji et al. reported a large ΔRA for CMS/Cr/CMS [61], which was a pioneering work to show a potential of Co-based full-Heusler alloys as a material to enhance the CPP-GMR effect. The next breakthrough of CPP-GMR was reported by Sakuraba and coworkers in 2009 [65, 66], in which the CPP-GMR ratio of 36% was observed at room temperature for CMS/Ag/CMS. Concerning the mechanism of the large CPP-GMR ratio in CMS/Ag/CMS, the ab initio studies suggested that the large

Table 36.3 A summary of CPP-GMR effects using full-Heusler alloys electrodes at room temperature

Material	Stacking structure of CPP-GMR	MR ratio (%)	ΔRA (m Ω μm^2)	References
Co_2MnSi	epi.-Co_2MnSi/Cr/Co_2MnSi	2.40	19	[61]
	epi.-Co_2MnSi/Cr/Co_2MnSi	5.20	19	[62]
	poly.-Co_2MnSi/Cu/Co_2MnSi	9.00	–	[63]
	epi.-Co_2MnSi/Cu/Co_2MnSi	8.60	14	[64]
	epi.-Co_2MnSi/Ag/Co_2MnSi	28.80	9	[65]
	epi.-Co_2MnSi/Ag/Co_2MnSi	36	12	[66]
Co_2(Fe–Mn)Si	epi.-$Co_2Fe_{0:4}Mn_{0:6}Si$/Ag/ $Co_2Fe_{0:4}Mn_{0:6}Si$	75	–	[67]
	epi.-$Co_2Fe_{0:4}Mn_{0:6}Si$/Ag/ $Co_2Fe_{0:4}Mn_{0:6}Si$	58	12	[68]
	epi.-$Co_2Fe_{0:4}Mn_{0:6}Si$/$Ag_{83}Mg_{17}$/ $Co_2Fe_{0:4}Mn_{0:6}Si$	49	17	[69]
	epi.-$Co_2Fe_{0:4}Mn_{0:6}Si$/$Ag_{78}Mg_{22}$/ $Co_2Fe_{0:4}Mn_{0:6}Si$	63	25	[71]
Co_2MnGe	poly.-Co_2MnGe/Cu/Co_2MnGe/Cu/ Co_2MnGe	6.90	7.4	[72]
	Co_2MnGe/Rh_2CuSn/Co_2MnGe	6.70	4	[73]
Co_2FeSi	epi.-Co_2FeSi/Ag/Co_2FeSi	23	7	[68]
$Co_2FeAl_{0:5}Si_{0:5}$	epi.-$Co_2FeAl_{0:5}Si_{0:5}$/Ag/ $Co_2FeAl_{0:5}Si_{0:5}$	6.90	7.4	[74]
	epi.-$Co_2FeAl_{0:5}Si_{0:5}$/Ag/ $Co_2FeAl_{0:5}Si_{0:5}$	34	8	[75]
$Co_2FeGa_{0:5}Sn_{0:5}$	epi.-$Co_2FeGa_{0:5}Sn_{0:5}$/Ag/ $Co_2FeGa_{0:5}Sn_{0:5}$	8.80	4	[76]
	epi.-$Co_2FeGa_{0:5}Sn_{0:5}$/NiAl/ $Co_2FeGa_{0:5}Sn_{0:5}$	7.00	3	[77]
$Co_2FeGa_{0:5}Ge_{0:5}$	epi.-$Co_2FeGa_{0:5}Ge_{0:5}$/Ag/ $Co_2FeGa_{0:5}Ge_{0:5}$	57	12	[78]
	epi.-$Co_2FeGa_{0:5}Ge_{0:5}$/Ag–Zn/ $Co_2FeGa_{0:5}Ge_{0:5}$	59.60	21.5	[79]
Co_2(Mn–Fe)Ge	poly.-Co–Fe–Ge/CoFe/Ag/InZnO/Zn/ CoFe/$Co_2Mn_{0:6}Fe_{0:4}Ge$	26	29	[80]

CPP-GMR effects originated from the good band matching between the Co-based full-Heusler alloys and the Ag spacer layer, leading to large interface spin-asymmetry [66, 81]. In addition to the development of Heusler alloys, the investigation of new material as a spacer layer has been carried out [69–71, 73, 77, 79, 80]. Among the studies, spacer materials of Ag–Mg [69–71], Ag–Zn [79], and InZnO [80] showed better device performances than that for the Ag spacer, which are attracting great interests for the read head application of HDDs with

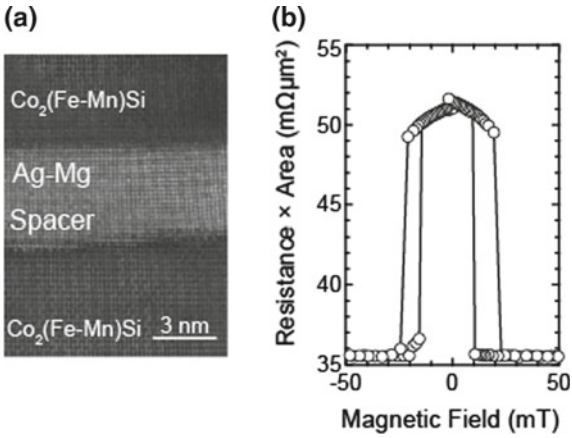

Fig. 36.5 **a** A high-angle annular dark field scanning transmission electron microscope (HAADF-STEM) image, and **b** a CPP-GMR curve for the Co_2(Fe–Mn)Si/Ag–Mg/Co_2(Fe–Mn)Si CPP-GMR device [71]. Copyright (2015) The Japan Society of Applied Physics

tera-bit-class areal recording density. Figure 36.5 shows examples of (a) a high-angle annular dark field scanning transmission electron microscope (HAADF-STEM) image, and (b) a CPP-GMR curve for the Co_2(Fe–Mn)Si/Ag–Mg/Co_2(Fe–Mn)Si CPP-GMR device [69].

As described above, full-Heusler alloys have been a mainstream for the CPP-GMR studies. However, there are also some experimental reports on CPP-GMR devices with half-Heusler alloys. Caballero et al. reported the MR ratio of 7.2% at 4.2 K for NiMnSb/Cu/NiMnSb in 1998 [82]. After the work in the early age, there have been few studies on CPP-GMR with half-Heusler alloys for a long period. In 2015, Wen et al. succeeded in achieving the MR ratio of 8% for NiMnSb/Ag/NiMnSb at room temperature, and it rose up to 21% at 4.2 K [83]. Although the MR ratios with NiMnSb layers were still smaller than those for full-Heusler alloys, room temperature CPP-GMR with half-Heusler alloys would be potentially a next breakthrough because of the large half-metallic band gaps of half-Heusler alloys compared with those of the full-Heusler ones [10–18].

36.4 Spin Torque Oscillation Using Heusler Alloys

36.4.1 Spin Angular Momentum Transfer

For a FM/NM/FM trilayer structure in a CPP-GMR device, the conduction electrons passing through one FM layer are spin-polarized, and the spin-polarized conduction electrons interact with local spins of the other FM layer. This interaction gives rise to the spin-dependent scattering of conduction electrons. In this scattering process, spin angular momenta carried by the conduction electrons are transferred to the local spins of the FM layer, which is called ‘spin angular momentum transfer’ (or simply ‘spin-transfer’). The basic concept of spin angular momentum transfer

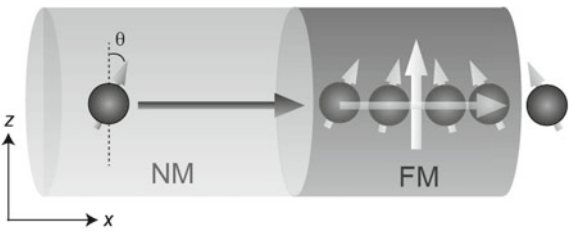

Fig. 36.6 A schematic illustration of the concept of spin angular momentum transfer from the conduction spin to the local spin

was proposed in 1996 by Slonczewski [84] and Berger [85], independently. Here, we consider a simple case as illustrated in Fig. 36.6. The incoming conduction electron is traveling in the x-direction and is spin-polarized along the direction tilted by θ from the z-direction in the z-x plane, i.e., $\hat{\mathbf{s}}_1 = (\sin\theta\cos\varphi, \sin\theta\sin\varphi, \cos\theta)$ in the polar coordinates of θ and φ. On the other hand, the local spin of the magnetic layer is oriented in the z-direction, i.e., $\hat{\mathbf{s}}_2 = (0, 0, 1)$. Due to the strong exchange interaction with the local spin of FM layer, the electron spin processes around the exchange field. Since many electrons would be propagating through the magnetic layer simultaneously in a real device, if one sums up the total spin angular momenta for all the conduction electrons, the non-negligible value is only the z component, and the perpendicular components in x and y directions become zero. This corresponds to the case of the absorption of spin by the FM layer, and the change of spin angular momentum (Δs) is described as

$$\Delta\hat{\mathbf{s}} = \frac{\hbar}{2}\begin{pmatrix} 0 \\ 0 \\ \cos\theta \end{pmatrix} - \frac{\hbar}{2}\begin{pmatrix} \sin\theta\cos\varphi \\ \sin\theta\sin\varphi \\ \cos\theta \end{pmatrix}, \tag{36.6}$$

where the first and second terms are the unit vectors indicating the directions of spin angular momenta for outgoing and incoming electrons, respectively. Then, Eq. (36.6) can be rewritten as

$$\Delta\hat{\mathbf{s}} = \frac{\hbar}{2}(\hat{\mathbf{s}}_2 \times (\hat{\mathbf{s}}_2 \times \hat{\mathbf{s}}_1)). \tag{36.7}$$

This is "Spin (transfer) torque". In order to conserve the spin angular momentum, this spin torque also acts on the local spin of the FM layer (for more details, see Ref. [86]).

36.4.2 Spin Torque Oscillation

The dynamics of a local spin ($\mathbf{S}_2$) under the effective magnetic field ($\mathrm{H_{eff}}$) is described using the Landau-Lifshitz-Gilbert (LLG) equation as

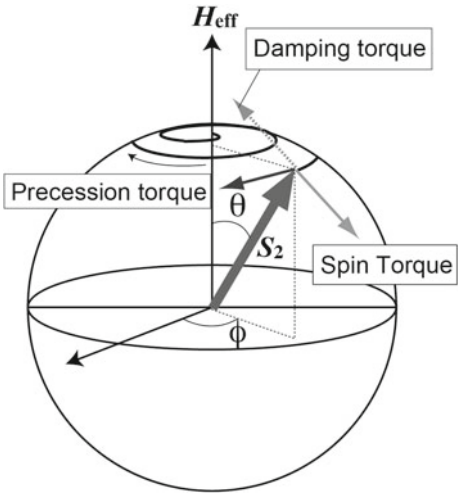

Fig. 36.7 Precession torque, damping torque and spin torque acting on $\mathbf{S}_2$ in the polar coordinates of θ and φ

$$\frac{d\mathbf{s}_2}{dt} = \gamma \mathbf{s}_2 \times \mathbf{H}_{eff} + \alpha \hat{\mathbf{s}}_2 \times \frac{d\mathbf{s}_2}{dt}, \tag{36.8}$$

where γ is the gyromagnetic ratio and α is the damping parameter. In this equation, the first and the second terms express the precession torque and the damping torque, respectively, of $\mathbf{S}_2$. When the spin torque acts on $\mathbf{S}_2$, using Eqs. (36.7) and (36.8) the magnetization dynamics is expressed by [84]

$$\frac{d\mathbf{s}_2}{dt} = \gamma \mathbf{s}_2 \times \mathbf{H}_{eff} - \alpha \hat{\mathbf{s}}_2 \times \frac{d\mathbf{s}_2}{dt} + g(\theta)\frac{I}{e}\frac{\hbar}{2}(\hat{\mathbf{s}}_2 \times (\hat{\mathbf{s}}_2 \times \hat{\mathbf{s}}_1)), \tag{36.9}$$

where e is the elementary charge, and $g(\theta)$ is the spin-transfer coefficient, which is a function of the spin polarization factor. Figure 36.7 depicts the precession torque, the damping torque and the spin torque acting on $\mathbf{S}_2$. One sees that the precession torque acts along the φ direction ($\hat{e}_\varphi$) while the damping torque and the spin torque act along the θ direction ($\hat{e}_\theta$). Thus, the time derivative of $\delta\mathbf{S}_2$ is described as

$$\begin{aligned}\frac{d\delta\mathbf{s}_2}{dt} &\approx \left\{\gamma \mathbf{s}_2 \left(\mathbf{H}_{eff} \cdot \hat{\mathbf{e}}_\theta\right)\right\}\hat{\mathbf{e}}_\varphi - \left\{\alpha\gamma \mathbf{s}_2 \left(\mathbf{H}_{eff} \cdot \hat{\mathbf{e}}_\theta\right)\right\}\hat{\mathbf{e}}_\theta + \left\{\frac{I}{e} g(\theta)\frac{\hbar}{2}\cos\theta\right\}\hat{\mathbf{e}}_\theta \\ &= T_\varphi \hat{\mathbf{e}}_\varphi + T_\theta \hat{\mathbf{e}}_\theta\end{aligned}, \tag{36.10}$$

where $T_\varphi = \gamma \mathbf{s}_2 \left(\mathbf{H}_{eff} \cdot \hat{\mathbf{e}}_\theta\right)$ and $T_\theta = -\alpha T_\varphi + g(\theta)\frac{I}{e}\frac{\hbar}{2}\cos\theta$. Equation (36.10) means the magnetization instability at the condition of $T_\theta = 0$, the current of which corresponds to the critical current for the magnetization instability (I_{c0}). In a condition of $T_\theta = 0$, spin torque induces the magnetization switching at $I = I_{c0}$. In addition to the magnetization switching, the magnetization steadily precesses on the iso-energy

trajectory when $T_\theta = 0$ and $dT_\theta/d\theta < 0$. This spin torque-induced steady magnetization precession is called spin torque oscillation.

The spin torque oscillation was first observed in GMR stacks [87, 88], and many investigations have been done to clarify the magnetic dynamics excited by spin torque [89]. In addition, the spin torque oscillation has a potential application such as a microwave oscillator, which is called a spin torque oscillator (STO). In the case of CPP-GMR device consisting of a free FM and a fixed FM layers that are separated by a NM spacer layer, the magnetization precession is induced in the free layer by applying dc electric current (I_{dc}) when the above requirements for the spin torque oscillation are satisfied. The steady magnetization precession in the free layer leads to a change in the device resistance through the magnetoresistance effect. Since I_{dc} is applied to the device, the time-dependent device resistance ($R(t)$) is converted into rf voltage (V_{rf}). Consequently, the device emits rf output power (P_{out}).

Before STOs can be put into practical use, there are several crucial issues that need to be solved. Those issues are as follows: the enhancement of P_{out}, improvement of the rf oscillation quality, and increasing the frequency tunability by I_{dc} and/or H_{ext}. Although MTJ-based STOs [90–92] may solve the first issue since the P_{out} is roughly proportional to the square of the MR ratio, the relatively wide oscillation linewidths (Δf) are not applicable for practical applications. On the other hand, a CPP-GMR device generally has a narrow Δf compared with the MTJ-based STOs [93]. Furthermore, a CPP-GMR stack is free from the risk of dielectric breakdown in a tunnel barrier material. Therefore, a CPP-GMR device showing a large MR ratio has potential for a high-performance STO.

36.4.3 Heusler-Based Spin Torque Oscillator

As mentioned in Sect. 36.3.2, half-metallic Heusler alloys enable us to obtain the high MR ratios even for CPP-GMR devices. CMS is one of the Heusler alloys theoretically predicted as a half metal and experimentally showing high MR ratios [61–66], leading to the enhancement of P_{out} even for a CPP-GMR-based STO [94, 95]. Figure 36.8a depicts a structure of the CPP-GMR device with a CMS/Ag/CMS trilayer and the measurement setup for spin torque oscillation. A stacking structure of Cr (5 nm)/Ag (40 nm)/CMS (40 nm)/Ag (5 nm)/CMS (5 nm)/Ag (2 nm)/Au (5 nm) was prepared on a MgO (100) single crystal substrate using an ultrahigh-vacuum magnetron sputtering system. The 40 nm-thick bottom CMS and the 5 nm-thick top CMS layers were grown at ambient temperature followed by in situ annealing at 500 °C to promote the chemical ordering. The film was patterned into a CPP nanopillar with an ellipsoidal shape ($0.06 \times 0.11\ \mu m^2$). In this device structure, the top and the bottom CMS layers behave as free and fixed layers, respectively, against spin torque given by I_{dc}. The CPP-GMR device was connected to the circuit with a two-terminal rf probe and I_{dc} was applied through a bias-Tee. Positive I_{dc} is defined as the direction that the electron flows from the upper to the lower CMS layer. V_{rf} was amplified by a

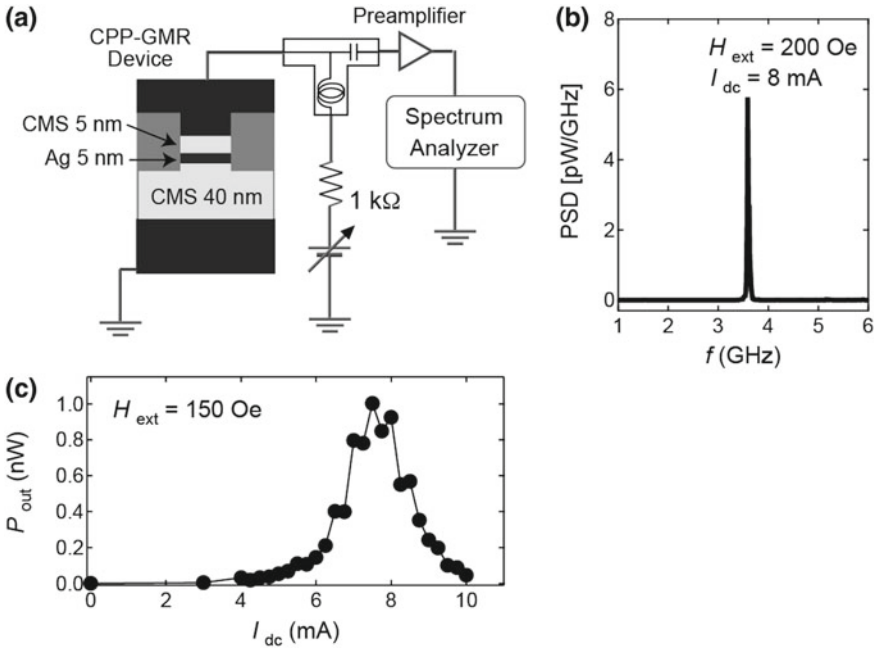

Fig. 36.8 **a** Structure of a current-perpendicular-to-plane (CPP) device with a Co_2MnSi (CMS)/Ag/CMS trilayer and measurement setup for spin torque oscillation. **b** Rf spectrum measured at I_{dc} = 8 mA and H_{ext} = 200 Oe. **c** Rf output power (P_{out}) as a function of I_{dc} at H_{ext} = 150 Oe [97]

preamplifier and was monitored in frequency-domain by a spectrum analyzer. The power spectral density (PSD) value was calculated by

$$PSD = \left(V_{rf}(I_{dc})\right)^2 \left(Z_0 \times \Delta f_{RB} \times \left(G_{amp}\right)^2\right)^{-1}, \tag{11}$$

where V_{rf} is the time-averaged value during the spectral measurement. G_{amp} is the frequency-dependent gain of the preamplifier and Δf_{RB} is the resolution bandwidth of the spectrum analyzer, which was set to 1 MHz. Z_0 is the characteristic impedance, which is 50 Ω for the present measurement. Figure 36.8b shows the rf spectrum at I_{dc} = 8 mA, where a clear peak is observed. This indicates that the spin torque oscillation is induced in the top CMS layer. I_{dc} dependence of P_{out} at H_{ext} = 150 Oe is shown in Fig. 36.8c. Once P_{out} increases monotonically after the onset of rf oscillation, and then it decreases with increasing I_{dc}. The large P_{out} of 1 nW is obtained at I_{dc} = 7.5 mA, which is much larger than the output power reported in CPP-GMR-based STOs using conventional ferromagnetic layers. However, the high power spin torque oscillation is observed only in a narrow I_{dc} region. Macrospin simulation suggests that the high spin polarization of CMS layers leads to narrowing the optimum I_{dc} region for the spin torque oscillation,

which is due to the narrow region for the condition balancing the large spin torque with H_{ext} [95], i.e.,

$$T_\theta = -\alpha T_\varphi + g(\theta)(I/e)(\hbar/2)\cos\theta = 0. \quad (12)$$

In order to improve spin torque oscillation characteristics, $Co_2Fe_{0.4}Mn_{0.6}Si$ (CFMS) is a more suitable Heusler alloy than the CMS because its lower magnetization damping than that for CMS [34] would be useful to obtain narrow oscillation linewidth. In addition, it was reported that the CPP-GMR devices with CFMS/Ag/CFMS exhibited the MR ratios larger than CMS/Ag/CMS [67, 68]. Thanks to the large CPP-GMR effect for the CFMS/Ag/CFMS, the value of P_{out} was significantly enhanced [96, 97]. For example, under the perpendicular H_{ext}, the large $P_{out} = 23.7$ nW was obtained and Δf showed the value of 10 MHz, giving the excellent Q factor of 1,124 [96]. Although the nanopillar-shaped STOs improve P_{out} and the Q factor, the other-type STOs also have several advantages. The point-contact-type STO with the CFMS layers exhibited the large P_{out} without applying H_{ext} [98]. This zero-field spin torque oscillation was induced by the combination of spin torque and the Oersted field due to the current injection. In addition, the dynamics of magnetic vortex can be exploited for improving the STO characteristics, e.g., narrowing the oscillation linewidth and the resultant high Q factor. The circular-shaped STO consisting of CFMS/Ag/CFMS showed the formation of magnetic vortex in the CFMS layer and exhibited the very high Q factor more than 4,000 [99, 100].

As described above, the large $P_{out} = 23.7$ nW was obtained for the CPP-GMR-based STO with CFMS/Ag/CFMS [96]. After calibrating the rf transmission loss, the value of P_{out} was calculated to be 0.3 μW. Then, the output efficiency of STO, which was given by the ratio of P_{out} to the input power (P_{in}), was 0.16% for the present STO. This value is of the same order as the largest one obtained for the CoFeB/MgO/CoFeB MTJ [101]. Consequently, the Heusler alloys such as CMS and CFMS are promising materials to improve the spin torque oscillation characteristics owing to their high MR ratios originating from the high spin polarizations and low damping constants.

References

1. M.N. Baibich, J.M. Broto, A. Fert, F. Nguyen Van Dau, F. Petroff, P. Etienne, G. Creuzet, A. Friedrich, J. Chazelas, Phys. Rev. Lett. **61**, 2472 (1988)
2. P. Grünberg, R. Schreiber, Y. Pang, M.B. Brodsky, H. Sowers, Phys. Rev. Lett. **57**, 2442 (1986)
3. D.H. Mosca, F. Petroff, A. Fert, P.A. Schroeder, W.P. Pratt Jr., R. Laloee, J. Magn. Magn. Mater. **94**, L1 (1991)
4. S. Araki, K. Yasui, Y. Narumiya, J. Phys. Soc. Jpn. **60**, 2827 (1991)
5. C.A. dos Santos, B. Rodmacq, M. Vaezzadeh, B. George, Appl. Phys. Lett. **59**, 126 (1991)
6. T. Shinjo, H. Yamamoto, J. Phys. Soc. Jpn. **59**, 3061 (1990)

7. B. Dieny, V.S. Speriosu, S.S.P. Parkin, B.A. Gurney, D.R. Wilhoit, D. Mauri, Phys. Rev. B **43**, 1297 (1991)
8. J. Bass, W.P. Pratt Jr., J. Magn. Magn. Mater. **200**, 274 (1999)
9. T. Valet, A. Fert, Phys. Rev. B **48**, 7099 (1993)
10. J.M.D. Coey, M. Venkatesan, M.A. Bari, in *High Magnetic Fields*, ed. by C. Berthier, L. P. Levy, G. Martinez. Lecture Notes in Physics, vol. 595 (Springer, Berlin, Heidelberg, 2001), pp. 377–396
11. I. Galanakis, P.H. Dederichs (eds.), *Half-Metalic Alloys* (Springer, Berlin, Heidelberg, 2005)
12. F. Heusler, Verh. Dtsch. Phys. Ges. **5**, 219 (1903)
13. T. Graf, C. Felser, S.S.P. Parkin, Prog. Sol. Stat. Chem. **39**, 1 (2011)
14. R.A. Groot, F.M. Mueller, P.G. Engen, K.H.J. Buschow, Phys. Rev. Lett. **50**, 2024 (1983)
15. J. Kübler, A.R. Williams, C.B. Sommers, Phys. Rev. B **28**, 1745 (1983)
16. S. Ishida, S. Asano, J. Ishida, J. Phys. Soc. Jpn. **53**, 2718 (1984)
17. J. Kübler, Phys. B **127**, 257 (1984)
18. E. Kulatov, I.I. Mazin, J. Phys. Condens. Mater. **2**, 343 (1990)
19. S. Ishida, S. Fujii, S. Kashiwagi, S. Asano, J. Phys. Soc. Jpn. **64**, 2152 (1995)
20. S.J. Youn, B.I. Min, Phys. Rev. B **51**, 10436 (1995)
21. I. Galanakis, S. Ostanin, M. Alouani, H. Dreysse, J.M. Wills, Phys. Rev. B **61**, 4093 (2000)
22. I. Galanakis, P.H. Dederichs, N. Papanikolaou, Phys. Rev. B **66**, 174429 (2002)
23. M. Julliere, Phys. Lett. A **54**, 225 (1975)
24. T. Miyazaki, N. Tezuka, J. Magn. Magn. Mater. **139**, L231 (1995)
25. J.S. Moodera, L.R. Kinder, T.M. Wong, R. Meservey, Phys. Rev. Lett. **74**, 3273 (1995)
26. K. Inomata, S. Okamura, R. Goto, N. Tezuka, Jpn. J. Appl. Phys. **42**, L419 (2003)
27. Y. Sakuraba, J. Nakata, M. Oogane, H. Kubota, Y. Ando, A. Sakuma, T. Miyazaki, Jpn. J. Appl. Phys. **44**, L1100 (2005)
28. Y. Sakuraba, M. Hattori, M. Oogane, Y. Ando, H. Kato, A. Sakuma, T. Miyazaki, Appl. Phys. Lett. **88**, 192508 (2006)
29. X.-F. Han, M. Oogane, H. Kubota, Y. Ando, T. Miyazaki, Appl. Phys. Lett. **77**, 283 (2000)
30. D. Wang, C. Nordman, J.M. Daughton, Z. Qian, J. Fink, IEEE Trans. Magn. **40**, 2269 (2004)
31. S. Kämmerer, A. Thomas, A. Hutten, G. Reiss, Appl. Phys. Lett. **85**, 79 (2004)
32. H. Kubota, J. Nakata, M. Oogane, Y. Ando, A. Sakuma, T. Miyazaki, Jpn. J. Appl. Phys. **43**, L984 (2004)
33. Y. Sakuraba, J. Nakata, M. Oogane, H. Kubota, Y. Ando, A. Sakuma, T. Miyazaki, Appl. Phys. Lett. **88**, 022503 (2006)
34. K. Inomata, S. Okamura, A. Miyazaki, M. Kikuchi, N. Tezuka, M. Wojcik, E. Jedryka, J. Phys. D Appl. Phys. **39**, 816 (2006)
35. S. Okamura, A. Miyazaki, S. Sugimoto, N. Tezuka, K. Inomata, Appl. Phys. Lett. **86**, 232503 (2005)
36. N. Tezuka, N. Ikeda, A. Miyazaki, S. Sugimoto, M. Kikuchi, K. Inomata, Appl. Phys. Lett. **89**, 112514 (2006)
37. T. Kubota, S. Tsunegi, M. Oogane, S. Mizukami, T. Miyazaki, H. Naganuma, Y. Ando, Appl. Phys. Lett. **94**, 122504 (2009)
38. S. Yuasa, A. Fukushima, T. Nagahama, K. Ando, Y. Suzuki, Jpn. J. Appl. Phys. **43**, L558 (2004)
39. S. Yuasa, T. Nagahama, A. Fukushima, Y. Suzuki, K. Ando, Nat. Mater. **3**, 868 (2004)
40. S.S.P. Parkin, C. Kaiser, A. Panchula, P.M. Rice, B. Hughes, M. Samant, S.-H. Yang, Nat. Mater. **3**, 862 (2004)
41. T. Ishikawa, T. Marukame, H. Kijima, K.-I. Matsuda, T. Uemura, M. Arita, M. Yamamoto, Appl. Phys. Lett. **89**, 192505 (2006)
42. T. Ishikawa, S. Hakamata, K.-I. Matsuda, T. Uemura, M. Yamamoto, J. Appl. Phys. **103**, 07A919 (2008)
43. S. Tsunegi, Y. Sakuraba, M. Oogane, K. Takanashi, Y. Ando, Appl. Phys. Lett. **93**, 112506 (2008)

44. H.-X. Liu, Y. Honda, T. Taira, K.-I. Matsuda, M. Arita, T. Uemura, M. Yamamoto, Appl. Phys. Lett. **101**, 132418 (2012)
45. T. Taira, T. Ishikawa, N. Itabashi, K. Matsuda, T. Uemura, M. Yamamoto, J. Phys. D Appl. Phys. **42**, 084015 (2009)
46. M. Yamamoto, T. Ishikawa, T. Taira, G. Li, K. Matsuda, T. Uemura, J. Phys, Condens. Matter. **22**, 164212 (2010)
47. W.H. Wang, H. Sukegawa, R. Shan, S. Mitani, K. Inomata, Appl. Phys. Lett. **95**, 182502 (2009)
48. N. Tezuka, N. Ikeda, F. Mitsuhashi, S. Sugimoto, Appl. Phys. Lett. **94**, 162504 (2009)
49. T. Marukame, T. Ishikawa, S. Hakamata, K. Matsuda, T. Uemura, M. Yamamoto, Appl. Phys. Lett. **90**, 012508 (2007)
50. T. Marukame, M. Yamamoto, J. Appl. Phys. **101**, 083906 (2007)
51. H.-X. Liu, T. Kawami, K. Moges, T. Uemura, M. Yamamoto, F. Shi, P.M. Voyles, J. Phys. D Appl. Phys. **49**, 164001 (2015)
52. S. Ikeda, J. Hayakawa, Y. Ashizawa, Y.M. Lee, K. Miura, H. Hasegawa, M. Tsunoda, F. Matsukura, H. Ohno, Appl. Phys. Lett. **93**, 082508 (2008)
53. P. Mavropoulos, M. Lezaic, S. Blugel, Phys. Rev. B **72**, 174428 (2005)
54. A. Sakuma, Y. Toga, H. Tsuchiura, J. Appl. Phys. **105**, 07C910 (2009)
55. L. Chioncel, Y. Sakuraba, E. Arrigoni, M.I. Katsnelson, M. Oogane, Y. Ando, T. Miyazaki, E. Burzo, L.I. Lichtenstein, Phys. Rev. Lett. **100**, 086402 (2008)
56. Y. Miura, H. Uchida, Y. Oba, K. Abe, M. Shirai, Phys. Rev. B **78**, 064416 (2008)
57. Y. Miura, K. Abe, M. Shirai, Phys. Rev. B **83**, 214411 (2011)
58. S. Tsunegi, Y. Sakuraba, M. Oogane, H. Naganuma, K. Takanashi, Y. Ando, Appl. Phys. Lett. **94**, 252503 (2009)
59. Y. Sakuraba, Y. Kota, T. Kubota, M. Oogane, A. Sakuma, Y. Ando, K. Takanashi, Phys. Rev. B **81**, 144422 (2010)
60. M. Takagishi, K. Yamada, H. Iwaski, H.N. Fuke, S. Hashimoto, IEEE Trans. Magn. **46**, 2086 (2010)
61. K. Yakushiji, K. Saito, S. Mitani, K. Takanashi, Y.K. Takanashi, K. Hono, Appl. Phys. Lett. **88**, 222504 (2006)
62. Y. Sakuraba, T. Iwase, K. Saito, S. Mitani, K. Takanashi, Appl. Phys. Lett. **94**, 012511 (2009)
63. T. Mizuno, Y. Tsuchiya, T. Machita, S. Hara, D. Miyauchi, K. Shimazawa, T. Chou, K. Noguchi, K. Tagami, IEEE Trans. Magn. **44**, 3584 (2008)
64. K. Kodama, T. Furubayashi, H. Sukegawa, T.M. Nakatani, K. Inomata, K. Hono, J. Appl. Phys. **105**, 07E905 (2009)
65. T. Iwase, Y. Sakuraba, S. Bosu, K. Saito, S. Mitani, K. Takanashi, Appl. Phys. Exp. **2**, 063003 (2009)
66. Y. Sakuraba, K. Izumi, Y. Miura, K. Fuasukawa, T. Iwase, S. Bosu, K. Saito, K. Abe, M. Shirai, K. Takanashi, Phys. Rev. B **82**, 094444 (2010)
67. J. Sato, M. Oogane, H. Naganuma, Y. Ando, Appl. Phys. Exp. **4**, 113005 (2011)
68. Y. Sakuraba, M. Ueda, Y. Miura, K. Sato, S. Bosu, K. Saito, M. Shirai, T.J. Konno, K. Takanashi, Appl. Phys. Lett. **101**, 252408 (2012)
69. H. Narisawa, T. Kubota, K. Takanashi, Appl. Phys. Exp. **8**, 063008 (2015)
70. T. Kubota, Y. Ina, M. Tsujikawa, S. Morikawa, H. Narisawa, Z. Wen, M. Shirai, K. Takanashi, J. Phys. D Appl. Phys. **50**, 014004 (2017)
71. T. Kubota, Y. Ina. Z. Wen, H. Narisawa, K. Takanashi, Phys. Rev. Mater. **1**, 044402 (2017)
72. M. Saito, N. Hasegawa, Y. Ide, T. Yamashita, Y. Hayakawa, Y. Nishiyama, M. Shizone, S. Yanagi, K.A. Takagishi, in *Digest of the Intermag Conference*, Paper No. FB-02 (2005)
73. K. Nikolaev, P. Kolbo, T. Pokhil, X. Peng, Y. Chen, T. Ambrose, L. Mrysaov, Appl. Phys. Lett. **94**, 222501 (2009)
74. T. Furubayashi, K. Kodama, H. Sukegawa, Y.K. Takahashi, S. Mitani, K. Hono, Appl. Phys. Lett. **93**, 222501 (2008)

75. T.M. Nakatani, T. Furubayashi, S. Kasai, H. Sukegawa, Y.K. Takahashi, S. Mitani, K. Hono, Appl. Phys. Lett. **96**, 212501 (2010)
76. N. Hase, BSDChS Varaprasad, T.M. Nakatani, H. Sukegawa, S. Kasai, Y.K. Takahashi, T. Furubayashi, K. Hono, J. Appl. Phys. **108**, 093916 (2010)
77. N. Hase, T.M. Nakatani, S. Kasai, Y.K. Takahashi, T. Furubayashi, K. Hono, J. Magn. Magn. Mater. **324**, 440 (2012)
78. S. Li, Y.K. Takahashi, T. Furubayashi, K. Hono, Appl. Phys. Lett. **103**, 042405 (2013)
79. Y. Du, T. Furubayashi, T.T. Sasaki, Y. Sakuraba, Y.K. Takahashi, K. Hono, Appl. Phys. Lett. **107**, 112405 (2015)
80. T.M. Nakatani, G. Mihajlovic, J.C. Read, Y. Choi, J.R. Childress, Appl. Phys. Exp. **8**, 093003 (2015)
81. Y. Miura, K. Futatsukawa, S. Nakajima, K. Abe, M. Shirai, Phys. Rev. B **84**, 134432 (2011)
82. J.A. Caballero, Y.D. Park, J.R. Childress, J. Bass, W.-C. Chiang, A.C. Reilly, W.P. Pratt Jr., F. Petroff, J. Vac. Sci. Tech. A **16**, 1801 (1998)
83. Z. Wen, T. Kubota, T. Yamamoto, K. Takanashi, Sci. Rep. **5**, 18387 (2015)
84. J.C. Slonczewski, J. Magn. Magn. Mater. **159**, L1 (1996)
85. L. Berger, Phys. Rev. B **54**, 9353 (1996)
86. T. Shinjo (ed.), *Nanomagnetism and Spintronics* (Elsevier, Oxford UK, 2009)
87. S.I. Kiselev, J.C. Sankey, I.N. Krivorotov, N.C. Emley, R.J. Schoelkopf, R.A. Buhrman, D. C. Ralph, Nature **425**, 380 (2003)
88. W.H. Rippard, M.R. Pufall, S. Kaka, S.E. Russek, T.J. Silva, Phys. Rev. Lett. **92**, 027201 (2004)
89. D.C. Ralph, M.D. Stiles, J. Magn. Magn. Mater. **320**, 1190 (2008)
90. A.M. Deac, A. Fukushima, H. Kubota, H. Maehara, Y. Suzuki, S. Yuasa, Y. Nagamine, K. Tsunekawa, D.D. Djayaprawira, N. Watanabe, Nat. Phys. **4**, 803 (2008)
91. H. Kubota, K. Yakushiji, A. Fukushima, S. Tamaru, M. Konoto, T. Nozaki, S. Ishibashi, T. Saruya, S. Yuasa, T. Taniguchi, H. Arai, H. Imamura, Appl. Phys. Exp. **6**, 103003 (2013)
92. H. Maehara, H. Kubota, Y. Suzuki, T. Seki, K. Nishimura, Y. Nagamine, K. Tsunekawa, A. Fukushima, A.M. Deac, K. Ando, S. Yuasa, Appl. Phys. Exp. **6**, 113005 (2013)
93. Q. Mistral, J.-V. Kim, T. Devolder, P. Crozat, C. Chappert, J.A. Katine, M.J. Carey, K. Ito, Appl. Phys. Lett. **88**, 192507 (2006)
94. R. Okura, Y. Sakuraba, T. Seki, K. Izumi, M. Mizuguchi, K. Takanashi, Appl. Phys. Lett. **99**, 052510 (2011)
95. T. Seki, Y. Sakuraba, R. Okura, K. Takanashi, J. Appl. Phys. **113**, 033907 (2013)
96. T. Seki, Y. Sakuraba, H. Arai, M. Ueda, R. Okura, H. Imamura, K. Takanashi, Appl. Phys. Lett. **105**, 092406 (2014)
97. T. Seki, H. Yako, T. Yamamoto, T. Kubota, Y. Sakuraba, K. Takanashi, J. Phys. D Appl. Phys. **48**, 164010 (2015)
98. T. Yamamoto, T. Seki, T. Kubota, H. Yako, K. Takanashi, Appl. Phys. Lett. **106**, 092406 (2015)
99. T. Yamamoto, T. Seki, K. Takanashi, Phys. Rev. B **94**, 094419 (2016)
100. T. Seki, T. Kubota, T. Yamamoto, K. Takanashi, J. Phys. D Appl. Phys. **51**, 075005 (2018)
101. Z. Zeng, P. Khalili Amiri, I.N. Krivorotov, H. Zhao, G. Finocchio, J.-P. Wang, J.A. Katine, Y. Huai, J. Langer, K. Galatsis, K.L. Wang, H. Jiang, ACS Nano **6**, 6115 (2012)

Chapter 37
Biosensors Based on Field-Effect Transistors

Miyuki Tabata and Yuji Miyahara

Abstract Field-effect transistor (FET)-based biosensors are used to detect charge density change as a result of biomolecular recognition on the gate of the transistor. To realize rapid detection and precise analysis of biomolecules using FET-based biosensors, design, and fabrication of chemical modifications at gate surface are important considerations. In this chapter, we showed fundamental working principles of a FET-based biosensor and described its application to the detection of DNA and electrically neutral biomolecules, and to the analysis of cell functions. Since the detection of electrically neutral molecules is one of challenges in electrical/electrochemical detection methods, we showed two possibilities employed stimuli-responsive polymer gel technique and aptamer-based chemistry for a FET-based biosensor. Furthermore, we indicated cell functional analysis results using ion-sensitive FET for a future alternative method of animal experiment. FET-based biosensors have potential advantages in miniaturization of the sensing device and parallel analysis. These advantages promote future medical care such as early diagnosis, telemedicine, and point-of-care test.

Keywords Biosensor · Ion-sensitive field-effect transistor · DNA sequencing · Cell analysis · Glucose sensing

M. Tabata
Institute of Bioengineering, École Polytechnique Fédérale de Lausanne, Lausanne, Switzerland

Y. Miyahara (✉)
Institute of Biomaterials and Bioengineering, Tokyo Medical and Dental University, Tokyo, Japan
e-mail: miyahara.bsr@tmd.ac.jp

Y. Setsuhara et al. (eds.), *Novel Structured Metallic and Inorganic Materials*, https://doi.org/10.1007/978-981-13-7611-5_37

37.1 Introduction

Over the last several decades, tremendous advances have been achieved in the field of micro- and nanoelectronics. Highly reliable and functional chips can be easily fabricated using a precisely controlled production process. Various kinds of information are now at our disposal using personal digital assistants. Moore's Law, which states that the number of transistors on a chip doubles every 18–24 months, has been used as a guide for the long-term planning of future development. This scaling works well for memories and microprocessors in digital electronics. Recently, however, the rate of development and progress has slowed due to the physical limitations of miniaturization. In order to overcome saturation of development in micro- and nanoelectronics, researchers in the micro- and nanoelectronics fields have been exploring new applications of semiconductor technologies. Applications such as radio frequency devices, power management subsystems, sensors, actuators, microelectromechanical systems, and biochips now play important roles in the semiconductor industry. Among these emerging technologies, biochips are critical for healthcare applications such as point-of-care diagnostic testing and treatment monitoring. In this chapter, we introduce and explain the fundamental principles and applications of biochips based on field-effect transistors (FETs).

Insulated gate FETs, the most fundamental devices in large-scale integrated circuits, must be fabricated in strictly controlled clean rooms. The first ion-sensitive FET (ISFET) was described by P. Bergveld in 1970 and was found to be sensitive to ion concentration changes in an aqueous solution [1]. ISFET continues to be used as an ion sensor for in-depth studies and is now commercially available as a pH sensor for laboratory use. ISFET is also used as a base device with various functional modifications at the gate for the selective detection of molecules. A wide variety of research has been reported on ISFET-based biosensors in which the surface of the gate was chemically or biologically modified with functional molecules. Functional molecules used in these studies include enzymes, proteins, nucleic acids, and cells [2, 3].

Major advantages of using semiconductor technology to fabricate sensing devices include the ability to miniaturize the device and integrate multiple sensing elements and signal-processing circuits in a single chip.

The rapid increase of knowledge in the field of molecular biology has created new applications for micro- and nanotechnologies in medicine and biology. Examples include the parallel processing of information, miniaturization of analysis systems, and exploring the molecular mechanisms of life. DNA chips with high-density DNA probes have been developed for high-throughput nucleic acid analyses, and microfluidic devices are contributing to the functional analysis of cells. In 2010, a high-density ISFET array was commercialized as a detector in a DNA sequencing machine in which hydrogen ions produced during single base extension reactions were detected with the ISFET array chip. This chip fully incorporates the large-scale integration of semiconductor devices, enabling parallel

processing and detection of multiple reactions for high-throughput DNA sequencing [4].

Charge-based detection using an FET-based biosensor can be utilized to register charged target molecules such as protein or DNA. Detection is the result of biomolecular recognition on the gate of the FET via electrostatic interactions. In this detection scheme, the shielding effect induced by abundant mobile counterions in an electrolyte solution hampers a direct detection of the charge of the target species. The electric charge of biomolecules in a solution is screened at a certain length termed the Debye screening length. The Debye length is expressed as a function of ionic strength of the solution ($\propto I^{-1/2}$) and yields no more than 10 nm even in a diluted buffer solution of 1 mM. Consequently, the intrinsic charges of target molecules localized within the range of the Debye length from the gate surface can be detected with the FET-based detection scheme. The possibilities and limitations of FET-based biosensors are also discussed in this chapter.

37.2 Principle of FET-Based Biosensors

A FET-based biosensor consists of ISFET and functional molecules with affinity toward the biomolecules to be detected. The materials for the hydrogen ion–sensitive layer on the gate insulator are usually composed of SiO_2, Al_2O_3, Si_3N_4, or Ta_2O_5. The mechanisms for pH-dependent charge alterations that occur on the surface of these materials have been explained by the site-binding model, taking into account a pH-dependent protonation (or deprotonation) of the surface-elaborated hydroxyl groups. To detect entities other than hydrogen ions, the surface of the hydrogen ion–sensitive layer is chemically or biologically modified with functional molecules. The conceptual structure of an FET-based biosensor with immobilized biomolecules is shown in Fig. 37.1a. The FET-based biosensor is immersed in a measurement solution together with an Ag/AgCl reference electrode in a saturated KCl solution. The potential of a measurement solution is controlled by the gate voltage (V_G) through the reference electrode. As a simple criterion for the operation of the FET-based biosensors, either reaction products or consumed reactants during the biomolecular recognition must be ions that can be detected with the ISFET. For example, urease is an enzyme that catalyzes hydrolysis of urea as shown in the following reaction.

$$(NH_2)_2CO + H_2O \rightarrow CO_2 + 2NH_3 \tag{37.1}$$

Hydrogen ions are consumed, and the local pH near the immobilized urease changes based on this reaction. The produced pH change is correlated with urea concentration, assuming that the quantity of urease is constant. Therefore, urea concentration can be quantitatively determined by measuring the produced pH change using the ISFET [5].

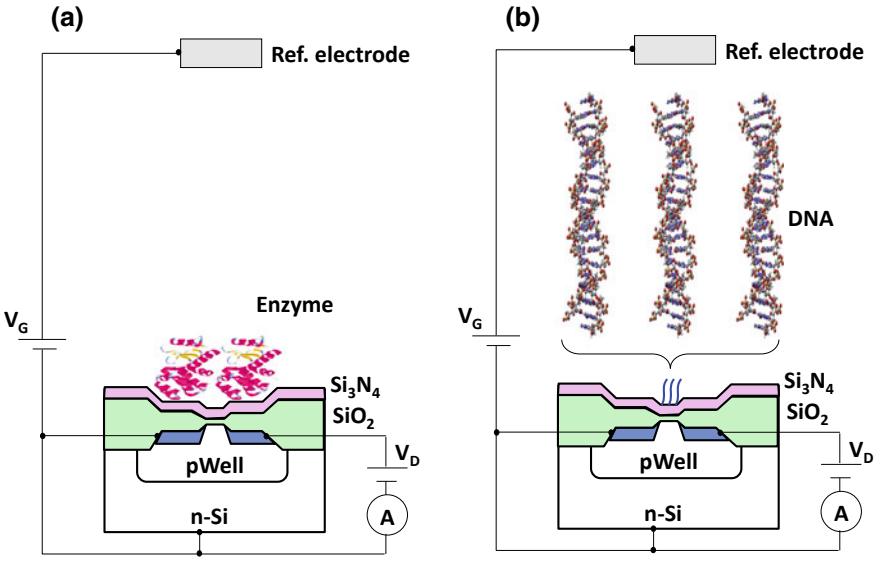

Fig. 37.1 Conceptual structures of FET-based biosensors. **a** FET-based biosensors with immobilized enzyme. **b** FET-based biosensors with immobilized oligonucleotide probes

Each enzyme used in this detection scheme has an optimum pH; therefore, a buffer solution is used to keep the enzyme activity as high as possible. The use of a buffer solution, however, suppresses the pH change produced by the detection reaction. To counteract this, a diluted buffer solution is often used. It is necessary to optimize buffer concentration so that enzymatic activity is not unduly compromised and the pH change can still be detected.

FET-based biosensors may also be used to detect charge density change as a result of biomolecular recognition on the gate of the transistor. When charged target molecules in aqueous solution are adsorbed on the surface of the gate, electrons in a silicon substrate electrostatically interact with adsorbed charged molecules. The electrical characteristics of the transistors, such as the relationship between the gate voltage (V_G) and the drain current (I_D), are influenced as a result of this electrostatic interaction. In the V_G–I_D characteristic, the voltage at which the drain current starts to flow is called the threshold voltage (V_T). One of the typical examples of this detection scheme is an FET-based biosensor for genetic analysis. In this device, oligonucleotide probes are immobilized on the surface of the gate insulator as shown in Fig. 37.1b. When cDNA molecules are contained in a sample solution, hybridization occurs at the surface of the gate area. Since DNA molecules are negatively charged in an aqueous solution, a hybridization event can be detected by measuring a shift of the threshold voltage V_T [6]. By measuring the direction and the amount of the V_T shift after hybridization, one can obtain information on the density of charge of hybridized DNA molecules. When an n-channel FET is used,

the V_T shifts in the positive direction in response to negatively charged DNA molecules.

Because the charges of the target biomolecules are directly detected with a transistor after specific binding on the gate, a fundamental limitation of this detection scheme originates from the "Debye length issue," namely, its susceptibility to counterions [7]. FET-based charge detection is inherently permitted only within a short distance of the electrical double layer or the Debye length, which is no greater than a few nanometers under the physiological ionic strength conditions. According to the Gouy-Chapman model, the Debye screening length is expressed in the following equation for an electrolyte containing an ionic species with a valence of z_i and a number density of n_i:

$$d = \sqrt{\frac{\varepsilon_0 \varepsilon_r kT}{\sum z_i n_i e^2}} \tag{37.2}$$

where ε_r, $\varepsilon_{0,}$ e, k, and T are the relative permittivity of the electrolyte, vacuum permittivity, elementary charge, Boltzmann constant, and absolute temperature, respectively. The Debye screening length gives a rough idea of how far the electric field extends from the surface. When the concentrations of a 1:1 electrolyte solution are 1 mM, 10 mM, and 100 mM, values of d are 10 nm, 3 nm, and 1 nm, respectively. Beyond this length, the counterions' screening effect predominates and the charge detection of proteins is severely hampered, since typical sizes of proteins (including antibodies) are in the order of 10 nm. In order to overcome this problem, a diluted buffer solution is usually used; however, the three-dimensional structure of biomolecules or the integrity of biomolecular recognition may be influenced by the diluted buffer.

37.3 DNA Sequencing

Because its results are used in defining the human genomes, as well as the genome of individual patients, DNA sequencing technology requires a robust methodology. It must also be cost-effective, fast, and easy to operate as its use in clinical research and practice becomes increasingly more common. DNA sequencing machines have been in a development race ever since Frederick Sanger developed the first approach in 1977. Currently available second- and third-generation DNA sequencing platforms are trying to decrease the run time while reducing the running cost. Ion Torrent™ is one of the major bench-top sequencing platforms [4, 8] and works by detecting the protons released during the elongation of a strand of nucleic acids by DNA polymerase. In Ion Torrent™, massively parallel ISFETs are integrated onto Ion Torrent™ chips fabricated using semiconductor technology. Three-micron beads that have DNA templates for use in emulsion PCR (emPCR) attached are loaded into individual wells that are capable of conducting pH sensing.

The DNA templates are then clonally amplified. During the amplification cycles, each of the nucleotide bases A, C, G, and T is sequentially added to the individual wells. If the added base is a complementary match to the template, elongation occurs and a proton is generated. This is detected as a change in pH by the pH sensor. If multiple copies of the same base are incorporated, a greater pH change occurs and stronger signal is detected. This ion semiconductor sequencing technology may have some advantages in terms of cost and high-throughput readout when compared to different technologies such as fluorescence-based DNA sequencers such as those marketed by Illumina™. These advantages are due to the ion semiconductor's compatibility with microfabrication techniques.

Because of the advantages of semiconductor devices, we proposed the use of FET for DNA sequencing [9] prior to the commercial availability of Ion Torrent™. This measurement principle was developed for exosomal microRNA (miRNA) detection using semiconductor-based microelectrode array [10]. We targeted miR-143 and miR-146, which are related to colorectal cancer and breast cancer metastasis, respectively. After ultracentrifuge collection of exosomes from cell culture supernatant, cDNAs were produced by reverse transcription from encapsulated miRNAs and amplified by PCR. For potentiometric recognition of cDNA, a 5′-SH-$(CH_2)_6$-DNA was immobilized together with sulfobetaine-3-undecanethiol (SB) on the Au array sensors. The hybridization event between immobilized DNA and cDNA directly changes the surface potential by inducing Coulomb charges. From the readout signal after hybridization, the detectable cDNA concentration was >20 pM and the detection rage was 2–200 pM. This miRNA detection platform realized label-free electrical sensing, although complicated pretreatment for preparation of target cDNAs was required.

To expand this research, we developed the combination of electrical detection devices and isothermal amplification methods for detection of nucleic acids [11, 12]. In principle, the characteristics and the stability of electrical devices including FET should be changed by thermal cycles of PCR. Isothermal nucleic acid amplification methods do not require a high-temperature denaturation step. Instead, they rely on strand displacement-type elongation at constant temperature. This is a strong advantage for electrical detection because it reduces the noise to signal ratio. We performed chronocoulometric miRNA detection combined with rolling circle amplification (RCA) in the presence of $[Ru(NH_3)_6]^{3+}$ as the signaling molecule [11]. Chronocoulometry (CC), which detects the produced charge by adsorbed reactant to the electrode surface, was conducted to detect RCA products on the Au electrode. As shown in Fig. 37.2a, detection sensitivity for DNA and miRNA (miR-143) were 100 fM and 1 pM, respectively. Furthermore, in order to realize a label-free detection, we fabricated an ethidium ion (Et^+)-selective electrode (Et^+ISE) and monitored isothermal DNA amplification by primer-generation RCA (PG-RCA) [12]. Since Et^+ is known as a typical intercalator, there's a potential decrease of elongation of PG-RCA amplicon due to the intercalation of positive charge by Et^+ added to the reaction mix. Since Et^+ sensitivity follows the Nernstian Eq. (37.3), output potential of Et^+ISE is proportional to the log of the Et^+ activity in the PG-RCA mixture.

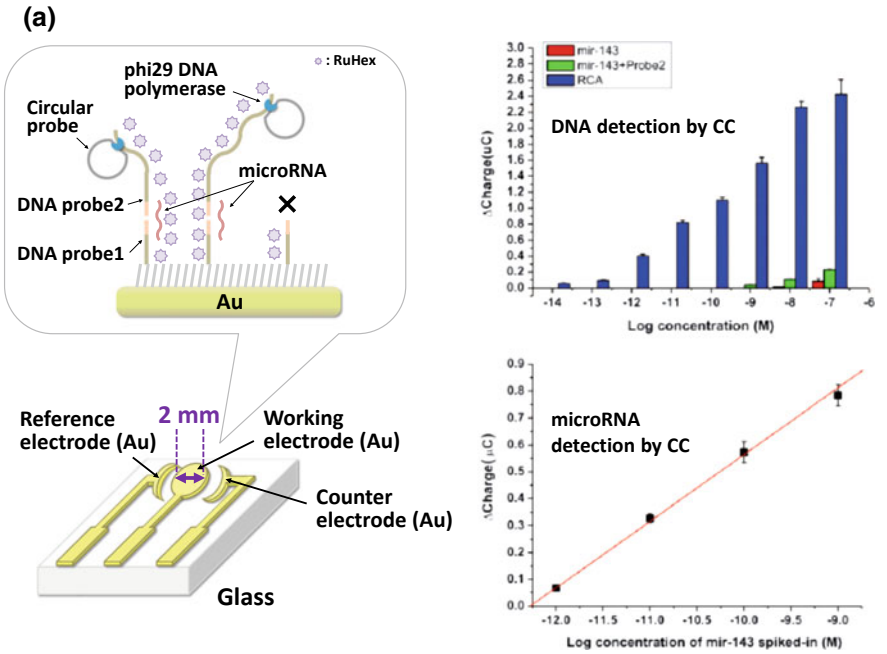

Fig. 37.2 Electrochemical biosensors for quantitative detection of nucleic acids. **a** Chronocoulometric DNA and microRNA detection combined with rolling circle amplification, reproduced from Ref. [10] with permission from the Royal Society of Chemistry. **b** Real-time DNA amplification monitoring using micro Et^+ sensor and primer-generation rolling circle amplification, reproduced from Ref. [12] with permission from the Japan Society for Analytical Chemistry

$$E = E_0 + (2.303\,RT/zF)\log\,a \tag{37.3}$$

where E_0 is the standard electrode potential at 25 °C, R is a gas constant, T is temperature, z is valence of ion, F is Faraday constant, and a is ion activity. The real-time potential shift during PG-RCA is shown in Fig. 37.2b. It was measured in the range of 10 nM–1 μM of initial target DNA as the difference between reference electrode (Ag/AgCl) and Et^+ISE using an electrometer.

Since these combinations of electrical/electrochemical devices and isothermal amplification could provide chip-based isothermal amplification devices, it could be a useful platform, particularly as a point-of-care testing device.

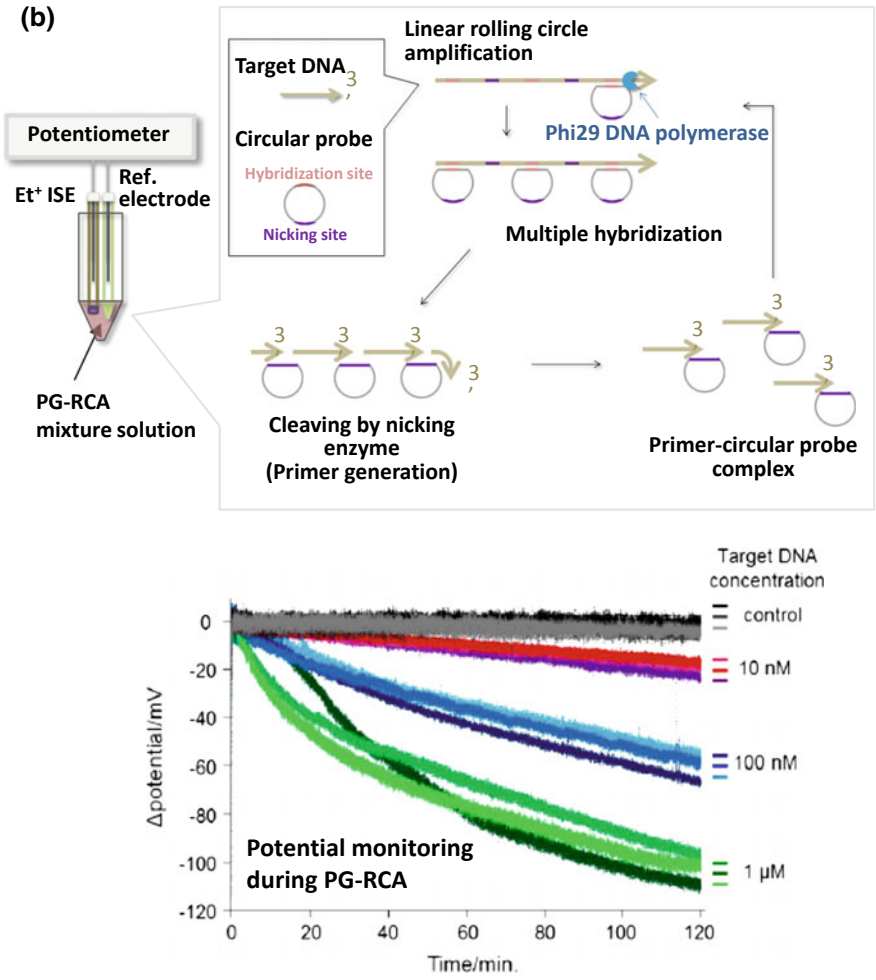

Fig. 37.2 (continued)

37.4 Functional Analysis of Cells

The first step in the evaluation of drug candidates is generally in vitro analysis using cultured cells. The development of cell-based biosensors promises to optimize this type of analysis.

We developed a microperfusion ISFET device for measuring proton-dependent membrane activity at the surface of *Xenopus laevis* oocytes [13]. The output voltages of this system under verified standard buffer solutions from pH 4.0 to pH 9.2 were calculated to pH according to the Nernstian equation. The pH sensitivity was −58.0 mV/pH, demonstrating the excellent pH-sensitive gate material of Ta_2O_5

(ideal Nernstian slope is −59.2 mV/pH at 25 °C). As shown in Fig. 37.3a, V_{SG} on oocytes heterologously expressing the proton-driven amino acid transporter (PAT1) significantly shifted to minus by exposure of 1 mM proline solution, reflecting the local pH increase at the ISFET interface associated with intracellular uptake of a proton and a proline. In contrast, the signal for oocytes heterologously expressing the electrogenic sodium-coupled phosphate cotransporter (NaPi-IIb) was reversed, indicating a decrease in the surface pH of the ISFET. These results are explained by equilibrium of divalent (HPO_4^{2-}) and monovalent (H_2PO^{4-}) phosphate species as shown in the following reaction.

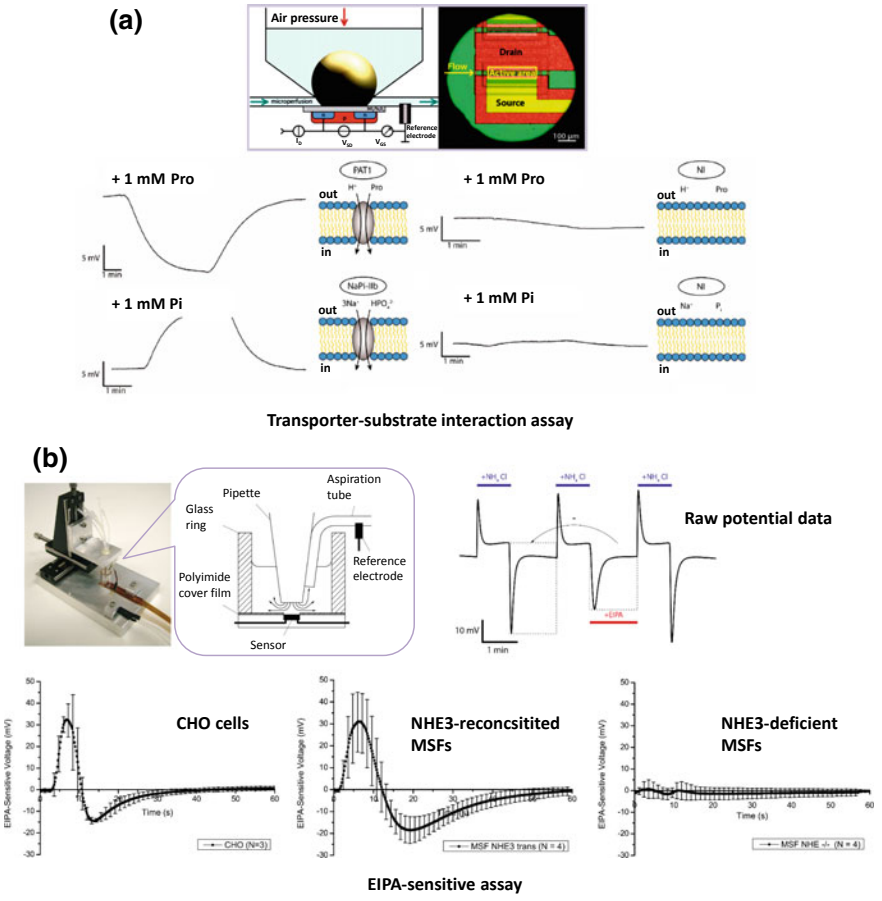

Fig. 37.3 Cell-based biosensor integrated with microperfusion system. **a** Evaluation of proton-dependent membrane activity using oocytes, reproduced from Ref. [13]. **b** Interaction monitoring between EIPA and sodium hydrogen exchangers using mammalian cells, reproduced from Ref. [14]

$$HPO_4^{2-} + H^+ \leftrightarrow H_2PO_4^- \tag{37.4}$$

After uptake of divalent Pi (HPO_4^{2-}), equilibrium shifted to the left-hand side in formula (37.4) because assumed pKa is 6.8 under physiological conditions, resulting in the generation of protons. This cell-based–transistor for the analysis of transporter function is expected to contribute to high-throughput screening in pharmaceutical research.

We next fabricated a nondestructive evaluation device based on sodium hydrogen exchangers (NHEs), which are ubiquitous ion transporters that serve multiple cell functions. This device combined ISFET, mammalian cells, and the microperfusion system [14]. The sensing system was capable of detecting not only transient changes caused by ammonia loading and unloading but also the steady-state signals that are likely to be influenced by the extracellular proton gradient. This suggests that the output signal of ISFET can be enhanced by using an intra/extracellular pH ammonia equilibrium reaction.

In the last set of experiments, 5-(N-ethyl-N-isopropyl) amiloride (EIPA) was used to analyze the cells' pH-regulatory response via the NHE. Figure 37.3b shows a series of results of the EIPA-sensitive assay. Chinese hamster ovary cells and NHE3-reconstituted mouse skin fibroblasts (MSF) showed a positive response, whereas NHE-deficient MSF showed no response. We further established the reliability of this device by examining dose-response and investigating other proton-sensitive membrane proteins. This cell-based transistor is expected to become a platform technology for drug discovery, screening and diagnostic tests, and the evaluation of induced immune response by chemical compounds.

37.5 Detection of Electrically Neutral Molecules

One of the big challenges for FET-based biosensors is the detection of electrically neutral molecules. In the case of FET-based biosensor for genetic analysis, DNA has abundant negative charges in nucleotides (−308 Da/charge) owing to the phosphate-deoxyribose backbone structure. Detection of proteins is more difficult due to lower charge density. Only five types of amino acids out of a possible 20 are primarily responsible for electrical properties. Arginine, lysine, and histidine are cationic, and aspartic acid and glutamic acid are anionic. Therefore, proteins are zwitterions in a certain range of pH, resulting in insufficient net charge. For example, the estimated charge density of human serum albumin is −5733 Da/charge at pH 7.4.

In order to overcome this problem, we have made use of a stimuli-responsive polymer gel formed directly on the gate of a transistor. Stimuli-responsive polymer gels are a class of material capable of undergoing marked changes in their physicochemical properties in response to a series of specific stimuli. As proof-of-principle, a phenylboronic acid-based polymer gel, a thoroughly synthetic

and well-characterized glucose-responsive material, was applied to the FET gate surface as a 50 μm thick layer as shown in Fig. 37.4a. This created an FET-based sensor for glucose [15], an electrically neutral molecule. In this configuration, an applied glucose stimulus triggered an abrupt volume change of the gel, termed a

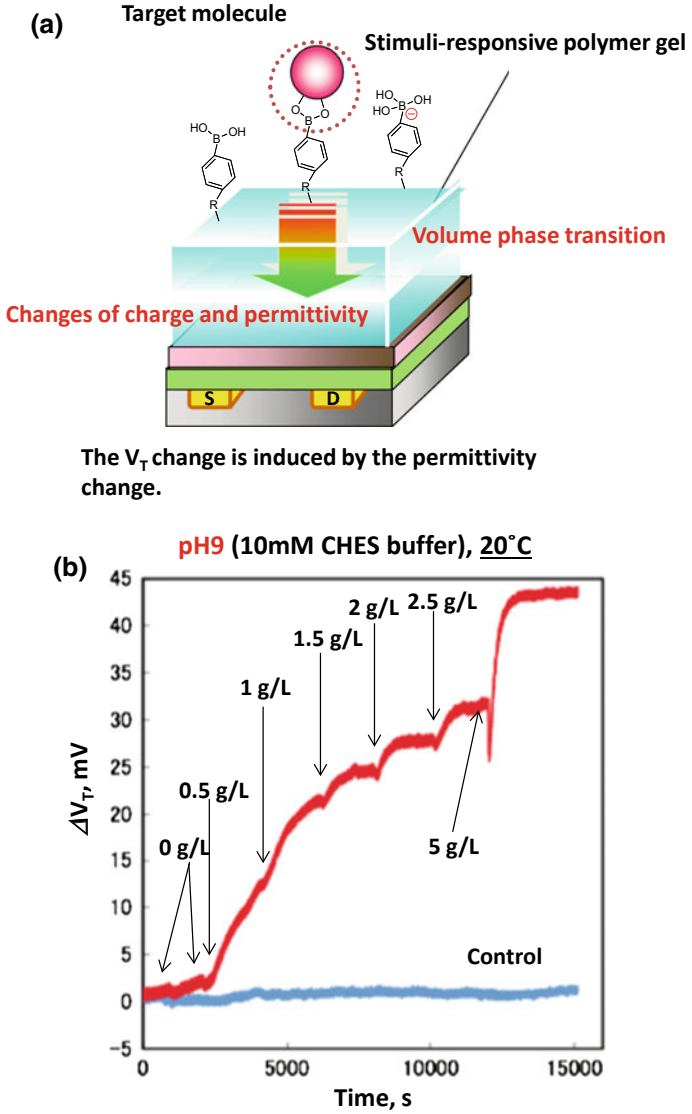

Fig. 37.4 FET-based biosensors with stimuli-responsive polymer gels, reproduced from Ref. [15] with permission from John Wiley and Sons with the license number of 4476360151639. **a** An FET-based glucose sensor with immobilized phenyl boronic acid. **b** Responses of an FET-based glucose sensor to various glucose concentrations

"volume phase transition". This transition also involved other physical parameter changes including thickness, charge density, and permittivity [16].

As the output signal of the FET-based biosensor, the shift of the threshold voltage, ΔV_T, can be expressed in the following formula.

$$\Delta V_T \propto (\Delta Q_{DL})/C_I \tag{37.5}$$

$$C_I = (\varepsilon_0 \varepsilon_i)/d \tag{37.6}$$

Here ΔQ_{DL}, C_I, d, and ε_r are the charge density change induced within the Debye length, the gate capacitance per unit area, the thickness of the gate insulator, and relative permittivity of the gate materials, respectively. Detection of DNA as described in Sect. 37.3 is based on the charge density change in formula (37.5), while the gate capacitance is considered to be constant. In the system described in Fig. 37.4a, a permittivity change of the gel is a major source of the threshold voltage change, rather than charge density change. The volume change of the polymer gel is practically equivalent to that of water content. A significantly high relative permittivity of water ($\sim$80) compared to those typical for condensed polymeric materials ($\sim$2) is responsible for this change. The permittivity change of the gate materials is another determining factor of the threshold gate voltage (V_T) as shown in formulae (37.5) and (37.6). Figure 37.4b shows a typical example of the glucose responses of the FET-based sensor with a phenylboronic acid-based polymer gel. The output signal of the transistor changes depending on the concentration of uncharged glucose. The reversibility of the signal was also confirmed. Thus, glucose concentrations could be measured as the change in permittivity of the gate materials in harmony with the volume phase transition of the gel.

We have developed another approach for the detection of electrically neutral molecules using an aptamer with a hairpin structure in combination with a groove binder for the DNA duplex. The conceptual structure of the device is shown in Fig. 37.5a. A hairpin-structured aptamer has a stem-loop configuration containing an adenosine-binding sequence in the loop structure. The hairpin-structured aptamer is immobilized on the surface of the Au gate electrode. Upon adenosine recognition and capture by the adenosine-binding sequence, the conformation of the hairpin structure changes from closed loop to open-loop, as shown in Fig. 37.5a. A positively charged DNA binder, 4′,6-diamidino-2-phenylindole (DAPI), is incorporated into the DNA duplex in advance and released from the stem of the hairpin aptamer upon adenosine-induced denaturation. The release of the cationic DNA binder from the gate–solution interface results in signal generation of the transistor, allowing detection of electrically neutral adenosine molecules. Figure 37.5b shows detection of adenosine in comparison with guanosine based on this detection scheme [17]. The sensitive and selective detection of electrically neutral adenosine was achieved within the dynamic concentration range of 10^{-8}–10^{-6} M. In this experimental condition, the calculated Debye length in 15 mM Dulbecco's phosphate-buffered saline was 2.5 nm. Considering the intramolecular distance between bases (0.34 nm), the 7-mer of the stem part at the 5′ end of the aptamer is always localized within the Debye length

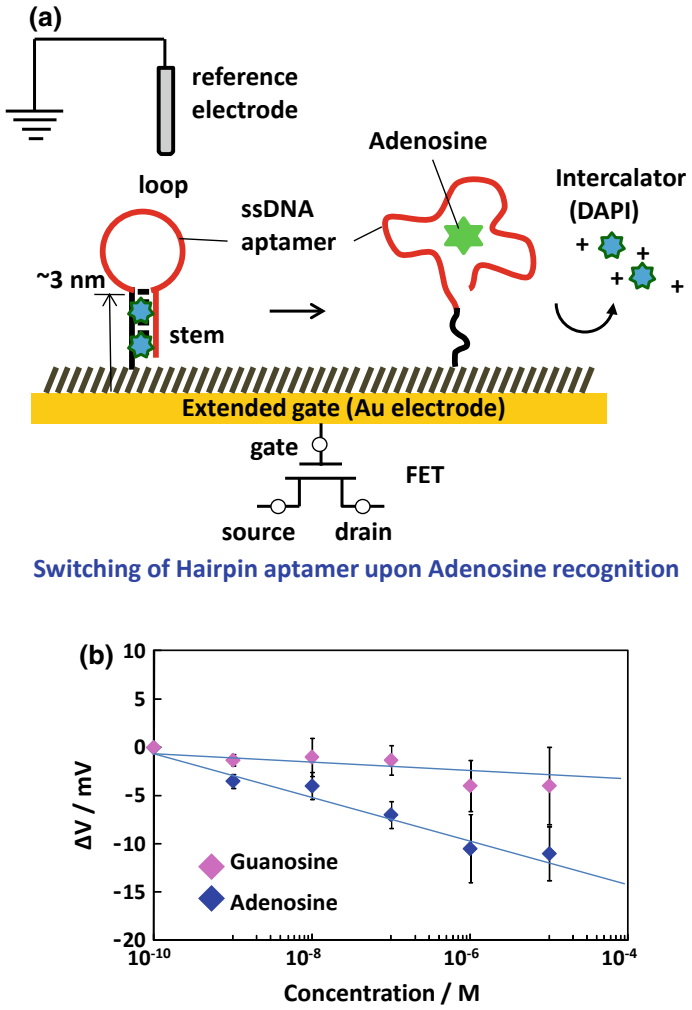

Fig. 37.5 Principle of FET-based biosensors with hairpin aptamer and intercalator, reproduced from Ref. [17] with permission from Elsevier with the license number of 4476341143732. **a** Detection scheme for electrically neutral adenosine. **b** Response curves for adenosine in comparison with guanosine

at the surface of the gate Au electrode. Therefore, the FET-based device is sensitive and specific to variations in the charges of the stem, induced by the dissociation of DAPI upon capture of adenosine.

37.6 Conclusion

In this chapter, we described several types of FET-based biosensors, focusing on the design and fabrication of chemical modifications at the surface of the gate. The fundamental principles of a FET-based biosensor and its application to the detection of DNA and electrically neutral biomolecules and to the analysis of cell functions are also described. In addition, we showed two examples of FET-based biosensors with which electrically neutral molecules could be detected. By designing and optimizing the structure and function of the interface between gate materials and solution, a wide variety of molecules can be detected with an FET. FET-based biosensors have potential advantages such as miniaturization of the sensing device and integration of multiple sensors and signal-processing circuits in a single chip. The potential small size of the clinical instruments provides a point-of-care diagnostic approach to detect biomarkers such as nucleic acids of viruses or microorganisms for infectious disease testing not only in a hospital but also in a physician's office. In developed countries, aging populations are leading to increased medical needs, while the ability to respond to those needs is limited by hospital capacity, the availability of doctors, and increasing healthcare costs. A possible solution to this problem is the increased use of home healthcare. A simple, small, sensitive, and user-friendly detection system is required to make this a reality.

Acknowledgements Our work was supported in part by the Center of Innovation (COI) Program from the Japan Science and Technology Agency (JST), Core Research of Evolutional Science & Technology (CREST), Japan Society for the Promotion of Science (JSPS), through the "Funding Program for World-Leading Innovative R&D on Science and Technology (FIRST Program)" initiated by the Council for Science and Technology Policy (CSTP); and by a JSPS Postdoctoral Fellowship for Foreign Researchers (No. P11355).

References

1. P. Bergveld, IEEE Trans. Biomed. Eng. **17**, 70 (1970)
2. S. Caras, J. Janata, Anal. Chem. **52**, 1935 (1980)
3. Y. Miyahara, T. Moriizumi, K. Ichimura, Sensor. Actuat. B-Chem **7**, 1 (1985)
4. J.M. Rothberg, W. Hinz, T.M. Rearick, J. Schultz et al., Nature **475**, 348–352 (2011)
5. Y. Miyahara, T. Moriizumi et al., Chemistry and industrial chemistry. J. Chem. Soc. Jpn. **6**, 823 (1983)
6. T. Sakata, M. Kamahori, Y. Miyahara, Jpn. J. Appl. Phys. **44**, 2854–2859 (2005)
7. P. Bergveld, Sensor. Actuat. A-Phys. **56**, 65 (1996)
8. C. Toumazou, L.M. Shepherd, S.C. Reed et al., Nat. Methods, **10**, 641–646 (2013)
9. T. Sakata, Y. Miyahara, Angew. Chem. Int. Ed. **45**, 2225–2228 (2006)
10. T. Goda, K. Masuno, J. Nishida et al., Chem. Commun. **48**, 11942–11944 (2012)
11. B. Yao, Y. Liu, M. Tabata et al., Chem. Commun. **50**, 9704–9706 (2014)
12. A. Seichi, N. Kozuka, Y. Kashima et al., Anal. Sci. **32**, 505–510 (2016)
13. D.F. Schaffhauser, M. Patti, T. Goda et al., PLoS ONE **7**(7), e39238 (2012)
14. D. Schaffhauser, M. Fine, M. Tabata et al., Biosensors **6**, 11 (2016)

15. A. Matsumoto et al., Adv. Mater. **21**(43), 4372–4378 (2009)
16. K. Kataoka, H. Miyazaki, M. Bunya, T. Okano, Y. Sakurai, J. Am. Chem. Soc. **120**, 12694 (1998)
17. T. Goda, Y. Miyahara, Biosens. Bioelectron. **32**, 244–249 (2012)

Chapter 38
Amorphous Oxide Semiconductor Thin-Film Transistors

Toshio Kamiya, Kenji Nomura, Keisuke Ide, Jungwhan Kim, Hidenori Hiramatsu, Hideya Kumomi and Hideo Hosono

Abstract Amorphous oxide semiconductor (AOS) is now commercialized in many flat-panel displays. On the other hand, its electronic structures and defects are largely different from conventional covalent semiconductors such as Si. This chapter explains their origins and reviews the defects that have been known to date. Finally, we will discuss how to fabricate high-quality, stabile AOS.

Keywords Amorphous oxide semiconductor · Thin-film transistor · Flat-panel display · Defects · Impurity hydrogen · Weakly-bonded oxygen · Stability

38.1 Introduction

Amorphous oxide semiconductor (AOS) represented by amorphous In–Ga–Zn–O (a-IGZO) is employed as thin-film transistors (TFTs) in many flat-panel displays (FPDs) from very high-resolution liquid-crystal displays (LCDs) to large (up to 88 in. diagonal prototype as of 2018) organic light-emitting diode (OLED) TVs because AOS TFTs have high field-effect mobilities (μ_{FE}) exceeding 10 $cm^2/(Vs)$ and can flow high-density current $\sim$100 times larger than that of conventional amorphous Si (a-Si) TFTs as seen in Fig. 38.1. In this chapter, we review the present status of AOS including applications to FPDs and integrated circuits as well as fundamental materials science. Here, we try to minimize the number of references due to the page limitation. Please see books and review papers [1–4] for details.

T. Kamiya (✉) · K. Nomura · K. Ide · J. Kim · H. Hiramatsu · H. Kumomi · H. Hosono
Tokyo Institute of Technology, Meguro, Japan
e-mail: kamiya.t.aa@m.titech.ac.jp

Y. Setsuhara et al. (eds.), *Novel Structured Metallic and Inorganic Materials*, https://doi.org/10.1007/978-981-13-7611-5_38

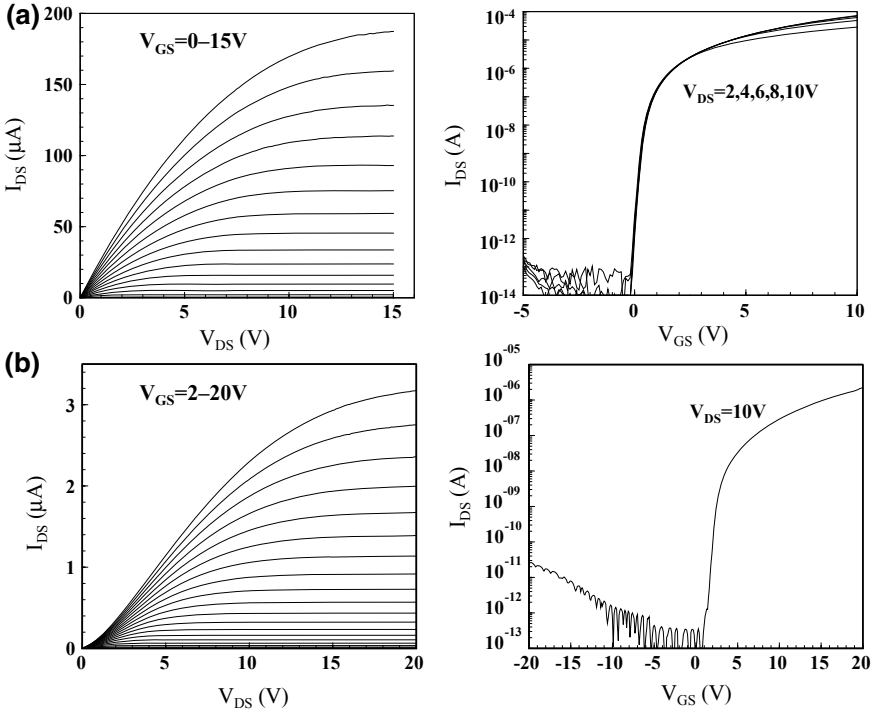

Fig. 38.1 Typical TFT characteristics of **a** a-IGZO and **b** a-Si TFTs

38.2 History and Present Status of AOS TFT Technology

The invention of TFT goes back to the CdS/CdSe TFTs by Schokley in 1948, followed by the invention of Si MOS field-effect transistors (FETs) in 1960. Research of oxide TFTs started in mid-1960s from crystalline ZnO, In_2O_3 and SnO_2 FETs and TFTs [1], but faded out from open-accessible literatures after that until 1990s. The next oxide TFT reappeared in 1996 with an epitaxial SnO_2 channel combined with a ferroelectric memory gate. Oxide TFT research became active in 2000s due to expectation that polycrystalline ZnO (poly-ZnO) can produce TFTs at low temperatures on large-size glass substrates comparable to the already-commercialized a-Si:H TFTs. However, the initial poly-ZnO TFTs suffered from low μ_{FE} up to 3 $cm^2/(Vs)$ and normally-on characteristics caused by high-density residual electron carriers and grain boundary (GB) defects [5]. It was also expected that polycrystalline TFTs would suffer also from nonuniformity issues arising from their GBs similar to poly-Si TFTs.

We reported the first AOS TFT in late 2014 with an a-IGZO channel deposited by pulsed laser deposition (PLD) [6]. Due to the amorphous structure without GBs, it overcomes the above deficiencies of polycrystalline oxide TFTs. Although the first AOS TFT was fabricated by PLD at room temperature (RT) without thermal

annealing, most of current AOS TFTs are fabricated by RF/AC/DC sputtering combined with post-deposition thermal annealing, e.g., at 300–400 °C. For the large-size sputtering systems, ULVAC [7] and AKT [8] provide Generation 8 or larger size sputtering systems. The first commercialization of oxide TFT was done by Sharp in March, 2012 for TFT backplane in retina LCD in Apple's new iPad, followed by commercialization of Sharp brand smartphones and tablet PCs. The AOS applications are now extended to very high-resolution LCDs for smartphones (e.g., 460 pixel per inch (ppi)), 27″ 5 K PC LCD monitors, and also for large-size (up to 88″) OLED TV. The OLED TV is now available as very thin "Picture-on-Wall display" that can be attached to a wall by magnets, and also prototype rollable OLED TV is demonstrated.

38.3 New Applications of AOS

The above products benefit from the intrinsic features of TAOS TFTs such as process compatibility to the existing a-Si:H TFT production lines, good uniformity owing to the amorphous structure, high $\mu_{FE} > 10$ cm^2/(Vs), and low process temperature owing to the strong iconicity of AOS as explained in Chap. 6. These features allow AOS TFTs to be applied to flexible devices. Actually, the first paper [6] demonstrated transparent and flexible TFT sheets fabricated on PET substrates using transparent conductive oxide electrode, and many flexible OLED displays have been demonstrated using AOS TFTs.

Another interesting feature of AOS is the transparency for human eyes, which enables completely transparent electronic devices. Facilitating the high transmittance of AOS TFTs, Toppan proposed a novel idea of front-drive structure [9]. In conventional color active-matrix (AM) electronic papers and displays, a color filter array is formed on a front plane and a TFT array on a back plane; therefore, fine alignment between these planes through a liquid-crystal (LC) layer or E-Ink microcapsules is necessary to avoid color misfit. However, the thickness of the E-Ink microcapsules (40–50 μm) is much larger than that of the LC layer (4–6 μm), making the alignment much difficult. This problem will be more critical for flexible displays because bending the display inevitably causes horizontal misalignment between the front and back planes. This issue is solved by integrating the TFT array on the color filter front plane (a similar structure is now referred to as COA, Color filter on TFT Array), where the high transparency of AOS TFTs is actually utilized.

AOS TFTs are expected also for integrating driving circuits in display panels (system-on-display) because their large μ_{FE} enables to fabricate high-frequency circuits as well. 410 kHz oscillation of 5-stage ring oscillator (RO) [10], and faster ones [11] were reported using a-IGZO TFTs. Ultra-miniaturization of oxide TFTs has also been examined for faster operation and integrated high-density memory devices. It is reported that a-IGZO TFTs are down-scalable to the channel length of 50 nm without suffering from the short-channel effect [12]. High-frequency

operation up to 180 MHz is reported for 1-μm-long a-In–Zn–O (a-IZO) TFTs [13]. These operation speeds are more than enough for gate/source driver circuits to drive AM-FPDs, and actually many current small-to-medium size FPDs driven by a-IGZO TFTs employ gate driver circuits integrated into the TFT backplanes.

For low power consumption applications, Hitachi, Ltd. reported very low-voltage (1.5 V) operation of AOS TFTs [14] and demonstrated 13.56 MHz RFID tag operating by 1 nA of driving current [15]. Facilitating the wide operation voltages from 1.5 to ~100 V of AOS TFTs, Renesas Electronics proposes integration of oxide (n-type IGZO and p-type SnO) TFTs in Si MOS ULSI, where the oxide TFTs bridges the low operation voltage ULSI circuit to an external high voltage load [16]. Further, AOSs are expected also for memories (see Ref. [1] for references). Many nonvolatile memories have been proposed using an a-IGZO including floating-gate memories, resistivity switching memories, and ferroelectric memories (FeRAM), where a-IGZO layers were used for the components different from TFT, such as floating node, resistivity switching media, etc.

AOS TFTs also have another advantage over Si FETs/TFTs. FETs/TFTs are used to keep the voltage states in switching TFTs in FPDs and memories; therefore, their retention time is limited by the off current I_{off} (or in other words, leakage current) of the FETs/TFTs, which are typically <1 nA for Si MOSFET, ~1 pA for poly-Si TFTs, and ~0.1 pA for a-Si:H TFTs. Display pixel and driving circuits are designed so that we cannot recognize image blinking at 60 Hz refresh rate. On the other hand, IGZO TFTs have much smaller I_{off}, which can be as low as the order of 10^{-26} A per μm in gate width at 27 °C [17]. The Sharp's smartphones and tablet PCs in market utilize this very low I_{off} and vary the refresh rate down to 1 Hz while a still image is displayed ("LCD idling stop technology"). The low I_{off} is effective in particular for reflective displays because only TFT backplanes consume electric power. Qualcomm MEMS technology (QMT) once released reflective displays based on MEMS ("Mirasol") display in smartwatches although the commercial products employed a-Si TFTs. QMT also demonstrated Mirasol display driven by a-IGZO TFTs [18]. Qualcomm Pixtronix has also developed a different type of MEMS display together with Sharp, which uses field sequential color control with RGB LEDs and digital micro-shutters. As the micro-shutter requires operation voltages as high as 20 V and higher speed than 0.1 ms, IGZO TFTs are used as the backplane [19]. Low I_{off} of IGZO TFTs also enables to realize nonvolatile DRAM/NOSRAM and normally-off CPU [20].

38.4 Electron Transport and Subgap Defects in TAOS

AOS has several common properties which are not seen in conventional amorphous semiconductors. First one is their large electron mobilities >10 $cm^2(Vs)^{-1}$, which is higher by 1–2 orders of magnitude than that in a-Si:H. Second is that a degenerate conduction state can be realized easily by doping. For instance, c-Si is easily changed to the degenerate state by carrier doping (~10^{18} cm^{-3}), but degenerate

state has never been attained in a-Si:H [21] to date. That is, carrier conduction takes place by hopping through tail states in conventional amorphous semiconductors, and therefore mobility is low. On the other hand, in AOS, degenerate conduction and the large electron mobilities >10 $cm^2/(Vs)$ are easily attained. This difference originates from that in chemical bonding nature as explained in Chap. 6.

Doping mechanism of AOS is also different from a-Si:H. In a-Si:H, aliovalent dopants such as P and B replaces the Si site in the tetrahedral coordination polyhedral; therefore, aliovalent doping works properly. On the other hand, such clear coordination structure has not been established in AOS, and DFT calculations for a-IGZO suggests that the coordination numbers around a metal cation have a large distribution [22–24]. Recent researches have revealed that the cation to oxygen ratio in AOS is very flexible. It is known that a-IGZO deposited by PLD and conventional sputtering contain high-density impurity hydrogens at 10^{20}–10^{21} cm^{-3} [25]. These hydrogens are considered to work as donors and generates mobile electrons, but compensated by excess oxygens. This situation would be understood by a simple ion charge counting rule summarized in Ref. [2], i.e., the total charge neutrality of the constituent ions determines the electron density. Therefore, aliovalent ion doping (e.g., Ga^{3+} doping to Zn^{2+} site) is expected to donate one mobile electron, but it is compensated by introducing excess 1/2 O atoms, which will be ionized to 1/2 O^{2-} ion upon trapping a mobile electron if appropriate deposition condition (P_{O2} etc.) or post-deposition thermal annealing is applied. A similar situation also happens if more impurity hydrogens are incorporated from a dirty deposition chamber; the mobile electrons generated from the hydrogens can be compensated by higher P_{O2} deposition or annealing conditions with more excess O (Fig. 38.2) [26].

It is important to notice that Hall mobility (μ_{Hall}) in AOS depends largely on N_e due to the presence of potential barriers in conduction band arising from its structural randomness. As seen in Fig. 38.3, μ_{Hall} increases with increasing N_e and finally exceeds 10 $cm^2(Vs)^{-1}$ if N_e exceeds $\sim 10^{18}$ cm^{-3} [6, 26]. Although the slopes, $d\mu_{Hall}/dN_e$, and the threshold N_e ($N_{e,th}$) depend on the IGZO films fabricated by different deposition conditions/with different structures, the positive slopes are commonly observed. This μ_{Hall} versus N_e behavior is explained by percolation

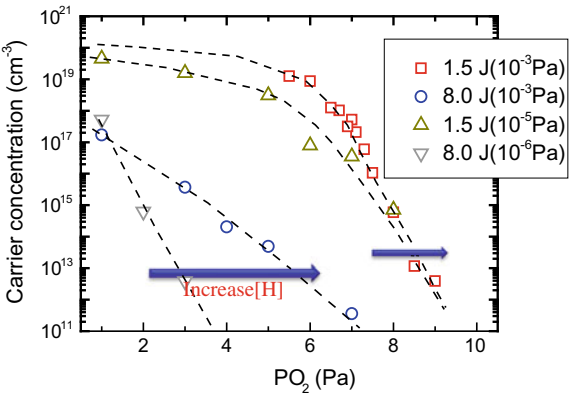

Fig. 38.2 Electron density in a-IGZO films deposited by PLD with different back pressures (10^{-3} and 10^{-5} Pa) in the deposition chamber. Two series of laser energies (1.5 and 8.0 J) are also compared

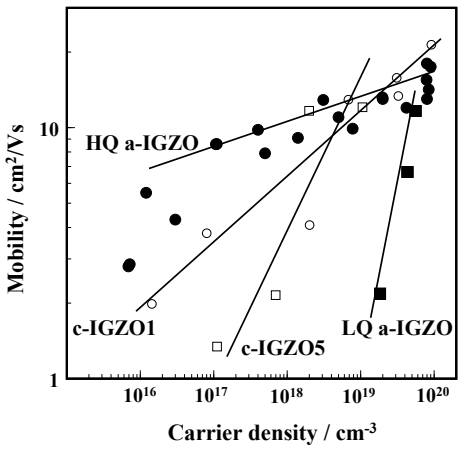

Fig. 38.3 Hall mobility versus electron density

conduction model, in which electron transport is controlled by distributed potential barriers above CBM [27].

The dominant factor of μ_{FE} is partly different from that of μ_{Hall} because μ_{FE} is expressed roughly by μ_{Hall} $(N_{ind} - N_{trap})/N_{ind}$, where N_{ind} is the total electron density induced by the gate voltage and N_{trap} is the density of the induced electrons trapped by subgap defects [2]. Therefore, low N_{trap} is important to obtain high μ_{FE}. It is confirmed by TFT analyses [28], C-V analyses [29, 30], etc. These studies have revealed that the subgap trap densities in AOSs are 2–3 orders of magnitude smaller than that of a-Si:H where E_F is close to CBM. The low trap density is explained also by the electronic structure specific to the strong iconicity of AOS as explained in Chap. 6. Figure 38.4 illustrates these electronic structures, which also shows reported defect states in the band gap of a-IGZO [2, 31].

38.5 Deposition Condition to Obtain Good AOS TFT

Figure 38.1 shows a typical (left) drain–source current (I_{DS}) − voltage (V_{DS}) characteristics at various gate biases (V_{GS}) (output characteristic) and (right) I_{DS} − V_{GS} characteristics at various V_{DS} (transfer characteristic) in comparison with those of a-Si:H TFT. It is seen that the on current (I_{on}) of a-IGZO TFT is two orders of magnitude larger than that of the a-Si:H TFT. In general, an OLED pixel requires several μA of driving current, indicating that only 5 V is enough for a-IGZO TFTs but 20 V is not satisfactory for a-Si:H TFTs. This is the reason why a-Si:H and organic TFT backplanes are not considered for practical OLED displays, and only oxide and poly-Si TFT backplanes are used. As explained above, a-IGZO TFTs easily attain high $\mu_{FE} > 10$ cm^2/(Vs), and I_{off} already reaches the measurement limit of $\sim 10^{-14}$ A and actually much lower than this value. In addition, the low operation voltage of a-IGZO TFT benefits also from the small subthreshold voltage swing (S value).

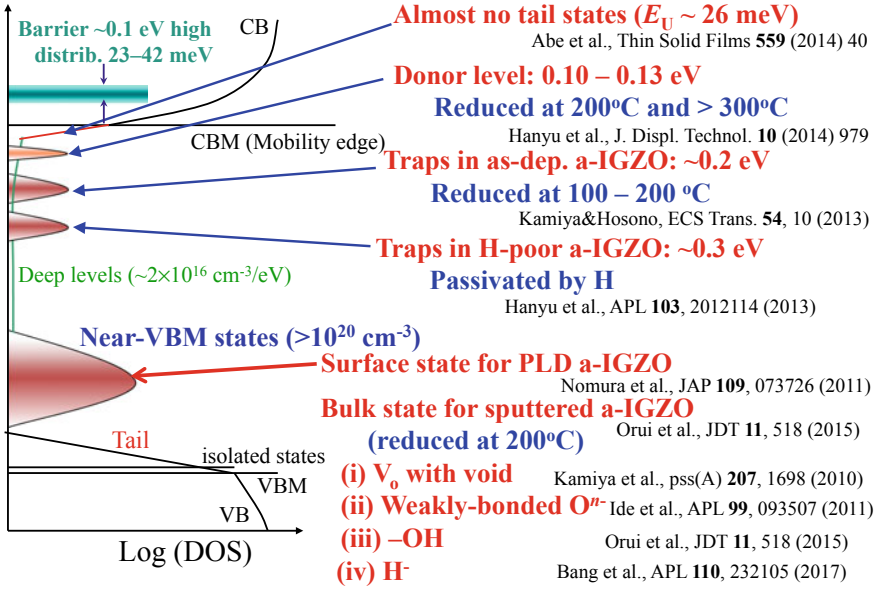

Fig. 38.4 Schematic electronic structure around the band gap of a-IGZO

To obtain such good TFTs, P_{O2} during film deposition is very important as seen in Fig. 38.5. It has been recognized that good TFTs are obtained with a-IGZO channels having the electrical conductivities 10^{-6}–10^{-3} S cm^{-1}, which corresponding to $N_e = 10^{12}$–10^{15} cm^{-3} upon supposition of $\mu_{Hall} = 10$ cm^2/(Vs). A key technology for producing practical TFTs is post-deposition thermal annealing. Although AOS TFTs operate with large $\mu_{FE} > 10$ cm^2/(Vs) even without substrate heating or thermal annealing; however, as seen in Fig. 38.6, unannealed TFTs exhibit serious non-uniformity issues as well as hysteresis and instability (V_{th} shift, ΔV_{th}). Post-deposition thermal annealing at 300–400 °C in air or O_2 improves the non-uniformity issues (Fig. 38.6d) [32, 33] and also the other issues. As explained above, a-IGZO TFTs deposited with the optimum condition (high-quality, HQ a-IGZO) operates with good μ_{FE}. On the other hand, that fabricated with off-optimized condition often causes poor operation characteristics as shown in Fig. 38.6b, but the poor characteristic is recovered to a good one comparable to Fig. 38.6a by the thermal annealing (Fig. 38.6c). However, although the resulting TFT characteristics appear similar, the annealed LQ a-IGZO still have high-density deep defects just above the VBM (near-VBM states) [34]; therefore, it is important to use the optimum condition so as to obtain high μ_{FE}, small S value, and V_{th} close to 0 V with minimum subgap optical absorption (corresponding to the density of the near-VBM states).

For depositing AOS films, other parameters should also be considered. It has been clarified that low total pressure (P_{tot}) produces higher density a-IGZO films and less-defective a-IGZO TFTs [35–37]. There is also a trend that higher RF/DC power is better [36]. These conditions (higher power, lower P_{tot}, smaller

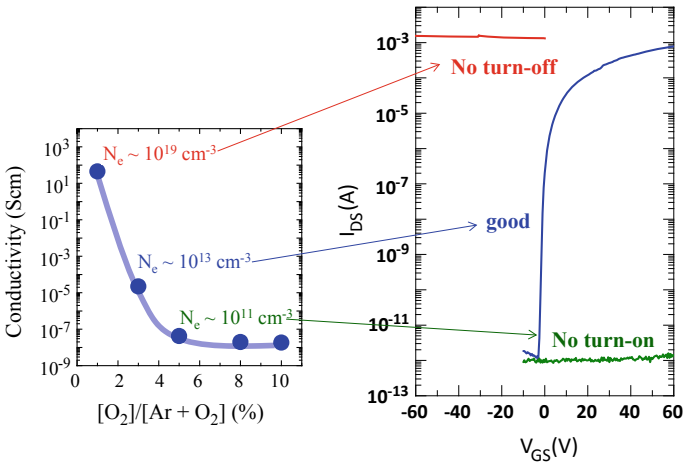

Fig. 38.5 Relationship among P_{O2}, conductivity (carrier concentration), and TFT characteristics

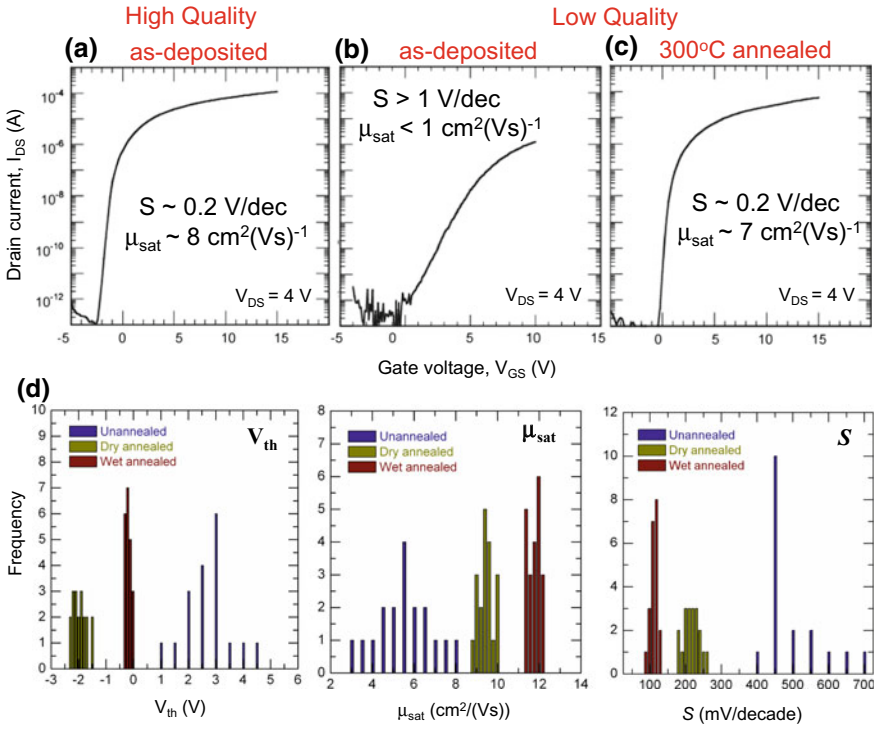

Fig. 38.6 Effects of post-deposition thermal annealing on **a**–**c** the performance and **d** uniformity of a-IGZO TFTs. For **d**, two thermal annealing, dry O_2 annealing, and wet O_2 annealing, are compared

substrate-target distance) appear to contradict with a common sense of plasma/sputtering depositions because these increases kinetic energy of deposition precursors and Ar^+ ions, and thus increase ion bombardment damage to the film. However, on the other hand, higher kinetic energy would be better to form a denser film, and the bombardment damage would be recovered by post-deposition thermal annealing for AOS films. Recent works have revealed that higher P_{tot} incorporates excess oxygen and Ar into a-IGZO films and causes low density [35, 37]. As for P_{O2}, too high P_{O2} also incorporate excess/weakly-bonded oxygen and create extra defects [38, 39]; therefore, P_{O2} during deposition should be tuned finely.

Another important issue to be considered is cleanness of deposition chamber and annealing system. As explained for Fig. 38.2, impurity hydrogen affects N_e and optimum P_{O2} very seriously. Further, the impurity hydrogen increases the near-VBM defects as –OH bonds [26]. For our conventional sputtering system, the optimum gas flow rate ratio, $R_{O2} = [O_2]/([O_2] + [Ar])$, is $\sim 3\%$, but is significantly reduced if ultrahigh-vacuum (UHV) sputtering system is employed [40] while increased if a dirty condition (poorer base pressure) is employed as seen in Fig. 38.2. This indicates that the optimum R_{O2} may be used as a measure of cleanness of deposition chamber and impurity hydrogen concentration. To date, it has been revealed that some hydrogens have good roles to reduce defects [41], but too many hydrogens cause extra instability [42].

38.6 Defects in AOSs (See Ref. [4] for the Latest Review)

As seen in Fig. 38.4, a-IGZO has very deep defects just above the valence band maximum (VBM, near-VBM states), which is observable by 6–8 keV excitation hard X-ray photoemission spectroscopy (HAXPES) [34, 43]. To date, various defects in AOSs have been clarified and proposed, which include (i) oxygen deficiency, (ii) weakly-bonded (wb-)/excess(ex-)/undercoordinated (uc-) oxygen, (iii) peroxide, (iv) low valence state cations, (v) hydrogen, and (vi) metastability due to flexible amorphous structure as summarized in Fig. 38.4 (references therein). These defects are related closely to TFT characteristics, hysteresis, and instability. Impurity H also have important roles on materials properties and TFT characteristics/stability as explained in the previous section. We have reported H works as shallow donors and exists mostly in the form of –OH bonds [25] while these donors are compensated by excess O (ex-O) in highly resistive, TFT-quality a-IGZO films [26]. More recently, a new chemical species of H, hydride ion H^-, was found experimentally [44]. Both the H states, $–O^{2-}H^+$ and $H^-@O^{2-}$, form shallow donor states and generate an electron each, while the latter is much thermally stable.

As for wb-/ex-O, if we employ a strong oxidation condition such as high R_{O2} during sputtering [39] and 300 °C O_3 annealing [38], a wb-/ex-O forms a bistable electron trap and produces a poor and unstable TFT. These two oxygen-related defects are formed under opposite fabrication conditions, and thus the optimum fabrication condition for AOS TFTs is limited in a narrow window.

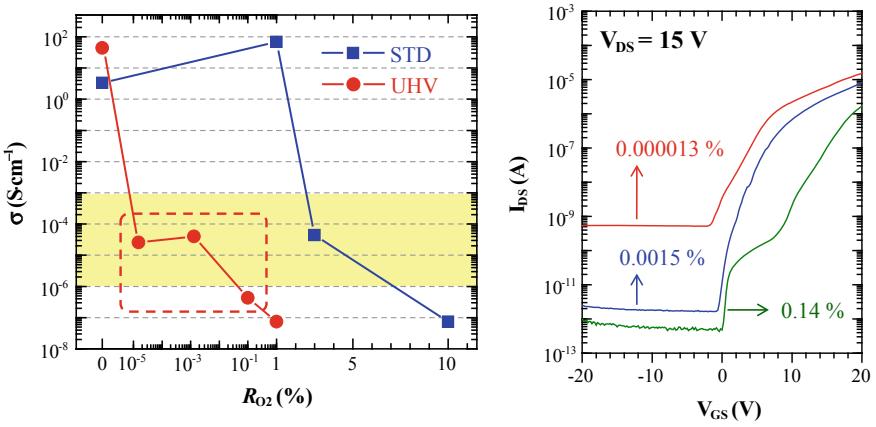

Fig. 38.7 Oxygen flow required for STD and UHV sputtered a-IGZO. (Left) Electrical conductivity and (right) transfer characteristics for STD and UHV sputtered a-IGZO films and channel TFTs

Hydrogen-related defects also have similar double-face behaviors [40–42]; some hydrogen causes TFT instability [42] while some passivate defects and improve TFT characteristics [41]. It should also be noted that the hydrogen impurity is related closely to excess oxygen because free electrons generated from hydrogen donors should be captured and compensated by incorporation of ex-O during film deposition or post-deposition annealing [25, 26]. This compensation effect by oxygen is more evident for the case of a-IGZO films deposited by ultrahigh vacuum (UHV) sputtering with the base pressure $\sim 10^{-7}$ Pa (Fig. 38.7). Conventional sputtering (STD) with the back pressure $\sim 10^{-4}$ Pa produces device-quality a-IGZO films and good TFTs if we control R_{O2} during sputtering at R_{O2} = 2.5–3.0% so that the electrical conductivity (σ) becomes 10^{-3}–10^{-6} S/cm. For the UHV sputtering case, this range of σ is obtained at very low $R_{O2} = 10^{-3}$–10^{-5}%, where operating TFTs can be fabricated. The big difference in the optimum R_{O2} is explained by impurity hydrogen ([H] > 10^{20} cm^{-3} for STD, while [H] is reduced to $\sim 10^{19}$ cm^{-3} [39]). This means that conventional sputtering for oxides, in usual, requires rather high R_{O2}, but most of the supplied oxygen is consumed to compensate the hydrogen impurity.

We also reported that high working pressure P_{tot} also introduces wb-/ex-O and causes deterioration of TFT operation and produces low-density a-IGZO films [35, 37]. It was considered that incorporation of ex-O and Ar would be an origin of the low film density, while more recent work revealed that the high P_{tot} condition enhances columnar growth with high-density nanopore structure [37] (Fig. 38.8). Both the films deposited at an optimum P_{tot} = 0.55 Pa (Fig. 38.8 (left)) and a very high P_{tot} = 5 Pa (center) have dense layers in the vicinity of the glass substrate surfaces, but then the growth mode changes to columnar-like one as observed by the increase in the surface roughness (Fig. 38.8 (right)). Even after the growth mode changes, the optimum a-IGZO keeps high-density structure, but the high P_{tot} film

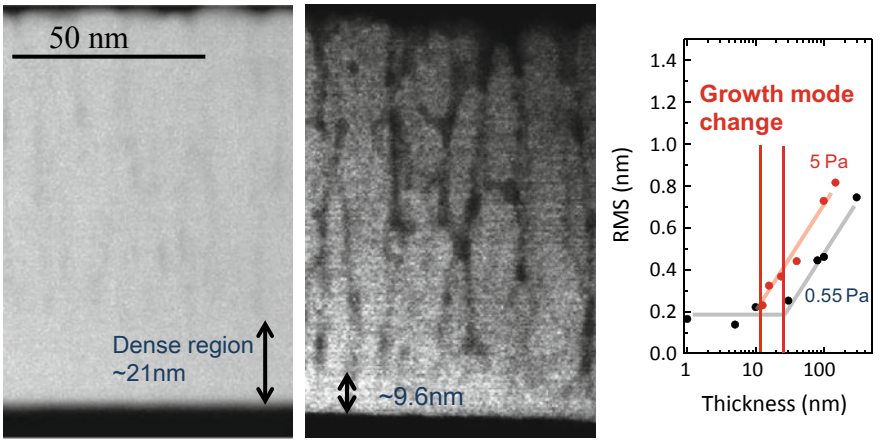

Fig. 38.8 STEM-HAADF images of a-IGZO films and growth mode change. Deposited at (left) optimum P_{tot} = 0.55 Pa and (center) high P_{tot} = 5 Pa. (Right) Surface roughness versus film thickness. Growth mode changes at the vertical lines indicated in the right figure

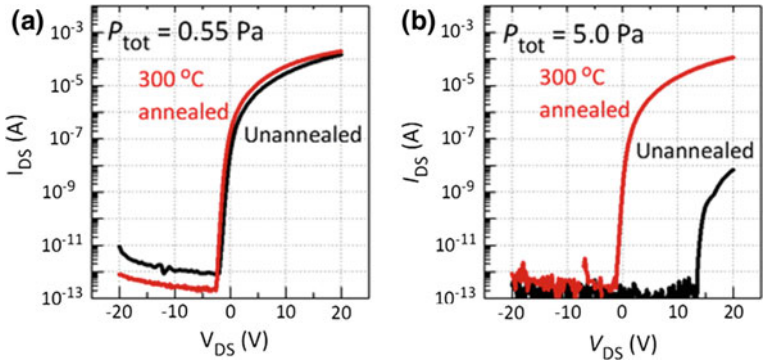

Fig. 38.9 Transfer characteristics of a-IGZO TFTs using a-IGZO channels deposited at different P_{tot}, **a** 0.55 and **b** 5.0 Pa

has high-density vertical nanopores and the film density is reduced drastically. Although TFTs using the high P_{tot} a-IGZO channel became to exhibit a reasonable performance after 300 °C annealing (Fig. 38.9), the nanopores were not annihilated by 300 °C annealing. It indicates that employing high P_{tot} should be avoided to obtain stable TFTs even if the static TFT characteristics will be better after annealing.

We should also notice that atomic-size nanovoids such as oxygen vacancy (oxygen deficiency with free space) would work as electron traps as suggested by DFT [22, 23]. A clear experimental evidence is shown in Fig. 38.10. The electrical resistivity decreases with decreasing P_{O2} during PLD deposition in the high P_{O2}

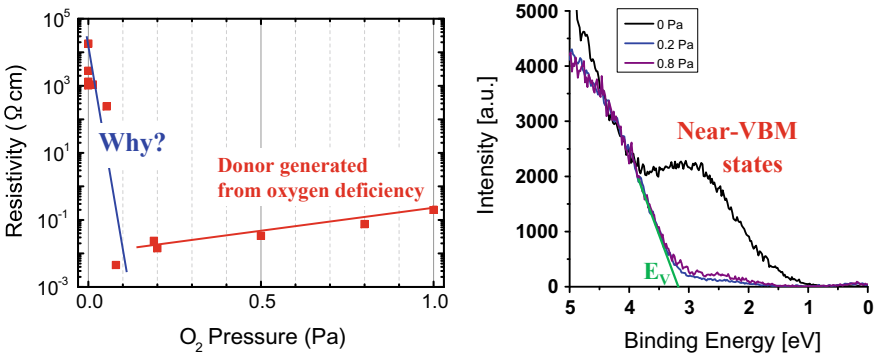

Fig. 38.10 Charge compensation in vacuum PLD-deposited a-IGZO. (Left) Resistivity versus P_{O2}. (Right) HAXPES spectra for $P_{O2} = 0$, 0.2, and 0.8 Pa. The a-IGZO films deposited in vacuum have a low density 6.01 g/cm^3

region as usually observed in oxide semiconductors. On the other hand, further decrease in P_{O2} below 1 Pa sharply increases the resistivity by several orders of magnitude (Fig. 38.10 (left)). Simultaneously, the formation of high-density near-VBM states is observed by HAXPES (Fig. 38.10 (right)). This can be explained that the low P_{O2} deposition produces oxygen-poor a-IGZO films and the oxygen deficiency would generate free electrons, but the free electrons are all captured by the near-VBM states, causing the perfect charge compensation.

38.7 Development of Amorphous GaO_x by Suppressing Charge Compensation

It is known crystalline β-Ga_2O_3 is a very wide band gap oxide semiconductor with the band gap ~4.9 eV. On the other hand, amorphous Ga–O (a-GaO_x) had never been converted to electronic conductor. As discussed for the high P_{O2} region in Fig. 38.10 (left), usual oxide semiconductors exhibit higher conductivity and higher electron densities at lower P_{O2}. However, for the case of a-GaO_x, the low P_{O2} condition including $P_{O2} = 0$ did not produce conducting films, which is similar to the insulating a-IGZO film in the low P_{O2} region in Fig. 38.10 (left); i.e., appropriate supply of O_2 reduced electron traps and increased electron density and conductivity. Similarly, supplying appropriate amount of O_2 reduced electron traps and realized electronic conduction also for a-GaO_x [45] (Fig. 38.11 (left)). This result reminds us of the importance of the charge compensation in particular for wide band gap semiconductors. As illustrated in the free electron density $N_e = n_0 \exp(-E_D/kT)$ and the trap density D_t relation in Fig. 38.11 (right), electron doping is realized when $N_e > N_t$. Conventional oxide semiconductors are easily doped to n-type and usually have high $N_e > 10^{19}$ cm^{-3}; therefore, the effect of D_t is usually

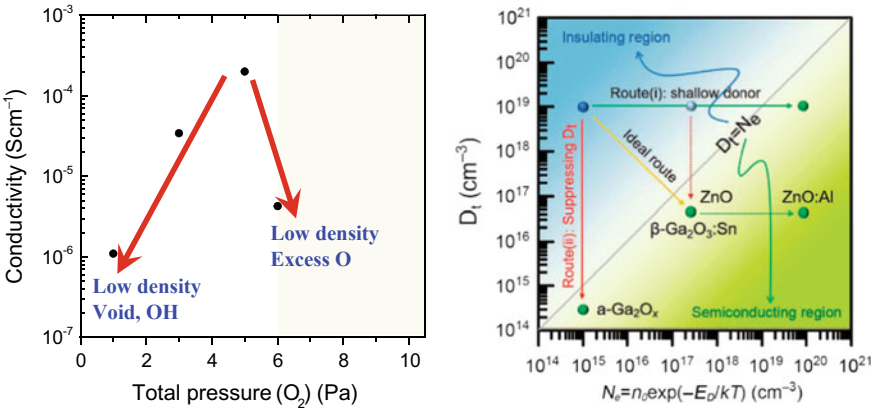

Fig. 38.11 Electrical properties of conducting *a*-GaO_x. (Left) Conductivity versus P_{O2}. (Right) Graph to explain doping region with respect to the doping density n_0 and trap density D_t

negligible. On the other hand, the donor level in a-GaO_x is deep, $E_D \sim 0.7$ eV from the CBM, N_e is only 10^{15} cm^{-3} at most at room temperature. This is the reason why the very trace $D_t \sim 10^{15}$ cm^{-3} is critical for a-GaO_x, and the electron doping was first attained by reducing D_t by increasing the deposition rate, optimizing P_{O2} in order to minimize electron traps due to V_O and ex-O.

References

1. T. Kamiya, H. Hosono, Oxide TFTs, in *Handbook of Visual Display Technology*, 2nd edn. (2016), pp. 1111–1144
2. T. Kamiya, K. Nomura, H. Hosono, Sci. Technol. Adv. Mater. **11**, 044305 (2010)
3. T. Kamiya, K. Nomura, H. Hosono, IEEE J. Display Technol. **5**, 273 (2009)
4. K. Ide, K. Nomura, H. Hosono, T. Kamiya, Phys. Status Solidi A **216**, 1800372 (2019)
5. R.L. Hoffman, B.J. Norris, J.F. Wager, ZnO-based transparent thin-film transistors. Appl. Phys. Lett. **82**, 733 (2003)
6. K. Nomura, H. Ohta, A. Takagi, T. Kamiya, M. Hirano, H. Hosono, Nature (London) **432**, 488–492 (2004)
7. M. Matsudai, S. Sato, K. Saito, Advanced sputtering technologies and targets for oxide semiconductor TFT, in *SID 2013 Digest*, 720 (2013)
8. A. Kloeppel, J. Liu, E. Scheer, Large area sputtered Al_2O_3 films for high mobility AM-TFT backplanes on PVD array system PiVot 55kVi^2, in *SID 2013 Digest*, 647 (2013)
9. M. Ito, M. Kon, C. Miyazaki, N. Ikeda, M. Ishizaki, Y. Ugajin, N. Sekine, IEICE Trans. Electron. **E90-C**, 2105–2111 (2007)
10. M. Ofuji, K. Abe, H. Shimizu, N. Kaji, R. Hayashi, M. Sano, H. Kumomi, K. Nomura, T. Kamiya, H. Hosono, IEEE Elect. Dev. Lett. **28**, 273–275 (2007)
11. S.I. Kim, C.J. Kim, J.C. Park, I. Song, S.W. Kim, H. Yin, E. Lee, J.C. Lee, Y. Park, in *International Electron Devices Meeting*, 15–17 Dec 2008. https://doi.org/10.1109/iedm.2008.4796617

12. I. Song, S. Kim, H. Yin, C.J. Kim, J. Park, S. Kim, H.S. Choi, E. Lee, Y. Park, IEEE Electron. Dev. Lett. **29**, 549–552 (2008)
13. Y.-L. Wang, L.N. Covert, T.J. Anderson, W. Lim, J. Lin, S.J. Pearton, D.P. Norton, J.M. Zavad, F. Ren, Electrochem. Solid State Lett. **11**, H60–H62 (2008)
14. T. Kawamura, H. Uchiyama, S. Saito, H. Wakana, T. Mine, M. Hatano, K. Torii, T. Onai, *Digest of International Electron Devices Meeting* 2008, 15–17 Dec 2008, pp. 1–4
15. H. Ozaki, T. Kawamura, H. Wakana, T. Yamazoe, H. Uchiyama, IEICE Electron. Exp. **8**, 225–231 (2011)
16. K. Kaneko, N. Inoue, S. Saito, N. Furutake, Y. Hayashi, *2011 VLSI Symposium*, 120 (2011)
17. T. Tanabe, K. Kusunoki, Y. Sekine, K. Furutani, T. Murakawa, T. Nishi, Yoshiharu Hirakata, H. Godo, J. Koyama, S. Yamazaki, K. Ozaki, T. Handa, M. Sakakura, *AM-FPD2011*, P-7 (2011)
18. J. Hong, E. Chan et al., in *SID 2014 Digest*, 793 (2014)
19. N. Hagood, L. Steyn, J. Fijol, J. Gandhl, T. Brosnihan, S. Lewis, G. Fike, R. Barton, M. Halfman, R. Payne, in *Proceedings of IDW'08*, 1345 (2008)
20. T. Nishijima, S. Yoneda, T. Ohmaru, M. Endo, H. Denbo, M. Fujita, H. Kobayashi, K. Ohshima, Y. Shionoiri, K. Kato, Y. Maehashi, J. Koyama, S. Yamazaki, in *SID 2012 Digest*, 583 (2012)
21. J.D. Oannopoulos, G. Luicovsky (eds.), *The Physics of Hydrogenated Amorphous Silicon* (Springer, 1984)
22. T. Kamiya, K. Nomura, H. Hosono, Phys. Status Solidi A **206**, 860–867 (2009)
23. T. Kamiya, K. Nomura, H. Hosono, Phys. Status Solidi A **207**, 1698–1703 (2010)
24. K. Nomura, T. Kamiya, H. Ohta, T. Uruga, M. Hirano, H. Hosono, Phys. Rev. B 75, 035212-1–5 (2007)
25. K. Nomura, T. Kamiya, H. Hosono, ECS J. Solid State Sci. Technol. **2**, P5–P8 (2013)
26. T. Orui, J. Herms, Y. Hanyu, S. Ueda, K. Watanabe, I. Sakaguchi, N. Ohashi, H. Hiramatsu, H. Kumomi, H. Hosono, T. Kamiya, J. Display Technol. **11**, 518–522 (2015)
27. T. Kamiya, K. Nomura, H. Hosono, Appl. Phys. Lett. **96**, 122103-1–3 (2010)
28. H.-H. Hsieh, T. Kamiya, K. Nomura, H. Hosono, C.-C. Wu, Appl. Phys. Lett. **92**, 133503-1–3 (2008)
29. M. Kimura, S.W.-B. Tam, S. Inoue, T. Shimoda, Jpn. J. Appl. Phys. **43**, 71–76 (2004)
30. M. Kimura, T. Nakanishi, K. Nomura, T. Kamiya, H. Hosono, Appl. Phys. Lett. **92**, 133512-1–3 (2008)
31. T. Kamiya, H. Kumomi, H. Hosono, Multiple origins of near-VBM defects and passivation effects in a-In-Ga-Zn-O, in *Proceedings of IDW'14*, 185 (2014)
32. H. Hosono, K. Nomura, Y. Ogo, T. Uruga, T. Kamiya, J. Non-Cryst. Sol. **354**, 2796–2800 (2008)
33. K. Nomura, T. Kamiya, H. Ohta, M. Hirano, H. Hosono, Appl. Phys. Lett. **93**, 192107-1–3 (2008)
34. K. Nomura, T. Kamiya, H. Yanagi, E. Ikenaga, K. Yang, K. Kobayashi, M. Hirano, H. Hosono, Appl. Phys. Lett. **92**, 202117-1–3 (2008)
35. J. Grochowski, Y. Hanyu, K. Abe, J. Kaczmarski, J. Dyczewski, H. Hiramatsu, H. Kumomi, H. Hosono, T. Kamiya, J. Display Technol. **11**, 523–527 (2015)
36. Y. Kikuchi, K. Nomura, H. Yanagi, T. Kamiya, M. Hirano, H. Hosono, Thin Solid Films **518**, 3017–3021 (2010)
37. K. Ide, M. Kikuchi, M. Ota, M. Sasase, H. Hiramatsu, H. Kumomi, H. Hosono, T. Kamiya, Jpn. J. Appl. Phys. **56**, 03BB03-1–5 (2017)
38. K. Ide, Y. Kikuchi, K. Nomura, M. Kimura, T. Kamiya, H. Hosono, Appl. Phys. Lett. **99**, 093507-1–3 (2011)
39. T. Kamiya, H. Hosono, ECS Trans. **54**, 103–113 (2013)
40. T. Miyase, K. Watanabe, I. Sakaguchi, N. Ohashi, K. Domen, K. Nomura, H. Hiramatsu, H. Kumomi, H. Hosono, T. Kamiya, ECS J. Solid State Sci. Technol. **3**, Q3085–Q3090 (2014)
41. Y. Hanyu, K. Domen, K. Nomura, H. Hiramatsu, H. Kumomi, H. Hosono, T. Kamiya, Appl. Phys. Lett. **103**, 2012114-1–3 (2013)

42. K. Domen, T. Miyase, K. Abe, H. Hosono, T. Kamiya, IEEE Electron Dev. Lett. **35**, 832–834 (2014)
43. K. Nomura, T. Kamiya, E. Ikenaga, H. Yanagi, K. Kobayashi, H. Hosono, J. Appl. Phys. **109**, 073726-1–8 (2011)
44. J. Bang, S. Matsuishi, H. Hosono, Appl. Phys. Lett. **110**, 232105-1–5 (2017)
45. J. Kim, T. Sekiya, N. Miyokawa, N. Watanabe, K. Kimoto, K. Ide, Y. Toda, S. Ueda, N. Ohashi, H. Hiramatsu, H. Hosono, T. Kamiya, NPG Asia Mater. **9**, e359-1–7 (2017)

Chapter 39
Electrode Formation Using Electrodeposition and Direct Bonding for 3D Integration

Tatsushi Kaneda, Hidetoshi Shinohara, Akiko Okada, Kaori Matsunaga, Shuichi Shoji, Mikiko Saito, Hiroshi Nishikawa and Jun Mizuno

Abstract This chapter describes a novel low-temperature Au–Au bonding method using nanoporous Au–Ag powder and vacuum ultraviolet irradiation in the presence of oxygen gas (VUV/O_3) pretreatment. The nanoporous powder, which was fabricated by dealloying Ag–Au alloy sheet, was used to form the bump structure on the Au substrate by simple filling process, while an Au-coated Si substrate was used as the chip. The VUV/O_3-treated bumps and chip were bonded under a bonding pressure of 20 MPa at 200 °C for 20 min in a vacuum atmosphere of 1 kPa. A ligament size of the nanoporous structure on powder surface was found to be grown dramatically during bonding process. The tensile strength reached 10.1 MPa which is 2.3 times higher than that without VUV/O_3 treatment. This suggests that organic contaminants on each ligament surface were effectively removed by VUV/O_3 treatment, and consequently, the diffusion of gold atoms in the nanoporous powder was significantly promoted to change into bulk structure. The proposed method will be highly a promising method for 3D-LSI and MEMS packaging. And, we investigated the composition, morphology, and dissolution behavior of an Au–Ag nanoporous structure formed by electrodeposition and dealloying. Formation of the films was carried out by changing the bath composition and the annealing temperature. The samples that were annealed at 50 °C before dealloying indicated a

T. Kaneda · H. Shinohara · A. Okada · S. Shoji
Waseda University, 3-4-1 Okubo, Shinjuku, Tokyo 169-8555, Japan

M. Saito · J. Mizuno (✉)
Research Organization for Nano & Life Innovation, Waseda University, 513 Waseda-tsurumakicho Shinjuku-ku, Tokyo 162-0041, Japan
e-mail: mizuno@waseda.jp

K. Matsunaga
Graduate School of Engineering, Osaka University, 2-1 Yamadaoka, Suita, Osaka 565-0871, Japan

H. Nishikawa
Joining and Welding Research Institute, Osaka University, 11-1 Mihogaoka, Ibaraki, Osaka 567-0047, Japan

Y. Setsuhara et al. (eds.), *Novel Structured Metallic and Inorganic Materials*, https://doi.org/10.1007/978-981-13-7611-5_39

finer nanoporous structure. This finer nanoporous structure is connected to the highest bond strength of the evaluated samples.

Keywords Flip chip bonding · Nanoporous powder · Vacuum ultraviolet · Low-temperature bonding · Electrodeposition · Dealloying

39.1 Introduction

Flip chip bonding technology has been widely accepted within microelectronics, including 3D-large-scale integration (LSI) [1, 2], optical device [3, 4], and micro electro mechanical system (MEMS) packaging [5, 6]. In the flip-chip bonding technology, metal bumps, which are formed on a substrate, are used to electrically connect between the chips. Hence, in comparison with a wire bonding technique, several advantages can be obtained by using the flip bonding, including reduction of interconnect delay and powder consumption because of the short wiring distance between chips and miniaturization of packaging area [7–9].

Various metals have been utilized as bump materials such as solder [1, 6, 10], Cu [2, 11, 12], Sn [13, 14], and Au [2, 3, 15, 16]. In particular, Au bumps have many advantages such as high conductivity and oxidation resistance [15, 16]. However, mechanical stress has been caused by different coefficients of thermal expansion (CTE) between the chips because Au–Au bonding has required high-temperature bonding process. To reduce the bonding temperature, several approaches have been reported recently, including material development of the bump itself [17, 18], as well as surface modification techniques such as plasma treatment [3, 19, 20]. Oppermann et al. proposed the nanoporous Au bump fabrication using electroplating and dealloying techniques and revealed that the fabricated bumps have highly reactive surface in nanoscale structure [17]. In our previous works, we proposed two kinds of low-temperature Au–Au bonding methods. One is a method using nanoporous powder bump [21]. In that work, novel nanoporous powder materials were prepared by dealloying Ag–Au alloy sheet and the bump structures were simply fabricated by filling resist holes with the prepared powders. The other is a method using vacuum ultraviolet irradiation in the presence of oxygen gas (VUV/O_3) [22–24]. Organic contaminations on the Au bumps were successfully removed by VUV/O_3 treatment, and low-temperature Au–Au bonding was achieved. The advantage of VUV/O_3 treatments is no ion bombardment damage compared to conventional plasma treatments.

In this study, we propose a novel low-temperature bonding method using nanoporous powder and VUV/O_3 pretreatment [25]. The overview of this bonding method is shown in Fig. 39.1 Nanoporous powder bump is fabricated by simple filling process. VUV/O_3 pretreatment was performed in order to increase bond strength without surface morphological damage.

Recently, developments in miniaturization and the high functionality of electronics packaging have been remarkable. Therefore, nanolevel control is required

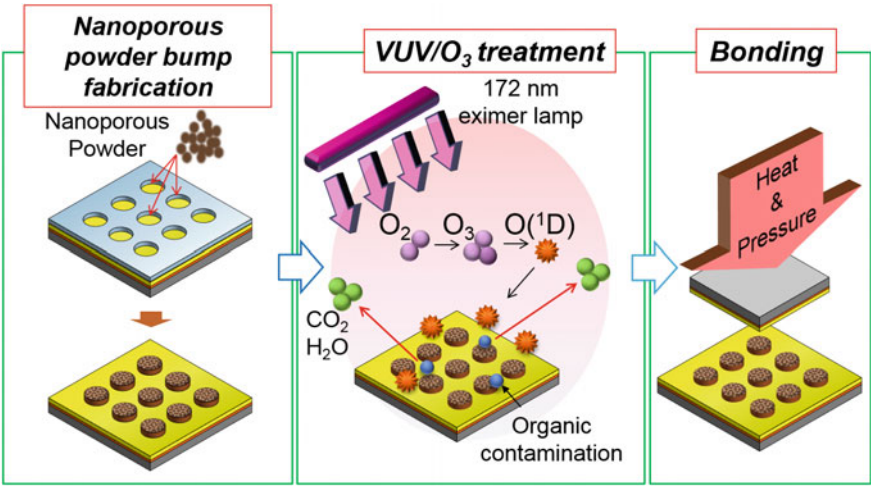

Fig. 39.1 Overview of bonding method in this study

for device formation. Electrochemical methods are used widely in electronics packaging because of the atomic-level control and the formation of thick materials with high aspect ratios. A sample of nanolevel electrode by electrodeposition is shown [26]. As another example for electrode formation using electrodeposition, TSV (Through-silicon via) technology has been investigated to raise packaging density. TSV technology has been used to three-dimensional packaging devices which draw electrodes out the backside through LSI chips, Si interposer, and the extracting electrodes of MEMS. The biggest problem of TSV technology is high producibility cost. Especially, at the process of plating, the quality of the films without voids and the high-speed plating time are needed. The cross-sectional image of Cu elec trodeposited TSV [27]. And, As an another technology using electrodeposition, there is an application for joining materials of Bump formation. Because of use these joining materials, metal nanoparticles are effective. Metal nanoparticles have been known to possess various properties that cannot be obtained in the bulk phase and expected to have applications in various fields, such as electronics and biotechnology [28–30]. Metal nanoparticles have achieved a low melting point and high chemical reactivity. Lower temperatures for some processes are expected when using nanosized particles. Au is applied to micro/nanoelectrochemical systems and biotechnology because it exhibits superior stability and conductivity over other metals. Dealloying is known to be the method to construct a nanoporous structure by selective etching of the poor metal from bimetals that consist of a noble metal and a poor metal [31, 32]. In the case of Au–Ag alloy films, the nanoporous structure was formed by dissolution of Ag and the formation of pores and the surface diffusion of Au [33]. An in situ scanning tunneling microscope (STM) was used to observe morphology changes [34]. The corrosion process leads to rough-ening of the surface by dissolution of Ag atoms

from terrace sites. The composition of Au–Ag corresponds to a critical potential, and this potential affects the porous structure [35]. In the formation of alloy films, sheets, arc melting, and electrochemical deposition have been reported [36, 37]. Electrochemical detection of hydrazine by using nanoporous gold has been reported. In this study, a solution containing sulfuric acid, thiourea, $HAuCl_4 \cdot 4H_2O$, and $AgNO_3$ was used. HNO_3 solution was used as a dealloying solution. Using a fabricated nanoporous Au electrode, the oxidation reaction of hydrazine was detected and the nanoporous Au electrode indicated greater stability [38]. On the other hand, we investigated low-temperature Au–Au bonding by using nanoporous Au–Ag sheets [38]. The strength of the Au–Au bond increased with the increase of the treatment temperature of the structure because of the diffusion of metals. The kinetic properties of the nanoporous structure for nanopore formation have been reported [39, 40]. However, the relation between the nanoporous structure and the formation process of metal has not been clarified. In this study, we attempted the formation of a nanoporous structure of Au–Ag films using the electrochemical method and dealloying process. We prepared the nanoporous structure on Cu pellets to investigate the bond strength. From these evaluations, we aimed to obtain the control and optimum morphology of the nanostructure [41].

39.2 Experimental Procedure

39.2.1 Fabrication of Nanoporous Powder

The fabrication process of the nanoporous powder is shown in Fig. 39.2. Here, we used an $Ag_{85}Au_{15}$ (atomic ratio) sheet as a base material [21, 42]. According to the powderization method reported in our previous work [43], the sheet was dealloyed in a 61 wt% (mass ratio) HNO_3 solution under ultrasonication for 15 min. The dealloying is a corrosion process in which the less novel metal of alloy is selectively removed by chemical or electrochemical means [44, 45]. Finally, the fabricated powder was rinsed in water and dried in atmosphere.

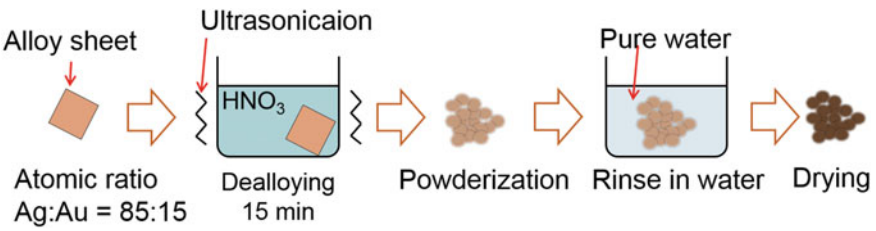

Fig. 39. 2 Fabrication process of nanoporous powder

39.2.2 *Fabrication of Nanoporous Powder Bump*

The fabrication process of the nanoporous powder bump is shown in Fig. 39.3 and proceeds as follows: (1) 50-nm-thick Ti and 300-nm-thick Au layer were deposited on a Si substrate using electron beam evaporation. (2) A 20-µm-thick dry film resist (H-Y920, Hitachi Chemical) was laminated on the Au-coated Si substrate. (3) Hole pattern was fabricated using photolithography. The diameter and pitch of hole pattern were 200 µm and 500 µm, respectively. The hole count on the chip was 100. (4) Organic contaminations on the Au surface were removed by O_2 plasma treatment. (5) Fabricated hole pattern was filled with nanoporous powder using a silicon scraper. (6) The sample was annealed to enhance adhesion of nanoporous powder to Au surface at 100 °C for 1 min. (7) Resist was removed by immersion in acetone, then bump pattern was obtained.

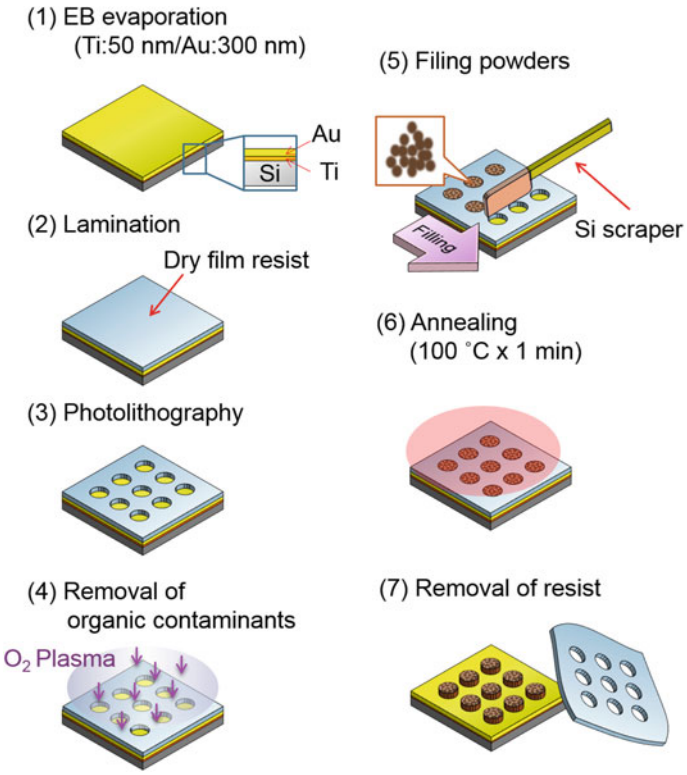

Fig. 39.3 Fabrication process of nanoporous powder bump

39.2.3 *VUV/O_3 Pretreatment*

The schematic image of the VUV/O_3 treatment system (UER 20-172, Ushio, Inc.) is shown in Fig. 39.4. The system consists of a lamp house and irradiation chamber. The VUV light has a central wavelength of 172 nm. The VUV light, which transmitted through the glass window of the lamp house, generated oxygen radical from oxygen and ozone in the irradiation chamber. The generated oxygen radicals cause breaking the chemical bonds and volatilization with organic contaminants of sample surface [22–24].

Table 39.1 shows VUV/O_3 pretreatment conditions. We selected the treatment conditions presented in our previous works [22, 24].

39.2.4 *Bonding Procedure and Evaluation*

The schematic image of bonding process is shown in Fig. 39.5a As a test vehicle for experiment, the Au-coated Si chip of 8 × 8 mm^2 and the substrate with nanoporous powder bump of 10 × 10 mm^2 were used. Table 39.2 shows its bonding conditions. For evaluation of bond strength and bump structure after bonding, tensile test and observation of fractured surface were performed, respectively.

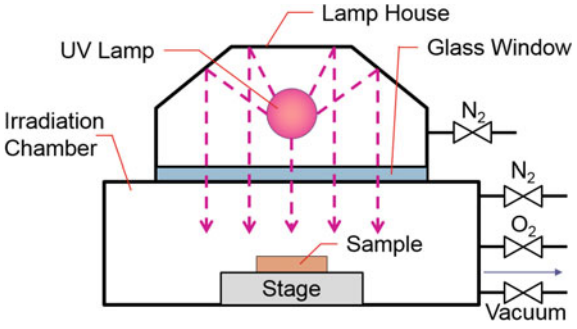

Fig. 39.4 Schematic image of VUV/O_3 treatment system

Table 39.1 VUV/O_3 treatment conditions

Lamp power	20 W
UV wavelength	172 nm
Light intensity	10 mW/cm^2
Exposure time	5 min
Temperature	Room temp.
Chamber pressure under oxygen gas	3.0 × 10^4 Pa

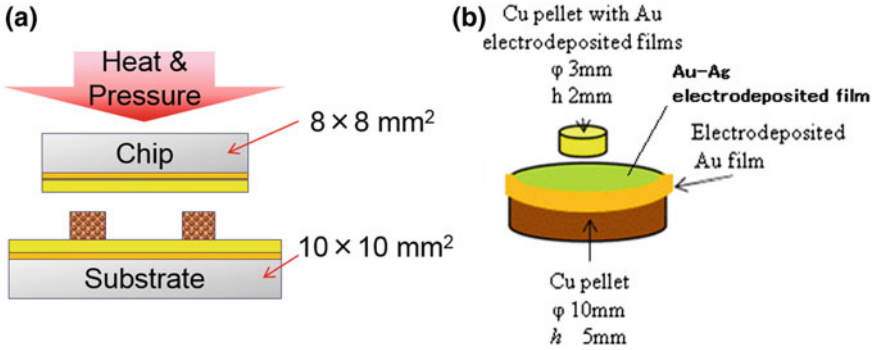

Fig. 39.5 **a** Schematic image of bonding process. **b** Schematic image of a sample for the evaluation of bond strength

Table 39.2 Bonding conditions

Applied pressure	20 MPa
Holding time	20 min
Temperature	200 °C
Chamber pressure	<1 kPa

39.2.5 Electrodeposition Procedure and Evaluation

Au or Pt seed layers were deposited on Si(111) wafers by sputtering. The thickness was 100 nm. Au–Ag films were electroplated at −0.7 V versus Ag/AgCl for 0.5 h by using an electrochemical analyzer (HZ-7000, Hokuto Denko). The Au–Ag bath composition is listed in Table 39.3. Field-emission scanning electron microscopy (FESEM S4800, Hitachi High-Technologies) was used to characterize the surface morphologies. The film composition was analyzed using inductively coupled plasma mass spectrometry (ICP-MS, Thermo Fisher Scientific). The schematic image of a sample for evaluation of bond strength is shown in Fig. 39.5b. To investigate bond strength, nanoporous Au–Ag films were deposited on a 10 mm φ disc with an electrodeposited Au film that had a thickness of 3 μm, and the 3-mm φ disc was set on it. The Cu-to-Cu disc joints with the deposited film were bonded at 350 °C for 30 min under 20 MPa in a nitrogen atmosphere.

Table 39.3 Bath composition

Chemicals	Concentration
$HAuCl_4 \cdot 4H_2O$	1 mM
$AgNO_3$	2 mM
Thiourea	0.2 M
H_2SO_4	0.01 M

39.3 Results and Discussion

39.3.1 Fabrication of Nanoporous Powder

Figure 39.6 shows a photograph of fabricated nanoporous powder. Sheet structure of $Ag_{85}Au_{15}$ alloy changed into powder structure (Fig. 39.6a). Furthermore, nanoporous structure was observed on the powder surface as shown in the scanning electron microscope (SEM) image (Fig. 39.6b). These results indicate that proposed process is effective for nanoporous powder fabrication.

39.3.2 Fabrication of Nanoporous Bump and VUV/O_3 Pretreatment

Figure 39.7 shows SEM images of fabricated nanoporous powder bump. Nanoporous powder bumps were successfully fabricated. Furthermore, nanoporous structure was observed on surface of nanoporous powder bump. Figure 39.8 shows SEM images of

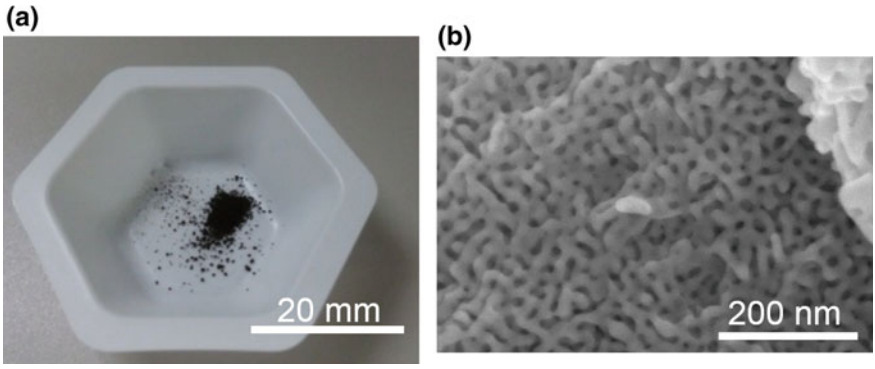

Fig. 39.6 **a** Photograph of nanoporous powder and **b** SEM image of nanoporous structure on nanoporous powder surface

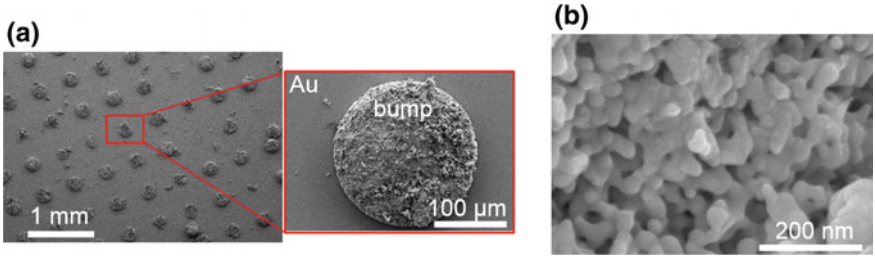

Fig. 39.7 SEM images of fabricated nanoporous powder bump: **a** whole and **b** magnified images

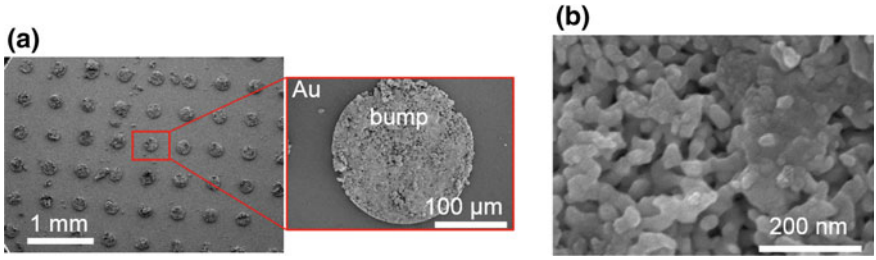

Fig. 39.8 SEM images of nanoporous powder bump after VUV/O_3 treatment: **a** whole and **b** magnified images

nanoporous powder bump after VUV/O_3 treatment. The nanoporous structure on the bump was maintained after VUV/O_3 treatment. This result indicates that VUV/O_3 treatment was possible to treat without destroying nanoporous structure.

39.3.3 Bonding Evaluation

Tensile strengths of untreated and VUV/O_3-treated samples were 10.1 and 4.4 MPa, respectively. Bulk destruction was observed on the fractured surfaces of both samples. Figure 39.9 shows SEM images of fractured surfaces of chip and substrate. Nanoporous structures were observed on each surface. On the other hand, the ligament size of VUV/O_3-treated sample (Fig. 39.9a, c) increased significantly compared with that of untreated one (Fig. 39.9b, d). The increase in ligament size indicates that the diffusion of gold atom was promoted during bonding process. The promotion of diffusion seems to be occurred by the VUV/O_3 treatment because organic contaminations on each ligament surface, which prevent diffusion from gold atoms, were decreased by the treatment [22]. Thus, bond strength of the VUV/O_3-treated sample increased compared with that of untreated one.

39.3.4 Preparation of the Nanoporous Au

Figure 39.10 shows the cyclic voltammetry of the solution for $HAuCl_4 \cdot 4H_2O$ and when thiourea is added the solution, respectively. Adding thiourea to the solution of $HAuCl_4 \cdot 4H_2O$ shifts the reduction potential in the direction of negative potential. This shift suggests that thiourea works as a complex reagent. Figure 39.11 shows the CV of the solution for $AgNO_3$ and the mix solution that is constituted by $HAuCl_4 \cdot 4H_2O$, $AgNO_3$, and thiourea. Compared with that of the solution of $AgNO_3$, the reduction potential of the mix solution shifted more negatively (from

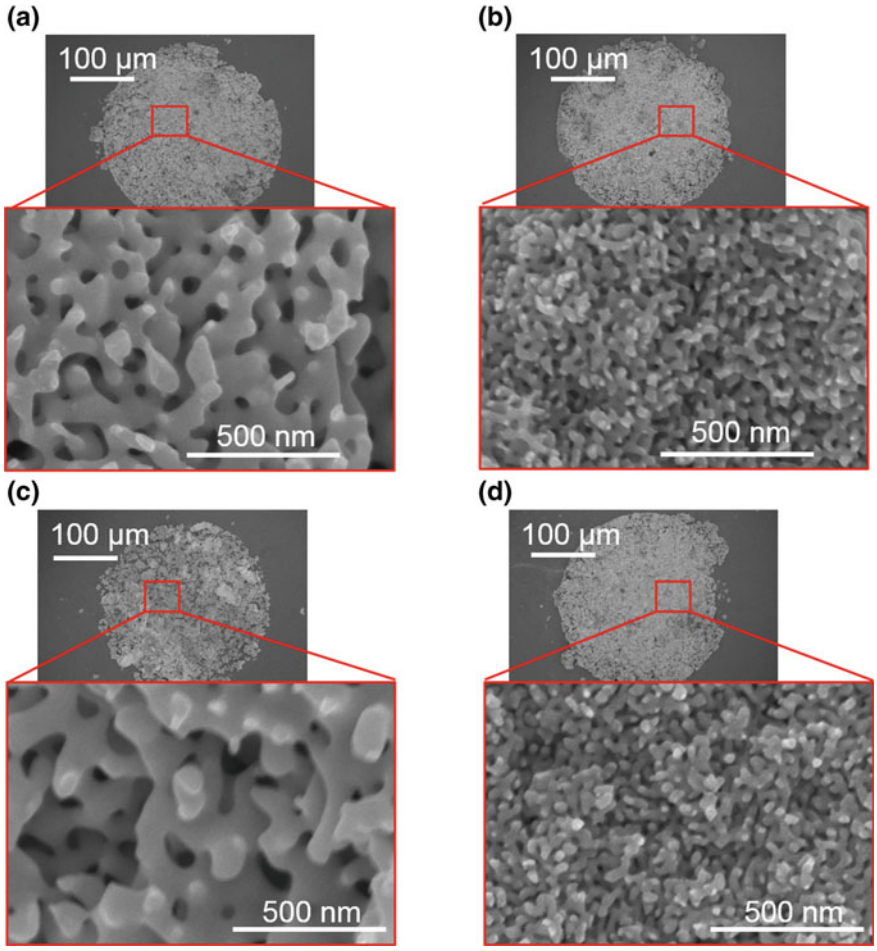

Fig. 39.9 SEM images of fractured surface of **a**, **b** chip and **c**, **d** substrate sides; **a**, **c** VUV/O_3 treated and **b**, **d** untreated samples

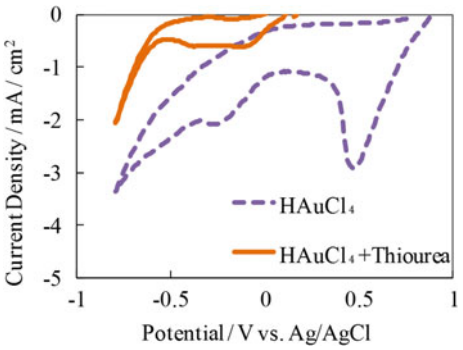

Fig. 39.10 Cyclic voltammograms for $HAuCl_4 \cdot 4H_2O$ and $HAuCl_4 \cdot 4H_2O$ + thiourea

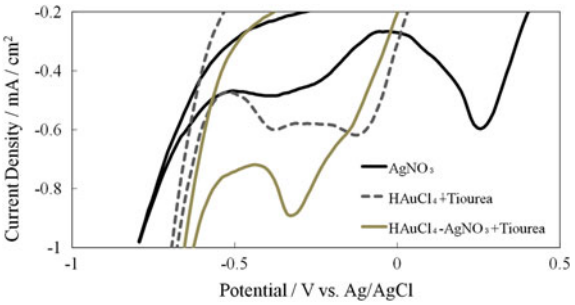

Fig. 39.11 Cyclic voltammetry for $AgNO_3$ and $HAuCl_4 \cdot 4H_2O$+ $AgNO_3$ + thiourea

+0.25 V to −0.32 V vs. Ag/AgCl). These results suggested that alloy films of Au–Ag would be formed. In the cyclic voltammetry measurements, a fixed potential of −0.7 V versus Ag/AgCl was applied to the electrode. The deposition time was selected at 0.5 h, resulting in a 0.15-μm-thick film. The Ag in the Ag–Au alloys could be selectively dealloyed by immersion in concentrated HNO_3 (60 wt%): H_2O = 2:1. To investigate the relation between temperature and the morphologies of nanoporous Ag–Au films, samples were treated at various temperatures. The composition results of the alloy films are shown in Fig. 39.12. The composition of as-deposited Ag–Au alloys was Ag_{68}-Au_{32}. After dealloying, the composition of Ag decreased from 68 to 65%. After annealing (50–100 °C), the composition of Ag became approximately 61 at.%. From the composition results, it was considered that the surface of the films are constituted by Au rich layer.

Figure 39.13 shows the anodic polarization curves for the Ag–Au films in 0.1 M HNO_3. The results reveal that the current density depends on the annealing temperature for the samples. The higher the temperature, the lower the current density. By doing annealing, the films morphology and the crystal status might be changed. Figure 39.14 shows the FE-SEM images of the samples on Si substrate with Au after dealloying. Figure 39.15 shows the FE-SEM images of the samples which are electrodeposited on Cu pellets. By annealing, ligament size became larger and each pore was isolated. In the case of samples on Cu pellets, the ligament size of a 50 °C

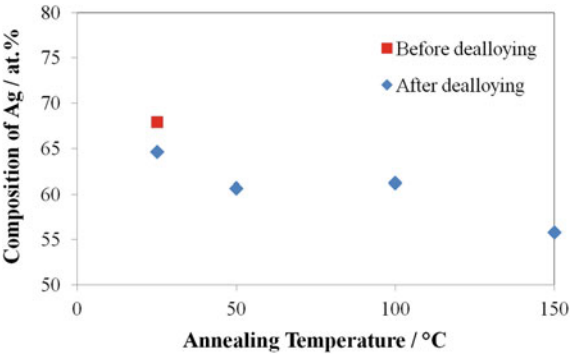

Fig. 39.12 Relation between annealing temperature and composition of Ag

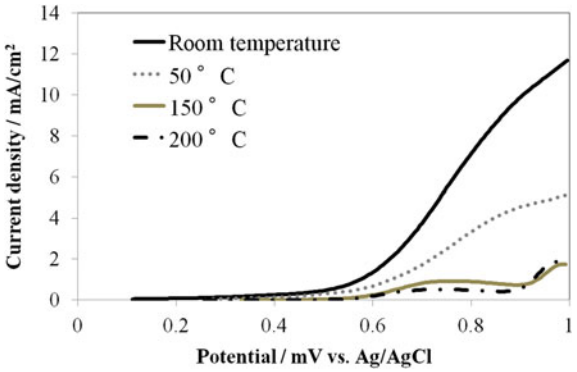

Fig. 39.13 Anodic polarization curves for the Ag–Au films in 0.1 M HNO_3

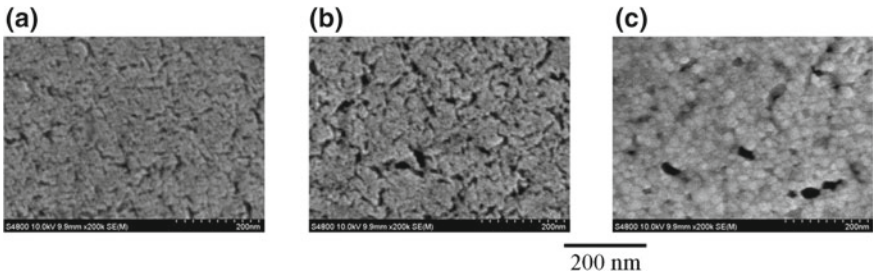

Fig. 39.14 FE-SEM images of the samples on Si substrate with Au after dealloying. **a** R. T. **b** 50 °C. **c** 150 °C

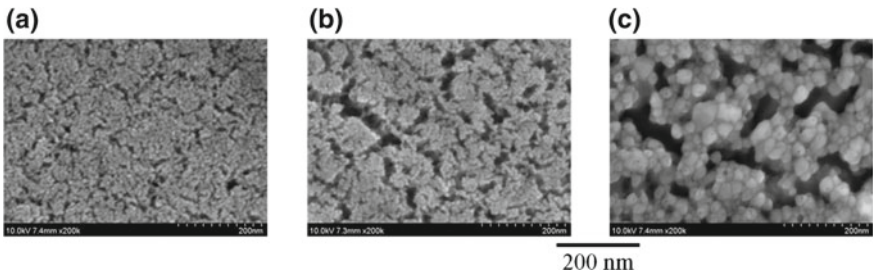

Fig. 39.15 FE-SEM images of the samples on Cu pellets after dealloying. **a** R. T. **b** 50 °C. **c** 150 ° C

sample was the same as that of a deposited sample. The size was under 10 nm. In the case of a 150 °C sample, the ligament size was larger. The size was 30–50 nm, and the pore size increased. It was assumed that this change of the morphology of the films resulted in the previous corrosion property.

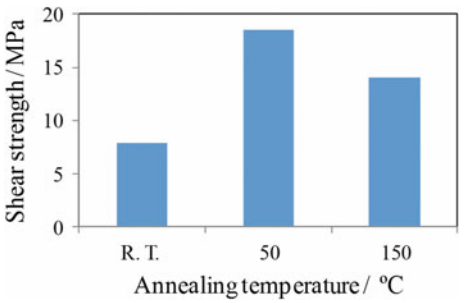

Fig. 39.16 Effect of process temperature on shear strength of a Cu-to-Cu joint under nitrogen atmosphere

39.3.5 Evaluation of Bond Strength

Figure 39.16 shows the results of the measurements for bond strength. From the results, the sample annealed at 50 °C indicated the highest bond strength of the examined samples.

The sample that was annealed at 50 °C before dealloying indicated a finer nanoporous structure, as observed from the FE-SEM images. This finer nanoporous structure connected to the highest bond strength of the examined samples. The results of anodic polarization measurements showed that the sample annealed at 50 °C exhibited high anodic current, except the as-deposited film. The composition of the as-deposited alloys did not drastically change before or after dealloying (Fig. 39.12), meaning selective etching occurred despite a high anodic current on the deposited film. The bond strength of the nanoporous structure depends on the pore size and ligament size.

39.4 Conclusions

In this study, we proposed a novel low-temperature Au–Au bonding method using nanoporous powder and VUV/O_3 pretreatment. A ligament size of the nanoporous structure on powder surface was found to be grown dramatically during bonding process. Tensile strength increased by using VUV/O_3 pretreatment, and highest tensile strength of 10.1 MPa was achieved even at the bonding temperature of 200 °C. The results indicate that removal of organic contaminations on each ligament surface by VUV/O_3 treatment promoted diffusion of gold atoms to change nanoporous bumps into bulk structure. Consequently, the proposed method is expected to be applied to 3D-LSI and MEMS packaging.

The morphology control of a nanoporous Au–Ag structure was investigated using electrochemical deposition and the electrochemical method. From the observation of the films, ligament size of electrodeposited Au-Ag films after dealloying became larger by annealing. The ligament size of 10–20 nm at as-deposited became 50–100 nm at 150 °C annealing. The samples that were

annealed at 50 °C before dealloying indicated a finer nanoporous structure. This finer nanoporous structure is connected to the highest bond strength of the evaluated samples. The volume of selective dissolution was small on as-deposited samples despite the anodic current being the largest of the examined films. ICP-MS analysis showed that the change of the composition of Ag of the films after dealloying on as-deposited samples indicated the smallest of the examined films. Small ligament size with a finer nanoporous structure leads to high bond strength.

Acknowledgements This work is partly supported by Japan Ministry of Education, Culture, Sports Science & Technology (MEXT) Grant-in-Aid for Scientific Basic Research (S) No. 23226010 and Scientific Basic Research (B) No. 2528924. The authors thank for MEXT Nanotechnology Platform Support Project of Waseda University.

References

1. K. Sakuma et al., 3D chip-stacking technology with through-silicon vias and low-volume lead-free interconnection. IBM J. Res. Dev. **52**(6), 611–622 (2008)
2. K. Takahashi et al., Ultra-high-density interconnection technology of three-dimensional packaging. Microelectron. Reliab. **43**(8), 1267–1279 (2003)
3. E. Higurashi, T. Imamura, T. Suga, R. Sawada, Low-temperature bonding of laser diode chips on silicon substrates using plasma activation of Au films. IEEE Photon Technol. Lett. **19**(24), 1994–1996 (2007)
4. K. Tadatomo et al., High output power InGaN ultraviolet light-emitting diodes fabricated on patterned substrates using metalorganic vapor phase epitaxy. Jpn. J. Appl. Phys. **40**(6B), L583–L585 (2001)
5. H.A.C. Tilmans, M.D.J. Van de Peer, E. Beyne, Indent reflow sealing (IRS) technique—a method for the fabrication of sealed cavities for MEMS devices. J. Microelectromech. Syst. **9** (2), 206–217 (2000)
6. K.M. Chu et al., Flip-chip bonding of MEMS scanner for laser display using electroplated AuSn solder bump. IEEE Trans. Adv. Packag. **30**(1), 27–33 (2007)
7. M.J. Wolf, G. Engelmann, L. Dietrich, H. Reichl, Flip chip bumping technology-status and update. Nucl. Instrum. Methods Phys. Res. A **565**(1), 290–295 (2006)
8. T. Braun et al., High-temperature reliability of flip chip assemblies. Microelectron. Reliab. **46** (1), 144–154 (2006)
9. V. Chidambaram, J. Hald, J. Hattel, Development of gold based solder candidates for flip chip assembly. Microelectron. Reliab. **49**(3), 323–330 (2009)
10. K.N. Tu, K. Zeng, Tin–lead (SnPb) solder reaction in flip chip technology. Mater. Sci. Eng. R. Rep. **34**(1), 1–58 (2001)
11. K. Tanida et al., Micro Cu bump interconnection on 3D chip stacking technology. Jpn. J. Appl. Phys. **43**(4B), 2264–2270 (2004)
12. L. Qiu et al., Room-temperature Cu micro joining with ultrasonic bonding of cone-shaped bump. Jpn. J. Appl. Phys. **52**(4), 04CB101–04CB105 (2013)
13. Z.G. Chen, Y.H. Kim, A new COP bonding using non-conductive adhesives for LCDs driver IC packaging. Displays **27**(3), 130–135 (2006)
14. S.M. Lee, B.G. Kim, Y.H. Kim, Non-conductive adhesive (NCA) trapping study in chip on glass joints fabricated using Sn bumps and NCA. Mater. Trans. **49**(9), 2100–2106 (2008)
15. K. Tanida et al., Au bump interconnection in 20 μm pitch on 3D chip stacking technology. Jpn. J. Appl. Phys. **42**(4B), 2198–2203 (2003)

16. M.M.V. Taklo et al., Strong, high-yield and low-temperature thermocompression silicon wafer-level bonding with gold. J. Micromech. Microeng. **14**(7), 884–890 (2004)
17. H. Oppermann, L. Dietrich, Nanoporous gold bumps for low temperature bonding. Microelectron. Reliab. **52**(2), 356–360 (2012)
18. Y.C. Lin et al., Nanoporous gold for MEMS packing applications. IEEJ Trans. Sens. Micromach. **133**(2), 31–36 (2013)
19. R. Takigawa, E. Higurashi, T. Suga, R. Sawada, Room-temperature bonding of vertical-cavity surface-emitting laser chips on Si substrates using Au microbumps in ambient air. Appl. Phys. Exp. **1**(11), 1122011–1122012 (2008)
20. E. Higurashi, D. Chino, T. Suga, R. Sawada, Au–Au surface-activated bonding and its application to optical microsensors with 3-D structure. IEEE J. Sel. Top. Q. Electron. **15**(5), 1500–1505 (2009)
21. H. Mimatsu et al., Study on low-temperature Au-Au bonding using nanoporous Au-Ag alloy powders as a joint layer, in *Technical Digest of the 20th Symposium on Microjoining and Assembly Technology in Electronics(MATE)* (Yokohama, 4–5 Feb 2014)
22. N. Unami, K. Sakuma, J. Mizuno, S. Shoji, Effects of excimer irradiation treatment on thermocompression Au-Au bonding. Jpn. J. Appl. Phys. **49**(6), 06GN121-06GN124 (2010)
23. K. Sakuma et al., Effects of vacuum ultraviolet surface treatment on the bonding interconnections for flip chip and 3-D integration. IEEE Trans. Electron. Packag. Manuf. **33**(3), 212–220 (2010)
24. A. Okada et al., Vacuum ultraviolet irradiation treatment for reducing Gold-Gold bonding temperature. Mater. Trans. **54**(11), 2139–2143 (2013)
25. T. Kaneda et al., (2015) Improved low temperature Gold-Gold bonding using nanoporous powder bump using vacuum ultraviolet irradiation pre-treatment, in *Proceedings of International Conference on Electronics Packaging and iMAPS All Asia Conference (ICEP-IAAC)* 2015 (Kyoto, 14–17 April 2015)
26. S.J. Yu, M. Fujimaki, K. Kawabe, H. Ohkubo, M. Hattori, Y. Ohki, M. Saito, Y. Wada, Development of a sub-micron processing method with ion implantation for the fabrication of optical communication devices. IEEJ Trans. Fundam. Mater. **125-A**(69) (2005)
27. M. Akazawa, K. Fujimoto, S. Kuramochi, K. Suzuki, M. Saito, in *The 27th Annual Conference* (The Japan Institute of Electronics Packaging, 15E09, 2013)
28. A. Pietrikova, E. Kapusanska, Kovove Mater. **29**(4), 262 (1991)
29. K. Mizugaki, K. Wada, K. Sakurada, T. Shintate, J. Yamada, T. Mikoshiba, N. Uehara, M. Yajima, J. Jan. Inst. Electron. Packag. **9**(7), 546–549 (2006)
30. M. Saito, J. Mizuno, H. Nishikubo, H. Fujiwara, T. Homma, Preparation of electrodeposited Pt nano patterned electrode using UV-nano imprinting lithography. ECS Trans. **16**, 131–136 (2008)
31. J. Erlebacher, M.J. Aziz, A. Karmer, N. Dimitrov, K. Sieradzki, Evolution of nanoporosity in dealloying. Nature **1410**, 450–453 (2001)
32. Z. Zhang, Y. Wang, Z. Qi, W. Zhang, J. Qin, J. Frenzel, Generalized fabrication of nanoporous metals (Au, Psd, Pt, Ag, and Cu). J. Phys. Chem. **113**, 12629–12636 (2009)
33. Y.K. Chen-Wiegart, S. Wang, I. McNulty, D.C. Dunand, Effect of Ag-Au composition and acid concentration on dealloying front velocity and cracking during nanoporous gold formation. Acta Mater. **61**, 5561–5570 (2013)
34. I.C. Oppenheim, D.J. Trevor, C.E.D. Chidsey, P.L. Trevor, K. Sieradzki, In situ scanning tunneling microscopy of corrosion of silver-gold alloys. Science **254**, 687–689 (1991)
35. K. Sieradzki, N. Dimitrov, D. Movrin, C. McCall, N. Vasiljevic, J. Erlebacher, The Dealloying Critical Potential. J. Electrochem. Soc. **149**, B370–B377 (2002)
36. M. Haokamada, Y. Chino, M. Mabuchi, Nanoporous surface fabricated on metal sheets by allying/dealloying technique. Mater. Lett. **64**, 2341–2343 (2010)
37. S. Parida, D. Kramer, C.A. Volkert, H. RÖsner, J. Erlebacher, J. Weissmüller, Volume change during the formation of nanoporous gold by dealloying. J. Phys. Lett. **97**, 035504-1–035504-4 (2006)

38. H. Mimatsu, J. Mizuno, M. Saito, T. Kasahara, H. Nishikawa, S. Shoji, Low-temperature Au-Au bonding using nanoporous Au-Ag sheets. J. Appl. Phys. **52**, 050204-1-3 (2013)
39. H. Siyu, L. Xinyu, L. Qingyu, M. Miamwu, L. Tengfa, W. Hongqiang, J. Zhiliang, The preparation of nanoporous gold electrodes by electrochemical alloying/dealloing process at room temperature and its properties. Mater. Lett. **64**, 2296–2298 (2010)
40. L.H. Qian, M.W. Chen, Ultrafine nanoporous gold by low-temperature dealloying and kinetics of nanopore formation. Appl. Phys. Lett. **91**, 083105-1-3 (2007)
41. M. Saito, K. Matsunaga, J. Mizuno, H. Nishikawa, in *5th Electronics System-Integration Technology Conference, ESTC 2014, Category Number CFP14TEM-ART*; Code 109411. Article number 6962819 (2014)
42. H. Mimatsu et al., Low-temperature gold-gold bonding using selective formation of nanoporous powders for bump interconnects, in *Proceedings of the 27th IEEE International Conference on Micro Electro Mechanical Systems (MEMS)* (San Francisco, 26–30 Jan 2014)
43. J. Erlebacher et al., Evolution of nanoporosity in dealloying. Nature **410**(6827), 450–453 (2001)
44. S. Parida et al., Volume change during the formation of nanoporous gold by dealloying. Phys. Rev. Lett. **97**(3), 035504-1–035504-4 (2006)
45. Y.H. Tan et al., Surface area and pore size characteristics of nanoporous gold subjected to thermal, mechanical, or surface modification studied using gas adsorption isotherms, cyclic voltammetry, thermogravimetric analysis, and scanning electron microscopy. J. Mater. Chem. **22**(14), 6733–6745 (2012)

Chapter 40
Carbon Nanotube Forests on SiC: Structural and Electrical Properties

Masafumi Inaba, Wataru Norimatsu, Michiko Kusunoki and Hiroshi Kawarada

Abstract Because carbon nanotube forest formed by surface decomposition of silicon carbide (CNT forest on SiC) is densely packed and vertically aligned with no entangle parts, it is useful to investigate the electrical properties of dense CNT forest. CNTs atomically bond to SiC substrates, causing good electrical contact for SiC power devices, where the Schottky barrier height is considerably low as $\sim$0.4 eV. CNTs contact with each other in dense CNT forest and contact conductance of CNT/CNT interface can be evaluated as $\sim 10^8$ S cm^{-2}. This value corresponds to the tunneling conductance between electron clouds of adjacent graphene sheets.

Keywords Carbon nanotube · Silicon carbide · Contact

40.1 Introduction

Carbon nanotubes (CNTs) have high one-dimensional current conductivity [1] and high thermal conductivity [2]. A dense forest of vertically aligned CNTs is advantageous for applying these properties because of its high CNT orientation. Although CNTs have the potential to withstand a very high current of up to $\sim 10^9$ A cm^{-2}, CNTs are generally used in applications with low conductance, such as CNT electrodes for biosensing [3], supercapacitors [4], and thin-film transistors [5]. Conversely, dense CNT forests are candidates for application in highly conductive devices such as power diodes and transistors. Densely packed CNT forests can be used to evaluate the electrical CNT contact. In this chapter, we evaluate the

M. Inaba (✉) · H. Kawarada
Faculty of Science and Engineering, Waseda University, 3-4-1 Okubo, Shinjuku, Tokyo 169-8555, Japan
e-mail: inaba-ma@ruri.waseda.jp

W. Norimatsu · M. Kusunoki
EcoTopia Science Institute, Nagoya University, Furo-cho, Chikusa, Nagoya, Aichi 464-8603, Japan

Y. Setsuhara et al. (eds.), *Novel Structured Metallic and Inorganic Materials*, https://doi.org/10.1007/978-981-13-7611-5_40

Schottky barrier height of the CNT/SiC interface and the contact conductivity of the CNT/CNT interface using a CNT forest formed by SiC surface decomposition. In Sect. 40.2, we introduce the CNT forest on SiC from the viewpoint of formation. In Sect. 40.3, the Schottky barrier height of the CNT/SiC interface is evaluated. In Sect. 40.4, the contact conductivity of the CNT/CNT interface is experimentally evaluated. We summarize this chapter in Sect. 40.5.

40.2 Formation of a CNT Forest on SiC

A CNT forest forms on SiC by surface decomposition [6]. At high temperatures above 1250 °C in vacuum, Si atoms at the surface of SiC are selectively attacked by chamber residual oxygen and sublimate as SiO. This has been confirmed by in situ transmission electron microscopy (TEM) observation [7]. The remaining carbon at the SiC surface first forms a lateral sp^2 structure, such as graphene flakes, and then a nanosized double-layer graphene dome structure [8–12]. The dome structures act as CNT caps, and CNTs with vertical walls grow as SiO sublimation proceeds. The lengths of the CNTs can be controlled by the treatment time because the decomposition ratio is relatively low. The CNTs have diameters of 5–20 nm from planar view TEM images [13]. Figure 40.1a and b show cross-sectional and planar TEM images of a CNT forest on SiC, respectively [14]. Double-wall CNTs were observed. Note that when the CNT length exceeded 500 nm as a result of long-term

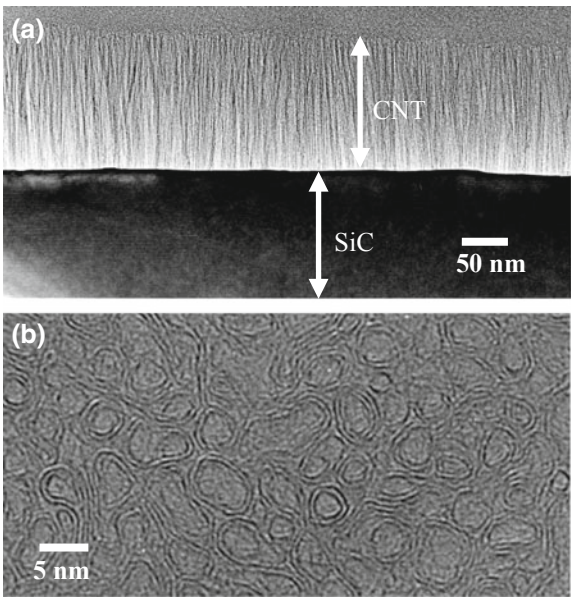

Fig. 40.1 **a** Cross-sectional view of CNTs on SiC with a CNT length of 100 nm obtained by high-resolution TEM. **b** Planar view of a CNT forest obtained by high-resolution TEM. Anfractuous graphene sheets exist between the tubes. Reproduced with permission from Ref. [14]. Copyright 2015, AIP Publishing LLC

decomposition, the quality of the subsequently formed underlayer became low and a graphite-like carbon layer formed.

The formed CNTs have zigzag chirality, which is confirmed by cross-sectional TEM diffraction patterns [15]. Zigzag-type CNTs have the chiral vector (n, 0), and they have both semiconducting and metallic properties. CNTs synthesized by catalyst chemical vapor deposition (C-CVD) tend to have near-armchair chirality, for example, (6, 5) and (7, 6) zigzag chirality. In addition, while CNTs synthesized by ordinal catalyst CVD are in weak contact with the catalyst or substrate, CNTs formed on SiC are atomically connected to the SiC substrate, which is advantageous for electrical applications. The contact area with the CNT is very small, and low contact resistivity is crucial.

40.3 Schottky Barrier Height of the CNT/SiC Interface

Wide bandgap semiconductors such as SiC, GaN, Ga_2O_3, and diamond have great potential for next-generation power devices. In particular, it is expected that SiC can be used for motor controlling inverters, where high current control with a high breakdown voltage is essential. However, it is difficult to form an electrical contact at SiC/metal interfaces because of the high Schottky barrier and formation of an amorphous carbon layer during high-temperature annealing. To overcome this difficulty, a heavily doped layer and a metal reactive layer are formed. Nickel silicide, which is widely used as a contact material for SiC, has a low Schottky barrier height of $\sim$0.4 eV (contact resistivity: 7×10^{-7} Ω cm^2) against n-type 4H-SiC [16], but its thermal conductivity is low, which causes poor heat dissipation from devices. CNT forest formation on SiC can be used in the SiC power device fabrication process. It is useful as an ohmic contact material for SiC. In this study, we measured the contact resistance and Schottky barrier height between the CNT forest and n-type 4H-SiC for application as a SiC ohmic contact [14, 17].

40.3.1 Experimental Model

The Schottky barrier height can be calculated from the relationship between the dopant density N_D and the contact resistivity ρ_C. The contact resistivity ρ_C is defined as

$$\rho_C = \left.\frac{dV}{dJ}\right|_{V=0}, \tag{40.1}$$

where V is voltage, and J is current density. Thus, it can be measured from the current–voltage characteristics. Note that the contact resistivity should be extracted from the slope near 0 V.

Figure 40.2 shows the experimental setup and its equivalent circuit. The current flows into the CNT forest and then into the SiC. The total resistance R_T is expressed as

$$R_T = R_{C,M/CNT} + R_{CNT} + R_{C,CNT/SiC} + R_{SiC} + R_{series}. \tag{40.2}$$

Here, $R_{C,M/CNT}$ and $R_{C,CNT/SiC}$ are the contact resistance of the metal electrode/CNT and CNT/SiC, and R_{CNT} and R_{SiC} are the CNT bulk and SiC bulk resistance, respectively. $\rho_{C,CNT/SiC}$ is the contact resistivity between the CNTs and the SiC substrate. The terms $R_{C,M/CNT}$, R_{CNT}, and $R_{C,CNT/SiC}$ are inversely proportional to the contact area S_{island}. Therefore, Eq. (40.2) can be rewritten as

$$R_T = \rho_{C,M/CNT/SiC} \Big/ S_{island} + R_{SiC} + R_{series}, \tag{40.3}$$

where

$$\rho_{C,M/CNT/SiC} = \rho_{C,M/CNT} + \rho_{CNT} l_{CNT} + \rho_{C,CNT/SiC}, \tag{40.4}$$

and $\rho_{C,M/CNT}$ is the metal electrode/CNT contact resistivity, ρ_{CNT} is the bulk CNT resistivity, l_{CNT} is the CNT length or CNT film thickness, and $\rho_{C,CNT/SiC}$ is the contact resistivity of the CNT/SiC interface. In the case where the terms $\rho_{C,M/CNT}$ and $\rho_{CNT} l_{CNT}$ are less than $\rho_{C,CNT/SiC}$, the contact resistivity of the CNT/SiC interface is extracted as the slope of the relationship between R_T and S_{island}.

The Schottky barrier height can be calculated from the contact resistivity. For a high dopant density, the contact resistivity is dependent on the barrier height and dopant density because the field emission contributes to carrier transfer. The contact resistivity of the CNT/SiC interface for high dopant density can be calculated by [18, 19]

$$\rho_C = \frac{k\sqrt{E_{00}}\cosh(E_{00}/kT)\coth(E_{00}/kT)}{qA^*T\sqrt{\pi(\Phi_B - (\Phi_C - \Phi_F))}} \exp\left(\frac{\Phi_B - (\Phi_C - \Phi_F)}{E_{00}\coth(E_{00}/kT)} + \frac{q(\Phi_C - \Phi_F)}{kT}\right), \tag{40.5}$$

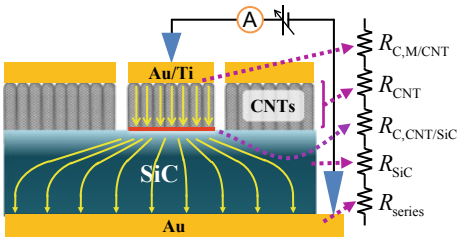

Fig. 40.2 Schematic diagram of the setup for electrical property measurement. The current paths are indicated by yellow arrows. Reproduced with permission from Ref. [14]. Copyright 2015, AIP Publishing LLC

where Φ_B is the Schottky barrier height, Φ_C is the conduction band level, Φ_F is the Fermi level of doped SiC, A^* is the Richardson constant, q is the elementary charge, k is the Boltzmann constant, T is the temperature, and E_{00} is the probability factor. E_{00} is given by

$$E_{00} = \frac{q\hbar}{2}\sqrt{\frac{N_D}{m^*\varepsilon_{SiC}}}, \tag{40.6}$$

where $\hbar$ is Planck's constant, m^* is the effective mass of an electron in SiC, and ε_{SiC} is the dielectric constant of SiC. Note that thermionic field emission (TFE) is predominant at a high doping density of approximately 10^{18} cm^{-3} and Eq. (40.5) holds in the case of TFE, where $E_{00} \approx kT$. Because the contact resistivity is a function of the Schottky barrier height and dopant density, the Schottky barrier height can be fitted from the relationship between the contact resistivity and the dopant density.

40.3.2 Device Fabrication

CNT forests were formed on (000 − 1) on-axis n-type 4H-SiC substrates by surface decomposition. The substrates were nitrogen doped at densities of (3×10^{16})—(8×10^{18}) cm^{-3} to become n-type with low resistivities of (5×10^{-1}) – (2×10^{-2}) Ω cm. They were annealed in vacuum at 1600 °C for 1 h (CNT length: 160 nm). As the top electrode, Au and Ti were deposited on the CNTs by magnetron sputtering. The formed CNT forests were nearly ideally packed with a surface density of $\sim 3 \times 10^{12}$ cm^{-2}. Electrically isolated contacts surrounded by trenches were formed using a focused ion beam (FIB), as shown in Fig. 40.3. The trenches surrounding the islands had a width of 500 nm and a depth of 350 nm.

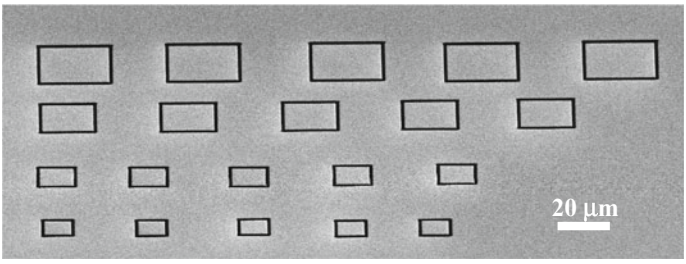

Fig. 40.3 Scanning electron microscopy image of islands formed by FIB from the 45°. The islands with sizes of 20 μm × 20 μm, 15 μm × 15 μm, and 10 μm × 10 μm are surrounded by 500-nm-wide trenches. Reproduced with permission from Ref. [14]. Copyright 2015, AIP Publishing LLC

40.3.3 Schottky Barrier Height

The current–voltage characteristics near zero voltage always showed a linear relationship, indicating that the contact was ohmic. The measured resistance R_T was calculated from the reciprocal of the slope of the current–voltage characteristics. We also examined the wide-range current–voltage characteristics from −3 to 3 V for an island size of 50 μm × 50 μm (Fig. 40.4). The inset of Fig. 40.4 shows the semilog plots. Two convex regions exist in each curve, as indicated by black arrows, which indicates that low and high barrier heights exist in the CNT/SiC contact. Similar results have been reported for a Ti/4H–SiC system [20]. These properties correspond to the existence of two Schottky barriers in contact, which will be discussed in Sect. 40.3.4.

Figure 40.5a shows the total resistance R_T plotted as a function of $1/S_{island}$ for 20 μm × 20 μm, 15 μm × 15 μm, and 10 μm × 10 μm islands and CNT lengths of 160 nm at each dopant density. Figure 40.5a1, a2 show plots and interpolated lines for dopant densities of 3×10^{16} and 5×10^{17} cm^{-3}, and 3×10^{18} and 8×10^{18} cm^{-3}, respectively. R_T linearly increases with increasing $1/S_{island}$, indicating that R_T depends on the CNT forest size. The R intercept obtained in the range 1.5–2.5 kΩ corresponds to the sum of the terms independent of S_{island} (i.e., R_{SiC} and $R_{serises}$).

The slope corresponds to $\rho_{C,M/CNT/SiC}$ in Eq. (40.4). It mainly originates from the contact resistivity at the CNT/SiC interface ($\rho_{C,CNT/SiC}$). The second term on the right-hand side of Eq. 40.4 should be proportional to the CNT length or the CNT film thickness (l_{CNT}). ρ_{CNT} is typically $\sim 10^{-4}$ to 10^{-2} Ω cm [21, 22] and l_{CNT} is of the order of 10–100 nm. Therefore, the term $\rho_{CNT} l_{CNT}$ is estimated to be of the order of 10^{-10}–10^{-7} Ω cm^2, which is 3–6 orders of magnitude lower than $\rho_{C,M/CNT/SiC}$, and thus negligible. Because the metal electrode/CNT interface is a metal/metal contact, the metal/CNT contact resistivity $\rho_{C,M/CNT}$ should be sufficiently small compared with the contact resistivity of the CNT/SiC interface $\rho_{C,CNT/SiC}$. Therefore, the CNT/SiC contact resistivity is $\sim 1.3 \times 10^{-4}$ Ω cm^2 at a

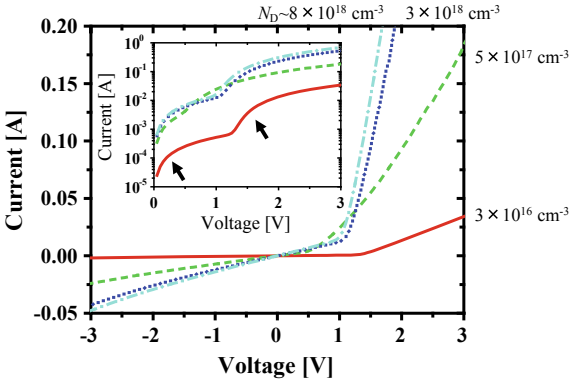

Fig. 40.4 Current–voltage characteristics determined by a probe for 50 μm × 50 μm islands at different dopant densities. The inset shows their semilog plots. Two convex regions exist in each curve, as indicated by black arrows, which indicates that low and high barrier heights exist in the CNT/SiC contact. Reproduced with permission from Ref. [14]. Copyright 2015, AIP Publishing LLC

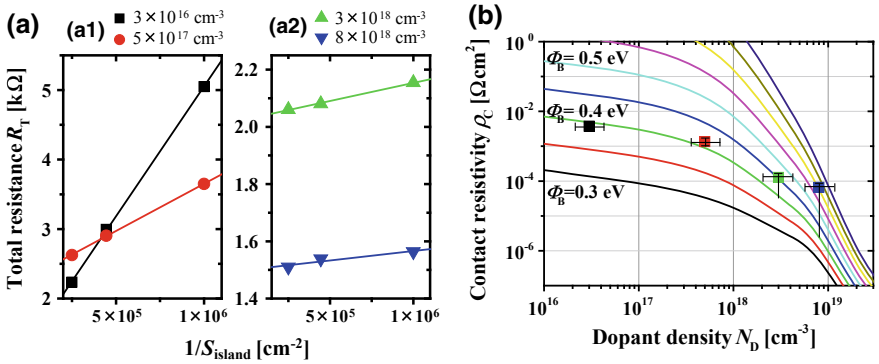

Fig. 40.5 **a** Total resistance R_T as a function of the reciprocal of the island area $1/S_{island}$ for different dopant densities. Plots and interpolated lines for dopant densities of **a1** 3×10^{16} and 5×10^{17} cm^{-3} and **a2** 3×10^{18} and 8×10^{18} cm^{-3}. **b** Contact resistivity ρ_C as a function of dopant density N_D, where the Schottky barrier heights are assumed to be from 0.3 to 0.7 eV at intervals of 0.05 eV. The plots correspond to the experimental results. Reproduced with permission from Ref. [14]. Copyright 2015, AIP Publishing LLC

dopant density of 3×10^{18} cm^{-3}. It mainly originates from the Schottky barrier at the CNT/SiC interface [14].

Figure 40.5b shows the relationship between $\rho_{C,CNT/SiC}$ and N_D. The lines correspond to the calculated result, where the Schottky barrier heights are assumed to be from 0.3 to 0.7 eV at intervals of 0.05 eV. When the dopant density is lower than 10^{18} cm^{-3}, the contact resistivity at each N_D falls on the line for Schottky barrier heights of 0.4–0.45 eV. When the doping concentration in the SiC substrate at the CNT/SiC interface increases to 10^{19} or 10^{20} cm^{-3}, field emission will dominate and the contact resistivity will rapidly decrease to $\sim 10^{-6}$ and $\sim 10^{-9}$ Ω cm^2 for dopant densities of 10^{19} and 10^{20} cm^{-3}, respectively. One of the lowest reported SiC/metal contact resistivities is of the order of 10^{-7} Ω cm^2, which was obtained with a Ni reactive layer [16]. The contact resistivity of CNTs with SiC has the potential to reach the same level or even lower, providing an ideal power device characteristic with high current density and thermal dissipation.

40.3.4 Model of the Low Schottky Barrier Height

The Schottky barrier height obtained in this study is compared with those in the literature. If the SiC/metal Schottky barrier height depended on the metal work function, the barrier height at the CNT/SiC interface would be estimated to be as high as 1.5 eV, where the CNT or graphene work function is 4.6–4.7 eV [23, 24]. This value is close to the Schottky barrier height between CNTs and 6H-SiC of 1.38 eV obtained by Maruyama et al. [25] using photoelectric spectroscopy.

However, Seyller et al. [26] obtained a barrier height of 0.3 eV at the graphene/6H-SiC interface using the same method as Maruyama et al. [25]. The Schottky barrier height estimated in the present work is approximately 1 eV less than that expected from the work function difference. This difference originates from the existence of two parallel Schottky barriers in the CNT/SiC system. In the inset of Fig. 40.4, there are two convex regions (indicated by black arrows), which indicate that low and high barrier heights exist in the CNT/SiC contact. In the CNT/SiC system, certain parts of the contact area have a low barrier height and other parts have a high barrier height. The barrier heights calculated by the Cheung method [27] at a dopant density of 3×10^{16} cm^{-3} are 0.52 and 1.07 eV. Although these values are slightly different from those in this study and the values report by Maruyama et al., the dual Schottky barrier well explains this difference. In electrical devices, the high barrier height indicated by photoelectron spectroscopy is usually higher than the effective electric barrier height. The effective contact resistivity is determined by the low barrier height estimated from the electrical properties.

A possible origin of this dual Schottky barrier is hydrogen termination of both the CNTs and the SiC C-face dangling bonds at the CNT/SiC interface. The carbon atoms of the CNTs and the SiC C-face edges are not connected. Only some of the vertical dangling bonds of the uppermost C–Si stack layer of the SiC C-face are connected to the carbon atoms of the CNTs, and others are terminated by hydrogen atoms. Similarly, part of the CNT edges is terminated by hydrogen atoms, which is confirmed by the secondary ion mass spectroscopy profiles [14]. Because the electronegativity of hydrogen (2.20) [28] is less than that of carbon (2.55), the hydrogen atoms in C–H bonds are positively charged by polarization. According to an ab initio study, the electron affinity of hydrogen-terminated CNT edges decreases by approximately 1 eV [29], leading to a 1 eV decrease of the CNT/SiC Schottky barrier height for electrons. However, the electron affinity of SiC edges also decreases if C–H bonds predominate, leading to an increase of the Schottky barrier height for electrons. Because the C-face SiC surface is not as smooth as before decomposition of SiC at 1600 °C, not only C–H termination but also Si–H termination exists. The electronegativity of silicon (1.90) is less than that of hydrogen (2.20). Therefore, Si–H bonds have the opposite polarity to C–H bonds [30], leading to an increase of the electron affinity and a decrease of Schottky barrier height for electrons. Figure 40.6 shows a schematic of the band diagram at the CNT/SiC interface. If the two opposite polarity effects on the SiC side cancel,

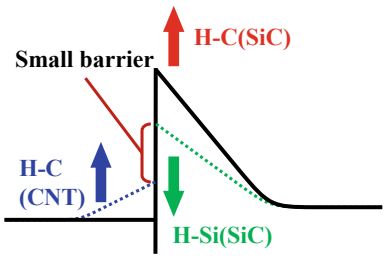

Fig. 40.6 Schematic diagram of the Schottky barrier at the CNT/SiC interface

the remaining effect of the dipole on the CNT side decreases the Schottky barrier height by 1 eV, as discussed above. The actual origin of the dual Schottky barriers should be investigated in the future. Contact materials for SiC with a low barrier height and high heat conductivity can be realized by applying appropriate contact conditions to obtain a suitable CNT/SiC interface.

40.4 CNT/CNT Contact Conductivity

For CNT forests formed by the catalyst-CVD method [31], although their distinctive properties are expected to be useful for very large-scale integrated vias [32, 33], supercapacitors [34–38], and so forth, many challenges must be overcome. For example, existence of voids and bundles, wavy parts, and entangled parts on their tops, existence of the metal catalyst as an impurity, and differentiation of CNT chiralities. A CNT forest formed on SiC is nearly ideally dense and highly uniform with no entangled parts on the top [6, 14]. This method is a non-catalytic method [39, 40] and only requires high-temperature annealing of the SiC substrate in vacuum. The CNT forest on SiC has only CNTs with zigzag chirality, which was confirmed by cross-section TEM diffraction by Kusunoki and Kato [41]. Norimatsu et al. reported the temperature dependence of the in-plane conduction of a CNT forest on SiC with caps [42]. In this study, we first investigated the in-plane conduction of an uncapped CNT forest on SiC as one of the electrical properties of a nearly ideally dense CNT forest. Second, we investigated the contact conductivity of the CNT/CNT interface from the in-plane conductivity of an uncapped CNT forest on SiC [43]. The in-plane conductivity of a dense CNT forest can be considered to be the aggregation of CNT/CNT contact conductances. Although some fluctuation exists in a dense forest, the obtained CNT forest conductivity should be useful for investigating the electrical properties of CNT/CNT contacts.

40.4.1 Sheet Conductivity

Low conductivity (under 10^{-8} S cm^{-1}) and C-face-polished 4H–SiC substrates were annealed at 1600 °C in vacuum. We assumed the conduction model shown in Fig. 40.7. There were assumed to be four conductive parts: the surface of the CNT forest (i.e., the CNT caps), the CNT bulk or the cylindrical part, the CNT/SiC interface, and the SiC bulk area. To identify the parts exhibiting conductivity, the CNT length (i.e., the CNT forest thickness) was varied in the range 30–350 nm by changing the decomposition time, and the sheet conductivity was measured by the van der Pauw method [44].

The variation of the sheet conductivity with the CNT length measured by the van der Pauw method is shown in Fig. 40.8. The red squares and red line correspond to the measured sheet conductivity, and the blue squares and blue line correspond to

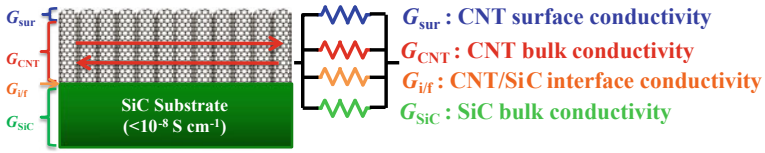

Fig. 40.7 Schematic diagram and equivalent circuit of a CNT forest on SiC. Reprinted with permission from Ref. [43]. Copyright 2016 American Chemical Society

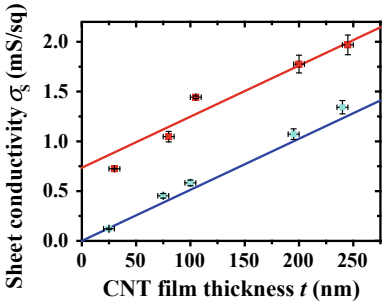

Fig. 40.8 Relationship between the sheet conductivity σ_S and the CNT film thickness t before and after mild oxidation by H_2O_2. The red squares and red line correspond to the data before oxidation. Blue circles correspond to the data after treatment. The blue line is the predicted line, whose slope is the same as that of the red line and whose intercept is zero. Reprinted with permission from Ref. [43]. Copyright 2016 American Chemical Society

the sheet conductivity after removing the CNT caps, which will be discussed later. The sheet conductivity increases with increasing CNT forest height. The sheet conductivity extrapolated to a CNT length of zero has a positive value. If this sheet conductivity was only from the CNT bulk region, the relation would be proportional and the intercept would be zero. This indicates the existence of conduction of other parts, that is, the CNT forest surface, CNT/SiC interface, and SiC bulk region. We assumed the existence of four conducting parts. The total conductance G_{total} can be expressed as

$$G_{total} = G_{sur} + G_{CNT} + G_{i/f} + G_{SiC}. \tag{40.7}$$

where G_{sur} is the in-plane conductance of the CNT surface region (i.e., the CNT caps), G_{CNT} is the in-plane conductance of the CNT bulk region, $G_{i/f}$ is the in-plane conductance of the CNT/SiC interface, and G_{SiC} is the in-plane conductance of the SiC bulk region. The CNT forest surface has a small plane composed of CNT caps and may exhibit conduction. The CNT/SiC interface was formed under very high-temperature vacuum conditions, so the interface may exhibit conduction.

To specify the possible conduction part(s) that corresponds to the intercept in Fig. 40.8, we removed the CNT surface region to remove conduction of the CNT cap region. The samples were treated in 15 wt% hydrogen peroxide solution at 100 °C for 3 h [45], and as a result, the CNTs were shortened by about 5 nm. From the Raman spectrum of the shortened CNTs, there was no significant damage because the intensity ratio of the G-peak to the D-peak did not change in the Raman spectrum. The measured sheet conductivity of the open-ended CNTs as a function of the CNT film thickness corresponds to the blue squares and line in Fig. 40.8. The sheet conductivity after etching is nearly proportional to the CNT length, and the intercept corresponds to the conductivity of the CNT cap region.

One possible origin of the conduction of the cap region is the existence of a graphene structure on top of the CNT forest on SiC. The sheet resistivity of a single-layered graphene sheet has been reported to be around 1 kΩ sq^{-1} [46–48]. Although the sheet conductivity of graphene depends on the existence of grain boundaries, wrinkles, and the conditions, the order of the sheet conductivity of the CNT cap region corresponds to that of graphene. This graphene structure is expected to have formed during the decrease in temperature after high-temperature annealing in the CNT formation process. During the temperature decrease, a small amount of gas may have leaked into the chamber, changing the top layer of the CNTs to the graphene structure. However, the graphene structure on the top layer of the CNTs was not observed, and further investigation is required.

40.4.2 CNT/CNT Contact Conductivity

The in-plane conductivity of the bulk CNT forest on SiC (σ_0) is estimated to be 50 S cm^{-1} from the slope of Fig. 40.8, which is two to three orders of magnitude lower than the conductivity of a CNT yarn [49]. This means that the CNT/CNT contact conduction is the dominant factor determining the CNT forest in-plane conduction, and the CNT on-axis conduction is much higher than the contact conductivity.

The in-plane conduction of the CNT bulk can be described as a series of contact conductances. To estimate the contact conductivity of the parallel adjacent CNTs, we assumed three approximations. First, the CNTs have the same diameter and are densely packed in a hexagonal pattern. Second, the CNT/CNT contact conductivity is the same for CNTs with the same diameter. Third, the CNT conductance is much higher than the CNT/CNT contact conductance. Based on these approximations, the CNT forest can be described as the netlike circuit in Fig. 40.9a, where each wire corresponds to a CNT/CNT contact path and each node corresponds to a CNT. Note that double-walled CNTs are dominant in the CNT forest, and the inner CNTs can be ignored because of the third assumption. The inner CNTs only contribute to the conductance of the CNTs. In the case of a CNT forest on SiC, the CNTs should be considered to be metallic owing to their large diameters [50]. Even though the chirality is semiconducting, the bandgap should be smaller for larger diameter CNTs [51]. The contact conductivity of a semiconducting/semiconducting or

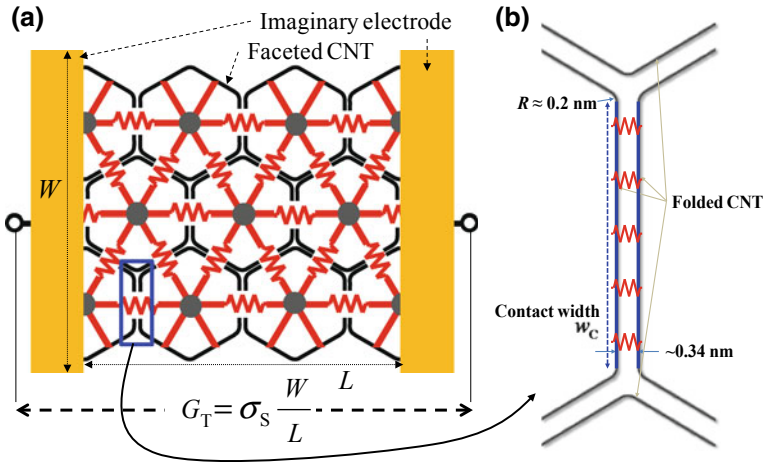

Fig. 40.9 **a** Approximated resistance network of parallel adjacent CNTs with a CNT width and interval of W and L, respectively. Each red wire indicates a CNT/CNT contact conductance $g_{C,CNT/CNT}$ and each node corresponds to a CNT. The total conductance G_T is expressed by Eq. (40.9). **b** Schematic diagram of the microscopic faceted CNT contact. Reprinted with permission from Ref. [43]. Copyright 2016 American Chemical Society

semiconducting/metallic contact should be lower than that of a metallic/metallic contact. The CNT/CNT contact conductivity normalized by the CNT film thickness t (CNT contact length) and contact width w_C is given by the following equations. The total conductance G_T [S] in terms of the contact conductance between each pair of CNTs $g_{C,CNT/CNT}$ [S] is given by

$$G_T = \sqrt{3}\frac{W}{L} g_{C,CNT/CNT} = \sqrt{3}\frac{W}{L}\sigma_{C,CNT/CNT} w_C t, \tag{40.8}$$

where W is the forest width, L is the distance between the electrodes, and $\sigma_{C,CNT/CNT}$ [S cm^{-2}] is the CNT/CNT contact conductivity per unit area. The total conductance G_T in terms of the sheet conductance σ_S is given by

$$G_T = \frac{W}{L}\sigma_S = \frac{W}{L}\sigma_0 t. \tag{40.9}$$

Finally, $\sigma_{C,CNT/CNT}$ is given by

$$\sigma_{C,CNT/CNT} = \frac{\sigma_0}{\sqrt{3} w_C}. \tag{40.10}$$

The CNT vacancies in a forest do not strongly affect the estimation of the contact resistivity or conductivity. To obtain $\sigma_{C,CNT/CNT}$, it is important to estimate the CNT/CNT contact width w_C. CNTs with large diameters should have a large

contact width. Although thin CNTs maintain their circular shape in the cross-section view, thick CNTs are faceted and adhere to each other as a result of changes in their cross-sectional shape [52–57]. This is because the energy of adhesion to the inside of the CNT exceeds the energy necessary to bend the CNT sheet (graphene). In particular, Tersoff and Ruoff [53] and Lopez et al. [54] reported that CNTs with a large diameter in a bundle are flattened in the areas where they are in contact with each other and are "polygonized" under van der Waals attractions from both theoretical and experimental aspects. In a CNT bundle or forest, CNTs that are parallel and adjacent to each other should have a deformed cross-section, in which the CNTs are in contact with each other over a larger area than in the case of a perfectly circular cross-section. For single-walled CNTs, the minimum curvature radius is ~0.2 nm [55]. For double-walled and multi-walled CNTs, the minimum curvature radius should be larger than that of a single-walled CNT. Figure 40.9b shows a schematic diagram of a microscopic faceted CNT contact. For large-diameter CNTs, the maximum contact width is estimated to be $\pi(D/2 - 0.1)/3$ nm, where D is the CNT diameter when the cross-section is circular. Assuming a CNT diameter D of 5–20 nm, the contact conductivity is in the range (0.3–1.2) × 10^8 S cm^{-2}, which corresponds to a contact resistivity of (0.8–3.6) × 10^{-8} Ω cm^2.

40.4.3 CNT/CNT Tunneling Conductivity

To verify the CNT/CNT contact conductivity, we calculated the tunneling conductance of a graphene/graphene interlayer system. The tunneling current density J_T [A cm^{-2}] is given by [58]

$$J_T = \left(\frac{q^2 V}{h^2 d_T}\right)\sqrt{2m_e\varphi}\exp\left(-\left(\frac{4\pi d_T}{h}\right)\sqrt{2m_e\varphi}\right), \tag{40.11}$$

where q is the elementary charge, V is the applied voltage, h is Planck's constant, d_T is the tunneling distance, m_e is the electron (effective) mass, and ϕ is the barrier height. This equation is for the case of $V \approx 0$. Note that the tunneling current is not affected by the density of states of the CNTs, because the CNTs in this study can be considered to be metallic. The tunneling contact conductance per unit area σ_{TC} [S cm^{-2}] is given by

$$\sigma_{TC} = \frac{J_T}{V} = \frac{q^2}{h^2 d_T}\sqrt{2m_e\varphi}\exp\left(-\left(\frac{4\pi d_T}{h}\right)\sqrt{2m_e\varphi}\right). \tag{40.12}$$

Graphene sheets are weakly connected by van der Waals forces, and the region between the sheets is assumed to be a vacuum [59]. We assumed that $m_e = m_0$ (electron mass) and ϕ = 5.0 eV [59]. In the CNT/CNT contact, d_T corresponds to the tunneling distance between the π electron clouds on the contact area of the

graphene sheets. From the relationship between the tunneling distance and the contact conductance, d_T = 0.24– 0.31 nm is suitable, which is indeed lower than the graphite interlayer distance ($\sim$0.34 nm). We also compared the results of our study with the theoretical results of Yoon et al. [60], who showed the calculated relationship between the intertube conductance and the contact distance. When the contact distance decreases by 0.7 Å, the intertube conductance increases by one order of magnitude. The conductivity of the CNT/CNT parallel contact of (0.3–1.2) $\times$ 10^8 S cm^{-2} is consistent with the tunneling contact conductivity. This result may also be useful for graphene/graphene interlayer contacts. Note that the in-plane conductivity of a graphene sheet composed of a few layers changes by one order of magnitude by changing the stack conditions [61]. For a CNT forest on SiC, the graphene sheets making up the CNT walls should be randomly stacked and may have low conductivity. Further study is required to investigate the electrical properties of the graphite interlayer.

40.5 Conclusion

The electrical contact of CNT/SiC and CNT/CNT interfaces was investigated using a CNT forest on SiC. The CNT forest was formed by SiC surface decomposition at high temperature in vacuum. Because the CNT forest on SiC is densely packed and well oriented, it is useful to evaluate the electrical contact. The CNT/SiC contact resistivity and Schottky barrier were measured from the relationships between the total resistance and the contact area, and the SiC dopant density and the measured contact resistivity, respectively. The Schottky barrier height of the CNT/SiC interface was $\sim$0.4 eV. This is comparable with that of nickel silicide, which is widely used as a SiC contact material. The CNT/CNT conductance was evaluated from the sheet resistivity of the CNT forest on SiC. Lateral conduction of the CNT forest is composed of CNT/CNT contacts. The evaluated CNT/CNT contact conductance was $\sim 10^8$ S cm^{-2}, which corresponds to the tunneling contact conductance. This study shows that a dense CNT forest on SiC can be used to investigate the unique properties of the CNT forest.

References

1. P. Avouris, Chem. Phys. **281**, 429 (2002)
2. E. Pop, D. Mann, Q. Wang, K. Goodson, H. Dai, Nano Lett. **6**, 96 (2006)
3. S.K. Vashist, D. Zheng, K. Al-Rubeaan, J.H. Luong, F. Sheu, Biotechnol. Adv. **29**, 2 (2011)
4. A. Izadi-Najafabadi, T. Yamada, D.N. Futaba, M. Yudasaka, H. Takagi, H. Hatori, H. Iijima, K. Hata, ACS Nano **5**, 2 (2011)
5. V. Sangwan, A. Southard, T. Moore, V. Ballarotto, D. Hines, M. Fuhrer, E. Williams, Microelectron. Eng. **88**, 10 (2011)
6. M. Kusunoki, M. Rokkaku, T. Suzuki, Appl. Phys. Lett. **71**, 2620 (1997)

7. T. Nagano, Y. Ishikawa, N. Shibata, Jpn. J. Appl. Phys. **42**, 1380 (2003)
8. H. Konishi, H. Matsuoka, N. Toyama, M. Naitoh, S. Nishigaki, M. Kusunoki, Thin Solid Films **464**, 295 (2004)
9. K. Hayashi, S. Mizuno, S. Tanaka, H. Toyoda, H. Tochihara, I. Suemune, Jpn. J. Appl. Phys. **44**, L803 (2005)
10. T. Maruyama, H. Bang, Y. Kawamura, N. Fujita, K. Tanioku, T. Shiraiwa, Y. Hozumi, S. Naritsuk, M. Kusunoki, Chem. Phys. Lett. **423**, 317 (2006)
11. H. Bang, Y. Ito, Y. Kawamura, E. Hosoda, C. Yoshida, T. Maruyama, S. Naritsuka, M. Kusunoki, Jpn. J. Appl. Phys. **45**, 372 (2006)
12. T. Maruyama, H. Bang, N. Fujita, Y. Kawamura, S. Naritsuka, M. Kusunoki, Diam. Relat. Mater. **16**, 1078 (2007)
13. M. Kusunoki, C. Honjo, T. Suzuki, T. Hirayama, Appl. Phys. Lett. **87**, 103105 (2005)
14. M. Inaba, K. Suzuki, M. Shibuya, C. Lee, Y. Masuda, N. Tomatsu, W. Norimatsu, A. Hiraiwa, M. Kusunoki, H. Kawarada, Appl. Phys. Lett. **106**, 123501 (2015)
15. M. Kusunoki, T. Suzuki, C. Honjo, T. Hirayama, N. Shibata, Chem. Phys. Lett. **366**, 458 (2002)
16. H. Na, H. Kim, K. Adachi, N. Kiritani, S. Tanimoto, H. Okushi, K. Arai, J. Electron. Mater. **33**, 2 (2004)
17. M. Inaba, K. Suzuki, Y. Hirano, W. Norimatsu, M. Kusunoki, H. Kawarada, Mater. Sci. Rep. **858**, 561 (2016)
18. F. Padovani, R. Stratton, Solid-State Electron **9**, 7 (1966)
19. C. Crowell, V. Rideout, Solid-State Electron **12**, 2 (1969)
20. S. Xu, Z.L. Wang, Nano Res. **4**, 11 (2011)
21. P. De Pablo, M. Martínez, J. Colchero, J. Gomez-Herrero, W. Maser, A. De Benito, E. Munoz, A. Baro, Mater. Sci. Eng. C **15**, 1 (2001)
22. W.B. Choi, E. Bae, D. Kang, S. Chae, B. Cheong, J. Ko, E. Lee, W. Park, Nanotechnology **15**, 10 (2004)
23. S. Suzuki, Y. Watanabe, Y. Homma, S. Fukuba, S. Heun, A. Locatelli, Appl. Phys. Lett. **85**, 127 (2004)
24. Z. Xu, X. Bai, E. Wang, Z.L. Wang, Appl. Phys. Lett. **87**, 163106 (2005)
25. T. Maruyama, S. Sakakibara, S. Naritsuka, W. Norimatsu, M. Kusunoki, H. Yamane, N. Kosugi, Appl. Phys. Lett. **101**, 092106 (2012)
26. T. Seyller, K. Emtsev, F. Speck, K. Gao, L. Ley, Appl. Phys. Lett. **88**, 242103 (2006)
27. S. Cheung, N. Cheung, Appl. Phys. Lett. **49**, 85 (1986)
28. L. Pauling, J. Am. Chem. Soc. **54**, 9 (1932)
29. F. Buonocore, F. Trani, D. Ninno, A. Di Matteo, G. Cantele, G. Iadonisi, Nanotechnology **19**, 025711 (2008)
30. S. Rajput, M. Chen, Y. Liu, Y. Li, M. Weinert, L. Li, Nat. Commun. **4**, 2752 (2013)
31. G. Zhong, T. Iwasaki, J. Robertson, H. Kawarada, J. Phys. Chem. B **111**, 1907 (2007)
32. D. Yokoyama, T. Iwasaki, K. Ishimaru, S. Sato, T. Hyakushima, M. Nihei, Y. Awano, H. Kawarada, Jpn. J. Appl. Phys. **47**, 1985 (2008)
33. Y. Awano, S. Sato, M. Nihei, T. Sakai, Y. Ohno, T. Mizutani, Proc. IEEE **98**, 2015 (2010)
34. R. Quintero, D.Y. Kim, K. Hasegawa, Y. Yamada, A. Yamada, S. Noda, RSC Adv. **4**, 8230 (2014)
35. B. Brown B, C. B. Parker CB, B. R. Stoner BR, W. M. Grill WM, and J. T. Glass JT, (2012) J. Phys. Chem. C 116:19526 (2012)
36. E. Teblum, M. Noked, J. Grinblat, A. Kremen, M. Muallem, Y. Fleger, Y.R. Tischler, D. Aurbach, G.D. Nessim, J. Phys. Chem. C **118**, 19345 (2014)
37. J. Kalupson, D. Ma, C.A. Randall, R. Rajagopalan, K. Adu, J. Phys. Chem. C **118**, 2943 (2014)
38. A.-R. Rautio, O. Pitkänen, T. Järvinen, A. Samikannu, N. Halonen, M. Mohl, J.-P. Mikkola, K. Kordas, J. Phys. Chem. C **119**, 3538 (2015)
39. M. Kusunoki, T. Suzuki, T. Hirayama, N. Shibata, K. Kaneko, Appl. Phys. Lett. **77**, 531 (2000)

40. Z.G. Cambaz, G. Yushin, S. Osswald, V. Mochalin, Y. Gogotsi, Carbon **46**, 841 (2008)
41. M. Kusunoki, H. Kato, Appl. Surf. Sci. **254**, 257 (2007)
42. W. Norimatsu, T. Maruyama, K. Yoshida, K. Takase, M. Kusunoki, Appl. Phys. Express **5**, 105102 (2012)
43. M. Inaba, C. Lee, K. Suzuki, M. Shibuya, M. Myodo, Y. Hirano, W. Norimatsu, M. Kusunoki, H. Kawarada, J. Phys. Chem. C **120**, 6232 (2016)
44. L. van der Pauw, Philips Res. Rep. **13**, 1 (1958)
45. R. Marega, G. Accorsi, M. Meneghetti, A. Parisini, M. Prato, D. Bonifazi, Carbon **47**, 675 (2009)
46. S. De, J.N. Coleman, ACS Nano **4**, 2713 (2010)
47. P.Y. Huang, C.S. Ruiz-Vargas, A.M. van der Zande, W.S. Whitney, M.P. Levendorf, J.W. Kevek, S. Garg, J.S. Alden, C.J. Hustedt, Y. Zhu, Nature **469**, 389 (2011)
48. S. Peng, Z. Jin, P. Ma, D. Zhang, J. Shi, J. Niu, X. Wang, S. Wang, M. Li, X. Liu, Carbon **82**, 500 (2015)
49. M. Miao, Carbon **49**, 3755 (2011)
50. M. Kusunoki, T. Suzuki, C. Honjo, H. Usami, H. Kato, J Phys D **40**, 6278 (2007)
51. R. Saito, T. Takeya, T. Kimura, G. Dresselhaus, M.S. Dresselhaus, Phys. Rev. B **57**, 4145 (1998)
52. R.S. Ruoff, J. Tersoff, D.C. Lorents, S. Subramoney, B. Chan, Nature **364**, 514 (1993)
53. J. Tersoff, R.S. Ruoff, Phys. Rev. Lett. **73**, 676 (1994)
54. M.J. Lopez, A. Rubio, J.A. Alonso, L.-C. Qin, S. Iijima, Phys. Rev. Lett. **86**, 3056 (2001)
55. C. Zhang, K. Bets, S.S. Lee, Z. Sun, F. Mirri, V.L. Colvin, B.I. Yakobson, J.M. Tour, R.H. Hauge, ACS Nano **6**, 6023 (2012)
56. M. Arai, S. Utsumi, M. Kanamaru, K. Urita, T. Fujimori, N. Yoshizawa, D. Noguchi, K. Nishiyama, Y. Hattori, F. Okino, Nano Lett. **9**, 3694 (2009)
57. X. Meng, M. Li, Z. Kang, X. Zhang, J. Xiao, J. Phys. D **46**, 055308 (2013)
58. J.G. Simmons, J. Appl. Phys. **34**, 2581 (1963)
59. P.W. Sutter, J. Flege, E.A. Sutter, Nat. Mater. **7**, 406 (2008)
60. Y. Yoon, M.S.C. Mazzoni, H. Joon Choi, J. Ihm, S.G. Louie, Phys. Rev. Lett. **86**, 688 (2001)
61. S. Bae, H. Kim, Y. Lee, X. Xu, J. Park, Y. Zheng, J. Balakrishnan, T. Lei, H.R. Kim, Y.I. Song, Nat. Nanotechnol. **5**, 574 (2010)